Transactions of the ASME

Journal of Heat Transfer

Published Quarterly by The American Society of Mechanical Engineers

VOLUME 108 • NUMBER 2 • MAY 1986

HEAT TRANSFER DIVISION
Chairman, **R. K. SHAH**
Secretary, **A. S. ADORJAN**
Senior Technical Editor, **G. M. FAETH**
Technical Editor, **I. CATTON**
Technical Editor, **R. GREIF**
Technical Editor, **P. J. MARTO**
Technical Editor, **R. H. PLETCHER**
Technical Editor, **R. VISKANTA**
Technical Editor, **M. M. YOVANOVICH**

BOARD ON COMMUNICATIONS
Chairman and Vice President
K. N. REID, JR.

Members-at-Large
W. BEGELL
J. T. COKONIS
W. G. GOTTENBERG
F. LANDIS
J. R. LLOYD
R. E. NICKELL
J. E. ORTLOFF
C. F. PHILLIPS
R. E. REDER
F. W. SCHMIDT

President, **L. S. FLETCHER**
Executive Director,
PAUL ALLMENDINGER
Treasurer,
ROBERT A. BENNETT

PUBLISHING STAFF
Mng. Dir., Publ., **J. J. FREY**
Dep. Mng. Dir., Pub.,
JOS. SANSONE
Managing Editor,
CORNELIA MONAHAN
Production Editor,
VALERIE WINTERS
Editorial Prod. Asst.,
MARISOL ANDINO

The Journal of Heat Transfer (ISSN 0022-1481) is published quarterly for $100 per year by The American Society of Mechanical Engineers, 345 East 47th Street, New York, N Y 10017. Second class postage paid at New York, NY and additional mailing offices. POSTMASTER: Send address changes to The Journal of Heat Transfer, c/o THE AMERICAN SOCIETY OF MECHANICAL ENGINEERS, 22 Law Drive, Box 2300, Fairfield, NJ 07007-2300.

CHANGES OF ADDRESS must be received at Society headquarters seven weeks before they are to be effective. Please send old label and new address.

PRICES: To members, $24.00, annually; to nonmembers, $100.00. Add $6.00 for postage to countries outside the United States and Canada.

STATEMENT from By-Laws. The Society shall not be responsible for statements or opinions advanced in papers or . . . printed in its publications (B7.1, para. 3).

COPYRIGHT © **1986** by the American Society of Mechanical Engineers. Reprints from this publication may be made on condition that full credit be given the TRANSACTIONS OF THE ASME, JOURNAL OF HEAT TRANSFER, and the author, and date of publication be stated.

INDEXED by Engineering Information

ANNOUNCEMENTS

TECHNICAL PAPERS

Downloaded 04 Feb 2011 to 194.85.80.107. Redistribution subject to ASME license or copyright; see http://www.asme.org/terms/Terms_Use.cfm

(Contents continued)

TECHNICAL NOTES

An Initial Value Approach to the Inverse Heat Conduction Problem

E. Hensel

R. G. Hills

New Mexico State University,
Mechanical Engineering Department,
Las Cruces, NM 88003

The one-dimensional linear inverse problem of heat conduction is considered. An initial value technique is developed which solves the inverse problem without need for iteration. Simultaneous estimates of the surface temperature and heat flux histories are obtained from measurements taken at a subsurface location. Past and future measurement times are inherently used in the analysis. The tradeoff that exists between resolution and variance of the estimates of the surface conditions is discussed quantitatively. A stabilizing matrix is introduced to the analysis, and its effect on the resolution and variance of the estimates is quantified. The technique is applied to "exact" and "noisy" numerically simulated experimental data. Results are presented which indicate the technique is capable of handling both exact and noisy data.

Introduction

One inverse problem of heat conduction consists of extrapolating temperature and heat flux information from the back surface or an interior point of a thermally conducting solid to the exposed surface of the body. The problem is encountered frequently in instrumentation systems, where it is often impossible to directly monitor the desired quantities. Typical examples include the estimation of surface heat transfer from measurements taken within the skin of a reentry vehicle, and predictions of temperature and heat flux from calorimeter-type instrumentation.

An exact solution to the inverse problem has been presented by Burggraf [1], along with a number of methods based on deconvolution [2–13], and finite element approaches [14–15]. Time-marching finite difference analyses of the inverse problem have been presented by a number of authors [16–19]. D'Souza [20], Weber [21], and the current authors [22] have implemented space-marching finite difference approaches. Model restructuring [23–26] has gained some attention recently, along with the method of regularizers which has received a great deal of attention in the Soviet Union [27–29].

Due to the diffusive nature of the heat conduction process, variations in the surface conditions of a solid will be attenuated at points interior to the solid. Conversely, as an inverse analysis procedure extrapolates from the interior locations of the solid to the exposed surface, the small random errors in the data are magnified. If the noise-to-signal ratio is too large it may be impossible to predict the surface conditions with the desired accuracy.

The solution to an inverse problem cannot be uniquely determined when the data at the interior location are known only at discrete times. An infinite number of surface histories can result in the same set of discrete measurements taken at the remote sensing location.

A number of authors have noted these features of the inverse problem [22–29], and have presented various smoothing techniques for reducing the effect of error growth and propagation. Murio [25] has used mullifiers to smooth the predictions at the surface, while others have used various smoothing functions [23, 24] to decrease the influence of errors in the measurement data. Relatively few of the techniques used in mechanical engineering give a quantitative method for determining what effect their smoothing operations have had on the accuracy of the estimates. Such techniques are illustrated in the work of Murio [25], Hills and Mulholland [23], Hills, Mulholland, and Matthews [24], Backus and Gilbert [26], and the current authors [22]. Lanczos [30] and Jackson [31] have discussed techniques which allow one to selectively discard those eigenvalues and eigenvectors of a particular system of equations that tend to magnify errors in the data vector. Jackson [31] has developed a technique whereby the impact of such a procedure on the resolution and variance of the predictions may be obtained. The question of uniqueness has been addressed in [22–24, 26].

The current discussion shall be limited to a one-dimensional planar geometry with constant thermal properties. The technique may be applied to problems having temperature-dependent thermal properties with suitable modification. This will be discussed in a future paper. The space-marching finite difference analysis developed shall be used to estimate surface conditions from data available at a location some distance beneath the exposed surface of a planar solid. A quantitative discussion of the resolving power and accuracy of the technique will be presented.

Analysis

Consider the one-dimensional linear inverse heat conduction problem illustrated in Fig. 1. The flux and temperature are assumed known as discrete functions of time at the location $x=0$. It is desired to predict the flux and temperature variation at the location $x=1$ as a function of time. The nondimensionalized governing equation may be broken into two equivalent first-order partial differential equations

$$\frac{\partial T}{\partial t} = -\frac{\partial q}{\partial x} \tag{1a}$$

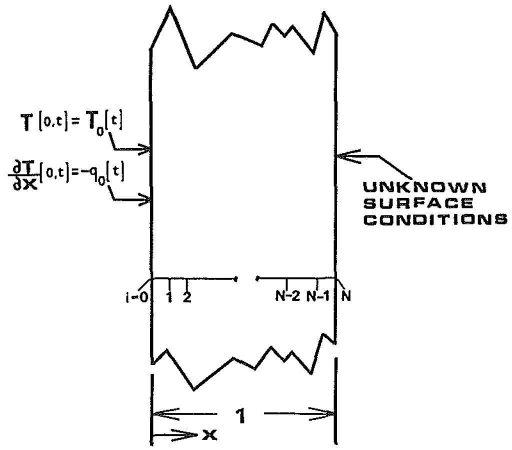

Fig. 1 Statement of known conditions and nodal spacing for an inverse problem of heat conduction

---

Contributed by the Heat Transfer Division for publication in the JOURNAL OF HEAT TRANSFER. Manuscript received by the Heat Transfer Division January 21, 1985. Paper No. 84-HT-48.

which must be solved simultaneously with

$$q = -\frac{\partial T}{\partial x} \tag{1b}$$

The known conditions are

$$T(0,\, t) = T_0(t) \text{ for discrete } t = t_j, \qquad j = 1, 2, \ldots, M \tag{2a}$$

$$\frac{\partial T}{\partial x}(0,\, t) = -q_0(t) \text{ for discrete } t = t_j \tag{2b}$$

Note that equations (1) and (2) are representative of an initial value problem in the spatial direction. Due to the location of the known conditions, it is reasonable to approach the problem with a space-marching algorithm. This formulation of the problem suggests that it is necessary to know two conditions at the measurement location $x=0$. Equation (1a) may be recast in finite difference form for $2 \le j \le M-1$ as

$$q^{j}_{i+1} = q^j_i - \frac{\Delta x}{2\Delta t}\left[T^{j+1}_i - T^{j-1}_i\right] \tag{3a}$$

For $j=1$, the temporal derivative will be replaced by a forward difference approximation, and at $j=M$ the temporal derivative will be replaced with a backward difference representation. Thus,

$$q^1_{i+1} = q^1_i - \frac{\Delta x}{2\Delta t}\left[T^2_i - T^1_i\right], \qquad j=1 \tag{3b}$$

$$q^M_{i+1} = q^M_i - \frac{\Delta x}{\Delta t}\left[T^M_i - T^{M-1}_i\right], \qquad j=M \tag{3c}$$

Equations (3) may be substituted into a backward difference representation of equation (1b) at $i+1$ and solved for T^j_{i+1} to yield, for $j=1$

$$T^1_{i+1} = -\Delta x\, q^1_i + \left(1 - \frac{(\Delta x^2)}{\Delta t}\right) T^1_i + \frac{(\Delta x^2)}{\Delta t} T^2_i \tag{4a}$$

for $2 \le j \le M-1$

$$T^j_{i+1} = -\Delta x\, q^j_i - \frac{(\Delta x^2)}{2\Delta t} T^{j-1}_i + T^j_i + \frac{(\Delta x^2)}{2\Delta t} T^{j+1}_i \tag{4b}$$

for $j=M$

$$T^M_{i+1} = -\Delta x q^M_i - \frac{(\Delta x^2)}{\Delta t} T^{M-1}_i + \left(1 + \frac{(\Delta x^2)}{\Delta t}\right) T^M_i \tag{4c}$$

Given the temperature and flux histories at spatial node i, equations (3) and (4) can be used to find the temperature and flux history at the adjacent spatial node $i+1$. Using the measured histories at $i=0$ ($x=0$), equations (3) and (4) can be used recursively to find the temperature and flux histories at the surface node, $i=N$.

Beck [17-19] has noted the advantages of using measurement data times in the future of the surface estimate time in the analysis of inverse conduction problems. Many standard techniques are not well suited for the utilization of future time data. As is readily apparent from equations (3) and (4), the current approach naturally incorporates future times in the analysis. Specifying twenty spatial nodes will result in the usage of 19 future and past measurements in the surface condition estimates for times far from a temporal boundary. This is accomplished without need for iteration. In order to examine the accuracy of the estimates of the surface conditions $x=1$ given by the above procedure, it is convenient to represent equations (3) and (4) in matrix form. Define a temperature vector

$$\bar{T}_i = [T^1_i, \ldots, T^j_i, \ldots, T^M_i]^T \tag{5}$$

Similarly, a heat flux vector

$$\bar{q}_i = [q^1_i, \ldots, q^j_i, \ldots, q^M_i]^T \tag{6}$$

Equations (3) and (4) may be written in matrix form as

$$\begin{bmatrix} \bar{T}_{i+1} \\ \hline \bar{q}_{i+1} \end{bmatrix} = \left[\begin{array}{c|c} A & B \\ \hline C & I \end{array}\right] \begin{bmatrix} \bar{T}_i \\ \hline \bar{q}_i \end{bmatrix} \tag{7}$$

where

$$A = \begin{bmatrix} 1 - \frac{\Delta x^2}{\Delta t} & \frac{\Delta x^2}{\Delta t} & & & \mathbf{0} \\ -\frac{\Delta x^2}{2\Delta t} & 1 & \frac{\Delta x^2}{2\Delta t} & & \\ & & \ddots & & \\ & & -\frac{\Delta x^2}{2\Delta t} & 1 & \frac{\Delta x^2}{2\Delta t} \\ \mathbf{0} & & & -\frac{\Delta x^2}{\Delta t} & 1 + \frac{\Delta x^2}{\Delta t} \end{bmatrix} \tag{8}$$

$$B = -\Delta x I, \text{ where } I \text{ is an } N \times N \text{ identity matrix} \tag{9}$$

Nomenclature

a_n = digital filter coefficient
A, B, C = finite-difference coefficient submatrix
D = finite-difference coefficient matrix
E = finite-difference matrix operator = D^N
F = stabilizing matrix when applied to estimates
I = identity matrix
L = half-width of digital filter
M = total number of measurement times
N = total number of Δx's
R = resolution matrix
$r_{k,l}$ = element in row k, column l of R
S = stabilizing matrix when applied to measurements
q = dimensionless heat flux
$\bar{q}$ = dimensionless heat flux vector
T = dimensionless temperature
$\bar{T}$ = dimensionless temperature vector
t = dimensionless time
Δt = dimensionless time between temporal nodes
x = dimensionless position
Δx = dimensionless distance between spatial nodes
$\bar{\gamma}$ = dimensionless temperature and heat flux vector
σ = Standard deviation

Subscripts and Superscripts

i = spatial node index, subscript
j = temporal node index, superscript
k, l = general counting indexes
¯ = indicates a vector
T = transpose of a matrix or vector
< > = indicates a stabilized quantity
ˆ = indicates a parameter containing random noise

$$C=\begin{bmatrix} \frac{\Delta x}{\Delta t} & -\frac{\Delta x}{\Delta t} & & & \mathbf{0} \\ \frac{\Delta x}{2\Delta t} & 0 & -\frac{\Delta x}{2\Delta t} & & \\ & & \blacklozenge & & \\ & & & \blacklozenge & \\ & & & & \blacklozenge \\ & & \frac{\Delta x}{2\Delta t} & 0 & -\frac{\Delta x}{2\Delta t} \\ \mathbf{0} & & & \frac{\Delta x}{\Delta t} & -\frac{\Delta x}{\Delta t} \end{bmatrix} \qquad (10)$$

For clarity of presentation, we define the $2M \times 2M$ finite difference coefficient matrix D and a temperature-heat flux vector $\bar{\gamma}$:

$$D=\left[\begin{array}{c|c} A & B \\ \hline C & I \end{array}\right] \qquad (11)$$

$$\bar{\gamma}_i=\left[\begin{array}{c} \bar{T}_i \\ \hline \bar{q}_i \end{array}\right] \qquad (12)$$

Using this notation, equation (7) becomes

$$\bar{\gamma}_{i+1}=D\bar{\gamma}_i \qquad (13)$$

All of the elements of D are constant for the current linear analysis, but may be spatially and or temperature-dependent in the general case. Since the elements of D are constant we may apply equation (13) in a recursive manner to obtain an explicit relationship between the desired surface conditions $x=1$ $(i=N)$, and the known conditions at $x=0$ $(i=0)$.

$$\bar{\gamma}_N=D^N\bar{\gamma}_0=E\bar{\gamma}_0 \qquad (14),(15)$$

where $E=D^N$. Numerical experimentation (not reported here) shows that, for the cases examined in our investigation, the eigenvalues of the D matrix always include values less than and greater than unity. This is also true for the inverse of the D matrix. As the dimensionless time between measurements is decreased, the ratio of the magnitude of the largest eigenvalue to that of the smallest eigenvalue increases. This implies that the matrix becomes increasingly ill conditioned as Δt is decreased. This characteristic is to be expected for inverse problems, and is reflected in the growth of the variance discussed in more detail later.

Discussion of Variance on Surface Condition Estimates

We wish to examine the errors in the estimates at spatial node N due to the errors in the measurements at $i=0$. We represent the measurement error information for both temperature and heat flux with the vector $\Delta\bar{\gamma}_0$. Assume that the errors are additive:

$$\hat{\bar{\gamma}}_0=\bar{\gamma}_0+\Delta\bar{\gamma}_0 \qquad (16)$$

where the $\hat{\bar{\gamma}}_0$ are the actual instrument readings, which consist of the true data $\bar{\gamma}_0$ and the additive noise (or error) in the measurements $\Delta\bar{\gamma}_0$. Applying equation (15) to (16) leads to

$$\hat{\bar{\gamma}}_N=E\hat{\bar{\gamma}}_0=E\bar{\gamma}_0+E\Delta\bar{\gamma}_0 \qquad (17)$$

If we define $\bar{\gamma}_N$ to be the surface condition as determined by our model when using perfect data, then

$$\bar{\gamma}_N=E\bar{\gamma}_0 \qquad (18)$$

$$\Delta\bar{\gamma}_N=E\Delta\bar{\gamma}_0 \qquad (19)$$

$\Delta\bar{\gamma}_N$ reflects the magnification of the errors $\Delta\bar{\gamma}_0$ due to the model E. If we assume the model to be correct, then the $\Delta\bar{\gamma}_N$ represents the error in the surface estimates due to the errors in the measurements. The error in our predictions $\Delta\bar{\gamma}_N$ can be determined if the error in our measurements $\Delta\bar{\gamma}_0$ is known. Postmultiplying equation (19) by $(\Delta\bar{\gamma}_N)^T$ we have

$$\Delta\bar{\gamma}_N(\Delta\bar{\gamma}_N)^T=E\Delta\bar{\gamma}_0(E\Delta\bar{\gamma}_0)^T=E\Delta\bar{\gamma}_0(\Delta\bar{\gamma}_0)^TE^T \qquad (20)$$

where

$$\Delta\bar{\gamma}_0(\Delta\bar{\gamma}_0)^T=\begin{bmatrix} \Delta\gamma_0^{1^2} & \Delta\gamma_0^1\Delta\gamma_0^2 & \cdots & \Delta\gamma_0^1\Delta\gamma_0^M \\ \Delta\gamma_0^2\Delta\gamma_0^1 & \Delta\gamma_0^{2^2} & \cdots & \Delta\gamma_0^2\Delta\gamma_0^M \\ \blacksquare & & & \blacksquare \\ \blacksquare & & & \blacksquare \\ \blacksquare & & & \blacksquare \\ \Delta\gamma_0^{M-1}\Delta\gamma_0^1 & \Delta\gamma_0^{M-1}\Delta\gamma_0^2 & \cdots & \Delta\gamma_0^1\Delta\gamma_0^M \\ \Delta\gamma_0^M\Delta\gamma_0^1 & \Delta\gamma_0^M\Delta\gamma_0^2 & \cdots & \Delta\gamma_0^{M^2} \end{bmatrix} \qquad (21)$$

Since the true errors in the data cannot be known, we estimate the $\Delta\bar{\gamma}_0(\Delta\bar{\gamma}_0)^T$ matrix with an estimate of the measurement covariance matrix, $\operatorname{cov}\{\Delta\bar{\gamma}_0(\Delta\bar{\gamma}_0)^T\}$. Beck and Arnold discuss various methods for estimating the covariance matrix in their text on parameter estimation [32, see Chapter Six]. Using our estimate for the covariance matrix in equation (20) gives us an estimate of the covariance matrix for the surface predictions

$$\operatorname{cov}\{\Delta\bar{\gamma}_N(\Delta\bar{\gamma}_N)^T\}=E\operatorname{cov}\{\Delta\bar{\gamma}_0(\Delta\bar{\gamma}_0)^T\}E^T \qquad (22)$$

If we assume the errors to be independent, random, have zero mean, and have a finite variance, then $\operatorname{cov}\{\Delta\bar{\gamma}_0(\Delta\bar{\gamma}_0)^T\}$ becomes a diagonal matrix. Additionally, to conserve space in presentation, and with no further apparent justification, we consider the special case of $\sigma_0^2=\text{const}$ (all of the measurements have the same variance). With these additional constraints, equation (22) simplifies to

$$\frac{\operatorname{cov}\{\Delta\bar{\gamma}_N(\Delta\bar{\gamma}_N)^T\}}{\sigma_0^2}=EE^T \qquad (23)$$

For analysis of actual experimental data, the more general expression (22) may be used for the error analysis.

Stabilizing Matrix

The inverse problem will inherently magnify measurement errors as we move toward the surface $x=1$. In the interest of reducing the variance of our estimates, we might choose to predict an averaged or smeared version of the surface conditions. We may do this by means of a stabilizing matrix, denoted either F or S. The rows of the stabilizing matrix may be thought of as "time-domain digital averaging filters" which act on the input data. F or S has the effect of smoothing the estimates of the surface conditions. The matrix F may be regarded as somewhat analogous to the continuous smoothing functions used by Backus and Gilbert [26] and is the digital analog of the smoothing functions used by Murio [25]. The stabilizing matrix may be applied to our system in two ways.

The first method is to apply the stabilizing matrix to the noisy input data $\hat{\bar{\gamma}}_0$ and then apply the finite difference matrix operator E, to obtain an estimate of the surface conditions.

$$<\hat{\bar{\gamma}}_N>=ES\hat{\bar{\gamma}}_0 \qquad (24)$$

A second technique is to first obtain the surface estimates and then apply the stabilizing matrix. We use the notation F to denote the stabilizing matrix when used in this manner.

$$<\hat{\bar{\gamma}}_N>=F\hat{\bar{\gamma}}_N=FE\hat{\bar{\gamma}}_0 \qquad (25)$$

In both cases the variance of the predictions will be reduced at the expense of a degradation in our ability to resolve small temporal scale fluctuations in the surface conditions. The estimates of the surface conditions will actually be a time-averaged "blur" (indicated by triangular brackets) of the unstabilized estimates. We define the partitioned stabilizing matrix to be composed of two banded submatrices as shown by equation (26)

$$S=\left[\begin{array}{c|c} S_{1,1} & 0 \\ \hline 0 & S_{2,2} \end{array}\right] \quad \text{or} \quad F=\left[\begin{array}{c|c} F_{1,1} & 0 \\ \hline 0 & F_{2,2} \end{array}\right] \qquad (26)$$

The rows of S (or F) contain the coefficients of a time domain digital filter which operates on the temperature-flux vector $\bar{\gamma}$. The elements of the upper left submatrix act to smooth the temperature history, while the lower right submatrix operates on the flux history. For the current work, the upper and lower submatrices are assumed equal for ease of physical interpretation. The values of the coefficients may be obtained from a discretized version of a Gaussian distribution or a standard digital filter, such as the Hanning filter. For the current work we employ a Hanning filter, with the coefficients given by

$$a_n = 0.5 + 0.5\cos\left(\frac{n\pi}{L}\right) \qquad (27)$$

where n varies from 0 to L. Other work [22] illustrates results obtained with different digital filter coefficients and half-widths. The a_n indicated in equation (27) are normalized by the summation

$$\Sigma a = a_0 + \sum_{n=1}^{L} 2a_n \qquad (28)$$

The filters applied to the temperature and flux measurements need not be the same width, nor even of the same type.

Near the beginning and end of the time period, the filter coefficients must be modified in order to avoid referencing a time node which does not exist. Here the filter coefficients which extend past a temporal boundary are simply added to the boundary node for that row. In this way, we ensure that the sum of the coefficients for a particular row is unity. The upper left and lower right submatrices are of the form

$$\begin{array}{c} S_{1,1}, S_{2,2} = \\ (\text{or } F_{1,1}, F_{2,2}) \end{array} \left[\begin{array}{ccccccccc} \sum_{n=0}^{L} a_n & a_1 & a_2 & \cdots & a_L & & & & \\ & & & & & & & \mathbf{0} & \\ \sum_{n=1}^{L} a_n & a_0 & a_1 & a_2 & \cdots & a_L & & & \\ & & \ddots & & & & & & \\ & a_L & \cdots & a_0 & \cdots & a_L & & & \\ & & & & \ddots & & & & \\ & & & & & a_L & \cdots & a_1 & a_0 \sum_{n=1}^{L} a_n \\ \mathbf{0} & & & & & a_L & \cdots & a_2 & a_1 \sum_{n=0}^{L} a_n \end{array}\right] \qquad (29)$$

This technique gives a heavier relative weighting to the temporal boundary nodes than to the measurements immediately surrounding it. If the conditions prior to and following the period for which the analysis is performed are at steady state, this causes no difficulty. For many experimental conditions, the initial time condition is at steady state. If data are not taken until the system returns to steady state following the transient under examination, we expect the error in our estimates to be larger throughout the last L time nodes, relative to the error during the rest of the time period, due to the bias introduced by the nonsymmetric filter coefficients.

Effect of Smoothing on Resolution and Variance

The introduction of a stabilizing matrix will reduce the variance of our estimates, while simultaneously degrading our ability to resolve small temporal scale fluctuations. We quantify these effects below.

For the case when the stabilizing matrix is first applied to the input data and then operated on by the finite difference matrix operator E, the ratio of the variance of the surface estimates to that of the measurements is, by replacing E with ES in equation (23)

$$\frac{\mathrm{cov}\{\Delta\bar{\gamma}_N(\Delta\bar{\gamma}_N)^T\}}{\sigma_0^2} = ES(ES)^T = ESS^TE^T \qquad (30)$$

Similarly, for the formulation given by equation (25), the variance is

$$\frac{\mathrm{cov}\{\Delta\bar{\gamma}_N(\Delta\bar{\gamma}_N)^T\}}{\sigma_0^2} = FE(FE)^T = FEE^TF^T \qquad (31)$$

We now turn our attention to an analysis of how the stabilizing matrix degrades the resolution of the surface estimates. The resolving power of a numerical technique may be interpreted as a measure of its ability to "see" small temporal scale variations. A numerical technique which provides high resolution is readily able to differentiate small temporal scale fluctuations. Due to the nature of the inverse problem, an improvement in the resolving power of the analysis will lead to a corresponding increase in the variance of the surface estimates. The resolution matrix as defined here relates the stabilized version of the surface estimates $<\hat{\bar{\gamma}}_N>$ to the estimates that would be obtained with no stabilization $\hat{\bar{\gamma}}_N$ as

$$<\hat{\bar{\gamma}}_N> = R\hat{\bar{\gamma}}_N \qquad (32)$$

Substituting equation (32) into equation (24) gives

$$R\hat{\bar{\gamma}}_N = ES\hat{\bar{\gamma}}_0 \qquad (33)$$

Substituting equation (15) into equation (33) yields

$$RE\hat{\bar{\gamma}}_0 = ES\hat{\bar{\gamma}}_0 \qquad (34)$$

Therefore,

$$RE = ES \qquad (35)$$

If we postmultiply equation (35) by E^{-1}, we arrive at an expression for the resolution matrix when the stabilizing matrix is applied directly to the input data

$$R = REE^{-1} = ESE^{-1} = D^N SD^{-1^N} \qquad (36a)$$

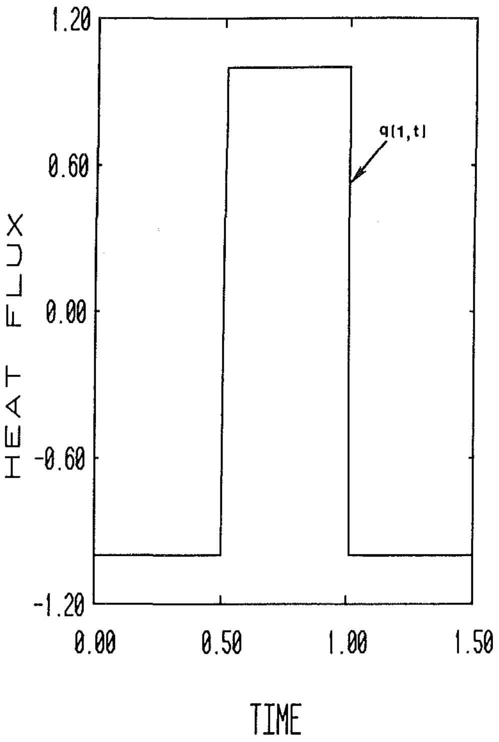

Fig. 2 Imposed surface flux

For the case of applying the stabilizing matrix F at the end of the computations, the resolution matrix may be found by comparing equation (25) with equation (32), which implies that

$$R = F \tag{36a}$$

This makes sense physically; the "filter" or "smoothing matrix" has operated directly on the surface estimates, and is thus a measure of the resolution of the surface predictions. From equation (32) we see that the kth row of the resolution matrix R gives precisely the blurring or averaging of the kth unstabilized surface estimate $\hat{\bar{\gamma}}_{Nk}$ due to the use of the stabilizing matrix S (or F)

$$< \hat{\gamma}_{Nk} > = \sum_{l=1}^{2M} r_{k,l} \hat{\gamma}_{Nl} \tag{37}$$

Equation (37) (as well as equation (32)) shows that the coefficients in the resolution matrix fully describe the blurring or averaging effects due to our stabilizing matrix. The resolution matrix is deterministic and independent of the measurements and their errors for the linear problem. See Jackson [31] for a more detailed discussion of the resolution matrix.

Sample Test Cases

To test the inverse method we choose a square wave for the surface flux history $q_1(t)$ and solve a forward problem to simulate the back surface measurements (temperature and flux). For our test cases, we assume the surface at $x=0$ to be insulated. Other test cases have been examined elsewhere [22]. Using the "data" generated in this manner, we attempt to reconstruct the surface flux $q_1(t)$ using the inverse technique. By adding random noise to the analytically generated measurements, we can simulate "real" experimental data. The response of our system to a step function in flux at the surface at time zero is governed by

$$\frac{\partial^2 v}{\partial x^2} = \frac{\partial v}{\partial t} \tag{38}$$

subject to the conditions on $v(x, t)$ of

$$v(x, 0) = 0 \tag{39a}$$

$$\frac{\partial v}{\partial x}(1, t) = -q_1(t) = 1 \tag{39b}$$

$$\frac{\partial v}{\partial x}(0, t) = 0 \tag{39c}$$

The exact solution to equations (38) and (39) is given in Carslaw and Jaeger [33, p. 112] as

$$v(x, t) = t + \frac{3x^2 - 1}{6} - 2 \sum_{n=1}^{\infty} (-1)^n \frac{\cos(\lambda_n x)}{\lambda_n^2} e^{-\lambda_n^2 t} \tag{40}$$

The eigenvalues are given by

$$\lambda_n = n\pi \tag{41}$$

To simulate the square wave surface flux shown in Fig. 2, we use superposition to obtain

$$T(x, t) = v(x, t); \quad 0 \le t < 0.5, \quad 0 \le x \le 1 \tag{42a}$$

$$T(x, t) = v(x, t) - 2v(x, t - 0.5); \quad 0.5 \le t < 1.0, \quad 0 \le x \le 1 \tag{42b}$$

$$T(x, t) = v(x, t) - 2v(x, t - 0.5) + 2v(x, t - 1.0); \quad 1.0 \le t < 1.5, \quad 0 \le x \le 1 \tag{42c}$$

$$T(x, t) = v(x, t) - 2v(x, t - 0.5) + 2v(x, t - 1.0) - 2v(x, t - 1.5); \quad 1.5 \le t < 2.0, \quad 0 \le x \le 1 \tag{42d}$$

Results

In this section, the estimates of the surface conditions ($x=1$) obtained from simulated measurement data generated by equations (40) through (42) for $x=0$ are compared with the true surface conditions for each of the test cases. The space-marching algorithm is first applied to "exact" measurement data, and subsequently to measurement data containing random noise.

For the results presented here, we used $N=32$, $\Delta t = 0.01$, and $\Delta x = 0.0313$. If we are only interested in estimating the surface conditions, and not the variances of these estimates or the resolution of the analysis, then we can use equations (3) and (4) directly to march toward the surface. If desired, the stabilizing matrix may be applied to the measurement vector before we begin marching, or directly to the surface estimates after we finish marching. If we are interested in a resolution and variance analysis, then we must compute D^N. By taking N as a power of 2, we are able to reduce computational requirements by squaring D to get D^2, squaring the result to get D^4, and so on, until we reach D^{32}. In this manner, only five matrix multiplications were needed to arrive at the matrix operator E. We can further reduce computational requirements by exploiting the banded substructure of D and using banded matrix multiplication algorithms.

We begin with an examination of the covariance matrix, equation (23). Shown in Fig. 3 are the ratios of the surface flux variances to the measurement variances for the sample problem considered here. These ratios are taken from the main diagonal elements of the surface estimate covariance matrix, which is independent of the actual values for the measurements for the linear problem. For the nodal spacing used here, the variance of the surface heat flux estimates was typically 100 times greater than the variance of the surface temperature estimates. In the interest of brevity we present only the variances for the surface heat flux. The ratio of variance in surface estimates to variance in measurements is constant throughout the center of the time period, and varies rapidly near a temporal boundary. From the magnitude of the variance terms, it is apparent that even a very small error in the measurements can lead to large errors in the surface estimates. The standard deviation of the surface estimates is

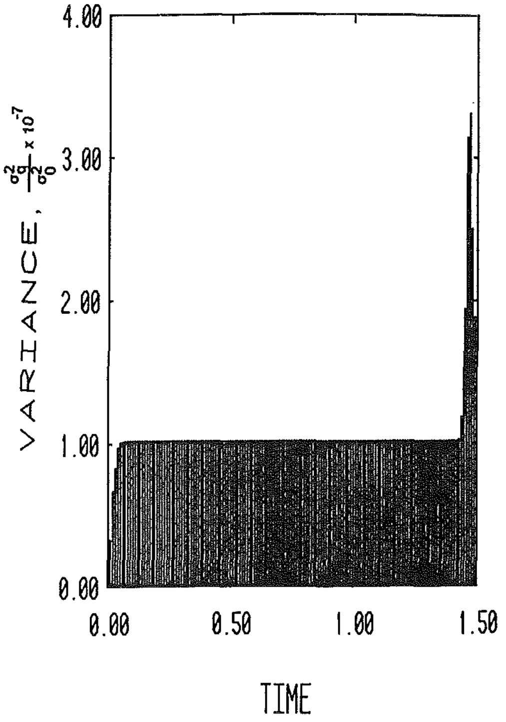

Fig. 3 Ratio of flux estimate variance to measurement variance, $N = 32$, $\Delta x = 0.0313$, $\Delta t = 0.01$

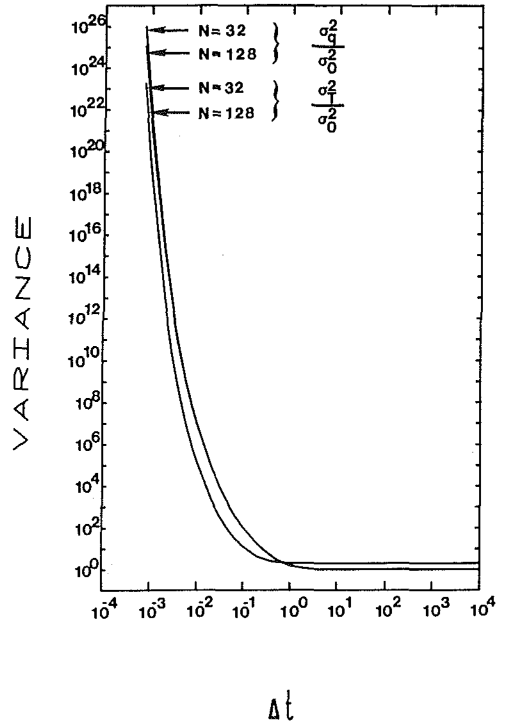

Fig. 4 Temperature and heat flux error magnification as a function of Δt, for various spatial nodings

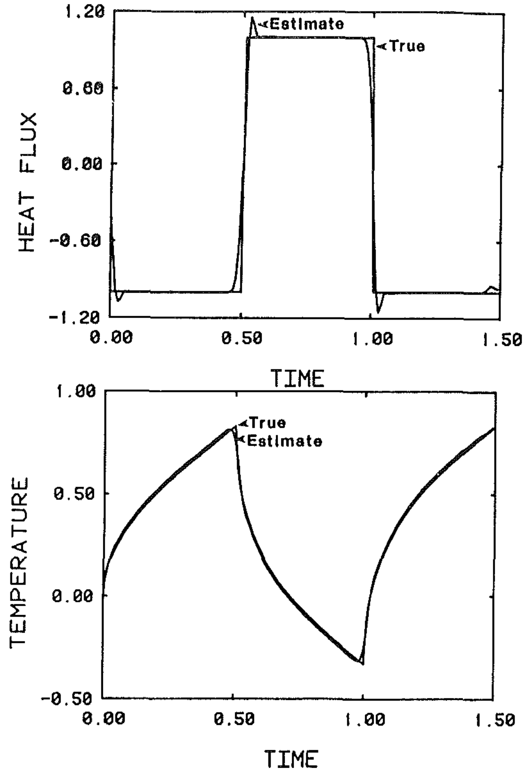

Fig. 5 Comparison between surface estimates and true conditions when using exact data, $\Delta t = 0.01$, $M = 150$, $\Delta x = 0.0313$, $N = 32$

roughly 3200 times the standard deviation of errors in the measurement data. This error magnification is primarily due to the small dimensionless temporal noding that we have used in the sample problems. Using a larger Δt would reduce the magnitude of the variance terms, but would inhibit our ability to resolve small time scale surface events. The large variance terms for the current noding indicate that it will be impossible to establish meaningful results from data containing even a small amount of random noise unless we smooth the data in some manner.

As we attempt to resolve finer temporal detail the errors are increasingly magnified, as graphically illustrated in Fig. 4. This plot shows the relation between the variance of surface estimates and the dimensionless time between measurements Δt. This illustrates what many investigators have observed; we can expect stability problems for small Δt. If we desire a very low variance in the surface estimates, we must be satisfied with larger time steps. Another way to stabilize the problem is by applying stabilizing matrices to the vector $\bar{\gamma}$. In this manner, we degrade the resolution in a specified fashion while still making use of all of the available measurement information.

Figure 5 shows the estimates given by equation (15) for the square wave surface flux along with the true surface conditions and the "exact" temperature measurements used at the insulated boundary $x = 0$. The flux estimates compare very well with the true surface conditions. The temperature estimates are better than the flux estimates, as suggested by the results of Fig. 4. The analysis fails to reliably estimate the true surface conditions where extremely rapid variations are occurring in heat flux, and near the end of the time period. We can not hope to resolve those fluctuations in the surface conditions which are near or above the digitizing frequency of the data acquisition system. The primary reason for the relatively poor estimates near the end of the time period is that we can no longer use the future time information shown to be valuable by many authors. One should thus continue to digitize data well after the time of interest in a testing environment. If the system is very near steady state at the end of the time period the inability to use "future time" information is not a limiting factor.

Figure 6 shows the effect of stabilizing matrices on the estimates. Once again, the measurement data used for this figure are "exact," and the noding is identical to above. We see from the results shown in Fig. 6 that the use of a

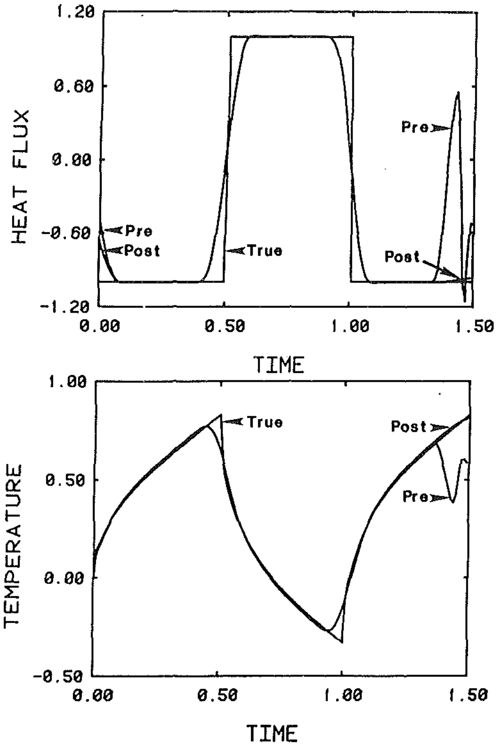

Fig. 6 Comparison between true surface conditions and estimates obtained with pre- and poststabilizing, using exact data, Hanning $L = 10$, $\Delta t = 0.01$, $M = 150$, $\Delta x = 0.0313$, $N = 32$

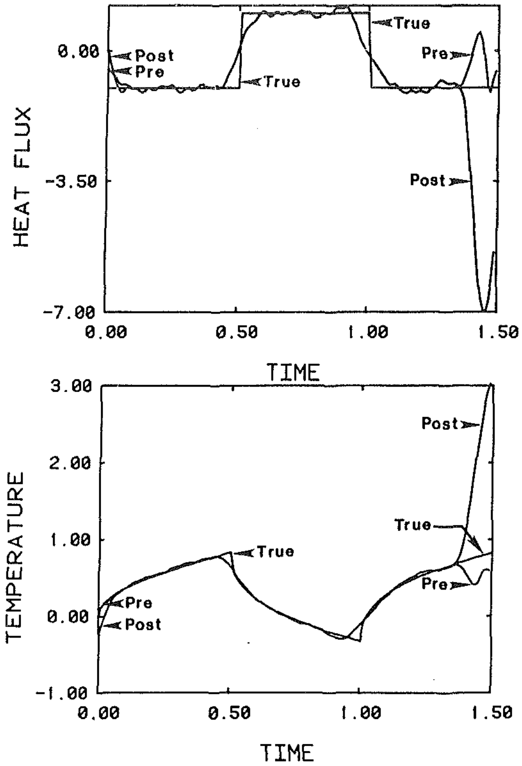

Fig. 7 Comparison between true surface conditions and estimates obtained with pre- and poststabilizing, using noisy data, $3\sigma_0 = 0.01$, Hanning $L = 10$, $\Delta t = 0.01$, $M = 150$, $\Delta x = 0.0313$, $N = 32$

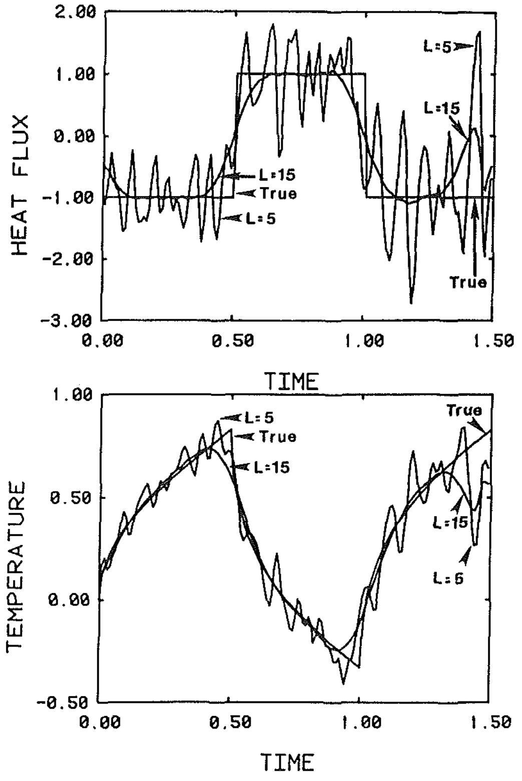

Fig. 8 Comparison between true surface conditions and estimates obtained with prestabilizing formulation, using noisy data, $3\sigma_0 = 0.01$, Hanning $L = 5, 15$, $\Delta t = 0.01$, $M = 150$, $\Delta x = 0.0313$, $N = 32$

stabilizing matrix (half-width $L = 10$) does indeed blur the estimates obtained. Since the data used are exact, our estimates with the stabilizing matrix appear worse than those without stabilization. Statistically, this implies that the use of the stabilizing matrix has introduced a bias into our estimates. The reason for applying stabilizers to "exact measurements" is twofold. First, we see the general effect of stabilizers on the estimates obtained by the analysis. Second, we are able to compare the relative attributes of formulations (24) and (25).

As discussed earlier, the manner in which the end points (in time) of the stabilizing matrix is handled introduces an additional bias into our estimates near these points, due to the asymmetry of the digital filter coefficients. If we apply the stabilizing matrix at the end of the computations, formulation (25), this bias does not appear to affect the estimates a great deal. If we apply the stabilizing matrix at the beginning of the analysis, formulation (24), the bias introduced by the digital filters is magnified by the analysis and results in estimates which rapidly fall away from the true conditions near the ends of the time period. Taken alone, this observation suggests that the poststabilizing approach (equation (25)) is preferable.

Figure 7 shows the estimates of the surface conditions obtained when we use "noisy" measurement data at $x = 0$, and a Hanning stabilizer with a half-width of 10. The noise added to the exact data has a normal distribution with $3\ \sigma_0 = 0.01$. When the unstabilized finite difference analysis equation (15) is used with the noisy data as input, the results are unintelligible. This is to be expected from the discussion presented with regard to Fig. 4. The estimates shown here once again compare the relative performance of formulations (24) and (25). In this case, the prestabilizing formulation (24) appears to perform better than the poststabilizing approach (25). This apparently conflicts with the observations made in the previous paragraph, when the measurement data were exact.

Occasionally, a problem may be encountered with formulation (25). If the data are too noisy, then we may encounter computer overflow difficulties before getting a chance to apply the stabilizing matrix.

The prestabilizing formulation is used to obtain the estimates shown in Fig. 8. Here we see the influence of two filter half-widths on the estimates. Since the noding used is the

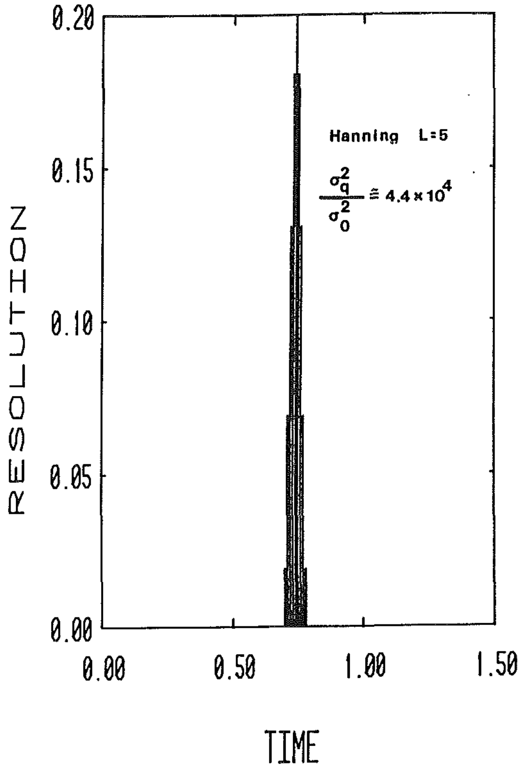

Fig. 9(*a*) Resolution and flux variance for Hanning $L = 5$

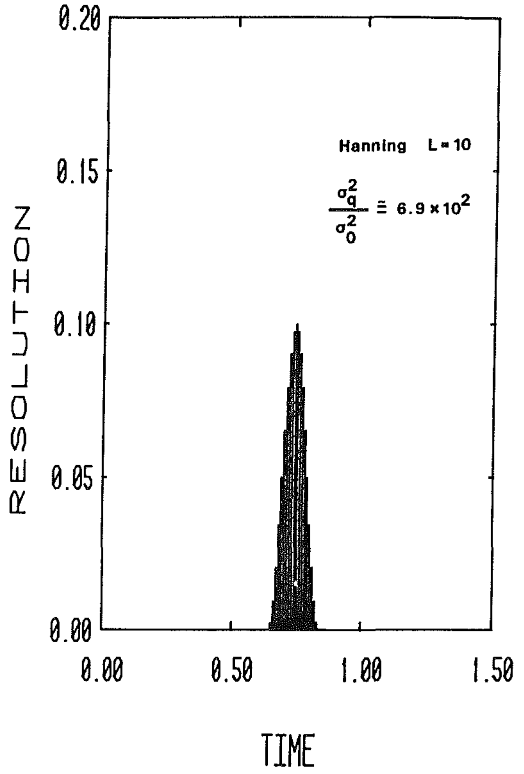

Fig. 9(*b*) Resolution and flux variance for Hanning $L = 10$

same for all of the sample results, these estimates may be compared against those of previous figures. Looking at the prestabilizing estimates of Figs. 7 and 8, we can see the increased smoothing caused as the strength of the filter is increased from $L=5$ to $L=15$.

Figure 9 graphically illustrates the effect that prefilter stabilizing matrices have on the resolving power of the

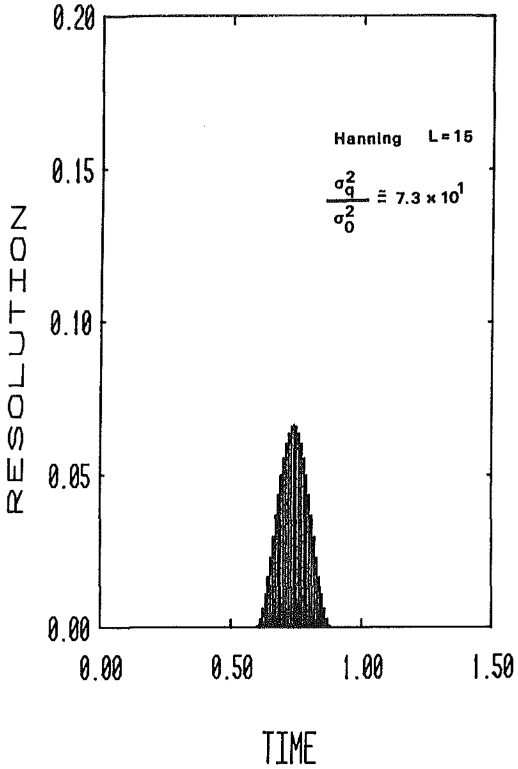

Fig. 9(c) Resolution and flux variance for Hanning $L = 15$

analysis. This figure represents a single row of the resolution matrix (see equation (36*a*)) for the various half-widths of Hanning filters. Also indicated on each plot is the variance of the surface flux estimate for the time t_j about which the particular filter is centered. The height of the vertical lines in Fig. 9 indicates the relative weights that are assigned to each data point surrounding the center time node. The estimate of the surface conditions for time node j is actually a weighted average of the unstabilized estimates $\pm L$ time nodes around node j. For a relatively narrow filter (such as $L=5$) the weighting will be strongly dependent on the current time node. This type of filter degrades the resolution of the estimates less than a wide filter (such as $L=15$). Accordingly, a narrow filter does less to reduce the variance than does a wide filter. For data which contain a relatively low level of noise, a narrow filter will suffice.

The numerical results presented in Figs. 6 and 7 indicate that the results provided by the pre- and poststabilizing formulations are identical throughout the center portion of the time period, and vary rapidly from one another near the temporal boundaries. Other results, not shown in this paper, indicate that the resolution and variance estimates show the same characteristics. Figure 9 illustrates the tradeoff between resolution and variance due to the use of the stabilizing matrix, as opposed to Fig. 4, which indicates the dependence of variance on the time between measurements.

Conclusions

A numerical technique has been presented which is capable of treating a class of linear inverse heat conduction problems with data containing random noise. The current approach utilizes future time data while requiring no iteration.

A quantitative as well as qualitative discussion has been presented regarding the tradeoff that must exist between the resolution and variance of estimates made by inverse techniques. A stabilizing matrix has been used to accomplish the necessary tradeoff. While similar surface estimate variances may be obtained by ignoring part of the data, the stabilizing matrix approach has the advantage of allowing us to use all of the available measurement data.

In an application environment, where we will not know the characteristics of the noise entirely, a median between the extremes of pre- and poststabilizing may provide the best results. A way to accomplish this would be through recursive application of a small width filter at each spatial step.

The technique presented may easily be extended to handle nonlinear inverse problems, with temperature-dependent thermal properties. In the nonlinear case, the finite-difference coefficient matrix D must be updated at each spatial node. The analysis of resolution and variance may be extended to incorporate this feature. A future paper (in preparation) will extend the analysis to nonlinear problems wherein we have more than one measurement location. A computationally efficient analysis of this problem requires an adjoint formulation, which would drastically increase the length of the present paper. To conserve space, we did not include the analysis here. The future work will also consider other geometries in addition to the planar one illustrated here.

References

1 Burggraf, O. R., "An Exact Solution of the Inverse Problem in Heat Conduction Theory and Applications," ASME JOURNAL OF HEAT TRANSFER, Vol. 86, 1964, pp. 373-382.

2 Anderson, S. A., Hale, L. A., Hunt, H. H., and Pulley, P. E., "A Technique for Determining the Transient Heat Flux at a Solid Interface Using the Measured Transient Interfacial Temperature," ASME JOURNAL OF HEAT TRANSFER, Vol. 95, Nov. 1973, pp. 492-497.

3 Arledge, R. G., and Haji-Sheikh, A., "An Iterative Approach to the Solution of Inverse Heat Conduction Problems," ASME Paper No. 77-WA/TM-2, 1977.

4 Arledge, R. G., and Haji-Sheikh, A., "An Iterative Approach to the Solution of Inverse Heat Conduction Problems," *Numer. Heat Transfer*, Vol. 1, 1978, pp. 365-376.

5 Beck, J. V., "Surface Heat Flux Determination Using an Integral Method," *Nucl. Eng. Des.*, Vol. 7, 1968, pp. 170-178.

6 Blackwell, B. F., "Some Comments on Beck's Solution of the Inverse Problem of Heat Conduction Through the Use of Duhamel's Theorem," *Int. J. Heat Mass Transfer*, Vol. 26, No. 2, 1983, pp. 302-305.

7 France, D. M., and Chiang, T., "Analytic Solution to Inverse Heat Conduction Problems With Periodicity," ASME JOURNAL OF HEAT TRANSFER, Vol. 102, 1980, pp. 579-581.

8 Frank, I., "An Application of Least Squares Method to the Solution of the Inverse Problem of Heat Conduction," ASME JOURNAL OF HEAT TRANSFER, Vol. 85, 1963, pp. 378-379.

9 Hagin, F., "A Stable Approach to Solving One-Dimensional Inverse Problems," *SIAM J. Appl. Math.*, Vol. 40, No. 3, 1981, pp. 439-453.

10 Imber, M., and Khan, J., "Prediction of Transient Temperature Distributions With Embedded Thermocouples," *AIAA J.*, Vol. 10, No. 6, 1972, pp. 784-789.

11 Sparrow, E. M., Haji-Sheikh, A., and Lundgren, T. S., "The Inverse Problem in Transient Heat Conduction," ASME *Journal of Applied Mechanics*, Vol. 86, 1964, pp. 369-375.

12 Stoltz, G., "Numerical Solution to an Inverse Problem of Heat Conduction for Simple Shapes," ASME JOURNAL OF HEAT TRANSFER, Vol. 82, 1960, pp. 20-26.

13 Woo, K. C., and Chow, L. C., "Inverse Heat Conduction by Direct Inverse Laplace Transform," *Numer. Heat Transfer*, Vol. 4, 1981, pp. 499-504.

14 Hore, P. S., Krutz, G. W., and Schoenhals, R. J., "Application of the Finite Element Method to the Inverse Heat Conduction Problem," ASME Paper No. 77-WA/TM-4, 1977.

15 Krutz, G. W., Schoenhals, R. J., and Hore, P. S., "Application of the *Finite-Element Method to the Inverse Heat Conduction Problem*," *Numer. Heat Transfer*, Vol. 1, 1978, pp. 489-498.

16 Blackwell, B. F., "Efficient Technique for the Numerical Solution of the One-Dimensional Inverse Problem of Heat Conduction," *Numer. Heat Transfer*, Vol. 4, 1981, pp. 229-238.

17 Beck, J. V., "Nonlinear Estimation Applied to the Nonlinear Inverse Heat Conduction Problem," *Int. J. Heat Mass Transfer*, Vol. 13, 1970, pp. 703-716.

18 Beck, J. V., "Review of Six Inverse Heat Conduction Computer Codes," ANL/RAS/LWR 81-1, Argonne National Laboratory, Argonne, IL, Feb. 1981.

19 Beck, J. V., Litkouhi, B., and Clair, C. R., "Efficient Sequential Solution of the Nonlinear Inverse Heat Conduction Problem," *Numer. Heat Transfer*, Vol. 5, 1982, pp. 275-286.

20 D'Souza, N., "Numerical Solution of One-Dimensional Inverse Transient Heat Conduction by Finite Difference Method," ASME Paper No. 75-WA/HT-81, 1975.

21 Weber, C. F., "Analysis and Solution of the Ill-Posed Inverse Heat Conduction Problem," *Int. J. Heat Mass Transfer*, Vol. 24, No. 11, 1981, pp. 1783-1792.

22 Hensel, E. C., and Hills, R. G., "A Space Marching Finite Difference Algorithm for the One Dimensional Inverse Conduction Heat Transfer Problem," ASME Paper No. 84-HT-48, 1984.

23 Hills, R. G., and Mulholland, G. P., "Accuracy and Resolving Power of One Dimensional Transient Inverse Heat Conduction Theory," *Int. J. Heat Mass Transfer*, Vol. 22, 1979, pp. 1221-1229.

24 Hills, R. G., Mulholland, G. P., and Matthews, L. K., "The Application of the Backus-Gilbert Method to the Inverse Heat Conduction Problem in Composite Media," ASME Paper No. 82-HT-26, 1982.

25 Murio, D. A., "The Mollification Method and the Numerical Solution of an Inverse Heat Conduction Problem," *SIAM J. Stat. Comput.*, Vol. 2, No. 1, 1981.

26 Backus, B., and Gilbert, F., "Uniqueness in the Inversion of Inaccurate Gross Earth Data," *Phil. Trans. R. Soc., Lond.*, Vol. 266, 1970, pp. 123-192.

27 Romanovsky, M. R., "On Regularization of Inverse Problems," *Teplofiz. Vysok. Temp.*, Vol. 18, No. 1, 1980, pp. 152-157.

28 Elubaev, S., "Regularization of a Particular Inverse Problem for the Heat Conduction Equation," *Izv. Akad. Nauk Kaz. SSR, Ser. Fiz. Mat. Nauk*, No. 3, 1980, pp. 21-26.

29 Tikhonov, A. N., Glasko, V. B., and Kulik, N. I., "On a Regularizing Algorithm for the Solution of Some Inverse Heat Conduction Problems," *Vestnik Mosk. Univ., Ser. 3, Fiz., Astronom.*, Vol. 22, No. 4, 1981, pp. 25-29.

30 Lanczos, C., *Linear Differential Operators*, VanNostrand, London, 1961.

31 Jackson, D. D., "Interpretation of Inaccurate, Insufficient and Inconsistent Data," *Geophys. J. R. Astr. Soc.*, Vol. 28, 1972, pp. 97-109.

32 Beck, J. V., and Arnold, K. J., *Parameter Estimation in Engineering and Science*, Wiley, New York, 1977.

33 Carslaw, H. S., and Jaeger, J. C., *Conduction of Heat in Solids*, Oxford University Press, Oxford, 1959.

Multinode Unsteady Surface Element Method With Application to Contact Conductance Problem

B. Litkouhi
Mechanical Engineering Department,
Manhattan College,
Riverdale, NY 10471
Mem. ASME

J. V. Beck
Mechanical Engineering Department,
Michigan State University,
East Lansing, MI 48824
Mem. ASME

The unsteady surface element method is a powerful numerical technique for solution of linear transient two- and three-dimensional heat transfer problems. Its development originated with the need of solving certain transient problems for which similar or dissimilar bodies are attached one to the other over a part of their surface boundaries. In this paper a multinode *unsteady surface element (MUSE) method for two arbitrary geometries contacting over part of their surface boundaries is developed and formulated. The method starts with Duhamel's integral (for arbitrary time and space variable boundary conditions) which is then approximated numerically in a piecewise manner over time and the boundaries of interest. To demonstrate the capability of the method, it is applied to the problem of two semi-infinite bodies initially at two different temperatures suddenly brought into perfect contact over a small circular region. The results show excellent agreement between the MUSE solution and the other existing solutions.*

Introduction

The heat transfer between two bodies with perfect or imperfect contact at the interface is of fundamental importance and it has accordingly received considerable attention over the last two or three decades. It is important in the problems involving electric contact, electronic cooling, weldings, fins, contact conductance, and many other applications for which two similar or dissimilar bodies are attached one to the other over small parts of their surface boundaries. Other related problems are those with mixed boundary conditions. In general it is difficult to obtain analytical solutions for such problems. The multinode unsteady surface element (MUSE) method described in this paper is particularly suited for such problems compared with other numerical methods.

The most widely used numerical procedures are the finite-difference method (FDM) and the finite-element method (FEM). Because of their great flexibility and power they can be used for a variety of problems involving composite bodies, nonhomogeneous boundary conditions, nonlinearity, and irregular geometries. However, for the problems mentioned above, the use of the FDM or the FEM is not entirely satisfactory. This is partly due to the necessity of setting up extremely fine grids near the interface, and many large grids farther from the interface. Further, both methods involve whole-body discretization schemes which require the solution of very large system of algebraic equations, especially for two- and three-dimensional problems. These methods unavoidably generate the solution at all internal nodes, whether or not this information is needed. This causes significant economic disadvantages for many applications where only interface results are of interest.

Closely related to the MUSE method is the boundary integral equation method (BIEM) which has become very popular in recent years. The BIEM is well suited for solving steady-state problems with infinite domain and irregular shaped boundaries. A number of papers have been written for steady-state heat conduction problems [1-4]. The application of the BIEM to transient problems has received less attention compared to the steady-state problems [5-8].

For the particular problems mentioned above (bodies connected over relatively small area) the MUSE method is superior to the FDM, FEM, or BIEM. In the MUSE method only the interface between the two geometries requires discretization as opposed to the discretization of the whole domain required in the FDM and FEM or the discretization of the whole boundary in the BIEM. This in turn reduces the size of numerical calculations and the computer time. Further, the MUSE method does not require any modifications or special handling of points near the domain boundaries unlike the abovementioned alternative methods.

The MUSE method uses Duhamel's integral and involves the inversion of a set of Volterra integral equations, one for each surface element. Although the method is limited to linear problems it can be used for nonlinear boundary conditions.

Two types of kernels (building blocks) can be employed in this method: temperature-based and heat flux-based. The method requires that these "building blocks" or kernels be known for the basic geometries under consideration. For many geometries the kernels are known or can be obtained simply by analytical or numerical procedures.

A precursor of the unsteady surface element method is the quasi-coupling method of Keltner [9]. Yovanovich [10] suggested the name "surface element" and did early work on a steady-state form of the surface-element method. Keltner and Beck [11] and later Beck and Keltner [12] were the first to employ the method for transient problems. They have considered only one element along the interface and utilized the Laplace transform technique to obtain "early" and "late" time analytical solutions for certain cases [11, 12]. Both types of kernels have been used in their solutions.

In this paper a MUSE method for two-dimensional heat conduction problems with linear boundary conditions is developed and formulated. The method is utilized to obtain the transient thermal response of the interface between two semi-infinite bodies suddenly brought together in a perfect contact over a circular region. The results are compared with those obtained by other investigators on the basis of the thermal constriction resistance and the heat flux across the contact area.

Multinode Surface Element Formulation

Consider the boundary value problem of heat conduction for a semi-infinite solid exposed to a time- and space-variable heat flux boundary condition over a portion of its surface boundary from $x=0$ to $x=L$ with the rest of the surface boundary being insulated (see Fig. 1). Utilizing Duhamel's

---

Contributed by the Heat Transfer Division for publication in the JOURNAL OF HEAT TRANSFER. Manuscript received by the Heat Transfer Division April 6, 1984. Paper No. 83-HT-80.

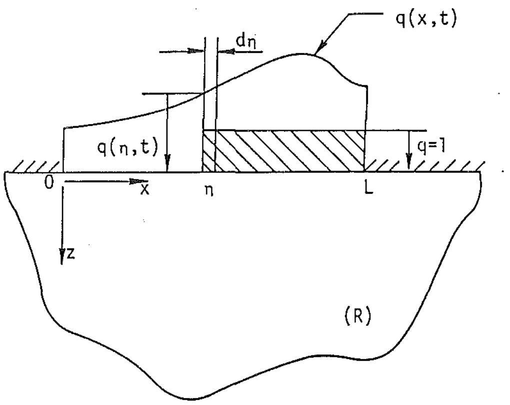

Fig. 1 Geometry showing a semi-infinite body heated by an arbitrary heat flux only over a portion of its surface boundary

theorem, the temperature of any point (x, z) of the semi-infinite solid, and at any time t can be given by [13]

$$T(x,z,t)-T_0=-\int_0^L\int_0^t q(\eta,\lambda)\,\frac{\partial^2\psi_q(x,z,\eta,t-\lambda)}{\partial t\,\partial\eta}\,d\lambda d\eta \tag{1}$$

where T_0 is the initial temperature, η is a point along the surface boundary between $x=0$ and $x=L$, and $\psi_q(x, z, \eta, t)$ is the temperature rise at position (x, z) and time t caused by a unit step change of heat flux at time $t=0$, from η to L as shown in Fig. 1 by the cross-hatched portion.[1] It is called the flux-based fundamental solution (FBFS), and is described by the following equation

$$\nabla^2\psi_q=\frac{1}{\alpha}\frac{\partial\psi_q}{\partial t} \tag{2a}$$

$$\psi_q(x,z,0)=0 \tag{2b}$$

$$\begin{aligned} k\frac{\partial\psi_q}{\partial z}&=0 \qquad \text{for } t<0 \text{ or } x<\eta \\ &=1 \qquad \text{for } t>0 \text{ and } \eta<x<L \end{aligned} \tag{2c}$$

Notice that, for fixed (x, z) and t, $\psi_q(x, z, \eta, t)$ decreases as η increases

$$\psi_q(x,z,\eta,t) > \psi_q(x,z,\eta+d\eta,t) \tag{3}$$

In equation (1) the input function is the heat flux along the boundary, and the solution is in terms of the FBFS ψ_q. If however, the surface temperature were known along the boundary as the input function, then the solution in terms of the temperature based fundamental solution (TBFS) ψ_T can be obtained as

$$T(x,z,t)-T_0 = -\int_0^L\int_0^t [T_s(\eta,\lambda)-T_0]\frac{\partial^2\psi_T(x,z,\eta,t-\lambda)}{\partial t\partial\eta}d\lambda d\eta \tag{4}$$

where $T_s(x, t)$ is the surface temperature, and $\psi_T(x, z, \eta, t)$ is the temperature rise at position (x, z) and time t due to a unit step change in surface temperature at time $t=0$, from $x=\eta$ to $x=L$. (It is assumed that the rest of the boundary, $x<0$ and $x>L$, is held at the initial temperature.)

Duhamel's integral equations (1) and (4) are rather general expressions for the case in which the input function varies with both space and time.[2] Both approaches can be used to determine the temperature history at any position (x, z) of the domain. However, depending upon the the type of boundary condition, one might be more appropriate than the other [13].

In the present paper only a heat flux-based approach is considered. Equation (1) is the basic starting point in the development of the multinode surface element formula in the following sections. Furthermore, only evaluation of the boundary data is considered here, since in many applications such as contact conductance and intrinsic thermocouple problems [14] only the interface results are of interest.

Both equations (1) and (4) can be related to the Green's function form for transient heat conduction problem [15, 16]. Because the Green's function formulation is better known than the multidimensional Duhamel's equations (1) and (4), an appendix is given to relate the heat flux-based expression, equation (1), to the Green's function equation. Some tabulations of Green's functions are given in [15, 17-19].

Discretization Over Space. In order to solve numerically the integral equation given by (1), the surface boundary is divided into N finite surface elements Δx_j as shown in Fig. 2. (Only the parts of the boundary with nonzero values of heat flux need to be discretized.) Equation (1) can be written as

$$T(x,z,t)-T_0= -\int_0^t\left[\sum_{j=1}^{N}\int_{\Delta x_j} q(\eta,\lambda)\frac{\partial^2\psi_q(x,z,\eta,t-\lambda)}{\partial t\,\partial\eta}d\eta\right]d\lambda \tag{5}$$

With uniform approximation of the heat flux over each surface element, one can write

Nomenclature

a = radius of the contact area
A_c = contact area
A_j = area of the surface element j
c_p = specific heat
$h(t)$ = time-variable contact conductance
k = thermal conductivity
L = length of interface shown in Fig. 1
M = time index
N = number of surface elements
q = heat flux
q_{cl} = center line heat flux
$\bar{q}_M$ = heat flux vector at time $t_M = M\Delta t$
Q_c = total heat flow through the contact area
r = radial coordinate
R_c = thermal constriction resistance
R_c^+ = normalized thermal constriction resistance
t = time
t^+ = dimensionless time
T = temperature
$\bar{T}_c$ = average contact area temperature
$\bar{T}_0$ = initial temperature vector
T_s = surface temperature
x = Cartesian coordinate
z = axial and Cartesian coordinate
α = thermal diffusivity
η = a point along the surface boundary; see Fig. 1
λ = dummy variable
ρ = density
ϕ = temperature rise for unit heat flux (influence function)
$\bar{\bar{\Phi}}_i$ = influence matrix at time $t_i = i\Delta t$
ψ_q = flux-based fundamental solution
ψ_T = temperature-based fundamental solution

---

[1] $\psi_q(x, y, \eta, t-\lambda)$ is the temperature rise at position (x, y) and time t due to a unit step change of heat flux at time λ, from η to L ($t-\lambda$ is the time elapsed since the step change at λ). For details, see [13].

[2] More general forms of these expressions are given in [13] which can be applied to any arbitrary two-dimensional geometry. For simplicity, however, the plain surface of a semi-infinite body is considered here.

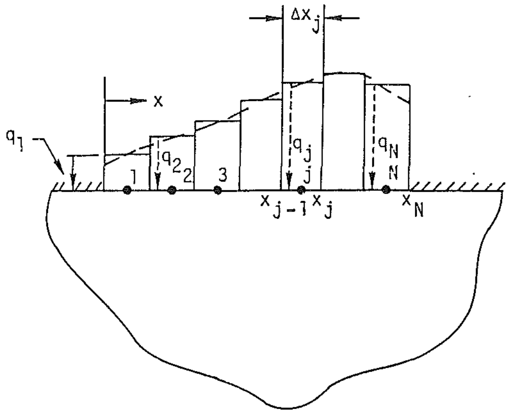

Fig. 2 Geometry showing discretization over heated portion of surface boundary

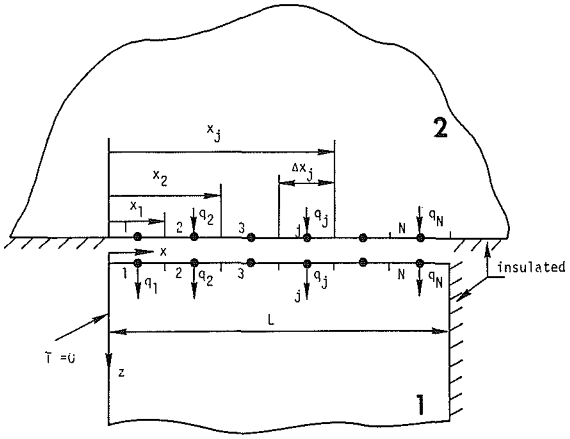

Fig. 3 Possible distribution of surface elements for connected semi-infinite body and slab

$$T(x,z,t)-T_0=$$

$$-\int_0^t \left\{\sum_{j=1}^{n} q_j(\lambda)\,\frac{\partial}{\partial t}\,[\Delta\psi_{q_j}(x,z,t-\lambda)]\right\}d\lambda \qquad (6)$$

$$\Delta\psi_{q_j}(x,z,t)=\psi_q(x,z,x_j,t)-\psi_q(x,z,x_{j-1},t) \qquad (7)$$

Further, if the temperature rise at point (x, z) and time t due to a unit step increase in heat flux q_j over the element j and $t=0$ is denoted $\phi_i(x, z, t)$, it can be shown that [13]

$$-\Delta\psi_{q_j}(x,z,t)\equiv\phi_j(x,z,t) \qquad (8)$$

Using (8) in (7) results in

$$T(x,z,t)-T_0=\sum_{j=1}^{N}\int_0^t q_j(\lambda)\frac{\partial\phi_j(x,z,t-\lambda)}{\partial t}d\lambda \qquad (9)$$

which gives the temperature rise at location (x, z) and time t due to the effect of N heat flux histories $q_1(t)$, $q_2(t)$, . . . , $q_N(t)$. The function $\phi_j(x, z, t)$ is the basic building block solution in the above expression and is termed an *influence function.*

The MUSE method requries that the influence functions ϕ be known for the geometries under consideration. For example the influence function needed for the geometry of Fig. 2 is the solution to the problem of a semi-infinite body heated by a constant heat flux over an infinite strip, which is provided in an exact closed form in [20]. A number of influence functions for various geometries are described and referenced in [21].

Two Bodies in Contact. Two different geometries of a semi-infinite body and a semi-infinite slab initially at uniform but different temperatures are brought into perfect (or imperfect) contact over the interface of width L. One side of the slab $x=0$ is held at zero temperature and the other parts of the boundaries are assumed to be insulated (see Fig. 3). The bodies may have different thermal conductivities k and density-specific heats ρc_p. The lower body is referred to as region 1 $(z>0)$, and the other body as region 2 $(z<0)$. The initial temperatures are denoted by T_{01} and T_{02} for regions 1 and 2, respectively.

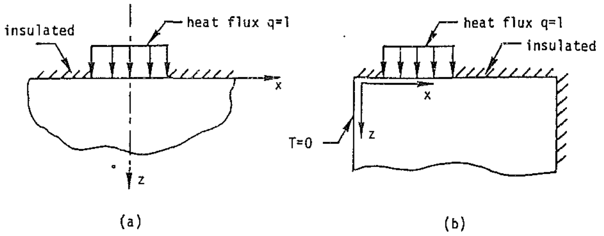

Fig. 4 Basic building blocks for the geometries of semi-infinite body and semi-infinite slab

To apply the MUSE method, the interface is divided into N finite elments (each being an infinite strip) as shown in Fig. 3. It is assumed that there is no spatial variation of temperature or heat flux over each element.

The heat flux $q_j(t)$ which leaves body 2 in Fig. 3 is the same heat flux that enters body 1 over the region $x=x_{j-1}$ to $x=x_j$; that is,

$$-k_1\frac{\partial T_1}{\partial z}=-k_2\frac{\partial T_2}{\partial z} \qquad \text{for } t>0,\ x_{j-1}\le x\le x_j,\ z=0 \qquad (10)$$

using (9), the temperature at element k $(z=0)$ in body 1 and time t can be given by

$$T_{k1}(t)=T_{01}+\sum_{j=1}^{N}\int_0^t q_j(\lambda)\,\frac{\partial\phi_{kj}{}^{(1)}(t-\lambda)}{\partial t}\,d\lambda \qquad (11)$$

where $\phi_{kj}{}^{(1)}(t)$ is the temperature rise at element k and time t due to a unit step heat flux at element j of surface 1; $\phi_{kj}{}^{(1)}(t)$ is the basic building block needed for body 1.

Similar to (11) an integral equation can be given for the kth surface element of body 2

$$T_{k2}(t)=T_{02}-\sum_{j=1}^{N}\int_0^t q_j(\lambda)\frac{\partial\phi_{kj}{}^{(2)}(t-\lambda)}{\partial t}d\lambda \qquad (12)$$

where $\phi_{kj}{}^{(2)}(t)$ is the temperature rise at element k and time t due to a unit step heat flux over element j of surface 2. The minus sign before the summation in (12) is used because the heat flux is pointing outward from body 2. The influence functions $\phi_{kj}{}^{(1)}(t)$ and $\phi_{kj}{}^{(2)}(t)$, can be found from the solution of a semi-infinite slab heated by a constant heat flux over an infinite strip with zero temperature on one side and insulated on the other side, and the solution of a semi-infinite body heated by a constant heat flux over an infinite strip [20], respectively (see Fig. 4).

For the case where the bodies are in perfect contact, one can write

$$T_{k1}(t)=T_{k2}(t) \qquad \text{for } k=1,2,\ .\ .\ .\ .\ ,N \qquad (13)$$

For the more general case of imperfect contact, (13) is replaced by

$$q_k(t)=h_k(t)[T_{k2}(t)-T_{k1}(t)] \qquad \text{for } k=1,2,\ .\ .\ .\ ,N \qquad (14)$$

where $h_k(t)$ is the time-variable contact conductance for surface element k. Relation (14) tends to the case of perfect contact as $h_k\to\infty$. It also includes the case of convection. By introducing (11) and (12) into (14), a set of integral equations for heat fluxes $q_k(t)$, $k=1,2,\ .\ .\ .\ .$, N, can be obtained

$$T_{02} - T_{01} = \frac{q_k(t)}{h_k(t)} + \sum_{j=1}^{N} \int_0^t q_j(\lambda) \frac{\partial \phi_{kj}(t-\lambda)}{\partial t} d\lambda \tag{15}$$

$$\phi_{kj}(t) = \phi_{kj}^{(1)}(t) + \phi_{kj}^{(2)}(t) \tag{16}$$

Discretization Over Time. Equation (15) represents a set of N Volterra equations of the second kind with the unknown heat fluxes $q_k(t)$ appearing both inside and outside the integrals. These integral equations can be approximated by a system of linear algebraic equations by replacing the integrals with suitable quadrature formulas. In the first step, the time region 0 to t is divided into M equal small time intervals Δt so that t_M represents the value of t and the end point of the Mth interval ($t_M = M\Delta t$). Next the heat flux histories $q_j(t)$ are assumed to have constant values in each time interval as shown in Fig. 5. Then (15) can be written as

$$T_0 = \frac{q_{kM}}{h_{kM}} + \sum_{j=1}^{N} \sum_{i=1}^{M} q_{ji}[\phi_{kj,M+1-i} - \phi_{kj,M-i}]$$

$$\text{for } k = 1,2, \ldots, N \tag{17}$$

where

$$T_0 = T_{02} - T_{01},\ q_{ji} \equiv q_j(t_i),\ \phi_{kj} \equiv \phi_{kj}(t_i) \tag{18a, b, c}$$

In the form given by (17), the heat fluxes q_{jM} (for $j = 1, \ldots, N$) can be determined at different time intervals one after another by marching forward in time for $M = 1,2,3, \ldots$; that is for each step, equation (17) represents a system of N equations with N unknowns; q_{1M}, $q_{2M}, \ldots, q_{NM}$.

Expressing (17) in matrix form with unknowns on the left and knowns on the right gives

$$(\bar{\bar{H}}_M + \bar{\bar{\Phi}}_1)\bar{q}_M = \bar{T}_0 + \sum_{i=1}^{M-1} \bar{\bar{\Phi}}_{M-i}\bar{q}_i - \sum_{i=1}^{M-1} \bar{\bar{\Phi}}_{M+1-i}\bar{q}_i \tag{19}$$

where $\bar{T}_0$ is the initial temperature vector, $\bar{\bar{H}}_m$ is the conductance matrix, and $\bar{\bar{\Phi}}_i$ and $\bar{q}_i$ are the influence matrix and the heat flux vector at time t_i, respectively

$$\bar{\bar{\Phi}}_1 \equiv \begin{bmatrix} \phi_{11i} & \phi_{12i} & \cdots & \phi_{1Ni} \\ \phi_{21i} & \phi_{22i} & & \phi_{2Ni} \\ \cdot & & & \\ \cdot & & & \\ \cdot & & & \\ \phi_{N1i} & \phi_{N2i} & & \phi_{NNi} \end{bmatrix}, \quad \bar{q}_i \equiv \begin{bmatrix} q_{1i} \\ q_{2i} \\ \cdot \\ \cdot \\ q_{Ni} \end{bmatrix}, \quad \bar{T}_0 \equiv \begin{bmatrix} T_0 \\ T_0 \\ \cdot \\ \cdot \\ T_0 \end{bmatrix} \tag{20a, b, c}$$

$$\bar{\bar{H}}_M \equiv \text{diag}\left[\frac{1}{h_{1M}}\ \frac{1}{h_{2M}} \cdots \frac{1}{h_{NM}}\right] \tag{20d}$$

If further $\bar{\bar{C}}_M$ and $\bar{\bar{D}}_M$ are defined to be the matrices

$$\bar{\bar{C}}_M = \bar{\bar{H}}_M + \bar{\bar{\Phi}}_1, \quad \bar{D}_M = \bar{T}_0 + \bar{E}_M - \bar{F}_M \tag{21a, b}$$

where

$$\bar{E}_M = \sum_{i=1}^{M-1} \bar{\bar{\Phi}}_{M-i}\bar{q}_i, \quad \bar{F}_M = \sum_{i=1}^{M-1} \bar{\bar{\Phi}}_{M+1-i}\bar{q}_i \tag{22a, b}$$

Then (19) can be written as

$$\bar{\bar{C}}_M \bar{q}_M = \bar{D}_M \tag{23}$$

and the solution is

$$\bar{q}_M = \bar{\bar{C}}_M^{-1} \bar{D}_M \tag{24}$$

The $\bar{\bar{C}}_M$ matrix, multiplier of $\bar{q}_M$, has to be calculated at each time step if the diagonal matrix $\bar{\bar{H}}_M$ is a function of time. However, for the case in which the contact conductances do not change with time, the $\bar{\bar{C}}_M$ matrix needs to be calculated only once during the entire solution.

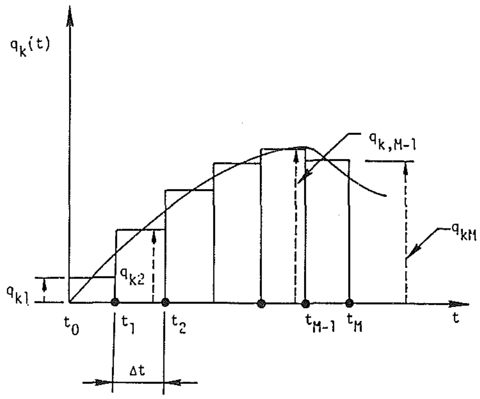

Fig. 5 Geometry illustrating uniform heat flux assumption over each time interval

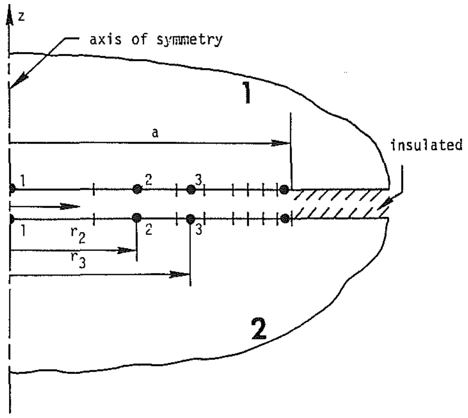

Fig. 6 Distribution of surface elements for two semi-infinite bodies in contact over a circular area

Application to Contact Conductance Problem

The MUSE method is used to obtain the transient thermal response of two semi-infinite bodies, initially at two different temperatures, that are suddenly brought into perfect thermal contact over a small circular region and insulated elsewhere (see Fig. 6). The solutions are given for the interface heat flux and temperatures, and the thermal constriction resistance of the contact area. Two different cases are investigated: (*a*) identical materials on both sides of the contact plane, and (*b*) different materials on the two sides of the contact plane. The former case is similar to the problem of a uniform step temperature change over a disk on the surface of a semi-infinite body and insulated elsewhere.

Due to the axisymmetric nature of the problem, in each case the contact area is divided into 10 annular variable-spaced elements with smaller elements being closer to the edge of the contact area. The influence functions for each geometry are obtained from the known available solutions given in [22, 23]. The results obtained from the surface element solutions are compared with those given by other investigators on the basis of the heat flux and the thermal constriction resistance across the contact area.

Previous Work. The transient problem for Case (*a*) has been analyzed by several authors by considering a single semi-infinite body with an isothermal disk on its surface [24–28]. Normington and Blackwell [24] and Blackwell [25] were the first to seek the solutions in oblate spheroidal coordinates. They developed an approximate solution by using Laplace and Legendre transform techniques. However, their solutions were

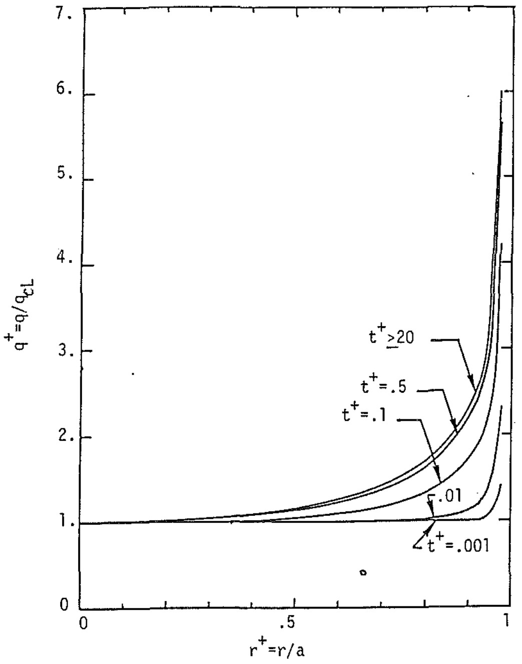

Fig. 7 Normalized heat flux distribution across the interface at various times for the geometry; Case (a)

valid only for long times ($t^+ > 4$) in the first paper and for short times ($t^+ < 0.1$) in the second one. Keltner [26] used the same coordinates to obtain a one-dimensional approximate solution using the heat balance integral method. Schneider et al. [27] developed finite difference solutions in oblate spheroidal coordinates for the two-dimensional axisymmetric case. In a recent paper [28], Marder and Keltner examined the problem using the method of separation of variables.

Case (*b*), where the materials on each side of the contact area are not identical, was first studied by Heasley [29] using an approximate method. His solution is approximately valid for long times. Other work was done by Schneider, Strong, and Yovanovich [30], Sadhal [31], and Beck and Keltner [12]. Schneider et al. [30] have employed finite difference techniques posed in oblate spheroidal coordinates to obtain the numerical solutions for the two-dimensional axisymmetric case. About 200 nodes were used inside each body. Sadhal [31] has solved the problem analytically by using Laplace and Legendre transform techniques. Beck and Keltner [12] were the first to employ the surface element method to solve the problem; only one element across the interface was used and the problem was solved analytically by utilizing Laplace transform technique.

The domain of validity of most of the abovementioned solutions is restricted in time or space [12, 24–26, 29, 31]. The finite difference approaches [27, 30] also have difficulties such as the effort in setting up large grids, and the restricted dimensionless time step that can be used.

Thermal Constriction Resistance for the Two Solids. In [1] the transient thermal constriction resistance is defined as "the difference between the average temperature of the contact area minus the temperature far from the contact area divided by the total instantaneous heat flow through the contact area." Based on the above definition one can write

$$R_{c1}(t) = \frac{\bar{T}_c(t) - T_{01}}{Q_c(t)}, \quad R_{c2}(t) = \frac{T_{02} - \bar{T}_c(t)}{Q_c(t)} \qquad (25a, b)$$

where $R_{c1}(t)$ and $R_{c2}(t)$ are the thermal constriction resistances for body 1 and body 2, respectively. The total thermal constriction resistance for the two semi-infinite bodies can be determined by

Table 1 Normalized area-averaged interface heat flux for the geometry of Case (a), $\bar{q}^+ = \bar{q}/\bar{q}_\infty$

		Beck & Keltner [12]		Marder & Keltner [28]	
t^+	MUSE	Eq. (56)	Eq. (22)	s = 2	s = 5
.001	15.057	12.357	14.522	13.088	8.645
.002	10.872	9.030	10.434	10.408	7.950
.005	7.169	6.079	6.792	7.063	6.485
.01	5.310	4.591	4.969	5.238	5.145
.02	3.998	3.539	3.688	3.948	3.943
.05	2.843	2.606	2.573	2.813	2.813
.1	2.268	2.136	2.038	2.248	2.248
.2	1.871	1.803	1.702	1.858	1.858
.5	1.533	1.508	1.530	1.515	1.526
1.	1.371	1.359	1.667	1.297	1.366
2.	1.259	1.254	2.334	1.104	1.257
5.	1.163	1.161		1.005	1.155
10.	1.114	1.113		1.	1.082
20.	1.080	1.080		1.	1.023
100.	1.036	1.036			1.
1000.	1.011	1.011			
10000.	1.004	1.004			
∞	1.0	1.			

$$R_c(t) = R_{c1}(t) + R_{c2}(t) = \frac{T_{02} - T_{01}}{Q_c(t)} \qquad (26)$$

The average contact area temperature $\bar{T}_c$ and the total heat flow through the contact area Q_c are given by

$$\bar{T}_c(t_M) = \sum_{j=1}^{N} T_{jM}(A_j/A_c), \quad Q_c(t_M) = \sum_{j=1}^{N} q_{jM}A_j \qquad (27a, b)$$

where A_c is the total contact area, A_j is the area of the jth element, and T_{jM} and q_{jM} are the temperature and the heat flux associated with element j at time t_M, respectively.

Results and Discussion. The results of the surface element solutions are presented in terms of the heat flux distributions across the interface, and the thermal constriction resistance of the contact area.

Figure 7 illustrates the normalized spatial variation of the surface heat flux at different dimensionless times. Normalization is obtained by dividing elemental values by the value of the centerline element which covers the area $0 \leq r^+ \leq 0.2$. After dimensionless time about 20, the normalized heat flux distribution remains constant. This indicates that for $t^+ \geq 20$, the heat flux across the disk can be approximated by a product of a function of t^+ and a function of r^+. Table 1 illustrates comparisons of *area-averaged interface heat flux*[3] calculations performed using the MUSE method with the results obtained from the two solutions given by equations (22) and (56) in [12] and the two other solutions given in [28] for values of $s = 2$ and $s = 5$.

Case (*b*) is considered with the glass being the material of one body and copper of the other. The glass–copper combination has also been investigated in [12, 30, 31]. The thermal conductivities k are 1.03 and 381 W/m-K and the thermal diffusivities α are 0.6×10^{-5} m^2/s and 13.2×10^{-5} m^2/s for glass and copper, respectively. For this case the dimensionless time is based on the lower thermal diffusivity $\alpha_1 < \alpha_2$. The results for spatial variation of the surface heat flux for Case (*b*) are similar to those of Case (*a*). In Fig. 8, the normalized interface temperature distribution is plotted versus dimensionless radius r^+ at several times. Normalization is obtained with respect to the initial temperature of body 2 (copper). For $t^+ = 0.1$ the interface temperature distribution is almost uniform.

The MUSE solution is also compared with the other available solutions on the basis of the dimensionless thermal constriction resistance across the contact area for both Cases (*a*) and (*b*). Table 2 provides the results for Case (*b*); for Case (*a*) see [13]. The first column in this table is the dimensionless

---

[3] The area-averaged interface heat flux $\bar{q}(t)$ was obtained by summing the products of the elemental heat flux and the fraction of the total interface area occupied by the element.

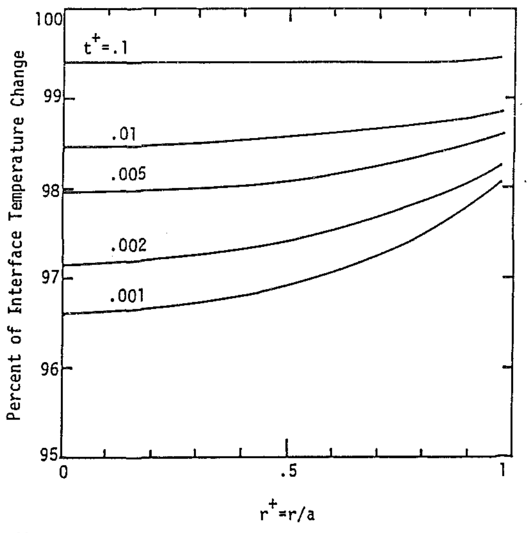

Fig. 8 Normalized interface temperature distribution for the geometry of Case (*b*) (normalized with respect to initial temperature of body 2, copper)

Table 2 Results for dimensionless constriction resistance for a disk-shaped interface of two semi-infinite bodies, one of copper and the other of glass; $R_c^+ = R_c/R_c(\infty)$

t^+	SSY [30]	Sadhal [31]	Beck & Keltner [12] Eq. (56)	Eq. (56)	MUSE
.001	.1549		.0820	.0701	.0676
.002	.1645		.1118	.0968	.0932
.005	.1870		.1655	.1462	.1890
.01	.2158		.2187	.1961	.1890
.02	.2595		.2833	.2570	.2507
.05	.3474		.3844	.3480	.3523
.1	.4382		.4688	.4101	.4413
.2	.5442		.5552	.4418	.5349
.5	.6869		.6637	.3857	.6610
1.	.7805	.7564	.7362	.2539	.7300
10.	.9495	.8992	.8982		.8973
100.	.9903	.9654	.9654		.9654
1000.	.9982	.9888	.9888		.9889
10000.	.9997	.9964	.9964		.9964
∞	1.	1.	1.		1.

time t^+, which extends over many decades. The results from the finite difference solution of Schneider et al. [30] are provided in the second column; they are least accurate at the early times and most accurate at the late times. The third column comes from the exact solution given by Sadhal [31] which is claimed to be very accurate at late times $t^+ > 10$. The fourth column is for the T-based solution given by Beck and Keltner [12], which is most appropriate for large times but is remarkably accurate down to $t^+ = 0.1$. Column 5 in the table is for the q-based solution [12] and is accurate at early times. The results obtained by the MUSE solution are displayed in the sixth column.

Conclusion

The multinode transient surface element formulation for solution of two-dimensional heat conduction problems with linear boundary conditions has been presented. The method uses Duhamel's integral and consequently can only be applied to problems with linear differential equations. It is applicable to homogeneous and composite geometries with perfect or imperfect contact.

The MUSE method is most suitable for calculating interface temperature and heat fluxes for the geometries connected over relatively small portion of their surface boundaries. Although the formulations were given for two-dimensional problems, they can also be applied to three-dimensional problems and the problems with multiple interfaces, providing the proper influence functions are used.

To show the flexibility and applicability of the method to two-dimensional homogeneous and composite bodies, the multinode surface element formulations were utilized to solve the problem of two semi-infinite bodies suddenly brought together over a small circular area. The results were in excellent agreement with existing analytical and numerical solutions. Very high accuracy is attainable with a relatively small number of surface elements for the complete time domain. This feature makes the method superior to alternative numerical techniques such as finite different or finite element which involve whole-body discretization.

Acknowledgments

This research was sponsored by NSF under Grant No. CME-79-20103.

References

1 Schneider, G. E., "Thermal Constriction Resistance Due to Arbitrary Contacts on a Half-Space-Numerical Solution of the Dirichlet Problem," *Progress in Astronautics and Aeronautics: Thermophysics and Thermal Control*, Vol. 65, R. Viskanta, ed., New York, 1979, pp. 103–119.

2 Schneider, G. E., and LeDain, B. L., "The Boundary Integral Equation Method Applied to Steady Heat Conduction With Special Attention Given to the Corner Problem," AIAA Paper No. 79-0176, 1979.

3 Khader, M. S., "Heat Conduction With Temperature Dependent Thermal Conductivity," ASME Paper No. 80-HT-4, 1980.

4 Khader, M. S., and Hanna, M. C., "An Iterative Boundary Integral Numerical Solution for General Steady Heat Conduction Problems," ASME Journal of Heat Transfer, Vol. 103, Feb. 1981, pp. 26–31.

5 Rizzo, F. J., and Shippy, D. J., "A Method of Solution for Certain Problems of Transient Heat Conduction," *AIAA Journal*, Vol. 8, No. 11, Nov. 1970, pp. 2004–2009.

6 Shaw, R. P.,, "An Integral Equation Approach to Diffusion," *International Journal of Heat and Mass Transfer*, Vol. 17, 1974, pp. 693–699.

7 Chang, Y. P., Kang, C. S., and Chen, D. J., "The Use of Fundamental Green's Functions for the Solution of Problems of Heat Conduction in Anisotropic Media," *Journal of Heat and Mass Transfer*, Vol. 16, 1973, pp. 1905–1918.

8 Wrobel, L. C., and Brebbia, C. A., "A Formulation of the Boundary Element Method for Axisymmetric Transient Heat Conduction," *International Journal of Heat and Mass Transfer*, Vol. 24, No. 5, 1981, pp. 843–850.

9 Keltner, N. R., "Heat Transfer in Intrinsic Thermocouples Application to Transient Measurement Errors," Report SC-RR-72-0719, Sandia National Laboratories, Albuquerque, NM, Jan. 1973.

10 Yonanovich, M. M., and Martin, K. A., "Some Basic Three-Dimensional Influence Coefficients for the Surface Element Method," AIAA Paper No. 80-1491, 1980.

11 Keltner, N. R., and Beck, J. V., "Unsteady Surface Element Method," ASME Journal of Heat Transfer, Vol. 103, No. 4, Nov. 1981, pp. 759–764.

12 Beck, J. V., and Keltner, N. R., "Transient Thermal Contact of Two Semi-infinite Bodies Over a Circular Area," *Progress in Astronautics and Aeronautics: Spacecraft Radiative Transfer and Temperature Control*, Vol. 33, 1982, pp. 66–82; Paper No. AIAA-81-1162.

13 Litkouhi, B., "Surface Element Method in Transient Heat Conduction Problems," Ph.D. Thesis, Department of Mechanical Engineering, Michigan State University, 1982.

14 Litkouhi, B., and Beck, J. V., "Instrinsic Thermocouple Analysis Using Multinode Unsteady Surface Element Method," to be published in *AIAA Journal*, Oct. 1985.

15 Beck, J. V., "Green's Function Solution for Transient Heat Conduction Problems," *Int. J. Heat Mass Transfer*, Vol. 27, 1984, pp. 1235–1244.

16 Ozisik, M. N., *Heat Conduction*, Wiley, New York, 1980.

17 Butkovskiy, A. G., *Green's Functions and Transfer Functions Handbook*, Halsted Press, NY, 1982.

18 Beck, J. V., "Green's Functions and Numbering System for Transient Heat Conduction," Paper No. AIAA-84-1741, 1984.

19 Carslaw, H. S., and Jaeger, J. C., *Conduction of Heat in Solids*, Cambridge University Press, Cambridge, 1959.

20 Litkouhi, B., and Beck, J. V., "Temperatures in Semi-infinite Body Heated by Constant Heat Flux Over Half Space," *Heat Transfer 1982—Munchen Conference Proceedings*, Vol. 2, Hemisphere, NY, 1982, pp. 21–17.

21 Beck, J. V., Keltner, N. R., and Schisler, I. P., "Influence Functions for the Unsteady Surface Element Method," Paper No. AIAA-84-0492.

22 Beck, J. V., "Transient Temperatures in a Semi-infinite Cylinder Heated by a Disk Heat Source," *Int. J. Heat Mass Transfer*, Vol. 24, 1981, pp. 1631–1640.

23 Beck, J. V., "Large Time Solutions for Temperatures in a Semi-infinite Body With a Disk Heat Source," *Int. J. Heat Mass Transfer*, Vol. 24, 1981, pp. 155–164.

24 Normington, E. G., and Blackwell, J. H., "Transient Heat Flow From Constant Temperature Spheroids and the Thin Circular Disk," *Quarterly Journal of Mechanics and Applied Mathematics*, Vol. 17, Part 1, 1964, pp. 65–72.

25 Blackwell, J. H., "Transient Heat Flow From a Thin Circular Disk Small-Time Solution," *Journal Australian Math. Soc.*, Vol. 14, 1972, pp. 433–442.

26 Keltner, N. R., "Transient Heat Flow in Half-Space Due to an Isothermal Disk on the Surface," ASME JOURNAL OF HEAT TRANSFER, Vol. 95, No. 3, 1973, pp. 412-414.

27 Schneider, G. E., Strong, A. B., and Yovanovich, M. M., "Transient Heat Flow From a Thin Circular Disk," AIAA 10th Thermophysics Conference, Denver, CO, May 27-29, 1975, AIAA Paper No. 75-707.

28 Marder, B. M., and Keltner, N. R., "Heat Flow From a Disk by Separation of Variables," *Numerical Heat Transfer*, Vol. 4, 1981, pp. 485-497.

29 Heasley, J. H., "Transient Heat Flow Between Contacting Solids," *Int. J. of Heat Mass Transfer*, Vol. 4, 1981, pp. 485-497.

30 Schneider, G. E., Strong, A. B., and Yovanovich, M. M., "Transient Thermal Response of Two Bodies Communications Through a Small Circular Contact Area," *Int. J. Heat Mass Transfer*, Vol. 20, 1977, pp. 301-108 [sic].

31 Sadhal, S. S., "Transient Thermal Response of Two Solids in Contact Over a Circular Disk," *Int. J. Heat Mass Transfer*, Vol. 23, 1980, pp. 731-733.

APPENDIX

Relation of Equation (1) to Green's Function Formulation

For the case of uniform initial temperature T_0 and a heat flux condition, equation (13) of [15] gives

$$T(\mathbf{r}, t) = T_0 + \frac{\alpha}{k}\int_{\lambda=0}^{t} \int_{S_i} q(\mathbf{r}_i', \lambda)\; G(\mathbf{r}, t/\mathbf{r}_i', \lambda)\; ds_i d\lambda \tag{A1}$$

For the coordinates $\mathbf{r} = x, z$, the heat flux at $z = 0$, and heating from $s' = \eta = 0$ to L, (A1) can be written as

$$T(x, z, t) = T_0 + \int_{\eta=0}^{L} \int_{\lambda=0}^{t} q(\eta, \lambda) \cdot \frac{\alpha}{k} G(x, z, t/\eta, 0, \lambda) d\lambda d\eta \tag{A2}$$

Comparing equation (1) and (A2) yields

$$-\frac{\partial^2 \psi_q (x, z, \eta, t-\lambda)}{\partial t \partial \eta} = \frac{\alpha}{k} G(x, z, t/\eta, 0, \lambda) \tag{A3}$$

and then integrating (A3) twice gives

$$\psi_q (x, z, \eta, t-\lambda) = -\int_{t'=0}^{t} \int_{x'=\eta}^{L} \frac{\alpha}{k} \cdot G(x, z, t/x', 0, t') dx' dt' \tag{A4}$$

which demonstrates a relationship between Duhamel's theorem equation given by (1) and a Green's function formulation.

An advantage of writing (1) in the present form is that $\psi_q(.)$ is finite for $t-\lambda \rightarrow 0$ for the heated surface while G(., .,) goes to infinity. On the other hand, an advantage of the Green's function formulation is the relatively easy access to the Green's functions [15-19].

M. H. N. Naraghi
Visiting Assistant Professor.
Assoc. Mem. ASME

B. T. F. Chung
Professor.
Mem. ASME

Department of Mechanical Engineering,
The University of Akron,
Akron, OH 44325

A Stochastic Approach for Radiative Exchange in Enclosures With Directional-Bidirectional Properties

The concept of multiple Markov chains is applied to the study of radiative heat transfer problems. A stochastic method for calculating radiative interchange in enclosures consisting of a number of isothermal surfaces with directional-bidirectional properties is developed. In this work, the Monte Carlo method is employed for calculating the multiple transition probabilities. Numerical examples have been presented to demonstrate the usefulness of the present approach.

Introduction

Most available methods of calculating radiative exchange in enclosures are only capable of treating enclosures with diffuse and specular surfaces [1-6]. Bobco [7] introduced a method for solving radiation transfer in enclosures with directional-bidirectional surfaces. His method includes only one bounce of the energy bundles and also requires bidirectional reflectance as an input. Calculating bidirectional reflectance from bidirectional reflectivity involves evaluation of four surface integrals or eight line integrals and is an extremely tedious task. The only practical method for determination of radiative interchange in enclosures with directional-bidirectional surfaces is the Monte Carlo method [8, 9]. However, the statistical errors involved in the Monte Carlo method can be large. Further improvement of this technique is necessary.

Recently, Naraghi and Chung [6] have demonstrated that the principle of multiple Markov chains can be used for calculating radiative interchange in enclosures consisting of diffuse and specular surfaces. The same concept will be used here to develop a method for calculating radiative exchange in enclosures consisting of directional-bidirectional surfaces.

It has been shown [6] that the stochastic process $X = \{x_0 = i_0, x_1 = i_1, x_2 = i_2, \ldots\}$ represents a radiation process in which the radiating energy bundle initially emitted from surface i_0 is reflected from surfaces, $i_1, i_2, \ldots$, etc., until it is absorbed by one of the participating surfaces. As an example, consider an enclosure consisting of 6 surfaces 1, 2, 3, 4, 5, and 6. The stochastic process $X = \{x_0 = 3, x_1 = 5, x_2 = 1, x_3 = 4, x_4 = 3, \ldots\}$ represents an energy bundle which initially is emitted from surface 3 and then reflected from surfaces 5, 1, 4, 3, ... sequentially until it is absorbed by one of the participating surfaces. Therefore, the radiative process in an enclosure can be represented by a stochastic process. The destination of an energy bundle after emission and each reflection is a random phenomenon and is influenced by emissivities and reflectivities of the participating surfaces. When the reflections are bidirectional the destination of the energy bundle after each reflection is influenced by a number of its past reflections. For example, if the destination of the energy bundle is influenced by its past l steps, then

$$P\{x_n | x_0, x_1, x_2, \ldots, x_{n-1}\} = P\{x_n | x_{n-l}, \ldots, x_{n-2}, x_{n-1}\} \tag{1}$$

This process is called multiple or l-dependent Markov chains [10-12]. The ordinary Markov chain theory can be applied to multiple Markov chains if we define a new random variable as

$$y_n = (x_n, x_{n+1}, \ldots, x_{n+l-1}) \tag{2}$$

Then $Y = \{y_n;\ n \in N\}$ is a stochastic process which holds the Markovian property. The stochastic process Y has no physical meaning and it is only created in order to carry out the calculations. The results obtained based on stochastic process Y have to be transformed into stochastic process X, which represents the radiation process in the enclosure. Since the random variables of the stochastic process Y are vectors, its transition probabilities matrix is in the form of

$$\mathbf{P} = [P_{(i_1, i_2, \ldots, i_l),\ (j_1, j_2, \ldots, j_l)}] \tag{3}$$

The transition from $(i_1, i_2, \ldots, i_l)$ to $(j_1, j_2, \ldots, j_l)$ is possible only if $i_2 = j_1, i_3 = j_2, \ldots, i_l = j_{l-1}$ or in general $i_k = j_{k-1}$ for $2 \le k \le l$. A more detailed description of stochastic processes and Markov chains can be found in [6, 10-12].

In this paper, the concept of multiple Markov chains is used to calculate the probabilities that radiation emitted from surface i of an enclosure is absorbed by surface j in the same enclosure. These probabilities are equivalent to the absorption factor $B_{i,j}$ of [1].

Analysis

Consider an enclosure with surfaces having directional emissivities $\epsilon'(\beta, \theta)$, absorptivities $\alpha'(\beta, \theta)$, and bidirectional reflectivities, $\rho''(\beta, \theta, \beta_r, \theta_r)$. The stochastic process $X = \{x_0, x_1, x_2, \ldots\}$ can be used to represent the radiation process in this enclosure. If the participating surfaces reflect bidirectionally the outcome of random variable x_n is influenced by the outcomes of l previous random variables. The stochastic process X can be transformed to stochastic process $Y = \{y_0, y_1, y_2, \ldots\}$ using the transformation shown by equation (2). The outcome of random variable y_n of stochastic process Y is only influenced by one preceding random variable, i.e., y_{n-1}. Therefore, the stochastic process Y holds a Markovian property. At the first $l-1$ transitions of stochastic process X, there are fewer than l past random variables; therefore, we must let the process go on for $l-1$ transitions in order to form the initial vector $y_0 = (x_0, x_1, \ldots, x_{l-1})$. The idea of the multiple Markov chains can be applied after $(l-1)$th transition has occurred, i.e., when the initial vector of stochastic process Y can be formed. Other techniques are necessary to calculate the energy absorbed by surfaces of the enclosure at first, second, ... $(l-1)$th transitions. Based on the above argument the absorption factor can be formulated by [6]

Contributed by the Heat Transfer Division for publication in the JOURNAL OF HEAT TRANSFER. Manuscript received by the Heat Transfer Division, July 20, 1984. Paper No. 84-HT-39.

$$\mathbf{B}=\mathbf{B}^{(1)}+\mathbf{B}^{(2)}+\ .\ .\ +\mathbf{B}^{(l-1)}+\mathbf{B}^{(l+)} \quad (4)$$

where $\mathbf{B}^{(k)}=[B^{(k)}_{i,j}]$ $(k<l)$ and $B^{(k)}_{i,j}$ is the probability that radiation initially emitted from surface i is absorbed by surface j in exactly k steps. The multiple Markov chains are used only to calculate the last term, i.e., $\mathbf{B}^{(l+)}$ in equation (4). $B^{(l+)}_{i,j}$ is defined as the probability of radiative energy bundle initially emitted from surface i being absorbed by surface j at the lth or later transitions.

The formulation given by equation (4) is referred to as a stochastic l model, e.g., the stochastic 2 model is given by

$$\mathbf{B}=\mathbf{B}^{(1)}+\mathbf{B}^{(2+)}$$

It represents a stochastic process in which the future of the radiation process depends on two previous reflections only.

The probability that radiation emitted from surface i is absorbed by surface j in exactly one transition is given by (refer to Fig. 1 for notations)

$$B^{(1)}_{i,j}=\frac{1}{\pi\,\epsilon_i A_i}\cdot\int_{A_i}\int_{A_j}\frac{\epsilon'_i(\beta_i,\theta_i)[\cos\beta_i\cos\beta_j]\alpha'_j(\beta_j,\theta_j)dA_i dA_j}{r^2_{i,j}} \quad (5)$$

where

$$\epsilon_i=\frac{1}{\pi}\int_0^{\pi/2}\int_0^{2\pi}\epsilon_i'(\beta,\theta)\cos\beta\sin\beta\,d\theta\,d\beta$$

$B^{(1)}_{i,j}$ can also be interpreted as the fraction of energy emitted from surface i absorbed by surface j in a single transition. The fraction of energy emitted from differential element dA_i along (β_i,θ_i) which is absorbed by differential element dA_j is given by

$$\frac{\epsilon'_i(\beta_i,\theta_i)[\cos\beta_i\cos\beta_j]\alpha'_j(\beta_j,\theta_j)\,dA_i\,dA_j}{\pi\,r^2_{i,j}}$$

Integrating the above expression with respect to surfaces A_i and A_j leads to the fraction of energy emitted from surface A_i absorbed by surface A_j. The use of equation (5) requires evaluation of two surface integrations or four line integrations. Expressions for $B^{(2)}_{i,j}, B^{(3)}_{i,j}, \ldots, B^{(l-1)}_{i,j}$ involve large numbers of integrations [10]. Evaluation of these integrations is a tedious job; therefore, it is more practical to use the Monte Carlo method to calculate $B^{(k)}_{i,j}$ $(k\leq l-1)$.

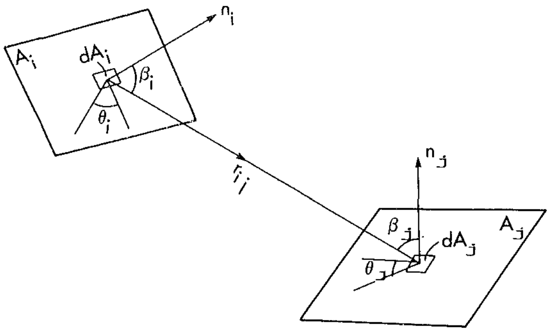

Fig. 1 Direct exchange of radiation between two surfaces, *i* and *j*

It has been shown [6] that stochastic 2 and 3 models provide solutions with reasonable accuracies. The stochastic 2 and 3 models correspond to one and two-bounce solutions, respectively. Hence, the Monte Carlo method will be used here for the evaluation of a small number of bounces of energy bundles (one or two bounces at most). Consequently it is expected that the statistical errors of the present techniques will be much less than the direct use of the Monte Carlo method in which several bounces of the energy bundles have to be evaluated by means of a random sampling. The formulation for equation (5) based on the Monte Carlo method is

$$B^{(1)}_{i,j}=\lim_{N_i\to\infty}\frac{N_{a(i,j)}}{N_i} \quad (6)$$

where N_i is the total number of energy bundles dispatched from surface i and $N_{a(i,j)}$ is the number of energy bundles

Nomenclature

$\mathbf{A}$ = absorptivity matrix
A_i = area of surface i
$\mathbf{B}$ = absorption factor matrix
$B_{i,j}$ = absorption factor (fraction of energy emitted from surface i and absorbed by surface j by direct radiation and multiple reflections)
$\mathbf{C}$ = matrix defined by equation (19)
$F_{i,j}$ = radiation shape factor from surface i to surface j
$\mathfrak{F}_{i,j}$ = $\epsilon_i\beta_{i,j}$
l = an integer denoting the dependence of the radiation process on its past steps
N_i = total number of energy bundles emitted from surface i
$N_{(i_1,i_2,\ldots,i_l)}$ = number of energy bundles initially emitted from surface i_1, and reflected from surfaces $i_2, i_3, \ldots, i_{l-1}$ sequentially, finally reaching surface i_l
$N_{a(i_1,i_2,\ldots,i_l)}$ = number of energy bundles initially emitted from surface i_1, reflected from surfaces $i_2, i_3, \ldots, i_{l-1}$ sequentially, and finally absorbed by surface i_l
$N_{r(i_1,i_2,\ldots,i_l)}$ = number of energy bundles initially emitted from surface i_1, reflected from surfaces $i_2, i_3, \ldots, i_{l-1}$ sequentially, and finally reflected from surface i_l
P = probability
$\mathbf{P}$ = transition probability matrix
$r_{i,j}$ = distance between differential surfaces dA_i and dA_j
$\bar{r}_{j,k,w}$ = nondimensional bidirectional reflectance of surface k for radiation arriving from surface j and directed toward surface w
$\overline{s_is_j}$ = total exchange area from surface i to surface j
R = random number between 0 and 1
$\mathbf{R}$ = reflectivity matrix
q = entries of matrix $\mathbf{Q}$ defined by equation (12)
$\mathbf{Q}$ = matrix defined by equation (14)
x = random variable
X = stochastic process
y = random variables vector
Y = stochastic process
α = absorptivity
β = angle from normal
δ = Krönecker delta
ϵ = emissivity
θ = circumferential angle
ρ = reflectivity

Superscripts

d = diffuse component of reflectivity
c = directional component of reflectivity
s = specular component of reflectivity
$'$ = quantity in one direction
$''$ = bidirectional quantity

which are emitted from surface i and absorbed by surface j in one transition. The formulations for emission direction and absorption are given in [13]. When the participating surfaces emit and absorb diffusely then the formulation given by equation (6) becomes

$$B^{(1)}_{i,j}=\alpha_j \lim_{N_i\to\infty} \frac{N_{(i,j)}}{N_i} \tag{7}$$

where $N_{(i,j)}$ is the number of energy bundles emitted from surface i and reaching surface j and α_j is hemispherical absorptivity. The right-hand side of equation (7) is identical to $F_{i,j}\,\alpha_j$ when the exact formulation is used. If the $F_{i,j}$'s are known, the use of exact formulation eliminates the statistical errors caused by the Monte Carlo method.

The probability that radiation emitted from surface i is absorbed by surface j in exactly two transitions is expressed by $B^{(2)}_{i,j}$ (i.e., one reflection, see Fig. 2)

$$B^{(2)}_{i,j} = \sum_{i_1} \lim_{N_i\to\infty} \frac{N_{a(i,i_1,j)}}{N_i} \tag{8}$$

where $N_{a_{(i,i_1,j)}}$ is the number of energy bundles initially emitted from surface i and reflected from surface i_1, and finally absorbed by surface j. $B^{(2)}_{i,j}$ represents the fraction of energy emitted from surface i which is reflected from one of the participating surfaces and finally absorbed by surface j.

When the participating surfaces emit and absorb diffusely the formulation given by equation (8) becomes

$$B^{(2)}_{i,j} = \alpha_j \sum_{i_1} \lim_{N_i\to\infty} \frac{N_{(i,i_1,j)}}{N_i} \tag{9}$$

where $N_{(i,i_1,j)}$ is the number of energy bundles initially emitted from surface i then reflected from surface i_1 and finally reaching surface j.

In general, the probability that radiation having emitted from surface i being absorbed by surface j in exactly k transitions ($k-1$ reflections, see Fig. 3) can be written as ($k < l$)

$$B^{(k)}_{i,j} = \sum_{i_1,i_2,\ldots,i_{k-1}} \lim_{N_i\to\infty} \frac{N_{a(i,i_1,i_2,\ldots,i_{k-1},j)}}{N_i} \tag{10}$$

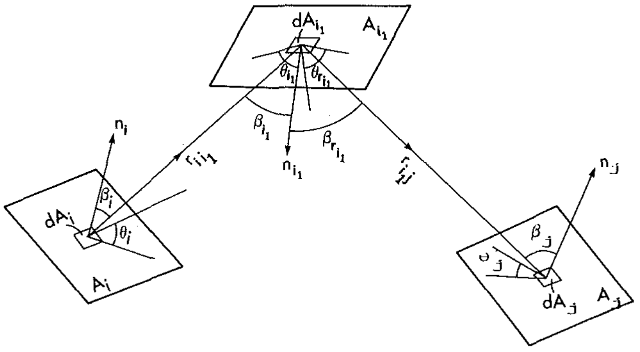

Fig. 2 Exchange of radiation between two surfaces, i and j with reflection from i_1

where $N_{a(i,i_1,i_2,\ldots,i_{k-1},j)}$ is the number of energy bundles initially emitted from surface i and reflected from surfaces i_1, $i_2, \ldots, i_{k-1}$ sequentially and finally absorbed by surface j.

$B^{(k)}_{i,j}$ can be interpreted as the fraction of energy emitted from surface i and absorbed by surface j having reflected from $k-1$ surfaces in the enclosure. When the participating surfaces emit and absorb diffusely equation (10) becomes

$$B^{(k)}_{i,j} = \alpha_j \sum_{i_1,i_2,\ldots,i_{k-1}} \lim_{N_i\to\infty} \frac{N_{(i,i_1,i_2,\ldots,i_{k-1},j)}}{N_i} \tag{11}$$

where $N_{(i,i_1,i_2,\ldots,i_{k-1},j)}$ is the number of energy bundles initially emitted from surface i and reflected from surfaces i_1, $i_2, \ldots, i_{k-1}$ sequentially and finally reaching surface j. To find $\mathbf{B}^{(l+)}$ (the last term in equation (4)), we use multiple Markov chain principles.

Let $q_{(i_1,i_2,\ldots,i_l)}$ be the probability of the radiative energy bundle not being absorbed by states $x_1 = i_2$, $x_2 = i_3, \ldots, x_{l-1} = i_l$. They are the entries of the vector $y_0 = (x_0, x_1, x_2, \ldots, x_{l-1})$. It also represents the probability of the initial state of stochastic process Y being formed, i.e., the initial distribution of stochastic process Y. $q_{(i_1,i_2,\ldots,i_l)}$ is expressed by the following equation

$$\begin{aligned} q_{(i_1,i_2,i_3,\ldots,i_l)} &= p\{x_0=i_1, x_1=i_2, x_2=i_3, \ldots, x_{l-1}=i_l, \\ &\qquad \text{and reflected from } i_l\} \\ &= \lim_{N_{i_1}\to\infty} \frac{N_{r(i_1,i_2,i_3,\ldots,i_l)}}{N_{i_1}} \end{aligned} \tag{12}$$

where $N_{r(i_1,i_2,i_3,\ldots,i_l)}$ is the number of energy bundles initially emitted from surface i_1, and reflected from surfaces i_2, $i_3, \ldots, i_l$, sequentially.

When the participating surfaces emit and absorb diffusely, equation (12) becomes

$$q_{(i_1,i_2,i_3,\ldots,i_l)} = \rho_{i_l} \lim_{N_{i_1}\to\infty} \frac{N_{(i_1,i_2,i_3,\ldots,i_l)}}{N_{i_1}} \tag{13}$$

where $N_{(i_1,i_2,i_3,\ldots,i_l)}$ is the number of energy bundles initially emitted from surface i_1, reflected from surfaces i_2, $i_3, \ldots, i_{l-1}$ sequentially, and finally reaching surface i_l.

We define an associated diagonal matrix $\mathbf{Q}$ as

$$\mathbf{Q} = [q_{(i_1,i_2,\ldots,i_l)}\,\delta_{(i_1,i_2,\ldots,i_l),(j_1,j_2,\ldots,j_l)}] \tag{14}$$

We also define the transition probability matrix $\mathbf{P}$

$$\mathbf{P} = [P_{(i_1,i_2,\ldots,i_l),(j_1,j_2,\ldots,j_l)}] \tag{15}$$

where $P_{(i_1,i_2,\ldots,i_l),(j_1,j_2,\ldots,j_l)}=0$; if $i_2 \neq j_1$ or $i_3 \neq j_2, \ldots,$ or $i_l \neq j_{l-1}$ then $P_{(i_1,i_2,\ldots,i_l),(i_2,i_3,\ldots,i_l,j_l)}$ is the probability of radiation reaching surface j_l initially emitted from i_1 and being reflected from i_2, $i_3 \ldots, i_l$. In this case $P_{(i_1,i_2,\ldots i_l),(i_2,i_3,\ldots,i_l,j_l)}$ is a conditional probability and is identical to $P\{x_l = j_l | x_0=i_1, x_1=i_2, \ldots, x_{l-1}=i_l\}$. The conditional probability is defined by [11, 12]

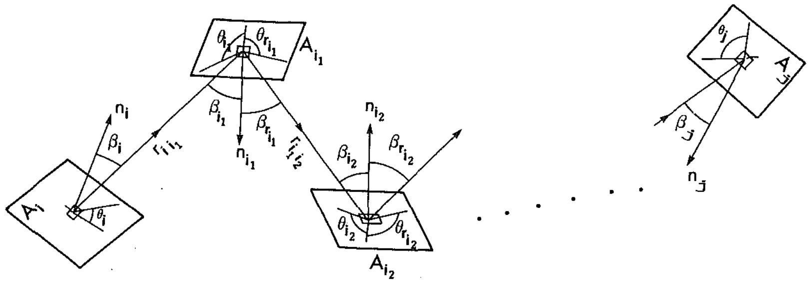

Fig. 3 Exchange of radiation between two surfaces, i and j with reflection from surfaces $i_1, i_2, i_3, \ldots$ sequentially

$$p\{x_2=b \mid x_1=a\}=p\{x_2=b, x_1=a\}/p\{x_1=a\}$$

Applying this relation we can write

$$P_{(i_1,i_2,\ldots,i_l),\,(i_2,i_3,\ldots,i_l,j_l)}=\frac{p\{x_0=i_1,\ x_1=i_2,\ \ldots,\ x_{l-1}=i_l,\ x_l=j_l\}}{p\{x_0=i_1,\ x_1=i_2,\ \ldots,x_{l-1}=i_l, \text{ and reflected from } i_l\}}$$

$$P_{(i_1,i_2,\ldots,i_l),\,(i_2,\ldots,i_l,j_l)}=\frac{\lim\limits_{N_{i_1}\to\infty}\dfrac{N_{(i_1,i_2,i_3,\ldots,i_l,j_l)}}{N_{i_1}}}{\lim\limits_{N_{i_1}\to\infty}\dfrac{N_{r(i_1,i_2,i_3,\ldots,i_l)}}{N_{i_1}}} \tag{16}$$

The hemispherical absorptivity and reflectivity matrices are defined as

$$\mathbf{A}=[\alpha_{j_l}\delta_{(i_1,i_2,\ \ldots,i_l),(j_1,j_2,\ldots,j_l)}] \tag{17}$$

and

$$\mathbf{R}=[\rho_{j_l}\delta_{(i_1,i_2,\ \ldots,i_l),(j_1,j_2,\ldots,j_l)}] \tag{18}$$

where α_{j_l} is hemispherical absorptivity and ρ_{j_l} is hemispherical total reflectivity of surface j_l. Then

$$\mathbf{C}=[C_{(i_1,i_2,\ldots,i_l),(j_1,j_2,\ldots,j_l)}]$$
$$=\mathbf{Q\,P\,A}+\mathbf{Q\,P\,R\,P\,A}+\mathbf{Q\,P\,R\,P\,R\,P\,A}+\ \ldots$$

or

$$\mathbf{C}=\mathbf{Q}[\mathbf{I}-\mathbf{P\,R}]^{-1}\,\mathbf{P\,A} \tag{19}$$

The interpretation of each term in equation (19) is as follows: **Q** is the probability that the initial state of stochastic processes Y is formed; the terms **Q P A**, **Q P R P A**, **Q P R P R P A** represent the probabilities that the radiative energy bundle is absorbed at the first, second, third, . . . transitions of stochastic process Y respectively. The first transition of stochastic process Y is equivalent to the lth transition of stochastic process X. This is due to the fact that the transiton from y_0 to y_1 is equivalent to transition from the last entry of $(x_0, x_1, \ldots, x_{l-1})$ to the last entry of $(x_1, x_2, \ldots, x_l)$, i.e., transition from x_{l-1} to x_l; but the transition from x_{l-1} to x_l is the lth transition of stochastic process X. Similarly, it can be shown that the second transition of stochastic process Y is equivalent to the $(l+1)$th transition of stochastic process X and so on. The matrix **C** gives the probabilities that the radiative energy bundle is absorbed by the states of stochastic process **Y**; therefore, we need to transform the matrix **C** into the original stochastic process X. This can be realized from the following relationship

$$B_{i,j}^{(l+)}=\sum_{\substack{i_2,i_3,\ldots,i_l\\ j_1,j_2,\ldots,j_{l-1}}} C_{(i,i_2,i_3,\ldots,i_l),(j_1,j_2,\ldots,j_{l-1},j)} \tag{20}$$

Once $\mathbf{B}^{(l+)}=[B_{i,j}^{(l+)}]$ is formed, the absorption factor matrix can be obtained by substituting $\mathbf{B}^{(1)}, \mathbf{B}^{(2)}, \ldots, \mathbf{B}^{(l+)}$ into equation (4). The one-bounce solution of the above method corresponds to $l = 2$ and equation (4) reduces to

$$\mathbf{B}=\mathbf{B}^{(1)}+\mathbf{B}^{(2+)} \tag{21}$$

If the view factors and mean bidirectional reflectance $\bar{r}_{i,j,k}$ are known, they can be used instead of the Monte Carlo method to evaluate the right-hand sides of equations (7), (13), and (16) when $l = 2$ (stochastic 2 model). These equations take the following forms

$$B_{i,j}^{(1)}=F_{i,j}\ \alpha_j \tag{22}$$

$$q_{(i_1,i_2)}=\rho_{i_2}\ F_{i_1,i_2} \tag{23}$$

Table 1 Surface properties for the enclosure shown in Fig. 4 [7]

				$\bar{r}_{w,i,j}$	
j	ϵ_j	ρ_j^s	ρ_j^d	$w = 2$	$w = 3$
1	0.10	—	—	0.	0.
2	0.05	0.95	0.	0.30	1.20
3	0.15	0.	0.85	1.20	0.75

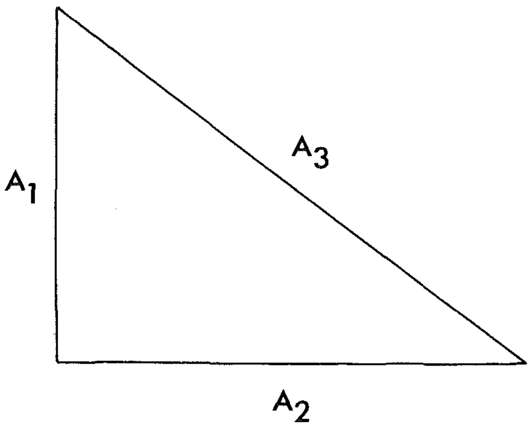

Fig. 4 An infinitely long triangular enclosure

$$P_{(i_1,i_2),(i_2,j_2)}=\frac{\bar{r}_{i_1,i_2,j_2}\ F_{i_1,i_2}\ F_{i_2,j_2}}{\rho_{i_2}\ F_{i_1,i_2}}=\frac{\bar{r}_{i_1,i_2,j_2}\ F_{i_2,j_2}}{\rho_{i_2}} \tag{24}$$

As will be shown in the next section, the present one-bounce solution (equations (21)–(24)) yields results identical to those of [7], for the same example problem solved in this reference. Note that the example given in [7] is restricted to the one-bounce solution only and it requires mean bidirectional reflectance as input. As pointed out earlier, calculation of mean bidirectional reflectance involves eight line integrals and is not an easy task. Furthermore, the present approach is capable of providing two, three, . . . bounce solutions, i.e., $l>2$. In these cases, the Monte Carlo method is used to evaluate the right-hand sides of equations (6)–(13) and (16). The reader should refer to [13] for details regarding emission and reflection direction of energy bundles in the Monte Carlo method.

Results and Discussion

The only existing solution for an enclosure with bidirectionally reflecting surfaces is given in [7]. The enclosure considered in this reference consists of three plane surfaces, A_1, A_2, and A_3, which reflect bidirectionally, specularly, and diffusely, respectively. The area ratio of the three surfaces is A_1:A_2:A_3 = 3:4:5, and the surface properties are given in Table 1.

The same problem will be resolved by the present approach. The simplest one-bounce formulation of the present approach, namely, stochastic 2 model gives

$$\mathbf{B}=\mathbf{B}^{(1)}+\mathbf{B}^{(2+)}$$

where

$$\mathbf{B}^{(1)}=[B_{i,j}^{(1)}]=[F_{i,j}\alpha_j]$$

and $B_{i,j}^{(1)}$ is the probability that energy bundles emitted from surface i are absorbed by surface j in one transition. The numerical value of matrix $\mathbf{B}^{(1)}$ is

$$\mathbf{B}^{(1)} = \begin{bmatrix} 0. & 0.01667 & 0.10000 \\ 0.02500 & 0. & 0.11250 \\ 0.04000 & 0.03000 & 0. \end{bmatrix}$$

To calculate $\mathbf{B}^{(2+)}$ the principle of multiple Markov chains is used. The possible states for this case are: (1, 2), (1, 3), (2, 1), (2, 3), (3, 1), and (3, 2). The transition probabilities are calculated from the following relations

$$P_{(1,2),\,(2,1)} = \frac{F_{1(2),\,1}}{F_{1,2}} = 0.$$

$$P_{(1,2),\,(2,3)} = \frac{F_{1(2),\,3}}{F_{1,2}} = 1.$$

$$P_{(1,3),\,(3,1)} = F_{3,1} = 2/5 \qquad P_{(1,3),\,(3,2)} = 3/5$$

$$P_{(2,1),\,(1,2)} = ((\bar{r}_{2,1,2}F_{2,1}F_{1,2})/\rho_1)/F_{2,1}$$

$$= (\bar{r}_{2,1,2}F_{1,2})/\rho_1 = 1/9$$

$$P_{(2,1),\,(1,3)} = ((\bar{r}_{2,1,3}F_{2,1}F_{1,3})/\rho_1)/F_{2,1} = (\bar{r}_{2,1,3}F_{1,3})/\rho_1 = 8/9$$

$$P_{(2,3),\,(3,1)} = F_{3,1} = 2/5 \qquad p_{(2,3),\,(3,2)} = F_{3,2} = 3/5$$

$$P_{(3,1),\,(1,2)} = ((\bar{r}_{3,1,2}F_{3,1}F_{1,2})/\rho_1)/F_{3,1}$$

$$= (\bar{r}_{3,1,2}F_{1,2})/\rho_1 = 4/9$$

$$P_{(3,1),\,(1,3)} = ((\bar{r}_{3,1,3}F_{3,1}F_{1,3})/\rho_1)/F_{3,1} = 5/9$$

$$P_{(3,2),\,(2,1)} = F_{3(2),1}/F_{3,2} = 1/5$$

$$P_{(3,2),\,(2,3)} = F_{3(2),3}/F_{3,2} = 2/3$$

where $\rho_1 = \rho_1^d + \rho_1^s$.

Matrix **Q**, based on equations (14) and (23), is given by

$$\mathbf{Q} = \begin{bmatrix} F_{1,2}\rho_2 & & & & & \\ & F_{1,3}\rho_3 & & 0 & & \\ & & F_{2,1}\rho_1 & & & \\ & & & F_{2,3}\rho_3 & & \\ & 0 & & & F_{3,1}\rho_1 & \\ & & & & & F_{3,2}\rho_2 \end{bmatrix}$$

$$= \begin{bmatrix} 0.31677 & & & & & \\ & 0.56667 & & 0 & & \\ & & 0.22500 & & & \\ & & & 0.63750 & & \\ & 0 & & & 0.36000 & \\ & & & & & 0.57000 \end{bmatrix}$$

The absorptivity matrix, equation (17), is given by

$$\mathbf{A} = \begin{bmatrix} 0.05 & & & & & \\ & 0.15 & & 0 & & \\ & & 0.10 & & & \\ & & & 0.15 & & \\ & 0 & & & 0.10 & \\ & & & & & 0.05 \end{bmatrix}$$

and the reflectivity matrix is

$$\mathbf{R} = \mathbf{I} - \mathbf{A}$$

Substituting the above matrices into equation (19) yields

$$\mathbf{C} = \begin{array}{c} \\ (1,2) \\ (1,3) \\ (2,1) \\ (2,3) \\ (3,1) \\ (3,2) \end{array} \begin{array}{c} \begin{array}{cccccc} (1,2) & (1,3) & (2,1) & (2,3) & (3,1) & (3,2) \end{array} \\ \begin{bmatrix} 0.01033 & 0.06093 & 0.02192 & 0.14271 & 0.04616 & 0.03462 \\ 0.02174 & 0.12827 & 0.04616 & 0.20044 & 0.09717 & 0.07288 \\ 0.00855 & 0.07305 & 0.01549 & 0.07084 & 0.03261 & 0.02446 \\ 0.02446 & 0.14430 & 0.05193 & 0.22550 & 0.10932 & 0.08199 \\ 0.01948 & 0.09773 & 0.02437 & 0.12863 & 0.05131 & 0.03848 \\ 0.01889 & 0.12863 & 0.05708 & 0.22509 & 0.08018 & 0.06013 \end{bmatrix} \end{array}$$

Equation (20) yields

$$B_{i,j}^{(2+)} = \sum_{i_2,j_1} C_{(i,i_2),(j_1,j)}$$

from which entries of matrix $\mathbf{B}^{(2+)}$ can be calculated

$$\mathbf{B}^{(2+)} = \begin{bmatrix} 0.21141 & 0.13947 & 0.53235 \\ 0.20935 & 0.13946 & 0.51369 \\ 0.21294 & 0.13698 & 0.58008 \end{bmatrix}$$

The absorption factor matrix is given by

$$\mathbf{B} = \mathbf{B}^{(1)} + \mathbf{B}^{(2+)} = \begin{bmatrix} 0.21141 & 0.15624 & 0.63235 \\ 0.23435 & 0.13946 & 0.62619 \\ 0.25294 & 0.16698 & 0.58008 \end{bmatrix}$$

The total exchange areas are related to the absorption factors according to

$$\overline{S_iS_j} = \epsilon_i A_i B_{i,j}$$

and hence the total exchange area matrix is represented by:

$$\overline{SS} = \begin{bmatrix} 0.06342 & 0.04687 & 0.18971 \\ 0.04687 & 0.02789 & 0.12524 \\ 0.18971 & 0.12524 & 0.43506 \end{bmatrix}$$

It is interesting to note that the entries of the above matrix are identical to the results given in [7].

The above example shows that the present stochastic approach provides a one-bounce solution exactly the same as that obtained earlier by Bobco [7]. However, Bobco's solution was restricted to the case of one bounce of energy bundles, while the present stochastic approach can improve the solution accuracy by considering two or three bounces of the energy bundles if the associated mean bidirectional reflectances are available. Furthermore, the existing method requires mean bidirectional reflectance ($\bar{r}_{i,j,k}$) as an input. As mentioned earlier, this requires evaluation of multiple integrations which is not preferable.

In the next example, the concept of mean bidirectional reflectance is abandoned; instead, the Monte Carlo method is employed. Consider an enclosure consisting of two infinitely long parallel plates, shown in Fig. 5. The radiative properties of the two plates are the same and their width is equal to the separation distance. The emissivities of the participating surfaces are diffuse and their bidirectional total reflectivities are shown in Fig. 6. Analogous to the idea of decomposition of radiation reflected by an oxidized brass sample into a specular component and a diffuse component ($\rho = \rho^d + \rho^s$) [5], we subdivide the bidirectional reflectivity into two components, diffuse and back-scattering components ($\rho = \rho^d + \rho^c$) as shown in Fig. 6.

The numerical values of emissivity and reflectivity components of the surfaces are given by

$$\epsilon_1 = \epsilon_2 = 0.1$$
$$\rho_1^d = \rho_2^d = 0.5$$
$$\rho_1^c = \rho_2^c = 0.4$$

We first employ the stochastic 2 model, i.e., the absorption factor is expressed by equation (21). A computer program which uses the Monte Carlo method for determination of one bounce of energy bundles is developed. This program uses 1000 random sampling and determines $N_{(i_1, i_2)}$ and $N_{(i_1, i_2, i_3)}$. Here $N_{(i_1, i_2)}$ is the number of energy bundles emitted from surface i_1 and reaching surface i_2, and $N_{(i_1, i_2, i_3)}$ is the number of energy bundles emitted from surface i_1, reflected from surface i_2 and finally reaching surface i_3. Using equation (7) we obtain

$$\mathbf{B}^{(1)} = \begin{bmatrix} 0 & 0.03900 & 0.61000 \\ 0.03900 & 0 & 0.61000 \\ 0.02935 & 0.02935 & 0.41300 \end{bmatrix} \qquad (25)$$

Since the participating surfaces emit diffusely, the elements of the above matrix are identical to $F_{i,j}\alpha_j$. The small difference between elements of the matrix in equation (25) and $F_{i,j}\alpha_j$ is due to the statistical errors associated with the Monte Carlo method.

Using equations (13) and (14) the following is obtained

$$\mathbf{Q} = \begin{bmatrix} 0.35100 & 0 & 0 & 0 & 0 & 0 \\ 0 & 0 & 0 & 0 & 0 & 0 \\ 0 & 0 & 0.35100 & 0 & 0 & 0 \\ 0 & 0 & 0 & 0 & 0 & 0 \\ 0 & 0 & 0 & 0 & 0.26415 & 0 \\ 0 & 0 & 0 & 0 & 0 & 0.26415 \end{bmatrix}$$

The transition probability matrix based on equation (16) is

$$\mathbf{P} = \begin{bmatrix} 0 & 0 & 0.67179 & 0.32821 & 0 & 0 \\ 0 & 1.00000 & 0 & 0 & 0 & 0 \\ 0.67179 & 0.32821 & 0 & 0 & 0 & 0 \\ 0 & 0 & 0 & 1.00000 & 0 & 0 \\ 0.23509 & 0.76491 & 0 & 0 & 0 & 0 \\ 0 & 0 & 0.23509 & 0.76491 & 0 & 0 \end{bmatrix}$$

The absorptivity matrix **A** is given by

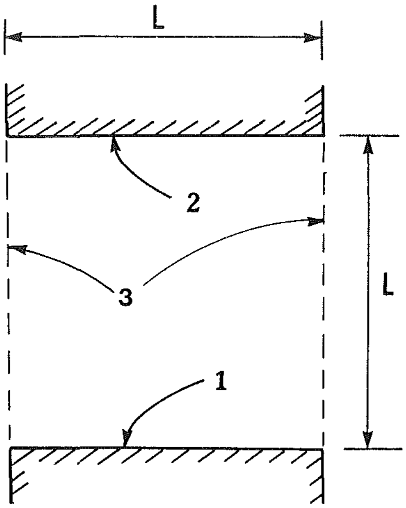

Fig. 5 Two infinitely long parallel plates

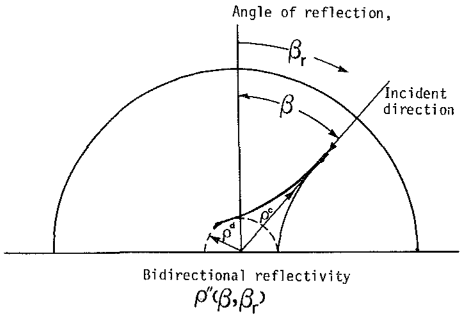

Fig. 6 Decomposition of bidirectional reflectivity distribution into diffuse and strictly directional components

$$\mathbf{A} = \begin{bmatrix} 0.1 & & & & 0 & \\ & 1 & & & & \\ & & 0.1 & & & \\ & & & 1 & & \\ & 0 & & & 0.1 & \\ & & & & & 0.1 \end{bmatrix}$$

and $\mathbf{R} = \mathbf{I} - \mathbf{A}$.

Substituting for **Q**, **P**, **R**, and **A** into equation (19) yields

$$\mathbf{C} = \begin{bmatrix} 0.02247 & 0.10978 & 0.03717 & 0.18158 & 0 & 0 \\ 0 & 0 & 0 & 0 & 0 & 0 \\ 0.03717 & 0.18158 & 0.02247 & 0.10978 & 0 & 0 \\ 0. & 0 & 0 & 0 & 0 & 0 \\ 0.00979 & 0.21953 & 0.00592 & 0.02891 & 0 & 0 \\ 0.00592 & 0.02891 & 0.00979 & 0.21953 & 0 & 0 \end{bmatrix}$$

From equation (20) we obtain

$$\mathbf{B}^{(2+)} = \begin{bmatrix} 0.03717 & 0.02247 & 0.29136 \\ 0.02247 & 0.03717 & 0.29136 \\ 0.01571 & 0.01571 & 0.49689 \end{bmatrix}$$

The absorption factor matrix for this case is

$$\mathbf{B}=\mathbf{B}^{(1)}+\mathbf{B}^{(2+)}=\begin{bmatrix}0.03717 & 0.06147 & 0.90136\\ 0.06147 & 0.03717 & 0.90136\\ 0.04506 & 0.04506 & 0.90989\end{bmatrix}.$$

In the above calculations the Monte Carlo method is used to determine the destination of energy bundles after one reflection in each dispatch. In the regular Monte Carlo method for the reflectivity of 0.9, the expected number of bounces before the energy bundle is absorbed is ten. Hence, ten bidirectional reflections have to be evaluated by the random sampling which requires considerable effort.

To check the computer program developed for the above calculations it is assumed that the participating surfaces reflect diffusely. The resulting absorption factors based on this assumption are found to be close to those obtained for the diffuse surfaces [6] (0.05 percent difference in $B_{1,3}$).

Another computer program based on the stochastic 3 model and Monte Carlo method for determination of two bounces of energy bundles was developed. The calculated absorption factor matrix based on this model is

$$\mathbf{B}=\mathbf{B}^{(1)}+\mathbf{B}^{(2)}+\mathbf{B}^{(3+)}=\begin{bmatrix}0.03788 & 0.06400 & 0.89812\\ 0.06400 & 0.03788 & 0.89812\\ 0.04244 & 0.04244 & 0.91512\end{bmatrix}$$

It would be expected that the stochastic 3 model provides better accuracy as compared to the stochastic 2 model. However, since the statistical errors involved in the use of the Monte Carlo method in stochastic 3 model are larger than that of stochastic 2 model, higher stochastic model does not guarantee better accuracy. To demonstrate this point the aformentioned programs are used to calculate the absorption factors of the enclosure when participating surfaces reflect diffusely, i.e., $\rho_1^d = \rho_2^d = 0.9$ and $\rho_1^c = \rho_2^c = 0$. This is a limiting case for which the exact solution exists [6]. Our numerical computations show that the average error in the resulting absorption factors using the stochastic 2 model is 1.7 percent while using the stochastic 3 model it is 2.3 percent.

It is believed that the stochastic 2 model provides the best accuracy since the Monte Carlo method is used to evaluate only one bidirectional reflection; therefore, the statistical errors involved are smaller than those of stochastic 3 model. The use of a higher order stochastic model is not justifiable because it introduces additional statistical error in calculating transition probabilities by Monte Carlo method. The present approach depends less on the random number generator and consequently provides more accurate results with less computer time as compared to the direct Monte Carlo method.

Conclusion

The stochastic method which was developed in [6] is extended to the analysis of radiative transfer in enclosures with directional-bidirectional surfaces and transparent media. Several numerical examples have been presented to demonstrate the usefulness of this technique. It has been shown that the present method yields results identical to those presented in the literature [7] if the idea of bidirectional reflectivity is used, which may not be readily available for most cases. The absorption factor $B_{i,j}$ obtained can be used to calculate other heat transfer parameters of the enclosures. Some other commonly used radiation variables such as Hottel's total exchange area, S_iS_j, and Bobco's $\mathfrak{F}_{i,j}$ can be obtained from the relationships

$$\overline{S_iS_j}=\epsilon_i\, A_i\, B_{i,j} \text{ and } \mathfrak{F}_{i,j}=\epsilon_i\, B_{i,j}$$

The resulting absorption factors obtained from the present scheme automatically satisfy the following relations

$$\sum_{j=1}^{n} B_{i,j}\approx 1 \text{ and } A_i\,\epsilon_i\,B_{i,j}\approx A_j\,\epsilon_j B_{j,i}$$

Two sides of these expressions are approximately equal instead of being identical because of the statistical errors involved in the Monte Carlo method for calculating the transition probabilities. In the example considered in this paper, the two sides of these equations are very close to each other (at most 0.02 percent relative difference between two sides). Usually, the directional components of reflectivities ρ^c are less than 0.5; therefore, the assumption of $l = 2$ yields a reasonable approximation from engineering point of view. Unlike the case involving an enclosure with specular surfaces [6] the accuracy of the results is not necessarily improved by using higher order stochastic models.

It should be noted that the use of the Monte Carlo method in this procedure is restricted to the calculation of transition probabilities only. Furthermore, the method is used only for one or two bounces of the energy bundles. It is therefore expected that the statistical errors involved in the calculations of this approach are much smaller than those of direct Monte Carlo technique in which many consecutive bounces of the energy bundles are evaluated. However, the statistical errors of stochastic models 2 and 3 caused by the Monte Carlo method could be reduced by using the linear regression technique to smooth away the departure from conservation [14].

The application of this stochastic method can be extended to enclosures with absorbing-emitting and anisotropically scattering medium. A preliminary work on the application of the stochastic approach to enclosures with participating medium is reported in [15].

Acknowledgments

The support of the National Science Foundation under the grant MEA-8314478 is gratefully acknowledged.

References

1 Gebhart, B., "Unified Treatment for Thermal Radiation Transfer Process—Gray, Diffuse Radiators and Absorbers," ASME Paper No. 57-A-34, Dec. 1957.

2 Sparrow, E. M., Eckert, E. R. G., and Jonsson, V. K., "An Enclosure Theory for Radiative Exchange Between Specularly and Diffusely Reflecting Surfaces," ASME JOURNAL OF HEAT TRANSFER, Vol. 84, 1962, pp. 294–300.

3 Bobco, R. P., "Radiation Heat Transfer in Semigray Enclosures With Specularly and Diffusely Reflecting Surfaces," ASME JOURNAL OF HEAT TRANSFER, Vol. 86, 1964, pp. 123–130.

4 Bevans, J. T., and Edwards, D. K., "Radiative Exchange in an Enclosure With Directional Wall Properties," ASME JOURNAL OF HEAT TRANSFER, Vol. 87, 1965, pp. 388–396.

5 Sarofim, A. F., and Hottel, H. C., "Radiative Exchange Among Non-Lambert Surfaces," ASME JOURNAL OF HEAT TRANSFER, Vol. 88, 1966, pp. 37–44.

6 Naraghi, M. H. N., and Chung, B. T. F., "A Stochastic Approach for Radiative Exchange in Enclosures With Non-participating Medium," ASME JOURNAL OF HEAT TRANSFER, Vol. 106, 1984, pp. 690–698.

7 Bobco, R. P., "A script-F Matrix Formulation for Enclosures With Arbitrary Surface Emission and Reflection Characteristics," ASME JOURNAL OF HEAT TRANSFER, Vol. 93, 1971, pp. 33–40.

8 Toor, J. S., and Viskanta, R., "A Numerical Experiment of Radiant Heat Interchange by the Monte Carlo Method," *International Journal of Heat and Mass Transfer*, Vol. 2, 1968, pp. 883–897.

9 Weiner, M. M., Tindall, J. W., and Candell, L. M., "Radiative Interchange Factors by Monte Carlo," ASME Paper No., 65-WA/HT-51, Nov. 1965.

10 Naraghi, M. H. N., "A Stochastic Approach for Radiative Exchange in Enclosures," Ph.D. Dissertation, Department of Mechanical Engineering, The University of Akron, 1984.

11 Doob, J., *Stochastic Processes*, Wiley, New York, 1953.

12 Cinlar, E., *Introduction to Stochastic Processes*, Prentice-Hall, New York, 1975.

13 Siegel, R., and Howell, J. R., *Thermal Radiation Heat Transfer*, 2nd ed., McGraw-Hill, New York, 1980, p. 371.

14 Vercammen, H. A. J., and Froment, G. F., "An Improved Zone Method Using Monte Carlo Techniques for the Simulation of Radiation in Industrial Furnaces," *International Journal of Heat and Mass Transfer*, Vol. 23, 1980, pp. 329–336.

15 Naraghi, M. H. N., and Chung, B. T. F., "A Unified Matrix Formulation for the Zone Method: Stochastic Approach," *International Journal of Heat and Mass Transfer*, Vol. 28, 1985, pp. 245–251.

M. P. Mengüç[1]

R. Viskanta
Fellow ASME

Heat Transfer Laboratory,
School of Mechanical Engineering,
Purdue University,
West Lafayette, IN 47907

Radiative Transfer in Axisymmetric, Finite Cylindrical Enclosures

A solution of the radiative transfer equation for an axisymmetric cylindrical enclosure containing radiatively participating gases and particles is presented. Nonhomogeneities of the radiative properties of the medium as well as of the radiation characteristics of the boundaries are allowed for, and the boundaries are assumed to be diffusely emitting and reflecting. The scattering phase function is represented by the delta-Eddington approximation to account for highly forward scattering by particulates. The model for radiative transfer is based on the P_1 *and* P_3*-spherical harmonics approximations. Numerical solutions of model equations are obtained using finite-difference as well as finite-element schemes.*

1 Introduction

In order to predict the thermal performance of practical systems such as furnaces, boilers, combustion chambers, and gas turbine combustors, the radiative heat transfer must be modeled properly. Many of these systems can be considered as finite-length cylindrical enclosures. Therefore, it is desirable to have an accurate and reliable model for solving the radiative transfer equation (RTE) for finite cylindrical geometries containing radiation participating media. This model should also be compatible with finite-difference methods required to solve the transport equations.

Cylindrical enclosures have one advantage in that for practical purposes they may be considered to be axisymmetric. As a result, the RTE is to be solved in two dimensions, rather than three. However, most of the studies reported in the literature are for one-dimensional, infinite cylindrical geometries (see [1] for an extensive literature survey). For multidimensional geometries, an up-to-date literature review has been published recently [2]. Here, only some of the more relevant studies are mentioned.

Some exact analytical expressions for radiative transfer in an absorbing, emitting medium in finite and infinitely long cylinders [3] and an absorbing, emitting, scattering, axially finite but radially infinite medium are available [4]. However, the analyses are not appropriate for a general combustion chamber. The Monte Carlo method [5, 6] and the zonal analysis [7, 8] may also yield acceptable predictions for radiative heat flux distributions in a cylindrical enclosure. Unfortunately, these methods are not compatible with the finite-difference equations for solving the transport equations with reasonable computational time and effort. An attempt to combine the zone method with the energy equation using average values has been made [8]; however, because of the averaging process the physical insight into the problem may be lost, and also the method can not be adapted to a scattering medium.

In the literature, some approximations such as first-order spherical harmonics (P_1) [9, 10], the two-flux model based on P_1 [11], discrete ordinates [12], and hybrid discrete transfer [13] methods have been reported. Applications and comparisons for some of the RTE models to practical systems have been discussed [14]. If the radiation field is anisotropic and if highly forward scattering particles are present in the medium, higher order approximations are required, and the scattering phase function must be properly approximated. In only one of these studies a linearly anisotropic scattering approximation of the medium was considered [12].

Recently, the third-order spherical harmonics (P_3) approximation has been formulated and solved for a three-dimensional rectangular enclosure containing absorbing, emitting, and highly anisotropic scattering inhomogeneous medium [15]. It has been shown that the P_3 approximation is elegant, reliable, easy to use, and can be readily combined with finite-difference equations for determining the flow and temperature fields. In this paper the formulation of P_1 and P_3 approximations are given for a two-dimensional axisymmetric cylindrical enclosure. The scattering phase function is modeled by the delta-Eddington approximation [16], which is capable of simulating the highly anisotropic scattering by the particles. The main purpose of this paper is to present methodology for solving the RTE in axisymmetric, finite-length cylindrical enclosures.

2 Analysis

2.1 Formulation. For an absorbing, emitting, and anisotropically scattering gas-particle mixture in local thermodynamic equilibrium, the time-independent spectral RTE for two-dimensional axisymmetric cylindrical enclosures is given by [17]

$$\left[\frac{1}{\beta}\left(\xi\frac{\partial}{\partial r}-\eta\frac{1}{r}\frac{\partial}{\partial\phi}+\mu\frac{\partial}{\partial z}\right)+1\right]I(r, z, \theta, \phi) = (1-\omega)I_b[T(r, z)]$$

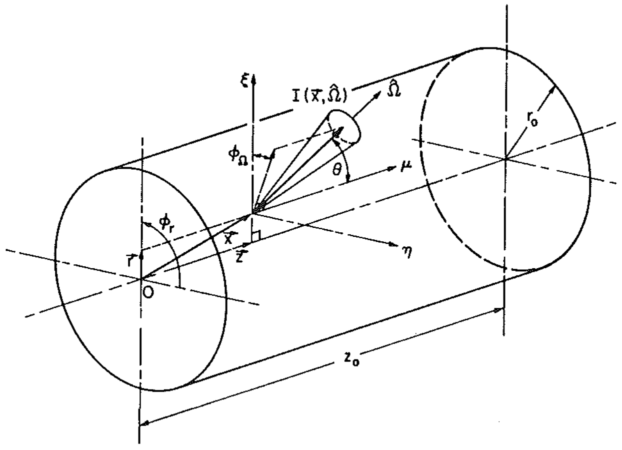

Fig. 1 Coordinate system for a cylindrical enclosure

---

[1] Present address: Department of Mechanical Engineering, University of Kentucky, Lexington, KY 40506

Contributed by the Heat Transfer Division and presented at the ASME Winter Annual Meeting, New Orleans, Louisiana, December 9-13, 1984. Manuscript received by the Heat Transfer Division February 11, 1985.

$$+\frac{\omega}{4\pi}\int_0^{2\pi}\int_0^{\pi} I(r, z, \theta, \phi)\Phi(\theta, \phi, \theta', \phi') \sin\theta' d\theta' d\phi' \qquad (1)$$

The subscript λ denoting spectral quantities in the RTE has been left off for the sake of clarity, but it is implied. In this equation ϕ corresponds to the difference of the azimuthal angles $\phi = \phi_\Omega - \phi_r$ (see Fig. 1). The direction cosines are given by

$$\xi = \cos\phi \sin\theta, \ \eta = \sin\phi \sin\theta, \ \mu = \cos\theta \qquad (2)$$

The delta-Eddington approximation for the phase function Φ is written as

$$\Phi(\theta, \phi, \theta', \phi') = 2f\delta(1 - \cos\psi) + (1 - f)(1 + 3g\cos\psi) \qquad (3)$$

where ψ is the scattering angle

$$\cos\psi = \xi\xi' + \eta\eta' + \mu\mu' \qquad (4)$$

and f and g are the parameters related to the coefficient of Legendre series expansion of the scattering phase function Φ [15, 16]. By using the moments of the intensity, and after the normalizations, the RTE equation (1) can be written as

$$\left[\xi \frac{\partial}{\tau_0 \partial \bar{r}} - \eta \frac{1}{\tau_0 \bar{r}} \frac{\partial}{\partial \phi} + \mu \frac{\partial}{\tau_0 \partial \bar{z}} + 1\right] I(\bar{r}, \bar{z}, \theta)$$

$$= (1 - \omega_0) I_b[T(\bar{r}, \bar{z})] + \frac{\omega_0}{4\pi}\left[I_0 + 3g(\xi I_1 + \eta I_2 + \mu I_3)\right] \qquad (5)$$

Note that the dependence of I on the azimuthal angle ϕ has been retained. It will be eliminated later by performing the necessary integrations over appropriate directions. In writing equation (5) some steps and details of the spherical harmonics method have been omitted since they have already been reported elsewhere [15, 18, 19]. The moments of intensity are defined as

$$\begin{aligned} I_0(r, z) &= \int_0^{2\pi}\int_0^{\pi} I(r, z, \theta, \phi) \sin\theta d\theta d\phi \\ I_{ij\,..\,k}(r, z) &= \int_0^{2\pi}\int_0^{\pi} (l_i l_j \,..\, l_k) I(r, z, \theta, \phi) \sin\theta d\theta d\phi \end{aligned} \qquad (6)$$

where l_i, l_j, l_k are direction cosines and each of them is either ξ, η, or μ [see equation (2)].

The intensity distribution in the medium is given in terms of the moments [15]. Note that in axisymmetric cylindrical enclosures the same intensity distribution reported for three-dimensional rectangular enclosures [15] can be adapted by introducing the following relations (for $i, j \neq 2$)

$$I_2 = I_{222} = I_{ij2} = 0, \ I_{22} = I_0 - I_{11} - I_{33} \qquad (7)$$

2.2 Governing Equations. In obtaining the model equations in terms of the moments of intensity, the following operation is employed

$$\int_{\phi=0}^{2\pi}\int_{\theta=0}^{\pi} [\text{equation (5)}]\, Y_n^{m*}(\theta, \phi) \sin\theta d\theta d\phi \qquad (8)$$

for $n = 0, 1, \ldots N$ and $m = -n, -n+1, \ldots n$, where N is the order of the P_N approximation. In this operation, the functions Y_n^{m*}, i.e., the complex conjugate of spherical harmonics [19], can be easily replaced with the appropriate multiples of direction cosines. This yields a single partial differential equation for the P_1 approximation

$$\left[\Gamma_{rr} + \Gamma_{zz} + \frac{1}{\bar{r}}\Gamma_r\right] I_0 = A_0 G(\bar{r}, \bar{z}) \qquad (9)$$

If the temperature distribution in a gray medium is specified the source term G can be expressed as

$$G(\bar{r}, \bar{z}) = 4\pi I_b[T(\bar{r}, \bar{z})] - I_0(\bar{r}, \bar{z}) = \frac{S r_0}{\tau_0(1 - \omega_0)} \qquad (10)$$

The coefficient A_0 is given by

$$A_0 = 3(1 - \omega_0)(1 - \omega_0 g)\tau_0^2 \qquad (11)$$

and the Γ operators are defined as

$$\Gamma_i = \frac{\partial}{\partial x_i}, \ \Gamma_{ij} = \frac{\partial^2}{\partial x_i \partial x_j} \qquad (12)$$

where x_i is either $\bar{r}$ $(i = 1)$ or $\bar{z}$ $(i = 3)$.

For the P_3 approximation, after some manipulations, four elliptic partial differential equations are obtained in terms of I_0, I_{11}, I_{33}, and I_{13}, moments such that

$$\left[\frac{4}{5}\Gamma_{rr} + \frac{4}{5}\Gamma_{zz} - B_1 \frac{1}{\bar{r}}\Gamma_r - \left(2\frac{B_2}{\bar{r}^2} + \frac{14}{3}\tau_0^2\right)\right] I_0$$

$$= -\frac{7}{3}\tau_0^2(1 - \omega_0) G(\bar{r}, \bar{z}) + A_1(\bar{r}, \bar{z}) \qquad (13)$$

Nomenclature

A_i = functions in equations (13)-(16)
B = coefficients of moment equations, equations (13)-(16)
f = scattering phase function parameter, equation (3)
g = scattering phase function parameter, equation (3)
G = normalized source term, equation (10)
h = boundary intensities, equation (22)
I = intensity
I_b = Planck's blackbody function
I_i = moments defined by equation (6)
$\bar{q}^r$ = radiative heat flux vector
r = radial coordinate
r_0 = radius of a cylindrical enclosure, see Fig. 1
S = volumetric source term, equation (10)
x = point on any boundary
Y_n^m = spherical harmonics
Y_n^{m*} = complex conjugate of spherical harmonics
z = axial coordinate
z_0 = length of a cylindrical enclosure, see Fig. 1
β = extinction coefficient
δ_{i1} = Kronecker delta function
ϵ = emissivity
κ = absorption coefficient
ω = single scattering albedo $= 1 - (\kappa/\beta)$
ω_0 = normalized albedo $= (1 - f)\omega/(1 - f\omega)$
ϕ = azimuthal angle, see Fig. 1
ρ = reflectivity
σ = Stefan-Boltzmann constant
τ_0 = normalized optical radius $= \beta(1 - f\omega)r_0$
θ = polar angle, see Fig. 1
Γ = differential operators, equation (12)
Ω = solid angle, see Fig. 1
Φ = scattering phase function, equation (3)
ψ = scattering angle, equation (4)

Superscripts

d = refers to diffuse reflectivity
i = refers to incident intensity or flux
$\bar{}$ = refers to normalized coordinates, equation (5)

Subscripts

b = refers to blackbody
w = refers to wall properties
0 = refers to zeroth movement
1, 2, 3 = refers to corresponding moments

Table 1 Moments for the boundary equations, see equation (21)

Moments of intensity	$\bar r$	$\bar z$
I_0	$\xi - \xi^3 - \xi\mu^2$	$\mu - \xi^2\mu - \mu^3$
I_{11}	ξ^3	$\xi^2\mu$
I_{33}	$\xi\mu^2$	μ^3
I_{13}	$\xi^2\mu$	$\xi\mu^2$

$$\left[3B_6\Gamma_{rr} + \Gamma_{zz} + B_7 \frac{1}{\bar r}\,\Gamma_r - \left(4\,\frac{B_4}{\bar r^2} + 7\tau_0^2\right)\right] I_{11}$$

$$= -\frac{7}{3}\,\tau_0^2(1-\omega_0)G(\bar r, \bar z) + A_2(\bar r, \bar z) \tag{14}$$

$$\left[\Gamma_{rr} + 3B_6\Gamma_{zz} + B_6 \frac{1}{\bar r}\Gamma_r - 7\tau_0^2\right] I_{33}$$

$$= -\frac{7}{3}\tau_0^2(1-\omega_0)G(\bar r, \bar z) + A_3(\bar r, \bar z) \tag{15}$$

$$\left[B_2\Gamma_{rr} + B_2\Gamma_{zz} - B_2 \frac{1}{\bar r}\,\Gamma_r\right.$$

$$\left. - \left(\frac{B_2}{\bar r^2} + 7\,\frac{\tau_0}{\bar r}\right)\right] I_{13} = A_4(\bar r, \bar z) \tag{16}$$

The functions A and the coefficients B are given in Appendix A. These four equations are to be solved simultaneously, which means that an iterative scheme must be employed to obtain the solution for the four moments of the intensity. Afterwards, the other moments are obtained by using relations between the moments of intensity and the intensity [15].

The divergence of the radiative flux in the medium is given by the conservation of radiant energy equation

$$\int_{\lambda=0}^{\infty} \nabla \cdot \mathbf{q}_\lambda d\lambda = \nabla \cdot \mathbf{q} = S(\bar r, \bar z) \tag{17}$$

where S is the net volumetric rate of radiant energy emission or absorption in the medium and is defined by equation (10). Using the first moment of intensity, the radiative flux distribution can be expressed as

$$\bar q_i(\bar r, \bar z) = I_i(\bar r, \bar z) \tag{18}$$

where i is either 1 ($=\bar r$ direction) or 3 ($=\bar z$ direction). For the P_1 approximation, I_i is given in terms of the zeroth order of moment

$$I_i(\bar r, \bar z) = -\frac{1}{3\tau_0(1-\omega_0 g)}\,\Gamma_i(I_0) \tag{19}$$

For the P_3 approximation, it can be expressed as

$$I_i(\bar r, \bar z) = -\frac{1}{\tau_0(1-\omega_0 g)}\,\left[\Gamma_i(I_{ii}) + \Gamma_j(I_{ij})\right.$$

$$\left. -\frac{\delta_{i1}}{\bar r}\,(I_0 - I_{11} - I_{33})\right] \tag{20}$$

where δ_{i1} is the Kronecker delta function.

2.3 Boundary Conditions. There are two different type of boundary conditions, namely, Mark's and Marshak's, which are to be used with the spherical harmonics approximations [17-19]. For the lower order approximations, such as P_1 or P_3, Marshak's boundary condition is preferable over Mark's and is obtained by taking the integral of the intensity over the appropriate hemispheres such that

$$\int_{2\pi} I(x_w, \Omega) Y_{2n-1}^m(\Omega) d\Omega = \int_{2\pi} h_w(x_w, \Omega) Y_{2n-1}^m(\Omega) d\Omega \tag{21}$$

where Y_{2n-1}^m are spherical harmonics, and $n = 1, 2, \ldots, (N+1)/2$, and $-2n+1 \le m \le 2n+1$. Here, h_w corresponds to the intensity at a diffusely emitting and reflecting opaque boundary and is given by

$$h_w(\bar x_w, \Omega) = \epsilon_w I_b(T_w) + \rho_w^d\, I^i\,(x_w, \Omega) \tag{22}$$

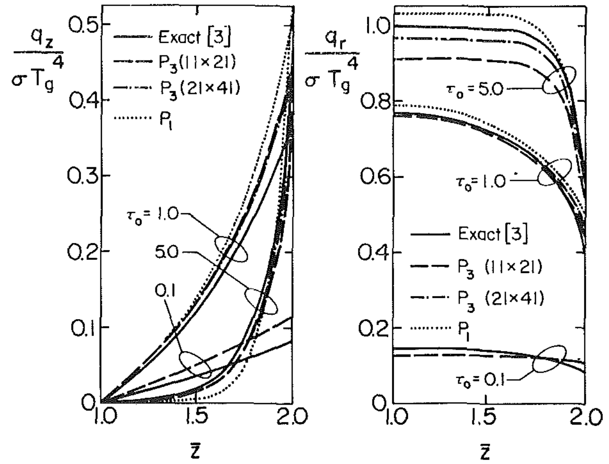

Fig. 2 Comparison of P_1 and P_3 approximation results with exact numerical results [3] for different optical radii, at $\bar r = 1$: $T_w = 0$, $\epsilon_w = 1$, $r_0 = 1$ m, $z_0 = 2$ m

The explicit forms of the boundary conditions at the walls required for an axisymmetric enclosure are similar to the expressions for a rectangular enclosure [15]. Therefore, they are not repeated here. At the centerline the symmetry conditions are used. The appropriate moments for boundary equations are listed in Table 1. It is worth noting that the multiplying factor for zeroth movement I_0 is obtained from the second relation given by equation (7). The other multiplying factors are similar to those used before [15].

2.4 Method of Solution. The governing equations, equation (9) for the P_1 approximation, and equations (13)-(16) for the P_3 approximation, are elliptic, linear partial differential equations. It is possible to solve the P_1 approximation equation analytically after some simplifying assumptions (see, e.g., [9, 10, 20]). However, if the source or temperature distribution in the medium and of the boundaries are nonuniform and if the radiative properties are nonhomogeneous, which is the case for practical systems, then an exact analytical solution is not possible. No analytical solution appears to be available for solving the four P_3 approximation equations simultaneously. Therefore, all of the results reported in this paper have been obtained numerically, either by a finite difference or a finite element scheme using a general computer code ELLPACK [21]. This code has been successfully employed in obtaining the numerical results for three-dimensional rectangular enclosures [15].

The results obtained for the P_1 approximation can be used to initiate the P_3 approximation solution, and equations (13)-(16) are solved simultaneously. The numerical results for the heat flux distributions are compared with the results for the previous iteration. When a predetermined convergence criterion is satisfied, the iteration is terminated. In the numerical calculations the mixed moment, i.e., I_{13} equation (16), has been left out of the solution scheme by assuming that $I_{13} \doteq 0$ everywhere in the medium. The main reason for this is the numerical instability caused by the double first-order derivatives of I_{13} moment in the governing equations near the singularity at $\bar r = 0$. Unless a more stable numerical scheme is developed, the solution for the I_{13} moment does not appear to be warranted as it improves the results little.

3 Results and Discussion

The predictions based on the P_1 and P_3 approximations for a finite cylindrical, black wall enclosure containing an absorbing and emitting medium are compared with the "exact"

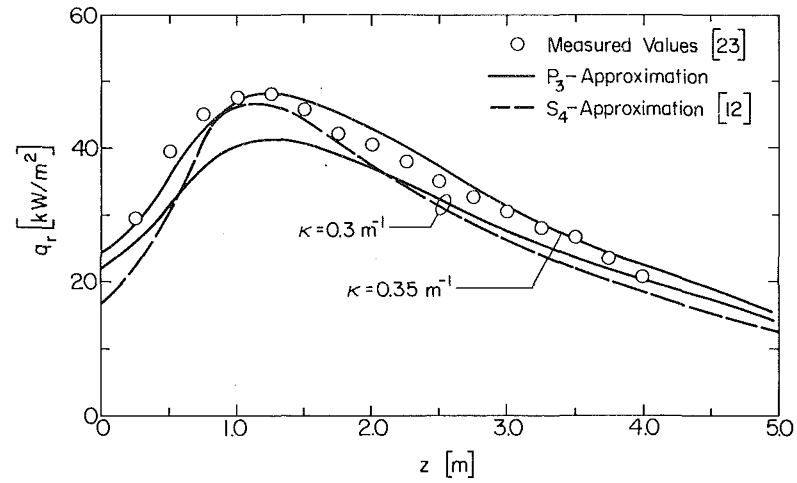

Fig. 3 Comparison of local radiative fluxes at the wall ($\bar{r} = 1$) based on P_3 approximation results for a combustion chamber with experimental data [23] and discrete ordinates model [12]: $r_0 = 0.45$ m, $z_0 = 5.1$ m

numerical results [3] in Fig. 2. The normalized heat fluxes obtained from the P_3 approximation in the axial and radial directions are generally in good agreement with those based on the exact analysis. By doubling the number of grid points, a slight increase in the radiative fluxes was obtained. Note that if the optical radius of the medium is large, then the finer grid scheme yields more accurate predictions. The finite element solutions of the P_3 approximation for $\tau_0 = 1.0$ and 5.0 were not distinguishable from the exact results. On the other hand, for $\tau_0 = 0.1$, both finite-element and finite-difference schemes gave the same numerical values for the wall heat fluxes.

All of the P_1 approximation results shown in Fig. 2 were obtained by the finite-element scheme. For the thin medium, i.e., $\tau_0 = 0.1$, the P_1 predictions were identical to those of the P_3 approximation. However, for $\tau_0 = 5.0$, it overpredicted the normalized heat fluxes and yielded values greater than unity near $z = 0$. The same unrealistic behavior of the P_1 approximation was also observed in a one-dimensional planar medium [22].

The P_3 approximation predictions are compared with the experimental data in Fig. 3 for a water-cooled cylindrical furnace [23]. The cylindrical walls are taken to be at a temperature of 425 K and to have an emissivity of 0.8. The end walls are at 300 K and are assumed to be black. The gray absorption coefficient is assumed to be 0.3 m^{-1} [12], and the temperature distribution in the medium is specified. The results based on the P_3 approximation shown in Fig. 3 follow the same trend as the data. The model predicts the location of peak heat flux accurately; however, the magnitude is underpredicted. Comparison of the results with the S_4-discrete ordinates approximation shows that, except near the peak heat flux, the P_3 approximation predictions are close to the results based on the S_4 method [12]. The difference between the experimental data and the P_3 results is at most 15 percent. It is believed that this deviation is mainly because of the small optical radius of the medium ($\tau_0 = 0.135$ in the radial direction). It was pointed out before that the P_3 approximation yields accurate results if the optical thickness of the medium is greater than or on the order of unity [15, 24]. Note that these calculations were performed by assuming that the gas absorption coefficient was temperature independent and constant throughout the medium. Indeed, it is difficult to justify this assumption physically, and also it is difficult to imagine how a single valued absorption coefficient can be chosen to model a real furnace. In order to examine the sensitivity of the P_3 approximation predictions to the gray absorption coefficient, calculations were also performed for $\kappa = 0.35$ m^{-1}. As seen from Fig. 3, this yielded, in general, better agreement with the data.

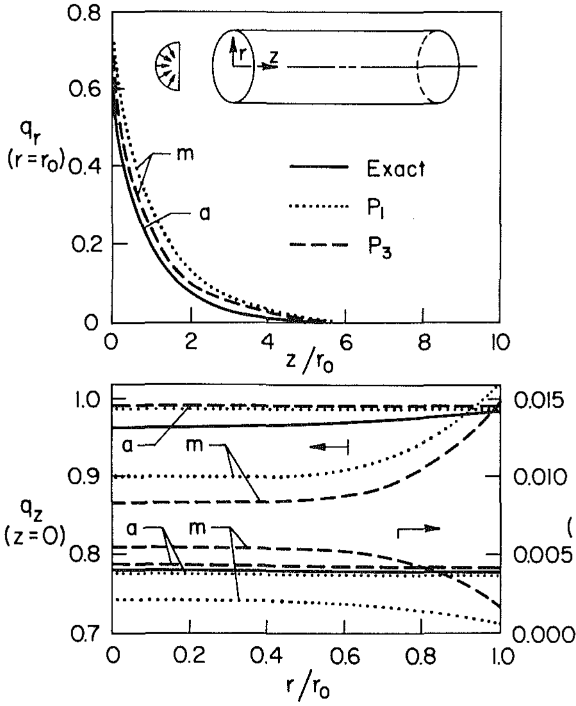

Fig. 4 Comparison of P_1 and P_3 approximation results with exact benchmark solution [25]: $r_0 = 0.1$ m, $z_0 = 1.0$ m, $\beta = 1.0$ m^{-1}, $\omega = 0.5$, $T_w = 0$, $\epsilon_w = 1$ (*m* refers to Marshak's boundary conditions, *a* refers to analytical boundary conditions).

In pulverized coal-fired furnaces the contribution of scattering particles to the radiative heat transfer is very important and must be accounted for. Therefore, it is desirable to evaluate the accuracy of the model for a scattering medium. Recently, Crosbie and Farrell [25] have obtained benchmark solutions for an isotropically scattering, nonemitting, homogeneous medium in a finite cylindrical enclosure with cold black walls subject to a diffuse radiant flux incident on one end. In Fig. 4, the predictions based on the P_1 and P_3 approximations are compared with the benchmark results. Since the walls are black and cold, it is possible to include the effect of uniform diffuse radiation flux incident on one end of the cylinder using a direct integration method. The corresponding integrals have been solved numerically employing a ten-point

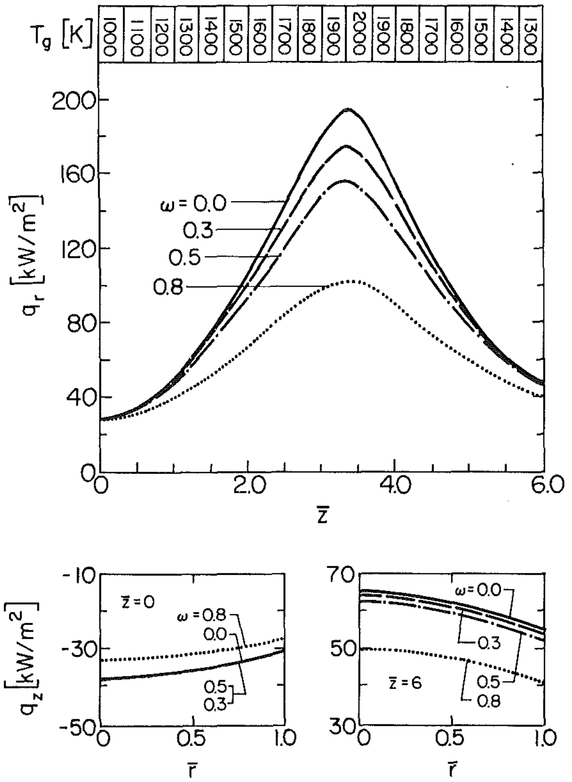

Fig. 5 Effect of scattering on the wall ($\bar{r} = 1.0$) radiative heat flux predictions of the P_3 approximation: $\beta = 1\ \mathrm{m}^{-1}$, $\epsilon_w = 0.7$, $T_w = 500$ K, $r_0 = 1$ m, $z_0 = 6$ m

Gaussian quadrature scheme. Additional numerical results and comparisons with benchmark solutions are available elsewhere [26].

The importance of scattering on the wall heat fluxes in a medium with nonuniform temperature distribution is examined in Fig. 5. The assumed temperature distribution in the medium as well as the dimensions of the enclosure and the radiative properties are shown on the figure. The radiative heat flux at the walls decreases with increased scattering, and more uniform distributions of the fluxes are obtained. This is expected, since with increasing ω the emission by the medium becomes less important in comparison to multiple scattering [see equation (1)]. Note that the effect of scattering albedo ω on the radial heat flux is more pronounced near the region where the temperature is high. It is clear from Fig. 5 that if scattering in the medium is neglected, the wall heat fluxes would be overpredicted by as much as 50 to 60 percent.

The effect of scattering phase functions (or the type of particles in the medium) on radiative heat flux distribution at the walls is shown in Fig. 6, for the same physical model given in Fig. 5. The parameters f and g [see equation (3a)] of the delta-Eddington phase function model are evaluated from the complete phase functions obtained from Mie theory for three different polydispersions. It is worth noting that the effect of anisotropic scattering on the radiative heat flux distribution at the cylindrical walls is not very critical. However, at the end walls, the change in heat fluxes can be as high as 20 to 40 percent. This small effect of anisotropic scattering by the particles on radiative heat fluxes is due to the cool walls. It is clear that, if the chamber wall temperatures are not much different from each other and not very high, the medium may be assumed isotropically scattering, and this assumption may not cause significant error in radiative heat flux predictions at the side walls. However, when there is a directional anisotropy in the radiative field, which is along the axial direction in this problem, then the effect of highly forward scattering becomes more pronounced in that direction. Because of this, the radiation fluxes calculated at the end walls show dramatic changes for different phase function model parameters.

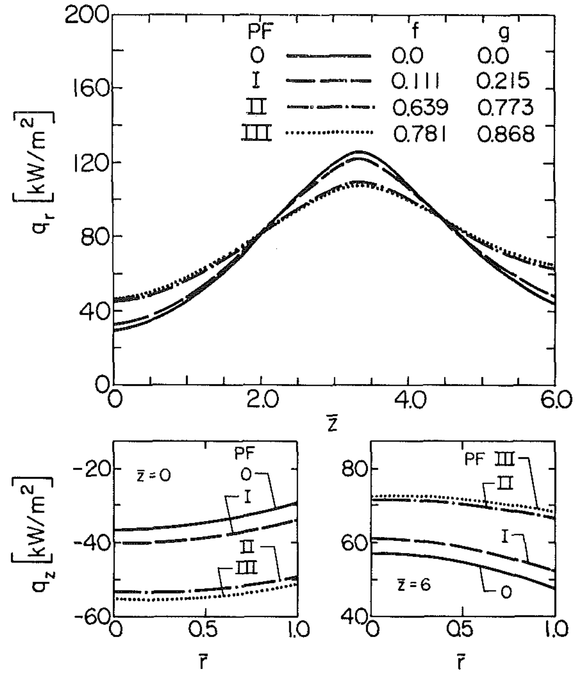

Fig. 6 Effect of scattering phase function on the wall ($\bar{r} = 1.0$) radiative heat flux predictions of the P_3 approximation: $\beta = 1\ \mathrm{m}^{-1}$, $\epsilon_w = 0.7$, $T_w = 500$ K, $r_0 = 1$ m, $z_0 = 6$ m

In the paper only the heat flux distributions at the walls are reported. However, in most engineering applications, the divergence of the radiative flux vector in the medium is required [see equation (17)] for coupling the RTE with the energy equation. Such divergence calculations have been reported for a cylindrical pulverized coal-fired furnace [26].

Most of the results reported in this paper required seven to nine iterations. For an 11 × 21 grid scheme the required CPU time on Vax-11/780 digital computer for a finite difference solution was about 250 s. For the same grid scheme, the solution using a finite element technique was obtained in about 3500 s.

4 Conclusions

A two-dimensional axisymmetric radiative transfer model for an absorbing, emitting, and anisotropically scattering nonhomogeneous medium, based on the third-order spherical harmonics approximation, has been developed. The governing differential equations were solved numerically by finite-difference as well as finite-element techniques. The computer time requirements show that the finite-difference solution of the model can be used successfully for accurate radiative heat flux predictions in combustion chambers. The model is compatible with available algorithms for solving the transport equations. Accounting for the nonhomogeneous radiative properties due to concentration and temperature variations in the medium and anisotropic scattering due to particulates yields more reliable heat transfer predictions by the model.

The P_3 approximation is sufficiently accurate for physical systems for which the optical thickness is greater than or on the order of 0.5 and yields improved radiative flux predictions over the P_1 approximation. It is shown that its accuracy can be further improved by using well-defined boundary relations, instead of Marshak's somewhat arbitrary boundary conditions. Also, when the mixed moment I_{13} is included in the solution scheme, somewhat more accurate predictions would be expected.

Acknowledgments

This work was supported, in part, by CONOCO, Inc. through a grant to the Coal Research Center of Purdue University.

References

1 Crosbie, A. L., and Linsenbardt, T. L., "Two-Dimensional Isotropic Scattering in a Semi-infinite Medium," *Journal of Quantitative Spectroscopy and Radiative Transfer*, Vol. 19, 1978, pp. 257–284.

2 Viskanta, R., "Radiative Heat Transfer," *Fortschritte der Verfahrenstechnik*, Vol. 22, Section A, 1984, pp. 51–81.

3 Dua, S. S., and Cheng, P., "Multi-dimensional Radiative Transfer in Non-isothermal Cylindrical Media with Non-isothermal Bounding Walls," *International Journal of Heat and Mass Transfer*, Vol. 18, 1975, pp. 245–259.

4 Crosbie, A. L., and Dougherty, R. L., "Two-Dimensional Radiative Transfer in a Cylindrical Geometry With Anisotropic Scattering," *Journal of Quantitative Spectroscopy and Radiative Transfer*, Vol. 25, 1981, pp. 551–562.

5 Perlmutter, M., and Howell, J. R., "Radiant Transfer Through a Gray Gas Between Concentric Cylinders Using Monte Carlo," ASME JOURNAL OF HEAT TRANSFER, Vol. 86, 1966, pp. 169–179.

6 Steward, F. R., and Cannon, P., "The Calculation of Radiative Heat Flux in a Cylindrical Furnace Using the Monte-Carlo Method," *International Journal of Heat and Mass Transfer*, Vol. 14, 1971, pp. 245–261.

7 Hottel, H. C., and Sarofim, A. F., *Radiative Transfer*, McGraw-Hill, New York, 1967.

8 Steward, F. R., and Tennankore, K. N., "Towards a Finite Difference Solution Coupled With the Zone Method for Radiative Transfer for a Cylindrical Combustion Chamber," *Journal of the Institute of Energy*, Vol. 107, 1979, pp. 107–114.

9 Higenyi, J., and Bayazitoglu, Y., "Differential Approximation of Radiative Heat Transfer in a Gray Medium – Axially Symmetric Radiation Field," ASME JOURNAL OF HEAT TRANSFER, Vol. 102, 1980, pp. 719–723.

10 Ou, S.-C. S., and Liou, K.-N., "Generalization of the Spherical Harmonic Method to Radiative Transfer in Multi-dimensional Space," *Journal of Quantitative Spectroscopy and Radiative Transfer*, Vol. 28, 1982, pp. 271–288.

11 Selcuk, N., and Siddall, R. G., "Two-Flux Spherical Harmonic Modeling of Two-Dimensional Radiative Transfer in Furnaces," *International Journal of Heat and Mass Transfer*, Vol. 19, 1976, pp. 313–321.

12 Fiveland, W. A., "A Discrete Ordinates Method for Predicting Radiative Heat Transfer in Axisymmetric Enclosures," ASME Paper No. 82-HT-20, 1982.

13 Lockwood, F. C., and Shah, N. G., "A New Radiation Solution Method for Incorporation in General Combustion Prediction Procedures," in: *Eighteenth Symposium (International) on Combustion*, The Combustion Institute, Pittsburgh, PA, 1981, pp. 1405–1414.

14 Khalil, E. E., *Modeling of Furnaces and Combustors*, Abacus, 1982.

15 Mengüç, M. P., and Viskanta, R., "Radiative Transfer in Three-Dimensional Rectangular Enclosures Containing Inhomogeneous, Anisotropically Scattering Media," *Journal of Quantitative Spectroscopy and Radiative Transfer*, Vol. 33, 1985, pp. 533–549.

16 Joseph, J. H., Wiscombe, W. J., and Weinman, J. A., "The Delta-Eddington Approximation for Radiative Heat Transfer," *Journal of Atmospheric Sciences*, Vol. 33, 1976, pp. 2452–2459.

17 Özisik, M. N., *Radiative Transfer and Interactions With Conduction and Convection*, Wiley, New York, 1973.

18 Davison, B., *Neutron Transport Theory*, Clarendon, Oxford, 1958.

19 Case, K. M., and Zweifel, P. F., *Linear Transport Theory*, Addison-Wesley, Reading, MA, 1967.

20 Özisik, M. N., *Heat Conduction*, Wiley, New York, 1980.

21 Rice, J. R., and Boisvert, R. F., *Solving Elliptic Problems Using ELLPACK*, Springer-Verlag, New York, 1985.

22 Mengüc, M. P., and Viskanta, R., "Comparison of Radiative Transfer Approximation for Highly Forward Scattering Planar Medium," *Journal of Quantitative Spectroscopy and Radiative Transfer*, Vol. 29, 1983, pp. 381–394.

23 Wu, L. H., and Fricker, N., "An Investigation of the Behavior of Swirling Jet Flames in a Narrow Cylindrical Furnace," International Flame Research Foundation Conference Paper, 1971.

24 Ratzel, A. C., III, and Howell, J. R., "Two-Dimensional Radiation in Absorbing-Emitting-Scattering Media Using the P-N Approximation," ASME JOURNAL OF HEAT TRANSFER, Vol. 105, 1983, pp. 333–340.

25 Crosbie, A. L., and Farrell, J. R., "Two-Dimensional Isotropic Scattering in a Finite Cylindrical Medium Exposed to Uniform Diffuse Radiation," *Journal of Quantitative Spectroscopy and Radiative Transfer* (in press).

26 Mengüc, P. M., "Modeling of Radiative Heat Transfer in Multidimensional Enclosures Using Spherical Harmonics Approximation," Ph.D. Thesis, Purdue University, 1985.

APPENDIX

In this appendix, the functions A and the coefficients B of the governing equations of the P_3 approximation are given. They are

$$A_1(\bar{r}, \bar{z}) = \left[-B_0\Gamma_{rr} + \Gamma_{zz} - B_3 \frac{1}{\bar{r}} \Gamma_r - \left(4 \frac{B_2}{\bar{r}^2} + 7\tau_0^2 \right) \right] I_{11}$$
$$+ \left[\Gamma_{rr} - B_0\Gamma_{zz} + B_0 \frac{1}{\bar{r}} \Gamma_r - \left(2 \frac{B_2}{\bar{r}^2} + 7\tau_0^2 \right) I_{33} \right.$$
$$- [2B_4\Gamma_{rz} + B_5\Gamma_z] I_{13} \tag{A1}$$

$$A_2(\bar{r}, \bar{z}) = \left[\frac{3}{5} \Gamma_{rr} + \frac{1}{5} \Gamma_{zz} + B_8 \frac{1}{\bar{r}} \Gamma_r \right.$$
$$\left. - \left(2 \frac{B_2}{\bar{r}^2} + \frac{7}{3} \tau_0^2 \right) \right] I_0$$
$$- \left[B_4\Gamma_{zz} + B_9 \frac{1}{\bar{r}} \Gamma_r - 2 \frac{B_2}{\bar{r}^2} \right] I_{33}$$
$$- \left[B_5\Gamma_{rz} + B_4 \frac{2}{\bar{r}} \Gamma_z \right] I_{13} \tag{A2}$$

$$A_3(\bar{r}, \bar{z}) = \left[\frac{1}{5} \Gamma_{rr} + \frac{3}{5} \Gamma_{zz} + B_{10} \frac{1}{\bar{r}} \Gamma_r - \frac{7}{3} \tau_0^2 \right] I_0$$
$$- B_4 \left[\Gamma_{rr} + \frac{3}{\bar{r}} \Gamma_r \right] I_{11} - B_5 \left[\Gamma_{rz} + \frac{1}{\bar{r}} \Gamma_z \right] I_{13} \tag{A3}$$

$$A_4(\bar{r}, \bar{z}) = \left[\frac{2}{5} \Gamma_{rz} + B_6 \frac{1}{\bar{r}} \Gamma_z \right] I_0$$
$$- B_6 \left[\Gamma_{rz} + \frac{2}{\bar{r}} \Gamma_z \right] I_{11} - B_6 \left[\Gamma_{rz} + \frac{1}{\bar{r}} \Gamma_z \right] I_{33} \tag{A4}$$

where

$$\begin{array}{llll} \alpha = \omega_0 g/(1-\omega_0 g), & B_0 = (7\alpha/5), & B_1 = (3/5 + B_0), \\ B_2 = (3 + B_0), & B_3 = (6 + 5B_0), & B_4 = (1 + B_0), \\ B_5 = (6 + 4B_0), & B_6 = (2 + B_0), & B_7 = (12 + 7B_0), \\ B_8 = (26/5 + 3B_0), & B_9 = (5 + 3B_0), & B_{10} = (6/5 + B_0) \end{array}$$

Free Convection in a Two-Dimensional Porous Loop

L. Robillard
Mem. ASME

T. H. Nguyen

P. Vasseur
Assoc. Mem. ASME

Génie civil,
Ecole Polytechnique,
Campus de l'Université de Montréal,
Montréal, Québec, Canada H3C 3A7

A study is made of the natural convection in an annular porous layer having an isothermal inner boundary and its outer boundary subjected to a thermal stratification arbitrarily oriented with respect to gravity. For such conditions, no symmetry can be expected for the flow and temperature fields with respect to the vertical diameter and the whole circular region must be considered. Two-dimensional steady-state solutions are sought by perturbation and numerical approaches. Results obtained indicate that the circulating flow around the annulus attains its maximum strength when the stratification is horizontal (heating from the side). This circulating flow is responsible for an important heat exchange between the porous layer and its external surroundings. The flow field is also characterized by the presence of two convective cells near the inner boundary, giving rise to flow reversal on this surface. When the maximum temperature on the outer boundary is at the bottom of the cavity, the convective motion becomes potentially unstable; for a Rayleigh number below 80, there exists a steady-state solution symmetrical with respect to both vertical and horizontal axes; for a Rayleigh number above 80, an unsteady periodic situation develops with the circulating flow alternating its direction around the annulus.

1 Introduction

Many studies have been conducted in the past on closed loop thermosyphons. In particular Creveling et al. [1] have studied experimentally and analytically the case of a vertical toroidal loop, heated from below and maintained at a constant temperature in the upper half. Some of their experimental results showed unsteadiness with the flow reversal. A one-dimensional analytical approach was developed to interpret the experimental results. Damerell and Schoenhals [2] have reconsidered the same problem for various angular positions of the heated and cooled sections. They have reported the presence of velocity profiles with reverse flow features in their experiments. More recently, Mertol et al. [3] have formulated for the same problem a two-dimensional model that neglects the radial velocity component. An extension of this work [4] describes the transient behavior of the toroidal loop. Bau and Torrance [5] have studied experimentally, within the framework of a one-dimensional model, the case of an open loop filled with a porous material. In all past studies where the fluid was heated from below, symmetry conditions were such that the circulating flow in the loop could develop in either direction with essentially equal probability.

The present study considers the two-dimensional free convection taking place in a saturated porous layer of annular shape with externally imposed temperatures on the boundaries. While the inner boundary is maintained at a constant uniform temperature, a thermal stratification of arbitrary orientation is imposed on the outer boundary. Consequently, the symmetry hypothesis with respect to the vertical diameter cannot be applied and the entire annular region must be considered, allowing for the possibility of a net circulation flow around the cavity. The main purpose of this study is to determine steady-state solutions, whenever they exist, of the flow and temperature fields for various imposed temperature distributions on the outer boundary.

Singh and Elliott [6] have already considered the free convection in a fluid contained between two horizontal concentric cylinders with the outer boundary subjected to a thermal stratification. However, their perturbation solution is limited to the case of stable vertical stratification for which a symmetry exists with respect to the vertical diameter and for which no circulating flow can develop.

2 Mathematical Model

The geometry of the problem is shown in Fig. 1. Inner and outer boundaries with corresponding radii r_i' and r_o' do not intersect and define a doubly connected region filled with a saturated porous medium. In fact, owing to the absence of corner effects, this particular geometry represents the most attractive form of a doubly connected region to be considered for free convection. While the inner boundary is maintained at a uniform temperature T_i', a temperature distribution of the form

$$T_o' = T_i' + \Delta T \cos(\phi - \phi_o) \qquad (1)$$

is imposed on the outer boundary so that extrema in temperature occur at opposite locations on this boundary, on a diameter oriented at an angle ϕ_o (heating phase angle, [7]) with the gravity direction. The Darcy-Oberbeck-Boussinesq approximations can be applied to the present problem. A

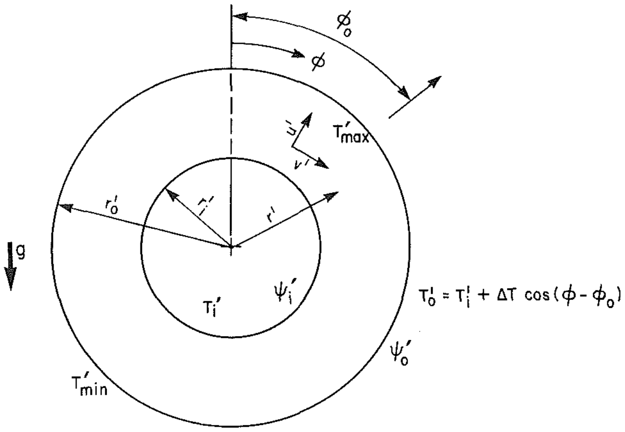

Fig. 1 Flow geometry and coordinate system

Contributed by the Heat Transfer Division for publication in the JOURNAL OF HEAT TRANSFER. Manuscript received by the Heat Transfer Division January 17, 1985.

discussion on the validity and the limits of those approximations is given in [8]. The governing equations are

$$\nabla \cdot \mathbf{V}' = 0 \tag{2}$$

$$\mathbf{V}' = \frac{K}{\mu}(\rho \cdot \mathbf{g} - \nabla p') \tag{3}$$

$$(\rho c)_p \frac{\partial T'}{\partial t'} + (\rho c)_f (\mathbf{V}' \cdot \nabla) T' = k \nabla^2 T' \tag{4}$$

$$\rho' = \rho_r'[1 - \beta(T' - T_i')] \tag{5}$$

where g is the gravitational acceleration; V', p', T', ρ', μ, and $(\rho c)_f$ are the filtration velocity, pressure, temperature, density, viscosity, and heat capacity of the fluid, respectively; K is the permeability of the saturated porous medium; β is the thermal expansion coefficient, and $(\rho c)_p$ and k are the heat capacity and the effective thermal conductivity of the porous medium. By scaling time, length, velocity, temperature, and pressure with $(\rho c)_p r_i^2/k$, r_i', $k/r_i'(\rho c)_f$, ΔT and $(\rho c)_f K/k\mu$, respectively, the following dimensionless equations can be obtained

$$\nabla \cdot \mathbf{V} = 0 \tag{6}$$

$$\mathbf{V} = \frac{\text{Ra}}{g} T\mathbf{g} - \nabla p \tag{7}$$

$$\frac{\partial T}{\partial t} + (\mathbf{V} \cdot \nabla) T = \nabla^2 T \tag{8}$$

with $\text{Ra} = Kg\beta(\rho c)_f r_i' \Delta T/\nu k$ being defined as an internal Rayleigh number. The initial and boundary conditions for temperature and velocity are

$$t \le 0: \quad T = \psi = V_r = V_\phi = 0$$

$$\text{for } 1 \le r \le R \text{ and } 0 < \phi < 2\pi \tag{9a}$$

$$\begin{cases} t > 0: \quad T = 0;\ V_r = 0 \\ \qquad \text{for } r = 1 \text{ and } 0 \le \phi \le 2\pi & (9b) \\ \qquad T = \cos(\phi - \phi_o);\ V_r = 0 \\ \qquad \text{for } r = R \text{ and } 0 \le \phi \le 2\pi & (9c) \end{cases}$$

where $R = r_o'/r_i'$ is the radius ratio of the annulus. It is possible to eliminate the pressure term of equation (7) in the usual way, i.e., by differentiating the equations of motion and subtracting one from the other. By expressing V_r and V_ϕ in terms of the stream function

$$V_r = \frac{1}{r}\frac{\partial \psi}{\partial \phi} \tag{10a}$$

$$V_\phi = -\frac{\partial \Psi}{\partial r} \tag{10b}$$

equation (7) becomes

$$\nabla^2 \psi = \text{Ra}\mathcal{L}(T) \tag{11}$$

where

$$\nabla^2 = \frac{1}{r}\frac{\partial}{\partial r}\left(r\frac{\partial}{\partial r}\right) + \frac{1}{r^2}\frac{\partial^2}{\partial \phi^2}$$

and

$$\mathcal{L}(\ ) = \sin\phi \frac{\partial}{\partial r} + \frac{\cos\phi}{r}\frac{\partial}{\partial \phi}$$

The boundary conditions (9*b*, *c*) for the velocity imply that the stream function ψ must be constant on each boundary

$$\begin{matrix} \psi = \psi_i, & r = 1 & 0 < \phi < 2\pi \\ \psi = \psi_o; & r = R & 0 < \phi < 2\pi \end{matrix} \tag{12}$$

When ψ_o is set to zero, ψ_i corresponds to the circulating flow around the annulus. Different ψ_i lead to different solutions for equations (8) and (11), one of which satisfies the original Darcy–Oberbeck–Boussinesq equation (7). In fact, by introducing the stream function, one has to keep in mind that the derivatives of equation (7) are increased by one order and that one more degree of freedom is introduced in the new equation (11). The additional boundary condition required to determine the solution is that of periodicity, i.e., $f(\phi + 2\pi) = f(\phi)$ where f stands for any physical variable. In particular, the pressure must be periodic (in the absence of a pump). As a consequence, by integrating equation (7) along a closed circular loop, we obtain

$$\Gamma = r\int_0^{2\pi} V_\phi d\phi = \begin{cases} 0 & r = 1 \\ -\text{Ra}\, r\int_0^{2\pi} T \sin\phi d\phi & 1 < r < R \\ -\text{Ra}\, R\pi \sin\phi_o & r = R \end{cases} \tag{13}$$

where Γ is the hydrodynamic circulation. More generally, Γ must be zero on any closed loop corresponding to an isotherm. Hence, there ought to be a flow reversal on such a loop, except for the trivial case where the tangential velocity is zero everywhere.

Nomenclature

g = gravitational acceleration, ms^{-2}
K = permeability of the porous medium, m^2
k = thermal conductivity of the saturated porous medium, $\text{Js}^{-1}\text{m}^{-1}\text{K}^{-1}$
Nu = overall Nusselt number defined by equations (29) and (30)
p = dimensionless pressure $= p'K(\rho c)_f/\mu k$
Q = local heat flux
r = dimensionless coordinate $= r'/r_i'$
R = radius ratio $= r_o'/r_i'$
Ra = internal Rayleigh number
t = dimensionless time $= t'k/r_i'^2(\rho c)_p$
T = dimensionless temperature $= (T' - T_i')/\Delta T$
ΔT = half the temperature difference between the hottest and coldest points on the boundary
$\mathbf{V}$ = dimensionless velocity $= \mathbf{V}'r_i'(\rho c)_f/k$
V_r = dimensionless velocity component in r direction
V_ϕ = dimensionless velocity component in ϕ direction
α = thermal diffusivity of the saturated porous medium, m^2s^{-1}
β = thermal expansion coefficient, K^{-1}
Γ = hydrodynamic circulation
μ = dynamic viscosity of fluid, $\text{kg}\,\text{m}^{-1}\,\text{s}^{-1}$
ν = kinematic viscosity of fluid, m^2s^{-1}
ρ = density of fluid, $\text{kg}\,\text{m}^{-3}$
$(\rho c)_f$ = specific heat capacity of fluid, $\text{J}\,\text{m}^{-3}\,\text{K}^{-1}$
$(\rho c)_p$ = heat capacity of saturated porous medium, $\text{J}\,\text{m}^{-3}\,\text{K}^{-1}$
ϕ = angular coordinate
ψ = dimensionless stream function $= \psi'(\rho c)_f/k$

Superscripts

$'$ = dimensional variable
$*$ = pure conduction
$-$ = average value

Subscripts

i = value on inner cylinder
o = value on outer cylinder

Equations (8) and (11), together with the boundary conditions (9), (12), and (13), completely determine the solution of the problem in terms of the Rayleigh number Ra, the radius ratio R, and the angle of stratification ϕ_o.

3 Methods of Solution

At low Rayleigh numbers, perturbation solutions, with the pure conduction temperature field as a starting point, may be used to obtain approximations of the flow and temperature fields. At higher Rayleigh numbers, solutions of the governing equations require a numerical approach.

3.1 Perturbation Approach. We attempt to solve the steady-state form of equations (8) and (11) subject to conditions (9) and (12) by expansions in powers of Ra. For the solution we assume the form

$$\psi = \sum_{n=0}^{\infty} \mathrm{Ra}^n \psi_n (r, \phi) \tag{14}$$

$$T = \sum_{n=0}^{\infty} \mathrm{Ra}^n T_n (r, \phi) \tag{15}$$

It can be easily shown that

$$T_o = \frac{R}{R^2-1}(r - r^{-1}) \cos (\phi - \phi_o) \tag{16a}$$

$$\psi_o = 0 \tag{16b}$$

Thus the expansion is about the pure conduction state. Substitution of equations (14) and (15) into equations (8) and (11) and collection of like power terms yields, for $n \geq 1$, a sequence of linear equations for successive ψ_n and T_n, i.e.,

$$\nabla^2 \psi_n = \mathrm{Ra}\left(\sin \phi \frac{\partial}{\partial r} + \cos \phi \frac{\partial}{r \partial \phi}\right) T_{n-1} \tag{17}$$

$$\nabla^2 T_n = \sum_{j=0}^{n} \left(\frac{\partial \psi_j}{r \partial \phi} \frac{\partial}{\partial r} - \frac{\partial \psi_j}{\partial r} \frac{\partial}{r \partial \phi} \right) T_{n-j} \tag{18}$$

For the purpose of this study, a two-term expansion has been obtained for the temperature and flow fields, such that:

$$T = T_o + \mathrm{Ra} T_1$$

and

$$\psi = \mathrm{Ra}\psi_1 + \mathrm{Ra}^2 \psi_2$$

where

$$\begin{aligned} \psi_1 = \frac{1}{2}\left(\frac{R}{R^2-1}\right)\bigg\{ & \left[\frac{r^2 - R^2}{2} - \ln \frac{r}{R}\right] \sin \phi_o \\ & + \left[\frac{r^2 + (R/r)^2}{2(R^2+1)} - \frac{1}{2}\right] \sin (2\phi - \phi_o)\bigg\} \end{aligned} \tag{19}$$

$$\begin{aligned} T_1 = {} & [\alpha_{11} r + \alpha_{12} r^{-1} + \alpha_{13}(r - r^{-1}) \ln r \\ & \quad + \alpha_{14} r^{-3} + \alpha_{15} r^3] \cos \phi \\ & + [\alpha_{21} r + \alpha_{22} r^{-1} + (\alpha_{23} r + \alpha_{24} r^{-1}) \ln r \\ & \quad + \alpha_{25} r^3] \sin (\phi - \phi_o) \\ & + [\alpha_{31} r^3 + \alpha_{32} r^{-3} + \alpha_{33} r^{-1} + \alpha_{34} r] \cos (3\phi - \phi_o) \end{aligned} \tag{20}$$

and

$$\begin{aligned} \psi_2 = {} & [\beta_{11} r^2 + \beta_{12} r^2 \ln r + \beta_{13} (\ln r)^2 + \beta_{14} r^4] \cos \phi_o \\ & + [\beta_{21} r^2 + \beta_{22} r^{-2} + \beta_{23} + \beta_{24} \ln r + \beta_{25} r^2 \ln r \\ & \quad + \beta_{26} r^{-2} \ln r + \beta_{27} r^4] \sin 2\phi \\ & + [\beta_{31} r^2 + \beta_{32} r^{-2} + \beta_{33} + \beta_{34} \ln r \\ & \quad + \beta_{35} r^2 \ln r + \beta_{36} r^4] \cos (2\phi - \phi_o) \\ & + [\beta_{41} r^2 + \beta_{42} r^{-2} + \beta_{43} + \beta_{44} r^4 \\ & \quad + \beta_{45} r^2 \ln r] \sin (2\phi - 2\phi_o) \\ & + [\beta_{51} r^4 + \beta_{52} r^{-4} + \beta_{53} + \beta_{54} r^2 \\ & \quad + \beta_{55} r^{-2}] \sin (4\phi - 2\phi_o) + \beta_{61} + \beta_{62} \ln r \end{aligned} \tag{21}$$

Coefficients α_{ij} and β_{ij} are rather lengthy expressions of R and ϕ_o and are not written explicitly here. Readers interested in those coefficients are invited to write to the authors.

3.2 Numerical Approach. Finite-difference techniques with regular mesh size (18×36) were used in the numerical approach to discretize the entire annulus. The Poisson equation (11) was solved by the method of successive overrelaxation. The energy equation, in its time-dependent form (8), was solved by an alternating direction implicit method. Central differences were used in the numerical formulation of the advective terms.

ψ_i must be corrected at each time step in order for condition (13) to be satisfied. An alternative to condition (13) consists in establishing a corrected flow from the first moment

$$\int_1^R \int_0^{2\pi} r^2 V_\phi dr d\phi = -\mathrm{Ra} \int_1^R \int_0^{2\pi} r^2 T \sin \phi dr d\phi \tag{22}$$

Equation (22) expresses the torque equilibrium with respect to the geometric center between the gravity forces arising from density differences and the viscous forces encountered by the fluid moving through the porous medium. Equation (22) must be satisfied at each time step. Otherwise a compensating flow $\Delta\psi_i$ around the annulus must be introduced. Assuming a uniform velocity ΔV_ϕ in r and ϕ directions for this flow leads to the following estimate

$$\Delta\psi_i = -\frac{3}{2}\left(\frac{1}{R^2+R+1}\right) \int_1^R \int_0^{2\pi} r^2 (V_\phi + \mathrm{Ra} T \sin \phi) dr d\phi \tag{23}$$

Thus equation (23) provides a way to adjust the value of ψ_i until (22) is satisfied. For fast convergence to the steady-state solution, it was found sufficient to correct ψ_i through equation (23) just once at each time step. The steady state was defined based on the following criteria

$$\frac{|\psi|_{\max}^{n+1} - |\psi|_{\max}^{n}}{|\psi|_{\max}^{n+1}} < 10^{-3}$$

where n refers to the time step.

The numerical approach was tested to reproduce standard cases in the literature for which symmetry conditions are assumed and a half cavity is considered. For instance the Nusselt numbers obtained from the present method correspond within 3 percent to the values mentioned in Caltagirone's paper [9]. A more detailed comparison between the results of the present numerical approach and those of Caltagirone can be found in [10].

4 Results and Discussion

4.1 Temperature and Flow Fields. On Fig. 2 are shown the steady-state flow and temperature fields obtained numerically for different heating phase angles ϕ_o between 0 and π. At $\phi_o = 0$ and π, the streamlines and isotherms are observed to be symmetrical with respect to the vertical and horizontal diameter. These symmetry characteristics arise from the fact that the governing equations (8) and (11), together with the boundary conditions (9*b*), become invariant under the transformations

$$(r, \phi, T, \psi \rightarrow r, -\phi, T, -\psi) \tag{24a}$$

$$(r, \phi, T, \psi \rightarrow r, \pi - \phi, -T, -\psi) \tag{24b}$$

Identical results to Figs. 2(*a*) and 2(*f*) may be obtained from a numerical approach involving the half cavity [11], since the circulating flow ψ_i is zero for those two figures. For $\phi_o = 0$, the upper half of the outer cylinder is relatively hotter than the inner cylinder while its lower half is relatively colder. Consequently the fluid will rise along the upper half of the outer

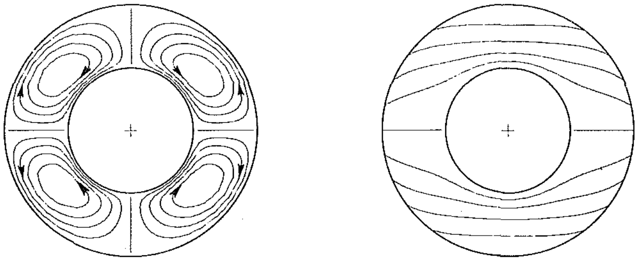

Fig. 2(*a*) $\psi_i = 0$; $\psi_{\max} = 1.35$; $\psi_{\min} = -1.35$; $\phi_o = 0$

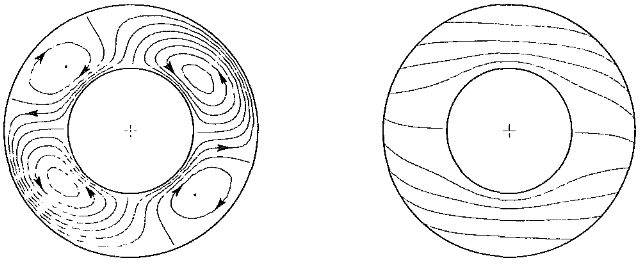

Fig. 2(*b*) $\psi_i = -0.87$; $\psi_{\max} = 0.58$; $\psi_{\min} = -2.16$; $\phi_o = \pi/32$

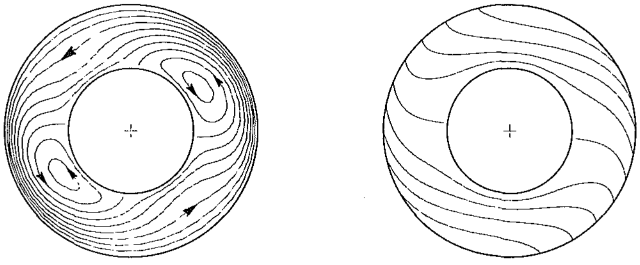

Fig. 2(*c*) $\psi_i = -3.43$; $\psi_{\max} = 0$; $\psi_{\min} = -4.58$; $\phi_o = \pi/8$

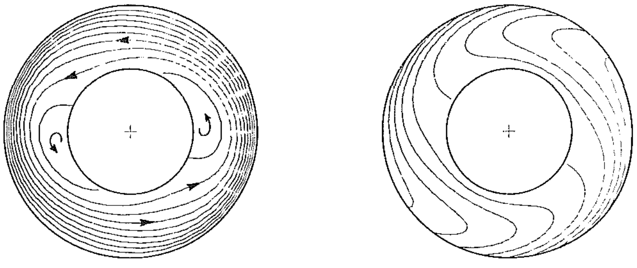

Fig. 2(*d*) $\psi_i = -11.34$; $\psi_{\max} = 0$; $\psi_{\min} = -12.15$, $\phi_o = \pi/2$

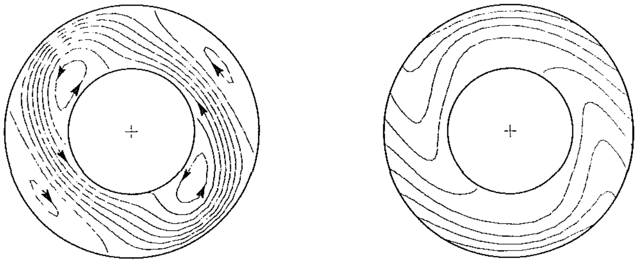

Fig. 2(*e*) $\psi_i = 5.80$; $\psi_{\max} = 1.08$; $\psi_{\min} = -7.38$; $\phi_o = 31\,\pi/32$

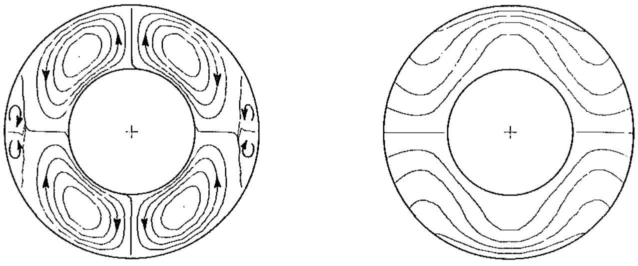

Fig. 2(*f*) $\psi_i = 0$; $\psi_{\max} = 3.79$; $\psi_{\min} = -3.79$; $\phi_o = \pi$

Fig. 2 Flow and temperature field for different values of ϕ_o, obtained from numerical results (Ra = 60 and $R = 2$)

cylinder and descend along its lower half. This convective motion straightens the isotherms and tends to establish a stable vertical stratification, except in the vicinity of the boundaries.

At $\phi_o = \pi$, the thermal stratification is potentially unstable and the problem becomes much more complicated. As mentioned in [11], there exist three convective regimes, namely, quadricellular, multicellular, and oscillating. For $0 < \mathrm{Ra} < 40$, the steady-state solution consists of four mirror image cells in the whole cavity. In fact the fluid motion as well as its effects on the temperature distribution are opposite to the previous case of stable configuration ($\phi_o = 0$). For $40 < \mathrm{Ra} < 80$ there still exists a steady fluid motion but additional symmetric vortices are created above and below the horizontal axis (Fig. 2*f*). The appearance of these additional cells was found to be unaffected by refining the mesh size. Their occurrence must be related to the particular distortion produced on the isotherms by the main flow: It is seen in Fig. 2(*f*) that the horizontal temperature gradient changes its sign somewhere between the inner and the outer boundary. Such a behavior promotes the formation of these additional cells. For $\mathrm{Ra} > 80$, no steady-state solution can be reached but a periodic time-dependent flow regime occurs with a circulating flow ψ_i reversing its direction. Such a threshold in the Rayleigh number beyond which there can be no more steady flow is not limited to $\phi_o = \pi$. In fact potential instability (cold fluid above hot fluid) exists for $\phi_o > \pi/2$. However this threshold reaches its minimum value at this particular angle. A thorough study of the oscillating regime is beyond the scope of the present work and will be treated in a subsequent article.

The presence of a stability limit and the periodic flow occurring above that limit are a strong incentive to relate the present problem to previous works on toroidal thermosyphons [1–4]. However, in an attempt to establish such comparisons, one must remember that the present problem deals with a saturated porous medium whereas the previous studies treated a fluid medium. Also the geometry and the thermal boundary conditions considered here are different. In addition, the references cited above dealt with convection regimes well above the threshold level beyond which there is a circulating flow within the torus. In the present study, the circulating flow obtained numerically was just above the threshold (Ra = 80) and its nature was found to be strongly dependent on the imposed thermal boundary conditions. For instance, adiabatic rather than isothermal boundary conditions were found to produce a steady-state circulating flow.

The sequence of Figs. 2(*b*) to 2(*e*) shows how the circulating flow develops when ϕ_o is increased from zero to π. For all these figures, the symmetry with respect to both horizontal and vertical diameters diameters has disappeared. There remains a symmetry with respect to the center, or centrosymmetry, for the set of streamlines and isotherms, in agreement with the invariance property of equations (8) and (11) together with the boundary condition (9), that exists for any ϕ_o, under the transformation

$$T(r, \phi) = -T(r, \phi + \pi) \tag{25a}$$

$$\psi(r, \phi) = \psi(r, \phi + \pi) \tag{25b}$$

In Fig. 2(*b*), the flow pattern contains two vortices responsible for flow reversal on the outer boundary. Beyond a critical value ϕ_{oc} of the heating phase angle, these vortices disappear (Figs. 2*c* and 2*d*). The term ϕ_{oc} for the pure conduction regime may be determined from the first-order perturbation solution. From equation (19) the velocities along the inner and outer boundaries may be deduced to be

$$V_\phi(R) = -\frac{R}{R^2+1}\,\frac{\mathrm{Ra}}{2}\left[\left(\frac{R^2-1}{R}\right)\sin\phi_o + \frac{1}{R}\left(\frac{R^2-1}{R^2+1}\right)\sin(2\phi-\phi_o)\right] \qquad (26a)$$

$$V_\phi(1) = -\frac{R}{R^2+1}\,\frac{\mathrm{Ra}}{2}\sin(2\phi-\phi_o) \qquad (26b)$$

It follows from equation (26*a*) that flow reversal near the outer boundary exists only when the following condition

$$\sin\phi_o < 1/(R^2+1) \qquad (27)$$

is satisfied. On the other hand, for any single angle ϕ_o it is seen from (26*b*) that the flow direction near the inner boundary must reverse twice from $\phi = 0$ to π. Thus the main circulating flow around the annulus must always contain two primary cells of opposite location near the inner boundary and this characteristic of the flow field is preserved for any aspect ratio.

According to equation (27), the flow reversal near the outer boundary should reappear when ϕ_o approaches π. More generally from equation (19) it can be readily verified that symmetrical results with respect to the horizontal diameter are obtained when ϕ_o is replaced by $(\pi - \phi_o)$. The two vortices creating the flow reversal on the outer boundary have reappeared in Fig. 2(*e*). However, important asymmetry effects are evident when comparison is made between this last flow pattern and the one in Fig. 2(*b*). Asymmetry arises from higher-order interaction between the velocity and temperature fields. It is worth mentioning at this point that similar flow reversals with recirculation cells have been experimentally observed [2, 12] in the three-dimensional case of a toroidal thermosyphon. For the present problem and its specific thermal boundary conditions, the occurrence of the flow reversals with recirculation cells is due to conditions (13) imposed on the circulation and the resulting inequality (27).

Although a detailed numerical study of the radius ratio R has not been made, it must be pointed out that the recirculation cells are a fundamental feature of the present problem. For instance, as evidenced by equation (26*b*) obtained from the perturbation approach, the inner cells do exist for any ϕ_o, independently of the value of R. A few numerical tests undertaken within the framework of the present study (not presented here) confirm that fact.

The circulating flow ψ_i, a function of the heating phase angle ϕ_0 and the Rayleigh number, is shown in Figs. 3(*a*-*c*). The numerical and analytical predictions for a Rayleigh number of 10 may be compared in Fig. 3(*a*). It can be seen in this figure that the addition of the second-order effect reproduces quite well the asymmetry with respect to $\pi/2$, observed in the numerical results. However, as shown in Fig. 3(*b*), where the circulating flow for $\phi_o = \pi/2$ is given as a function of Ra, discrepancies between numerical and analytical results develop rapidly when Ra is increased. This condition is due to the natural, inherent limitation of the perturbation technique. Numerical results for the circulating flow, up to Ra = 200, are given in Fig. 3(*c*). It is seen that the circulating flow, at any fixed angle ϕ_o, remains strongly dependent of Ra. It is also noticed that the distortion from the sinusoidal shape of the conduction regime in Fig. 3(*a*) is amplified at higher Ra. As mentioned earlier, above Ra = 80, an oscillating regime characterizes the flow when ϕ_o is in the neighborhood of π; hence the curves corresponding to Ra = 100 and 200 do not extend to π.

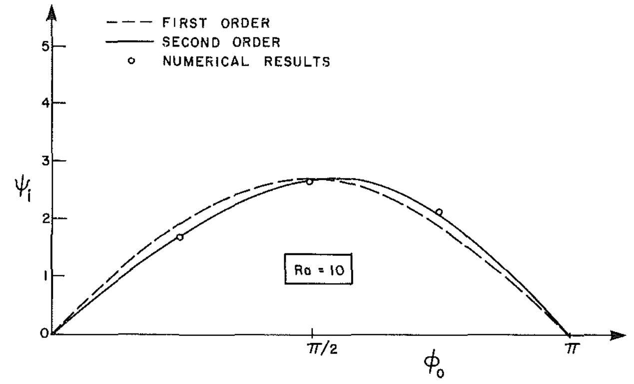

Fig. 3(*a*) Comparison between analytical and numerical results for Re = 10 and $R = 2$

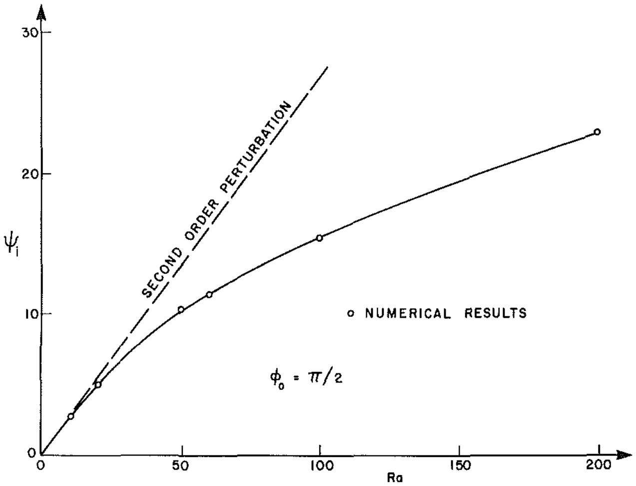

Fig. 3(*b*) Comparison between analytical and numerical results for $\phi_o = \pi/2$ and $R = 2$

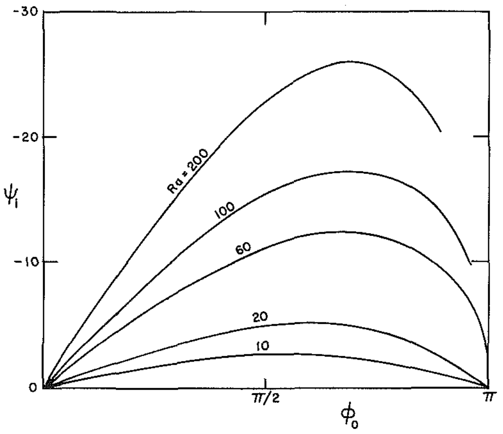

Fig. 3(*c*) Numerical results ($R = 2$)

Fig. 3 Circulating flow around the cavity

Figure 3 presents steady-state flows below the threshold level for oscillations. In particular, for $\phi_o = \pi$ and $0 < \mathrm{Ra} < 80$, the fluid motion is generated by the horizontal temperature gradients originating from the imposed thermal boundary conditions; the potential instability, i.e., the cold fluid above the hot fluid, is insufficient to destroy the symmetry observed in Fig. 2(*f*) and to induce a circulating flow. Consequently,

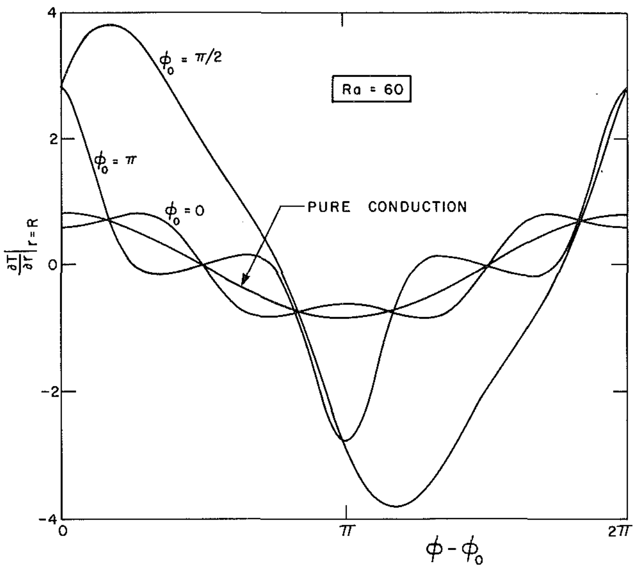

Fig. 4(*a*) **Local heat flux along the outer boundary (Ra = 60 and *R* = 2)**

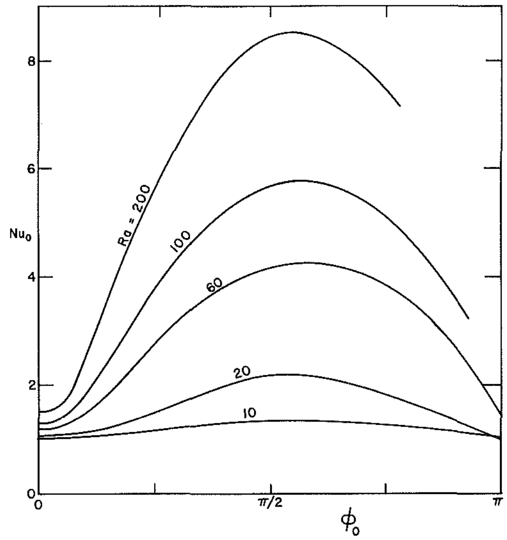

Fig. 4(*b*) **Nusselt number function of ϕ_o and Ra (R = 2)**

Fig. 4 **Heat transfer through the outer boundary from numerical results**

for Ra < 80, the maximum value of the circulating flow has to be produced by "side heating."

4.2 Heat Transfer. Some quantities of interest are the dimensionless local heat fluxes through the inner and outer boundaries, defined respectively as

$$Q_i = \left.\frac{\partial T}{\partial r}\right|_{r=1} \tag{28a}$$

$$Q_o = \left.\frac{\partial T}{\partial r}\right|_{r=R} \tag{28b}$$

Q_o, corresponding to Ra = 60 and to $\phi = 0$, $\pi/2$, and π, is given in Figs. 4(*a*) and 4(*b*). The choice of the abscissa facilitates the comparison with the pure conduction curve. The circulating flow is zero for a heating phase angle of 0 and π. Corresponding Q_o curves are symmetrical with respect to the vertical diameter and antisymmetrical with respect to the horizontal diameter, in agreement with relationships (24*a*, *b*). The presence of a circulating flow different from zero, for $\phi_o = \pi/2$, is seen to enhance the local heat flux.

As a consequence of the centrosymmetrical behavior, the integration of Q_i and Q_o over the inner and outer boundary, respectively, must be zero, which means that there is no net heat transfer at both inner and outer boundaries. Each curve in Fig. 4(*a*) fulfills that condition, including the one corresponding to $\phi_o = \pi/2$. In fact, for any value of ϕ_o, the net heat flux integrated over each of the two circular boundaries is zero. Nevertheless it is possible to introduce overall Nusselt numbers of the form

$$\mathrm{Nu}_i = \frac{1}{4\pi \mathrm{Nu}*_i} \int_0^{2\pi} \left| \frac{\partial T}{\partial r} \right|_{r=1} d\phi \tag{29a}$$

$$\mathrm{Nu}_o = \frac{1}{4\pi \mathrm{Nu}*_o} \int_0^{2\pi} \left| \frac{\partial T}{\partial r} \right|_{r=R} R d\phi \tag{29b}$$

where

$$\mathrm{Nu}*_i = \frac{1}{2\pi} \int_0^{2\pi} \left| \frac{\partial T_o}{\partial r} \right|_{r=1} d\phi = 0.8488 \tag{30a}$$

$$\mathrm{Nu}*_o = \frac{1}{2\pi} \int_0^{2\pi} \left| \frac{\partial T_o}{\partial r} \right|_{r=R} R d\phi = 1.0610 \tag{30b}$$

are the overall Nusselt numbers for pure conduction. The terms Nu_i and Nu_o are related to the heat exchange between the porous medium and its surroundings. They are equal to twice the net inflow (or twice the net outflow) of heat through the inner and outer boundaries respectively. In Fig. 4(*b*), Nu_o is given as a function of ϕ_o for different values of Ra. A comparison of this figure with Fig. 3(*c*) shows the strong correlation that exists between the circulating flow around the cavity and the heat exchange with the exterior surroundings. Owing to the presence of flow reversal near the inner boundary for any ϕ_o, such a correlation becomes unclear for the heat exchange with the interior surroundings. In fact numerical results indicate that Nu_i is maximum at $\phi_o = 0$.

5 Conclusion

The steady-state free convection in an annular porous medium with nonuniform temperature distribution around the outer boundary has been solved numerically and analytically. The main conclusions drawn from the present two-dimensional study are:

1 The existence of a strong circulating flow in the case of side heating. This circulating flow is responsible for the high rate of heat exchange with the exterior surroundings;

2 The existence of primary cells embedded in the circulating flow, producing flow reversals on the inner boundary. These primary cells exist for any angle of stratification and may be inferred directly by evaluating the circulation on the inner boundary from the Darcy-Oberbeck-Boussinesq equation;

3 The existence of a relatively low critical Rayleigh number (Ra ≈ 80) above which the flow is changed from a steady to an unsteady (periodic) regime for inverse stratification. The oscillations involved are rather slow (for Ra = 100, the nondimensional time required for one cycle is ≈ 1.8) and there is a circulating flow around the cavity reversing its direction twice during one cycle;

4 The presence of primary cells in the flow field demonstrates the incompatibility between a one-dimensional approach and the present problem. However there exist, for the same geometry, specific thermal boundary conditions for which the stream function, as established from the first-order perturbation approach, becomes independent of the angular coordinate.

Acknowledgments

This work was supported by the National Research Council of Canada through grant CRSNG-G 1292.

References

1 Creveling, H. F., De Paz, J. F., Baladi, J. Y., and Schoenhals, R. J., "Stability Characteristics of a Single-Phase Free Convection Loop," *J. Fluid Mech.*, Vol. 67, 1975, pp. 65-84.

2 Damerell, P. S., and Schoenhals, R. J., "Flow in a Toroidal Thermosyphon With Angular Displacement of Heated and Cooled Sections," ASME JOURNAL OF HEAT TRANSFER, Vol. 101, 1979, pp. 672-676.

3 Mertol, A., Greif, R., and Zvirin, Y., "Two Dimensional Study of Heat Transfer and Fluid Flow in a Natural Convection Loop," ASME JOURNAL OF HEAT TRANSFER, Vol. 104, 1982, pp. 508-514.

4 Mertol, A., Greif, R., and Zvirin, Y., "Two Dimensional Analysis of Transient Flow and Heat Transfer in a Natural Circulation Loop," *Wärme- und Stoffübertragung*, Vol. 18, 1984, pp. 89-98.

5 Bau, H. H., and Torrance, K. E., "Transient and Steady Behavior of an Open, Symmetrically Heated, Convection Loop," *Int. J. Heat Mass Transfer*, Vol. 24, 1981, pp. 597-609.

6 Singh, S. N., and Elliott, J. M., "Free Convection Between Horizontal Concentric Cylinders in a Slightly Thermally Stratified Fluid," *Int. J. Heat Mass Transfer*, Vol. 22, 1979, pp. 639-646.

7 Ostrach, S., "Natural Convection in Enclosures," *Advances in Heat Transfer*, Academic Press, New York, 1972.

8 Vasseur, P., Robillard, L., Nguyen, T. H., Robillard, L., and Tong Thi, V. K., "Natural Convection Between Horizontal Concentric Cylinders Filled With a Porous Layer With Internal Heat Generation," *Int. J. Heat Mass Transfer*, Vol. 27, 1984, pp. 337-349.

9 Caltagirone, J. P., "Thermoconvective Instabilities in Porous Medium Bounded by Two Concentric Horizontal Cylinders," *J. Fluid Mech.*, Vol. 76, 1976, pp. 337-362.

10 Vasseur, P., Nguyen, T. H., Caltagirone, J. P., and Chandra Shekar, "Convection in a Horizontal Annular Porous Layer With Non-Linear Density Effects," *Chem. Eng. Comm.*, Vol. 26, 1984, pp. 55-71.

11 Vasseur, P., Robillard, L., Nguyen, T. H., and Shekar, B. S., "A Numerical Study of Free Convection in Thermally Stratified Porous Layer," *3rd Int. Conf. on Num. Methods in Heat Transfer*, Seattle, Vol. III, 1983, pp. 607-618.

12 Britt, T. E., and Wood, D. C., "Free Convection in a Partially Submerged Loop," ASME Paper No. 83-HT-67, 1983.

J. G. Georgiadis
Graduate Research Assistant.

I. Catton
Professor.
Fellow ASME

Mechanical, Aerospace and
Nuclear Engineering Department,
University of California,
Los Angeles, CA 90024

Prandtl Number Effect on Bénard Convection in Porous Media

A numerical study of buoyancy-driven two-dimensional convection in a fluid-saturated horizontal porous layer is reported emphasizing the nonlinear inertial effect on heat transport. The Forchheimer-Brinkman-Darcy-Boussinesq formulation and a single energy equation for the volume-average temperature are used. Closure to the wavenumber selection problem is sought through a criterion based on the Glansdorff and Prigogine theory of nonequilibrium thermodynamics. Good agreement with laboratory data and the analogy with the Rayleigh-Bénard problem are corroborative facts which justify similar non-Darcian formulations and demonstrate the role of the quadratic inertial terms in decreasing the mean convective heat transfer across the layer.

1 Introduction

Based on the concept of bulk (average) flow quantities, continuum mechanics models for single-phase flow in fully saturated porous media are not well developed except for slow filtration in isothermal fields. For high flow rates, the hydraulic gradient is found to be a quadratic function of the filtration flux and this observation has led to phenomenological extensions of the Darcian law, cf. Forchheimer [1] and Ergun [2]. Wooding [3] simply introduced the convective inertial term in Darcy's law but we may note in passing that such a formulation fails to account for the quadratic drag in unidirectional flows. Suggesting that the deviation from Darcy's law can be attributed to inertial drag on the fluid filtering through the tortuous porous matrix, Irmay [4] incorporated Forchheimer's quadratic term and the time derivative term to obtain the motion equation postulated earlier by Polubarinova-Kochina [5]. Choudhary et al. [6] supported the vectorial form of Forchheimer's motion equation with the convective inertial term included, but the role of the latter was proven to be negligible.

Vafai and Tien [7] utilized the local volume-averaging technique and the semi-empirical models mentioned above to formulate a two-dimensional momentum equation which would complement the empirical energy conservation equation. Brinkman's extension was also used but its validity in conjunction with the no-slip condition at the porous medium-solid boundary interface still remains unjustified. Chan et al. [8] showed numerically that Brinkman's term, which was used by Katto and Masuoka [9] for "convenience," has a negligible effect on the convective heat transfer across a two-dimensional porous enclosure for (physically) reasonable values of Da. Tong and Subramanian [10] did a boundary layer analysis for the same vertical enclosure heated from the side and demonstrated that the deviation (in Nusselt number) from the Darcian results is less than 4 percent only when the product of the porous Rayleigh number and Darcy number (based on the enclosure width) divided by the aspect ratio of the box (height/width) is less than 10^{-3}. Other boundary layer analyses using non-Darcian formulations have been reported for free convection, cf. Plumb and Huenefeld [11] and Bejan and Poulikakos [12] (inertia effects), and forced convection, cf. Vafai and Tien [7] (boundary and inertia effects). In order to study both of the latter effects in a simple configuration, free convection in a vertical infinite two-dimensional porous slot has been analyzed by the present authors, cf. [13]. In all the above studies, the non-Darcian effects were proven to become more significant as the convection rate increases.

In horizontally unbounded porous layers confined between two impermeable walls and heated isothermally from below, the onset of convection is marked by the following critical values, cf. Lapwood [14]

$$\mathrm{Ra}_m^{\mathrm{crit}} = 4\pi^2, \quad \alpha^{\mathrm{crit}} = \pi \tag{1}$$

Katto and Masuoka [9] showed that the Darcian limit for the first bifurcation point given by equation (1) is essentially reached when $\mathrm{Da} \leq 10^{-3}$, a result that cannot be influenced by the quadratic term in the motion equation. Straus [15] used a Galerkin technique to find the finite amplitude steady solutions of the two-dimensional Darcy-Bénard problem and employed a maximum heat transfer criterion to select the wavenumber. He developed the stability envelope (in the form of a balloon that delineates the Ra_m-α space where two-dimensional rolls can exist) and predicted a monotonic increase of the wavenumber with the Rayleigh number. His heat transfer predictions fall within the range of experimental data and between the predictions of Gupta and Joseph [16] and those of Combarnous [17]. The same problem was addressed by Somerton et al. [18], who employed the Brinkman-Darcy-Boussinesq formulation with arguments from the thermodynamic theory of Glansdorff and Prigogine [19]. They predicted a monotonic decrease of the preferred wavenumber with the Rayleigh number. As far as the mode of steady convection is concerned, in contrast to the two-dimensional rolls observed by Caltagirone et al. [20], who used a thin slotlike convection cell, observations in slablike boxes reveal steady polyhedral (hexagonal) cells between the first two bifurcation points, the second bifurcation marking the onset of fluctuating convection, cf. Combarnous and Bories [21]. Straus and Schubert [22] suggested that of the steady two-dimensional or three-dimensional convection states possible, when the wavenumber lies within Straus' [15] balloon, the two-dimensional mode is "probably preferred." Outside that balloon, the motion in an infinite porous slab is necessarily three dimensional. However, as proven by Schubert and Straus [23], the transition from two-dimensional steady to two-dimensional oscillatory mode is impossible for the infinite layer.

In his review article, Cheng [24] presented a compilation of experimental heat transfer results for convection in horizontal porous layers. In his summary plot of the Nusselt number versus the porous Rayleigh number (Fig. 37 in [24]), one can see a large spread in the data. It is obvious to many researchers that more physics has to be included in the model to account for this scatter. Combarnous and Bories [25] implemented a two-energy equation model and assumed a finite heat transfer coefficient between the solid and fluid phases. Somerton [26] isolated some weaknesses of the above formulation and showed that the Nusselt number experimental values increase with a modified porous Prandtl number. Unfortunately in his

---

Contributed by the Heat Transfer Division for publication in the JOURNAL OF HEAT TRANSFER. Manuscript received by the Heat Transfer Division February 25, 1985. Paper No. 84-HT-115.

formulation, the momentum equation is rather unrealistic since the vector corresponding to Forchheimer's quadratic term is not parallel to the filtration velocity vector. Prasad et al. [27] employed an "effective" medium thermal conductivity that depends on Ra_m, in order to reduce the scatter of the heat transfer results for porous enclosures but neglected the quadratic term in favor of the convective inertia term. In an experimental investigation of convection in boxes heated from the side, Seki et al. [28] suggested that the divergence in the data is an explicit effect of the porous medium Prandtl number and gave a correlation of the form

$$\mathrm{Nu} = C\mathrm{Ra}_m^r \mathrm{Pr}^p \tag{2}$$

The constant C in equation (2) depends on the aspect ratio of the box and the exponents r, p are evaluated experimentally. Jonsson [29] obtained heat transfer data for free convection in porous cylindrical cells heated from below and reported a correlation in the form of (2) but with a modified Prandtl number ($\mathrm{Pr} \cdot \mathrm{KC}$). The factor KC depends on the geometric characteristics of the porous medium and the correlation yields prediction with ±10 percent scatter, cf. Catton [30].

In the following, we present a numerical solution of a non-Darcian model which accounts for the inertial (Forchheimer term) and boundary effects (Brinkman extension). It is our objective to validate and explain such effects in the simplest realization of the canonical porous Bénard problem. We postulate that the scatter in the Nusselt number laboratory data can be reduced by including the quadratic inertia terms in the formulation. Although the celebrated simplicity of the Darcian formulation is lost, our mixed finite difference-pseudospectral scheme remains economical. Since there are no lateral boundaries in the theoretical domain, horizontal wavenumber selection is an additional complication to the problem that requires closure.

2 Formulation of the Governing Equations

For an incompressible infiltrating fluid, the (local average) filtration velocity field is solenoidal

$$\nabla \cdot \mathbf{q} = 0 \tag{3}$$

and the momentum equation can be written in terms of macroscopic (physically) measurable properties of the flow, cf. Georgiadis [31]

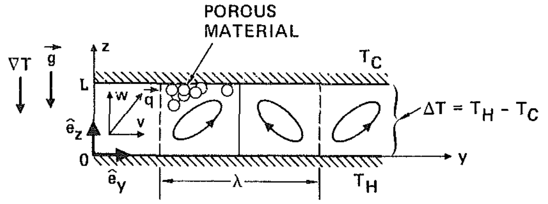

Fig. 1 Two-dimensional convection cells inside the infinite porous layer heated uniformly from below

$$\frac{1}{\epsilon}\frac{\partial \mathbf{q}}{\partial t} = -\frac{\nabla P}{\rho} + \mathbf{g} + \frac{\nu}{\epsilon}\nabla^2 \mathbf{q} - \frac{\nu}{\gamma}\mathbf{q} - \frac{b}{\gamma}|\mathbf{q}|\mathbf{q} \tag{4}$$

where γ and b are assumed to remain constant everywhere inside the porous medium. Their values are given by Ergun [2] for packed beds of bead diameter d and porosity ϵ

$$\gamma = \frac{d^2\epsilon^3}{150(1-\epsilon)^2}, \quad b = \frac{1.75\, d}{150(1-\epsilon)} \tag{5}$$

Assuming local thermodynamic equilibrium between the solid and liquid phases, cf. Wong and Dybbs [32], and that the (saturated) medium is isotropic with respect to thermal conduction, we can adopt a local volume average energy equation with an equivalent thermal conductivity k_m, cf. Combarnous and Bories [21]

$$(\rho c)_m \frac{\partial T}{\partial t} + (\rho c)_f \mathbf{q} \cdot \nabla T = k_m \nabla^2 T \tag{6}$$

In all the above, constant properties and the Boussinesq approximation have been tacitly assumed with the following equation of state for the infiltrating fluid

$$\rho = \rho_c[1 - B(T - T_c)] \tag{7}$$

We consider the flow field confined between two isothermal impermeable walls of infinite horizontal extent (see Fig. 1). Taking the temperature of the cold wall T_c and the pressure of the isothermal (static) field P_{hydro} as reference values, the temperature and pressure fields can be expressed as

Nomenclature

a_m = thermal diffusivity $= k_m/(\rho c)_f$
A_0, A_k = Fourier coefficients of the velocity amplitude, equation (15)
b = inertial resistance coefficient in equation (5), m
B = volumetric thermal expansion coefficient of the fluid
c = specific heat
d = diameter of the beads in the porous packed bed
Da = Darcy number $= \gamma/L^2$
$\mathbf{g}$ = gravitational acceleration in the $-z$ direction
k_m = equivalent (stagnant) thermal conductivity coefficient, W/(mK)
K = number of terms in the truncated Fourier series expansion (13)
KC = Kozeny-Carman inertial coefficient $= \gamma/(b\,L)$
L = thickness of the porous layer, Fig. 1
Nu = Nusselt number
P = average pressure of the interstitial fluid
Pr = Prandtl number $= \nu(\rho c)_f/k_m$
$\mathbf{q}$ = average filtration velocity
Ra = Rayleigh number $= gB\,\Delta T \cdot L^3/(\nu_f a_m)$
Ra_m = porous Rayleigh number $= \mathrm{Da} \cdot \mathrm{Ra}$
t = time
T = temperature
ΔT = temperature difference $= T_H - T_C$
v, w = horizontal, vertical velocity components respectively, Fig. 1
y, z = horizontal, vertical Cartesian coordinates respectively
α = dimensionless wavenumber $= 2\pi/\lambda$, Fig. 1
γ = porous medium permeability, m^2
ϵ = porosity
ν = kinematic viscosity of infiltrating fluid
ρ = fluid density
Φ = entropy production functional, equation (16)
ω = inertial drag coefficient $= (\mathrm{Pr} \cdot \mathrm{KC})^{-1}$
Ω = heat capacity ratio $= (\rho c)_f/(\rho c)_m$

Subscripts

C = cold
f = fluid
H = hot
k = kth order mode
m = porous medium
0 = horizontal average

Superscripts

$*$ = perturbation
crit = critical value

Special symbols

D = z derivative

$$T = T_c + T^*,\ P = P_{\text{hydro}} + P^* \tag{8}$$

Using (7), the hydrostatic part of the pressure gradient in the momentum equation (4) is canceled out by the uniform gravity term in the buoyancy force. The momentum equation yields

$$-\frac{1}{\epsilon}\frac{\partial \mathbf{q}}{\partial t} + \frac{\nu}{\epsilon}\nabla^2\mathbf{q} - \frac{\nu}{\gamma}\mathbf{q} - BT^*\mathbf{g} - \frac{\nabla P^*}{\rho} = \frac{b}{\gamma}|\mathbf{q}|\mathbf{q} \tag{9}$$

Introducing the following scales for nondimensionalization

$$\begin{aligned} &\text{time} : L^2/a_m, && \text{length} : L \\ &\text{temperature} : \Delta T = T_H - T_C, && \text{pressure} : \rho\nu_f a_m/L^2 \end{aligned} \tag{10}$$

and suppressing any new notation, the two-dimensional steady-state form of the governing equations (3), (6), and (9) becomes

$$\frac{\partial v}{\partial y} + \frac{\partial w}{\partial z} = 0 \tag{11a}$$

$$\frac{1}{\epsilon}\left(\frac{\partial^2 v}{\partial y^2} + \frac{\partial^2 v}{\partial z^2}\right) - \frac{1}{\text{Da}}v - \frac{\partial P^*}{\partial y} = \omega|\mathbf{q}|v \tag{11b}$$

$$\frac{1}{\epsilon}\left(\frac{\partial^2 w}{\partial y^2} + \frac{\partial^2 w}{\partial z^2}\right) - \frac{1}{\text{Da}}w + \text{Ra}T^* - \frac{\partial P^*}{\partial z} = \omega|\mathbf{q}|w \tag{11c}$$

$$\frac{\partial^2 T^*}{\partial y^2} + \frac{\partial^2 T^*}{\partial z^2} = v\frac{\partial T^*}{\partial y} + w\frac{\partial T^*}{\partial z} \tag{11d}$$

with the following boundary conditions (no penetration, no slip, and isothermal):

$$w = v = 0,\ T^* = 0 \text{ at } z = 1;\ w = v = 0,\ T^* = 1 \text{ at } z = 0 \tag{12}$$

3 Method of Solution

We assume that the steady-state solution of the system of equations (11) subject to (12) exhibits a horizontal periodicity (two-dimensional rolls) at low values of $\text{Ra}_m > \text{Ra}_m^{\text{crit}}$. Using the discrete spectrum $\{\alpha_k\} = k\alpha$ with $k = 1, 2, \ldots K$, we form a truncated Fourier series representation of the solution in the functional space spanned by an orthonormal basis as follows

$$\begin{Bmatrix} v(y,z) \\ w(y,z) \\ T^*(y,z) \\ P^*(y,z) \end{Bmatrix} \cong \begin{Bmatrix} 0 \\ 0 \\ T_0(z) \\ P_0(z) \end{Bmatrix} + \sqrt{2}\sum_{k=1}^{K} \begin{Bmatrix} v_k(z)\sin\alpha_k y \\ w_k(z)\cos\alpha_k y \\ T_k(z)\cos\alpha_k y \\ P_k(z)\cos\alpha_k y \end{Bmatrix} \tag{13}$$

Preserving the primitive variable formulation of the problem, we can eliminate the pressure between (11*b*, *c*). Then, by substituting (13) into the resulting governing equations, weighting with the appropriate basis and forming inner products (integrating in the y direction over the convection cell), we obtain the following weak formulation of the problem as a system of Galerkin O.D.E.'s

$$\alpha_k v + Dw_k = 0 \tag{14a}$$

$$\left[\frac{1}{\epsilon}(D^2 - \alpha_k^2) - \frac{1}{\text{Da}}\right](D^2 - \alpha_k^2)w_k$$

$$-\alpha_k^2\text{Ra}T_k = -\omega(\alpha_k Df_1^k + \alpha_k^2 f_2^k) \tag{14b}$$

$$DP_0 = -\omega\sum_{k=1}^{K} A_k w_k + \text{Ra}T_0 \tag{14c}$$

$$P_k = \frac{\omega}{\alpha_k}f_1^k + \frac{1}{\epsilon\alpha_k^2}D^3 w_k - \left(\frac{1}{\epsilon} + \frac{1}{\alpha_k^2\text{Da}}\right)Dw_k \tag{14d}$$

$$D^2 T_0 = \sum_{m=1}^{K} D(w_m T_m) \tag{14e}$$

$$(D^2 - \alpha_k^2)T_k = f_3^k \tag{14f}$$

with the index k ranging through 1, 2, 3, . . . K.

In the system of equations given above, the velocity amplitude $|\mathbf{q}|$ has been assumed to have a spectral representation of the same form and order as the velocity components

$$\frac{1}{\sqrt{2}}|\mathbf{q}| \cong A_0 + \sum_{k=1}^{K} A_k\cos\alpha_k y = \left[\left(\sum_{k=1}^{K} w_k\cos\alpha_k y\right)^2\right.$$

$$\left. + \left(\sum_{k=1}^{K} v_k\sin\alpha_k y\right)^2\right]^{1/2} \tag{15}$$

The following functionals are also defined for $k = 1$, 2, 3, . . . K

$$f_1^k \ \hat{=}\ \sqrt{2}A_0 v_k + \frac{1}{\sqrt{2}}\sum_{n,m=1}^{K} v_n A_m I_1(k, n, m)$$

$$f_2^k \ \hat{=}\ \sqrt{2}A_0 w_k + \frac{1}{\sqrt{2}}\sum_{n,m=1}^{K} w_n A_m I_2(k, n, m)$$

$$f_3^k \ \hat{=}\ DT_0 w_k$$

$$+\frac{1}{\sqrt{2}}\sum_{n,m=1}^{K}\left[\frac{n}{m}Dw_m T_n I_1(n, m, k) + w_m DT_n I_2(k, n, m)\right]$$

and the following convolution products have been used

$$I_1(k, n, m) = \frac{4\alpha}{\pi}\int_0^{\pi/\alpha}\sin\alpha_k y\sin\alpha_n y\cos\alpha_m y\,dy = \begin{cases} 1, & m = |k-n| \\ -1, & m = k+n \\ 0, & \text{other} \end{cases}$$

$$I_2(k, n, m) = \frac{4\alpha}{\pi}\int_0^{\pi/\alpha}\cos\alpha_k y\cos\alpha_n y\cos\alpha_m y\,dy = \begin{cases} 1, & m = |k-n| \\ & \text{or } m = k+n \\ 0, & \text{other} \end{cases}$$

Given the wavenumber α (and of course the direction of the rotation in the roll), equations (14*b*, *e*, *f*) form a closed system of nonlinear ordinary differential equations along with the boundary conditions

$$v_k = w_k = T_k = 0, \text{ at } z = 0, 1;\ T_0 = 1 \text{ at } z = 0,\ T_0 = 0 \text{ at } z = 1$$

A standard iterative algorithm is used to solve the above system of equations after approximating the nonlinear r.h.s. of the equations with a Frechét-Taylor series expansion and retaining only linear terms (Newton-Kantorovich quasilinearization). Due to the high storage requirement of the matrix operator of the quasi-linearized system, we apply total modal decomposition solving for each w_k, T_k separately, cf. McDonough and Catton [33]. The resulting $(2K+1)$ O.D.E.'s are coupled only through iterations. The terms that correspond to the quadratic Forchheimer r.h.s. of (11*b*, *c*) are evaluated first in the physical plane by (15) and transformed to the spectral plane by using the discrete Fourier transform at each iteration. Centered finite differences are used to approximate the z-differential operators in the Galerkin O.D.E.s (14).

The general problem is well posed only as an initial value problem. In the absence of lateral walls that would remove the

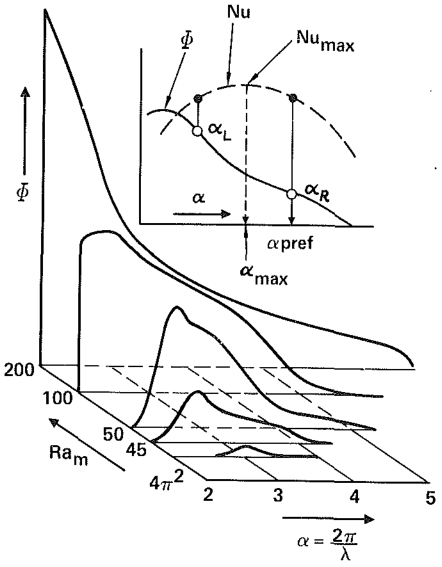

Fig. 2 Behavior of the thermodynamic functional and the inflection criterion for the selection of the preferred wavenumbers

degeneracy of the steady state, we seek a criterion to determine the most probable weavelength of convection. Although a finite band of wavenumbers is realizable (stable) under different initial conditions, we postulate that only discrete values occur for each supercritical Rayleigh number in direct analogy to the Rayleigh-Bénard system.

Letting s denote the specific entropy of the fluid, we can use $[s-(\mathbf{q}\cdot\mathbf{q})/(2T_0)]$ as a Liapunov function, cf. Glansdorff and Prigogine [19]. The stability of the (stationary) convective state is given by the following global stability criterion (integration over the convection roll), cf. Georgiadis [31]

$$\Phi = \frac{c}{g\,B\,L}\mathrm{Ra}\Omega\frac{\pi}{\alpha}\int_0^1 T_0(d^2T_0/dz^2)dz \geq 0 \qquad (16)$$

Denoting $\delta T = T^* - T_0$, the mean heat transfer across the layer, as expressed by the Nusselt number, can be written as follows

$$\mathrm{Nu} = -\frac{dT_0(0)}{dz} = \frac{\alpha}{\pi}\int_0^{\pi/\alpha}\int_0^1 |\nabla T^*|^2 dz dy$$

$$= \frac{\alpha}{\pi}\int_0^{\pi/\alpha}\int_0^1 \left(\left|\frac{dT_0(0)}{dz}\right|^2 + |\nabla \delta T|^2\right) dz dy \qquad (17)$$

Now we can integrate the relation (16) by parts and finally reduce it to

$$\Phi = \frac{c}{g\,B\,L}\mathrm{Ra}\Omega\int_0^{\pi/\alpha}\int_0^1 |\nabla\delta T|^2 dz dy \qquad (18)$$

The functional above expresses the entropy production rate in a single roll due to convective temperature fluctuations around the mean temperature field $T_0(z)$ and is always positive definite after the onset of convection.

For constant Ra, considering infinitesimal fluctuations $d\alpha$ around the stable convective states (inside the balloon of Straus [15]) characterized by the value of the wavenumber α, we can associate $\{\partial\Phi/\partial\alpha\}$ to the "excess local potential" of Glansdorff and Prigogine [19]. Consequently, the most probable state is identified by the extremum of this potential, namely

$$\{\partial^2\Phi/\partial\alpha^2 = 0\} \text{ at the preferred wavenumber} \qquad (19)$$

Within the limits of computational accuracy, we identified certain features of the $\mathrm{Nu} = \mathrm{Nu}(\alpha)$, $\Phi = \Phi(\alpha)$ curves with the Ra_m number as a parameter (see Fig. 2). For low supercritical Ra_m numbers, the functional Φ has a maximum whereas for higher values of Ra the maximum moves toward lower values of the wavenumber α that are not physically realizable. There is a value of the wavenumber $\alpha_{\max}$ that maximizes the heat transfer across the layer, as expressed by the Nu number. There are generally two inflection points on the $\Phi = \Phi(\alpha)$ curve for each supercritical Ra_m number. These correspond to a pair of α_L (Left) and α_R (Right) wavenumbers which we identify with the "preferred" wavenumbers according to the selection criterion (19).

4 Numerical Results and Discussion

The following evaluation tests were performed on the code via numerical computations. The convergence of the grid functions and Nusselt number as the grid size decreases was checked. An accuracy of 2 percent in the Nusselt number was achieved with a uniform mesh of 50 grid points across the layer thickness. The convergence rate of Newton-Kantorovich iterations with respect to the max-norm pointwise error was found to be close to linear due to the damping employed in the iterations for the computation of T_0, T_k. A max-norm error tolerance of 10^{-3} was used to terminate the iterations. The Fourier series convergence, and consequently the absolute and uniform convergence of the expansion (13), was also verified. A six-term approximation yielded negligible truncation error, and therefore was used throughout the computation. The power integral solution given in [21] was used as an initial guess to start the Newton-Kantorovich iterations for some value of Ra_m safely close to the critical value. Then for each wavenumber α, the continuation mode enabled us to march up in Ra_m in small increments so as to keep the number of iterations below some economical value (less than 100).

Measured physical properties (ϵ, γ, k_m), and values of the other parameters such as Pr and b estimated by means of equation (5), were used as inputs to the numerical scheme that models the porous Bénard problem. These systems correspond to packed spherical particle beds used in the experimental work of Jonsson [29]. They were selected so as to span a wide range of values of $\omega = (\mathrm{KC}\cdot\mathrm{Pr})^{-1}$, and to have data available for comparison with our calculation. Numerical solutions to the thermohydrodynamic field were obtained for the three sets of input data given in Table 1 which correspond to similar packed beds (random packing $\mathrm{Da} \sim 10^{-5}$, $\gamma \sim 10^{-8}$ m^2) saturated with oil or water. The Prandtl numbers (or ω) vary from a low (high) of $\mathrm{Pr} = 0.58$ ($\omega \sim 300$) as in steel-water, to a high (low) of $\mathrm{Pr} = 236.0$ ($\omega \leq 0.7$) as in the case of glass-oil (1 Stokes).

The heat transfer results for glass-water with $\mathrm{Pr} = 4.5$ ($\omega \sim 50$) are plotted in Fig. 3 for the range $100 \leq \mathrm{Ra}_m \leq 275$, along with the thermodynamic functional given by (16) and the selected wavenumbers according to the inflection point criterion (19). A dramatic decrease of the heat transfer, as expressed by the Nusselt versus wavenumber curve, is observed for the high ω case (steel-water) (see Fig. 3). Concerning the physics of the roll-type convective flow in this case, there is a smaller loss of kinetic energy in each period of circulation by dissipation due to the Darcy and Brinkman terms. The larger part of the kinetic energy is stored in the fluid of increased inertia (flywheel effect) and consequently there is smaller release of potential energy (by convection). This is analogous to the "inertial" regime in the Rayleigh-Bénard convection. The inertial effect is less explicit for the high Prandtl number (low ω) system since the Nu-α curve for each Ra_m differs very little from the corresponding one for glass-water (moderate ω). The same type of asymptotic behavior of the Nusselt number has also been observed in the Rayleigh-Bénard problem for Pr of order one and higher. The Nu-α curves for the medium and low ω systems are very close to the predictions by Straus [15] for $\mathrm{Ra}_m = 200$ (Darcian model, infinite Prandtl number). This verifies numerical results that show that the existence of the Brinkman term has a negligible effect on the mean heat transfer for $\mathrm{Da} \sim 10^{-5}$ and lower (this is the range for most

Table 1 Thermophysical data for the porous packed beds

Glass-oil	Ra_m	$Da \times 10^5$	$KC \times 10^2$	ω
	65.4	0.955	0.59	0.718
$Pr = 236$	107.4	1.13	0.642	0.66
$d = 6$ mm	150	"	"	"
$\epsilon = 0.394$	200	"	"	"
$\gamma = 3.67 \times 10^{-8}$ m^2	225	"	"	"
$b = 0.116$ mm	250	"	"	"
$k_m = 0.6$ W/(mK)	275	"	"	"
Glass-water	Ra_m	$Da \times 10^5$	$KC \times 10^2$	ω
$Pr = 4.5$	100	0.9247	0.5	44.5
$d = 6$ mm	150	0.5201	"	"
$\epsilon = 0.394$	200	"	0.43	51.5
$\gamma = 3.67 \times 10^{-8}$ m^2	225	"	"	"
$b = 0.116$ mm	250	"	"	"
$k_m = 1.1$ W/(mK)	275	"	"	"
Steel-water	Ra_m	$Da \times 10^5$	$KC \times 10^2$	ω
	80	0.642	0.168	1026
$Pr = 0.58$ mm	100	1.194	0.73	236
$d = 4.8$ mm	150	"	"	"
$\epsilon = 0.393$	200	0.568	0.5	344
$\gamma = 1.91 \times 10^{-8}$ m^2	225	"	"	"
$b = 0.092$ mm	250	"	"	"
$k_m = 8.6$ W/(mK)	275	"	"	"
	300	0.368	0.4	431

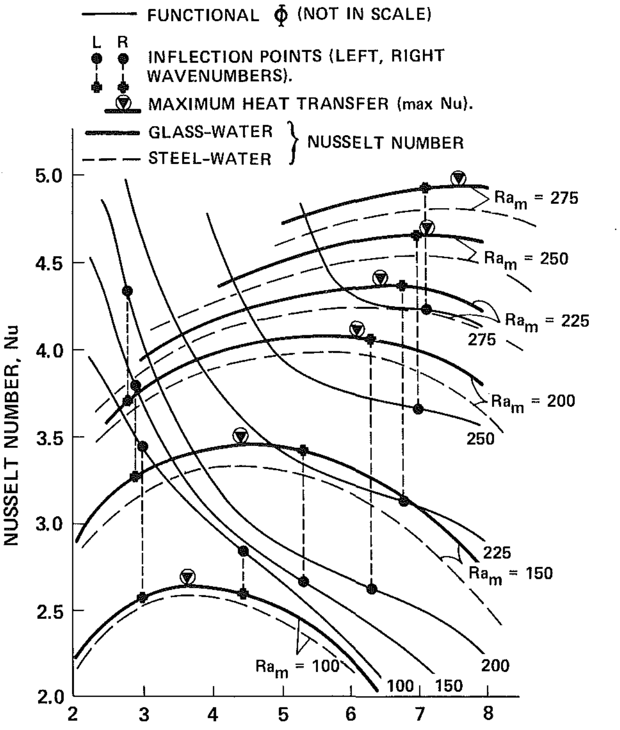

Fig. 3 Computed heat transfer versus wavenumber results for the glass-water and steel-water packed beds; wavenumber selection for glass-water

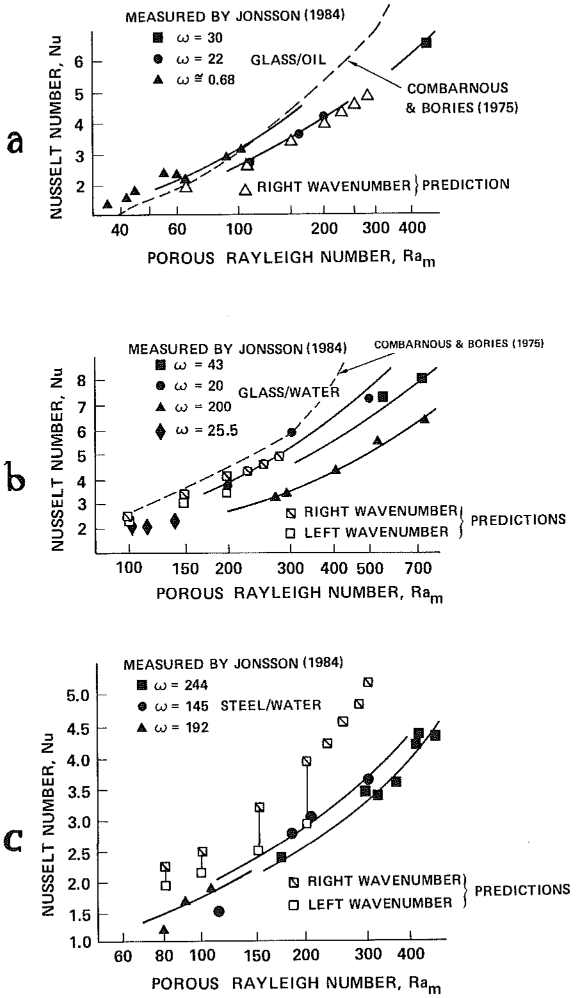

Fig. 4 Comparison of the Nusselt number predictions with laboratory measurements: (*a*) glass-oil, (*b*) glass-water, and (*c*) steel-water

laboratory experiments and geothermal flows) for $Ra_m \leq 300$, in direct agreement with the criterion presented in [10], see also [26]. For fixed ω, higher values of Da (or permeability) lower the Nusselt number and this can have a physical explanation in terms of lowering the dissipation due to the Darcy term; see discussion above.

The heat transfer data predicted according to the criterion (19) are plotted against the corresponding laboratory measurements by Jonsson [29] and also by Combarnous and Bories [21] in Figs. 4(*a*, *b*, *c*). With the exception of glass-oil, our closure criterion produced pairs of preferred wavenumbers. The ad-hoc theory that supports it gives no indication as to which of the two, α_L or α_R, is the wavenumber that the system selects "naturally," or whether it selects any one at all. Our results indicate that the best agreement is obtained by using the "Left" wavenumbers, which decrease monotonically with the porous Rayleigh number. The similarity with the Rayleigh-Bénard problem should be mentioned; see data by Willis et al. [34]. We could not locate (numerically)

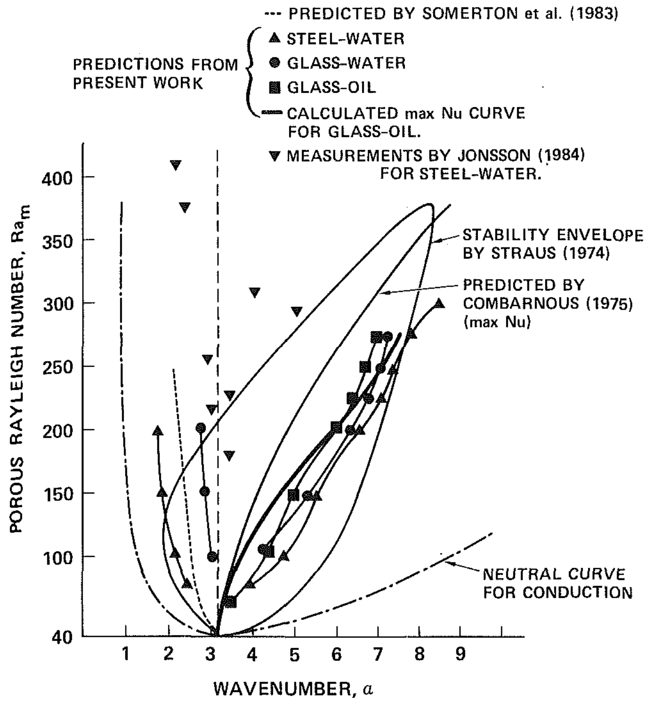

Fig. 5 Wavenumber predictions for the two-dimensional porous Bénard problem in a horizontally unbound domain

"Left" wavenumbers for values of Ra_m higher than 200, but there is enough evidence, both analytical and experimental, to support the existence of a different (fluctuating) mode of convection in porous cavities above that Rayleigh number. The onset of this different mode is marked by an abrupt change of the slope of the Nu-Ra_m curves just below $Ra_m = 300$ in the data reported by Combarnous and Bories [21] (see Figs. 4*a*, *b*).

The agreement between predicted and measured Nusselt numbers by using ω as a parameter and the absence of any competing formulation of convective flow in porous media with constant properties (easy to estimate or measure) lend support to our postulate that the large-scale divergence of heat transfer data reported by many investigators is primarily due to inertia effects. Since ω is the pertinent parameter, such effects can become important even for moderate porous Prandtl numbers. For example, the Nusselt numbers for glass-water with $\omega = 200$ in Fig. 4(*b*) (obtained with small beads of low permeability and high inertia resistance) are consistently lower than the other measured glass-water data, although the porous Prandtl number is almost the same ($Pr \sim 4$), and agree with the high ω (steel-water) data of Fig. 4(*c*). Our Nusselt number predictions agree with the measured values by Combarnous and Bories [21] in Figs. 4(*a*, *b*) only as far as the trend to decrease with increasing ω is concerned. The manner in which geometry enters into ω makes much of the published heat transfer data troublesome to use as most investigators neglect to report the plate spacing for each data point or other physical parameters of the laboratory packed beds.

Although the agreement is always better when the "Left" wavenumber α_L is used, the difference between Nu_L-Nu_R (if any) is negligible in the high and middle Pr number cases. In the case of low Pr number system (steel-water) however, it is only the left wavenumber α_L that produces the most favorable results. By using the maximum-Nu criterion to select the wavenumbers for each different system, we notice a definite monotonic increase of the wavenumber α versus the Ra_m (see Fig. 5) in analogy to similar trends in computations for the classical Rayleigh-Bénard computations. Comparison with measurements shows that the maximum heat transfer criterion fails since it generally overpredicts the Nusselt number. The wavenumber predictions by Somerton et al. [18] using the selection criterion $\{d^2\Phi/d\mathrm{Ra}^2 = 0\}$ are also presented in Fig. 5.

Our wavenumber predictions according to the criterion (19) are plotted in Fig. 5, along with some measured values of α for the steel-water system by Jonsson [29]. The latter were estimated from pointwise temperature measurements inside the cylindrical convection cell used and therefore their measurement accuracy is contingent upon wall and curvature effects. Although the deviations between predicted and measured values for the "preferred" wavenumbers are far from being tolerable, the divergence of the measured values serves as an indication of a possible multiplicity of wavenumbers in porous convection, maybe in the form of competing patterns. The predicted wavenumbers presented in Fig. 5 exhibit the same qualitative feature as in the Rayleigh-Bénard problem (cf. [34]): The lower (higher) the Pr number (ω), the more rapidly the wavenumber changes, especially near the onset of convection.

5 Conclusion

The formulation of the motion equation (4) showed how Darcy's law can be extended in a buoyancy-driven flow to include the inertia effects whose relative importance is expressed by the nondimensional parameter $\omega = (b\ L)/(\mathrm{Pr}\ \gamma)$, provided that the Darcy number is less than 10^{-5} and $4\pi^2 < Ra_m \leq 300$. The inertia terms affect the free convective heat transfer in much the same way as in the Rayleigh-Bénard problem; that is, the lower the inertial drag coefficient ω, the larger the Nusselt number, until an asymptotic regime is reached where Nu becomes insensitive to further decrease of ω.

Although the (inflection point) wavenumber selection criterion (19) is not conclusive, it remains operational since it reproduces the divergence observed in the heat transfer results when measured values of the thermophysical parameters of the packed bed are used. Best agreement with the experimental data of Jonsson [29] is found when the set of wavenumbers monotonically decreasing with the Rayleigh number is selected. However, due to the ad-hoc nature of the wavenumber selection criterion, a point of major contention is not resolved: the existence of uniqueness of a "preferred" value of the horizontal wavenumber.

Acknowledgments

The authors wish to thank Dr. McDonough for his helpful suggestions. The financial support of D.O.E. under grant No. DE-AT03-82ER12021 is gratefully acknowledged as well as the reviewers' constructive criticism.

References

1 Forchheimer, P., "Wasserbevegung durch Boden," *Z. Ver. Deutsch. Ing.*, Vol. 45, 1901, pp. 1782–1788.

2 Ergun, S., "Fluid Flow Through Packed Columns," *Chem. Engng. Prog.*, Vol. 48, No. 2, 1952, pp. 89–94.

3 Wooding, R. A., "Steady State Free Thermal Convection of Liquid in a Saturated Permeable Medium," *J. Fluid Mechanics*, Vol. 2, 1957, pp. 273–285.

4 Irmay, S., "On the Theoretical Derivation of Darcy and Forchheimer Formulas," *Trans. Amer. Geophys. Union*, Vol. 39, No. 4, 1958, pp. 702–707.

5 Polubarinova-Kochina, P. Ya., *Teoriya dvizheniya gruntovȳkh vod. Gosudarstv.*, Izdat. Tekh. Teoret.-Lit., Moscow, 1952.

6 Choudhary, M., Propster, M., and Szekely, J., "On the Importance of the Inertial Terms in the Modeling of Flow Maldistribution in Packed Beds," *AIChE Journal*, Vol. 22, No. 3, 1976, pp. 600–603.

7 Vafai, K., and Tien, C. L., "Boundary and Inertia Effects on Flow and Heat Transfer in Porous Media," *Int. J. Heat Mass Transfer*, Vol. 24, Part 2, 1981, pp. 195–203.

8 Chan, B. K. C., Ivey, C. M., and Barry, J. M., "Natural Convection in Enclosed Porous Media With Rectangular Boundaries," ASME JOURNAL OF HEAT TRANSFER, Vol. 92, 1970, pp. 21–27.

9 Katto, Y., and Masuoka, T., "Criterion for the Onset of Convection in a Fluid in a Porous Medium," *Int. J. Heat Mass Transfer*, Vol. 10, 1967, pp. 297–309.

10 Tong, T. W., and Subramanian, E., "A Boundary-Layer Analysis for

Natural Convection in Vertical Porous Enclosures – Use of the Brinkman-Extended Darcy Model," *Int. J. Heat Mass Transfer*, Vol. 28, Part 3, 1985, pp. 563-571.

11 Plumb, O. A., and Huenefeld, J. C., "Non-Darcy Natural Convection From Heated Surfaces in Saturated Porous Media," *Int. J. Heat Mass Transfer*, Vol. 24, Part 4, 1981, pp. 765-768.

12 Bejan, A., and Poulikakos, D., "The Non-Darcy Regime for Vertical Boundary Layer Natural Convection in a Porous Medium," *Int. J. Heat Mass Transfer*, Vol. 27, Part 5, 1984, pp. 717-722.

13 Georgiadis, J. G., and Catton, I., "Free Convective Motion in an Infinite Vertical Porous Slot: the Non-Darcian Regime," *Int. J. Heat Mass Transfer*, 1985 (in press).

14 Lapwood, E. R., "Convection of a Fluid in a Porous Medium," *Proc. Cambridge Phil. Soc.*, Vol. 44, 1948, pp. 508-521.

15 Straus, J. M., "Large Amplitude Convection in Porous Media," *J. Fluid Mechanics*, Vol. 64, Part 1, 1974, pp. 51-63.

16 Gupta, V. P., and Joseph, D. D., "Bounds for Heat Transport in a Porous Layer," *J. Fluid Mech.*, Vol. 57, 1973, pp. 491-514.

17 Combarnous, M., "Etude numérique de la convection naturelle dans une couche poreuse horizontale," *Comptes Rendus Acad. Sci. Paris*, Ser. B, Vol. 271, 1970, pp. 357-360.

18 Somerton, C. W., McDonough, J. M., and Catton, I., "Natural Convection in Porous Media: a Mixed Finite Difference-Galerkin Solution With Wavenumber Predictions," *Proc. VII Int. Heat Transfer Conference*, Hemisphere, New York, 1983.

19 Glansdorff, P., and Prigogine, I., *Thermodynamic Theory of Structure, Stability and Fluctuations*, Wiley Interscience, New York, 1971.

20 Caltagirone, J. P., Cloupeau, M., and Combarnous, M. A., "Convection naturelle fluctuante dans une couche poreuse horizontale," *Comptes Rendus Acad. Sci. Paris*, Ser. B, Vol. 273, 1971, pp. 833-836.

21 Combarnous, M., and Bories, S. A., "Hydrothermal Convection in Saturated Porous Media," *Advances in Hydroscience*, Vol. 10, Academic Press, 1975, pp. 231-307.

22 Straus, J. M., and Schubert, G., "On the Existence of 3-D Convection in a Rectangular Box Containing Fluid-Saturated Porous Material," *J. Fluid Mechanics*, Vol. 87, Part 2, pp. 385-394.

23 Schubert, G., and Straus, J. M., "3-D and Multicellular Steady and Unsteady Convection in Fluid-Saturated Porous Media at High Ra," *J. Fluid Mechanics*, Vol. 94, Part 1, 1979, pp. 25-38.

24 Cheng, P., "Heat Transfer in Geothermal Systems," *Adv. Heat Transfer*, Vol. 14, 1978, pp. 1-105.

25 Combarnous, M., and Bories, S. A., "Modélization de la convection naturelle au sein d'une couche poreuse horizontale à l'aide d'un coefficient de transfert solide-fluide," *Int. J. Heat Mass Transfer*, Vol. 17, 1974, pp. 505-515.

26 Somerton, C. W., "The Prandtl Number Effect in Porous Layer Convection," *Appl. Sci. Res.*, Vol. 40, 1983, pp. 333-344.

27 Prasad, V., Kulacki, F. A., and Keyhani, M., "Natural Convection in Porous Media," *J. Fluid Mechanics*, Vol. 150, 1985, pp. 89-119.

28 Seki, N., Fukusako, S., and Inaba, H., "Heat Transfer in a Confined Rectangular Cavity Packed With Porous Media," *Int. J. Heat Mass Transfer*, Vol. 21, 1978, pp. 985-989.

29 Jonsson, T., "Natural Convection in Porous Media: Prandtl Number Effects," M.S. thesis, Department of Engineering, UCLA, Los Angeles, 1984.

30 Catton, I., "Natural Convection Heat Transfer in Porous Media," *Natural Convection: Fundamentals and Applications*, Hemisphere, New York, 1985.

31 Georgiadis, J. G., "Numerical Study of the Inertial Effect on Natural Convection in an Infinite Horizontal Fluid-Saturated Porous Layer," M.S. thesis, Department of Engineering, UCLA, Los Angeles, 1984.

32 Wong, K., and Dybbs, A., "An Experimental Study of Thermal Equilibrium in Liquid Saturated Porous Media," *Int. J. Heat Mass Transfer*, Vol. 18, 1976, pp. 234-235.

33 McDonough, J. M., and Catton, I., "A Mixed Finite Difference-Galerkin Procedure for 2-D Convection in a Square Box," *Int. J. Heat Mass Transfer*, Vol. 25, Part 8, 1982, pp. 1137-1146.

34 Willis, G. E., Deardorff, J. W., and Somerville, R. C., "Roll-Diameter Dependence in Rayleigh Convection and Its Effect Upon the Heat Flux," *J. Fluid Mechanics*, Vol. 54, Part 2, 1972, pp. 351-367.

Natural Convection Heat Transfer From a Horizontal Cylinder Between Vertical Confining Adiabatic Walls

F. Karim

B. Farouk
Assoc. Mem. ASME

I. Namer
Mem. ASME

Mechanical Engineering and Mechanics
Department,
Drexel University,
Philadelphia, PA 19104

This paper reports an experimental study of natural convection heat transfer from a horizontal isothermal cylinder between vertical adiabatic walls. Some of the industrial applications of this problem are cooling and casing design of electronic equipment, nuclear reactor safety, and heat extraction from solar thermal storage devices. Heat transfer from 3.81 cm and 2.54 cm diameter cylinders was determined by measuring the electric power supplied to the heater, which was placed inside the cylinders, and correcting for radiation and end losses. Average Nusselt numbers were determined for a Rayleigh number range of 2×10^3 to 3×10^5 and wall spacing to cylinder diameter ratios of 1.5, 2, 3, 4, 6, 8, 10, 12, and ∞. It was found that the confinement of a heated horizontal cylinder by adiabatic walls enhances the heat transfer from the cylinder continuously. This effect is more pronounced at low Rayleigh numbers. A maximum relative enhancement of 45 percent was obtained over the range of experimental conditions studied. Schlieren and flow visualization studies were conducted at selected values of Rayleigh number and wall spacing to cylinder diameter ratios to further explain the heat transfer characteristics and the associated flow physics of the present problem.

Introduction

Natural convection heat transfer from isothermal horizontal cylinders between confining walls has many practical applications. Cooling and casing design of electronic equipment, nuclear reactor safety devices, ocean thermal energy conversion, and heat extraction for solar thermal storage devices are some examples of the applications of this problem. Despite its importance, this problem has attracted little attention up to now, even though natural convection heat transfer from an unconfined horizontal cylinder has been extensively investigated in the past. Buoyancy-induced convection mechanisms become more complex when there are interactions of the flow with solid boundaries, obstructions, or enclosures. In the present configuration, that of a heated cylinder in a two-dimensional channel whose walls are adiabatic, the heated cylinder provides buoyancy to the fluid in the channel and, in effect, acts as a pump. This establishes a directed flow far upstream of the heated cylinder. The problem is considerably more complicated than that of a cylinder in an infinite medium.

An experimental investigation designed to systematically study the influence of confinement of the flow on heat transfer characteristics was performed and the results are reported in the present paper. A schematic of the problem studied can be found in Fig. 1. A horizontal heated cylinder was placed midway between two vertical insulated walls. The cylinder was maintained at a uniform surface temperature. Average Nusselt numbers were measured as a function of Rayleigh number Ra and wall spacing to cylinder diameter ratio W/D. From these measurements the qualitative and quantitative influence of such confinement on heat transfer were deduced. As will be seen, heat transfer is found to be enhanced by confinement over the range of parameters studied. These studies were conducted at wall spacing to cylinder diameter ratios of 1.5, 2, 3, 4, 6, 8, 10, 12, and ∞ and for a Rayleigh number range of 2×10^3 to 3×10^5. To explain the heat transfer characteristics of the present problem and the associated fluid flow behavior, Schlieren and flow visualization studies were also conducted.

Background

When a horizontal heated cylinder is placed between abiabatic vertical walls the Nusselt number will be a function of both Rayleigh number and wall spacing to cylinder diameter ratio W/D. In contrast, when such a cylinder is placed in an unbounded fluid the Nusselt number is only a function of Rayleigh number. The purpose of this study was to quantify the effect of such confinement on heat transfer and qualitatively study the temperature and flow fields near the cylinder.

The natural convection heat transfer from a horizontal

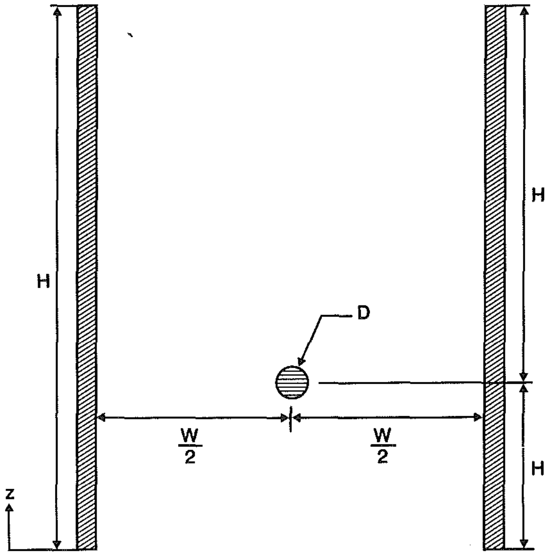

Fig. 1 Schematic of the problem

Contributed by the Heat Transfer Division for publication in the JOURNAL OF HEAT TRANSFER. Manuscript received by the Heat Transfer Division October 22, 1984.

isothermal cylinder in an infinite medium has been studied extensively. There is an abundance of experimental data extending over a wide range of Rayleigh numbers. Empirical correlations as well as numerical solutions of this problem are also available. Besides their own correlations for their experimental data, Fand et al. [1] and Fand and Brucker [2] give an extensive survey of published work on this subject through 1983. Sparrow [3] has found that the empirical correlations of Morgan [4], Raithby and Holland [5], and Fand [1] correlate all the available data equally well. Churchill and Chu [6] proposed a more recent correlation for a wide range of Rayleigh number (laminar and turbulent). However, the correlation of Churchill and Chu [6] lies consistently below the data on which their correlation is based for the range of Rayleigh numbers studied here. This correlation also fell below data for the natural convection from a free cylinder obtained as part of this study.

The available data of heat transfer from a horizontal isothermal cylinder between confining walls are very sparse. Limited experimental data have been obtained by Marsters [7], and Marsters and Paulus [8] for a single cylinder and an array of cylinders between confining walls, respectively. Farouk and Guceri [9] have performed a numerical study of heat transfer from a single cylinder between confining walls by employing a vorticity-stream function formulation. Farouk and Guceri [9] have predicted the existence of an optimum separation of the walls for maximum heat transfer. They assert that this optimum spacing depends upon the Rayleigh number. Farouk and Guceri [9] have also asserted that at low Rayleigh numbers where the boundary layer is thick, wall spacing has a more significant effect upon heat transfer characteristics than at high Rayleigh numbers where the boundary layer is thin. Sparrow and Pfiel [10], on the other hand, have recently suggested that there is no optimal wall spacing and that heat transfer increases with greater confinement. They also suggested that the heat transfer characteristics are, in addition, functions of the parameter H/D (see Fig. 1).

Experimental Apparatus

The apparatus consisted of a cylinder mounted horizontally between insulated vertical walls. Two cylinders of different diameters were used to obtain a wide range of Rayleigh number. This was necessary because, for a given cylinder, there are large uncertainties associated with heat transfer measurements when $(T_s - T_\infty)$ is small (below 1.5°C) for the instrumentation used in this study. It should be noted that, for a given cylinder diameter, Rayleigh number does not increase monotonically with cylinder surface temperature at atmospheric pressure. For a given cylinder diameter in air at atmospheric pressure, the Rayleigh number increases to a maximum and then decreases with increasing temperature difference $(T_s - T_\infty)$. One can easily understand why this happens by considering the definition of Rayleigh number. The fluid properties, such as kinematic viscosity, the coefficient of thermal expansion, and Prandtl number, are evaluated at the film temperature $T_f = (T_s + T_\infty)/2$. In particular, the kinematic viscosity squared increases rapidly with increasing film temperature and eventually increases at a faster rate than the numerator in the definition of Rayleigh number. The maximum Rayleigh number for these experiments occurred when $(T_s - T_\infty)$ was about 140°C.

The restrictions described above limited to range of Rayleigh number in these experiments to between 2×10^3 and 3×10^5. The larger cylinder was made of 0.64-cm wall aluminum tube with an outside diameter of 3.81 cm. The smaller cylinder was made of 0.32-cm wall aluminum tube with an outside diameter of 2.54 cm. The length of the cylinders was chosen such that L/D was large and the induced flow was largely two dimensional. The lengths of the cylinders were 66 cm. Inside each tube was a 61-cm-long electrical cartridge heater with 1.59-cm diameter for the larger cylinder and 0.95-cm diameter for the smaller cylinder. The cartridge heaters were supported concentric with the tube using two copper sleeves at both ends (Fig. 2*a*). The space between the tube and the heater was filled with fine-grade sand. The cylinders were highly polished using car wax (polishing and buffing compound).

To minimize end losses, transite end caps were fabricated and attached to each end of the cylinders. For the larger cylinder, the end caps were 2.54 cm long and had a diameter of 3.81 cm. For the smaller cylinder, the end caps were 3.81 cm long with a diameter of 2.54 cm. The thermal conductivity of the end caps was 0.649 W/m°C.

Using a sufficiently thick-walled aluminum tube in con-

Nomenclature

A = surface area of the cylinder
B = coefficient in equation (10)
C = coefficient in the power law least-square fit, equation (7)
D = diameter of the cylinder
E, F = coefficients in equation (10)
g = acceleration of gravity = 9.8 m/s^2
H = total height of the walls
H_1 = height from the cylinder center to the top of the walls
H_2 = height from the cylinder center to the bottom of the walls
$\bar{h}$ = average heat transfer coefficient for the cylinder
h_o = heat transfer coefficient for the outside surface of the adiabatic walls
k = thermal conductivity
L = length of the cylinder
m = index in the power law least-square fit, equation (7)
$\overline{\mathrm{Nu}}$ = average Nusselt number = $\bar{h}D/k_a$
Pr = Prandtl number
Q = heat transfer rate
Ra = Rayleigh number = $g\beta_a(T_s - T_\infty)D^3\mathrm{Pr}/\nu_a^2$
t = thickness of vertical walls
T = temperature
T_f = film temperature = $(T_s + T_\infty)/2$
T_s = cylinder surface temperature
T^* = nondimensional temperature = $(T - T_\infty)/(T_s - T_\infty)$
T_{ow} = outside surface temperature of the vertical walls
$T_w(z)$ = inside surface temperature of the vertical walls
W = wall spacing
x = distance measured along the axis of the cylinder
z = vertical distance measured from the bottom of the walls
β = volume coefficient of expansion of air = $1/T_f$
ϵ = total normal emissivity
θ = nondimensionalized adiabatic wall temperature = $(T_w(z) - T_\infty)/(T_s - T_\infty)$
ν = kinematic viscosity
σ = Stefan-Boltzmann constant = 5.669×10^{-8} W/m^{2}K^4
ψ^* = nondimensionalized stream function, see [9]

Subscripts

a = air
end = end caps
s = cylinder surface
∞ = ambient

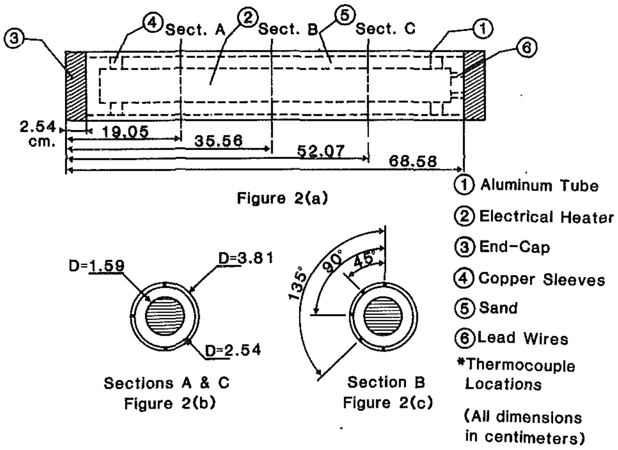

Fig. 2 Internal arrangement of the 3.81-cm-dia cylinder and thermocouple locations

junction with this particular design provided a cylinder with a constant and uniform surface temperature distribution. Eleven type T (copper-constantan) thermocouples were embedded just below the surface of the cylinder (see Fig. 2*a*) to monitor the surface temperature distribution of the cylinder. Measurements confirmed the uniformity of surface temperature distribution of the cylinder. The thermocouples were placed at various locations axially and circumferentially along the cylinder (see Figs. 2*b* and 2*c*). Two thermocouples, separated by a distance of 1.27 cm, were positioned centrally within each of the end caps to determine end losses. An Omega Digicator (model 410-B-T, 0.1°C resolution) in conjunction with a 16-channel selector switch were used to measure temperature.

The adiabatic walls were urethane insulating boards with aluminum sheeting surface (Thermax). The thermal conductivity of the walls was 0.0259 W/m°C. The walls were 2.44 m by 0.69 m (0.66 m for the smaller cylinder) and 2.54 cm in thickness. This gave a wall height to diameter ratio H/D of 64 and 96 for the larger and smaller cylinders, respectively, which provided a good approximation to an infinite channel. The Nusselt number was independent of H/D for such values of H/D. Measurements to confirm this are discussed in a later section. The walls were supported using assemblies (made from steel angles) that could be moved to provide the variations in wall spacing. For the experiments performed H_1 and H_2 were kept equal.

The entire setup was housed within a rigid frame made of steel angles, of dimensions 3.05 m by 0.91 m by 1.52 m. The cylinder was hung from the frame using 0.35-mm-dia steel music wires attached to the ends of the cylinder. The frame was covered with a transparent plastic sheet open at the bottom and at the top. Thin plexiglass boards were used as endplates for the cylinder to prevent axial extrainment of air and minimize three-dimensional effects.

Five type K (Chromel-Alumel) thermocouples were placed at locations $z/H = 0$, 0.25, 0.5, 0.75, and 1.0 on the inside surface of each wall. These provided the wall surface temperature distributions $T_w(z)$, which were needed for radiation correction calculations.

Three theromocouples (type K) were placed at heights 1.22 m, 2.44 m, and 3.66 m above the floor to check the stratification of room air. The stratification of the ambient air in the laboratory was found to be negligible.

Electrical power was supplied to the heater through a voltage regulated a-c source. A rheostat was used to vary the power to the heater. Two digital multimeters (Fluke model 8050 A) were used to measure the voltage supplied to and the current through the heater. The frame was grounded electrically for safety.

Flow and density (temperature) fields near the cylinder were investigated qualitatively. The density field was observed using a 25.4-cm-dia Schlieren system and a 100 W mercury light source and was photographically recorded. For flow visualization, a narrow sheet of light was generated and passed through the top of the test section. This sheet of light illuminated the very fine-powdered chalk that was introduced from the bottom of the test section and was entrained by the flow. A 35 mm SLR camera was placed perpendicular to the flow direction and was used to take photographs of the flow field. The same camera was used to take pictures of the Schlieren image.

All experiments were performed in a well-insulated room located in the basement of the Mechanical Engineering and Mechanics Department Laboratories of Drexel University.

Data Reduction

The major objective of the data analysis procedure was to determine the average Nusselt number for a given Rayleigh number and wall spacing to cylinder diameter ratio W/D. The surface temperature of the cylinder was determined from the average of the eleven surface temperatures measured by the thermocouples. The heat transferred by convection from the cylinder, Q_{conv}, is equal to the electric power delivered to the cartridge heater, Q_{elect}, with appropriate corrections for radiation Q_{rad} and end losses Q_{end} so that

$$Q_{\mathrm{conv}} = Q_{\mathrm{elect}} - Q_{\mathrm{rad}} - Q_{\mathrm{end}} \qquad (1)$$

The electric power was determined by multiplying the voltage across the heater and the current through the heater as measured by the digital multimeters.

The heat loss by conduction from the end caps was determined from Fourier's law of conduction. Knowing the geometry of each end cap, its thermal conductivity, and the temperature at two known locations within it, end losses from each end cap are given by

$$Q_{\mathrm{end}} = -k_{\mathrm{end}} A_{\mathrm{end}} \frac{\Delta T_{\mathrm{end}}}{\Delta x} \qquad (2)$$

where

$$\Delta T_{\mathrm{end}} = T_{\mathrm{end},2} - T_{\mathrm{end},1} \qquad (3)$$

$T_{\mathrm{end},1}$ and $T_{\mathrm{end},2}$ were the temperatures measured within the end caps at locations separated by a distance $\Delta x = 1.27$ cm and A_{end} is the cross-sectional area of the end cap.

The heat loss by radiation from a free cylinder within an infinite medium is given by

$$Q_{\mathrm{rad}} = \epsilon \sigma A (T_s - T_\infty) \qquad (4)$$

where the emissivity of the aluminum cylinder is taken as 0.079 [11]. However, when the adiabatic walls are present radiation loss calculations from the cylinder were performed as given by [12]. A two-dimensional enclosure was considered for the analysis which consisted of the two adiabatic walls and two open (the top and the bottom) surfaces along with the isothermal cylinder inside. For ease of analysis, the adiabatic wall was divided into several isothermal sections based on experimental measurements. The theory for radiation exchange in an enclosure (with gray diffuse surfaces) was then applied. The emissivity of the adiabatic walls was taken as 0.04 [11]. As mentioned earlier, the adiabatic walls were urethane insulating boards with aluminum sheeting surfaces. Assuming higher values of the emissivity of the walls would result in slightly higher Nusselt numbers for the cylinder since, in that case, the radiation losses would be smaller. Additional details of the calculations are given in [13].

Once the heat transferred by convection was determined, the average heat transfer coefficient was obtained from

$$\bar{h} = \frac{Q_{\mathrm{conv}}}{A(T_s - T_\infty)} \qquad (5)$$

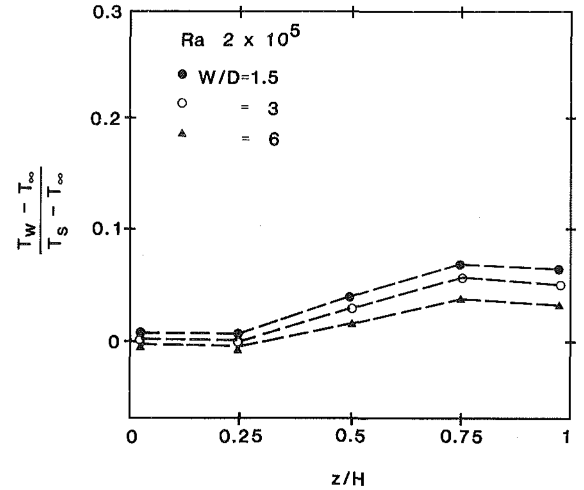

Fig. 3 Temperature distribution of the adiabatic vertical walls

Table 1 Empirical coefficients for equation (7)

W/D	*C*	*m*
1.5	0.6183	0.2475
2	0.6062	0.2468
3	0.4942	0.2600
4	0.4923	0.2577
6	0.4514	0.2648
8	0.3855	0.2780
10	0.3703	0.2783
12	0.3204	0.2914
∞	0.3103	0.2895

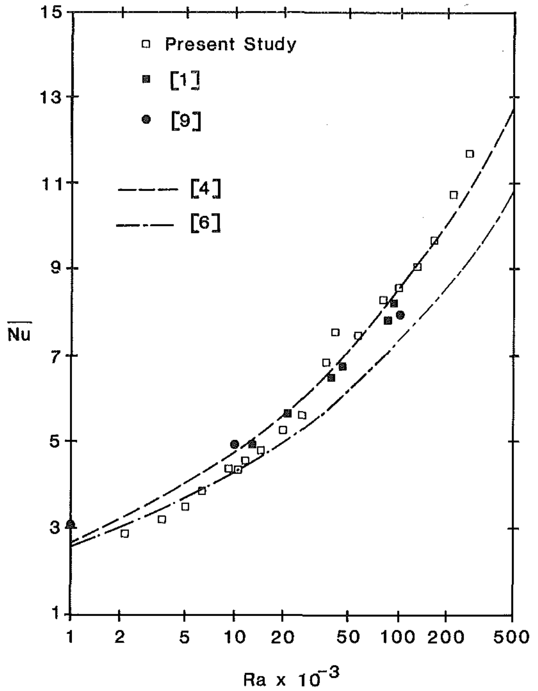

Fig. 4 Variation of average Nusselt number with Rayleigh number for a free cylinder

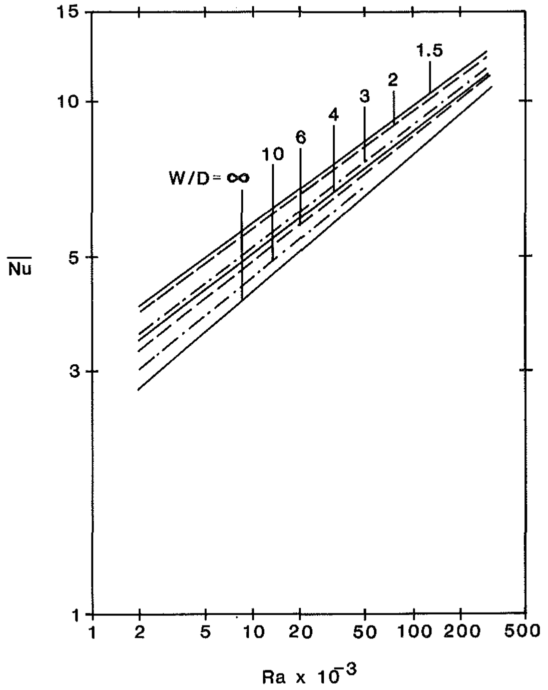

Fig. 5 Least-square fit representation of the effect of Ra on $\overline{\mathrm{Nu}}$ for various *W/D*

The Rayleigh number was calculated from

$$\mathrm{Ra} = \frac{g\beta_a (T_s - T_\infty) D^3 \, \mathrm{Pr}}{\nu_a^2} \tag{6}$$

All air properties were evaluated at the film temperature.

Results

Average Nusselt numbers for Ra ranging from 2×10^3 to 3×10^5 were obtained for various wall spacing to cylinder diameter ratios. The uncertainty in the measurement of $\overline{\mathrm{Nu}}$ decreased from 10 to 0.8 percent as Ra increased from 2×10^3 to 3×10^5 [13]. The temperature difference $(T_s - T_\infty)$ was varied from 1.4°C to 45.3°C for the 2.54-cm-dia cylinder and from 2°C to 128.8°C for the 3.81-cm-dia cylinder. Axial and circumferential variations of surface temperature did not exceed 2.75 and 1 percent, respectively, for the entire range of Ra studied. Heat loss by radiation was found to vary from 0.1 to 6.17 percent of the total electrical power supplied to the heater. End losses accounted for no more than 0.95 percent of the total electrical power supplied. Stratification of the air in the room was found to be negligible during a typical run. The results presented are for $H_1/D = H_2/D = 32$ for the 3.81-cm-dia cylinder and $H_1/D = H_2/D = 48$ for the 2.54-cm-dia cylinder. In addition, measurements were made for H_1/D and H_2/D of 40 and 24, respectively, for the 3.81-cm-dia cylinder. It was found that the variation of H_1/D from 32 to 40 did not alter the $\overline{\mathrm{Nu}}$ results significantly. Hence the walls were large enough to provide the H/D independence desired.

Temperature measurements along the vertical confining walls $T_w(z)$ were used for radiation correction calculation as mentioned earlier. These measurements indicated that a significant variation of T_w from T_∞ is only experienced for $W/D = 1.5$ and Ra higher than 10^5. A maximum of 9°C for $(T_w - T_\infty)$ was observed. Figure 3 shows the effect of W/D on the vertical variation of dimensionless wall temperature distribution, $\theta = (T_w(z) - T_\infty)/(T_s - T_\infty)$ for $\mathrm{Ra} = 2 \times 10^5$. These measurements compare well with those of Sparrow and Pfeil [10] for adiabatic walls. A maximum value of 0.151 was obtained for θ in [10] at $\mathrm{Ra} = 1.75 \times 10^4$ and $W/D = 1.5$. In this study a value of 0.130 for θ was found when $\mathrm{Ra} = 2 \times 10^4$ and $W/D = 1.5$ which is in good agreement with [10]. An absolute maximum of $\theta = 0.416$ was obtained for $\mathrm{Ra} = 2 \times 10^3$ and $W/D = 1.5$.

The measurements of $T_w(z)$ were also used to determine

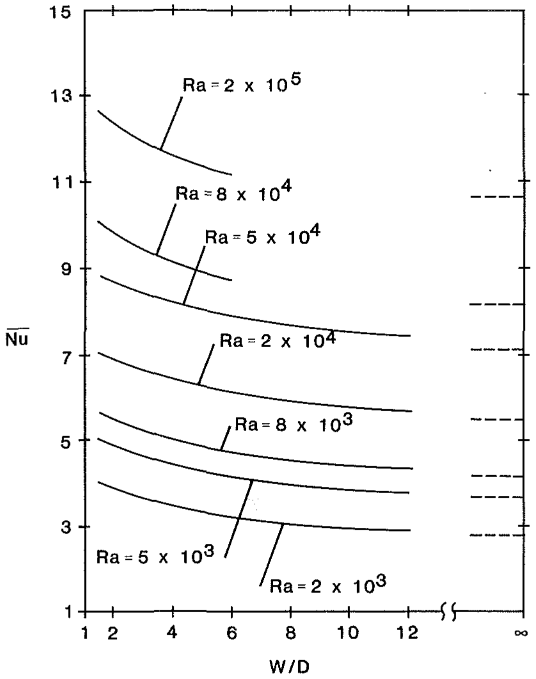

Fig. 6 Effect of Rayleigh number on the variation of the average Nusselt number with W/D

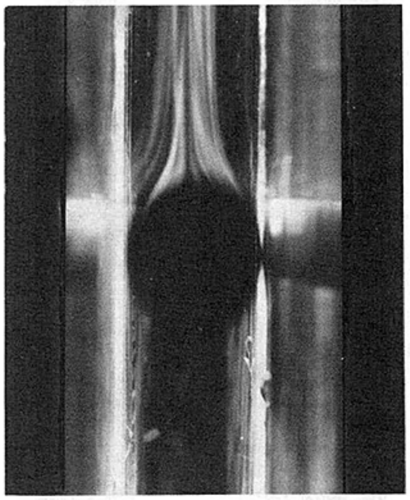

Fig. 7(*a*) Flow field around the confined heated horizontal cylinder, Ra = 3 × 10^4, W/D = 1.5

the reasonableness of the adiabatic walls assumption. In order for the walls to be perfectly adiabatic the temperature on the outside surface T_{ow} would have to be equal to T_∞. Although direct measurement of this was not made, a reasonable estimate can be made from the measurements of $T_w(z)$ and assuming a quasi-one-dimensional conduction through the walls. This is a fairly good assumption because the walls are very thin compared to their height H. The distribution of T_w for three values of W/D and Ra = 2 × 10^5 is shown in Fig. 3. The distribution of T_w for other Ra showed similar trends. As expected, the walls (inside surface) remain rather cool below the cylinder, are somewhat hotter near the cylinder, and get hottest near the top of the channel where the plume of the cylinder fills the cross section of the channel. With the abovementioned analysis one obtains

$$(T_{ow}-T_\infty)=\left(\frac{k}{th_o}\right)(T_w-T_\infty)/\left(1+\frac{k}{th_o}\right).$$

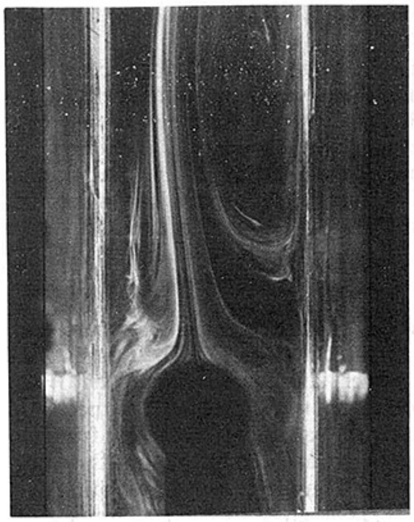

Fig. 7(*b*) Flow field around the confined heated horizontal cylinder, Ra = 3 × 10^4, W/D = 3

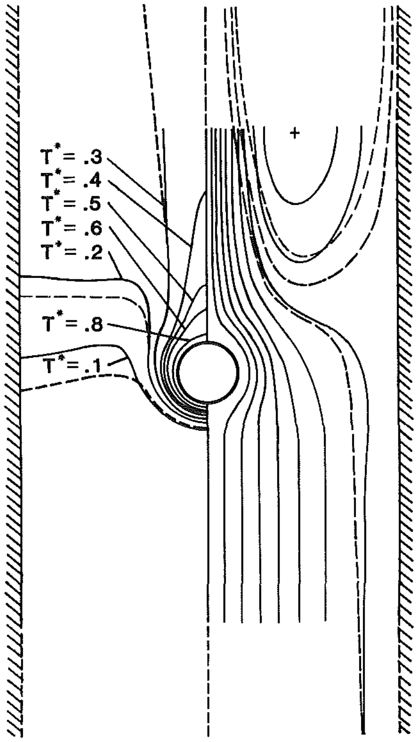

Fig. 7(c) Isotherms and streamlines for the confined heated cylinder, Ra = 10^3, W/D = 6, $\Delta\psi^*$ = −2.65 ($\psi_W{}^*$ = −19.1 for smaller flow domain, $\psi_W{}^*$ = −20.3 for larger flow domain), from Farouk and Guceri [9]

The worst case occurs when $(T_s - T_\infty) \approx 130°\mathrm{C}$ and W/D = 1.5. Using data such as those presented in Fig. 3, and 10 $\mathrm{W/m^2\,°C}$ for h_o one gets $(T_{ow} - T_\infty) \approx 0.8°\mathrm{C}$ in the worst case. Therefore, the vertical walls can be considered adiabatic.

Figure 4 shows the effect of Ra on the average Nusselt number for a horizontal cylinder in infinite medium (free cylinder in air). The experimental data were compared to the empirical equations of Morgan [4] and Churchill and Chu [6], the experimental data of Fand et al. [1], and numerical results of Farouk and Guceri [9] for a heated horizontal cylinder in air. The data obtained here compared well with the data from the literature.

Maintaining a desired cylinder surface temperature is not possible when the power supplied to the heater is kept constant and W/D is varied. This is due to the increase of T_s as W/D is increased which leads to a moderate to small change in Ra. Hence, cross plotting of the data becomes difficult unless a suitable interpolation equation is used for $\overline{\text{Nu}}$ versus Ra for given W/D. An empirical equation of the form

$$\overline{\text{Nu}} = C\,\text{Ra}^m \tag{7}$$

is used in the literature to represent the dependence of $\overline{\text{Nu}}$ on Ra for a free cylinder [1–3, 12]. The experimental data were fit to this power law equation for each W/D case. The equations obtained were used to interpolate the average Nusselt number for values of Ra different from those at which measurements were made. Table 1 shows the value of C and m for various W/D. Figure 5 shows the variation of $\overline{\text{Nu}}$ with Ra for various W/D as given by the least-square fits. The convergence of the lines as Ra increases is clearly seen here and is a consequence of the reduction of the relative increase of Nusselt number ($\overline{\text{Nu}}/\overline{\text{Nu}}_\infty$) with increasing Ra. This is attributed to the thinning of the boundary layer as Ra increases so that flow near the cylinder remains essentially unaffected by the presence of the walls.

Figure 6 shows the variation of the average Nusselt number with W/D for select values of Ra. Interpolation based on the results in Table 1 was used to obtain these plots. Figure 6 demonstrates that $\overline{\text{Nu}}$ increases with decreasing W/D for all Ra considered. For a given Ra, $\overline{\text{Nu}}$ decreases with increasing W/D and asymptotically approaches its corresponding free cylinder value $\overline{\text{Nu}}_\infty$. The asymptotic limits are shown as dashed lines on Fig. 6. Further, it can be seen that as Ra increases, approach to $\overline{\text{Nu}}_\infty$ occurs at smaller values of W/D. In other words, the effect of confinement remains significant for lower Ra. It seems that there is no optimal W/D for maximum heat transfer. This result is in contrast with the conclusions of Farouk and Guceri [9]. The discrepancy is believed to be due to the small H/D ratio studied in [9] versus the H/D of 64 and higher studied here.

In order to explain the heat transfer characteristics and the associated buoyancy-induced flow physics, flow visualization and Schlieren studies were performed. Figures 7(*a*) and 7(*b*) show the flow field due to the heated confined cylinder at Ra $= 3 \times 10^4$ and $W/D = 1.5$ and 3.0, respectively. The photographs reveal interesting details of the flow field, caused by the confinement. (The bright vertical lines in the photographs are due to the finite wall widths.) The presence of the walls considerably affects the flow pattern. As the plume forms at the wake region, a flow reversal occurs at the downstream side of the flow domain. The recirculation loop was found to be finite and extends about 10 to 20 diameters downstream, beyond which the flow becomes unidirectional. Qualitatively, similar observations were made by Farouk and Guceri [9]. Figure 7(*c*) shows the isotherms and streamlines for a confined cylinder taken from [9]. The predicted recirculation loop was, however, not bounded in [9] due to the approximate hydrodynamic boundary conditions considered in the exit plane. The heat transfer coefficient for the heated cylinder is affected by the presence of the recirculation region. The confinement decreases the net flow induced by the cylinder as compared to the heated unconfined cylinder. Hence, there are two competing effects that appear due to confinement which have influence on the heat transfer characteristics. In this study, it was observed that the overall effect is always an increase in heat transfer over the unconfined case for the Ra and W/D ranges studied.

Figures 8(*a*) and 8(*b*) show the temperature fields (Schlieren photographs) around an unconfined and confined heated cylinder at Ra $= 5 \times 10^4$. The W/D in Fig. 8(*b*) was equal to 2.0. Due to the confinement, there is a significant lengthening of the plume length. This information is important from a computational viewpoint. For elliptic equations a finite solution domain is necessary. The Schlieren photographs can give an estimate of the H_1/D ratio to be considered for a reasonable approximation of the thermal boundary conditions for such computations (see Fig. 7*c*).

Fig. 8(*a*) Schlieren photograph for the unconfined heated cylinder, Ra $= 5 \times 10^4$, $W/D = \infty$

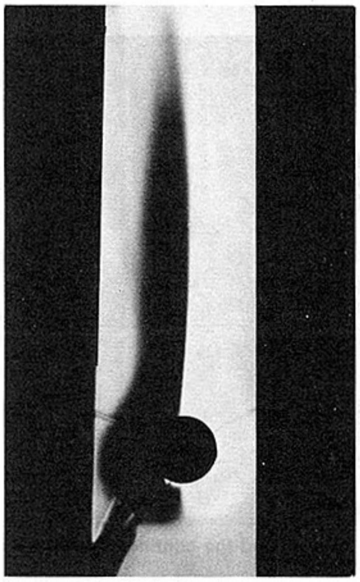

Fig. 8(*b*) Schlieren photograph for the confined heated cylinder, Ra $= 5 \times 10^4$, $W/D = 2$

Figure 9 shows the relative enhancement of the heat transfer $\overline{\text{Nu}}/\overline{Nu}_\infty$ due to confinement. The enhancement of heat transfer increases with decreasing Ra or decreasing W/D. As W/D becomes large all the curves merge together and $\overline{\text{Nu}}/\overline{\text{Nu}}_\infty$ approach unity. The curves for large Ra approach unity faster than the curves for low Ra.

Figure 10 is an alternative crossplot of the relative enhancement of heat transfer as a function of Ra for various

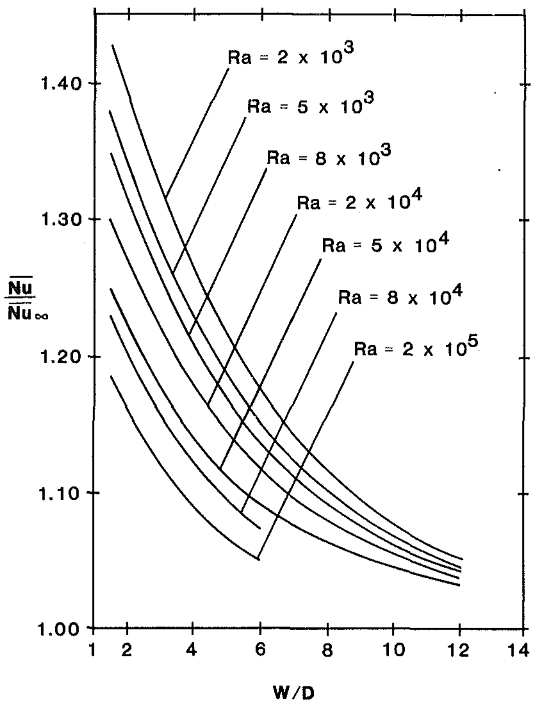

Fig. 9 Effect of Rayleigh number on the variation of $\overline{Nu}/\overline{Nu}_\infty$ with W/D

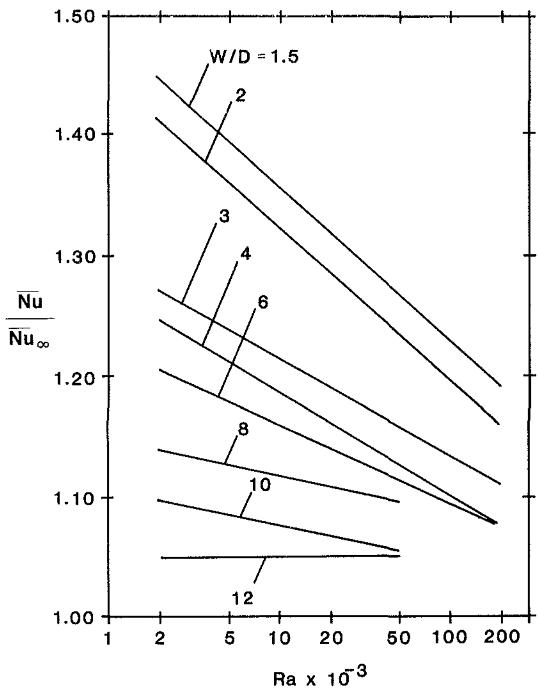

Fig. 10 Effect of W/D on the variation of $\overline{Nu}/\overline{Nu}_\infty$ with Rayleigh number

W/D ratios. Here again it can be seen that as Ra increases $\overline{Nu}/\overline{Nu}_\infty$ decreases for all values of W/D. Also, the enhancement of the heat transfer for a given Ra decreases with increasing W/D. As W/D increases, the slope of the lines decreases continuously and at $W/D = 12$ the slope becomes nearly zero. This figure shows that a maximum of 45 percent enhancement in heat transfer is obtained for the smallest wall spacing, $W/D = 1.5$, and the smallest Ra studied, 2×10^3. Marsters' experimental results [7] predict a maximum of 48 percent enhancement for $W/D = 4$ at Ra $= 10^4$, and 50 percent for $W/D = 2$ at Ra $= 10^3$, when $H/D = 64$. Sparrow and Pfeil [10] measured enhancement of up to 40 percent at $W/D = 1.5$ and $H/D = 20$. Sparrow and Pfeil, however, do not give any information about the effect of the Rayleigh number on enhancement for given W/D and H/D. All three studies suggest a significant enhancement of heat transfer by confinement. The slight discrepancy between the results of [10] and this study can be attributed to the different H/D values selected (a maximum H/D of 20 versus 64).

In order to obtain an empirical correlation for the entire range of W/D and Ra considered in this study, the form

$$\overline{Nu} = g(W/D) f(\mathrm{Ra}) \tag{8}$$

is proposed. To represent $f(\mathrm{Ra})$, the following form was used

$$f(\mathrm{Ra}) = \mathrm{Ra}^m \tag{9}$$

which is consistent with equation (7). The value of $m = 0.25$ was chosen as the best value of the exponent from the available literature for a free cylinder [1-3]. An exponential behavior of $g(W/D)$ with W/D was chosen such that

$$g(W/D) = B + E\exp[-F(W/D)] \tag{10}$$

This form has been suggested by Fernandez and Schrock [14] for a geometrically similar problem of natural convection from a cylinder buried in porous medium. Using equations (9) and (10) and finding the coefficients from a least-squares fit, $\overline{Nu}$ can be represented as

$$\overline{Nu} = [0.481 + 0.172\exp(-0.258(W/D))]\mathrm{Ra}^{0.25} \tag{11}$$

The correlation coefficient for this fit was 0.9978. The data are plotted against this correlation in Fig. 11. Also included in this figure are data from [7] and [9]. There is clearly a discrepancy between the data from [7] and the data from this study. The reason for this is not obvious but may be due to the different values of H/D considered in the two studies. The H/D used by Masters was much smaller than what was used in these experiments. It is very likely that at the small values of H/D that parameter has a significant role in controlling $\overline{Nu}$. Further, Marsters positioned the heated cylinder near the very bottom of the channel whereas it was centrally located in these experiments ($z/H = 0.5$). There is good agreement between our experimental correlation and the numerical results presented in [9]. In [9] approximate boundary conditions (for velocities and temperature) were employed in the solution

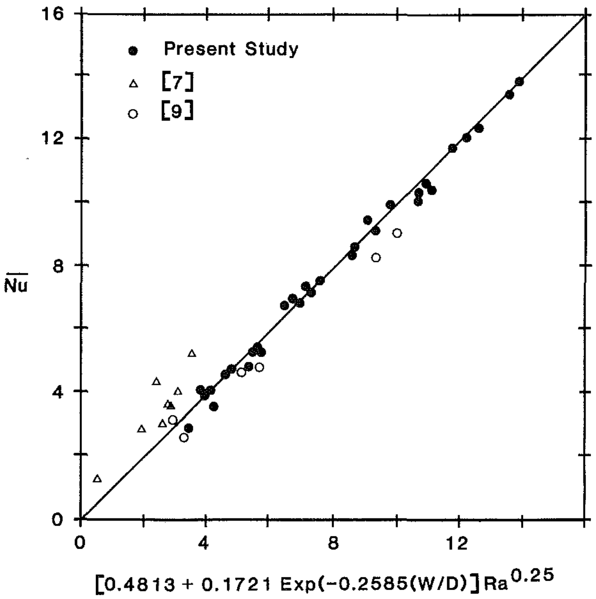

Fig. 11 Comparison of experimental data with predictions of correlation equation (11)

scheme. A stream function–vorticity formulation was used to obtain the numerical solutions. Since the mass flow rate through the walls is not known a priori, an iterative procedure was employed for defining the stream function boundary condition along the walls. Another drawback of the above computations was the use of a composite grid structure (polar near the cylinder and Cartesian for the rest of the domain) which involved interpolation of the dependent variables. Nevertheless, in spite of the limitations of the numerical calculations in [9], the agreement with the experimental correlation (equation (11)) is quite good. Unfortunately, no specific data points from [10] could be plotted on Fig. 11 as that information was not provided in [10]. However, it is clear that the present data exhibit an excellent degree of self-consistency and low scatter and the data collapse nicely onto one curve (equation (11)).

Conclusions and Recommendations

The major conclusion of this study was that the confinement of a heated horizontal cylinder by vertical adiabatic walls enhances the heat transfer from the cylinder. The magnitude of relative enhancement decreases with increasing Rayleigh number for all W/D. Furthermore, the enhancement of heat transfer from the cylinder decreases with increasing spacing of the walls for the entire range of Rayleigh number studied. A maximum enhancement of 45 percent was obtained. This occurred at the smallest Ra and W/D studied. An empirical correlation was obtained to describe the dependence of the average Nusselt number on Ra and W/D jointly. For the range of Rayleigh number studied, no optimal W/D was obtained for maximum heat transfer as suggested by either Farouk and Guceri [9] or Marsters [7]. Further investigation of this problem for Ra lower than 2×10^3 and for small H/D ratios (5, 10, 15, 20 for example) is necessary to determine whether such an optimum exists. It may be that such an optimum is due to the H/D. The heights H_1 and H_2 may also have a dominant role in determining if there is an optimal heat transfer for various spacings. Nevertheless, a clear and significant effect of confinement on heat transfer rates has been demonstrated.

References

1 Fand, R. M., Morris, E. W., and Lum, M., "Natural Convection Heat Transfer From Horizontal Cylinders to Air, Water and Silicone Oils for Rayleigh Numbers Between 3×10^2 and 2×10^7," *International Journal of Heat and Mass Transfer*, Vol. 20, No. 11, 1977, p. 1173–1184.

2 Fand, R. M., and Brucker, J., "A Correlation for Heat Transfer by Natural Convection From Horizontal Cylinders That Accounts for Viscous Dissipation," *International Journal of Heat and Mass Transfer*, Vol. 26, No. 5, 1983, pp. 709–726.

3 Sparrow, E. M., "Effect of Vertical Separation Distance and Cylinder-to-Cylinder Temperature Imbalance on Natural Convection for a Pair of Horizontal Cylinders," ASME JOURNAL OF HEAT TRANSFER, Vol. 103, Nov. 1981, pp. 638–644.

4 Morgan, V. T., "The Overall Convective Heat Transfer From Smooth Circular Cylinders," *Advances in Heat Transfer*, Vol. 11, Academic Press, New York, 1975, pp. 638–644.

5 Raithby, G. D., and Hollands, K. G. T., "Laminar and Turbulent Free Convection From Elliptic Cylinders With a Vertical Plate and Horizontal Circular Cylinders as Special Cases," ASME JOURNAL OF HEAT TRANSFER, Vol. 98, 1976, pp. 72–80.

6 Churchill, S. W., and Chu, H. H. S., "Correlating Equations for Laminar and Turbulent Free Convection From a Horizontal Cylinder," *International Journal of Heat and Mass Transfer*, Vol. 18, No. 9, 1975, pp. 1049–1053.

7 Marsters, G. F., "Effects of Confining Walls Upon Natural Convection From a Heated Horizontal Cylinder," *Proceedings of the Fourth Canadian Congress of Applied Mechanics*, May 28–June 1, 1973, Montreal, pp. 789–790.

8 Marsters, G. F., and Paulus, G., "Effects of Confining Walls on Heat Transfer From a Vertical Array of Heated Horizontal Cylinders," *Transactions of the CSME*, Vol. 1, No. 4, 1972, pp. 219–222.

9 Farouk, B., and Guceri, S. I., "Natural and Mixed Convection Heat Transfer Around a Horizontal Cylinder Within Confining Walls," *Numerical Heat Transfer*, Vol. 5, No. 3, 1982, pp. 329–341.

10 Sparrow, E. M., and Pfeil, D. R., "Enhancement of Natural Convection Heat Transfer From a Horizontal Cylinder Due to Vertical Shrouding Surfaces," ASME JOURNAL OF HEAT TRANSFER, Vol. 106, Feb. 1984, pp. 124–130.

11 Holman, J. P., *Heat Transfer*, 5th ed., McGraw-Hill, New York, 1981, p. 547.

12 Siegel, R., and Howell, J. R., *Thermal Radiation Heat Transfer*, 2nd ed., McGraw-Hill, New York, 1980, pp. 233–280.

13 Karim, F., "Natural Convection Heat Transfer From a Horizontal Cylinder Between Vertical Confining Adiabatic Walls," Master's Thesis, Drexel University, Philadelphia, 1984.

14 Fernandez, R. T., and Schrock, V. E., "Natural Convection From Cylinders Buried in a Liquid-Saturated Porous Medium," *Proc. of the Int. Heat Transfer Conf.*, Vol. 2, Munich, 1982, pp. 335–340.

Win Aung
Deputy Director,
Division of Chemical, Biochemical
and Thermal Engineering,
National Science Foundation; and
Adjunct Professor,
Department of Mechanical Engineering,
Howard University,
Washington, D.C.
Fellow ASME

G. Worku
Grove Engineering Inc.,
Gaithersburg, MD

Developing Flow and Flow Reversal in a Vertical Channel With Asymmetric Wall Temperatures

Numerical results are presented for the effects of buoyancy on the hydrodynamic and thermal parameters in the laminar, vertically upward flow of a gas in a parallel-plate channel. Solutions of the governing parabolic equations are obtained by the use of an implicit finite difference technique coupled with a marching procedure. It is found that buoyancy dramatically increases the hydrodynamic entry length but diminishes the thermal development distance. At a fixed wall temperature difference ratio, buoyancy enhances the heat transfer on the hot wall but has little impact on the cool wall heat transfer. Flow reversal is observed in some cases. Based on an analytical solution for fully developed flow, criteria for the occurrence of flow reversal are presented. The present numerical solutions yield results that asymptotically approach those from the analytical solution.

Introduction[1]

Free and forced convection flows in vertical ducts have been investigated extensively. The majority of the recent studies have dealt with the circular tube geometry, but increasing attention is being focused on the parallel-plate duct. This configuration is relevant to solar energy collection, as in the conventional flat plate collector and the Trombe wall, and in the cooling of modern electronic systems. In the latter application, electronic components are mounted on circuit cards, an array of which is positioned vertically in a cabinet forming vertical flat channels through which coolants are passed [1, 2]. The coolant may be propelled by free convection, forced convection, or mixed convection, depending on the application.

Existing literature for the parallel-plate vertical channel deals mostly with the limiting cases of free and forced convection; little information is available for mixed convection. Consider the situation in which the channel walls are cooled by forced flow in the upward direction at a prescribed coolant flow rate at the duct entrance. Assume that the wall heating is sufficiently intense that free convection effects are significant. Such a mixed convection problem has not been fully treated in the literature. For this problem, the quantitative effects of buoyancy cannot be extrapolated from the tube flow case, and the phenomenon of flow reversal has not been adequately discussed. The feature of asymmetric heating and therefore its impact on the flow dynamics, indigenous to the parallel-plate system, is worthy of additional attention and forms the focus of the present paper.

Four papers have appeared recently that concern convection in vertical flat channels. In the first of these papers, Wirtz and Stutzman [3] performed measurements on free convection in air on a channel with the walls heated uniformly and symmetrically. Their results are in close agreement with the finite difference calculations of a previous study by Aung, Fletcher, and Sernas [4], and lead to a design equation that is accurate to ±5 percent. The second paper, by Sparrow, Chrysler, and Azevedo [5] with water as the working medium, also deals with free convection. This paper provides insight into the reversed flow phenomenon mentioned in the last paragraph, for the limiting case of free convection. In the third paper, Yao [6] presents an analysis of combined convection in a channel with symmetric uniform temperature and uniform flux heating. The solutions, valid in the developing flow region, reveal fundamental information on different length scales that distinguish various convective mechanisms traversed by the fluid before reaching the fully developed state. However, the author did not present quantitative information on the effects of buoyancy, but conjectured that reversed flow may be present in the fully developed flow region, when the channel walls are maintained at uniform temperatures. In the fourth paper, Cebeci, Khattab, and LaMont [7] describe a numerical analysis for combined convection in the entrance region of a parallel-plate channel. The results are presented in terms of boundary layer flow parameters, and show the effects of flow reversal and of the Prandtl number.

The present paper is part of a theoretical study of mixed convection in a vertical flat channel. In the developing region and up to the point of flow reversal, when it occurs, the flow problem is described by means of parabolic partial differential equations and solutions are obtained by a fully implicit numerical method. The flow in the fully developed (FDF) region, whether or not flow reversal is present, is obtained by an analytical solution of a simplified version of the describing equations. Boundary conditions of uniform wall temperature (UWT) and uniform heat flux (UHF) are considered. The theoretical approaches, analysis and results are presented for UWT with asymmetric heating. Results for UHF appear in [10]. There are interesting differences and similarities between UWT and UHF cases; for a discussion see [9]. The overall focus of the study is to obtain quantitative information on the effects of buoyancy on the heat transfer in mixed convection.

Analysis

Developing Flow. Consider laminar mixed convection between two vertical plates. The flow is assumed to be two dimensional and steady, and the fluid properties are constant except for the variation of density in the buoyancy term of the momentum equation. The fluid has a uniform vertically upward streamwise velocity distribution at the channel entrance. The walls are heated at UWT but the temperatures on the two

---

[1] Opinions expressed in this paper are the personal views of the authors.

Contributed by the Heat Transfer Division for publication in the JOURNAL OF HEAT TRANSFER. Manuscript received by the Heat Transfer Division September 19, 1983.

walls may be different, resulting in an asymmetric heating situation. The boundary layer equations appropriate for this problem are:

Continuity

$$\frac{\partial U}{\partial X}+\frac{\partial V}{\partial Y}=0 \qquad (1)$$

x momentum

$$U\frac{\partial U}{\partial X}+V\frac{\partial U}{\partial Y}=-\frac{\partial P}{\partial X}+\frac{\mathrm{Gr}}{\mathrm{Re}}\,\theta+\frac{\partial^2 U}{\partial Y^2} \qquad (2)$$

y momentum

$$\frac{\partial P}{\partial Y}=0 \qquad (3)$$

Energy

$$U\frac{\partial \theta}{\partial X}+V\frac{\partial \theta}{\partial Y}=\frac{1}{\mathrm{Pr}}\frac{\partial^2 \theta}{\partial Y^2} \qquad (4)$$

In equation (2), use has been made of the Boussinesq equation of state, $\rho-\rho_0 = -\beta\rho(T-T_0)$, and of the definition $p = p'-p''$, where p'' is the pressure at any streamwise position if the temperature were T_0 everywhere. The latter definition gives $dp''/dx = -\rho_0 g$. Hence

$$-\frac{dp'}{dx}-\rho g=-\frac{dp}{dx}+g\beta\rho(T-T_0)$$

It is noted that the dimensionless pressure is $P = (p'-p'')/\rho u_0^2$; if the channel were horizontal, we would have $P = p'/\rho u_0^2$, the conventional definition in pure forced flow. The boundary conditions are

$$\begin{aligned}&\text{At } X=0,\ 0\leq Y\leq 1:\ U=1,\ V=0,\ \theta=0,\ P=0\\ &\text{At } X>0,\ Y=0:\ U=0,\ V=0,\ \theta=r_T\\ &\text{At } X>0,\ Y=1:\ U=0,\ V=0,\ \theta=1.\end{aligned} \qquad (5)$$

In the above, dimensionless parameters have been defined as

$$\begin{aligned}&U=u/u_0; && V=v\,b/\nu\\ &X=x/(b\,\mathrm{Re}) && Y=y/b\\ &P=(p'-p'')/\rho u_0^2\\ &\theta=(T-T_0)/(T_2-T_0)\end{aligned} \qquad (6)$$

To obtain a solution of the mixed convection problem formulated above, an additional equation expressing the global conservation of mass at any cross section in the channel is also required. This becomes

$$\int_0^1 U\,dy=1 \qquad (7)$$

Table 1 Mesh sizes for uniform wall temperature

	ΔX	ΔY
$0<X\leq 0.001$	0.0001	0.00625
$0.001<X\leq 0.005$	0.00025	0.0125
$0.005<X\leq 0.02$	0.0005	0.025
$0.02<X\leq 0.05$	0.001	0.05
$0.05<X<\infty$	0.005	0.1

The system of nonlinear equations (1)-(4) is solved by a numerical method based on finite difference approximations. An implicit difference technique is employed whereby the differential equations are transformed into a set of simultaneous linear algebraic equations. The solution procedure is identical to that described in [4]. The implicit finite difference technique used is universally stable for all mesh sizes [11]. The mesh sizes selected in the solution are uniform in the transverse (i.e., Y) direction at all streamwise positions. At increasing X the mesh sizes increase as the computation marches into regions where sharp gradients are of lesser likelihood. The mesh sizes used in the present investigation are given in Table 1.

In the initial stages of the present investigation, the numerical techniques were validated by application to a situation for which known solutions exist. The case chosen for comparison was pure forced convection between parallel plates. The computed hydrodynamic and heat transfer results have been reported by Bodoia and Osterle [12] and Hwang and Fan [13]. In terms of streamwise velocity, pressure drop, bulk temperature, and average Nusselt number, the present method produces excellent agreement with those from the earlier studies. Details of the comparison are given in [9].

Fully Developed Flow. When the channel height is much larger than the channel spacing, the flow in the channel may reach a state in which streamlines are parallel to one another. The velocity component V is zero in the entire cross section of flow. This condition leads to a major simplification of equations (1), (2), and (4), making it possible to derive the solutions in closed form. Details of the derivations and the results are given in [9, 10].

Nomenclature

A = surface area
b = spacing between plates
c_p = specific heat at constant pressure
D_e = hydraulic diameter
g = acceleration due to gravity
Gr = Grashof number = $g\beta(T_2-T_0)b^3/\nu^2$
k = thermal conductivity
Nu = Nusselt number
p = pressure difference = $p'-p''$
p' = static pressure
p'' = hydrostatic pressure
P = dimensionless pressure difference; see equation (6)
r_T = ratio of wall temperature differences = $(T_1-T_0)/(T_2-T_0)$
Re = Reynolds number = u_0b/ν
T = temperature
u = axial velocity
U = dimensionless streamwise velocity = u/u_0
v = transverse velocity
V = dimensionless transverse velocity = vb/ν
x = streamwise distance from channel entrance
X = dimensionless streamwise distance from channel entrance = $x/b/\mathrm{Re}$
y = transverse coordinate (measured from cool wall)
Y = dimensionless transverse coordinate = y/b
β = thermal expansion coefficient
θ = dimensionless temperature difference = $(T-T_0)/(T_2-T_0)$
μ = dynamic viscosity
ν = kinematic viscosity
ρ = density

Subscripts

1 = cool wall (i.e., value at y = 0)
2 = hot wall (i.e., value at y = b)
m = mean value
m,1 = mean value on cool wall
m,2 = mean value on hot wall
0 = value at channel entrance (i.e., at x = 0)
b = bulk value
c = value at centerline

Table 2 Maximum Gr/Re for no flow reversal

r_T	$(\mathrm{Gr/Re})_{\max}$
1.0	∞
0.8	360.00
0.5	144.00
0.3	102.86
0.0	72.00

Results

In the present study, quantitative information on the effects of buoyancy and asymmetric heating have been obtained for Pr = 0.72 at Gr/Re = 0, 25, 50, 100, 250, and 500. Typical results are given below.

Qualitative Flowfield Results. The present results show that at small Gr/Re the velocity profile, specified as $U = 1$ at the channel entrance, remains positive throughout at all X. At a sufficiently high value of Gr/Re for a fixed r_T, the streamwise velocity is everywhere positive up to a certain X, then a separation point (i.e., $\partial U/\partial Y = 0$) develops on the cool wall when $r_T < 1$. Such a situation occurs for $r_T = 0.5$, Gr/Re = 250. In the latter instance, the solution procedure was successfully "marched" past the separation point, and the velocity profile eventually exhibited both positive and negative flows that finally became fully developed. This represents the only case where a stable solution was obtained in the presence of flow reversal, aided probably by relatively large streamwise step sizes when marching across the separation point and the rapid evolution of the flowfield into FDF past this point in this instance. In all other cases, such as for $r_T = 0.3$, Gr/Re = 250, the solutions became unstable.

In [10], analytical solutions for the FDF region have been presented. The solution for the streamwise velocity distribution indicates that both unidirectional flow (in the positive X direction) as well as bidirectional flow are possible, with the latter case representing a parallel-streamline shear flow. The controlling parameters are r_T and Gr/Re. In general, bidirectional FDF is promoted by small r_T or large Gr/Re with larger negative flow (in magnitude and in extent) stemming from larger Gr/Re. Bidirectional flow is impossible in FDF when $r_T = 1$; for more details, see [10]. For any given r_T, the maximum Gr/Re for which no flow reversal occurs anywhere in the channel for a duct of any length may be derived from the criterion given in [10]. The quantitative results are listed in Table 2. It is to be noted that the FDF theory does not predict the location of the separation point; for any given r_T, separation always occurs, if at all, in the developing region, and the location moves upstream with increasing Gr/Re.

Since parabolic partial differential equations have been utilized in the present investigation, the solutions immediately downstream of separation are not examined in great detail. Boundary layer equations have been traditionally applied, in external flow situations, up to the point of separation but not beyond; see, for instance, Schlichting [14]. However, several studies have been reported (e.g., [7]) where boundary layer equations, with the neglect of the streamwise convective term, have been used to obtain quantitative or qualitative information across the point of separation in duct flow. This approach was not used in the present study.

The present numerical approach yielded stable solution in one particular case involving reversed flow. The calculation was carried out for Gr/Re = 250 and $r_T = 0.5$. The results are reported in [10] to afford comparison with the analytical solution for FDF, and point to the need for additional clarification of the usefulness and limitations of the present approach for situations involving flow recirculation. Also in need of further investigation is the concept of fully developed flow in the presence of bidirectional flow. Some investigations, e.g., [6], have conjectured that in mixed convection, FDF may involve a periodic flow structure. On the other hand, the recent work of Sparrow, Chrysler, and Azevedo [5], carried out concurrently with our study, illustrates the fact that a parallel-streamline, bidirectional FDF can exist. The study in [5] deals with the limit of Gr/Re → ∞ with $r_T = 0$. By means of a thymol blue method, the authors observed the direction of fluid flow inside the channel. Beyond a certain threshold value of the Rayleigh number, they found a pocket of recirculating flow situated adjacent to the unheated wall in the upper part of the channel. This recirculation is sustained by fluid drawn in from the ambient at the top of the channel. This downward flow passes along the cool wall, reverses direction somewhere inside the channel, and flows out of the top. The axial extent of the recirculation region depends on the system and thermal parameters, but is increased as buoyancy increases.

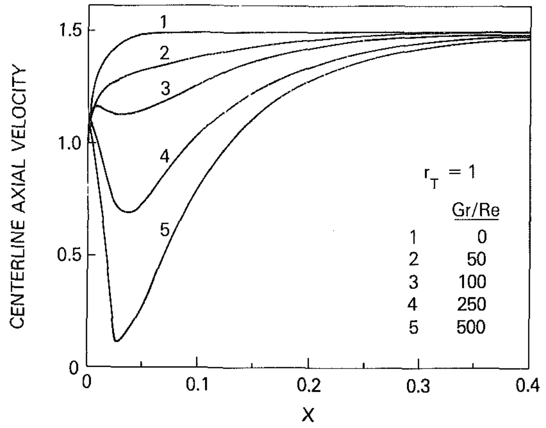

Fig. 1 Streamwise variation of the centerline velocity for symmetric heating

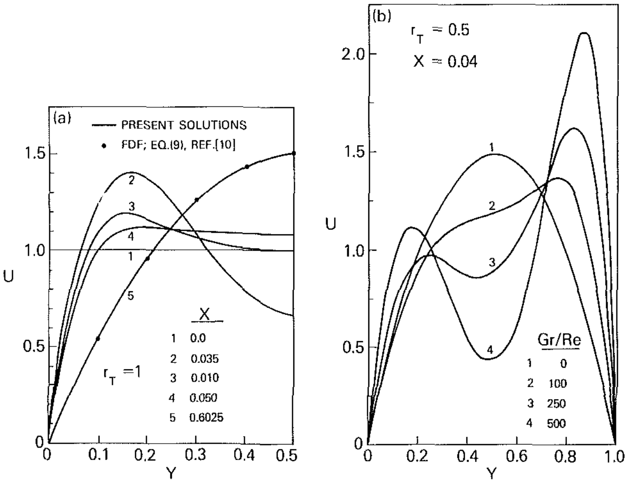

Fig. 2 Streamwise velocity distribution as a function of position and of Gr/Re for symmetric and asymmetric heating

An additional discussion of flow reversal in the context of FDF is given in [10] where, for example, it is shown that even in the presence of flow reversal, the centerline velocity is always positive at any r_T and has a numerical value of 1.5, the same as when buoyancy is absent. It should be recognized that flow separation as a fundamental fluid flow phenomenon is still poorly understood, even in laminar flow. For a recent review, see [15].

Hydrodynamic Parameters. For a channel with symmetric heating at UWT ($r_T = 1$), the streamwise variation of the centerline velocity is indicated in Fig. 1. It can be seen that buoyancy effects are felt very close to the channel entrance ($X = 0$). Buoyancy causes increased mass flow close to the walls, and since the global mass flow is fixed, the fluid

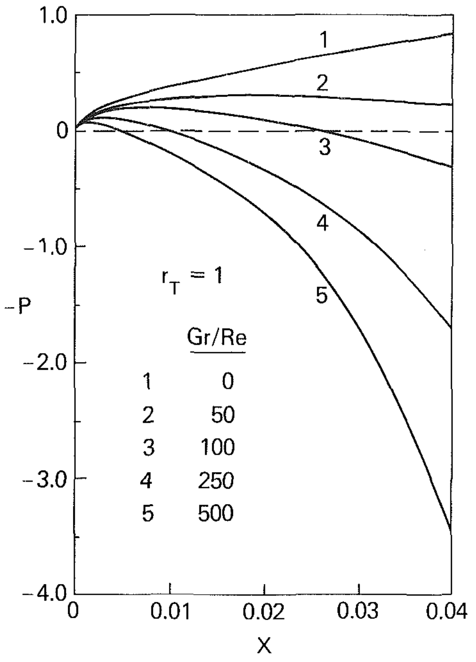

Fig. 3 Variation of the pressure with streamwise distance for symmetric heating at various Gr/Re

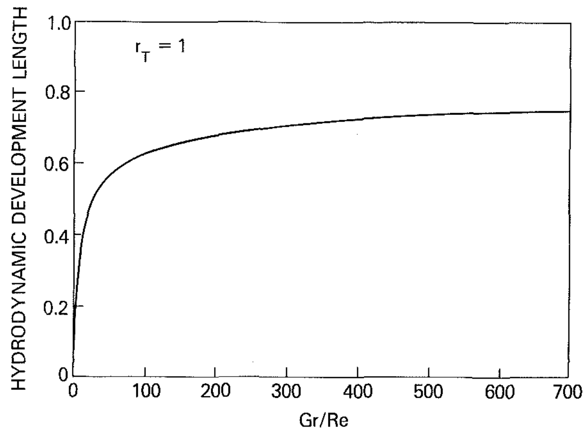

Fig. 4 Hydrodynamic development length versus Gr/Re for symmetric heating

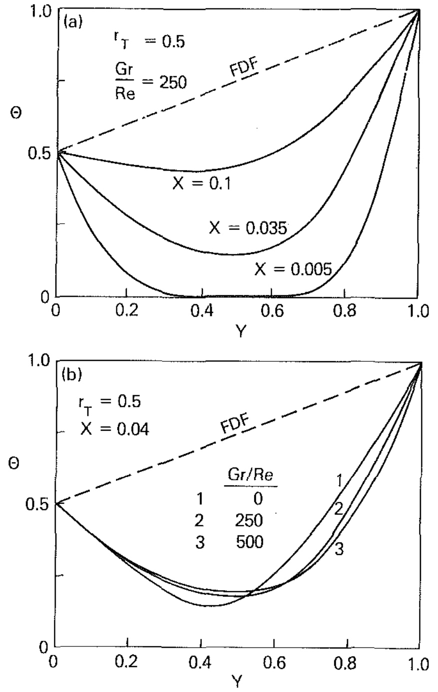

Fig. 5 Dimensionless temperature distribution at r_T = 0.5 at different X and Gr/Re

velocities near the centerline decrease. At a sufficiently high value of Gr/Re (larger than 100), the centerline velocity undergoes a minimum, then once again increases monotonically. In all cases, the curves approach a value close to 1.5 at large X.

Since buoyancy leads to increased velocities near the walls, the velocity profile attains a concave shape near the center and the concavity becomes more severe as Gr/Re increases. However, for $r_T = 1$ at all values of Gr/Re, the concavity eventually disappears and the profile develops into the fully developed shape predicted by the fully developed flow theory given in [10]. This effect is illustrated in Fig. 2(*a*). For asymmetric wall temperatures ($r_T < 1$), the concavity never completely disappears, as the FDF theory also predicts [10]. A skewness in the velocity profile also appears as the fluid moves toward the hot wall ($Y = 1$). The smaller r_T, the greater is the skewness. The distortion of the profile is, however, reduced at increased X. On the other hand, increased buoyancy introduces a more severe distortion, as illustrated in Fig. 2(*b*).

Figure 3 shows the variation of the dimensionless pressure parameter P for $r_T = 1$. The figure indicates the streamwise variation of the parameter at different Gr/Re. At some point along the channel, for Gr/Re values of 50, 100, 250, and 500, the pressure attains a minimum (i.e., $-P$ achieves a maximum) and starts increasing. In the upper range of the Gr/Re values (Gr/Re $\geq$ 250), the maximum pressure occurs at about the point where buoyancy effects begin to be felt and the centerline velocity starts to decrease. In the same range, it is also observed that P becomes positive when the centerline velocity attains a value less than that of the entry velocity, i.e., $U = 1$. This phenomenon is not observed for Gr/Re less than 250, although the general behavior of the pressure parameter is the same. As in the case of the velocity profiles, the higher the value of Gr/Re, the earlier (i.e., at smaller X) the inflection point occurs. Such a behavior was also discerned in the results of Lawrence and Chato [16] for flow in a vertical pipe. At large X, the pressure gradient attains a constant value, which agrees with the predictions given by the FDF theory [10]. It should be noted that to interpret the meaning of a positive pressure gradient properly for the curves in Fig. 3 that represent Gr/Re $\geq$ 50, it is necessary to recall that, by the definitions stated following equation (4), dP/dX denotes the difference between the static and hydrostatic pressure gradients.

The above discussion indicates that in UWT with asymmetric wall temperature heating, buoyancy initially distorts the entering flat velocity profile into one with a concavity near the centerline. However, the concavity disappears ($r_T = 1$) or at least diminishes ($r_T \leq 1$) downstream and, in the case of $r_T = 1$, a fully developed flow with a parabolic profile takes place at large values of X. For fully developed flow, theory predicts that the velocity profile is asymmetric when $r_T < 1$. It may be ascertained from Fig. 1 that the hydrodynamic development length initially increases rapidly with Gr/Re, but then approaches an asymptotic value at large Gr/Re. This behavior is quantified for $r_T = 1$ in Fig. 4, where the development length has been taken as the value of X at which the centerline velocity is within 0.06 percent of that given by equation (8) of [10]. Figure 4 shows that buoyancy can increase the hydrodynamic development length very dramatically.

Thermal Parameters. The development of the temperature field is exemplified by Fig. 5(*a*). The FDF temperature distribution is a function only of r_T and not of Gr/Re. The ef-

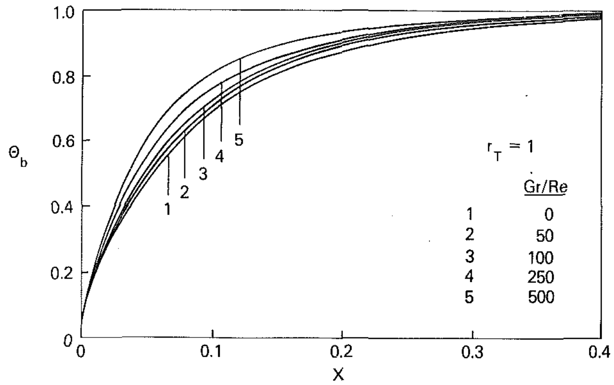

Fig. 6 Axial variation of the bulk temperature (symmetric heating)

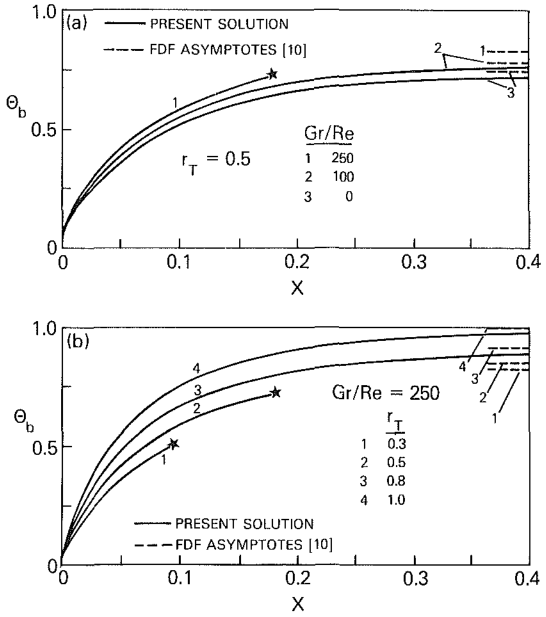

Fig. 7 Bulk temperature as a function of axial distance at various r_T and Gr/Re (star symbols represent positions of flow reversal)

fect of the latter parameter is felt in the developing region, where the buoyancy decreases the temperature in the region adjacent to the hot wall while increasing the temperature elsewhere in the flow. The phenomenon is evident in Fig. 5(*b*). Thus, buoyancy tends to equalize the temperature in the fluid. An examination of the streamwise development of the centerline temperature at various Gr/Re reveals that as buoyancy increases, its effect is felt closer to the entrance [9]. While the thermal development length is usually smaller than the velocity development length for gas flows, buoyancy effects, which on the one hand lengthen the hydrodynamic development and on the other equalize fluid temperatures, have increased the discrepancy between the thermal and hydrodynamic development distances.

The axial variation of the bulk temperature for $r_T = 1$ at different Gr/Re is displayed in Fig. 6. The bulk temperature is defined as

$$\theta_b = \frac{\int_0^1 U\theta dY}{\int_0^1 U dY} \tag{8}$$

It may be noted that buoyancy effects are noticeable through a long segment of the channel, but not for small or large X. At large X, all the curves converge to the value 1. Beyond $X = 0.3$, the forced convection solution, curve 1, may be used to predict bulk temperatures at all values of Gr/Re. A similar trend is observed at $r_T = 0.5$, shown in Fig. 7(*a*). As predicted by equation (10) of [10], with r_T fixed the asymptote is still a function of Gr/Re; similarly at a fixed Gr/Re, θ_b is a function of r_T, as indicated in Fig. 7(*b*). The bulk temperature is seen to be less than the value of 1 (for $r_T = 1$), and decreases as r_T is reduced.

The "star" symbols in Figs. 7(*a*) and 7(*b*) represent the locations where flow separation occurs. For the case $r_T = 0.5$ and Gr/Re = 250, stable solutions were obtained across the separation point, even though results are not plotted past the separation points in Figs. 7. It may be noted from the latter that the flow is nearly fully developed when reversal occurs, as has been alluded to in the previous discussion. It may be noted also that at a fixed Gr/Re, the point of separation moves upstream when the value of r_T is reduced.

The thermal information presented thus far points to increased heat transfer rates as Gr/Re increases. The average Nusselt number based on the log-mean temperature difference, a definition commonly employed in forced convection, may be plotted as a function of the Graetz number. For $r_T = 1$, Gr/Re = 0, the Nu_m results of the present investigation were compared against the solutions of Hwang and Fan leading to no detectable difference [9]. Typical axial variations of the average Nusselt number on the two walls for $r_T \leq 1$ and specified values of Gr/Re are given in [9]. It should be noted that the cool wall Nusselt number is decreased drastically when r_T is reduced. At any fixed X, the average Nusselt number on either wall is only mildly sensitive to changes of Gr/Re, when r_T is fixed. Reference [10] shows that FDF in these cases implies a linearity of the temperature profile, so that there is no net heat addition to the fluid and what occurs is simply heat conduction, across the fluid layer, from the hot wall to the cool wall. Thus, in the FDF region when $r_T < 1$, $\mathrm{Nu}_{m,2}$ and $\mathrm{Nu}_{m,1}$ are equal in absolute values but are opposite in sign. An illustration of this effect appears in the experimental and theoretical results presented in [4].

After the conclusion of the study reported by Worku [9], Ormiston [17] published the results of a study of the same problem in which elliptic partial differential equations were employed. Ormiston compared his results for U_c, U, θ_c, θ with those of the present investigation and the agreement is generally good; however, the two results for U_c do not match well in the immediate vicinity of the duct entrance and Ormiston ascribes the discrepancy to the fact that finer grid spacings were used near the duct entrance in the present study that employs the parabolic partial differential equations.

Conclusions

The theoretical results obtained in this study show that the velocity profiles in the developing regions can become highly distorted in mixed convective flows. For $r_T = 1$ at large distances from the entrance the profile attains a constant parabolic shape in fully developed flow. In both the developing and the fully developed flow regions, asymmetric wall temperatures lead to a skewness in the velocity profiles. The hydrodynamic development length increases dramatically as Gr/Re increases from zero to about 100, and then gradually approaches an asymptotic value. While buoyancy elongates the hydrodynamic development region, the thermal entry length is shortened. In general, the thermal parameters are less sensitive to buoyancy effects; however, the latter are still significant. The value of the bulk temperature when $r_T < 1$ is shown, in the asymptotic limit of large X, to increase with buoyancy. At a fixed Gr/Re, flow separation is observed to move upstream (i.e., down the vertical channel) as r_T decreases. Clearly, the phenomenon of flow reversal in internal mixed convection involves many unresolved issues, and is an area that deserves further attention.

References

1 Aung, W., Kessler, T. J., and Beitin, K. I., "Free Convection Cooling of

Electronic Systems," *IEEE Trans. Parts, Hybrids, and Packaging*, Vol. 9, No. 2, 1973, pp. 75-86.

2 Aung, W., "Heat Transfer in Electronic Systems With Emphasis on Asymmetric Heating," *Bell System Technical Journal*, Vol. 52, No. 6, 1973, pp. 907-925.

3 Wirtz, R. A., and Stutzman, R. J., "Experiments on Free Convection Between Vertical Plates With Symmetric Heating," ASME JOURNAL OF HEAT TRANSFER, Vol. 104, 1982, pp. 501-507.

4 Aung, W., Fletcher, L. S., and Sernas, V., "Developing Laminar Free Convection Between Vertical Flat Plates With Asymmetric Heating," *International Journal of Heat and Mass Transfer*, Vol. 15, 1972, pp. 2293-2308.

5 Sparrow, E. M., Chrysler, G. M., and Azevedo, L. F., "Observed Flow Reversals and Measured-Predicted Nusselt Numbers for Natural Convection in a One-Sided Heated Vertical Channel," ASME JOURNAL OF HEAT TRANSFER, Vol. 106, No. 2, 1984, pp. 325-332.

6 Yao, L. S., "Free and Forced Convection in the Entry Region of a Heated Vertical Channel," *International Journal of Heat and Mass Transfer*, Vol. 26, No. 1, 1983, pp. 65-72.

7 Cebeci, T., Khattab, A. A., and LaMont, R., "Combined Natural and Forced Convection in Vertical Ducts," *Heat Transfer 1982, Proceedings of 7th International Heat Transfer Conference*, Munich, West Germany, 1982, Vol. 2, pp. 419-424.

8 Aung, W., and Worku, G., "Developing Flow and Fully Developed Flow in Mixed Convection-Asymmetric Uniform Wall Heat Fluxes," submitted to ASME JOURNAL OF HEAT TRANSFER.

9 Worku, G., "Developing Laminar Combined Natural and Forced Convection Flow Between Vertical Parallel Plates," M.S. Thesis, Department of Mechanical Engineering, Howard University, Washington, D.C., May 1982.

10 Aung, W., and Worku, G., "Theory of Fully Developed Mixed Convection Between Parallel Vertical Plates," ASME JOURNAL OF HEAT TRANSFER, this issue.

11 Hornbeck, R. W., "Numerical Marching Techniques for Fluid Flows With Heat Transfer," NASA SP-297, 1973.

12 Bodoia, J. R., and Osterle, J. F., "The Development of Free Convection Between Heated Vertical Plates," ASME JOURNAL OF HEAT TRANSFER, Vol. 84, 1962, pp. 40-44.

13 Hwang, C. L., and Fan, L. T., "Finite Difference Analysis of Forced Convection Heat Transfer in Entrance Region of Flat Rectangular Duct," *Applied Scientific Research*, Sec. A, Vol. 13, 1964, pp. 401-422.

14 Schlichting, H., *Boundary Layer Theory*, 6th ed., McGraw-Hill, New York, 1968, pp. 150-151.

15 Aung, W., "Separated Forced Convection," *Proc. ASME/JSME Thermal Engineering Conference*, Mar. 20-24, 1983, Honolulu, Hawaii, Vol. 2, pp. 499-515.

16 Lawrence, W. T., and Chato, J. C., "Heat Transfer Effects on the Developing Laminar Flow Inside Vertical Tubes," ASME JOURNAL OF HEAT TRANSFER, Vol. 88, 1966, pp. 214-222.

17 Ormiston, S. J., "A Numerical Study of Two-Dimensional Natural Convection in a Trombe Wall System Including Vent and Room Effects," Master's Thesis, Department of Mechanical Engineering, University of Waterloo, Ontario, Canada, 1983.

Y. L. Chan
Assistant Professor,
Department of Aerospace and
Mechanical Engineering,
University of Notre Dame,
Notre Dame, IN 46556
Assoc. Mem. ASME

C. L. Tien
Professor,
Department of Mechanical Engineering,
University of California,
Berkeley, CA 94720
Fellow ASME

Laminar Natural Convection in Shallow Open Cavities

Experimental investigation on natural convection in a two-dimensional open cavity was performed using laser-Doppler velocimetry. The cavity is rectangular with one vertical heated wall facing a vertical opening, and with the two horizontal walls insulated. Studies for an open shallow cavity with an aspect ratio of 0.143 and Rayleigh numbers ranging from 10^6 to 10^7 under the steady laminar conditions were carried out using water as the working fluid. Heat transfer was found to approach that for a vertical heated flat plate. The measured velocity and temperature profiles illustrate the effect of the open boundary which can be viewed as consisting of two parts: the outgoing hot fluid flow exhibiting strong characteristics of the cavity condition, and the incoming flow influenced by outside conditions.

Introduction

Buoyancy-driven natural convection is an important mode of heat transfer in many engineering systems. Among various problems of natural convection, internal flows arising within enclosures have received a lot of attention in recent years [1, 2]. However, relatively few studies have been directed to buoyant flows in open cavities or partial enclosures. The open two-dimensional rectangular cavity in the present study is shown in Fig. 1. It has two horizontal insulated walls of length L, one heated vertical wall of height H maintained at a constant temperature T_H (hot), and a vertical face open to a surrounding at a constant temperature T_∞ (ambient, cold). It is assumed that at a sufficient distance away from the opening, the ambient or reservoir can be described by an overall characteristic temperature T_∞. In this problem of natural convection in an open cavity, there are internal flows, external flows, and their interactions. The internal flows in the cavity usually involve boundary layers at the walls enclosing a core region. The external flows include the rising plume of hot fluid exiting from the opening and the inflow of cold fluid drawn from the ambient. Examination of these interactions is one of the objectives of the present study.

A shallow open cavity is one with a small height-to-length (H/L) ratio. An example of a system modeled by such a geometry is a pipe with one end connected to a reservoir and the other to a closed valve. The temperature difference between the valve and the reservoir provides a driving force for a natural convective loop. The interest can be in the prediction of heat transfer in cryogenic fluid storage. From a nuclear reactor safety design viewpoint, the pipe can be part of a coolant transfer system to the hot reactor core. Knowledge about the temperature distribution along the pipe wall will be useful for thermal stress analysis. The use of a two-dimensional rectangular model is evidently a great simplification of the real system, but it should give some basic information of the physical phenomena involved.

There have been few experimental studies on natural convection in open cavities. Chen et al. [3] studied natural convection in rectangular open cavities heated on all sides. Visualization of the flow and temperature measurements were conducted at different angles of inclination. Sernas and Kyriakides [4] made measurements in a two-dimensional square open cavity in air at a Grashof number of 10^7. The bottom wall was maintained at ambient temperature and no turbulence was observed. Hess [5] obtained velocity profiles for Ra between 10^{10} and 10^{11} for both constrained and unconstrained square open cavity geometries with insulated top and bottom walls. Bejan and Rossie [6] studied natural convection in a horizontal duct connecting two fluid reservoirs. Fluid velocity and temperature profiles were measured in the region of the channel. Other related studies include natural convection in a closed shallow enclosure by Imberger [7] and Al-Homond and Bejan [8]. A considerable amount of work has been done on partial enclosures by the fire research community including experimental and numerical studies of the buoyant flow generated by fire [9–13]. Relatively little attention has been paid to the interaction of the flows at the open boundary. By setting the opening far away from the heated wall, as in a shallow open cavity, the conditions at the open boundary can be examined independently.

In the present study, natural convection in a shallow open cavity has been investigated under the steady laminar conditions using water as the working fluid. The overall heat transfer rates have been obtained by measuring electrical power input to a wall heater. These results are supplemented by velocity measurements using laser-Doppler velocimetry (LDV) and by temperature measurements using a thermocouple probe.

Experimental System and Measurements

Figure 2 shows a simplified diagram of the apparatus for the experiment. The cavity is 4.45 cm high, 31.1 cm long, and 61.0 cm wide. The two-dimensional shallow cavity therefore has a height-to-length aspect ratio of 0.143. It has a vertical heated wall of aluminum with the opposite end open to a large cubic tank 61.0 cm on the side. The ratio of the volume of the tank to that of the cavity is greater than 20 and the tank models a reservoir or an ambient surrounding. The top and bottom horizontal walls of the cavity are thermally insulated by plexiglass walls and glass wool. The side walls of the cavity and the tank are constructed of 0.95-cm-thick plexiglass. This allows optical access of laser beams to the flow. A cooling water coil

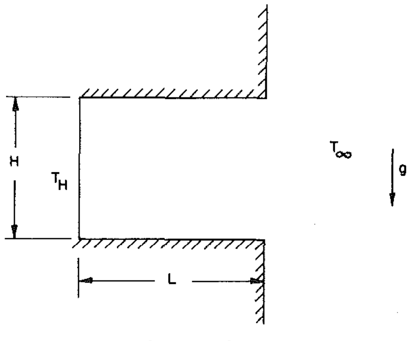

Fig. 1 Open cavity geometry

Contributed by the Heat Transfer Division and presented at the National Heat Transfer Conference, Seattle, Washington, August 1983. Manuscript received by the Heat Transfer Division March 16, 1984.

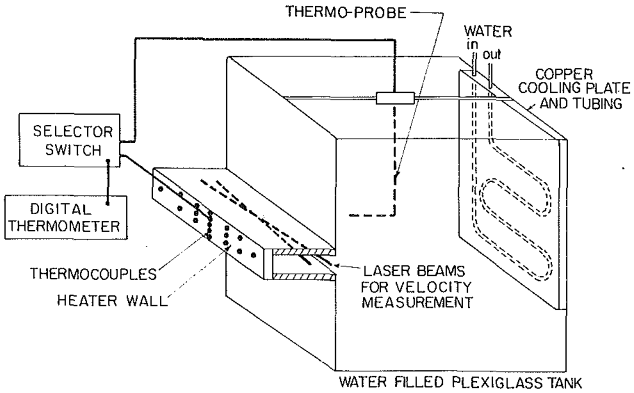

Fig. 2 Experimental apparatus

on a copper plate is positioned at the far end of the tank about 60 cm away from the opening. This permits the circulating water to cool down before returning to the cavity. The heater wall consists of a tubular electric heater embedded in a 1.27-cm-thick aluminum plate. The backside of the heater plate is insulated with glass wool. Input power to the heater is measured by an ammeter and a voltmeter. The voltage supply is monitored by a variable voltage controller. Copper-constantan thermocouples have been inserted to a depth of 0.08 cm (1/32 in.) from the heater wall. Their positions are roughly shown as circular dots in Fig. 2. Several of them are placed in the lateral (third dimension) direction so that the two-dimensionality assumption can be checked. A thermoprobe is used to measure the temperature of water in the cavity and the tank. It consists of a thermocouple inside a stainless steel tube, which is mounted on a traversing mechanism. Temperatures are read directly from a digital thermometer.

During the heat transfer measurements, the two vertical plexiglass end walls of the cavity were further insulated by glass wool to give a better modeling of the two dimensionality and to minimize heat losses from the end walls. Heat losses from the top and bottom walls were estimated from the temperature readings in the inner side and the outer side of the plexiglass wall, and those in the insulation at several locations. Heat leaks were largest from the top wall at places near the heater. As the losses occurred downstream of the heated wall, the results of the experimental Nusselt number were not corrected with these estimated losses. This was based on the assumption that the heat transfer mechanism was very similar to that for a vertical flat plate and that assumption was supported by the numerical results [14]. Due to the elliptical nature of the problem, this assumption admittedly represented an approximation. When the variable voltage power supply was adjusted to a specific setting, steady state was achieved, usually in about 6 h. The voltage and current to the heater were recorded, and the power input to the cavity was calculated after the correction of the estimated heat leaks from the backside of the heater. The error in the heater power input was estimated to be less than 18 percent. The heater wall temperature T_H was obtained from averaging the wall temperatures along the vertical center line. The water tank temperature T_∞ was taken at a location about 25 cm from the opening, at about the same depth as that of the bottom wall of the cavity.

An LDV system with dual beam forward scattering was used to measure the small velocities occurring in natural convection. A laser beam from a 2 W argon-ion laser ($\lambda = 514.5$ nm) was split into two parallel beams separated by 50 mm. One of the beams was frequency shifted optically by 40 MHz in an acousto-optic (Bragg) cell. The shift made it possible to distinguish the direction of the flow. The beams were focused by a lens with focal length 598 mm and crossed to form a measuring volume of diameter 0.66 mm and length 16 mm. The longer dimension lay parallel to the width of the cavity and did not greatly affect the measurement accuracy in the two-dimensional flow. The half angle of the intersecting laser beam was 2.39 deg and the fringe spacing was 6.2 μm. The whole laser and transmitting optics were mounted on a milling table with a three-dimensional traversing mechanism which allowed manual positioning accurate to 0.025 cm (0.01 in.). The collecting optics had a lens of focal length 134 mm which focused the scattered light on a pinhole of 0.025 mm diameter. A photomultiplier tube (RCA-4526) converted the light signal to an electrical signal which was amplified, electronically downshifted, filtered, and then processed by a TSI-1090 tracker. No seeding was required as the laboratory water provided enough particles for scattering. The tracker usually verified about 800 samples per second. The typical Doppler frequencies were about 500 Hz and the system could resolve velocities as low as 0.03 cm/s.

In the velocity measurements, the laser beams were allowed to enter and cross near the middle of the cavity width. Horizontal velocity profiles were obtained by sweeping vertically from top to bottom at the opening or other horizontal positions inside and outside the cavity. Vertical velocities were measured by horizontal sweeps at different depths, after first rotating the transmitting optics by 90 deg. The change in refractive index of water with temperature presented a problem for measurements of vertical velocities near the heated wall. As one beam traveled from the top (hot) to the bottom (colder) through the long cavity width, while the other beam did the reverse, they were thrown off their intended position of crossing. Other difficulties encountered involved the geometric relation between the beams and the walls which sometimes interfered with one of the beams. These problems were partly solved by moving the transmitting optics so that the optical axis was at an angle to the heated wall. The laser beams therefore would avoid the thermal boundary layer as much as possible. The validity of the two-dimensional assumption was checked by moving the measuring volume along the width of the cavity. Steadiness of the flow was examined by looking at the signal over a period of time at a specific location.

After completing the flow measurements, the temperature measurements were taken by traversing the thermoprobe inside the cavity and the tank, in the same manner and location

Nomenclature

B = ratio of length to height $= L/H$
g = gravitational acceleration
H = height of cavity
$\bar{h}$ = average heat transfer coefficient for the heated wall
k = thermal conductivity of water
L = length of cavity
Nu_e = experimental Nusselt number, equation (1)
Pr = Prandtl number = ν/α
$\dot{Q}$ = power input to heated wall
Ra = Rayleigh number, equation (4)
T = temperature
T_f = film temperature, equation (3)
T_H = hot wall temperature
T_∞ = ambient temperature
ΔT = temperature difference, equation (2)
W = width of experimental cavity
α = thermal diffusivity of water
β = coefficient of thermal expansion of water
λ = wavelength of laser beam
ν = kinematic viscosity of water

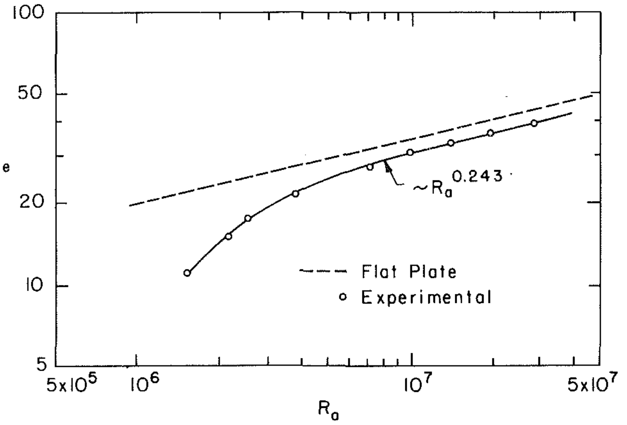

Fig. 3 Variation of experimental Nusselt number Nu_e with Ra for shallow open cavity

as that for the laser measuring volume. Because the temperature differences were small, measurements became difficult especially inside the thermal boundary layer. The two-dimensionality and steady-state assumptions were also checked by the temperature readings. One important piece of information obtained from the temperature measurements was that the water in the tank was stratified. The stratification was much stronger in the lower half of the tank. This finding helped to explain the observation that the fluid was drawn horizontally into the cavity.

Experimental Results

Heat transfer results have been obtained and plotted in Fig. 3, showing the variation of overall Nu_e with Ra ranging from 1.5×10^6 to 2.9×10^7. The results were repeatable under the experimental conditions. The wall temperatures along the vertical center line were about uniform to within 0.2°C. The two-dimensionality assumption on the heater wall was reasonable around this center line but did not hold as well near the two ends.

If an average heat transfer coefficient $\bar{h}$ can be obtained for the heated wall such that

$$\dot{Q} = \bar{h}(HW)\Delta T$$

then an experimental Nusselt number Nu_e can be defined as $\bar{h}H/k$, or

$$Nu_e = \frac{\dot{Q}}{kW\Delta T} \tag{1}$$

where

$$\Delta T = T_H - T_\infty \tag{2}$$

In the calculation of the results, the properties are evaluated at the film temperature T_f where

$$T_f = (T_H + T_\infty)/2 \tag{3}$$

The Rayleigh number is defined as

$$Ra = g\beta\Delta TH^3/\nu\alpha \tag{4}$$

The experimental data can essentially be separated into two regions. For Ra greater than or equal to 10^7, the data points lie on a straight line with Nu_e varying with Ra to the power 0.243. From $Ra = 1.5 \times 10^6$ to 10^7, the data points follow a smooth rising curve, then the slope levels off and approaches the asymptotic relation dependence for higher Ra. Physically, at low Ra, conduction and convection jointly contribute to heat transfer. As Ra increases, convection gradually increases the rate of heat transfer and eventually dominates in the boundary layer regime. The approach of the heat transfer to that of a vertical heated flat plate [15] agrees with the conclusions from the experimental work of Sernas and Kyriakides [4].

The errors in the data points presented in Fig. 3 involve both Ra and Nu_e. The error in the measurement of the temperature difference ΔT included both the uncertainties for the wall temperature T_H, of about 0.2°C, and the ambient water temperature T_∞, of 0.1°C. This yielded, for the range of temperature difference considered, an error in Ra from 22 percent for the low Ra value to 2 percent for the high values. Error in the experimental Nusselt number Nu_e as defined in equation (1) included both the errors in $\dot{Q}$, about 18 percent as stated previously, and those in ΔT. This gave a percent error for Nu_e from 28 to 18 percent for low to high Ra values.

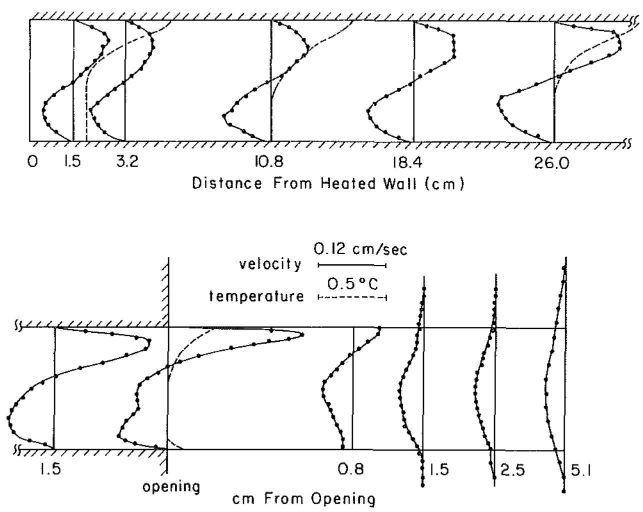

Fig. 4 Horizontal velocity and temperature profile for $Ra = 1.05 \times 10^6$, $Pr = 8.7$

In another set of experiments, velocity and temperature profiles were obtained in a shallow open cavity for $Ra = 1.05 \times 10^6$ and $Ra = 1.27 \times 10^7$. The basic flow patterns were essentially the same for both values of Ra. Fluid was drawn horizontally into the cavity toward the heater wall. As the fluid was heated, it rose, turned around 90 deg, and accelerated slightly as it moved toward the opening. The fluid went out of the opening, up the vertical wall, across horizontally as the top layer in the water tank, down the cooling plate, and completed its cycle when it was drawn toward the opening. This was the dominant fluid motion. Very little movement occurred in the lower half of the tank. This region was thermally stratified and relatively stagnant. The fluid was drawn into the cavity from the fluid layer situated in the tank at the same depth as the cavity opening. In a real situation, the fluid could be expected to be drawn into the cavity radially, as if by suction. The experiment showed that the flow was essentially steady and two dimensional except near the end walls.

$Ra = 10^6$

Figure 4 shows the horizontal velocities measured for $Ra = 1.05 \times 10^6$ ($\Delta T = 1.4$°C, $T_\infty = 12.8$°C, $Pr = 8.7$). The temperature profiles are presented at several locations. Conservation of mass across each section is good to within 12 percent. The temperature profiles are essentially stratified or linear inside the outgoing flow at the top part of the cavity, and are uniform at almost the ambient temperature for the incoming flow. The outgoing and incoming flows occupy roughly equal upper and lower halves of the cavity except near the opening where the outgoing flow accelerates. The outgoing flow occupies about 32 percent of the cavity opening and has a pointed profile as the hot fluid goes up and out of the opening. The incoming flow has a shape different from the expected smooth round profile. It shows a "bump" near the bottom part of the entrance. This occurred during the experiment when the natural convective flow went up to the lower vertical wall of the tank, which was warmer than the surrounding water due to insufficient insulation. In the flow region just

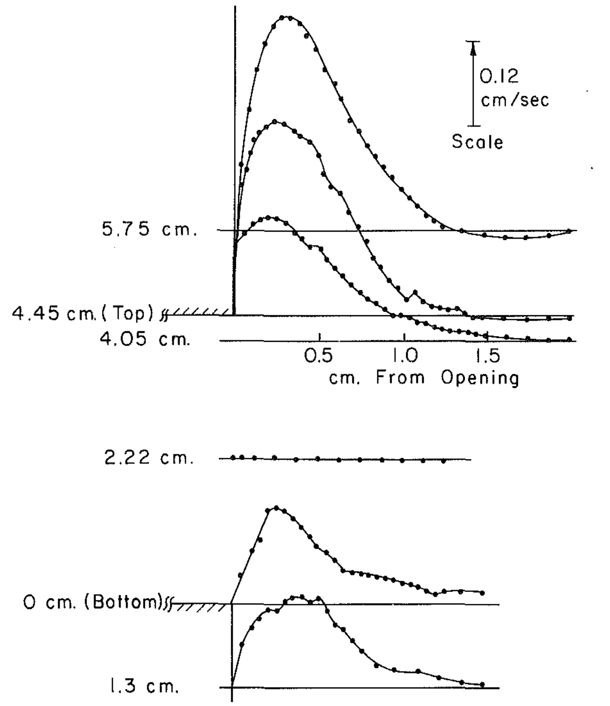

Fig. 5 Experimental vertical velocities near opening for Ra = 1.05 × 10^6, Pr = 8.7

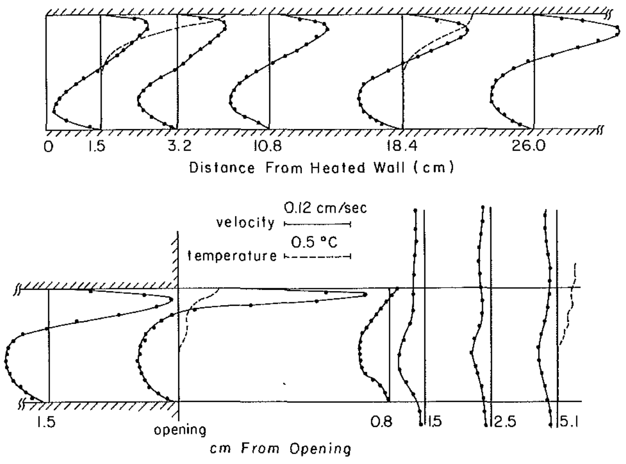

Fig. 6 Horizontal velocity and temperature profile for Ra = 1.27 × 10^7, Pr = 6.2

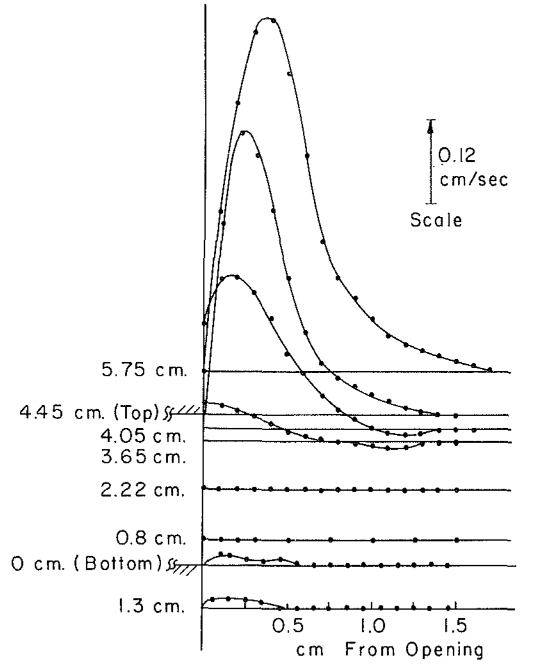

Fig. 7 Experimental vertical velocities near opening for Ra = 1.27 × 10^7, Pr = 6.2

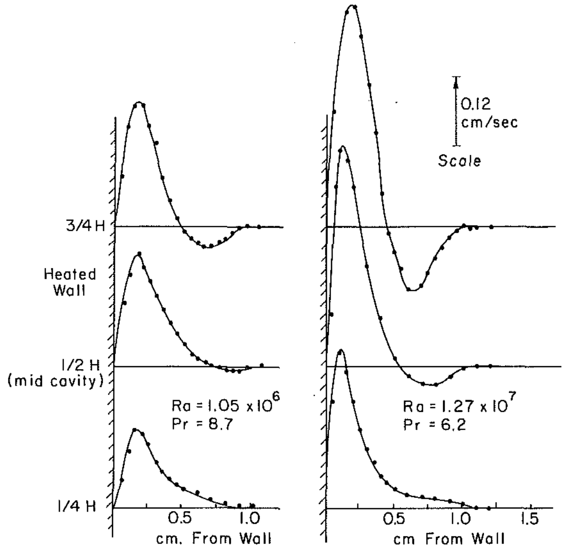

Fig. 8 Vertical velocities at heated wall for two values of Ra

outside the cavity, the incoming flows are essentially horizontal. The temperature profile in the outgoing flow is not linear at the opening as the upper part of the incoming flow is warmed by conduction. The temperature profile at the bottom of the incoming flow illustrates the effect of natural convection up the vertical wall.

Figure 5 presents the vertical velocities near the opening. The wall plume profile is very well defined at 1.3 cm from the top of the cavity. Its shape compares well with that of a plume arising from a line thermal source on an adiabatic wall [16]. Vertical velocity profiles due to natural convection along the lower vertical wall are not smooth. The flow is driven by both natural convection and suction toward the cavity. At the mid-cavity depth, the vertical velocities are essentially zero.

Ra = 10^7

Velocity and temperature profiles have also been obtained for $\Delta T = 7.4$°C and $T_\infty = 21.3$°C. This gives Ra = 1.27 × 10^7 and Pr = 6.2. Figure 6 shows the horizontal velocities. The outgoing flow occupies a narrower passage and has a higher maximum velocity than the incoming flow. The incoming flow at the opening has a smooth profile. The natural convection up the lower vertical wall was eliminated at higher tank temperatures, closer to the room temperature during the experiment. The incoming flow again enters horizontally due to stratification in the tank. The outgoing flow occupies 23 percent of the opening. The narrowing of the flow width is accompanied by a more pointed velocity profile. The approaching flows from the far field have patterns similar to those for Ra = 10^6, except for the higher velocities at levels above the top of the cavity. They are due to increased entrainment to the wall plume along the upper vertical wall. The temperature profile at the opening is masked by the stratification of the fluid in the tank. Because of increased heating, the stratification effect becomes more severe. This can be observed from the uneven temperature profile at 5.1 cm from the opening.

Figure 7 shows the vertical velocities near the opening. The flow along the lower vertical wall is very small. The vertical velocities are zero around midcavity depth as the approaching flow enters the cavity horizontally. The wall plume profiles are well defined, with increased buoyancy effect at the higher Ra.

Vertical velocities at the heater wall were also measured in spite of the difficulties encountered as explained earlier. Figure 8 shows the cases for $Ra = 10^6$ and $Ra = 10^7$. Even though the heat transfer results resemble those for a flat plate, the velocity profiles are different. Downward flows are present to supply entrainment to the upgoing flow. These are the effects of the restrictive horizontal walls.

It should be pointed out that the two different Ra cases lie within a close range and the flow and heat transfer characteristics are quite similar. They are investigated to examine the general trend of changes with varying Ra.

For both Ra cases, the temperature measurements were accurate to 0.1°C in the whole field outside the thermal boundary layer and the accuracy from the LDV system was 0.03 cm/s for the velocity measurements.

Discussion

One of the objectives of the present study is to obtain an understanding of the flow characteristics near the open boundary. Different regimes of flow near the open boundary have been observed in the experiments. The outgoing flow is made up of hot fluid force driven by the cavity heating and this fluid also "escapes" from under the restrictive horizontal wall. When the horizontal exit velocities are not high enough to form a buoyant jet, as in the experiments, a wall plume rises up the vertical wall above the opening. This plume entrains fluid from the ambient surrounding. The approaching flow from the ambient far field feeds this entrainment and also the incoming flow entering the cavity. When the fluid is thermally stratified, this approaching flow is essentially horizontal, proceeding right into the cavity. If there is little stratification, the flow is expected to approach radially toward the lower part of the opening which acts like a mass sink. The flow along the lower vertical wall arises from suction toward the opening and also from a possible natural convective flow when this wall is at a higher temperature than the ambient. Thus the incoming flow at the opening is affected by these various external conditions. In addition, flow separation due to the flow turning around the corner may occur if the velocity is high enough. However, this was not observed in the experiments.

If Ra is small, or if the cavity is sufficiently shallow (long), flow inside the cavity can closely resemble that in a core region where the flow is everywhere parallel to the horizontal walls. In the experimental study the flow inside the cavity remains "unicellular" throughout. No recirculation or secondary cell was observed. The open boundary seems to produce a stabilizing effect in allowing the strongly driven flow to escape freely. The absence of an opposing shear flow from below, in contrast to that of a closed enclosure, may be the reason for this phenomenon.

The major conclusion of this study with an open boundary condition is that the outgoing flow is forced by the cavity heating while the incoming flow is affected by the external conditions. The overall flow near the open boundary is rather complicated and will be an interesting subject for further investigation.

References

1 Ostrach, S., "Natural Convection in Enclosures," *Advances in Heat Transfer*, Vol. 8, 1972, pp. 161–227.

2 Catton, I., "Natural Convection in Enclosures," *Proceedings of the Sixth International Heat Transfer Conference*, Toronto, 1978, Vol. 6, 1979, pp. 13–43.

3 Chen, K. S., Humphrey, J. A. C., and Miller, L., "Note on the Pulsating Nature of Thermally Driven Open Cavity Flows," *International Journal of Heat and Mass Transfer*, Vol. 26, 1983, pp. 1090–1093.

4 Sernas, V., and Kyriakides, I., "Natural Convection in an Open Cavity," *Proceedings of Seventh International Heat Transfer Conference*, Munich, Germany, 1982, Vol. 2, Hemisphere, Washington, D.C., pp. 275–286.

5 Hess, C. F., and Henze, R. H., "Experimental Investigation of Natural Convection Losses From Open Cavities," ASME JOURNAL OF HEAT TRANSFER, Vol. 106, 1984, pp. 333–338.

6 Bejan, A., and Rossie, A. N., "Natural Convection in Horizontal Duct Connecting Two Fluid Reservoirs," ASME JOURNAL OF HEAT TRANSFER, Vol. 103, 1981, pp. 108–113.

7 Imberger, J., "Natural Convection in a Shallow Cavity With Differentially Heated End Walls. Part III: Experimental Results," *Journal of Fluid Mechanics*, Vol. 65, 1974, pp. 247–260.

8 Al-Homond, A. A., and Bejan, A., "Experimental Study of High Rayleigh Number Convection in a Horizontal Cavity With Different End Temperatures," Report CUMER-79-1, Department of Mechanical Engineering, University of Colorado, Boulder, 1979.

9 Markatos, N. C., and Malin, M. R., "Mathematical Modelling of Buoyancy-Induced Smoke Flow in Enclosures," *International Journal of Heat and Mass Transfer*, Vol. 25, 1982, pp. 63–75.

10 Ku, A. C., Doria, M. L., and Lloyd, J. R., "Numerical Modeling of Unsteady Buoyant Flows Generated by Fire in a Corridor," *16th Symposium (Intl.) on Combustion*, The Combustion Institute, 1976, pp. 1373–1384.

11 Yang, K. T., and Chang, L. C., "UNDSAFE-I. A Computer Code for Buoyant Flow in an Enclosure," University of Notre Dame Technical Report TR-79002-77-1, 1977.

12 Liu, V. K., and Yang, K. T., "UNDSAFE-II. A Computer Code for Buoyant Turbulent Flow in an Enclosure With Thermal Radiation," University of Notre Dame Technical Report TR-79002-78-3, 1978.

13 Steckler, K. D., Quintiere, J. G., and Rinkinen, W. J., "Flow Induced by Fire in a Compartment," *19th Symp. (Intl.) on Combustion*, The Combustion Institute, 1982, pp. 913–920.

14 Chan, Y. L., and Tien, C. L., "A Numerical Study of Two-Dimensional Laminar Natural Convection in Shallow Open Cavities," *International Journal of Heat and Mass Transfer*, Vol. 28, 1985, pp. 603–612.

15 Churchill, S. W., and Chu, H. H. S., "Correlating Equations for Laminar and Turbulent Free Convection From a Vertical Plate," *International Journal of Heat and Mass Transfer*, Vol. 18, 1975, pp. 1323–1329.

16 Gebhart, B., and Jaluria, Y., "Buoyancy-Induced Flow Arising From a Line Thermal Source on an Adiabatic Vertical Surface," *International Journal of Heat and Mass Transfer*, Vol. 20, 1977, pp. 153–157.

Pseudo-Steady-State Natural Convection Heat Transfer Inside a Vertical Cylinder

Y. S. Lin

R. G. Akins
Mem. ASME

Department of Chemical Engineering,
Kansas State University,
Manhattan, KS 66506

The SIMPLER numerical method was used to calculate the pseudo-steady-state natural convection heat transfer to a fluid inside a closed vertical cylinder for which the boundary temperature was spatially uniform and the temperatures throughout the entire system were increasing at the same rate. (Pseudo-steady state is comparable to the steady-state problem for a fluid with uniform heat generation and constant wall temperature.) Stream functions, temperature contours, axial velocities, and temperature profiles are presented. The range of calculation was $0.25<H/D<2$, $Ra<10^7$, *and* $Pr=7$. *This range includes conduction to weak turbulence. A characteristic length defined as* $6\times$ *(volume)/(surface area) was used since it seemed to produce good regression results. The overall heat transfer for the convection-dominated range was found to be correlated by* $Nu=0.519\ Ra^{0.255}$, *where the temperature difference for both the Nusselt and Rayleigh numbers was the center temperature minus the wall temperature. Correlations using other temperature differences are also presented for estimating the volumetric mean and minimum temperatures.*

Introduction

Natural convection in enclosures commonly occurs in nature and in technological applications. This phenomenon plays an important role in such diverse applications as cooling of cans of beverages, heating of buildings and fluid storage vessels, emergency cooling of nuclear reactors, temperature stratification in cryogenic fuel tanks, and cooling (heating) chemical reactors generating (consuming) heat uniformly, to name but a few. In these cases, the fluid is driven by density variations in a body-force field, and the flow pattern depends critically on the applied heating conditions and the boundaries. These kinds of systems are governed by the Navier–Stokes equations, but, due to the complexity of the equations and the coupling of the dependent variables, general analytical solutions are still not possible. Most previous research efforts have been based on experimental work and, recently, on numerical approaches.

The purpose of this work was to aim for an improved understanding of internal natural convection problems. Recently there has been substantial work on the analysis of thermal convection in vertical cylinders heated from below and in cylindrical annuli. In the following introduction we only mention work with two-dimensional temperature gradients and within single vertical cylinders. A characteristic of this group of studies is the existence of a surface heat source or a heat sink, but not both.

Previous studies include a step change in the wall temperature of cylinders with H/D ratios from 0.75 to 2.0 by Evans and Stefany [1]. For Rayleigh numbers (based on initial temperature difference and diameter) from 6×10^5 to 6×10^9, the heat transfer was correlated by $\mathrm{Nu}=0.55\ \mathrm{Ra}^{0.25}$. Evans et al. [2] have presented a thorough treatment of transient natural convection in a partially filled vertical cylinder subjected to a uniform side wall heat flux. A range of Grashof numbers from 10^3 to 10^{11}, H/D ratios from 1 to 3, and Prandtl numbers from 2 to 8000 were studied, encompassing both laminar and turbulent flow regions.

Natural convection heat transfer of a uniformly heat-generating fluid is difficult to achieve experimentally. In Murgatroyd and Watson's [3] experiments, a solution of HCl ($3<\mathrm{Pr}<9$) was heated by passing an alternating current between two copper electrodes, one at each end of the cylinder. A high flow rate of cooling water around the outside of the cylinder was used to keep the wall temperature constant and uniform. Modified Rayleigh numbers, based on rate of heating per unit volume, from 2×10^3 to 3×10^6 were used (which corresponded to laminar flow). This type of system can be numerically simulated by a uniform internal heat source or by pseudo-steady state. The analogy between pseudo-steady state and uniform internal heat source has been discussed by Daney [4]. Daney used a cooling bath to provide a constant temperature difference between the internal fluid and the cylindrical vessel wall. The cooling rate was controlled by the amount of evaporation from the cooling bath; therefore a specific bath fluid was required for each temperature difference desired. Horizontal temperature gradients were found to be negligible for the insulated ends of the cylinder. Vertical temperature distributions as well as Nusselt numbers were reported for Rayleigh numbers from 7×10^8 to 6×10^{11}.

Efforts to solve pseudo-steady-state (or uniform heat generation) natural convection inside vertical cylinders with moderate height-to-diameter ratios by analytical methods has received limited attention. Seemingly, there has been no previous work using primitive variables to solve this problem. The only solution available was presented by Kee et al. [5], who used the stream function-vorticity method to formulate the uniform heat generation problem. An instrumented cylinder containing radioactive tritium gas was used to demonstrate experimental and analytical agreement. Their work provided a valuable comparison for the lower Rayleigh number results of this paper.

Compared with experimental investigations, the proper numerical method can offer the advantages of low cost, high speed, the ability to provide complete information, and ease of application to different conditions. Numerical results require the solution of the Navier–Stokes and energy equations, which are highly nonlinear and inseparably coupled. For this case of natural convection, the temperature gradient is the only driving force for flow; therefore, both fields are coupled and must be calculated simultaneously. This substantially increases the difficulty of calculation compared to forced convection problems where the flow field is usually determined prior to temperature field. In addition to the complexity of the

---

Contributed by the Heat Transfer Division for publication in the JOURNAL OF HEAT TRANSFER. Manuscript received by the Heat Transfer Division July 10, 1984.

equations, a wide range of parameters must be taken into account. In usual applications, the Prandtl number covers about five orders of magnitude and the Rayleigh number can span ten orders of magnitude. These facts make the calculation algorithm not only difficult, but also parameter dependent.

The Semi-Implicit Method for Pressure-Linked Equations, Revised (SIMPLER) algorithm was proposed by Patankar and is fully described in his book [6]. The essence of the algorithm is to successively correct the pressure field so as to satisfy the boundary conditions and the continuity equation with the velocities calculated via the momentum equations. Recently, this method has become a powerful tool for solving fluid flow problems, and numerous papers based on it have been published. However, Pollard and Thyagaraja [7] pointed out that this method appears to encounter convergence difficulties when the momentum equations are driven by body forces, even if no physical instability occurs. They proposed a Pressure Reduction by Force Decomposition (PRFD) method in conjunction with the SIMPLE algorithm to avoid numerical instability. A new variable as function of position was defined and a Poisson equation was solved in addition to the governing equations.

Formulation of the Problem

The system studied consisted of a fluid completely enclosed in a vertical cylinder. Initially the fluid was motionless and at a uniform temperature. Suddenly, the temperature of the cylinder walls (top, bottom, and side) underwent a step change. A transient period started, during which the fluid temperature and velocity changed with time due to heat conduction through walls and natural convection inside the cylinder. Following the step change, the wall temperature was also adjusted dynamically to sustain a constant wall-to-center temperature difference equivalent to the step change. Calculation were carried out through the transient period until pseudo-steady state was reached, at which time the temperature difference between any two points in the fluid was time invariant.

To formulate this problem, it was assumed that: (1) all variables were θ-direction independent; (2) the fluid was viscous and incompressible; (3) dissipation terms were negligible; and (4) all physical properties were constant except for the density in buoyancy term, which was expressed as a linear function of temperature (the Boussinesq assumption) $\rho=\rho_0(1-\beta(T-T_0))$. If pressure is defined as

$$P=p-(p_h-\pi)=p+\rho_0 gz \tag{1}$$

where p is the actual pressure at any point in the fluid, p_h is the hydrostatic pressure of a column of fluid at the reference temperature, and π is a reference pressure at the bottom of the cylinder, then P is a pressure term without hydrostatic influence. Using the following dimensionless variables

$$\begin{aligned} r &= r'/D,\ z=z'/D,\ t=\frac{t'}{(D^2/\nu)} \\ v_r &= \frac{v_r'}{(\nu/D)},\ v_z=\frac{v_z'}{(\nu/D)} \\ T &= \frac{T'-T_0'}{T_w'-T_0'},\ P=\frac{P'}{\rho(\nu/D)^2} \end{aligned} \tag{2}$$

the governing equations can be expressed in the following dimensionless form

$$\frac{\partial(rv_r)}{\partial r}+\frac{\partial(rv_z)}{\partial z}=0 \tag{3}$$

$$\frac{\partial v_r}{\partial t}+v_r\frac{\partial v_r}{\partial r}+v_z\frac{\partial v_r}{\partial z}=-\frac{\partial P}{\partial r}+\nabla^2 v_r-\frac{v_r}{r^2} \tag{4}$$

$$\frac{\partial v_z}{\partial t}+v_r\frac{\partial v_z}{\partial r}+v_z\frac{\partial v_z}{\partial z}=-\frac{\partial P}{\partial z}+\nabla^2 v_z+\mathrm{Gr}\bullet T \tag{5}$$

$$\frac{\partial T}{\partial t}+v_r\frac{\partial T}{\partial r}+v_z\frac{\partial T}{\partial z}=\frac{1}{\mathrm{Pr}}\nabla^2 T \tag{6}$$

with dimensionless initial conditions of

$$T=0,\ v_r=v_z=0 \qquad \text{for } t=0 \tag{7}$$

and dimensionless boundary conditions of

$$\begin{aligned} &v_r=v_z=0,\ T=T_c+1 && \text{at solid boundaries} \\ &v_r=\frac{\partial v_z}{\partial r}=\frac{\partial T}{\partial r}=0 && \text{at } r=0 \end{aligned} \tag{8}$$

where all unprimed variables and operators are dimensionless.

The distribution of the local heat flux may be evaluated from Fourier's law, $q'=-k(\partial T'/\partial n')$ since the convective terms are zero at the boundaries. Letting $n=n'/D$, the local and the overall Nusselt numbers (based on diameter) can be expressed as

$$\mathrm{Nu}_x{}^*=\frac{h_x'D}{k}=-\frac{\partial T}{\partial n} \quad \text{(local)} \tag{9}$$

$$\mathrm{Nu}^*=\frac{\int_A \mathrm{Nu}_x{}^* dA}{A} \quad \text{(overall)} \tag{10}$$

In defining the Rayleigh and Nusselt numbers, several characteristic lengths were evaluated. The following gave the best correlation

$$L=6\bullet\frac{\text{volume}}{\text{surface area}}=D\left[\frac{3(H/D)}{1+2(H/D)}\right]=D\bullet f \tag{11}$$

Nomenclature

A = area
D = diameter
f = H/D function, equation (10)
g = acceleration of gravity
Gr = Grashof number
h = heat transfer coefficient
H = height
k = thermal conductivity
L = characteristic length $=D\bullet f$
n = normal vector
Nu = nusselt number based on L
p = actual pressure
p_h = hydrostatic pressure $=\pi-\rho_0 gz$
P = $p+\rho_0 gz$
Pr = Prandtl number
q = heat flux
r = radial position
Ra = Rayleigh number based on L
t = time
T = temperature
V = velocity
z = axial position
α = thermal diffusivity
β = coefficient of thermal expansion
μ = dynamic viscosity
ν = kinematic viscosity
π = reference pressure
ρ = density
∇^2 = two-dimensional Laplacian operator

Subscripts

c = center
0 = initial
r = radial-component property
w = wall
x = local variable
z = axial-component property

Superscripts

$'$ = dimensional variables
$*$ = based on diameter

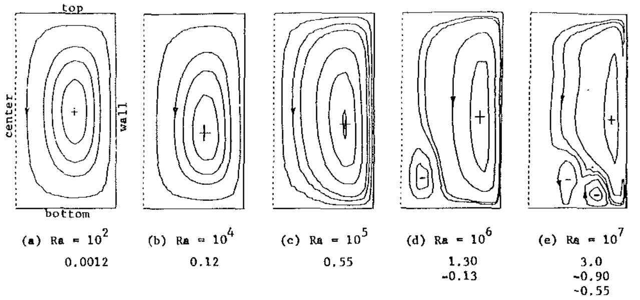

(a) Ra = 10^2 0.0012

(b) Ra = 10^4 0.12

(c) Ra = 10^5 0.55

(d) Ra = 10^6 1.30 −0.13

(e) Ra = 10^7 3.0 −0.90 −0.55

Fig. 1 Stream function contours for $H/D = 1$ cylinder; maximum (minimum) stream function value of each circulation is shown after Ra

This choice of L also had the following advantages: (1) $L = D$ when $D = H$; (2) L takes into account both D and H: When they are close, more weight is put on the smaller of the two, which is intuitively realistic; (3) L depends only on the smaller dimension as one becomes very large compared to the other. The Rayleigh number and the Nusselt number using L and D can be related as

$$\mathrm{Nu} = f\,\mathrm{Nu}^* \tag{12}$$

$$\mathrm{Ra} = f^3\,\mathrm{Ra}^* \tag{13}$$

Numerical Method

The equations above, with the associated initial and boundary conditions, provide a complete mathematical description of the problem. These equations were solved by the SIMPLER algorithm which is briefly described here. The grid structure was based on the Marker and Cell (MAC) method of Harlow and Welch [8], which involves the use of primitive variables (velocities, pressure, and temperature). A special feature was that the grid points at which the velocity components were computed were shifted along the coordinate direction to the edge of the control volume where other fields were computed so that there was a close relationship between the velocities and the motive pressure differences. The partial differential equations were discretized by a power-law scheme [9]. The resulting finite-difference equations included the velocity equations, temperature equation, and pressure equation. The pressure equation was derived by substituting the velocity (in terms of the pressure) into the equation of continuity. This method made the velocity field satisfy continuity only if the correct pressure field was also employed. A line-by-line method was used to simplify the solution of the general MN-variable system to iteratively solving MN-variable and NM-variable tridiagonal systems.

The calculation parameters were Rayleigh number and the height-to-diameter ratio. Cases with a Rayleigh number up to 10^7, H/D of 0.125, 0.25, 0.5, 1, and 2 were calculated. A Prandtl number of 7 was used, corresponding to water; however, the influence of the Prandtl number was not expected to be significant since it is generally accepted that steady-state natural convection can be described by geometric parameters and the Rayleigh number alone when the Prandtl number is greater than 5. To further support this, two cases (with the Prandtl number equal to 7 and 180, $\mathrm{Ra} = 10^5$, and $H/D = 1$) were calculated for comparison, and the resulting temperature profiles coincided exactly.

To establish the finite-difference equation involving boundary points and to solve the discontinuity problem at the boundary, the harmonic-mean method of Patankar [10] was used. Considerably finer grids were applied to the region close to the boundaries to reduce errors due to this boundary condition approximation and rapid changes in that area, and to increase the accuracy of heat flux calculations. Grids of 10×10, 10×28, and 19×19 were generally used and the results were determined to be grid independent by a comparison of solutions obtained with different grids.

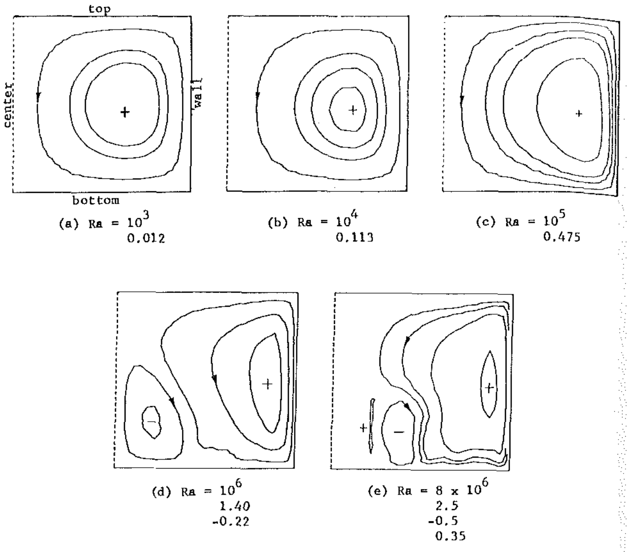

(a) Ra = 10^3 0.012

(b) Ra = 10^4 0.113

(c) Ra = 10^5 0.475

(d) Ra = 10^6 1.40 −0.22

(e) Ra = 8×10^6 2.5 −0.5 0.35

Fig. 2 Stream function contours for $H/D = ½$ cylinder; maximum (and minimum) stream function value of each circulation is shown after Ra

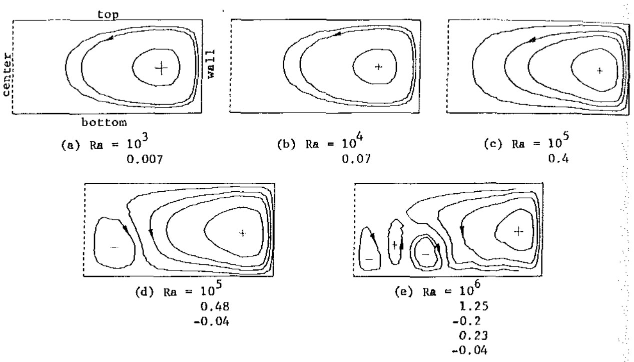

(a) Ra = 10^3 0.007

(b) Ra = 10^4 0.07

(c) Ra = 10^5 0.4

(d) Ra = 10^5 0.48 −0.04

(e) Ra = 10^6 1.25 −0.2 0.23 −0.04

Fig. 3 Stream function contours for $H/D = ¼$ cylinder; maximum (and minimum) stream function value of each circulation is shown after Ra

The pseudo-steady-state solution was calculated by marching through transient steps until temperatures at all grid points were changing at the same rate. The size of a time step was determined by assuming that the change between two contiguous steps was inversely proportional to the step size. Smaller initial dimensionless time steps were required for larger Rayleigh numbers. Time steps from 10^{-3} to 10^{-5}, corresponding to the Rayleigh number of 10 to 10^7, were used. The size of the time steps increased as the calculation approached steady state.

Patankar [6] suggested that this scheme would not converge without underrelaxation of the momentum and energy equations. However it was found that for small Rayleigh numbers, or for small time steps, or close to steady state, the use of the underrelaxation coefficient would greatly overdamp the response resulting in excessive computer time. Therefore, different relaxation coefficients, ranging from 0.3 to 1, were used, depending on the convergence rate.

Results

The results are presented in the form of streamline and isotherm contours. Axial velocity and temperature profiles at several heights and Rayleigh numbers are also presented to provide supplementary information. Heat transfer results are presented as the Nusselt number versus Rayleigh number. Local Nusselt numbers are then discussed to give details about heat transfer at the boundaries.

Streamlines. Stream functions were assumed zero at all solid boundaries and were calculated by integrating the velocity field. Integrations along both axial and radial directions

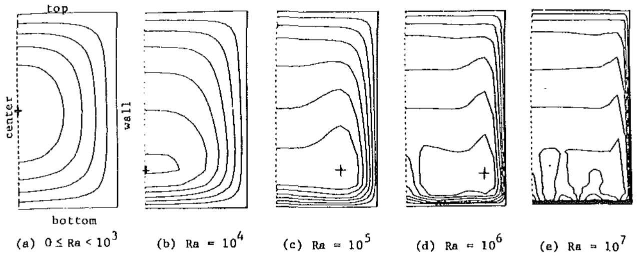

(a) $0 \leq \mathrm{Ra} < 10^3$ (b) $\mathrm{Ra} = 10^4$ (c) $\mathrm{Ra} = 10^5$ (d) $\mathrm{Ra} = 10^6$ (e) $\mathrm{Ra} = 10^7$

Fig. 4 Temperature contours for $H/D = 1$ cylinder; contour values equal 1.0 at the solid boundary and 0 at the center; 0.2 increments

were made to check the accuracy. Representative streamline contours are presented in Figs. 1-3. Each figure consists of five diagrams, each showing the right-hand half of the vertical cross section passing through the center of the cylinder for various Rayleigh numbers.

Figure 1 shows results for $H/D = 1$. The main feature of these flow fields is the circulation up along the heated side wall and down through the center core. The dimensionless stream function ψ provides a direct index of the volumetric flow rate. The ψ values for larger Ra were substantially higher than those for smaller Ra, indicating increased circulation. For $\mathrm{Ra} \leq 10^3$, conduction dominates and there is horizontal symmetry. In reality, there is no flow if the Rayleigh number is smaller than a critical value. However, due to the fact that dissipation terms were neglected, the existence of flow was predicted even for an infinitesimal driving force. As the Rayleigh number and, thus, convection increases, the center of the circulation moves downward and then toward the side wall. This indicates that convection is stronger in the region closer to the side wall and the bottom. When the Ra is greater than 10^5, a secondary (and reverse) flow begins in the vicinity of the bottom center. For larger Rayleigh numbers, multiple circulations were found. Flow patterns of this type have been observed experimentally [11] in cubical enclosures. Figures 2 and 3 are similar to Fig. 1, with H/D equal to 0.5 and 0.25, respectively. As H/D decreases, the vertical confinement increases and stronger top-to-bottom symmetry is evident. In Fig. 3 the side wall is so remote (relatively) that there is a large central region without significant primary circulation, leaving room for the development of multiple cells. The heat entering through the top tended to stabilize the fluid motion, so the multiple circulations occurred in the lower part of the cylinder. It should be noted that both Fig. 3(*c*) and (*d*) are stable solutions for $\mathrm{Ra} = 10^5$ (this will be discussed later). Since changes in H/D did not influence the major flow structures significantly in this range, it was thought that other characteristics such as the Nusselt number might also be correlated without considering H/D as a parameter.

Isotherms. Figures 4-6 present dimensionless temperatures in the same format as the streamlines. In interpreting these diagrams, it should be remembered that the contour values at the solid walls are defined equal to 1 and those at the center equal to zero. For small Rayleigh numbers, where conduction is essentially controlling, the temperature contours are independent of the Rayleigh number and are characterized by top-to-bottom symmetry. As convection increases, the minimum temperature moves from the center downward and then toward the wall. The relative increase in the temperature at the bottom of the center core provides the driving force for a rising flow along the center line. This can lead to the formation of secondary circulation in the flow field. At high Rayleigh numbers, when the minimum temperature is close to the side wall and the bottom, thermal boundary layers which are found in this region are indicated by a crowding together of the isotherms adjacent to the walls; vigorous heat transfer is to be expected in this region. When $\mathrm{Ra} \geq 10^6$ the isotherms close to the bottom become wavy and develop into the multiple circulating flow patterns. The convergence of the numerical calculations for these high Rayleigh number cases was much slower and the error terms could only be reduced to small values, but not to zero. Therefore, it may be that the unevenness observed in the isotherms is due to numerical instabilities in the calculation scheme. Since similar flow patterns have been observed experimentally, it seemed worthwhile to report them here. Even at the high Ra numbers, the isotherms at the walls were smooth and the overall heat transfer was not significantly affected by the unevenness farther from the bottom.

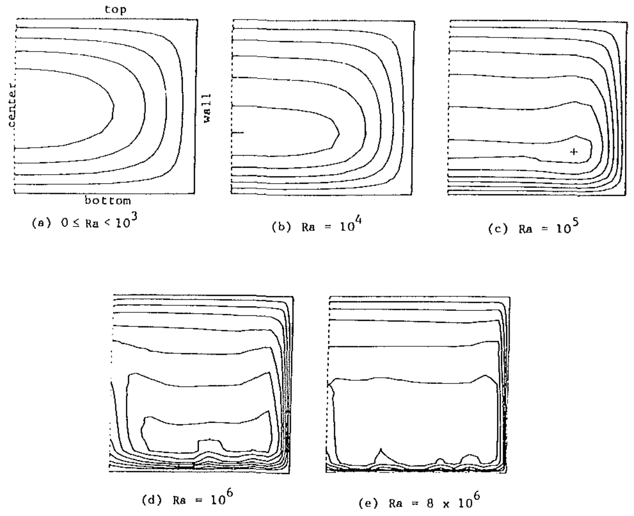

(a) $0 \leq \mathrm{Ra} < 10^3$ (b) $\mathrm{Ra} = 10^4$ (c) $\mathrm{Ra} = 10^5$

(d) $\mathrm{Ra} = 10^6$ (e) $\mathrm{Ra} = 8 \times 10^6$

Fig. 5 Temperature contours for $H/D = 0.5$ cylinder; contour values equal 1.0 at the solid boundary and 0 at the center; 0.2 increments

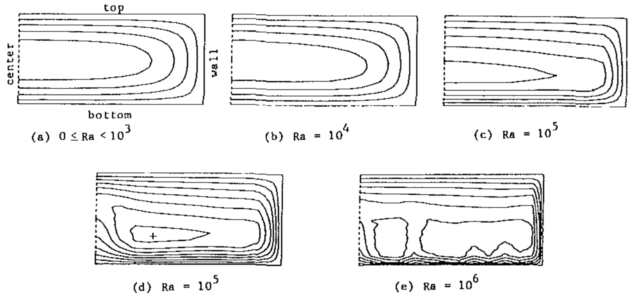

(a) $0 \leq \mathrm{Ra} < 10^3$ (b) $\mathrm{Ra} = 10^4$ (c) $\mathrm{Ra} = 10^5$

(d) $\mathrm{Ra} = 10^5$ (e) $\mathrm{Ra} = 10^6$

Fig. 6 Temperature contours for $H/D = 0.25$ cylinder; contour values equal 1.0 at the solid boundary and 0 at the center; 0.2 increments

In addition to the overall temperature distribution, there is another noteworthy effect of H/D on temperatures. For $H/D = 1$ the center line temperature is mostly influenced by the hot fluid that circulates from the side walls across the top of the cylinder and down the center. This global circulation pushes the minimum temperature toward the bottom. As H/D decreases, the influence of side walls becomes smaller, and the center temperature is additionally affected by the upward movement of hot fluid from the bottom. This elevates the minimum temperature location. The heating effect of the bottom becomes increasingly important as the H/D ratio decreases. For H/D of 0.25 and Ra between 8×10^4 and 2×10^5, two solutions were found for the same Ra. Diagrams (*c*) and (*d*) of Figs. 3 and 6 present these two solutions for $\mathrm{Ra} = 10^5$.

Axial Velocity Profiles. Figure 7 shows several axial velocity distributions in a cylinder with $H/D = 1$. Each diagram presents profiles at three different vertical positions: one at the center (designed by *c*), one at one-quarter height from the top (*t*), and one at one-quarter height from the bottom (*b*). In Fig. 7(*a*), profiles *t* and *b* coincide, indicating top-to-bottom symmetry. Also, the maximum axial velocity occurs in the central downward flow. At higher Ra numbers (Fig. 7*b*), a boundary layer develops at the side wall, which is in-

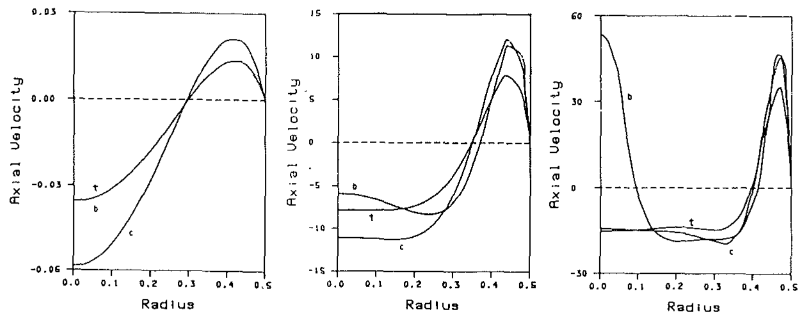

(a) Ra $=10^2$ (b) Ra $=10^5$ (c) Ra $=10^6$

Fig. 7 Radial profiles of the axial velocity for $H/D=1$ cylinder

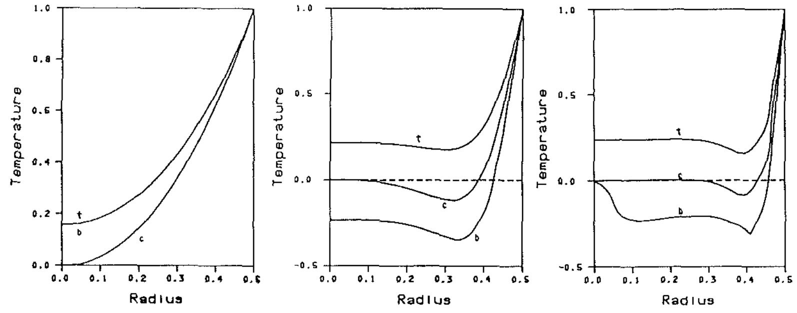

(a) Ra = 0 (b) Ra $=10^5$ (c) Ra $=10^6$

Fig. 8 Radial temperature profiles for $H/D=1$ cylinder

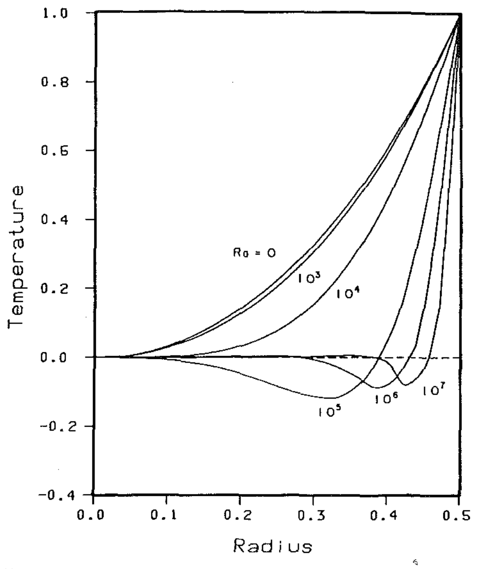

Fig. 9 Effect of the Rayleigh number on the temperature distribution for $H/D=1$ and at midheight

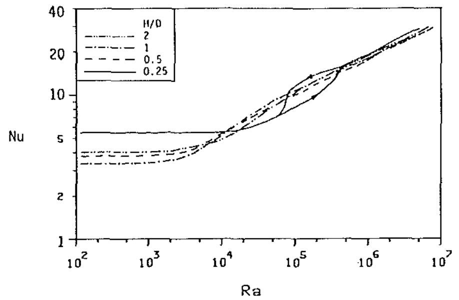

Fig. 10 Heat transfer correlation for vertical cylinders; $\Delta T=(T_w-T_c)$

dicated by the increased velocity gradient next to wall and the large, constant velocity region in the center. The magnitudes of the maximum positive and negative velocities are about the same. For even higher values of Ra (Fig. 7*c*), the boundary layer becomes thinner and the center core larger, except in the bottom region where a secondary circulation is located. At high Rayleigh numbers, the maximum positive velocities are much greater than the maximum negative velocities.

Temperature Profiles. Figure 8 shows temperature profiles of three Rayleigh numbers at three different heights, the format and nomenclature being the same as Fig. 7. These profiles correspond to temperature contours presented in Fig. 4; therefore no further description is provided here. Figure 9 is provided to show the effects of increasing Rayleigh number. Six temperature profiles at the midheight of the cylinder with $H/D=1$ are plotted with the smallest Ra of zero representing conduction. The increasing slope at wall and the increasing center core region show the development of the boundary layer at the side wall.

Heat Transfer. Figure 10 shows the relationship between the overall Nusselt number and the Rayleigh number. In defining the Nusselt and Rayleigh numbers, a characteristic temperature difference of (T_w-T_c) was used since that would be the easiest to measure practically. Other temperature differences were also used and their effects will be discussed. The low Rayleigh number region of Fig. 10 shows horizontal lines for the various H/D ratios, indicating that conduction dominates the heat transfer. Hence, when conduction is the only significant mode, the Nusselt number depends only on the H/D ratio. As the Rayleigh number increases, the curves for different H/D ratios merge into one straight line. This indicates that the overall heat transfer rate does not significantly depend on the configuration ratio for $0.25<H/D<2$ and Nu and Ra can be successfully correlated by $\mathrm{Nu}=a\cdot\mathrm{Ra}^b$. Table 1 lists the values of the coefficients a and b for several Rayleigh numbers based on different characteristic temperature differences. The temperature difference for defining the Nusselt number in Table 1 was (T_w-T_c). By knowing the Rayleigh number based on any of these temperature differences, the Nusselt number may be determined, and then the other two temperature differences can be calculated. Note that the cor-

Table 1 Coefficients for heat transfer correlation

Temperature difference	a	b	Correlation coefficient R^2
wall-mixed-cup	0.727	0.234	0.971
wall-center	0.519	0.255	0.963
wall-minimum	0.536	0.248	0.967

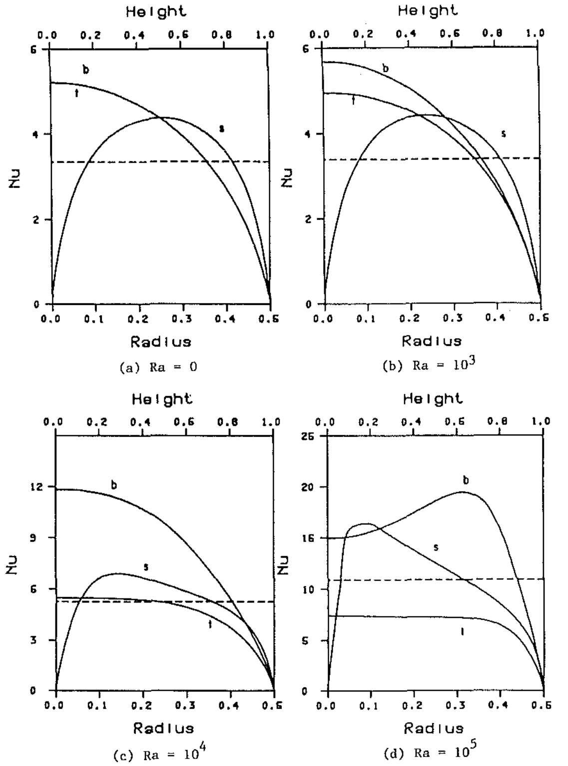

(a) Ra = 0 (b) Ra = 10^3

(c) Ra = 10^4 (d) Ra = 10^5

Fig. 11 Local Nusselt number for $H/D = 1$ cylinder; ------ is the mean

relations for the three different definitions are not significantly different as far as ability to fit the data is concerned.

It is important to notice the hysteresis in the data for $H/D=0.25$ and $8\times10^4<\mathrm{Ra}<2\times10^5$. As H/D is decreased, the importance of the heat transfer through the side walls is also decreased, and the problem evolves into one of horizontal plates in which the bottom has greater influence. As previously mentioned, the pseudo-steady-state results were approached by marching through transient time steps until no significant changes were observed. But, in this hysteresis region, the transient terms oscillated between two small values instead of decreasing monotonically toward zero. The hysteresis represents the solutions at these two minimums. The two solutions are considerably different in detail (e.g., one versus two circulation patterns) which shows up as a 10-20 percent difference in the Nusselt number. The hysteresis phenomenon is believed to represent the transition between a side-wall dominated process and one in which the bottom has the major influence. The arrows in Fig. 10 are to indicate that the solutions on the upper branch of the hysteresis are similar in shape to those at higher Rayleigh numbers, whereas the solutions on the lower branch are similar to the solutions at lower Rayleigh numbers. Due to the complexity of the phenomenon, extrapolation of these results to smaller H/D ratios is not recommended.

Figure 11 shows the typical local Nusselt number distribution for the $H/D = 1$ cylinder. The dashed line in each diagram is the mean Nusselt number for the cylinder. The local Nusselt numbers along the top and bottom of the cylinder are plotted versus radius, whereas the local Nusselt number for the side wall is plotted versus height. Figure 11(a) shows the case for conduction. As expected, the local Nusselt numbers of the top and bottom walls coincide. In Fig. 11(b), as Ra increases to 10^3, the local Nusselt number at the bottom increases, while that at the top decreases, causing the mean Nusselt number to remain essentially unchanged. Thus, if only the overall Nusselt number was observed, one might conclude that there was no convection when the Rayleigh number was 10^3. Further increase in Ra, Fig. 11(c), shows the development of a region of constant Nusselt number at the top and an increased importance of heat transfer through the bottom. The position of the maximum local Nusselt number on the side wall also moves downward. All of these effects are due to the movement of minimum temperature down the center line. For even larger values of Ra the minimum temperature moves off of the center line and, as a result, the maximum local Nusselt number on the bottom no longer occurs at the center. This is shown in Fig. 11(d).

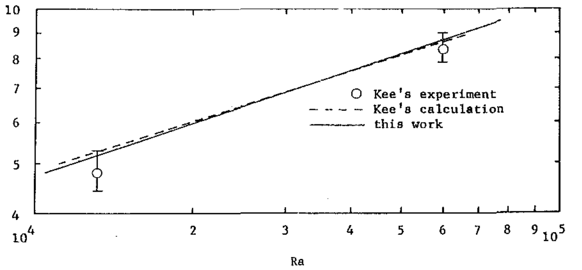

Fig. 12 Comparison of heat transfer results with those of Kee [5]; error bounds of the experimental data are also shown

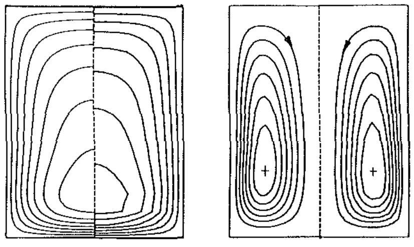

(a) Temperature (b) Stream Function

Fig. 13 Comparison of the temperature and stream function contours with Kee's [5] (at left): $H/D = 1.315$, $\mathrm{Pr} = 0.7$, $\mathrm{Ra} = 1.21\times10^4$

Discussion

The numerical and experimental results of Kee [5] may be used for comparison with these results at low Rayleigh numbers. Figure 12 shows the comparison, with their experimental data at Ra of 1.21×10^4 and 5.76×10^4 included. According to Kee's paper, their numerical results were well within the experimental error, and the low values of the measured heat transfer rate were explained by the nonuniformity of the wall temperature. Figure 13 is another comparison with the work of Kee. In Fig. 13(a), the same values of the temperature isotherms are presented for this work and that of Kee. Although the stream functions in Fig. 13(b) look almost identical, they may have different contour values since the numerical values were not given in Kee's paper. Generally good agreement was found between these two results except in the very low temperature regions.

In this work, the low temperature range (usually between -0.2 and -0.4) became unstable as the Rayleigh number increased to over 10^7. There are several possible reasons for this phenomenon. Pollard [7] has pointed out that the SIMPLE method might diverge, even if no physical instability occurs, if the momentum equation is driven by the body force. Another possible cause could be the transition from laminar flow to weak turbulence. McLaughlin and Orszag [12] have studied the transition of the Benard convection to turbulence in a flat layer system. It is believed that the development of unstable solutions from a state of steady convective flow may be qualitatively described by their study. However, these two systems are too dissimilar to make quantitative comparison. According to Raithby's [13] analysis, finite-difference methods are subject to false diffusion error if the flow is not in the direction of a grid line. However, the results will still be reasonable as long as the true diffusion is significantly greater than the false diffusion. The false diffusion coefficient is proportional to the velocity and is greater for larger grid sizes. This may explain why the unstable phenomenon only occurs for the very high velocity cases and at large grid size areas. In addition, the grid size used may not be small enough to accurately produce the details of the complex flow patterns. The purpose in mentioning the unstable phenomenon is to indicate the upper bound of this work and to show that the numerical scheme was functional to that point.

Conclusions

A numerical method was used to investigate pseudo-steady-state natural convection inside a closed vertical cylinder. The range of parameters was $0 \leq \mathrm{Ra} \leq 10^7$, $\mathrm{Pr} = 7$, and $H/D = 1/4$, 1/2, 1, and 2. The results include the stream function contours, isotherms, heat transfer coefficient correlation, and profiles of the axial velocity, temperature, and local Nusselt numbers. The following were concluded from the study:

1 The heat transfer for all H/D ratios was successfully correlated by $\mathrm{Nu} = 0.519\ \mathrm{Ra}^{0.255}$ based on the wall-to-center temperature difference.

2 The heat transfer results for all H/D ratios investigated were similar as long as the special characteristic length (defined by 6 × volume/surface area) was used. The use of this characteristic length was essential for correlation of the data since neither H nor D alone was sufficient to characterize the system dimension.

3 Secondary flows were observed for $\mathrm{Ra} \geq 2 \times 10^5$ and for all H/D ratios.

4 Two solutions were found for the case where $H/D = 0.25$ when $8 \times 10^4 \leq \mathrm{Ra} \leq 2 \times 10^5$, which may represent an actual sustained oscillation in the natural convection process.

5 Based on the local Nusselt number, the heat flux through the bottom was found to be higher than that through side wall, which, in turn, was much higher than that through the top. The maximum flux for large Rayleigh numbers was located at about $0.15D$ from side wall on the bottom, and $0.15H$ from the bottom on the side wall. This location is closely associated with the minimum temperature location.

References

1 Evans, L. B., and Stefany, N. E., "An Experimental Study of Transient Heat Transfer to Liquids in Cylindrical Enclosures," *CEP Symp. Series*, Vol. 62, No. 64, 1966, pp. 209–215.

2 Evans, L. B., Reid, R. C., and Drake, E. M., "Transient Natural Convection in a Vertical Cylinder," *AIChE Journal*, Vol. 14, 1968, pp. 251–259.

3 Murgatroyd, W., and Watson, A., "An Experimental Investigation of the Natural Convection of a Heat Generating Fluid Within a Closed Vertical Cylinder," *J. Mech. Engg. Sci.*, Vol. 12, 1970, pp. 354–363.

4 Daney, D. E., "Turbulent Natural Convection of Liquid Deuterium," *Int. J. Heat Mass Transfer*, Vol. 19, 1976, pp. 431–441.

5 Kee, R. J., Landram, C. S., and Miles, J. C., "Natural Convection of a Heat-Generating Fluid Within Closed Vertical Cylinders and Spheres," ASME JOURNAL OF HEAT TRANSFER, Vol. 98, 1976, pp. 55–61.

6 Patankar, S. V., *Numerical Heat Transfer and Fluid Flow*, Hemisphere, New York, 1980.

7 Pollard, A., and Thyagaraja, A., "A New Method for Handling Flow Problems With Body Forces," *Comp. Methods Appl. Mech. Engg.*, Vol. 19, 1979, pp. 107–116.

8 Harlow, F. H., and Welch, J. E., "Numerical Calculation of Time-Dependent Viscous Incompressible Flow of Fluid With Free Surface," *Phys. of Fluids*, Vol. 8, 1965, pp. 2182–2189.

9 Patankar, S. V., and Baliga, B. R., "A New Finite Difference Scheme for Parabolic Differential Equations," *Numerical Heat Transfer*, Vol. 1, 1978, pp. 27–37.

10 Patankar, S. V., "A Numerical Method for Conduction in Composite Materials, Flow in Irregular Geometries, and Conjugate Heat Transfer," *Proc. 6th Heat Transfer Conf.*, Toronto, 1978, Vol. 3, pp. 297–302.

11 Lin, Y. S., and Akins, R. G., "An Experimental Study of Flow Patterns and Heat Transfer by Natural Convection Inside Cubical Enclosures," *Natural Convection in Enclosures, The 21st Nat. Heat Trans. Conf.*, Seattle, 1983, Vol. 26, pp. 35–42.

12 McLaughlin, J. B., and Orszag, S. A., "Transition From Periodic to Chaotic Thermal Convection," *J. Fluid Mech.*, Vol. 122, 1982, pp. 123–142.

13 Raithby, G. D., "A Critical Evaluation of Upstream Differencing Applied to Problems Involving Fluid Flow," *Computer Methods in Applied Mechanics and Engineering*, Vol. 9, 1976, pp. 75–103.

T. L. Bergman[1]
Assoc. Mem. ASME

F. P. Incropera
Professor.
Fellow ASME

R. Viskanta
Professor.
Fellow ASME

Heat Transfer Laboratory,
School of Mechanical Engineering,
Purdue University,
West Lafayette, Indiana 47907

Transient Behavior of a Radiatively Heated Double-Diffusive System

A mathematical model is developed to predict the transient response of a salt-stratified, double-diffusive system which is destabilized by radiation absorption at its bottom boundary. An accepted k–ε turbulence model is used to predict the response of the salt-stratified solution to bottom heating, and a discrete ordinates solution of the radiative transfer equation is used to predict the radiation field. Verification is achieved through comparisons of predicted and measured temperature distributions, which have been previously reported. Parametric calculations are performed to investigate the influence of the radiation source temperature, bottom surface reflectivity, optical extinction coefficient, and top surface boundary condition on system response.

Introduction

In order to investigate double-diffusive phenomena relevant to many engineering and geophysical systems [1, 2], considerable attention has been given to initially isothermal, salt-stratified solutions which are thermally destabilized by bottom heating [3, 4]. In such systems, the mixed layer which develops above the heated surface expands into and transfers thermal energy to the overlying stratified fluid. In other systems of interest, bottom heating may be achieved by the absorption of applied irradiation. Such a destabilizing heating process is relevant to the salt-stratified solar pond [5], radiative heating of walls adjacent to cool binary gas mixtures in combustion systems [6], and to salt-stratified layers in the ocean [7].

Recently a one-dimensional turbulence model was successfully used to predict mixed-layer growth, as well as temperature and salinity profile development, in a salt-stratified system electrically heated from below [8]. Model predictions of mixed-layer growth and temperature profiles were confirmed by comparison with experimental results. In addition, one-dimensional models for radiative transfer in liquid systems have been developed and experimentally verified [9, 10]. With these models well established, it is now possible to use a hybrid turbulent/radiative transport model to predict the response of salt-stratified solutions to an imposed radiation field. The objective of this study has been to use such a hybrid model to evaluate the effect of important radiation parameters on system response. Verification of the hybrid model is achieved by comparing predicted system behavior with experimental measurements for a radiatively driven salt-stratified system [11]. The experiments were performed in a small test cell containing a salt-stratified fluid which was irradiated from filtered overhead quartz, tungsten filament lamps equipped with parabolic reflectors. A schematic of the physical system is provided in Fig. 1, and details of the experiments are available elsewhere [11, 12].

Mathematical Model

By assuming one-dimensional transport in the vertical (z) direction, a turbulent Lewis number of unity, applicability of gradient diffusion, and appropriate expressions for effective viscosities and Prandtl numbers, the energy and species conservation equations for the salt-stratified system may be expressed as

$$\frac{\partial}{\partial t}(\rho c T)=\frac{\partial}{\partial z}\left[\left(\frac{\mu_e}{\mathrm{Pr}_e}c\right)\frac{\partial T}{\partial z}\right]+\frac{\partial F}{\partial z} \tag{1}$$

$$\frac{\partial}{\partial t}(\rho m_s)=\frac{\partial}{\partial z}\left[\left(\frac{\mu_e}{\rho \mathrm{Pr}_e}\right)\frac{\partial}{\partial z}(\rho m_s)\right] \tag{2}$$

where the radiative flux divergence $\partial F/\partial z$ accounts for the absorption of applied radiation (source term) within the system.

A one-dimensional low turbulence Reynolds number, k–ϵ model [8] is used to evaluate the effective viscosity and Prandtl number in equations (1) and (2). The k and ϵ equations include source terms accounting for buoyant production or destruction of turbulent quantities due to local unstable or stable density gradients, respectively. The local density gradient is determined by evaluating local temperature and salinity gradients. Vertical turbulence diffusion is considered, as is dissipation in the k equation and viscous destruction in the ϵ equation. However, convective transport and shear production are neglected. A complete discussion of the turbulence model is provided elsewhere [8].

Values of the source term in the energy equation (1) and the bottom heat flux resulting from radiation absorption govern local temperature gradients and, hence, can provide for the buoyant production of turbulence within the system. The source term and the bottom heat flux are obtained by solving the one-dimensional radiative equation of transfer. Using the

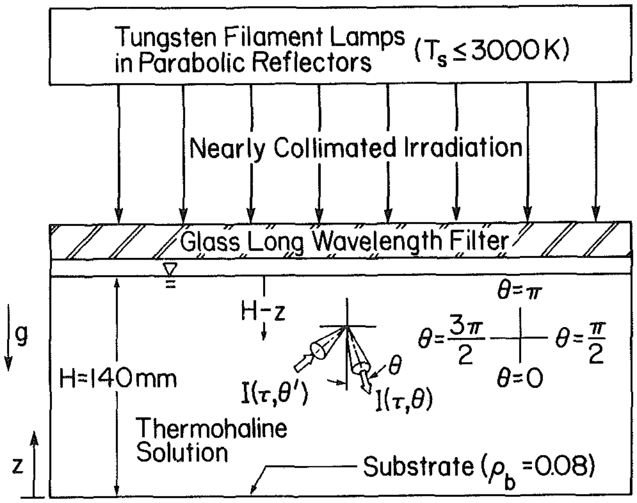

Fig. 1 Experimental apparatus and coordinate systems

---

[1] Presently at the Department of Mechanical Engineering, The University of Texas at Austin, Austin, Texas 78712

Contributed by the Heat Transfer Division for publication in the JOURNAL OF HEAT TRANSFER. Manuscript received by the Heat Transfer Division January 28, 1985.

coordinate system of Fig. 1, the appropriate form of the equation is

$$\cos\theta \frac{dI_\lambda}{d\tau_\lambda} = -I_\lambda + \frac{\omega_\lambda}{2}\int_0^\pi I_\lambda p_\lambda(\theta', \theta)\sin\theta' d\theta' \qquad (3)$$

where the salt solution is considered to be a plane-parallel, nonemitting, absorbing, and anisotropically scattering medium. The net spectral radiation flux at an optical depth $\tau_\lambda = \beta_\lambda (H-z)$ is

$$F_\lambda(\tau_\lambda) = 2\pi\int_0^\pi I_\lambda(\tau_\lambda, \cos\theta)\cos\theta\sin\theta d\theta \qquad (4)$$

Although the radiative flux distribution may be most accurately predicted by employing a multiple-band radiation model, it was found that a simple two-band model acceptably predicts system behavior. Since water is effectively opaque to long wavelength radiation [13], incident radiation of $\lambda > 1000$ nm which is transmitted by the glass filter of Fig. 1 is assumed to be absorbed at the top of the salt solution. For the band below 1000 nm, a spectrally averaged extinction coefficient, which accounts for spectral variations in source emission, glass transmission, and the water extinction coefficient, is used

$$\beta = \frac{\int_{\lambda=0}^{1000 \text{ nm}} \epsilon_{\lambda,s} E_{\lambda,b}(T_s)\tau_{\lambda,g}\beta_{\lambda,w} d\lambda}{\int_{\lambda=0}^{1000 \text{ nm}} \epsilon_{\lambda,s} E_{\lambda,b}(T_s)\tau_{\lambda,g} d\lambda} \qquad (5)$$

Values of $\tau_{\lambda,g}$, $\beta_{\lambda,w}$, and $\epsilon_{\lambda,s}$ are available elsewhere [9, 14, 15]. Although salt content can influence the optical properties of an aqueous solution [16], the degree to which these properties are affected in the infrared is small [17, 18] and the available data concerning the variation are minimal. As such, it is assumed that use of the optical properties of pure water is valid. A spectrally averaged albedo ω was obtained in a manner similar to β and used in conjunction with a highly forward peaked Henyey-Greenstein approximation ($g_{hg} = 0.90$) to the scattering phase function [19] in a discrete ordinates prediction of the radiance, radiation flux, and volumetric absorption within the fluid. The collimated irradiation in the semitransparent band was assumed to be normally incident and was calculated from

$$G_{(0\text{-}1000 \text{ nm})} = G\,\frac{\int_{\lambda=0}^{1000 \text{ nm}} \epsilon_{\lambda,s} E_{\lambda,b}(T_s)\tau_{\lambda,g} d\lambda}{\int_{\lambda=0}^{\infty} \epsilon_{\lambda,s} E_{\lambda,b}\tau_{\lambda,g} d\lambda} \qquad (6)$$

Due to the presence of the glass filter, heat loss from the top of the thermohaline solution is considered negligible ($q_t = 0$). Also, since the bottom is externally insulated and the absorbed radiation is conducted to the fluid, the bottom heat flux may be expressed as

$$q_b = F(z=0) \qquad (7)$$

The boundaries at the top and bottom of the system are impermeable to salt transfer

$$\left.\frac{\partial m_s}{\partial z}\right|_{z=0} = \left.\frac{\partial m_s}{\partial z}\right|_{z=H} = 0 \qquad (8)$$

while appropriate boundary conditions for the k and ϵ equations are discussed in [8]. Appropriate upper and lower surface boundary conditions for the radiance in the solution are expressed in terms of the reflectivity of the air-liquid interface, as determined by the Fresnel equations [20], and the diffuse hemispherical reflectivity of the bottom surface, $\rho_b = 0.08$ [11]. The expressions and a discussion of the solution technique are presented elsewhere [9].

Results and Discussion

Measured (symbols) and predicted (dashed lines) temperature distributions are shown in Figs. 2 and 3 for experiments 1 and 2, respectively. Temperature distributions were measured [11, 12] with a rake housing thermocouples separated by a vertical distance of 4.76 mm near the top and bottom and 19.05 mm near the center of the 140-mm-deep test cell. The two experiments were performed with initial stabilizing salinity gradients of approximately 19 and 24 percent/m. The experimental irradiation was varied by adjusting the power to the tungsten lamps, and an optical pyrometer was used to determine tungsten filament temperatures of 2600 and 3000 K for experiments 1 and 2, respectively. Values of the total, transmitted irradiation were 1120 and 1720 W/m^2 and were determined by matching the predicted and actual internal energy change of the solution over a period of one hour.

Interferograms taken at $t = 1$ h are shown for both experiments, and a shadowgraph, which was obtained at $t = 1$ h by blocking the reference leg of the Mach-Zehnder interferometer, is shown for experiment 1. The interferometer was not used to measure temperature (or salinity) profiles since salinity and temperature gradients are both stabilizing in the upper portions of the test cell, leading to an irresolvably fine fringe spacing [12]. Rather, the interferograms were used to infer mixed layer heights within the system. The vertical scale on the interferograms and shadowgraph corresponds to the vertical scale of the temperature distribution. As is evident in Fig. 2, the height of the mixed layer, denoted by the bright

Nomenclature

c = specific heat
E = emissive power
F = radiative flux
g_{hg} = Henyey-Greenstein phase function coefficient
G = total transmitted irradiation
h = convective heat transfer coefficient at the air-liquid interface
H = height of the double-diffusive system
I = radiance
k = turbulence kinetic energy or thermal conductivity
m_s = salt mass fraction
p = scattering phase function
Pr = Prandtl number = $\mu c/k$
q = heat flux
t = time
T = temperature
z = vertical coordinate (positive upward)
β = spectrally averaged extinction coefficient for semitransparent band
ϵ = turbulence kinetic energy dissipation or emissivity
λ = wavelength
θ = polar angle
θ' = polar angle of incoming radiation for scattering
μ = viscosity
ρ = mass density or reflectivity
τ = optical depth
ω = single scatter albedo

Subscripts

b = bottom
e = effective
g = glass
s = source
t = top
λ = spectral quantity
w = thermohaline solution

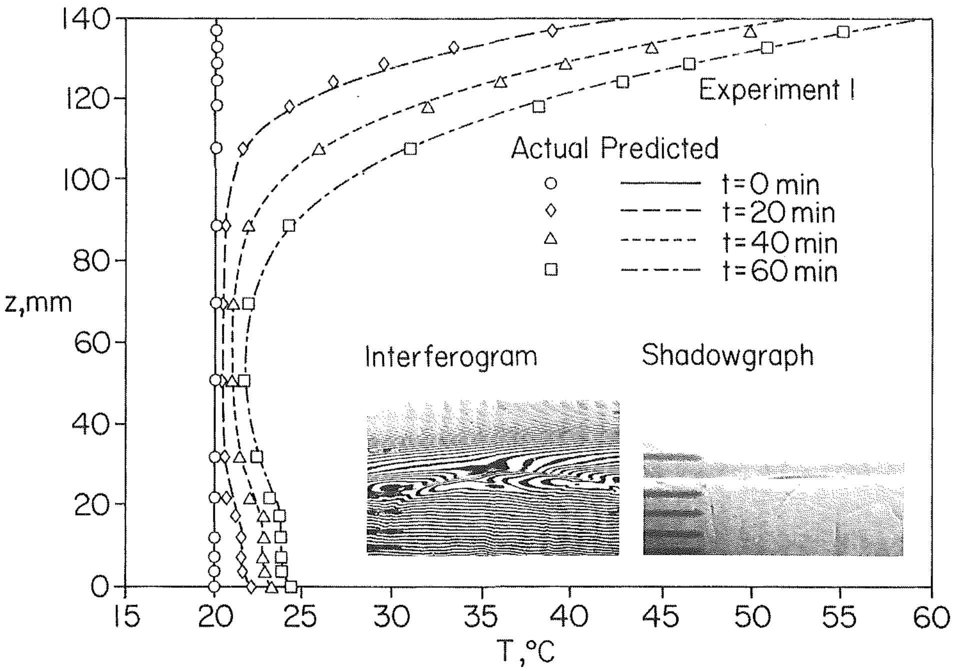

Fig. 2 Predicted and actual temperature profiles and interferogram and shadowgraph of Experiment 1

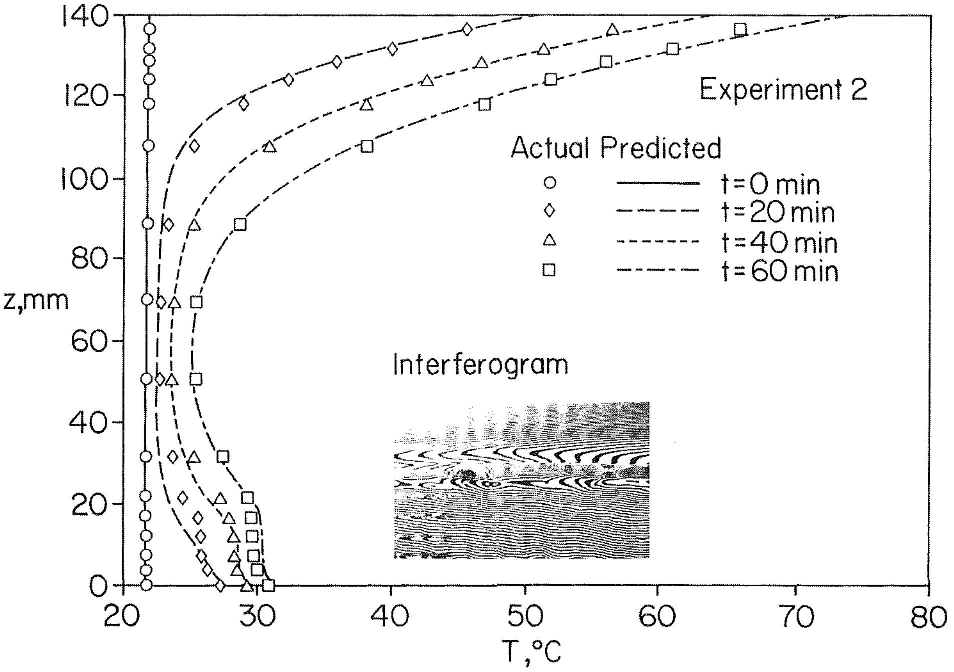

Fig. 3 Predicted and actual temperature profiles and interferogram of Experiment 2

horizontal band in the shadowgraph, corresponds to the disturbance in the interferogram and the inflection point in the measured temperature profile at $z \approx 20$ mm. Dark horizontal lines at the left of the interferograms and the shadowgraph are shadows of the thermocouples used to measure the temperature distribution.

Values of the average extinction coefficient and scattering albedo for experiments 1 and 2, which were determined from equation (5), are shown in Table 1. The shift of the blackbody spectrum to lower wavelengths for the increased source temperature of experiment 2 causes β to decrease and ω to increase.

The strong absorption of long ($\lambda > 1000$ nm) wavelength irradiation at the upper surface induces a stable temperature distribution in the underlying fluid. Shorter wavelength ($\lambda \leq 1000$ nm) radiation is transmitted through the air-liquid interface and is locally absorbed within the remainder of the system. Bottom heat fluxes of approximately 130 and 300 W/m^2, which result from the absorption of transmitted radiation at the black substrate, induce thermal instabilities in the fluid and the development of a bottom mixed layer.

Due to the manner in which the irradiation is determined, comparison between predicted and measured global internal energy variations is meaningless. However, agreement between the predicted and measured temperature profiles is excellent suggesting acceptable prediction of the local

Table 1 Spectrally averaged extinction coefficients and albedos

Experiment	T_s (K)	β (m^{-1})	ω
1	2600	6.02	0.027
2	3000	5.01	0.043
Parametric calculations			
Base case	5800	2.34	0.110
Source	5000	2.93	0.100
Temperature	4000	4.01	0.070
Variation	3000	5.87	0.034
Extinction	5800	4.44	0.110
Coefficient	5800	6.66	0.110
Variation	5800	8.88	0.110

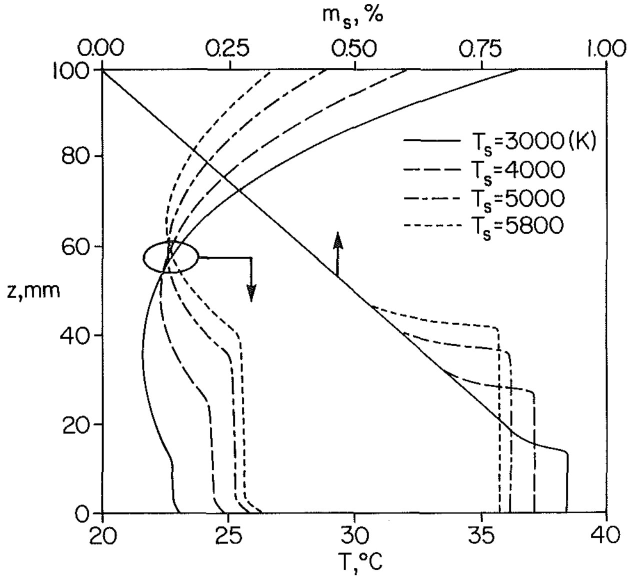

Fig. 4 Predicted temperature and salinity profiles at t = 1 h for various radiation source temperatures

radiative flux divergence. Agreement between the predicted and measured mixed layer heights at $t = 1$ h, which are denoted by the inflection point in the predicted temperature profiles and the discontinuities in the interferograms, is good. Since experimental salinity measurements are limited to a single measurement below 20 mm [12], comparison of predicted and measured salinity distributions is not possible. However, salt concentration distributions have been acceptably predicted by the turbulence model for thermohaline systems in the absence of radiation [8].

It should be noted that corroboration of the data by the model may be due to compensating errors associated with uncertainties in measuring T_s and G and/or to applicability of the model assumptions to the experimental conditions. Higher order effects such as small beam divergence resulting from imperfect parabolic reflectors, sidewall reflections, multiple reflections between the glass cover plate and the air-liquid interface, variations or fluctuations of optical properties, and uncertainties concerning values of the optical properties of the salt solution may also contribute to differences between the predicted and measured results. Nevertheless, the model does predict important trends associated with warming of the surface layers, bottom mixed layer growth, and radiation absorption at intermediate layer depths. Hence it may be used to perform parametric calculations of system behavior.

Since the spectral variation of optical properties is large, the radiation source temperature T_s can have a pronounced effect on system behavior. To investigate this effect, particularly with respect to mixed layer growth, T_s was varied from 3000 to 5800 K. Fixed conditions for the calculations included a salt stratification of $\partial m_s/\partial z = 10$ percent/m, a depth of 100 mm, and a black ($\rho_b = 0$) bottom. The spectrally averaged extinction coefficients and scattering albedos are shown in Table 1. An increase in the source temperature results in decreased β and increased ω, and scattering becomes important only at high source temperatures. Variations in the optical properties associated with experiment 2 and the parametric calculation with $T_s = 3000$ K are due to the presence of the glass filter in the experiment and to the assumption of a radiation source with a spectral distribution proportional to that of a blackbody in the parametric calculation. In addition, an initial fluid temperature of 20°C and irradiation of 500 W/m^2 were prescribed for each of the simulations.

Predicted temperature and salinity profiles at $t = 1$ h for various source temperatures are shown in Fig. 4. As T_s increases, radiation absorption decreases at the air-liquid interface and increases at the bottom substrate. The trend is due to an increase in the fraction of the incident irradiation in the semitransparent band ($\lambda \leq 1000$ nm), as well as to optical property variations, with increasing source temperature. An important consequence of this trend is an increase in mixed layer growth with increasing T_s. Hence, double-diffusive systems driven by high-temperature radiation sources, such as solar ponds [5] or the upper layers of the ocean [7], will, in general, be characterized by deeper and warmer mixed layers than laboratory systems [8] driven by lower temperature sources. The salinity distributions show the effects of mixing driven by unstable temperature distributions above the bottom surface. The salinity distribution in the overlying stable region experiences little change except for a very slight redistribution at the impermeable upper surface. To retain clarity in the figures, this redistribution has been omitted from Fig. 4 and subsequent figures.

In a radiatively driven system, substrate reflectivity ρ_b can also influence mixed layer development. The base case ($T_s = 5800$) was used while simulations were performed for the complete range of ρ_b. As seen in Fig. 5, mixed layer growth may be decreased or eliminated by increasing ρ_b. Such a control scheme (increasing or decreasing ρ_b) would be useful when either the maintenance of a stratified species distribution, as in stratified-charged combustion studies [6, 21], or attainment of maximum mixed layer temperatures, as in the salt-stratified solar pond [5], is desirable.

Optical properties of the thermohaline solution also affect mixed layer heights and temperatures, as shown in Fig. 6. Temperature and salinity profiles were predicted for $T_s = 5800$ K and $\rho_b = 0$, while the extinction coefficient in the semitransparent band was increased from 2.34 to 8.88 m^{-1}. The scattering albedo was held at the base case value of 0.11. With increasing β, there is increased absorption in the upper regions of the thermohaline solution and a corresponding reduction in the bottom heating rate. Hence, the mixed layer height and temperature decrease with increasing β. As such, the "turbidity" of a thermohaline solution affects temperature and salinity profile development, and optical property control may be used to enhance system performance.

Conditions at the upper surface of the system also affect behavior. In general, convective, evaporative, and radiative

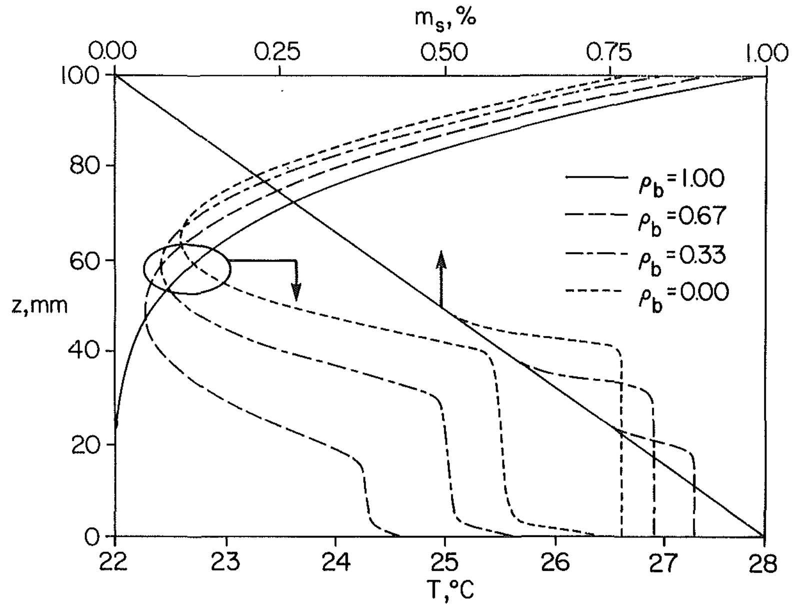

Fig. 5 Predicted temperature and salinity profiles at $t = 1$ h for various bottom substrate reflectivities

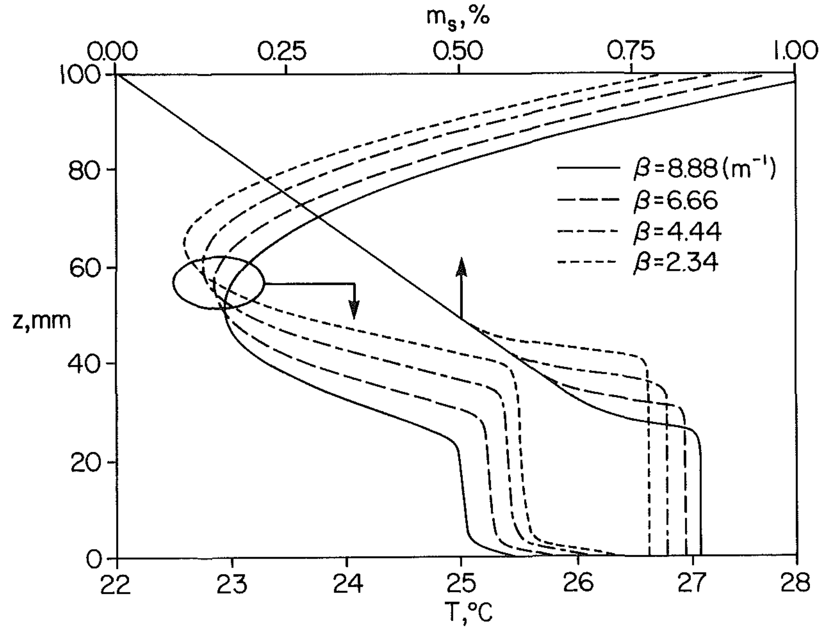

Fig. 6 Predicted temperature and salinity profiles at $t = 1$ h for various semitransparent band extinction coefficients

transfer may occur at the air-liquid interface. Predicted temperature profiles are shown in Fig. 7 for the base case simulation with various convective heat transfer coefficients imposed at the air-liquid interface. The evaporative mass transfer coefficient was determined by the heat-mass transfer analogy, while radiative exchange at the interface was evaluated with the Stefan-Boltzmann law using a liquid surface emissivity of 0.96 [22]. Ambient and surrounding temperatures of 20°C and an ambient relative humidity of 0.5 were used in evaluating the convective, radiative, and evaporative heat transfer, at the air-liquid interface. Salinity variations at the interface, resulting from water evaporation, were ignored.

As the heat transfer coefficient is increased, surface heat losses become important and for $h = 10$ W/m^2 K a shallow mixed layer develops below the air-liquid interface. As h increases, increased mixing occurs at the top of the system. Heat losses at the air-liquid interface also affect the bottom mixed layer, with decreased bottom mixed layer temperatures and slightly greater mixed layer heights (resulting from more unstable temperature gradients above the bottom mixed layer) occurring for larger h.

Summary and Conclusions

A mathematical model has been used to predict the response of a salt-stratified, double-diffusive system to radiative heating. Model results are in good agreement with previously reported experimental data, and key features of system behavior have been predicted. Radiation absorption at the upper surface induces thermal stratification, which enhances existing salt-stratified conditions, while absorption at the bottom substrate induces a thermal instability and bottom mixed layer growth. Parametric calculations reveal the influence of the radiation source temperature, bottom substrate reflectivity, solution optical properties, and top surface thermal boundary conditions on system response.

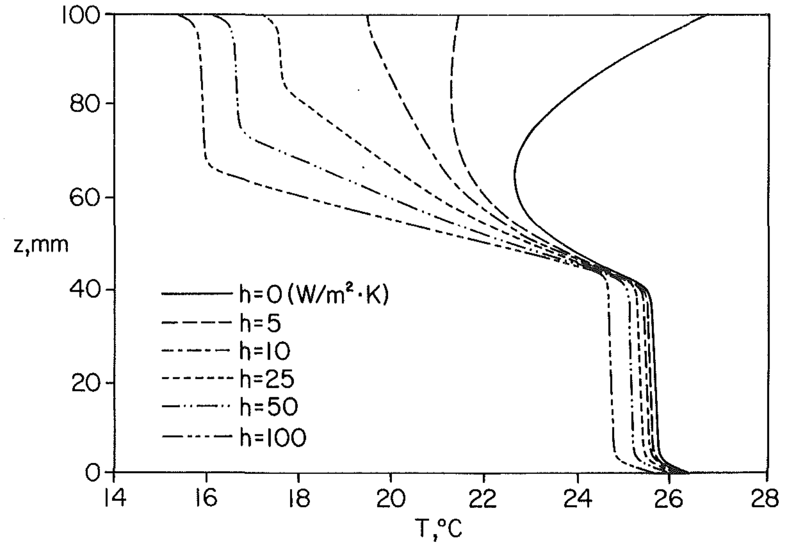

Fig. 7 Predicted temperature profiles at $t = 1$ h for various top surface thermal boundary conditions

Acknowledgments

Support of this work by the National Science Foundation under Grant No. MEA-8316580 is gratefully acknowledged.

References

1 Turner, J. S., *Buoyancy Effects in Fluids*, Cambridge University Press, 1979.

2 Viskanta, R., Bergman, T. L., and Incropera, F. P., "Double-Diffusive Convection," in: *Natural Convection: Fundamentals and Applications*, S. Kakac et al., ed., Hemisphere, Washington, 1985, pp. 1075-1099.

3 Turner, J. S., "Double Diffusive Phenomena," *Annual Reviews of Fluid Mechanics*, Vol. 6, 1974, pp. 37-56.

4 Huppert, H. E., and Linden, P. F., "On Heating a Stable Salinity Gradient From Below," *Journal of Fluid Mechanics*, Vol. 95, 1979, pp. 431-464.

5 Tabor, H., "Solar Ponds," *Solar Energy*, Vol. 27, 1981, pp. 181-184.

6 Fendell, F. E., and Feldman, P. S., "On the Interpenetration of Initially Separated Binary Mixtures," *Combustion Science and Technology*, Vol. 15, 1977, pp. 83-92.

7 Miller, J. R., "The Salinity Effect in a Mixed Layer Ocean Model," *Journal of Physical Oceanography*, Vol. 6, 1976, pp. 29-35.

8 Bergman, T. L., Incropera, F. P., and Viskanta, R., "A Differential Model for Salt-Stratified, Double-Diffusive Systems Heated From Below," *International Journal of Heat and Mass Transfer*, Vol. 28, 1985, pp. 779-788.

9 Houf, W. G., and Incropera, F. P., "An Assessment of Techniques for Predicting Radiative Transfer in Aqueous Media," *Journal of Quantitative Spectroscopy and Radiative Transfer*, Vol. 23, 1980, pp. 101-115.

10 Wagner, T. R., Incropera, F. P., and Houf, W. G., "Visible Radiation Transfer in a Black Ink Suspension," ASME JOURNAL OF HEAT TRANSFER, Vol. 102, 1980, pp. 709-714.

11 Lewis, W. T., Incropera, F. P., and Viskanta, R., "Interferometric Study of Mixed Layer Development in a Laboratory Simulation of Solar Pond Conditions," *Solar Energy*, Vol. 28, 1982, pp. 389-401.

12 Lewis, W. T., "Interferometric Study of Buoyancy-Induced Mixing in Salt-Stratified Fluid Layers," M.S.M.E. Thesis, Purdue University, West Lafayette, IN, 1980.

13 Viskanta, R., and Toor, J. S., "Radiant Energy Transfer in Waters," *Water Resources Research*, Vol. 8, 1972, pp. 595-608.

14 Viskanta, R., and Toor, J. S., "Effect of Multiple Scattering of Radiant Energy Transfer in Waters," *Journal of Geophysical Research*, Vol. 78, 1973, pp. 3538-3551.

15 Branstetter, J. R., "Radiant Heat Transfer Between Nongray Parallel Plates of Tungsten," NASA Technical Note TND-1088, 1961.

16 Viskanta, R., and Toor, J. S., "Absorption of Solar Radiation in Ponds," *Solar Energy*, Vol. 21, 1978, pp. 17-25.

17 Querry, M. R., Waring, R. C., Holland, W. E., Hale, G. M., and Nijm, W., "Optical Constants in the Infrared for Aqueous Solutions of NaCl," *Journal of the Optical Society of America*, Vol. 62, 1972, pp. 849-855.

18 Querry, M. R., Holland, W. E., and Waring, R. C., "Complex Refractive Index in the Infrared for NaCl, NaN_3, and $NaHCO_3$ in Water," *Journal of the Optical Society of America*, Vol. 66, 1976, pp. 830-836.

19 Bergman, T. L., Houf, W. G., and Incropera, F. P., "Effect of Single Scatter Phase Function Distribution on Radiative Transfer in Absorbing-Scattering Liquids," *International Journal of Heat and Mass Transfer*, Vol. 26, 1983, pp. 101-107.

20 Hottel, H. C., and Sarofim, A. F., *Radiative Transfer*, McGraw-Hill, New York, 1967.

21 Ishikawa, N., "Flame Structure and Propagation Through an Interface of Layered Gases," *Combustion Science and Technology*, Vol. 31, 1983, pp. 109-117.

22 Incropera, F. P., and DeWitt, D. P., *Fundamentals of Heat Transfer*, Wiley, New York, 1981.

R. Kumar[1]
Assoc. Mem. ASME

R. J. Adrian

Department of Theoretical
and Applied Mechanics,
University of Illinois at
Urbana-Champaign,
Urbana, IL 61801

Higher Order Moments in the Entrainment Zone of Turbulent Penetrative Thermal Convection

In a simulation of the lifting of an atmospheric inversion layer in the laboratory, measurements have been made to understand the dynamics in the interfacial region capped by a stable, linearly stratified layer. Instantaneous values of vertical and horizontal components of velocity have been measured using a two-component dual-beam laser Doppler anemometer. Temperature fluctuations have been made simultaneously. Detailed measurements of all relevant horizontally averaged one-point moments including heat flux and third-order joint vertical velocity-temperature moments have been obtained. The negative heat flux region is well defined in the entrainment zone, and varies in thickness with different stable layer temperature gradients. The entrainment mechanism is probably most important only in the top part of the interfacial zone. The present data supplement data obtained in the atmosphere, and they compare favorably with the existing data in the literature.

Introduction

Daytime changes in solar radiation set up a cycle of cooling and heating of the lower atmosphere. Before sunrise, the air layer above the ground is stably stratified because the ground is cooler than the air above it. After sunrise, solar irradiation warms the ground, creating thermal convection in the air above; thermals penetrate into the stable region and some of the warm fluid is entrained downward. The result is a mixing of air that makes the potential temperature in the convective layer almost constant. In the course of the day, the convective layer increases in thickness at a rate that is determined by the heat flux from the ground. Thus, the flow consists of a nonturbulent stable region and a well-mixed convective region, separated from the stable region by an entrainment zone. Although the interface is envisioned as a sharp layer for the convenience of the theoretical studies, in reality it is a highly convoluted region deformed by thermals and plumes. For a thorough understanding of the growth of the convection layer, one must consider the details of the mixing processes in the interfacial region.

Betts [1], Carson [2], Stull [3], Tennekes [4], and Deardorff [5] have developed various first-order models in which the rate of rise of the inversion layer and the entrainment rate have been parameterized. More complex models based on the equations for the pertinent second-order moments of the turbulent velocity and temperature field have been developed by Wyngaard [6], Zeman and Lumley [7], and Lenschow, Wyngaard, and Pennell [8]. In the second-order models, third-order moments are parameterized in terms of second-order moments to close the equations for kinetic energy, temperature variance, and turbulent heat flux. Zeman and Lumley [7] found that traditional gradient transport models were inadequate and that buoyancy effects have to be accounted for in the transport if the entrainment mechanism is to be predicted correctly.

Direct measurements of third-order moments are useful in determining empirical coefficients in the closure models and in refining the models themselves. Measurements of second and/or third-order moments have been performed in atmospheric convection layers by Telford and Warner [9], Lenschow [10], Kaimal, Wyngaard, Haugen, Coté, and Izumi [11], and Caughey and Palmer [12]. Aside from the second-order data of Caughey and Palmer [12], atmospheric data on the entrainment zone are very limited. Laboratory studies of moments in turbulent convection have been performed by Deardorff and Willis [13], Willis and Deardorff [14], Adrian [15], Ferreira [16], and Adrian and Ferreira [17]. Only Willis and Deardorff [14] provide data in the entrainment zone, although Adrian [15] does present detailed measurements in the entrainment zone of water-over-ice convection.

Available data need to be supplemented to support theoretical studies and numerical models. This paper presents the results obtained in the laboratory simulation of atmospheric penetrative convection.

Experimental Apparatus and Procedure

The test section consists of a rectangular chamber (150 cm × 148 cm) insulated on its top and sides (Fig. 1). It is filled with water with a horizontal aluminum plate at the bottom. The heat is supplied uniformly to the aluminum plate by means of heating mats covering the bottom of the plate. In the initial condition of the experiment the water is stably stratified throughout the test section, and the temperature gradient is nearly constant. This condition is established using a grid of steel rods wound with heating wire and arranged in such a way that it can be moved upward and fixed at various heights in the water layer. A stepwise temperature gradient is set up by positioning the grid at different heights for time intervals calculated from the heat balance equation for the layer of water between the grid and the top of the convection chamber. Moving the grid to known heights, the time step is calculated for the required temperature step. The resulting temperature steps are smeared out by conduction to give a nearly perfect linear profile. When the grid reaches the top, it is applied with a heat flux which is sufficient to sustain the linear temperature gradient. This step method is faster (typically 30 to 40 min) than the traditional method of adding progressively warmer layers of water using wooden floats. A faster method, which utilizes a laser Doppler anemometer, is crucial to our experiment, since the flow has to be seeded and the scattering particles settle downward with time, rendering unacceptable dropouts in the velocity signal in the stable layer if the time to set up the experiment is too long.

---

[1] Presently at the Department of Mechanical Engineering, Clemson University, Clemson, SC 29631.

Contributed by the Heat Transfer Division for publication in the JOURNAL OF HEAT TRANSFER. Manuscript received by the Heat Transfer Division September 5, 1984. Paper No. 84-HT-82.

Table 1

Case	Symbol	Γ, °C/cm	$Q_0 = H_0/\rho c_p$, °C cm/s	z_*, cm	w_*, cm/s	θ_*, °C	$Re_* = w_* z_*/\nu$	$\frac{dz_*/dt}{w_*}$
A	Δ	0.29	0.0133	13	0.371	0.036	560	0.0109
B	○	0.55	0.0133	13	0.371	0.036	560	0.0056
C	*	1.026	0.0133	13	0.371	0.036	560	0.0025
D	□	0.55	0.0241	17	0.494	0.049	975	0.0049

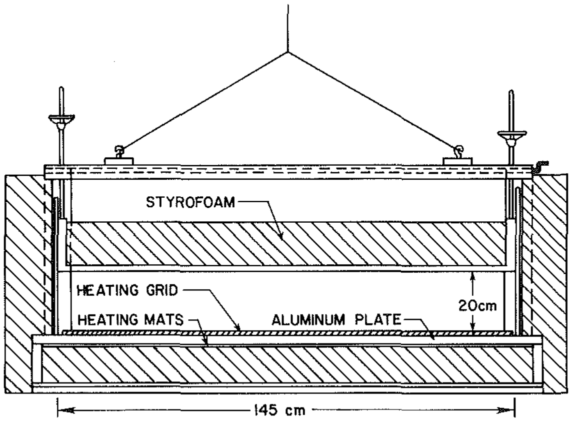

Fig. 1 Cross section of the test section

Experiments are performed using three different stable layer temperature gradients Γ, and two different bottom layer heat fluxes $Q_0 = H_0/\rho c_p$, as shown in Table 1. The turbulent Reynolds number $w_* z_*/\nu$ lies between 560 and 975. These values are believed to be high enough to permit comparison with atmospheric convection (Ferriera [16]). The effective Rayleigh number calculated using the mixed layer depth as a length scale, $\beta g z_*^3 \Delta T/\alpha\nu$, is 4.5×10^8. This value is 9000 times greater than the critical value of 5×10^4 at which the transition to turbulent flow occurs. Thus, the flow is in a regime far removed from the initial cellular instabilities that occur at low Rayleigh numbers, and deterministic cellular patterns are neither expected nor observed.

The vertical mean temperature profile is measured using a Teflon-coated alumel wire strung across a stainless steel ring of 196 mm diameter. The sensitivity of the resistance wire is 2.096°C/V and the wire is scanned vertically upward at 0.478 cms^{-1} to obtain vertical profiles. The rate of warming of the convective layer is sufficiently small (see last column of Table 1) that the time delay did not cause significant bias in temperature measurements. Instantaneous temperature is measured using a thermocouple probe, 0.038 mm in diameter, constructed of chromel-constantan duplex wire with a frequency response of 50 Hz. The horizontal and vertical components of the instantaneous velocity are measured with a two-component, dual-beam, laser Doppler anemometer in backscatter mode with a spatial resolution of 0.15 mm × 0.15 mm × 1.7 mm. The light source is a 1 W argon ion laser. The geometry of the three-beam configuration used to find the two components of velocity has been reported by Adrian [18]. Details of the optics and signal processing system are given by Kumar [19]. The light scattering particles used are Dow Saran microspheres with a diameter range of 5 to 8 μm and a specific gravity of 1.07. The optical components and the support for the thermocouple are rigidly connected to an optical table which is mounted on a hydraulically driven lathe bed.

The fluctuations of temperature and the associated fluctuating temperature gradients disturb the propagation of the laser beams and cause beam swinging, beam distortion, and phase modulation of the beam. The consequences are signal dropouts if the beam swinging causes the beams to misalign, and noise in the velocity measurements. The magnitude of the refractive index noise is not large, except in regions of intense temperature fluctuations and large mean temperature gradients, i.e., the entrainment zone or the conduction layer adjacent to the lower plate.

In the entrainment zone, we have found that the signal quality decreases with increasing Γ and/or increasing Q_0. The maximum value of Γ at which velocity data can be measured reliably is 1.026°C cm^{-1}, for the lower heat flux in Table 1. At the highest heat flux, $Q_0 = 0.024$°C cms^{-1}, velocity data cannot be measured for $\Gamma = 0.55$°C cm^{-1}. These limitations occurred even though the optical axis of the laser Doppler anemometer is tilted 2 deg so that only a portion of the lower two laser beams passes through the entrainment zone.

To evaluate systematically the magnitude of the noise added to the velocity signal by refractive index fluctuations, a plexiglass target is placed in the test section, and scratches on its surface are used as a source of laser anemometer signals with zero velocity. Fluctuations in the resulting velocity measurements then correspond to refractive index noise fluctuations. Surveys show that under the worst case conditions ($\Gamma = 1.026$°C cm^{-1}, $Q_0 = 0.0133$°C cms^{-1}) the maximum value of the root-mean-square noise is 0.1 w_*, where w_* is the velocity scale of the convection layer (Table 1). This value corresponds to approximately 0.04 cms^{-1}, and it occurs close to the middle of the entrainment at a point where the temperature fluctuations are the most intense.

Measurements of $\overline{w\theta}$, $\overline{w\theta^2}$, and $\overline{w^2\theta}$ are not expected to be affected by refractive index noise if the noise is not well correlated with the local temperature fluctuations.

Nomenclature

c_p = specific heat
g = acceleration due to gravity
H_0 = heat flux at $z=0$
p = pressure fluctuation
$\bar{q}^2$ = kinetic energy
Q_0 = kinematic heat flux at $z=0$ $(H_0/\rho c_p)$
t = time
t_1 = time at which mixed layer height $= z_1$
T = mean temperature
u = horizontal velocity fluctuation
w = vertical velocity fluctuation
$\overline{w\theta}$ = kinematic heat flux
w_* = convective velocity scale
z = vertical coordinate
z_* = mixed layer height
z_i = height of the mixed layer where heat flux is most negative
α = thermometric conductivity
β = volumetric coefficient of thermal expansion
Γ = constant temperature gradient in the stable layer
ΔT = temperature difference
ϵ = rate of dissipation of kinetic energy
ϵ_θ = rate of dissipation of thermal variance
$\epsilon_{w\theta}$ = rate of dissipation of kinematic heat flux
θ = temperature fluctuation
θ_* = convective temperature scale
ν = kinematic viscosity
ρ = density
ρ_0 = reference density
σ_u = root-mean-square horizontal velocity
σ_w = root-mean-square vertical velocity
σ_θ = root-mean-square temperature fluctuation

Measurements of the root-mean-square velocity will contain a component due to noise, but the magnitude of these components is less than 6 percent of the total root-mean-square velocity in the region above $z/z_* = 1$.

Data Collection and Analysis

The thermocouple is positioned 2 mm downstream from the measurement volume so that the wake of the probe does not interfere with the velocity measurements. The data are taken by scanning the optical table in the middle third of the test section at a speed of 2.735 cm/s. Each scan consists of 1024 points, with a digitization time interval of 0.0144 s between successive points and a Nyquist frequency of 35 Hz.

For our studies, the aspect ratio of the mixed layer ranges from 7.25 to 15, width to height, over the entire set of data. Hence, mean flow is assumed to be absent in the convection and interfacial layers. The other assumptions governing the flow situation are that: (*a*) the flow is horizontally homogeneous; (*b*) the mixed layer grows so slowly that there is a statistically quasi-steady state in which all moments are constant during the time for two successive scans. Under the conditions of stationarity and homogeneity all turbulent moments are functions of the height above the lower boundary z only.

Using standard notation and the above assumptions, the equations for kinetic energy, the temperature variance, the turbulent heat flux, and the mean temperature are, respectively

$$\frac{\partial}{\partial t}\left[\frac{1}{2}\overline{q^2}\right]+\frac{\partial}{\partial z}\left[\overline{w\left(\frac{1}{2}q^2+\frac{P}{\rho_0}\right)}\right]=\beta g\overline{w\theta}+\nu\frac{\partial^2\left[\frac{1}{2}\overline{q^2}\right]}{\partial z^2}-\epsilon \qquad (1)$$

$$\frac{\partial}{\partial t}\left[\frac{1}{2}\overline{\theta^2}\right]+\frac{\partial}{\partial z}\left[\overline{w\frac{1}{2}\theta^2}\right]+\overline{w\theta}\frac{\partial T}{\partial z}=\alpha\frac{\partial^2\left[\frac{1}{2}\overline{\theta^2}\right]}{\partial z^2}-\epsilon_\theta \qquad (2)$$

$$\frac{\partial}{\partial t}[\overline{w\theta}]+\frac{\partial}{\partial z}[\overline{w^2\theta}]+\overline{w^2}\frac{\partial T}{\partial z}=-\frac{1}{\rho_0}\overline{\theta\frac{\partial p}{\partial z}}-\beta g\overline{\theta^2}-\epsilon_{w\theta} \qquad (3)$$

$$\frac{\partial T}{\partial t}=-\frac{\partial}{\partial z}[\overline{w\theta}]+\alpha\frac{\partial^2 T}{\partial z^2} \qquad (4)$$

Profiles of the mean temperature from selected experiments are presented in Fig. 2 for the four cases A, B, C, and D (see Table 1). The height of the interface z_*, determined from mean temperature profiles taken at successive times, is presented in Fig. 3 for each case.

To get several data points inside the interfacial layer, it is desirable to move the optical table in the vertical direction after a scan is completed. However, the unsteadiness of the flow makes this feature very difficult to accomplish. Hence, consecutive scans of data are taken along a horizontal line throughout the experiment, letting the interface migrate upward, and noting the time at which convection starts and the time of each scan. From the time of each scan, the height z_* can be interpolated from the growth rate profile (Fig. 3). Thus, two scans of data are grouped for a particular z_*. However, two scans are found to be inadequate to perform ensemble averages at a particular height. Therefore four to six experiments are performed for the same temperature gradient, which is reproducible within 3 percent error. Starting from $z/z_* = 1$, two scans from each experiment are classified in a sequential order for several z/z_* ranging from 0.6 to 1.3. These are later grouped with similar classes from other experiments, to form the ensemble averages. The time taken for two successive scans is typically 60 s in which time the interface moves up by about 0.5 mm for case C and 2.4 mm for case A. Any error caused by the overlap that may have occurred in predicting z_* is assumed to be insignificant since each profile consists of more than 25 points within the 4-4.5 cm thickness of the entrainment zone. The interface height z_* is defined as the height at which the r.m.s. value of the temperature fluctuations reaches a maximum. This fact makes it easier to determine $z/z_* = 1$ accurately for each experiment and group several scans from several experiments for any z/z_*. More details of this procedure are available in Kumar [19].

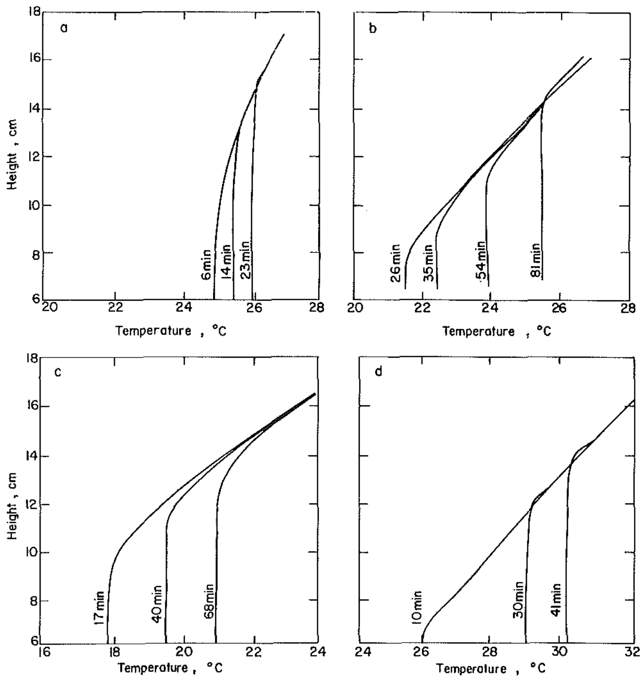

Fig. 2 Vertical profiles of mean temperature for (*a*) case *A*, (*b*) case *B*, (*c*) case *C*, (*d*) case *D*; profile labels give time in minutes

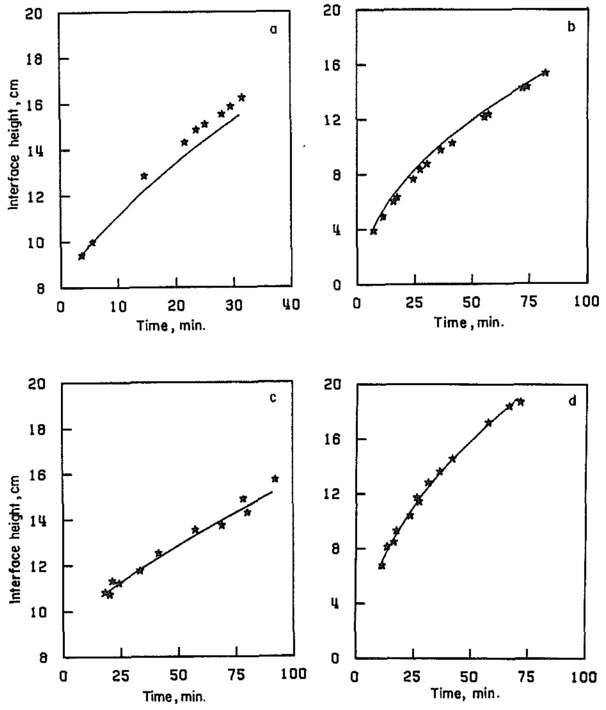

Fig. 3 Interfacial growth rate: comparison of measured values (*) with the zero-order model (———) for (*a*) case *A*, (*b*) case *B*, (*c*) case *C*, (*d*) case *D*

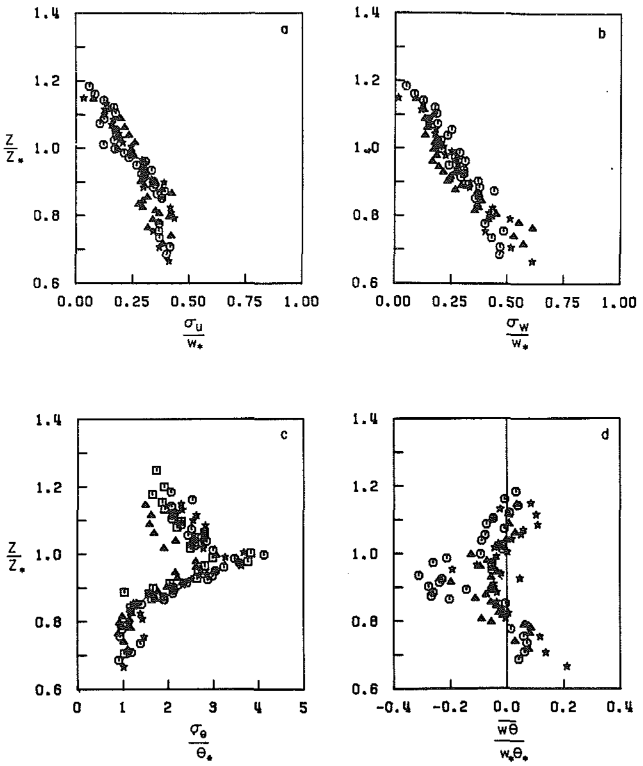

Fig. 4(*a*) Root-mean-square horizontal velocity fluctuations; (*b*) root-mean-square vertical velocity fluctuations; (*c*) root-mean-square temperature fluctuations; (*d*) kinematic heat flux: Δ, case *A*; ○, case *B*, *, case C; □, case *D*

Results and Discussion

The mean temperature profiles in Fig. 2 show that the mean temperature in the mixed region is essentially constant. In the stable region the mean temperature gradient is nearly constant. The behavior of the mean temperature in the interfacial region depends upon the stability of the stable layer and the heat flux at the bottom of the mixed layer. For times more than approximately 15–20 min after the start of heating, the profiles are nearly self-similar, although some small discrepancies do exist. For example, the curve at 81 min in Fig. 2(*b*) exhibits an anomalous low temperature region in the stable layer. Regions in which the mean temperature falls below the stable layer profile are easily seen in Fig. 2(*d*). These regions imply that interfacial cooling occurs as the mixed layer grows upward. This phenomenon has been observed by a number of investigators. In cases *A* and *D*, the cooling region is more pronounced and appears to develop as the interface progresses. This cooling causes the interface to be more stable than the nonturbulent stable region above.

Using a simple zero-order model of Deardorff et al. [20], a closed form solution for the convection layer height z_* can be obtained as

$$z_*^2 - z_1^2 = \frac{2Q_0(t-t_1)}{\Gamma} \tag{5}$$

where Q_0 is kinematic heat flux at the bottom plate, Γ is the temperature gradient in the stable layer, and z_1 is the initial height of the interface at initial time t_1. Even though this model assumes that the thickness of the interface is negligible, it compares well with our experimental growth rate. The experimental points are curve-fitted to determine the entrainment parameter $(dz_*/dt)/w_*$.

The geometry of the boundaries determines the large scales of the flow. Therefore, z_* is an appropriate length scale for the convection region. We have used the same scale to nondimensionalize all the moments. From dimensional analysis, Deardorff [21] obtained a set of velocity and temperature scales for the convection layer

$$w_* = (\beta g Q_0 z_*)^{1/3}; \qquad \theta_* = \frac{Q_0}{w_*} \tag{6}$$

These scales do not involve the temperature gradient of the stable layer, and they are not necessarily appropriate in the stable layer. All the moments are made dimensionless using z_*, w_*, and θ_*.

The r.m.s. values of the horizontal component of velocity σ_u, the vertical component σ_w, and temperature σ_θ, and the kinematic heat flux are given in Fig. 4. Noise level has been removed from the mean square velocity by subtracting the mean square velocity measured deep in the stable region (where the velocity is zero) from the mean square velocity obtained at different z/z_*. Below $z/z_* = 0.9$, σ_u reaches a constant value in the convection layer. It is observed that the motion of the ascending hot fluid is not entirely vertical. This behavior is also seen by Ferreira [16] in a nonpenetrative convection experiment. From the σ_u profile, it is also seen that below $z/z_* = 1$, the vertical motion is decelerated, but it is comparable to the horizontal motions associated with thermals spreading to the sides due to impacts. Data for all three cases seem to collapse well for both σ_u and σ_w.

In the convection layer σ_θ is essentially constant at about $\sigma_\theta \approx \theta_*$. At $z/z_* = 1$, the temperature fluctuations attain a sharp peak, nearly $4\theta_*$. It should be brought to the attention of the reader that σ_θ in the entrainment zone may not scale with θ_*.

Vertical profiles of heat flux in Fig. 4(*d*) show that there is a region of negative heat flux which is a significant fraction of the bottom layer heat flux Q_0, making the interface a well-defined region. In the convection layer, the fluid elements have a vertical velocity that exceeds that of the interface, and therefore they overshoot. Above $z/z_* = 0.9$, the slope of $\overline{w\theta}$ is generally positive. From equation (4), we can infer that the negative value $[-\partial/\partial z\,(\overline{w\theta})]$ gives rise to relative cooling at the interface. If the region of negative heat flux is defined as the interface, we can see that this region extends to near 4 cm for case *B* and about 2.6 cm for case *C*. This smaller interfacial thickness for case *C* is due to the inability of the thermals to penetrate deep into the stable region. Data for case *A* do not behave as expected giving a value of the interfacial thickness close to 4 cm, as in case *B*. However, the overall behavior of the heat flux data suggests that the thickness of the interface could be a possible length scale in this region. A similar length scale based on "interfacial distortion" was proposed by Wyatt [23]. The small positive heat flux seen at the top of the interface was also observed by Deardorff [24] who rejected it as being spurious. One explanation might be that the cold thermals penetrate upward contributing to $+w$ and $-\theta$ and when the density does not match with the local density they recede, contributing to $-w$ and $-\theta$, resulting in positive $\overline{w\theta}$. Obviously, several mechanisms take place in this region and the dominating one can be inferred only from conditional averages.

If, as we have supposed, the flow were perfectly homogeneous in horizontal planes, the mean velocity would necessarily vanish and moments such as $\overline{uw}$, $\overline{u^2w}$, and $\overline{u^3}$ would also be zero. From Fig. 5, we see that this is true to within experimental accuracy, although there is a tendency for $\overline{u^3}$ to be slightly negative, particularly in case *A*.

Profiles of various terms in equations (1)–(3) are given in Fig. 6. The measurements of these third-order moments are useful not only in parameterization, but also because their signs reveal the direction of the velocity and the relative temperature of the thermals in the interfacial region. The scatter in the $\overline{w\theta^2}$ data in case *B* was originally high. It is assumed that more scans of data are needed to perform en-

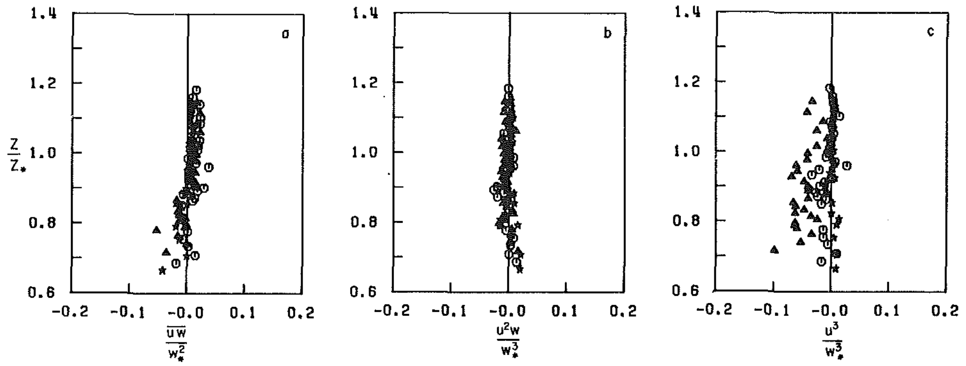

Fig. 5(*a*) Cross moment of horizontal and vertical velocites; (*b*) vertical transport of horizontal velocity fluctuations; (*c*) third-order moment of horizontal velocity fluctuations: ▵, case *A*; ○, case *B*; *, case *C*; ○, case *D*

semble averages. Hence, four consecutive scans from each experiment are grouped, at the expense of vertical spatial resolution, to form ensemble averages for case *B*. The resulting profile exhibits the same sort of variations as the other two cases. Even so, the scatter is considerable, so a solid line is sketched through the data to indicate what we believe is the general trend. All third-order moments change signs rapidly, suggesting that two or more mechanisms compete in the entrainment zone. This behavior was also seen at the interface in water-over-ice convection [18].

The diffusion of kinetic energy $d(\overline{w^3} + 2\ \overline{wu^2})\ /\ dz$ decreases slowly toward the interface and vanishes abruptly at about $z/z_* = 0.9$. Hence, in the region $0.9 < z/z_* < 1.0$, the pressure diffusion term, which is not measured, is the only source to maintain the turbulence against the losses due to dissipation and negative buoyant flux that exists in that region.

The profile of $\overline{\theta^3}$ exhibits a sharp peak in a narrow region of 2 mm to 3 mm width at $z/z_* = 1$ for all the cases, where σ_θ reaches a maximum. This shows that, on the average, most fluid elements penetrate up to $z/z_* = 1$. The negative heat flux below $z/z_* = 1$ is primarily due to the ascending thermals that turn relatively cold when they enter the interface. The tiny negative region slightly above $z/z_* = 1$ in the $\overline{w\theta^2}$ profile and the corresponding positive regions in the $\overline{\theta^3}$ and $\overline{w^2\theta}$ profiles indicate that the negative heat flux in the top part of the interface could be due to entrainment. The entrainment does not seem to play an active role further below $z/z_* = 1$. However, this cannot be ascertained without evidence from probability density distributions and conditionally averaged moments. Slightly below $z/z_* = 1$, $\overline{w\theta^2}$ and $\overline{w^3}$ vanish, suggesting that rising and falling elements contribute equally so that their opposing statistical characteristics cancel out. This behavior is similar to that observed by Adrian [18].

From the above discussions, it seems possible to interpret the higher order moments to understand the physical structure of the flow. The rising fluid originates from the bottom plate near the conduction layer where its typical temperature is more than the surrounding fluid temperature, and hence it is positively buoyant. When the fluid reaches a region of equal density, it decelerates, but it still penetrates into the interfacial region, contibuting to negative fluctuations of temperature. The temperature fluctuations become increasingly negative as the fluid penetrates to levels of increasing local mean temperature. The same fluid elements contribute to two mechanisms: One takes the form of large, intermittent, positive velocity fluctuations associated with small negative temperature fluctuations; the other contributes to large negative temperature fluctuations and small positive velocity fluctuations, as the elements penetrate upward. In the lower parts of the interfacial region, deep entrainment seems to be insignificant. This may be due to the fact that the entrainment parameter $(dz_*/dt)/w_*$ achieved in the laboratory is lower than that found in the atmosphere (0.018 and higher).

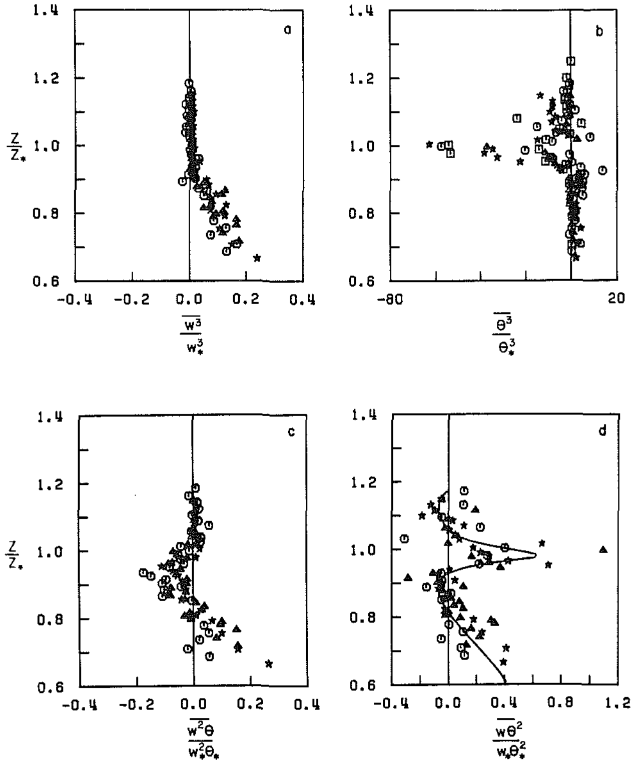

Fig. 6(*a*) Vertical transport of vertical velocity fluctuations; (*b*) third-order moment of temperature fluctuations; (*c*) vertical transport of heat flux; (*d*) vertical transport of temperature fluctuations

The vertical profiles of moment data obtained from laboratory experiments, numerical model calculations, and atmospheric measurements are compared with the moments measured in the present study in Fig. 7. The vertical height is nondimensionalized using z_i, the height of the interface where the heat flux reached a minimum, instead of z_*, to facilitate comparison with the existing data. The value of the characteristic velocity w_* calculated using z_i differs from the value calculated using z_* by less than 3 percent. The solid line in the figures represents the average of cases *A*, *B*, and *C*.

The r.m.s. vertical velocity shows a slow decrease toward the interface, and reaches nearly $0.3w_*$ near z_i. This is in excellent agreement with the atmospheric measurements. The minimum heat flux occurs at least 0.1 z/z_i below the σ_θ peak and is consistent with the laboratory results of Willis and Deardorff [14] and field measurements. The complete description of the entrainment zone provided by the Ashchurch data of Caughey and Palmer [12] compares very well

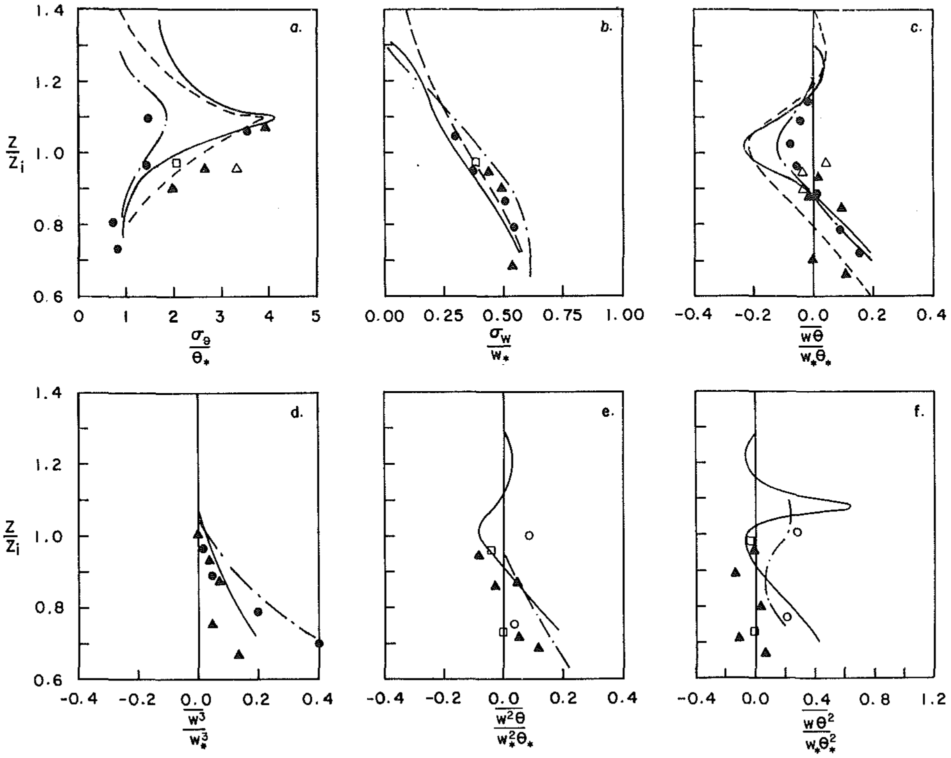

Fig. 7 Higher order moments compared with data in the literature.
Legend: Laboratory measurements: ●, Willis and Deardorff [14]
Atmospheric measurements:
□, Telford and Warner [9]
△, Lenschow [10]
▲, Lenschow et al. [8]
○, Kaimal et al. [11]
-----, Caughey and Palmer [12]
Second-order numerical model:
_._._. Zeman and Lumley [7]
___, present study, average of cases *A*, *B*, and *C*

with the present measurements of σ_θ, σ_w, and $\overline{w\theta}$. The heat flux measurements show a predominantly negative region crossing over the zero mark at about the same heights in the atmosphere. The solid line is weighted toward cases *A* and *B* since their entrainment parameter is closer to that of the atmosphere. Even though some effect can be expected due to the presence of mean wind in the atmosphere, the present data show good agreement with the atmospheric measurements of heat flux, including a slightly positive region at the top of the interface. The diffusion of kinetic energy agrees well within the existing data, vanishing near $z/z_i=1$. The vertical transport of energy given by Zeman and Lumley [7] includes the pressure distribution term, and shows large values in the mixed layer. The transport of pressure energy is largely responsible for the supply of energy in the interfacial layer. Only a few scattered data points are available in the literature to compare some of the third-order moments in the interface. However, the trend seems to agree with the present measurements.

Conclusions

The temperature gradient Γ has little effect on r.m.s. values σ_u, σ_w, and σ_θ below $z/z_*=1$. Since there may be a large sampling error in the cross correlation of w and θ to obtain heat flux, there is no strong evidence to suggest that $\overline{w\theta}$ depends significantly upon Γ. However, in the limit $\Gamma=0$, with no "capping" inversion present, there would be no negative heat flux in the entrainment zone. Above $z/z_*=1$, σ_θ appears to be affected by Γ as σ_θ data are not well correlated above $z/z_*=1$. Since the large temperature fluctuations in this region may generally be due to internal gravity waves, the temperature scale may be dependent upon the temperature gradient in the entrainment zone.

The r.m.s. values of horizontal and vertical velocities are of comparable magnitude in the entrainment zone. The extent of the negative heat flux defines a thickness of the entrainment zone. This thickness is seen to decrease with increasing stratification.

The value of $\overline{w^3}$ is positive in a region where $d(\overline{w^2})/dz$ is negative, in agreement with a simple gradient transport model. However, results from Ferreira [16] show that $\overline{w^3}$ remains positive when $d(\overline{w^2})/dz$ vanishes in the vicinity of $z_*/2$.

The net transport of turbulent kinetic energy $d(\overline{w^3}+2\overline{wu^2})/dz$ is very small above $z/z_*=0.9$. The estimates of the time rate of change of turbulent kinetic energy in the entrainment zone from the equation given by Zilitinkevich [25]

$$\frac{\partial\left(\frac{1}{2}\overline{q^2}\right)}{\partial t}=-\frac{\partial\left(\frac{1}{2}\overline{q^2}\right)}{\partial z}\cdot\left(\frac{dz}{dt}\right)_i \qquad (7)$$

show that it is also negligible. The implication is that the pressure–velocity energy transport balances the net resultant from dissipation and buoyant energy production in the entrainment zone. Furthermore, in this zone, the production of kinetic energy by buoyancy is negative, so the pressure energy transport must be positive.

Around $z/z_*=1$, the negative values of $\overline{\theta^3}$ and $\overline{w^2\theta}$ occur when $\overline{w\theta^2}$ is positive, implying that the larger fluctuations in θ are negative and associated with positive velocities, that is, ascending fluid penetrating into the warmer stable region. This means that the entrainment mechanism is probably most important only in the top of the interfacial layer.

Measurements of second and third-order moments scaled with convection scales correlate reasonably well with the atmospheric data of Lenschow et al. [8] and Caughey and Palmer [12]. We conclude that the Reynolds numbers in our laboratory experiments are large enough to yield reasonable simulation of the full-scale atmosphere.

Acknowledgments

This research is based on work supported by the National Science Foundation under Grant No. ATM 8203521, and was part of the Ph.D. Dissertation of the first author at the University of Illinois at Urbana-Champaign.

References

1 Betts, A. K., "Non-precipitating Cumulus Convection and Its Parameterization," *Quart. J. Roy. Meteor. Soc.*, Vol. 99, 1973, pp. 178-196.

2 Carson, D. J., "The Development of a Dry, Inversion-Capped Convectively Unstable Boundary Layer," *Quart. J. Roy. Meteor. Soc.*, Vol. 99, 1973, pp. 450-467.

3 Stull, R. B., "Inversion Rise Model Based on Penetrative Convection," *J. Atmos. Sci.*, Vol. 30, 1973, pp. 1092-1099.

4 Tennekes, H., "A Model for the Dynamics of the Inversion Above a Convective Boundary Layer," *J. Atmos. Sci.*, Vol. 30, 1973, pp. 558-567.

5 Deardorff, J. W., "Prediction of Convective Mixed Layer Entrainment for Realistic Capping Inversion Structure," *J. Atmos. Sci.*, Vol. 36, 1979, pp. 424-436.

6 Wyngaard, J. C., "Atmospheric Boundary Layer-Modeling and Measurements," *Turbulent Shear Flows II, Proc. of the Second Symposium on Turbulent Shear Flows*, London, 1979.

7 Zeman, O., and Lumley, J. L., "Modeling Buoyancy Driven Mixed Layers," *J. Atmos. Sci.*, Vol. 33, 1976, pp. 1974-1988.

8 Lenschow, D. H., Wyngaard, J. C., and Pennell, W. L., "Mean Field and Second Moment Budgets in a Baroclinic, Convective Boundary Layer," *J. Atmos. Sci.*, Vol. 37, 1980, pp. 1313-1326.

9 Telford, J. L., and Warner, J., "Fluxes of Heat and Vapor in the Lower Atmosphere Derived From Aircraft Observations," *J. Atmos. Sci.*, Vol. 43, 1964, pp. 539-548.

10 Lenschow, D. H., "Model of the Height Variation of the Turbulence Kinetic Energy in the Unstable Planetary Boundary Layer," *J. Atmos. Sci.*, Vol. 31, 1974, pp. 465-474.

11 Kaimal, J. C., Wyngaard, J. C., Haugen, D. A., Coté, O. R., Izumi, Y., Caughey, S. J., and Readings, C. J., "Turbulence Structure in a Convective Boundary Layer," *J. Atmos. Sci.*, Vol. 33, 1976, pp. 2152-2169.

12 Caughey, S. J., and Palmer, S. G., "Some Aspects of Turbulence Structure Through the Depth of the Convective Boundary Layer," *Quart. J. Roy. Meteor. Soc.*, Vol. 105, 1979, pp. 811-827.

13 Deardorff, J. W., and Willis, G. E., "Investigation of Turbulent Thermal Convection Between Horizontal Plates," *J. Fluid Mech.*, Vol. 28, 1967, pp. 675-704.

14 Willis, G. E., and Deardorff, J. W., "A Laboratory Model of the Unstable Planetary Boundary Layer," *J. Atmos. Sci.*, Vol. 31, 1974, pp. 1297-1307.

15 Adrian, R. J., "Turbulent Convection in Water Over Ice," *J. Fluid Mech.*, Vol. 69, 1975, pp. 753-781.

16 Ferreira, R. T. D. S., "Unsteady Turbulent Thermal Convection," Ph.D. Thesis, Univ. of Illinois at Urbana-Champaign, 1978.

17 Adrian, R. J., and Ferreira, R. T. D. S., "Higher Order Moments in Turbulent Thermal Convection," 2nd International Turbulence Symposium, London, 1979.

18 Adrian, R. J., "A Bi-Polar Two Component Laser Velocimeter," *J. Phys. E: Sci. Instrum.*, Vol. 4, 1975, pp. 723-726.

19 Kumar, R., "Studies in Unsteady Penetrative Thermal Convection," Ph.D. thesis, Univ. of Illinois at Urbana-Champaign, 1983.

20 Deardorff, J. W., Willis, G. E., and Lilly, D. K., "Laboratory Investigation of Non-steady penetrative Convection," *J. Fluid Mech.*, Vol. 35, 1969, pp. 7-31.

21 Deardorff, J. W., "Convective Velocity and Temperature Scales for the Unstable Planetary Boundary Layer," *J. Atmos. Sci.*, Vol. 27, 1970, pp. 1211-1213.

22 Townsend, A. A., "Natural Convection in Water Over an Ice Surface," *Quart. J. Roy. Meteor. Soc.*, Vol. 90, 1964, pp. 248-259.

23 Wyatt, L. R., "The Entrainment Interface in a Stratified Fluid," *J. Fluid Mech.*, Vol. 86, 1978, pp. 293-311.

24 Deardorff, J. W., "Three-Dimensional Numerical Study of Turbulent in an Entraining Mixed Layer," *Bdy. Layer Met.*, Vol. 7, 1974b, pp. 199-226.

25 Zilitinkevich, S. S., "Comments on 'A Model for the Dynamics of the Inversion Above a Convective Boundary Layer'," *J. Atmos. Sci.*, Vol. 32, 1975, pp. 991-992.

Heat Transfer Enhancement in Natural Convection Enclosure Flow

R. Anderson
Assoc. Mem. ASME

M. Bohn
Mem. ASME

Solar Energy Reseach Institute,
Goldon, CO 80401

The results of an experimental investigation that examines the effects of one type of surface roughness upon heat transfer in a water-filled cubical enclosure are reported. The experiments covered the range from the beginning of transition to the point where the flow over 60 percent of the length of the heated side had undergone transition. Tests were conducted using both isothermal and constant flux boundary conditions. The largest increase in overall *Nusselt number was 15 percent at* $Ra = 3.3 \times 10^{10}$ *on the isothermal heated plate. Increases of the* local *Nusselt number on the isothermal heated plate were as large as 40 percent. The roughness elements used in the present study were found to be ineffective on the upper portion of the heated plate where fluid detrains from the vertical boundary layer.*

Introduction

There has been a large volume of research in recent years that examines natural convection in enclosures with differentially heated vertical walls [1, 2]. This research has been stimulated to a large degree by interest in evaluating energy transfer in buildings, solar collectors, and fluid-filled thermal storage tanks. In the present study we report the results of an experimental investigation of the effect of surface roughness upon natural convection heat transfer in a cubical enclosure at high Rayleigh numbers. The inclusion of surface roughness in a natural convection study is of interest from a fundamental point of view because the effects of roughness upon natural convection flows are not well understood. There is a broad literature on the use of roughness to provide heat transfer enhancement in forced convection [3, 4], but the conditions under which rough surfaces can produce enhancement in natural convection are not clear.

The earliest experiments on the effects of surface roughness upon natural convection were carried out by Prasolov [5] using distributed roughness elements on the surface of a horizontal cylinder. The experiments were carried out in air in the laminar-to-turbulent transitional Rayleigh number range 3×10^3 to 3×10^6. Roughness heights varied from 0.08 to 0.36 mm. Prasolov found that the roughness increased heat transfer by 50 to 100 percent for $10^5 < Ra < 3 \times 10^6$. The degree of enhancement reached a maximum and then decreased to zero as the Rayleigh number increased. Prasolov attributed this increase in heat transfer to "turbulization" of the flow in the transitional regime. Heya, Takeuchi, and Fujii [6] recently repeated Prasolov's experiments using air in the range $6 \times 10^4 < Ra < 7 \times 10^5$ and water in the range $4 \times 10^6 < Ra < 2 \times 10^8$ and concluded that surface roughness had little or no influence upon the heat transfer coefficient. Unfortunately, there is a gap in their data in the region where Prasolov found maximum enhancement to occur. In addition, the difference in Pr number between water and air makes it difficult to draw any definite conclusions from comparison of the water data of Heya et al. with the air data of Prasolov.

Jofre and Barron [7] experimented with an isothermal vertical plate in air for $Ra = 1\text{–}2 \times 10^9$. Their rough surface consisted of horizontal ribs with triangular cross sections which were 0.76 mm high. Based upon comparisons with smooth plate experiments by Eckert and Jackson [8] they found the rough surface increased heat transfer by about a factor of two. Jofre and Barron did not collect smooth plate data using their own apparatus.

Fujii, Fujii, and Takeuchi [9] examined the effect of rough surfaces upon heat transfer from a vertical cylinder with a constant surface heat flux. They carried out experiments in water and spindle oil in the range $10^{10} < Ra^* < 10^{15}$ using a variety of rough surfaces and found the maximum difference in the local heat transfer in the turbulent regime to be on the order of 10 percent. More recently, Sastry, Murthy, and Sarma [10] examined the effect of roughness created by wrapping various gauges of copper wire around a vertical cylinder. Their experiments were carried out in air with Rayleigh numbers in the range from 7×10^8 to 3.5×10^9. They found that the overall heat transfer in this configuration was enhanced by up to 50 percent over that of a smooth cylinder. They were apparently unaware of the earlier work by Fujii et al., and thus did not attempt to explain the difference between their results and the previous ones.

The above review indicates that there is a disagreement among previous investigators concerning the amount of heat transfer enhancement which can occur in a natural convection flow. The objective of the present study is to examine the effect of one type of distributed roughness element upon the heat transfer in the transitional regime between fully laminar and fully turbulent flow in a cubical enclosure. The transitional regime was chosen because it can extend over a considerable range in Ra and is the regime most likely to be influenced by finite-sized roughness elements. The Rayleigh numbers of several important applications (including buildings) are high enough that the flows fall in the transitional range between laminar and turbulent motion. The present study is fundamentally different from previous work on external flows cited above in that the main flow consists of a recirculating cell with a quiescent core which possesses a high degree of thermal stratification. These differences will be the focus of further discussion below.

In addition to the work on small roughness elements reviewed above, there have been a number of studies involving natural convection heat transfer from extended surfaces [11–14]. These extended surface studies are primarily concerned with the performance of different fin geometries and are not directly related to effects caused by small surface roughness elements.

Experimental Method

A schematic drawing of the convection test cell is shown in Fig. 1. The heat transfer surfaces of the hot and cold ends are constructed of 1.27-cm aluminum and the adiabatic side walls are constructed of 1.27-cm and 0.635-cm lucite. The top and bottom walls are reinforced with 1.27-cm aluminum and the entire apparatus is insulated on the outside with 5.08 cm of extruded styrofoam insulation. The height of the test cell interior is 29.2 cm and the width and length are 30.5 cm. The resulting aspect ratios H/L and W/L are 0.96 and 1.0. In

---

Contributed by the Heat Transfer Division and presented at the ASME Winter Annual Meeting, New Orleans, Louisiana, December 9–13, 1984. Manuscript received by the Heat Transfer Division February 15, 1984.

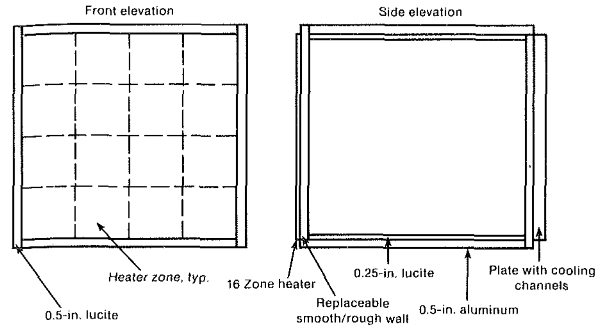

Fig. 1 Test cell schematic

order to limit corrosion, all aluminum surfaces were plated with a 0.001-in. layer of electroless nickel. The heated wall has 16 equal area resistance heaters attached to its outer surface and the cold wall has milled channels through which cooling water is circulated. The temperature at the center of each heater is individually monitored by thermocouples placed in wells 1.6 mm from the inside surface of the wall. The power input to each heater is independently controlled through the use of solid-state relays and a microcomputer data acquisition system. All tests were run using water as the heat transfer fluid. The water was deionized and dissolved gases were eliminated by boiling before use. All fluid properties used in the calculation of Nu, Ra, and Ra* were evaluated at the bulk temperature $T_B = T_C + \Delta T/2$.

In the present study only the roughness of the heated wall was varied. The effect of the roughness was directly measured by conducting all tests with the same apparatus. Since a number of different thermal boundary conditions are possible in real applications, all measurements were repeated for the two cases of "constant flux" and constant temperature at the heated surface. In the present paper the terminology "constant flux" refers to the boundary condition at the surface of the heaters used to provide power to the test cell wall. Due to the finite conductivity of the test cell wall, the boundary condition at the inner surface of the heated wall deviates slightly from a pure constant flux condition. This deviation will be discussed in more detail during our presentation of experimental results.

The cold surface was held isothermal to within ±4 percent of the overall temperature difference throughout the experiment. In the isothermal mode, the temperature variation across the heated plate was less than ±0.4°C. This was achieved by computer control over the 16 independent heaters. The algorithm was a proportional, integral, differential control scheme [15]. This algorithm varied the fraction of the time that each heater was on from 0–92 percent. This percentage was adjusted once every 60 s. In order to determine when the apparatus reached a steady-state condition, the temperature of the hot plate and power input were monitored on a chart recorder. A steady-state condition was generally reached within 3–4 h. The resistance of each heater was measured and recorded before each run. The power input to the apparatus was calculated by combining this resistance measurement with an rms measurement of the voltage supplied to each heater.

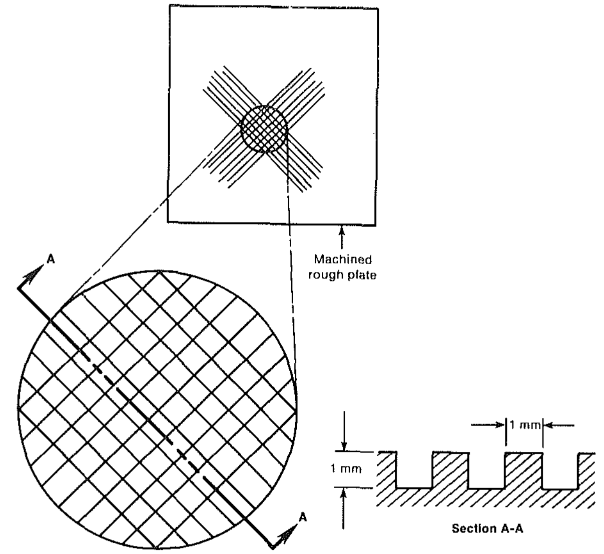

Fig. 2 Detail of distributed roughness elements used on heated surface

The laminar thermal boundary layer thicknesses based upon a scaling analysis for an isolated boundary layer in a fluid with Pr > 1 are

$$\left(\frac{\delta}{H}\right)_{iso} \approx \frac{1}{\mathrm{Ra}^{1/4}} \tag{1}$$

$$\left(\frac{\delta}{H}\right)_{CF} \approx \frac{1}{\mathrm{Ra}^{*1/5}} \tag{2}$$

The roughness elements used during the experiment are shown in Fig. 2 and consist of a series of intersecting grooves rotated 45 deg from the horizontal. The height of the elements l/H was chosen to be the same order of magnitude as the thickness

Nomenclature

Bi = Biot number = $k_p t/kH$
h = average heat transfer coefficient based upon midheight temperature difference between hot and cold walls
H = enclosure height
k = thermal conductivity
L = enclosure length
l = height of roughness elements
Nu = Nusselt number = hH/k
n = index of refraction
Pr = Prandtl number
q = average heat transfer per unit area
Q = total heat transfer

Ra = $g\beta H^3 \Delta T/\nu\alpha$
Ra* = $g\beta H^4 q/\nu\alpha k$
t = plate thickness
T = temperature
ΔT = midheight temperature difference between hot and cold walls
W = enclosure width
Y = vertical coordinate
y = nondimensional vertical coordinate = Y/H
δ = thermal boundary layer thickness
ϕ = nondimensional temperature $= \dfrac{T-T_C}{\Delta T}$

Subscripts

b = base area
B = bulk
C = cold side
CF = constant flux
cr = critical
H = hot side
iso = isothermal
p = vertical plate
y = local value
1 = based upon $\Delta T_1 = (T_p|_{y=0.125} - T_C)$
2 = based upon $\Delta T_2 = (T_p|_{y=0.375} - T_C)$
3 = based upon $\Delta T_3 = (T_p|_{y=0.625} - T_C)$
4 = based upon $\Delta T_4 = (T_p|_{y=0.875} - T_C)$

of the thermal boundary layer as evaluated from equations (1) and (2). This thickness corresponds with the location of the velocity maximum and is the same length scale over which turbulent temperature fluctuations reach their maximum [16]. It was felt that this height would be large enough to disrupt the thermal boundary layer in the turbulent region and small enough to avoid causing the boundary layer to undergo immediate transition. All heat transfer and temperature measurements were based upon the temperature and area at the base of the roughness elements. The parameter range investigated in the present experiment is summarized in Table 1.

The major sources of experimental error were measurement of the power input Q and the temperature of the heated plate. Radiation heat transfer was neglected because water is opaque to infrared radiation. Conduction losses through the neoprene gaskets and through insulation external to the test cell were calibrated at 1.1 W/°C overall temperature difference. This conduction loss was accounted for in the actual wall heat transfer measurement and was generally less than 4 percent of the total end-to-end heat transfer in the test cell.

Due to the control scheme used to turn the 16 heaters on and off, the average power did not ever become totally steady. Errors in computing Q due to this oscillation were approximately ± 2 percent of the indicated value. Oscillations in T_H of ± 0.4°C contribute to uncertainty in the measurement of Ra and Nu for the rough and smooth tests. This error in T_H produces an error in $T_H - T_C$ of approximately 2 percent. As shown in Table 2 the error in Q and $T_H - T_C$ gives an uncertainty in Ra and Ra* of ± 2 percent and in Nu of ± 4 percent. Therefore, we may consider differences in Nu between the rough and smooth surface to be significant if they are larger than 4 percent.

Determination of the Location of Transition

For the purpose of interpreting our results it is necessary to be able to visualize the important features of the natural convection flow. In the present case, the most important feature is the boundary layer on the heated vertical wall. The temperature gradient across the boundary layer makes feasible any of several possible visualization techniques. The method we have chosen here is similar to the "mirage" method first described by Fujii, Takeuchi, Suzaki, and Uehara [17].

Table 1 Parameter range investigated by present experiments

Ra	7.7×10^9–7.3×10^{10}
Ra*	6.8×10^{11}–9.2×10^{12}
$\left(\frac{\delta}{H}\right)_{iso}$	0.0034–0.0019
$\left(\frac{\delta}{H}\right)_{CF}$	0.0043–0.0025
Pr	3.7–6.3
Q (watts)	165–1800
H/L, W/L	1, 0.96
ΔT(°C)	12–55
l/H	0.0034
A/A_b	2
Hot wall Biot number, $\frac{k_p t}{kH}$	10.0

Table 2 Experimental errors (percent)

Q	ΔT	Ra	Ra*	Nu
± 2	± 2	± 2	± 2	± 4

This method utilizes the index of refraction gradient in the boundary layer which results from the large changes in temperature which occur near the heated plate. At high Ra numbers the thermal boundary layer is quite thin, leading to an abrupt reduction of the index of refraction in the thermal boundary layer as compared to the core. This difference makes it possible to place an object on one side of the apparatus and view the distortion of the image which is reflected and refracted by the thermal boundary layer. The image of the object appears chaotic in the turbulent portion of the thermal boundary layer, making the mirage method especially useful for observing boundary layer transition. The object used in the present study was a series of vertical lines drawn parallel to the heated wall.

Transition was defined to occur at the y location where finite-amplitude oscillations could be observed in the boundary layer using the "mirage" flow visualization technique (see Fig. 3). Preliminary visual observations indicated that the average location of transition as determined by this method was interrupted occasionally by transient turbulent bursts rolling upward from the laminar region. We did not include these transient bursts in our determination of the average location of transition.

Experimental Results

The temperature profile on the surface of the hot wall for the constant flux condition is shown in Fig. 4. Each data point in the figure represents the average of the temperature at the center of all four heaters at a given vertical location on the smooth surfaces. As has been pointed out by Balvanz and Kuehn [18], this profile is a function of the wall Biot number Bi $= k_p t/kH$. The Biot number of the aluminum plate used in the present experiment was 10. The numerical predictions of Balvanz and Kuehn for a two-dimensional enclosure with an aspect ratio of 5 are in good agreement with present ex-

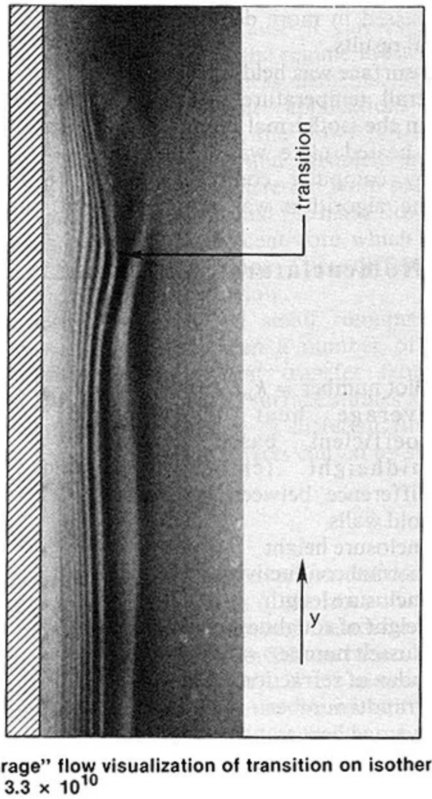

Fig. 3 "Mirage" flow visualization of transition on isothermal heated plate; Ra = 3.3×10^{10}

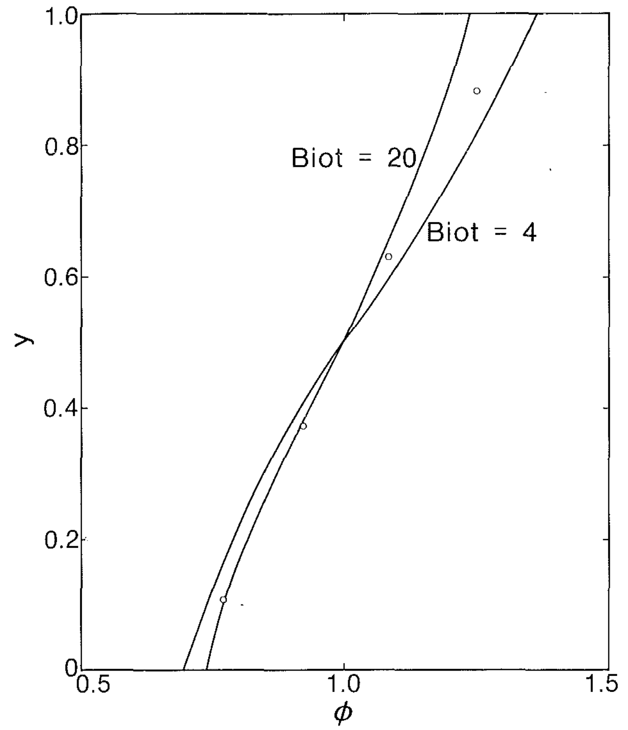

Fig. 4 Constant flux hot plate temperature profile: —— = numerical predictions by Balvanz and Kuehn [18]; ○ = present results

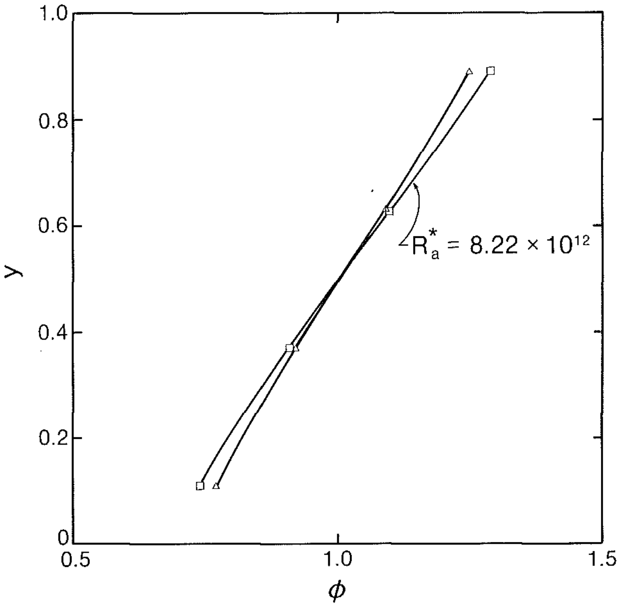

Fig. 5 Variation in surface temperature caused by the rough surface: △ = smooth plate and rough plate for Ra* < 4 × 10^{12}; □ = rough plate, Ra* = 8.22 × 10^{12}

perimental results, except near the bottom of the wall, where our measured temperature is higher than expected. Balvanz and Kuehn indicate that a constant flux wall with Bi = 10 will result in a rate of overall heat transfer that is reduced by a factor of ~0.94 over that of a wall with Bi = 0. This reduction in heat transfer reflects the reduction in the temperature difference between the top and bottom of the wall caused by conduction along the wall.

The surface temperature of the constant flux wall was found to be relatively independent of Ra* when the heated surface was smooth. However, ϕ did depend upon Ra* when the wall surface was roughened. This dependence is illustrated in Fig. 5. For values of Ra* < 4 × 10^{12} the rough surface and smooth surface profiles coincide. As Ra* increases, the profile for the rough surface rotates clockwise. Because the nondimensional surface temperature ϕ is normalized by the midheight temperature difference between the hot and cold walls of the test cell, the rotation shown in Fig. 5 indicates an overall decrease in the surface temperature of the rough wall relative to that of a smooth surface for Ra* > 4 × 10^{12}. Previous studies of isolated vertical walls with constant heat flux boundary conditions in isothermal media have observed a sudden drop in the local surface temperature of the upper portion of the wall and used this as a criterion for the onset of transition [17, 19]. This drop in local surface temperature was not observed in the Ra* range covered by the present experiments.

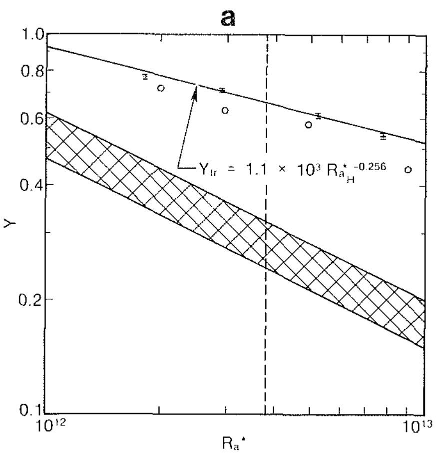

Fig. 6(*a*) Influence of roughness upon transition for the constant flux boundary layer: ···· = beginning of heat transfer enhancement; + = smooth plate; ○ = rough plate; cross hatching = transition in external flow [21]

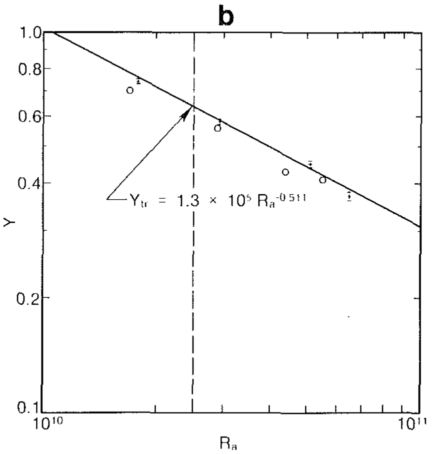

Fig. 6(*b*) Influence of roughness upon transition for the isothermal boundary layer; symbols have the same meaning as in Fig. 6(*a*)

The vertical locations of transition determined from photographs like Fig. 3 are shown as a function of Ra* and Ra in Figs. 6(*a*) and 6(*b*). The points in these figures represent the average of three different observations. It can be seen from examination of these figures that transition on the rough plate occurs ~5 percent earlier than on the smooth plate. Godaux and Gebhart [20] have shown that velocity fluctuations occur much earlier than temperature fluctuations when Pr > 1 as a result of the fact that the thermal boundary layer thickness is smaller than the velocity boundary layer

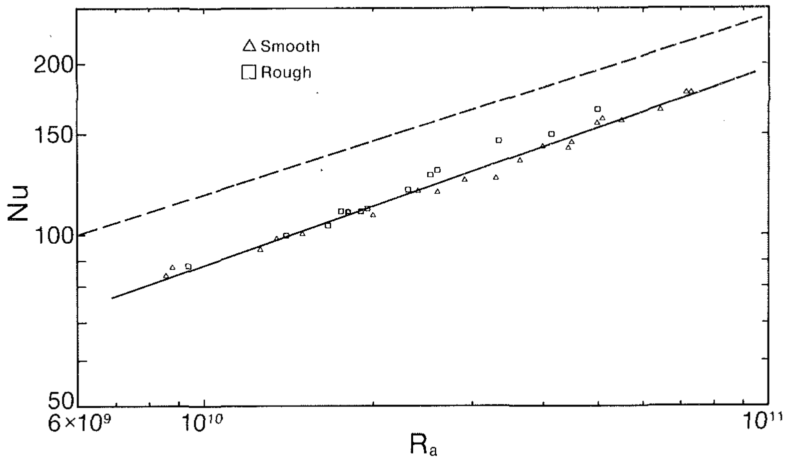

Fig. 7 Average Nusselt number for isothermal heated plate: △ = smooth plate; □ = rough plate; —— = 0.033 $Ra^{0.343}$; ---- = 0.166 · $Ra^{0.285}$ as reported by Schinkel et al. [22]

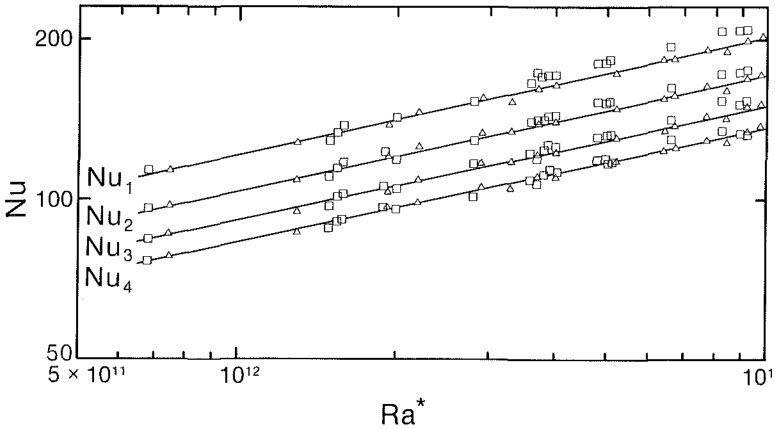

Fig. 8 Average Nusselt number for constant flux heated plate as a function of the temperature difference upon which the Nusselt number is based: subscripts refer to the surface location at which the temperature difference is calculated; △ = smooth plate; □ = rough plate

thickness when $Pr > 1$. We did not measure velocity or temperature fluctuations in the present study but feel that our transition criterion is more closely related to thermal transition than velocity transition since it depends upon the difference in index of refraction of the thermal boundary layer and the core. Based upon the information presented in Figs. 6(*a*) and 6(*b*), the largest portion of the boundary layer which underwent transition during the present experiment was ~60 percent of the length of the vertical heated plate.

The cross-hatched area in Fig. 6(*a*) is the location of transition in an external natural convection flow as determined by Jaluria and Gebhart [21]. The lower border of the cross-hatched area represents the onset of velocity fluctuations while the upper border of the cross-hatched area represents the onset temperature fluctuations. Transition in the external flow studied by Jaluria and Gebhart occurs at a Ra* number roughly an order of magnitude smaller than the Ra* number for transition observed in the present study of an internal flow.

The average Nusselt numbers for the smooth and rough surface are shown as a function of Ra and Ra* in Figs. 7–9. The maximum increase in overall Nusselt number observed during the experiment was 15 percent at $Ra = 3.3 \times 10^{10}$ on the isothermal heated plate (Fig. 7). The dashed lines in Figs. 6(*a*) and 6(*b*) indicate the location at which heat transfer enhancement first occurs for the isothermal and constant flux boundary conditions. In each case, enhancement in overall heat transfer is not detectable until ~40 percent of the vertical height of the plate has undergone transition.

The four series of constant flux data which appear in Fig. 8 differ only in terms of the temperature difference upon which the Nusselt number is based. It can be seen that the general dependence of the Nusselt number upon Ra* and the onset of heat transfer enhancement is *not* affected by the surface location which is used to calculate the temperature difference upon which the Nusselt number is based. This result supports our previous conclusion that the enhancement which results from the presence of the rough surface is caused by a decrease in the surface temperature along the entire length of the heated wall. Enhancement is exaggerated when basing Nu upon ΔT calculated from temperature measurements made at the bottom of the heated wall because these ΔT experience the largest *relative* change in the temperature difference between the smooth and rough surface.

The solid lines in Figs. 7 and 9 indicate the recommended correlations for the average Nusselt number. For the isothermal boundary condition this correlation is

$$Nu = 0.033\, Ra^{0.343} \tag{3}$$

The corresponding correlation for the constant flux case is

$$Nu = 0.234\, Ra^{*0.218} \tag{4}$$

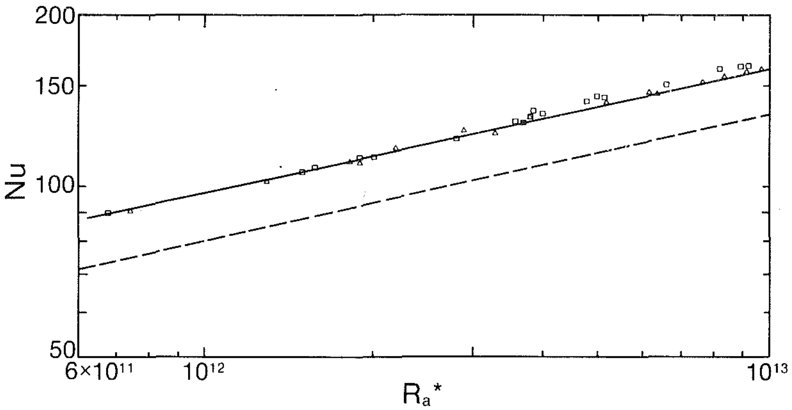

Fig. 9 Average Nusselt number for constant flux heated plate based upon midheight temperature difference: △ = smooth plate; □ = rough plate; —— = $0.234\ \mathrm{Ra}^{*0.218}$; ···· = $0.194\ \mathrm{Ra}^{*0.218}$ as reported by Landis and Yanowitz [23]

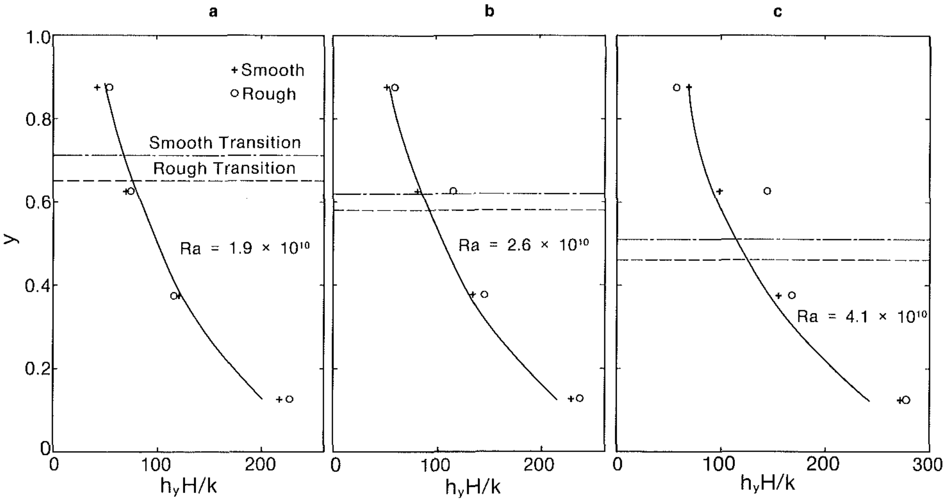

Fig. 10(*a*) Local Nusselt number for the isothermal heated plate: $\mathrm{Ra} = 1.9 \times 10^{10}$; + = smooth plate; ○ = rough plate; —— = $0.526\ \mathrm{Ra}^{1/4} \cdot y^{-1/4}\ (0.73 - 0.46y)^{1.25}$ as reported by Schinkel et al. [22]; —·—·— = location of transition on smooth plate; ······ = location of transition on rough plate; (*b*) $\mathrm{Ra} = 2.6 \times 10^{10}$; (*c*) $\mathrm{Ra} = 4.1 \times 10^{10}$

Also included in Fig. 7 for comparison is an extrapolation of the numerical prediction of Schinkel, Linthorst, and Hoogendoorn [22] based on calculations for a two-dimensional air-filled enclosure in the range $10^4 < \mathrm{Ra} < 10^6$ with $H/L = 1$. The dashed line in Fig. 9 is a correlation based upon experimental measurements made by Landis and Yanowitz [23] using water and silicone oil in the range $2 \times 10^6 \leq \mathrm{Ra} \leq 1.5 \times 10^9$ with $H/L = 10$. The trends reported by Schinkel et al. [22] and Landis and Yanowitz [23] agree with the present results as to Rayleigh dependence but differ by about 20 percent as far as the absolute magnitude of the Nusselt number is concerned. This difference is assumed to be a result of the use of a different apparatus in the case of Landis and Yanowitz and differing boundary conditions in the case of Schinkel et al.

Local Nu number information for the isothermal plate is presented as a function of Rayleigh number in Fig. 10. The data displayed in this figure cover the range $1.9 \times 10^{10} < \mathrm{Ra} < 4.1 \times 10^{10}$ and represent the average heat transfer from a horizontal strip 7.6 cm high which is centered on the y location shown in the figures. Each horizontal strip is composed of four of the 16 heaters which were used to control the temperature of the plate. During the course of the experiment we found local heat transfer measurements such as these to be repeatable to within ±7 percent. The solid line in the figures is extrapolated from a correlation provided by Schinkel et al. [22] in the laminar regime for $A \geq 4$, $\mathrm{Pr} = 0.7$, and $10^5 \leq \mathrm{Ra}/A^3 \leq 4 \times 10^5$. The horizontal solid and dashed lines indicate the approximate location of transition of the smooth and rough plate, respectively, as determined from Fig. 7. Figure 10(*a*) is for a Rayleigh number at which no enhancement in the average Nusselt number occurs and indicates that there is also no enhancement of the local Nusselt number. Figures 10(*b*) and 10(*c*) are for Rayleigh numbers for which the average Nusselt number is increased by the presence of the rough plate. Figures 10(*b*) and 10(*c*) demonstrate that this increase in the average Nusselt number is a result of a dramatic increase in local heat transfer near $y = 0.6$.

Summary and Conclusions

We have conducted an experimental investigation of the effect of one type of distributed roughness element upon natural convection heat transfer in a cubical enclosure. These experiments covered the range from the beginning of transition up to the point where 60 percent of the length of the heated vertical surface had undergone transition. The distributed roughness used in the present study reduced the location of transition by about 5 percent. No enhancement occurred until ~40 percent of the length of the heated plate had undergone transition. Enhancement was larger for the isothermal boundary condition than for the constant flux boundary condition due to a dramatic increase in local heat transfer of as much as 40 percent at $y \cong 0.6$, slightly above the midpoint of the heated plate. Based upon the findings of this study, the local heat transfer appears to be relatively insensitive to the presence of the rough surface in the regions of the enclosure boundary layers which detrain fluid into the core. In the regions where the rough surface produces enhancement, it appears to do so by disrupting the thermal boundary layer and increasing thermal contact with the core.

The results of this study confirm that surface roughness can be used to produce heat transfer enhancement in natural convection enclosure flows. However, the level of enhancement measured in the present investigation is much less than that reported in [5, 7, 10]. This difference appears to be primarily a result of the insensitivity of the detrainment region in an enclosure boundary layer to the presence of a rough surface. There is a need for further research with other types of roughness elements to determine if the large increases in local heat transfer which were measured in the present experiment can be extended to produce a larger effect upon the overall heat transfer.

References

1 Catton, I., "Natural Convection in Enclosures," *Proceedings of the 6th International Heat Transfer Conference*, Hemisphere, Washington, D.C., Vol. 6, 1978, pp. 106–120.

2 Ostrach, S., "Natural Convection Heat Transfer in Cavities and Cells," *7th International Heat Transfer Conference*, Munich, Germany, Vol. 6, 1982, pp. 365–379.

3 Bergles, A. E., "Enhancement of Heat Transfer," *Proceedings of the 6th International Heat Transfer Conference*, Hemisphere, Washington, D.C., Vol. 6, 1978.

4 Nakayama, W., "Enhancement of Heat Transfer," *Proceedings 7th International Heat Transfer Conference*, Hemisphere, Washington, D.C., Vol. 1, 1982.

5 Prasolov, R. S., "The Effects of Surface Roughness of Horizontal Cylinders on Heat Transfer to Air," *Inzh.-fiz. Zh.*, Vol. 4, 1961, pp. 3–7.

6 Heya, N., Takeuchi, M., and Fujii, T., "Influence of Surface Roughness on Free-Convection Heat Transfer From a Horizontal Cylinder," *Chem. Eng. J.*, Vol. 23, 1982, pp. 185–192.

7 Jofre, R. J., and Barron, F., "Free Convection Heat Transfer to a Rough Plate," ASME Paper No. 67-WA/HT-38, 1967.

8 Eckert, E. R. G., and Jackson, T. W., "Analysis of Turbulent Free Convection Boundary Layer on Flat Plate," NACA Report 1015, 1951.

9 Fujii, T., Fujii, M., and Takeuchi, M., "Influence of Various Surface Roughness on the Natural Convection," *Int. J. Heat Mass Transfer*, Vol. 16, 1973, pp. 629–640.

10 Sastry, C. V. N., Murthy, V. N., and Sarma, P. K., "Effect of Discrete Wall Roughness on Free Convective Heat Transfer From a Vertical Tube," in: *Heat Transfer and Turbulent Buoyant Convection*, Vol. 2, Hemisphere, Washington, D.C., 1976, pp. 651–661.

11 Al-Arabi, M., and El-Refaee, M. M., "Heat Transfer by Natural Convection From Corrugated Plates to Air," *Int. Journal Heat Mass Transfer*, Vol. 21, 1978, pp. 357–359.

12 Elsherbiny, S. M., Hollands, K. G. T., and Raithby, G. D., "Free Convection Across Inclined Air Layers With One Surface V-Corrugated," ASME Journal of Heat Transfer, Vol. 100, 1978, pp. 410–415.

13 Sparrow, E. M., and Prakash, C., "Enhancement of Natural Convection Heat Transfer by a Staggered Array of Discrete Vertical Plates," ASME Journal of Heat Transfer, Vol. 91, 1980, pp. 215–220.

14 Prakash, C., and Sparrow, E. M., "Natural Convection Heat Transfer Performance Evaluations for Discrete (in-line or staggered) and Continuous-Plate Arrays," *Numerical Heat Transfer*, Vol. 3, 1980, pp. 89–105.

15 Weber, T. W., *An Introduction to Process Dynamics and Control*, Wiley, New York, 1973.

16 Qureshi, Z. H., and Gebhart, B., "Transition and Transport in a Buoyancy Driven Flow in Water Adjacent to a Vertical Uniform Flux Surface," *Int. J. Heat Mass Transfer*, Vol. 21, 1978, pp. 1467–1479.

17 Fujii, T., Takeuchi, M., Suzaki, K., and Vehara, H., "Experiments on Natural Convection Heat Transfer From the Outer Surface of a Vertical Cylinder to Liquids," *Int. J. Heat Mass Transfer*, Vol. 13, 1970, pp. 753–787.

18 Balvanz, J. L., and Kuehn, T. H., "Effect of Wall Conduction and Radiation on Natural Convection in a Vertical Slot With Uniform Heat Generation on the Heater Wall," *Natural Convection in Enclosures*, ASME, New York, Vol. 8, 1980, pp. 55–62.

19 Vliet, G. C., and Liu, C. K., "An Experimental Study of Turbulent Natural Convection Boundary Layers," ASME Journal of Heat Transfer, Vol. 91, 1969, pp. 517–531.

20 Godaux, F., and Gebhart, B., "An Experimental Study of the Transition of Natural Convection Flow Adjacent to a Vertical Surface," *Int. J. of Heat Mass Transfer*, Vol. 17, 1974, pp. 93–107.

21 Jaluria, Y., and Gebhart, B., "On Transition Mechanisms in Vertical Natural Convection Flow," *J. Fluid Mech.*, Vol. 66, 1974, pp. 309–337.

22 Schinkel, W. M. M., Linthorst, S. J. M., and Hoogendoorn, C. J., "The Stratification in Natural Convection in Vertical Enclosures," ASME Journal of Heat Transfer, Vol. 105, 1983, pp. 267–272.

23 Landis, F., and Yanowitz, H., "Transient Natural Convection in a Narrow Vertical Cell," *Third International Heat Transfer Conference*, AIChE, Vol. 2, 1966, pp. 139–151.

L. Sharpe, Jr.
Associate Professor,
Department of Mechanical Engineering,
N. C. A&T State University,
Greensboro, NC 27411
Assoc. Mem. ASME

F. A. Morrison, Jr.[1]
Director, Earth Sciences Division,
Lawrence Livermore National Laboratory,
Livermore, CA 94583
Mem. ASME

Numerical Analysis of Heat and Mass Transfer From Fluid Spheres in an Electric Field

Steady-state heat or mass transfer to a drop in an electric field at low values of the Reynolds number is investigated. The energy equation is solved using finite difference techniques; upwind differencing is used in approximating the convective terms. Far from the sphere, a "transmitting" boundary condition is introduced; the dimensionless temperature is held at zero for inward radial flow and the dimensionless temperature gradient is held at zero for outward radial flow at a fixed distance from the sphere's surface. Numerical solutions are obtained using an iterative method. Creeping flow heat transfer results are obtained for Peclet numbers up to 10^3.

Introduction

When a uniform electric field is applied to a dielectric fluid in which a drop of another dielectric fluid is suspended, charge accumulates at the interface. The field acting on the free charges at the interface produces an electrostatic force which generates liquid motion both within and outside the drop. This flow has been studied analytically [1] and experimentally [2].

Taylor [1] analyzed the steady, creeping motion generated by an electric field imposed on a drop. He determined the relation among the ratios of the electrical conductivity, viscosity, and dielectric constant for the drop to remain spherical when subjected to an electric field. Taylor also found the velocity distribution and the stresses acting to distort the drop and described two types of circulatory motion. In both cases, the streamlines are shown in Fig. 1 for flow within and outside the drop. The direction of the fluid motion was found to be independent of the orientation of the applied electric field. The circulation is from equator to pole at the interface when the product of the dielectric constant and electrical resistivity of the surrounding fluid is greater than the corresponding product for the drop. The flow is from pole to equator otherwise.

Stewart and Morrison [3] examined the flow at small nonzero Reynolds numbers. The effects of convective acceleration on the stream function and deformation were investigated using a regular perturbation expansion with Reynolds number as the perturbation parameter.

The use of electric fields to enhance heat or mass transfer has been proven effective in such disparate areas as boiling heat transfer [4], condensation heat transfer [5], and convection from horizontal wires [6]. Electric field enhanced heat or mass transfer from drops has also been widely considered. Experimental results of Lazarenko et al. [7] for heat transfer and Thornton [8] for mass transfer have demonstrated large increases in the transfer rate.

Theoretical results have been obtained for both the low Peclet number [9] and high Peclet number [10] cases. The low Peclet number results of Griffiths and Morrison [9] were obtained assuming dominant continuous phase resistance and steady state. Regular perturbations were successful for analyzing the heat transfer because far from the body the fluid velocity is $O(Ua^2/r^2)$ and the ratio of convection to conduction far from the body is, correspondingly,

$$\frac{\mathbf{v}\cdot\nabla t}{\alpha\nabla^2 t} = 0[(a/r)\mathrm{Pe}]$$

Therefore, the conduction solution is a uniformly valid approximation for the zeroth order solution for small Peclet number. This is not true for the translating sphere. In that case, conduction cannot dominate far from the body so that the conduction solution is not uniformly valid for a zeroth order solution [11, 12].

An exact solution for transport from a translating fluid sphere at high Peclet number was obtained by Chao [13]. A similar approach was used by Morrison [10] in analyzing the high Peclet number, transient transport in circulating flows generated by an electric field. The special case of steady-state, continuous phase resistance can be derived from those results. Morrison found that the high Peclet number heat transfer coefficient was proportional to the magnitude of the applied field.

Thus, results for circulating flows at zero Reynolds number have been established for both the low and high Peclet number cases. In this paper, steady heat transfer results for the intermediate Peclet number are obtained using finite difference techniques. The known solutions for low and high Peclet numbers are useful as limit checks for the numerical solutions.

Another powerful global check is the overall Nusselt number. Brenner [14] has shown that the Nusselt number for transport from an isothermal body of any shape to a fluid of uniform temperature remains unaltered when the flow is everywhere reversed. Although local fluxes differ greatly, the overall heat transfer is independent of the direction of flow. This phenomenon was observed in both the high Peclet number and low Peclet number results.

Mathematical Formulation

Consider steady electroconvective flow about a drop of radius a. Attention will be restricted to the case where the dominant thermal resistance is found outside the drop. For this external flow, the stream function is [1]

$$\psi = Ua^2[(a/r)^2 - 1]\sin^2\theta\cos\theta \tag{1}$$

As shown in Fig. 1, r is the radial distance measured from the center of the drop and θ is the polar angle.

The speed U is the maximum speed produced by the electric field. This maximum speed occurs at the interface where θ is $\pi/4$. Taylor found this to be

$$U = \frac{-9E^2 a\epsilon_2}{8\pi(2+\sigma_1/\sigma_2)^2}\left[\frac{\sigma_1\epsilon_1/\sigma_2\epsilon_2 - 1}{5(\mu_1+\mu_2)}\right] \tag{2}$$

---

[1] Deceased.

Contributed by the Heat Transfer Division for publication in the JOURNAL OF HEAT TRANSFER. Manuscript received by the Heat Transfer Division March 16, 1984. Paper No. 83-WA/HT-29.

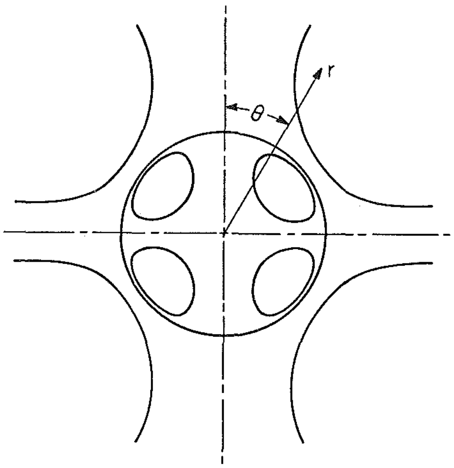

Fig. 1 Streamlines of the creeping motion generated by an electric field

The subscripts 1 and 2 refer to the surrounding fluid and the drop, respectively. E is the magnitude of the applied field, σ is the electrical resistivity, ϵ is the dielectric constant, and μ is the viscosity.

If the convection of surface charge by the fluid motion is neglected, then the steady-state temperature distribution is governed by the energy equation, which for axisymmetric flow with constant properties may be written in nondimensional form as

$$\frac{1}{R^2}\frac{\partial}{\partial R}(R^2 u_r T)+\frac{1}{R\sin\theta}\frac{\partial}{\partial\theta}(\sin\theta\, u_\theta T)= \frac{2}{\mathrm{Pe}}\left(\frac{\partial^2 T}{\partial R^2}+\frac{2}{R}\frac{\partial T}{\partial R}+\frac{1}{R^2}\cot\theta\frac{\partial T}{\partial\theta}+\frac{1}{R^2}\frac{\partial^2 T}{\partial\theta^2}\right) \qquad (3)$$

The Peclet number Pe is defined in terms of the maximum speed U, the thermal diffusivity α_1 of the continuous region, and the drop radius a

$$\mathrm{Pe}\equiv\frac{2Ua}{\alpha_1} \qquad (4)$$

The dimensionless temperature T is defined as

$$T\equiv\frac{t-t_\infty}{t_s-t_\infty} \qquad (5)$$

where t is the local temperature, t_∞ is the temperature of the surrounding fluid far from the drop, and t_s is the temperature of the drop. A dimensionless distance is defined by

$$R\equiv r/a \qquad (6)$$

The dimensionless velocity components are

$$u_r\equiv v_r/U \qquad (7)$$

and

$$u_\theta\equiv v_\theta/U \qquad (8)$$

where v_r and v_θ are the velocity components determined from the stream function ψ and are given by

$$v_r=\frac{1}{r^2\sin\theta}\frac{\partial\psi}{\partial\theta} \qquad (9)$$

and

$$v_\theta=\frac{-1}{r\sin\theta}\frac{\partial\psi}{\partial r} \qquad (10)$$

The boundary conditions for equation (3) are

$$T=1 \text{ at } R=1 \qquad (11)$$

and

$$T\to 0 \text{ as } R\to\infty \qquad (12)$$

Symmetry tangential boundary conditions are also used.

Introducing the transformation

$$x=R^{-1} \qquad (13)$$

equation (3) becomes

$$x^4\frac{\partial}{\partial x}(U_x T)+\frac{x}{\sin\theta}\frac{\partial}{\partial\theta}(U_\theta T)= \frac{2}{\mathrm{Pe}}\left(x^4\frac{\partial^2 T}{\partial x^2}+x^2\cot\theta\frac{\partial T}{\partial\theta}+x^2\frac{\partial^2 T}{\partial\theta^2}\right) \qquad (14)$$

where

$$U_x=(1-x^2)(2\cos^2\theta-\sin^2\theta) \qquad (15)$$

and

$$U_\theta=2x^4\sin^2\theta\cos\theta \qquad (16)$$

The boundary conditions for equation (14) are

$$T=1 \text{ at } x=1 \qquad (17)$$

$$T\to 0 \text{ as } x\to 0 \qquad (18)$$

$$\frac{\partial T}{\partial\theta}=0 \text{ at } \theta=0 \text{ and } \theta=\pi/2 \qquad (19)$$

Nomenclature

a = sphere radius
E = magnitude of the applied field
Nu = average Nusselt number
Nu_θ = local Nusselt number
O = order of magnitude
Pe = Peclet number
Pe_x, Pe_θ = false diffusion terms
r = spherical radial position
R = dimensionless spherical radial position
t = local temperature
t_s = temperature of the sphere
t_∞ = ambient temperature
T = dimensionless temperature
u_r = dimensionless radial velocity component
u_θ = dimensionless tangential velocity component
U = the maximum circulation speed
U_x = radial velocity used in the finite-difference equation
U_θ = tangential velocity used in the finite-difference equation
v_r = radial velocity component
v_θ = tangential velocity component
$\mathbf{v}$ = velocity vector
x = transformation (R^{-1})
X = horizontal axis = $R\sin\theta$
Y = vertical axis = $R\cos\theta$
α = thermal diffusivity
ϵ = dielectric constant
θ = polar angle
μ = viscosity
σ = electrical resistivity
ψ = Stokes stream function
ω = relaxation parameter

Subscripts

1 = outside drop
2 = inside drop
i,j = node indices

Superscripts

n = iteration

Equation (14) along with equations (15) and (16) are solved numerically subject to the boundary conditions given in equations (17), (18), and (19).

Numerical Procedure

In approximating the diffusive terms, second-order central differences are appropriate. There are no instabilities associated with approximating the diffusive terms in this way. The centered difference form of these terms has a truncation error of order $(\Delta z)^2(\partial^4 T/\partial z^4)$.

The difficulties encountered in numerical solutions of transport equations arise from the convective terms. Initially, one would be tempted to use second-order central differences for these terms. This leads to a truncation error of order $(\Delta z)^2(\partial^3 T/\partial z^3)$, but the requirement of stability prevents this approximation from being effective. For a one-dimensional problem, the cell Peclet number must be less than or equal to two for the solution to be stable [15].

A method used to overcome this difficulty was developed by Lelevier, e.g., see [16]. The method is known as upwind differencing, the donor cell technique, or the method of positive coefficients. A one-sided difference is used in approximating the convective terms. In this first-order method, information is advected into a cell only from cells that are upwind of it.

An error analysis of the upwind differencing method reveals a false diffusion term. Theoretically, this false diffusion term can easily exceed the physical diffusion term by orders of magnitude, but the practical situation is not quite this severe. It can be shown, however, that in regions where the Prandtl boundary layer approximations are valid, this false diffusion effect is negligible [17]. A Taylor series expansion shows that equation (14) is equivalent to

$$x^4 \frac{\partial}{\partial x}(U_x T) + \frac{x}{\sin\theta}\frac{\partial}{\partial\theta}(U_\theta T) = x^4 \frac{\partial^2 T}{\partial x^2}\left(\frac{2}{\mathrm{Pe}} + \mathrm{Pe}_x\right) + \frac{2}{\mathrm{Pe}} x^2 \cot\theta \frac{\partial T}{\partial \theta} + x^2 \frac{\partial^2 T}{\partial \theta^2}\left(\frac{2}{\mathrm{Pe}} + \mathrm{Pe}_\theta\right) \tag{20}$$

where

$$\mathrm{Pe}_x = (\Delta x) U_x/2 \tag{21}$$

and

$$\mathrm{Pe}_\theta = (\Delta\theta) U_\theta/2 \tag{22}$$

Pe_x and Pe_θ are the radial and tangential components, respectively, of the artificial diffusion terms. In any region where the boundary-layer approximations apply, $\partial^2 T/\partial\theta^2$ will be small and the effect $(2/\mathrm{Pe} + \mathrm{Pe}_\theta)$ will be small in equation (20). Also, U_x will be small, so Pe_x may be less than 2/Pe. Therefore, the artificial viscosity terms are negligible. The main advantage of upwind differencing is that it is not stability limited by a cell Peclet number.

A conservative finite difference representation of the convective terms, developed by Torrance [18], is employed

$$\frac{\partial(uT)}{\partial z} = \begin{cases} (\bar{u}_i T_i - \bar{u}_{i-1} T_{i-1})/\Delta z; & (\bar{u}_i, \bar{u}_{i-1} > 0) \\ \\ (\bar{u}_i T_{i+1} - \bar{u}_{i-1} T_i)/\Delta z; & (\bar{u}_i, \bar{u}_{i-1} < 0) \end{cases} \tag{23}$$

where

$$\bar{u}_m = (u_{m+1} + u_m)/2 \tag{24}$$

If the two mean velocity coefficients are of different signs, one term from the numerator of each of the two approximations shown is required.

Successive overrelaxation is used to solve the system of equations associated with the finite difference approximations. A relaxation parameter was introduced

$$T_{i,j}^{n+1} = (1-\omega) T_{i,j}^{n} + \omega \bar{T}_{i,j}^{n+1} \tag{25}$$

where the overbar indicates the Gauss–Siedel value.

Convergence of the computed values of temperature was assumed when the difference between successive iterations was less than 5×10^{-6}. The mesh used was 121 × 121 resulting in the transformed radial step size of 0.00825 and the grid size for the angle of 0.75 deg. For comparison, calculations were also made with a mesh of 61 × 61. At a Peclet number of 10^3, the calculated Nusselt number was within 1.8 percent of that found using the 121 × 121 grid.

The position of the outer boundary was held constant for all Peclet numbers, that boundary being $R = 100$. Conditions imposed at the outer boundary have a dramatic effect on computational effectiveness. The easiest method is to completely specify the temperature along the outer boundary. This can be achieved either by using "infinity" boundary conditions at the extremes of the mesh or by using asymptotic solutions applicable at large but finite distances from the drop's surface. Imposing different conditions on inflow and outflow portions of the boundary proves to have decided advantages. This usually allows a considerably shorter computational mesh for comparable accuracy in the region near the interface. The boundary condition used at the outer boundary was $T = 0$ for inflow and $\partial T/\partial x = 0$ for outflow [16].

The evaluation of the average Nusselt number given by

$$\mathrm{Nu} = 2\int_0^{\pi/2} \left(\frac{\partial T}{\partial x}\right)_{x=1} \sin\theta \, d\theta \tag{26}$$

was obtained using the trapezoidal rule for integration.

The gradient $(\partial T/\partial x)_{x=1}$ can be evaluated using first or second-order finite difference techniques or even higher order accurate techniques for that matter. For the gradient in this case, first-order finite difference methods will be shown to be appropriate by examining the limiting analytical solution.

The first-order finite difference approximation is given by

$$\left(\frac{\partial T}{\partial R}\right)_i = -\frac{1}{(\Delta R)}(T_i - T_{i+1}) + O\left[\left((\Delta R)\frac{\partial^2 T}{\partial R^2}\right)_i\right] \tag{27}$$

and the second-order finite difference approximation is given by

$$\left(\frac{\partial T}{\partial R}\right)_i = -\frac{1}{2(\Delta R)}(3T_i - 4T_{i+1} + T_{i+2}) + O\left[(\Delta R)^2\left(\frac{\partial^3 T}{\partial R^3}\right)_i\right] \tag{28}$$

Consider now the exact solution for large Peclet number given by Morrison [10]

$$T = 1 - \mathrm{erf}[\mathrm{Pe}^{1/2}(R-1)f] \tag{29}$$

$$\frac{\partial^2 T}{\partial R^2} = 4\pi^{-1/2} f^3 \mathrm{Pe}^{3/2}(R-1)\exp[-(R-1)^2 \mathrm{Pe} f^2] \tag{30}$$

$$\frac{\partial^3 T}{\partial R^3} = 4\pi^{-1/2} f^3 \mathrm{Pe}^{3/2}[1 - 2f^2 \mathrm{Pe}(R-1)^2] \cdot \exp[-(R-1)^2 \mathrm{Pe} f^2] \tag{31}$$

where $f = \cos\theta$ for pole to equator flow and $f = \sin^2\theta/(1+\sin^2\theta)^{1/2}$ for equator to pole flow. The error term for the first-order finite difference approximation of the gradient at $R = 1$ is identically zero. This is not the case for the second-order finite difference of the gradient at $R = 1$. In

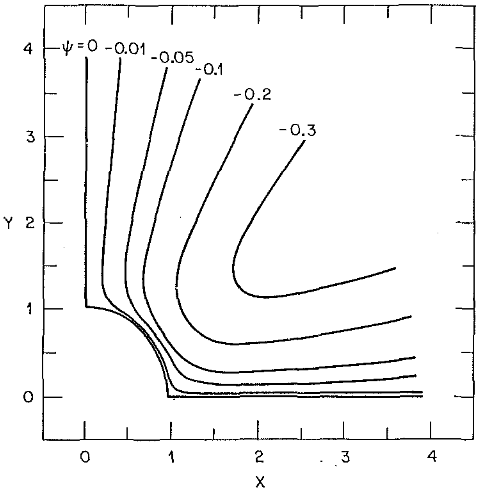

Fig. 2 Streamlines for flow outside the drop

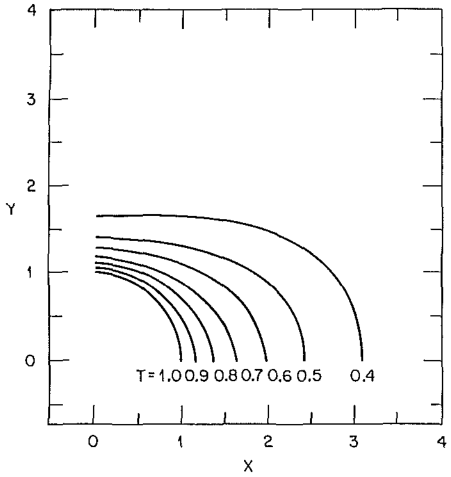

Fig. 3 Isotherms for pole to equator flow at Pe = 10

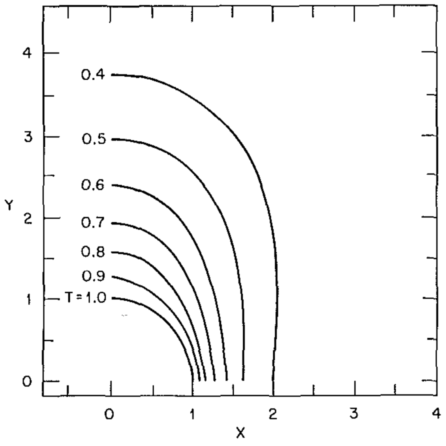

Fig. 4 Isotherms for equator to pole flow at Pe = 10

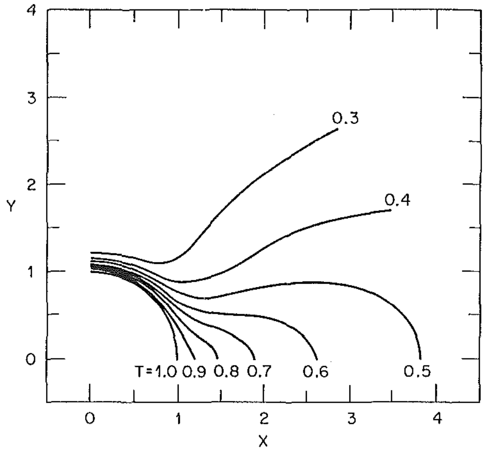

Fig. 5 Isotherms for pole to equator flow at Pe = 50

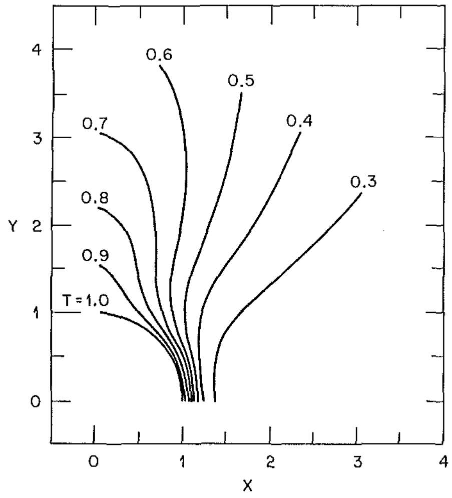

Fig. 6 Isotherms for equator to pole flow at Pe = 50

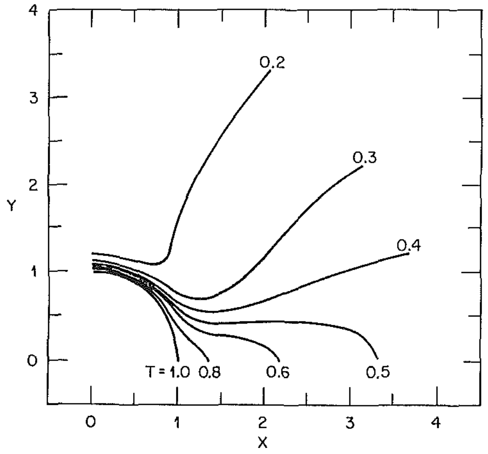

Fig. 7 Isotherms for pole to equator flow at Pe = 100

that case, the error term is $4\pi^{-1/2}(\Delta R)^2 f^3 \mathrm{Pe}^{3/2}$. Therefore, the first-order approximation is fitting for determining the gradient. It is easier and just as good at high Peclet numbers.

Numerical Results

The streamlines for the steady electroconvective flow are shown in Fig. 2 and the isotherms are shown in Figs. 3-8. At Pe = 0, which corresponds to pure conduction, isotherms coincide with lines of constant R. At low Peclet numbers, as in Fig. 3 and Fig. 4, the isotherms diverge from the conduction solution as lines of constant R and resemble prolate and oblate spheroids. As the Peclet number is increased

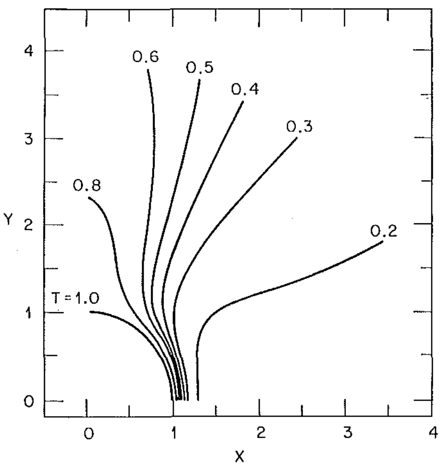

Fig. 8 Isotherms for equator to pole flow at Pe = 100

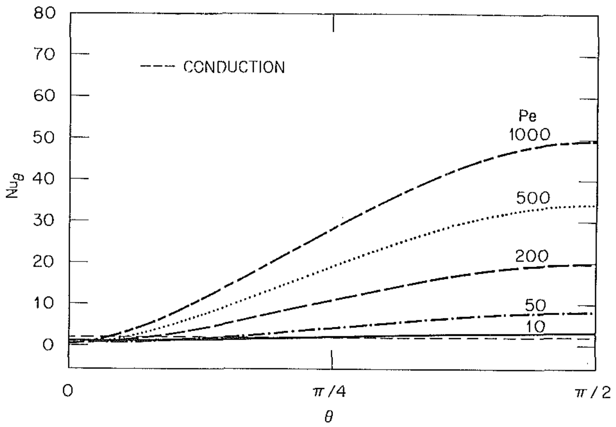

Fig. 10 Local Nusselt number variation for equator to pole flow

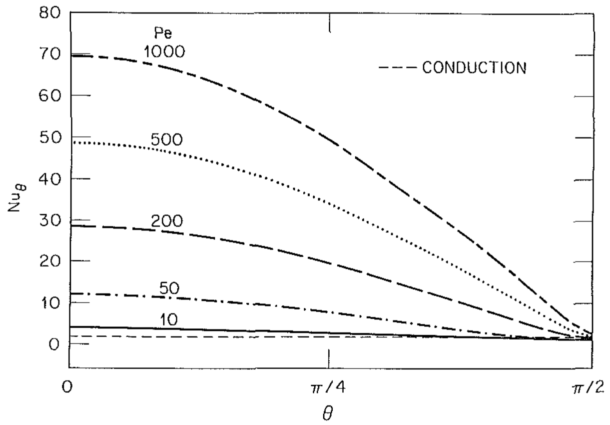

Fig. 9 Local Nusselt number variation for pole to equator flow

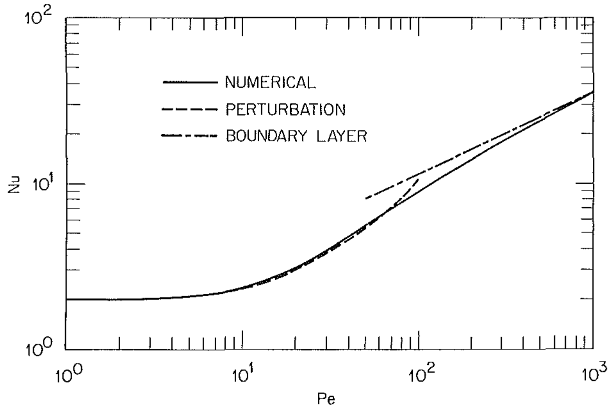

Fig. 11 Variation of mean Nusselt number with Peclet number

further, as in Fig. 5 and Fig. 6, the isotherms are compressed at the frontal stagnation point and thicken as the rear stagnation point is approached. As the Peclet number inwake. At large Peclet numbers, as in Fig. 7 and Fig. 8, isotherms near the drop's surface are very close to each other at the frontal stagnation point and thickens as the rear stagnation point is approached. As the Peclet number increases, transport rates at the front of the sphere increase while those at the rear stagnation point decrease.

The local Nusselt number given by

$$\mathrm{Nu}_\theta = 2\left(\frac{\partial T}{\partial x}\right)_{x=1} \qquad (32)$$

is shown in Fig. 9 for pole to equator flow and Fig. 10 for equator to pole flow. The local Nusselt number increases for increasing Peclet number at the frontal stagnation point. At higher Peclet numbers, the local heat transfer should decrease at the rear stagnation point. Figures 9 and 10 show that the local transfer actually increases at higher Peclet numbers. The local Nusselt number is quite sensitive near the rear stagnation point because the temperature gradients are quite small. Even at high Peclet numbers, the temperature distribution approaches the conduction solution far from the drop's surface. Because of this infinity boundary condition and machine storage capacity, accurate solutions near the rear stagnation point were not feasible. The average Nusselt number is relatively unaffected because little transfer takes place near the rear stagnation point.

Figure 11 shows the overall Nusselt number obtained by the perturbation analysis of Griffiths and Morrison [9], boundary layer analysis of Morrison [10], and the present numerical results. The perturbation results agree with the numerical results within 4.3 percent up to a Peclet number equal to 75. The numerical results approach the exact boundary layer analysis at high Peclet numbers; at a Peclet number of 750 the numerical results agree with the boundary layer solution within 3 percent.

The overall calculated Nusselt number for the pole to equator flow was always within a percent of the equator to pole flow. Since the temperature distributions and local Nusselt numbers of equator to pole flow differed greatly from their counterparts in pole to equator flow, this global check provides valuable evidence of computational accuracy.

Since the dimensionless equations and boundary conditions governing mass transfer are identical to those of heat transfer, the solution to these equations are also identical. Equivalent results for mass transfer may, therefore, be found by simply replacing the Nusselt number by the Sherwood number and the dimensionless temperature by the dimensionless concentration.

Dedication

This paper is dedicated to the memory of Frank A. Morrison, Jr., my teacher, my advisor, my friend.

References

1 Taylor, G. I., "Studies in Electrohydrodynamics. I. The Circulation Produced in a Drop by an Electric Field," *Proceedings of the Royal Society*, Vol. 291, 1966, pp. 159-166.

2 McEwan, A. D., and deJong, L. N. J., "Addendum, Experimental

Verification," *Proceedings of the Royal Society*, Vol. 291, 1966, p. 166 (addendum to Reference [1]).

3 Stewart, M. B., and Morrison, F. A., Jr., "Small Reynolds Number Electrohydrodynamic Flow Around Drops and the Resulting Deformation," ASME *Journal of Applied Mechanics*, Vol. 46, 1979, pp. 510-512.

4 Olinger, J. L., and Colver, C. P., "A Study of the Effect of a Uniform Field on Nucleate and Film Boiling," *Convective and Interfacial Heat Transfer, Chemical Engineering Progress Symposium Series*, Vol. 67, No. 113, 1971, pp. 19-29.

5 Choi, H. Y., "Electrohydrodynamic Condensation Heat Transfer," ASME JOURNAL OF HEAT TRANSFER, Vol. 90, 1968, pp. 98-102.

6 Ahsmann, G., and Kronig, R., "The Influence of Electric Fields on the Convective Heat Transfer in Liquids," *Applied Science Research*, Vol. A2, 1950, pp. 235-244.

7 Lazarenko, B. R., Kozhukhar, I. A., and Bologa, M. K., "Heat Transfer in Emulsions of Poor Conductors Under Electric Fields," *International Journal of Heat and Mass Transfer*, Vol. 18, 1975, pp. 589-596.

8 Thornton, J. D., "The Applications of Electrical Energy to Chemical Rate Processes," *Reviews of Pure and Applied Chemistry*, Vol. 18, 1968, pp. 197-218.

9 Griffiths, S. K., and Morrison, F. A., Jr., "Low Peclet Number Heat and Mass Transfer in an Electric Field," ASME JOURNAL OF HEAT TRANSFER, Vol. 101, 1979, pp. 484-488.

10 Morrison, F. A., Jr., "Transient Heat and Mass Transfer to a Drop in an Electric Field," ASME JOURNAL OF HEAT TRANSFER, Vol. 99, 1977, pp. 269-273.

11 Kronig, R., and Bruijsten, J., "On the Theory of Heat and Mass Transfer From a Sphere in a Flowing Medium at Low Values of Reynolds' Number," *Applied Scientific Research*, Vol. A2, 1951, pp. 439-446.

12 Acrivos, A., and Taylor, T. D., "Heat and Mass Transfer From Single Sphere in Stokes Flow," *Physics of Fluids*, Vol. 5, No. 4, 1962, pp. 387-394.

13 Chao, B. T., "Transient Heat and Mass Transfer to a Translating Droplet," ASME JOURNAL OF HEAT TRANSFER, Vol. 91, 1969, pp. 273-281.

14 Brenner, H., "On the Invariance of the Heat Transfer Coefficients to Flow Reversal in Stokes and Potential Streaming Flow Past Particles of Arbitrary Shape," *Journal of Mathematics and Physical Sciences*, Vol. 1, 1967, pp. 173-179.

15 Gutfinger, C., *Topics in Transport Phenomena*, Hemisphere, Washington, 1975.

16 Roache, P. J., *Computational Fluid Dynamics*, Hermosa, Albuquerque, NM, 1972.

17 Schlichting, H., *Boundary Layer Theory*, 6th ed., McGraw-Hill, New York, 1968.

18 Torrance, K. E., "Comparison of Finite-Difference Computations of Natural Convection," *Journal of Research of the National Bureau of Standards*, Vol. 72B, No. 4, 1968, pp. 281-301.

V. Kadambi
Corporate Research and Development,
General Electric Company,
Schenectady, NY 12301

E. K. Levy
Mem. ASME

S. Neti
Mem. ASME

Department of Mechanical Engineering
and Mechanics,
Lehigh University,
Bethlehem, PA 18017

Heat Transfer and Pressure Drop in a Helically Coiled Rectangular Duct

The present paper deals with experiments using air in three helically coiled rectangular ducts of mean diameters 12.7 cm, 17.8 cm, and 22.8 cm, respectively, made of rectangular wave-guide tubing of dimensions 1.27 cm × 0.64 cm. Pressure variations observed around the ducts were qualitatively in agreement with the expectations for secondary flow. The friction factors change gradually with increasing Reynolds numbers over the range 1200–10,000 without exhibiting a sudden transition from laminar flow to turbulence. At all Reynolds numbers, these are higher than those for a straight duct by 20–100 percent. The heat transfer coefficient is also higher than that for straight ducts ranging between 20–300 percent, depending on the Reynolds number. The largest increases are seen in the Reynolds number range 1200–2500.

1 Introduction

Curved or rotating ducts of rectangular cross section with coolants flowing through them find several applications in industry. Large generators have hydrogen flowing through ducts rotating parallel to an axis, while several types of large motors have air entering radially through small ducts and flowing out axially thereafter. In all these cases, the temperature limitation on the material being cooled and the associated heat transfer play an important role in determining the power outputs and machine sizes. For appropriate design, it is essential to know the heat transfer and the pressure drop during fluid flow under the actual conditions encountered in these machines. At present, this information is not available and the design is often based on stationary straight tube data.

The fluid flowing through a stationary curved duct or a rotating straight duct is subjected to forces which act locally in a direction normal to the main flow direction. Depending upon the duct curvature or the speed of rotation, these forces can reach values which are very large compared with normal gravitational acceleration. As a result, secondary flows transverse to the main flow direction are set up, with the formation of vortex cells. The number and the geometry of these cells depend upon the duct geometry (circular or rectangular) and the Reynolds number as well as other nondimensional parameters. For a curved duct (Fig. 1*a*), the parameter of interest depends on the duct geometry and curvature, while it is a function of the rotational speed, the duct size, and other variables for rotating ducts.

The type of cross flow one can envision in a curved channel is indicated in Fig. 1(*b*). This appears to be similar to that generated in rotating straight ducts, since the secondary flows are caused by either centrifugal or Coriolis forces. There is strong evidence to indicate that they affect the stability of the main flow so as to reduce the sharpness of transition between laminar and turbulent conditions. The result may be a gradual variation of friction factor with Reynolds number. The friction factors and heat transfer coefficients often become much higher than in straight tubes of the same diameters and at similar Reynolds numbers.

Trefethen [1] experimented with water in long circular tubes and found that in the laminar region, the friction factor increases with rotational speed. In the turbulent region, the rotational speed has only a small influence on the friction factor, as compared with that of a stationary duct. Trefethen also showed that the forces acting on the fluid would result in secondary flows that are similar in curved stationary tubes and straight rotating tubes.

Several other studies dealing with curved tubes can be found in the literature [2–4]. Mori and Nakayama [5, 6] have analyzed curved circular tube flow by dividing it into two parts: a core region which is potential in nature and a boundary-layer region affected by viscosity and confined to the walls. They show that the effect of secondary flow increases markedly with increase in duct curvature. Mori and Nakayama found that the curvature has much less influence in fully developed turbulent flow than in laminar flow.

Humphrey et al. [7], Melling and Whitelaw [8], and Buggeln

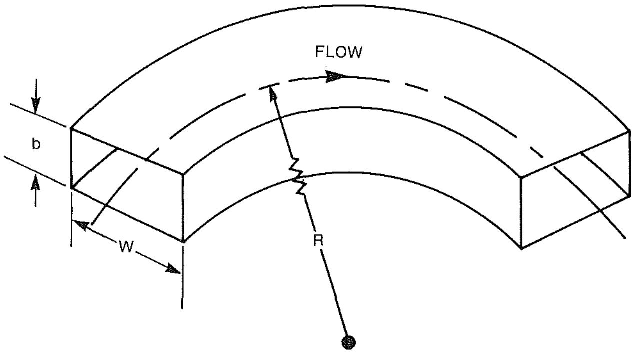

Fig. 1(*a*) Curved rectangular duct nomenclature

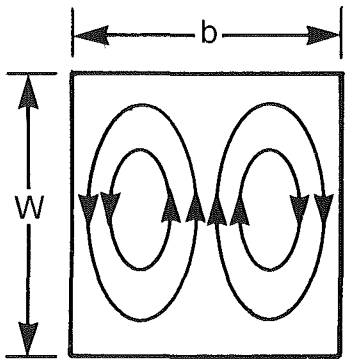

Fig. 1(*b*) Secondary streamlines

Contributed by the Heat Transfer Division for publication in the JOURNAL OF HEAT TRANSFER. Manuscript received by the Heat Transfer Division March 16, 1984. Paper No. 83-WA/HT-1.

et al. [9] have reported numerical solutions of flows in curved ducts. In these reports, the flows have been assumed to be completely turbulent and the appropriate equations of motion solved by using a suitable turbulence model. In both [7] and [9], the calculated results agree reasonably well with experimental data up to a bend angle of 45 deg. A similar calculation applying to laminar flow in a straight rectangular duct rotating about an axis parallel to itself has been developed by Neti et al. [11].

Measurements of developing flow in right angled and 180 deg bends have also been reported in the literature [7, 9, 24]. It has been observed that inlet boundary-layer thickness influences the secondary flow and may affect turbulence as well as heat transfer.

Cheng and Akiyama [12] have obtained numerical solutions to flow in curved rectangular channels of various aspect ratios and computed heat transfer coefficients as well. Their analysis is applicable in laminar flow for Dean numbers in the range 0–10,000. Mori et al. [13] have used a momentum integral approach similar to that of Mori and Nakayama [5, 6] to calculate heat transfer in a curved square duct. It is clear from Cheng and Akiyama's analysis that the assumptions of Mori et al. [13] are valid only for Dean numbers in excess of 700.

Even though rectangular curved ducts are widely used in industrial applications, not much of information relating to them exists in the literature. A considerable amount of information relating to circular curved tubes exists, though there is an uncertainty about the effects of secondary flow on transition to turbulence as well as on heat transfer during transition.

Srinivasan et al. [14] carried out a review of available data on helically curved circular coils as well as on spirally curved circular coils and concluded that the Reynolds number for transition between laminar and turbulent flows is larger than for straight circular tubes. Srinivasan et al. [15] have also published the results of a series of experiments on ten different helically coiled circular tubes and obtained both the transition Reynolds numbers and friction factors for these tubes. They have established three correlations for friction factors depending upon the tube-to-coil diameter ratio, each correlation valid in a certain range of Dean numbers. An interesting aspect of their correlations is that a critical Reynolds number is proposed for turbulent flow, in addition to a transition region stretching over a range of Reynolds numbers. This implies that there is no sharp cutoff point for transition between laminar and turbulent flows. Indeed, an examination of their graphs indicates that straight lines have been drawn through regions of scatter in the data and that the secondary flow due to curvature so modifies the friction factor that it is not possible to determine specific points of break in the data heralding the onset of turbulence. The friction factor curve is so smooth that the "critical Reynolds number" for transition could have been picked at one or more of several points more or less arbitrarily. A continuous change from laminar flow to turbulence occurs, deviating more and more from the classical laminar straight tube data, until fully turbulent flow is noticed. In view of these uncertainties and lack of other information, it was thought fit to establish data on curved ducts relating to both heat transfer and pressure drop. A rectangular geometry was chosen primarily because of its applications in industry.

In the present paper, the results of experiments on helical rectangular ducts with mean coil diameters of 12.7 cm (5.0 in.), 17.8 cm (7.0 in.), and 22.86 cm (9.0 in.) are described. Friction factors and Nusselt numbers have been calculated for each duct. As opposed to observations for a straight duct, there exists a regime where the flow is dominated by secondary flow effects and it is therefore difficult to tell whether it is laminar or turbulent by observing the friction factor curve. This regime extends over a wide range of Reynolds numbers betweem 1000 and 10,000, so that the classical transition between laminar and turbulent flows does not occur in curved ducts. With increasing Reynolds numbers the friction factor, which is influenced by secondary flows, gradually changes from laminar values to those in turbulent flow. Also, curvature can raise the friction factors and heat transfer by as much as 100–300 percent in the range $1000 < \mathrm{Re} < 3000$, while the increases are much smaller at large Reynolds numbers.

2 Experimental Details

A schematic diagram of the fluid flow loop used in the study is shown in Fig. 2. The coiled rectangular ducts were made of wave-guide tubing, 1.27 cm × 0.64 cm (0.5 in. × 0.25 in.) outer dimensions and walls 1 mm (0.04 in.) thick. Tests have been conducted on three helices, with respective mean diameters 12.7 cm (5.0 in., $b/R = 0.068$), 17.8 cm (7.0 in., $b/R = 0.0486$), and 22.9 cm (9.0 in., $b/R = 0.0378$).

Air at 600 kP (90 psia) was cooled, dehumidified, filtered and then led into the duct through a pressure regulator and a control valve. The rate of air flow could be adjusted to lie anywhere between 4.5×10^{-4}–4.5×10^{-2} m³/s (0.1 and 10 scfm), as necessary.

The air flow rate was measured with a Datametrics linear flow meter (Model 800-L, range $4.5 \times 10^{-4} - 2.5 \times 10^{-2}$ m³/s

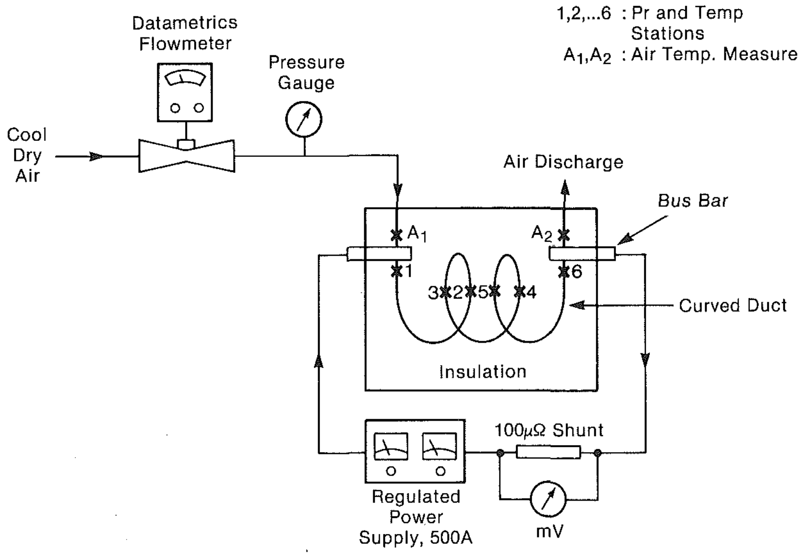

Fig. 2 Schematic diagram of apparatus

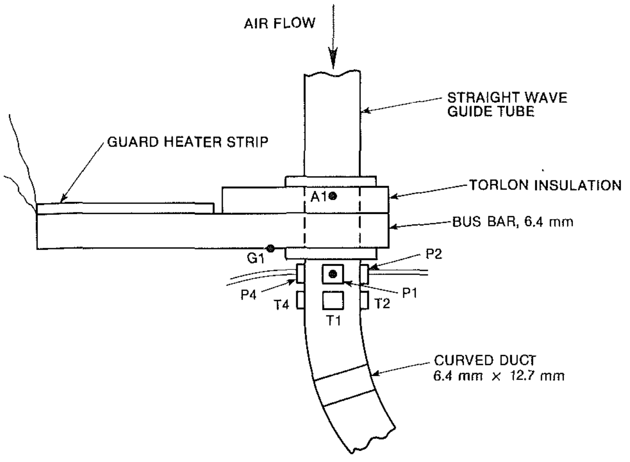

Fig. 3 Guard heaters and instrumentation at the duct inlet

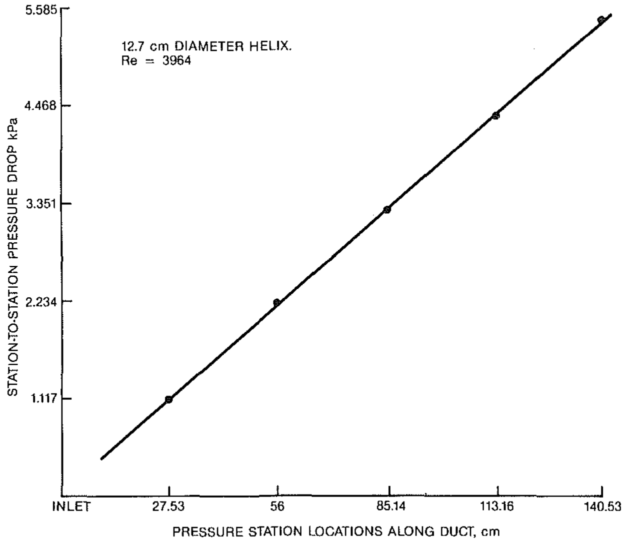

Fig. 4(*a*) Pressure variation along the duct axis

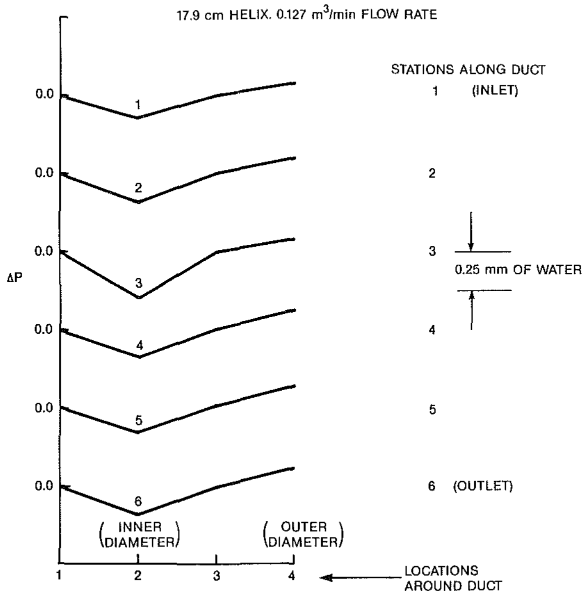

Fig. 4(*b*) Pressure variation around the duct

or 0.1-5 scfm and accuracy 0.5 percent of the set scale value) or a Cox turbine flow meter (range $2.5\text{-}7.5 \times 10^{-2}$ m^{-2}/s, accuracy 0.2 percent of set value). The meters were connected in parallel with shutoff valves, so that either of them could be used for flow measurement at any given time. (In Fig. 2, only one instrument has been shown for purposes of clarity.) The total range of flow in which the experiments were conducted was between $4.5 \times 10^{-4} - 3.6 \times 10^{-2}$ m^3/s (0.1-8 scfm), corresponding to a Reynolds number range of 450-35,000.

A straight wave-guide tube of the same internal and external cross sections as the helical duct, 2 m (6 ft) long (length/hydraulic mean diameter = 300), was connected tangentially to the helix to provide a well-developed and smooth flow at the inlet. A similar straight section, 0.6 m (2 ft) long, was connected at the exit end of the test section.

The air pressures were monitored with static pressure taps at six stations along the duct, spaced equally apart and half a turn away from one another. In addition, pressures were measured at every station with taps, located one on each wall of the duct. These measurements were used to obtain an estimate of the velocity of secondary flow, as compared with that of the main flow. A scanivalve connected to the taps and a Validyne pressure transducer permitted the pressure at every tap to be monitored as required. The whole system was precalibrated and could provide accurate data, within 0.25 kP (0.2 in. of water). In addition to these, the air pressures at the inlet of the duct and at the flow-metering instruments were measured with a Heise bourdon tube instrument that had a least count of 0.3 kP (0.05 psig).

For heat transfer studies, the duct was heated electrically by passing a d-c current through its walls, controlled by a regulated power supply, capable of providing a maximum of 500 A. The current flow was measured with a calibrated 100 microhm shunt (rating: 100 mV at 1000 amp). The duct was well insulated with fiberglass and styrofoam packing pellets, so that thermal losses were reduced to a minimum.

Heavy copper bus bars, connected one at each end, transmitted power to the duct from the power supply. In order to minimize heat transfer from the duct to the bus bars, secondary electrical heating was provided with 40 W flat strip heaters glued to each bus. The strip heaters could be maintained at any desired temperature by using variacs operating off a-c 110 V mains. During each test, the bus temperatures could be controlled within 0.3°C (0.5°F) of those on the duct at these points. At these temperature differences, the end losses were estimated to be less than 0.5 percent of the power input to the duct.

The temperatures at six stations along the duct (as well as around the duct at each station), were measured with copper-constantan thermocouples glued to each flat face of the duct. In addition, the temperatures of the air at the entry and the exit of the curved duct were measured with thermocouples that were inserted into the duct, through an insulating material, 6.3 cm (0.25 in.) thick, placed above the bus. The details of the thermocouple locations and the pressure taps at the inlet are indicated in Fig. 3.

Adiabatic flow data were first obtained by passing dry, dehumidified air through the unheated duct. The pressures at all the locations, the mass flow rate, and the air temperatures at the inlet and the outlet were measured. These data enabled the calculation of friction coefficient and the Reynolds number, corresponding to the mean temperature within the duct.

Before performing the heat transfer tests, the energy losses through the insulation were determined by turning on the heaters and the current through the duct without any air flow. The bus-bar temperatures were matched with those of the

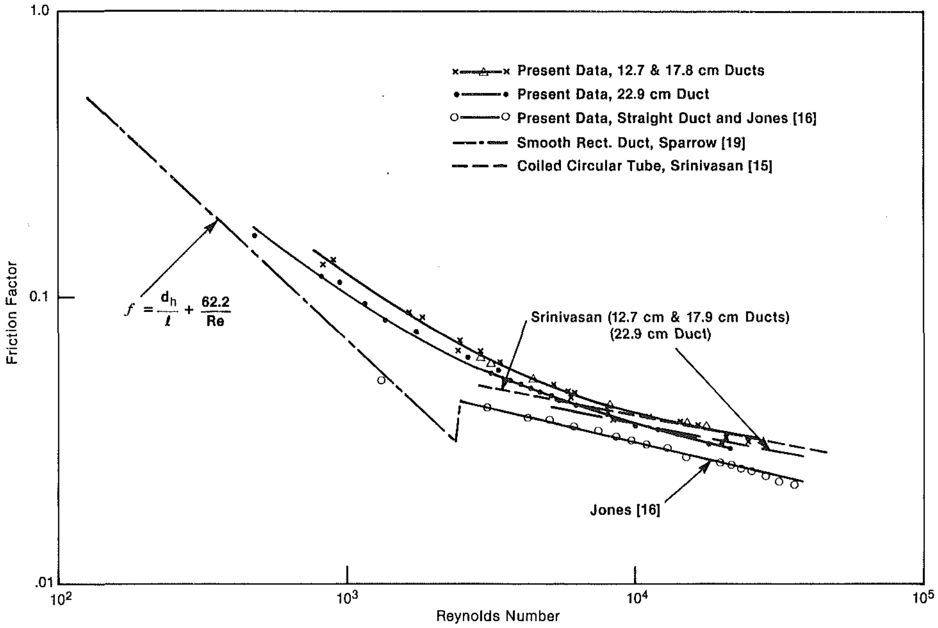

Fig. 5 Measured friction factors

thermocouples located close to the duct ends, within 0.3°C (0.5°F), so that the duct ends could be treated as insulated. The total power input to the duct and the temperatures at various locations along the duct were measured to obtain a power loss versus average duct temperature curve, one for each duct.

During the heat transfer test with air flow, the duct surface temperatures at the inlet and the exit were again matched with those of the bus bars. All the temperatures, pressure drops, the flow rate, and other data were recorded after steady state was reached.

3 Results and Discussion

In order to check the instrumentation, a few tests were first run on a straight duct 1.2 m (4 ft) long, provided with pressure taps as well as thermocouples, one each at the inlet and the exit and at two other intermediate positions, 0.38 m (15 in.) apart from each other. Pressure drops were measured and the friction factors calculated at each Reynolds number in the range 1300-32,000, resulting in the graph shown in Fig. 5. The results have been compared with the graphic data given by Jones [16], applicable to rectangular ducts of aspect ratio 2:1. The data points agree reasonably with the predictions of Jones. A few data points were also obtained for comparison with heat transfer correlations in straight duct flow and are indicated in Fig. 7 as squares. They show that the instrumentation for friction factor and heat transfer used in the present experiment is reasonable.

The graph of measured pressures along the curved duct (Fig. 4*a*) shows that the pressure drops linearly along the duct. Further, the graphs (Fig. 4*b*) show that the difference in pressure between the outer radius and the inner radius is essentially the same, no matter at what station it is measured. Both these results indicate that the effect of entrance was confined to a very short section at the inlet and that the secondary flow was fully established all along the duct. Hence, it could be assumed that the flow was hydrodynamically fully developed.

The friction factors calculated from fully developed adiabatic flow data are shown in Fig. 5. For both the 12.7 cm and 17.8 cm (5.0 in. and 7.0 in.) helices, very nearly the same values were obtained within the limits of experimental accuracy. For the 22.9 cm (9.0 in.) duct, the friction factor data fall between those of the straight duct and those of the other two ducts. The values for all the curved ducts are above those of straight ducts by 20-100 percent, depending upon the duct size and the Reynolds number. The 12.7 cm and 17.8 cm ducts exhibit friction factors which are about 30 percent larger, while the 22.9 cm duct exhibits increases of about 20 percent above those of a straight duct, both for small Reynolds numbers (Re = 850) and for large Reynolds numbers (Re > 10,000). What is interesting is that while there exists a clearly discernible transition between laminar and turbulent flows in a straight duct, no such sharp transition exists in the curved duct. The friction factors change gradually with increasing Reynolds numbers, so that it is impossible to tell by looking at the friction factor curve where laminar flow ends and where turbulent flow begins. This is the region which is dominated by secondary flow effects. These curves are similar to those of Johnson and Morris obtained from pressure measurements in a circular duct rotating about a parallel axis [17]. In that test, air was passed through the duct without heating and the friction factors caused by entrance effects were measured. The curves of friction factors plotted against Reynolds numbers look much like the curves for friction factors presented in Fig. 5, except that they vary with distance from the inlet. Johnson and Morris observe that there is no "dip" in the friction factor-Reynolds number relationship which is characteristic of stationary straight tubes.

Rayleigh [18] has shown that flows with curved streamlines are stable if the circulation increases with radial distance from the center of curvature. Otherwise, the flow will become unstable. Assuming the Rayleigh criterion to hold in the present case, the flow may be expected to become unstable near one wall of the duct and to be stable near the other wall. Also, Kelleher et al. [23] have performed measurements and flow visualization experiments in a curved rectangular channel. From their data, it can be seen that flow disturbances exist at the inner wall even below Re = 800 (Dean No. = 140). In addition, if one assumes in a simple-minded way that the secondary flow near the walls is of the boundary-layer type (Mori and Nakayama [5]), it is likely to be unstable in the area where it faces an adverse pressure gradient. Similarly, it is likely to be stable in the area where the pressure gradient is favorable. Hence, once secondary flow is established, there may exist a range of Reynolds numbers where the secondary vortices dominate and maintain laminar flow over part of the cross section and turbulent flow over the remaining part. With

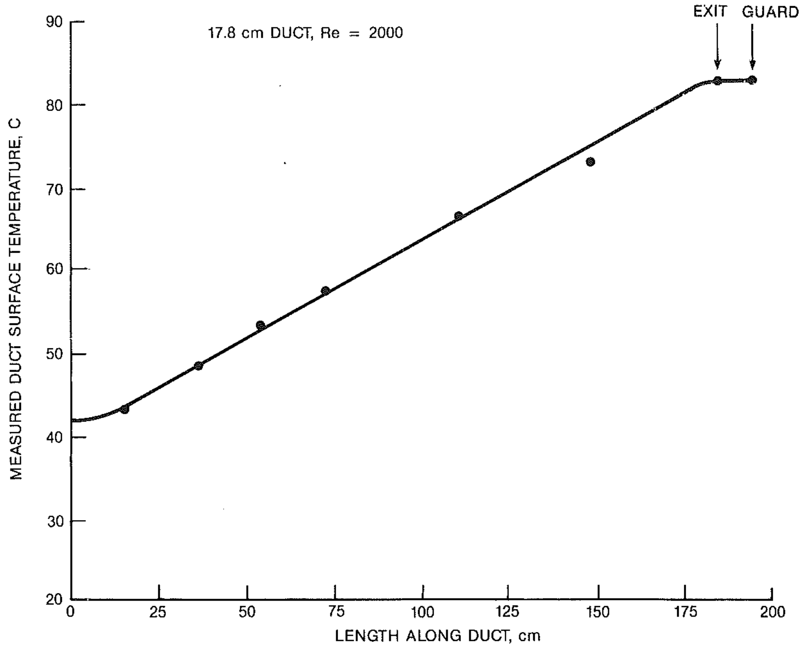

Fig. 6 Temperature variation along the duct

increasing Reynolds numbers, it is conceivable that the character of the flow changes gradually, until turbulence is reached all over the cross section. This could result in the behavior that is exhibited in Fig. 5. Further experimentation along with flow visualization is necessary to determine the flow pattern in the duct, before the reasons for the observed variation in friction factors are known. At any Reynolds number, the secondary vortices tend to increase the friction factor as compared with that in a straight tube, due to the increased length of fluid path in the duct.

Srinivasan et al. [15] have established empirical correlations for predicting the critical Reynolds number and turbulent friction factors in coiled circular tube flow as given by the equations:

$$\mathrm{Re}_{\mathrm{crit}} = 2100[1 + 12(d/D)^{0.5}] \tag{1a}$$

$$f(D/d)^{0.5} = 0.336[\mathrm{Re}(d/D)^2]^{-0.2} \tag{1b}$$

where

Re = Reynolds number based on tube diameter
$\mathrm{Re}_{\mathrm{crit}}$ = critical Reynolds number
f = friction factor

Here, d is the tube diameter while D is the helix mean diameter. A plot of equation (1a) (using the hydraulic diameter in place of d) is also shown in Fig. 5 as a dashed line, for comparison with the present data. For both the 12.7 cm and 17.8 cm helices, essentially the same line is obtained, since the dependence of friction factor on the helix diameter in the above equation is not strong enough to show up in the plot. For Reynolds numbers above 8000, the agreement of this equation with the present data is excellent. For smaller Reynolds numbers, the rectangular duct data show a higher friction factor than circular tube data.

During the heat transfer tests, because of constancy of generated energy flux at the surface and good insulation around the duct, the axial variation in wall temperature was nearly linear over a very large portion of the duct length. The differences in thermocouple readings around the duct at any axial location never exceeded 0.6°C, so that they were averaged to obtain the duct wall temperature at the location. A typical temperature profile obtained with the 17.8 cm (7.5 in.) duct at a Reynolds number of 2000 is indicated in Fig. 6. At the inlet and the exit sections where guard heating was employed, the temperature gradients are nearly zero.

By knowing the energy input, the losses through the insulation at various temperatures and the axial energy conduction, an energy balance was carried out to determine if the energy transferred to the air was equal to the net energy transfer at the duct walls. For all the data reported, the energy balance was correct within 10 percent. Finally, the heat transfer coefficient and the Nusselt number were calculated from a knowledge of air temperatures and the surface temperatures by using the logarithmic mean temperature difference. The results applicable to the middle duct section where the end effects were considered as negligible are exhibited in Fig. 7. Again, these may be expected to apply in fully developed flow, since very little variation in heat transfer coefficient was noticed among the middle three sections.

In analogy with the behavior of friction factor, one should expect the Nusselt number at very small Reynolds numbers to approach the value of 2.88, which applies to a stationary straight rectangular duct of aspect ratio 2. Even though the points indicate that they approach this value at Reynolds numbers below 1000, it is likely that free-convection effects in the curved duct have influenced the data resulting in lower heat transfer coefficients than would occur with purely forced flow. A rough estimate of the effect of free convection due to duct orientation indicates that its influence is such as to oppose the main flow and its magnitude is comparable with that of forced convection at low Reynolds numbers. Above a Reynolds number of about 1200, free-convection effects are quite small and the data presented can be considered as realistic. Based on an error analysis, experimental uncertainties have been estimated as ±2 percent in Reynolds numbers and ±9 percent in Nusselt numbers. The heat transfer coefficient first rises rapidly with increasing Reynolds numbers between 1200 and 2500 and then, more gradually, for Reynolds numbers above 2500. In fully developed turbulent flow the Nusselt number becomes 10–20 percent higher than for straight duct flow [20, 21]. Like friction factors, the heat transfer coefficients too are higher than for straight tubes at all Reynolds numbers by amounts varying between 10–300 percent, the largest differences occurring between Reynolds numbers of 1200 and 2500.

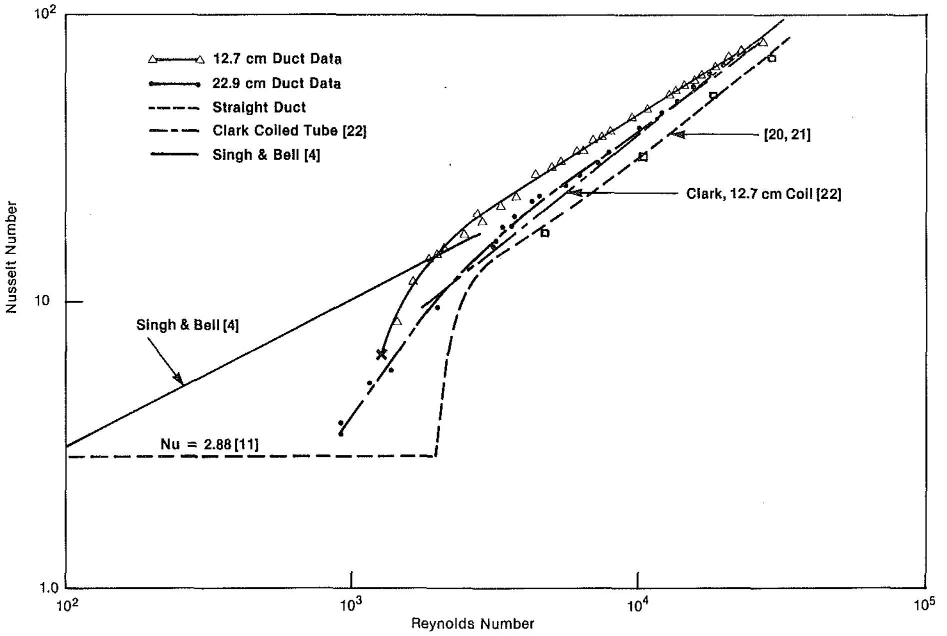

Fig. 7 Variation of Nusselt number with Reynolds number

Singh and Bell [4] have obtained data on circular curved tubes ($0.024 < d/D < 0.05$) and have correlated them in the range $70 < \mathrm{Re} < 7000$ by the expression

$$\mathrm{Nu}_c = [0.224 + 1.369(d/D)][\mathrm{Re}^{(0.501 + 0.318(d/D))}]\mathrm{Pr}^{(1/3)} \tag{2}$$

where

d = tube diameter
D = coil diameter
Nu_c = Nusselt number for the coiled tube
Pr = Prandtl number of the fluid flowing through the duct

A plot of this equation for air ($\mathrm{Pr} = 0.7$) is shown in Fig. 7. What is surprising here is that at very small Reynolds numbers, Singh and Bell's data do not seem to show a tail leading asymptotically to the straight tube result which is well known to be around 3.46 for circular tubes. Also, there is no pronounced change in the heat transfer coefficients due to transition, as presently observed for rectangular ducts. These differences may be due to the different fluids used in the two cases: All of Singh and Bell's data apply to liquids of relatively high Prandtl number ($3.46 < \mathrm{Pr} < 5.4$), while the present data apply to air. Some recent data for water flow obtained by the present authors and not exhibited here seem to agree with Singh and Bell's correlation better.

A comparison of the present data with the correlation of Clark [22] obtained by a regression analysis of several data points is also shown in Fig. 7. Clark's equation is

$$\mathrm{Nu}_c/\mathrm{Nu}_s = 1.0 + 2.12(d/D)^{0.731} \tag{3}$$

where

$$\mathrm{Nu}_s = 0.023\mathrm{Re}^{0.8}\mathrm{Pr}^{0.4}$$

is the Dittus-Boelter correlation applicable to straight tube heat transfer. Equation (3) applies in turbulent flow and agrees reasonably with the present data for Reynolds numbers above 5000. For smaller Reynolds numbers, the agreement is not good. This is probably due to differences in geometry as well as due to transition effects which are different between tubes and rectangular ducts. As already seen, friction factors for coiled circular tubes and rectangular ducts are not the same in the region where secondary flow effects dominate. In this range of Reynolds numbers, therefore, it is not surprising that the heat transfer data do not agree well with those of circular tubes.

Pressure drop measurements were also made for flow with heat transfer, for comparison with adiabatic flow results. Because of low thermal fluxes and temperature differences, negligible changes in friction factors were noticed with and without heat transfer. Hence, friction factor data with heat transfer have not been separately presented.

Curve fits have been obtained for friction-factor and heat transfer, applicable to all the ducts. The friction factor correlation curve chosen as an asymptote to the laminar duct data at low Reynolds numbers and an asymptote to Srinivasan's correlation at high Reynolds numbers is given by

$$f = [(62.2/\mathrm{Re} + C_1)^{e_1} + C_2/\mathrm{Re}^{e_2}]^{1/e_1} \tag{4}$$

where f is defined by the equation

$$f = 2g_c D\,\Delta p/(\rho l V^2) \tag{5}$$

Here

Δp = pressure drop in a duct of length l
ρ = density of fluid
g_c = dimensional constant

The rest of the quantities have the same significance as in the earlier equations. The quantities C_1, C_2, e_1, and e_2 are constants depending upon the duct diameters.

For the 12.7 cm and 17.8 cm mean diameter ducts

$$C_1 = 0.01; \qquad e_1 = 0.753$$

$$C_2 = 0.2364; \qquad e_2 = 0.1883$$

For the 22.9 cm mean diameter duct

$$C_1 = 0.0058; \qquad e_1 = 1.255$$

$$C_2 = 0.217; \qquad e_2 = 0.314$$

The correlations above are applicable only in the Reynolds number range $600 < \mathrm{Re} < 25{,}000$. Within this range, the correlations provide results with a root mean square error of 3.55 percent for the 12.7 cm and 17.8 cm ducts, and 4.44 percent for the 22.9 cm duct. The maximum errors are -8.62 percent for the 12.7 cm duct and -8.8 percent for the 22.9 cm duct.

The correlation applicable to heat transfer data is

$$\mathrm{Nu} = C_3\mathrm{Re}^{C_4}\mathrm{Pr}^{0.4} \tag{6}$$

Here again, C_3 and C_4 are constants, depending upon the helix mean diameters. For the 12.7 cm duct

$$C_3 = 0.1754; \quad C_4 = 0.6198$$

For the 22.9 cm duct

$$C_3 = 0.0592; \quad C_4 = 0.7227$$

This correlation is applicable in the Reynolds number range $3000 < \mathrm{Re} < 25{,}000$. The root mean square and maximum errors for the heat transfer correlations are respectively 2.65 percent and −7.82 percent for the 12.7 cm duct, while they are 2.94 percent and −7.2 percent for the 22.9 cm duct.

An appropriate correlation which is applicable to several ducts of differing hydraulic diameters and curvatures should involve the ratio d_h/D (hydraulic diameter/helix diameter) as a parameter. However, the above correlations do not contain such a parameter, since it was thought to be inappropriate to specify a general correlation based upon data from only three sets of experiments. The correlations provided in equations (4) and (6) apply only to the particular geometries for which they have been obtained and should not be construed as being of general applicability or to hold outside the range of Reynolds numbers specified above.

It appears from the above that one can obtain very large increments in heat transfer as compared with those of straight ducts, if the flow can be maintained at Reynolds numbers of about 1800, with a curvature corresponding to that of the 12.7 cm (5.0 in.) helix. The penalty in increased frictional pressure drop is not large, as compared with the increase in heat transfer. It may be possible to utilize this fact to design heat exchangers with improved performance.

4 Conclusions

1 Experimental data obtained on curved rectangular ducts show that there is no well-defined transition point between laminar and turbulent flows. There exists an extended range of Reynolds numbers over which the friction factor changes gradually under the influence of secondary vortices, until fully developed turbulent flow is reached. At large Reynolds numbers, the present results agree quite well with circular tube data.

2 The friction factors are higher than those of a straight duct by amounts ranging between 20 and 100 percent, depending upon the Reynolds number and duct curvature. The largest differences occur below a Reynolds number of about 3000.

3 For Reynolds numbers above 5000, the present heat transfer data agree reasonably with those of coiled circular tubes. In this range, the Nusselt numbers are above those of straight tube values by about 13-20 percent.

4 At Reynolds numbers between 1200 and 5000, the present heat transfer data differ considerably from those of straight tubes as well as those of coiled circular tubes. Overall, the curved duct heat transfer coefficients exceed those of straight ducts by magnitudes ranging from 20 to 300 percent, depending upon the Reynolds number and the helix diameter.

Acknowledgments

The authors would like to express sincere thanks to Mr. Steve Brzozowski, who helped in the design of the apparatus and especially to Mr. Karl Hardcastle, without whose diligent efforts this work would not have been completed. Mr. Hardcastle undertook the painful task of making all the connections, checking for leaks and put in such other effort as was necessary to make the experiment a success.

The authors are also grateful to the National Science Foundation, Washington, D.C., for providing partial funding for this research, under grant MEA-7923751.

References

1 Trefethen, L., "Fluid Flow in Radial Rotating Tubes," *Proc. IX Congres Int. Meca. Appli.*, Univ. Bruxelles, 1957, Vol. II, pp. 341-350.

2 Pratap, V. S., and Spalding, D. B., "Numerical Computations of the Flow in Curved Ducts," *Aero. Quart.*, Vol. 26, 1975, pp. 219-228.

3 Rao, K. V., "Secondary Flow in a Curved Channel as Revealed by a Laser-Doppler Anemometer," *Proc. LDA Symp.*, Copenhagen, 1975, pp. 710-718.

4 Singh, S. P. N., and Bell, K. H., "Laminar Flow Heat Transfer in a Helically Coiled Tube," *Fifth Int. Heat Trans. Conf.*, Tokyo, Vol. 2, Pap. FC5.3, 1974, pp. 193-197.

5 Mori, T., and Nakayama, W., "Study on Forced Convection Heat Transfer in Curved Pipes," *Int. J. Heat Mass Trans.*, Vol. 8, 1965, pp. 67-82.

6 Mori, T., and Nakayama, W., "Study on Forced Convective Heat Transfer in Curved Pipes," *Int. J. Heat Mass Trans.*, Vol. 10, 1967, pp. 37-59.

7 Humphrey, J. A. C., Whitelaw, J. H., and Yee, G., "Turbulent Flow in a Square Duct With Strong Curvature," *J. Fluid Mech.*, Vol. 103, 1981, pp. 443-463.

8 Melling, A., and Whitelaw, J. H ., "Turbulent Flow in a Rectangular Duct," *J. Fluid Mech.*, Vol. 78, 1976, pp. 289-315.

9 Chang, S. M., Humphrey, J. A. C., and Modavi, A., "Turbulent Flow in a Strongly Curved U-Bend and Downstream Tangent of Square Cross-sections," Rep. No. FM-82-1, Dept. Mech. Engg., Univ. California, Berkeley, Oct. 1982.

10 Buggeln, R. C., Briley, W. R., and McDonald, H., "Computation of Laminar and Turbulent Flow in Curved Ducts, Channels and Pipes Using the Navier-Stokes Equations," Rep. No. R80-920006-F, Office of Naval Research, Dec. 1980.

11 Neti, S., Warnock, A. S., Levy, E. K., and Kannan, K. S., "Computation of Laminar Heat Transfer in Rotating Rectangular Ducts," presented at National Heat Transfer Conference, Seattle, WA, 1983.

12 Cheng, K. C., and Akiyama, M., "Laminar Forced Convection Heat Transfer in Curved Rectangular Channels," *Int. J. Heat Mass Trans.*, Vol. 13, 1970, pp. 471-490.

13 Mori, Y., Uchida, Y., and Ukon, T., "Forced Convective Heat Transfer in a Curved Channel With a Square Cross-section," *Int. J. Heat Mass Trans.*, Vol. 14, 1971, pp. 1787-1805.

14 Srinivasan, P. S., Nandapurkar, S. S., and Holland, F. A., "Pressure Drop and Heat Transfer in Coils," *Chem. Engr.*, London, No. 218, 1968, pp. CE113-119.

15 Srinivasan, P. S., Nandapurkar, S. S., and Holland, F. A., "Friction Factors for Coils," *Trans. Inst. Chem. Engrs.*, Vol. 48, 1970, pp. T156-161.

16 Jones, O. C., "An Improvement in the Calculation of Turbulent Friction in Rectangular Ducts," *J. Fluids Engg.*, Vol. 98, June 1976, pp. 173-181.

17 Johnson, R. A., and Morris, W. D., "Pressure Loss Measurements in Circular Tubes Which Rotate About a Parallel Axis," XIV ICMHT Symp. Heat Mass Trans. Rot. Mach., Dubrovnik, Aug. 30-Sept. 3, 1982.

18 Lord Rayleigh, "On the Dynamics of Revolving Fluids," *Proc. Roy. Soc., London*, Series A, Vol. 93, 1916, pp. 148-154.

19 Sparrow, E. M., Hixon, C. W., and Shavit, G., "Experiments on Laminar Flow Development in Rectangular Ducts," ASME *Journal of Basic Engineering*, Mar. 1967, pp. 116-124.

20 Notter, R. H., and Sleicher, C. A., "A Solution to the Turbulent Graetz Problem—III: Fully Developed and Entry Region Heat Transfer Rates," *Chem. Engg. Sci.*, Vol. 27, 1972, pp. 2073-2093.

21 Kadambi, V., "Forced Convection in Circular Tubes," TIS Rep. No. 80CRD252, General Electric Co., Schenectady, Oct. 1980.

22 Clark, J. W. G., "Heat Transfer in Coiled Tubes," ICI Rep. No. CL-B, Res. Note. JWGC/74/9, 1974.

23 Kelleher, M. D., Flentie, D. L., and McKee, R. J., "An Experimental Study of the Secondary Flow in a Curved Rectangular Channel," ASME *Journal of Fluids Engineering*, Vol. 102, No. 1, Mar. 1980, pp. 92-96.

24 Yee, G., Chilukuri, R., and Humphrey, J. A. C., "Developing Flow and Heat Transfer in Strongly Curved Ducts of Rectangular Cross-Section," ASME JOURNAL OF HEAT TRANSFER, Vol. 102, May 1980, pp. 285-291.

E. Levy
Mem. ASME

S. Neti
Mem. ASME

G. Brown

F. Bayat

Energy Research Center,
Lehigh University,
Bethlehem, PA

V. Kadambi
GE Corporate R&D,
Schenectady, NY
Assoc. Mem. ASME

Laminar Heat Transfer and Pressure Drop in a Rectangular Duct Rotating About a Parallel Axis

Experimental results were obtained on pressure drop and heat transfer in a laminar flow of air in a rotating heated rectangular duct. The duct had a 2 to 1 aspect ratio, and was parallel to, but displaced from, the rotor axis. Data presented on Nusselt number in the inlet region and dimensionless pressure drop in the inlet and fully developed regions were found to be in close agreement with numerical finite difference solutions to the laminar flow equations. Laminar heat transfer and pressure drop are strongly affected by rotation, beginning to increase for values of Grashof number in excess of 10^3. For a Grashof number of 10^6, the Nusselt number is approximately twice the value of that in a flow with zero Grashof number. The effect of rotation on dimensionless pressure drop is smaller, with increases of the order of 35 percent occurring from $Gr = 0$ to 10^6.

Introduction

Cooling passages are frequently used in the rotor windings of large high-performamce electrical generators to allow for increased electrical and magnetic loadings. In some of these designs, a major portion of a typical rotor cooling circuit involves flow channels which are parallel to, but displaced from, the rotor axis (Fig. 1). In such a geometry, the density gradients caused by the heated wall interact with the centrifugal acceleration to cause flows in the lateral plane. The cooler and more dense fluid in the core flows radially outward while the warmer fluid near the walls flows inward toward the axis of rotation. In addition, Coriolis accelerations induced by the transverse velocity components lead to further adjustments in the flow patterns.

The effects of rotation on the axial development of laminar flow of air in a heated rectangular duct with a 2 to 1 aspect ratio are illustrated in Fig. 2, where the arrows represent the velocity vectors in the transverse plane. These solutions, shown here for one half of the duct, where obtained by a numerical finite difference procedure [1]. The inlet velocity and temperature profiles were uniform and the duct was heated uniformly around its circumference and along its length. For the case illustrated in Fig. 2, $Re = 1800$, $Gr = 3.5 \times 10^5$, and $Ro = 0.067$. At the inlet, the flow develops as a classical boundary layer, where all the transverse velocities are directed toward the center of the duct. As the fluid reaches a nondimensional axial distance $Z^* \sim 0.005$, the effects of the body forces start to dominate, resulting in a reorganization of the transverse flow patterns. Further downstream, the flow exhibits a typical mixed convection behavior with the fluid rising along the hot wall against the body force. The effects of these secondary flows on the axial variation of Nusselt number are shown in Fig. 3 (see Table 1). The bottom curve represents a duct flow with no centrifugal or Coriolis effects. Rotation increases Nusselt number both in the inlet and fully developed regions, with values of Gr in excess of 10^3 required to influence Nu.

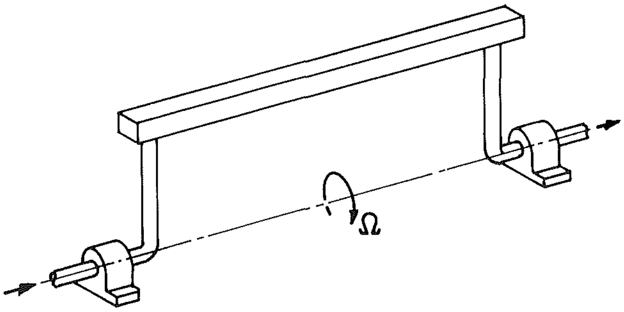

Fig. 1(*a*) Flow circuit with parallel rotating duct

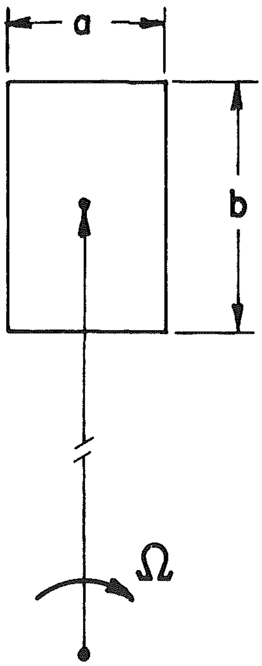

Fig. 1(*b*) Cross section of duct flow passage

Most investigations reported in the literature which are concerned with laminar flow in parallel rotating passages, deal with flows in circular pipes. These include theoretical solutions by Morris [2], Mori and Nakayama [3], Woods and Morris [4], and Skiadaressis and Spalding [5]. Experimental results on the effects of rotation on laminar heat transfer and pressure drop have been reported by Morris and Woods [6], Woods [7], Woods and Morris [8], Johnson and Morris [9], Morris [10], Davies and Morris [10], and Sakamoto and Fukui [10]. Research on laminar flow in square passages has been reported by Dias [11] and Morris and Dias [12].

The present paper describes a laboratory study of the effects

---

Contributed by the Heat Transfer Division for publication in the JOURNAL OF HEAT TRANSFER. Manuscript received by the Heat Transfer Division January 25, 1985.

of rotation on heat transfer and pressure drop for air flowing in a parallel axis duct with a rectangular cross section and a 2 to 1 aspect ratio. Experimental results are presented over a range of Reynolds numbers from 1500 to 2370 and Grashof numbers which extend to maximum values in excess of 10^6. Comparisons are made with the numerical finite difference solutions of [1].

Experimental Apparatus

The experiments were performed using the rotating duct facility shown in Fig. 4. This consists of a motor-driven shaft and rotor which drive a 76-mm-dia. by 1.7-m-long hollow tube located at a radius of 0.32 m from the axis of rotation. The tube, which is open at the ends, is used to hold the heated rectangular duct test section. The rotor is driven by a 30 kW variable speed d-c motor which is mounted on the base frame and connected to the rotor shaft by a timing belt. Rotor speed is measured by an induction-type tachometer. Tubes, electrical cables, thermocouple wires, and other connections from the test section are carried along the axis of the hollow rotor shaft. Tube connections for the working fluid are made through rotary couplings, one located at each end of the shaft. The inlet fluid coupling and power slip rings are located next to the drive belt. These rings and brushes transmit power to the heaters and transducer, and transmit the switching signals to the rotary solenoids. The rotating instrument package is located on the exhaust side of the rotor. This package contains the equipment for measuring and switching between various thermocouple and pressure lines. The output signals from these devices are transmitted through low-noise slip rings, made by LeBow Associates.

Air was supplied by house air compressors at 550 kPa pressure. The line from the compressors was connected to a pressure-regulated tank, which allowed the air pressure in the circuit to be varied and also aided in filtering out small pressure and flow variations caused by compressor cycling. After flowing from the tank, the air entered a chamber filled with desiccant, to remove water vapor. For the heat transfer experiments, air flow rate was measured using an orifice plate of standard ASME design [13]. A positive displacement flowmeter was used to measure flow rate for the pressure drop experiments.

Two different rectangular test sections, both with 2/1 aspect ratios, were used in this study. One, with a 3.18-mm hydraulic diameter, was used for the laminar pressure drop measurements; and the second, with a 10.53-mm hydraulic diameter, was used to obtain the laminar heat transfer data.

The test section used for the pressure drop measurements is shown in Fig. 5. This was machined from Type 315 stainless steel and was 1.5 m in length and 25 mm by 25 mm in outer cross section. The rectangular flow passage was 2.381 mm wide by 4.763 mm deep. The dimensions of the test section and apparatus needed for data analysis and comparison are summarized in Table 2.

Chromel-alumel thermocouple signal leads were inserted in holes drilled in the duct wall at 14 intervals along its length for measurement of axial variation of wall temperature. Thermocouples were also mounted in the inlet and exit passages to measure fluid inlet and exit temperature.

The duct was heated by electric thermofoil resistance heaters attached to the outer walls of the test section. The Kapton type strip heaters, manufactured by Minco Products, Inc., were each rated for 15 W at 208 V. Both sides of the heaters were coated with silicon conducting paste to smooth out hot spots. Thin 309 stainless steel strips were used to support each heater and assure good thermal contact with the duct wall. This prevented damage to the heaters and promoted uniform heat flux through the walls. The duct was insulated with cork pads layered over the stainless steel strips, arranged

Nomenclature

a = width of flow passage
A = cross-sectional area of duct flow passage
A_{duct} = cross-sectional area of duct wall
b = height of flow passage
C_p = specific heat of working fluid
D_H = hydraulic diameter
f = dimensionless pressure drop

$$= \frac{\left(\frac{dP}{dZ}\right) D_H}{\frac{1}{2}\rho_b(Z) w_b(Z)^2}$$

Gr = Grashof number

$$= \frac{\beta(Z)\left(\frac{q}{A}\right)_F H\Omega^2 D_H{}^4}{\nu(Z)^2 k(Z)}$$

H = radial distance from rotor axis to center of duct flow passage
k = fluid thermal conductivity
k_{duct} = thermal conductivity of duct wall
L = length of heated test section
$\dot{m}$ = flow rate of working fluid
P = pressure
Pr = Prandtl number
q_c = rate of heat transfer by conduction to elemental section of duct
Q_c = rate of heat transfer by conduction through ends of duct
q_∞ = rate of heat transfer from elemental sections of duct to ambient
Q_∞ = overall rate of heat transfer from test section to ambient
q_F = rate of heat transfer to working fluid in elemental section of duct
$\left(\frac{q}{A}\right)_F$ = rate of heat transfer per unit area to working fluid in elemental section of duct
Q_F = total rate of heat transfer to working fluid
q_H = power dissipated in heaters within elemental section of duct
Q_H = total power dissipated in heaters
R = gas constant
Re = Reynolds number

$$= \frac{w_b(Z) D_H}{\nu(Z)}$$

Ro = Rotation number

$$= \frac{\Omega D_H}{w_b}$$

T_b = fluid bulk temperature
T_∞ = ambient temperature
T = temperature
$\bar{T}_w$ = average wall temperature
U_i = overall heat loss coefficient from duct wall to surroundings
W_i = heat loss weighting coefficient
w = average axial velocity
Z = axial position
$Z^* = \frac{Z}{D\text{Re}}$
ΔZ = length of elemental section of duct
α = duct aspect ratio $= \frac{b}{a}$
β = coefficient of thermal expansion
Ω = angular velocity
ν = kinematic viscosity
ρ = fluid density

Subscripts

b = bulk
w = wall

to provide an equal thickness of insulation along the length of the duct. The cork was chosen because of its low weight and high insulation value.

The test section used for the heat transfer studies consisted of rigid copper-bronze 10.53-mm hydraulic diameter waveguide tubing, enclosed in a hollow micarta rod. The tubing was rectangular and 1.5 m long with 1.58-cm × 0.79-cm inside dimensions and a wall thickness of 1.02 mm (see Fig. 6).

This duct was also heated by electric thermofoil heaters attached to its four outer walls. The heaters on the side walls were each 90 mm long and were mounted with 11.4-mm gaps between them to provide room for wall thermocouples. Flat cement-on type thermcouples, 6.4 mm by 8.9 mm in size, were attached to the wall at 15 such positions along the length of the duct. Similarly the heaters on the top and bottom walls were positioned with 22.9-mm gaps between them to provide spaces for pressure taps. The high conductivity wall material (52 W/mK) established an axial conduction effect which helped to minimize problems of cold spots at the short unheated sections of the wall. For data analysis purposes, the power dissipated in the heaters was assumed to be distributed uniformly along the entire 1.4 m heated length of the duct.

A micarta rod was used to insulate the heated duct and to act as a supporting element for the wave guide tube. An increase in rotational speed produces high centrifugal forces, which would cause the wave guide tube to bend if left unsupported. Because of micarta's high mechanical properties, it is good supporting material. Micarta also has a low conductivity

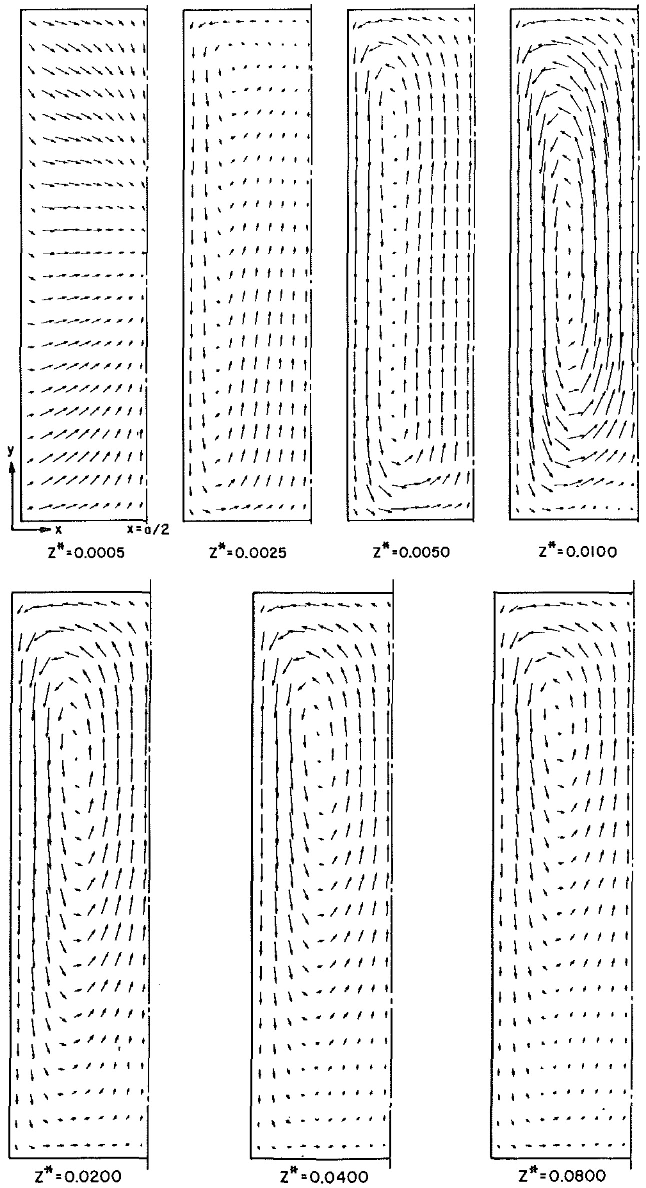

Fig. 2 Development of transverse flow patterns: Re = 1800, Ro = 0.066, Gr = 3.5 × 10^5, Pr = 0.7, α = 2.0 [1]

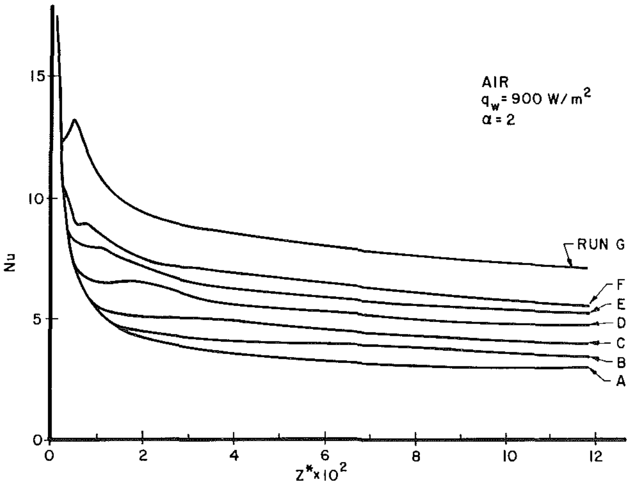

Fig. 3 Nusselt number variation along duct for different Gr (see Table 1)

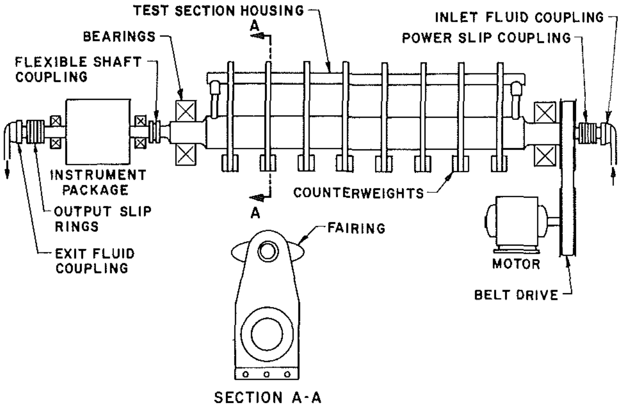

Fig. 4 Sketch of rotor with motor drive, instrument package, rotating couplings, and slip rings

Table 1 Tabulation of Gr, Re, and Ro at $Z^* = 0$ and $Z^* = 0.12$; $q_w = 900$ W/m^2

Run	Gr(0)	Gr(0.12)	Re(0)	Re(0.12)	Ro(0)	Ro(0.12)
A	0	0	2000	1800	0	0
B	6.3 × 10^4	2.1 × 10^4	500	450	0.082	0.066
C	1.6 × 10^5	5.4 × 10^4	250	225	0.26	0.21
D	6.4 × 10^5	2.25 × 10^5	500	450	0.26	0.21
E	1.6 × 10^6	5.5 × 10^5	1000	900	0.21	0.17
F	2.5 × 10^6	8.8 × 10^5	2000	1800	0.13	0.1
G	1 × 10^7	3.3 × 10^6	2000	1800	0.26	0.21

Table 2 Important dimensions of test sections (See Figs. 1, 5, and 6)

Hydraulic diameter	$D_H = 3.175$ mm	10.53 mm
Height of flow passage	$b = 4.763$ mm	15.8 mm
Width of flow passage	$a = 2.381$ mm	7.9 mm
Heated length of duct	$L = 1.5$ m	1.4 m
Distance from axis of rotation to duct centerline	$H = 0.32$ m	0.32 m

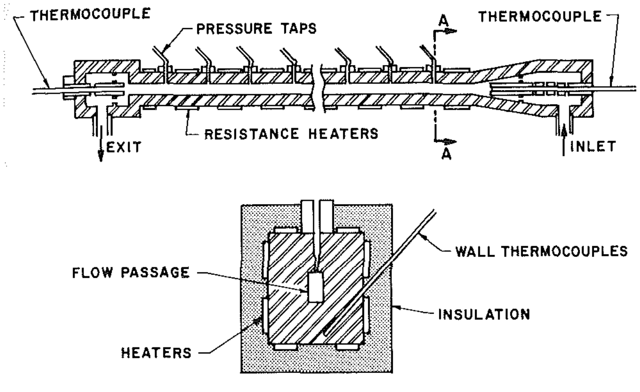

Fig. 5 Sketch of test section used for pressure drop measurements

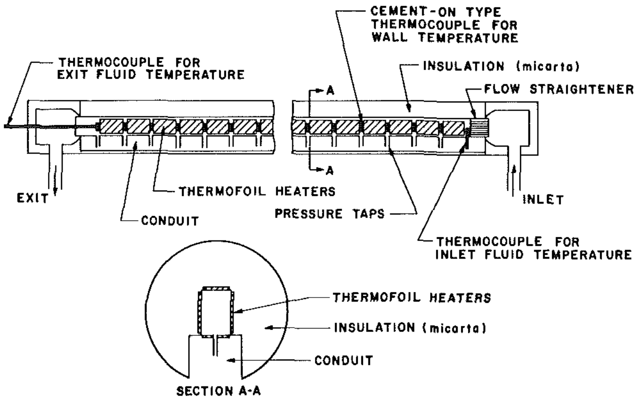

Fig. 6 Sketch of test section used for heat transfer measurements

which makes it possible to limit the heat loss to the ambient.

Three thermocouples were inserted in the air stream at the upstream end of the duct. These were located at different vertical positions across the flow passage and their average reading was used to indicate the inlet fluid temperature. Another thermocouple was mounted in the air stream at the downstream end of the duct. The sensing tip of this thermocouple was located at the center of the flow channel and was used to indicate outlet fluid temperature.

The wall and fluid thermocouples were connected to a rotary solenoid switch located inside the instrument package. This switch was used to select from among the different pairs of leads. The switch was advanced by applying a 2.5 A, 28 V d-c pulse through the power slip rings. One pair of thermocouple leads was then connected between the solenoid switch and the output slip rings, from which connections to a potentiometer were made for monitoring the thermocouple signals.

Static pressure taps, located along the lengths of the test sections, were used to measure axial variations in wall static pressure. The pressure signals were transmitted from the taps through teflon tubes connected to a solenoid driven fluid switch located in the instrument package. This fluid switch, manufactured by Scanivalve Corp., was activated by applying 1.5 A, 28 V d-c pulses through the slip rings connected to the solenoid leads. The output pressure tubing from the Scanivalve switch was connected to a Validyne Model DP7 pressure transducer, also located in the rotating instrument package. The transducer used a Validyne Model CD 16 miniature carrier demodulator to convert the electrical signal produced by the pressure differential to a linear d-c voltage. This signal was then measured across the output slip rings by a digital voltmeter. The transducer was mounted in an orientation such that the diaphragm sensing element was located in the rotational plane and was centered about the axis of rotation. This location minimizes diaphragm distortion caused by centrifugal acceleration.

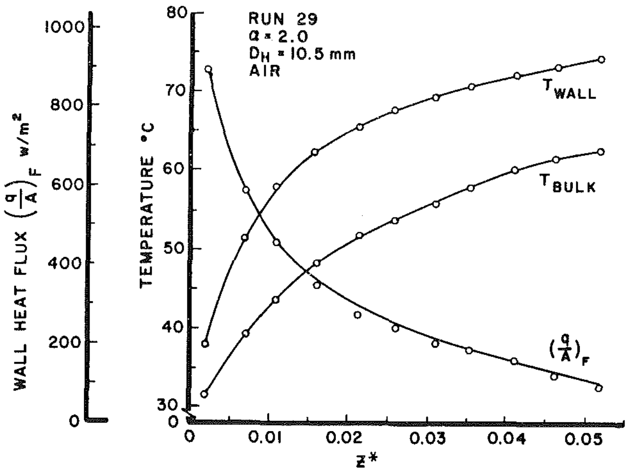

Fig. 7 Axial variations of temperatures and heat flux for run 29

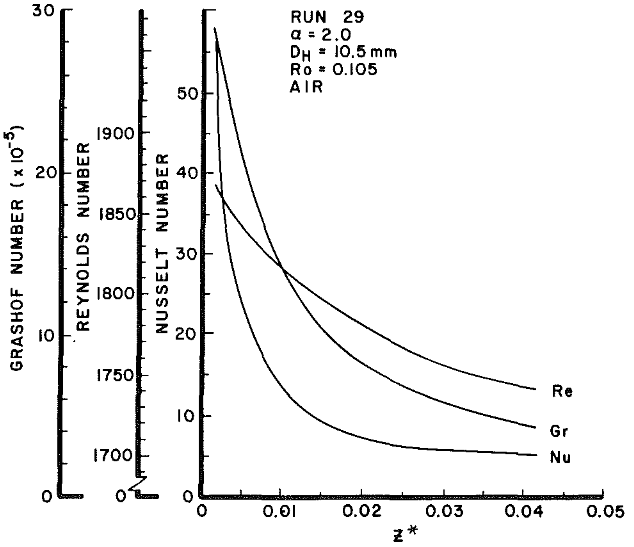

Fig. 8 Axial variations of Grashof, Reynolds, and Nusselt numbers for run 29

All of the heat transfer data were obtained with a flow straightener inserted in the inlet plenum of the 10.53-mm-dia duct. The flow straightener, fabricated from a bundle of 4-cm-long sections of 0.08-cm hypodermic tubing, was used to eliminate inlet swirl and provide controlled inlet flow conditions.

Data Analysis Procedure

To correlate the pressure drop and heat transfer results properly and relate pressure drop and Nusselt number to Grashof number, Reynolds number, and Z^*, information on *local fluid bulk temperature, wall temperature, and wall heat* flux is needed. For each run, the wall temperatures were recorded, as well as the entrance and exit fluid thermocouple

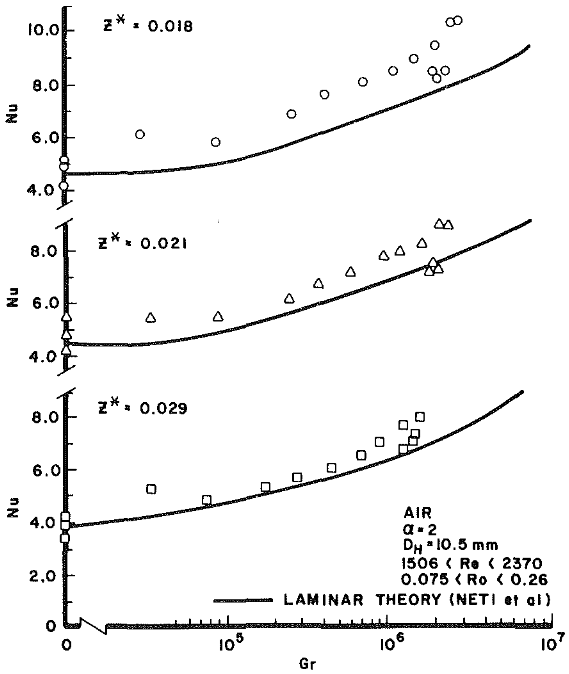

Fig. 9 Variation of Nusselt number with Grashof number in the inlet region

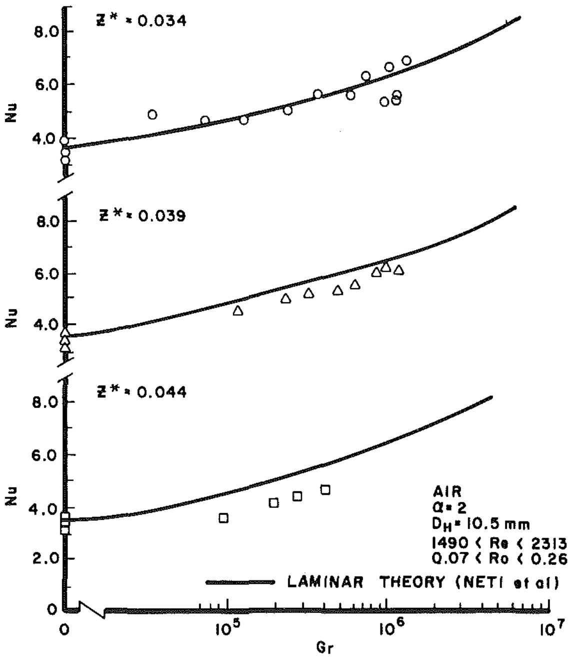

Fig. 10 Variation of Nusselt number with Grashof number in the inlet region

voltages, rotor speed, ambient temperature, heater voltage and power dissipation. In addition, the voltages produced by the pressure transducer (as it was switched between pressure taps), and the air flow rate were recorded. The pressure transducer was calibrated after every experimental run. The transducer calibration data were fitted with a linear least-squares curve and the equation for this line was used to convert the transducer voltage measurement into pressure measurements.

A fourth-degree least-squares polynominal curve was fitted to the wall temperature data and was used to calculate local wall temperatures as well as to obtain values for axial conduction through the test section wall. Energy balances for the entire duct and for small incremental lengths of duct were then computed to obtain the axial variation of bulk fluid temperature. In this procedure, the duct was divided into 16 equal sections, each centered about a thermocouple location. It was assumed that in each section the power dissipated in the heaters was transferred into the working fluid, conducted axially upstream or downstream through the duct walls, and conducted outward into the test section housing and from there to the surroundings.

Energy conducted axially was found by differentiating the fourth degree curve fit for wall temperature and evaluating it at the section boundaries. At any axial location Z

$$q_c(Z) = -[(k_{\mathrm{duct}}A_{\mathrm{duct}})]\frac{dT_w}{dZ} \tag{1}$$

Once the axial conduction was known, an energy balance was performed on the entire test section, exclusive of the inlet nozzle and exit plenum. The power dissipated in the heaters was equated to the sum of the rate of energy gained by the working fluid, conducted out of the duct ends, and transferred from the test section housing to the ambient according to the equation

$$Q_\infty = Q_H - Q_F - Q_C \tag{2}$$

which was then used to calculate Q_∞.

The rate of heat transfer to the surroundings from each of the 16 elemental sections was then found from

$$q_\infty = W_i U_i \Delta Z(T_w(Z) - T_\infty) \tag{3}$$

where U_i, the overall heat loss coefficient, is

$$U_i = \frac{Q_\infty}{(\bar{T}_w - T_\infty)L} \tag{4}$$

$\bar{T}_w$ = average wall temperature
L = length of heated heat section

and

W_i = heat loss weighting coefficient

The weighting coefficient W_i was used to account for nonuniform thermal resistance between the heaters and the surroundings along the length of the duct due to differences in thickness of thermal insulation. The value for W_i was found for each element through a calibration procedure performed when the duct was heated to steady-state conditions and rotated without flow of working fluid through the passage. Evaluation of these constants shows that they ranged from 0.9 to 1.10 for the 3.18-mm-dia duct and were 1.0 for the 10.53-mm duct.

Once q_∞ was found for each element volume, an energy balance was performed on each to give the energy gained by the fluid in that volume

$$q_F = q_H - q_\infty - q_C \tag{5}$$

The rise in bulk temperature of the working fluid for each element was then found from

$$\Delta T_{bi} = \frac{q_F}{\dot{m}c_p} \tag{6}$$

In the case of the pressure drop experiments performed in the 3.18-mm-dia duct, the inlet bulk temperature of the fluid was measured with a thermocouple located 0.6 cm upstream of the actual inlet to the test section. Calculations were performed to correct the inlet fluid temperature for heat transfer to the working fluid between the location of the thermocouple and the actual inlet to the test section. See [16, 17] for the details of the calculation procedure.

Local values of air density and average fluid velocity were then found as follows:

$$\rho_b(Z) = P(Z)/RT_b(Z) \tag{7}$$

$$w_b(Z) = \dot{m}/\rho(Z)A \tag{8}$$

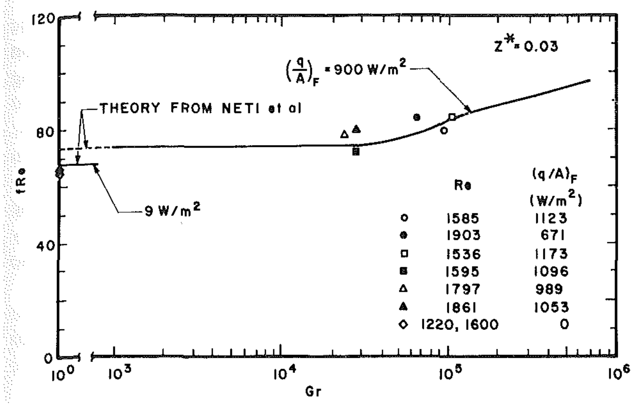

Fig. 11 Variation of dimensionless pressure drop with Grashof number at $Z^* = 0.03$

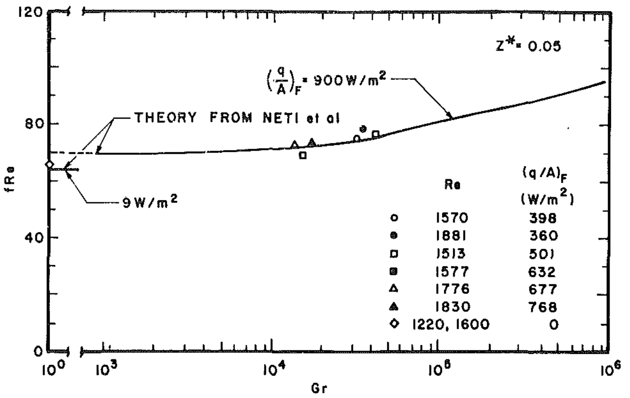

Fig. 12 Variation of dimensionless pressure drop with Grashof number at $Z^* = 0.05$

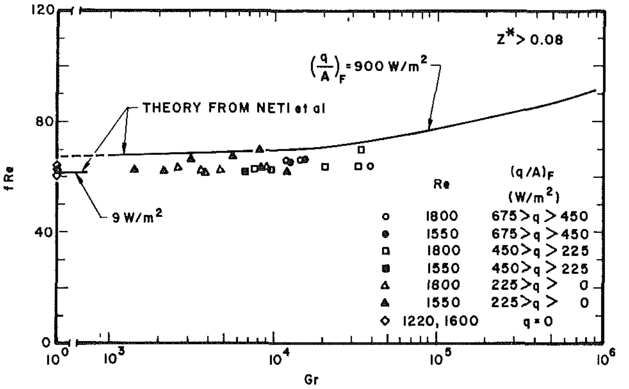

Fig. 13 Variation of dimensionless pressure drop with Grashof number for $Z^* > 0.08$

The local dimensionless pressure drop f, Nu, Gr, and Re were computed as shown below

$$f = \frac{\left(\frac{dP}{dZ}\right) D_H}{\frac{1}{2}\rho_b(Z) w_b(Z)^2} \qquad \mathrm{Nu} = \frac{\left(\frac{q}{A}\right)_F \frac{D_H}{k}}{[T_w(Z) - T_b(Z)]}$$

$$\mathrm{Re} = \frac{w_b(Z) D_H}{\nu(Z)} \qquad \mathrm{Gr} = \frac{\beta(Z)\left(\frac{q}{A}\right)_F H\Omega^2 D_H{}^4}{\nu(Z)^2 k(Z)}$$

where values of dP/dZ were obtained by differentiating a curve fit to the measured axial variation in wall static pressure. The form of the Grashof number used here is similar to that for a constant heat flux wall, except that $H\Omega^2$ has been substituted for g, the acceleration due to gravity.

Theoretical Solutions for Uniform Wall Heat Flux

In this paper, the experimental results are compared with the theoretical solutions of [1]. The procedure used to obtain those uniform wall heat flux results involved the numerical finite difference solution of the three momentum equations, continuity, the energy equation, and the equation of state for the fluid. Both Coriolis and buoyancy terms were included in the momentum equations, but the axial diffusion terms in the momentum and energy equations were ignored. To account for axial variations in bulk fluid temperature and fluid properties, the properties were allowed to vary in the axial direction with T_b where the local bulk temperature T_b was obtained from the uniform wall heat flux condition. Transverse variations of flow properties were not accounted for in this analysis except as they occur in the buoyancy term in the momentum equation. The analysis assumed both uniform velocity and temperature profiles at the duct inlet. The wall heat flux was held constant both in the circumferential and axial directions. The solution procedure involved a marching technique to calculate the sequential development of the flow along its primary direction. More specific details of this procedure are given in [1].

Discussion of Experimental Results

Shown in Fig. 7 for a typical heat transfer test run with the 10.53-mm-dia test section are the axial variations of wall temperature, bulk fluid temperature, and local heat flux to the fluid $(q/A)_F$. For the same run, Fig. 8 gives the corresponding axial variations of Reynolds number, Nusselt number, and Grashof number. The Reynolds number varies along the length of the duct due to the axial variation in viscosity caused by the heating of the working fluid. The axial variation in Grashof number is due, in part, to changes in fluid properties with heating. In addition, Gr is directly proportional to the local heat flux to the fluid $(q/A)_F$ and as illustrated in Fig. 7, this varied over the length of the duct in the experiments.

Similar experiments were carried out over a range of inlet flow conditions, wall heat fluxes, and speeds of rotation to achieve experimental values of Nusselt number for Grashof numbers from 10^5 to 10^7 and Reynolds numbers from 1500 to 2370. The conditions for the pressure drop experiments covered the range of Re from 1500 to 1900 and Gr to 10^5.

In the inlet region, the Nusselt number and dimensionless pressure drop are influenced by flow development and rotational effects. The theoretical results taken from [1] are based on a wall heat flux which is constant in both the circumferential and axial directions. In the experiments, the wall heat flux varied circumferentially in some unknown way due to wall conduction. No attempt was made to account for this in the data analysis. Instead average circumferential values of heat flux were used for computing Nusselt number. More importantly, the heat flux also varied along the length of the test section due to heat losses to the surroundings and axial conduction. This is accounted for in the data analysis procedure described in equations (1)-(6).

To make it possible to compare constant heat flux theoretical solutions to experimental data with axially varying heat flux, local comparisons were made between the theoretical and experimental values, where conditions of comparable Gr and Z^* were used. The results of this comparison are shown in Figs. 9 through 13 as plots of dimensionless pressure drop and Nusselt number versus Gr for values of constant Z^*. The points are from the measurements and the solid lines are from the numerical finite difference analysis [1]. The flow is in the entrance region for most of the values of Z^*

shown here, approaching fully developed flow for Z^* in excess of 0.08.

Heat transfer data obtained in the range of Grashof numbers from 10^5 to 10^7 are in good agreement with the theoretical solutions. These show increases in Nusselt number of the order of 100 percent as the Grashof number extends to 10^7 (Figs. 9 and 10). The theoretical solutions of [1] show that values of Grashof number in excess of 10^3 are needed to influence the Nusselt number. However it was not possible to verify this experimentally because the experimental Grashof numbers were too high.

The results for pressure drop are summarized in Figs. 11-13. Two different theoretical solutions (the solid lines) are given in each graph, representing the limiting cases of very low wall heat flux and a relatively high heat flux of 900 W/M^2. Using this comparison technique, the results show good agreement between the measurements and theory. Rotation increases pressure drop in both the inlet and fully developed regions. The local Grashof number must be increased to a value in excess of 10^3 to have an influence on pressure drop. To achieve the same percentage increase in f, larger local values of Gr are required in the inlet region than are needed further downstream.

The experimental $f \cdot \mathrm{Re}$ values depend on measured values for pressure gradient, flow rate, temperature, pressure, and the duct dimensions. For the range of flow rates and test conditions shown here, an error propagation analysis indicated a relative uncertainty in $f \cdot \mathrm{Re}$ of 5 percent. In the case of the heat transfer measurements, the fraction of the power dissipated in the heaters which was transferred to the working fluid varied from 70 percent at the duct inlet to 10 percent at $Z^* \approx 0.05$. The corresponding uncertainties in Nusselt number were estimated to vary from 4 percent near the duct inlet to 11 percent at $Z^* \approx 0.04$. The estimated uncertainties indicated above are of the same order as the scatter in the measured values of Nu and $f \cdot \mathrm{Re}$.

Summary and Conclusions

Data are presented on the effects of rotation on heat transfer and pressure drop in a laminar flow of air in a heated rectangular duct with a 2 to 1 aspect ratio. The data for Nusselt number extend from Reynolds numbers of 1500 to 2370 and to Grashof numbers in excess of 10^6. The results on pressure drop extend from Re of 1500 to 1900 and Gr to 10^5. The pressure drop data are from both the inlet and fully developed regions. The results for Nusselt number cover only the inlet region. Both types of data are in good agreement with numerical finite difference solutions of Neti et al. [1].

Rotation increases both heat transfer and pressure drop but has an effect only for values of Gr in excess of 10^3. Increases in dimensionless pressure drop of 30 to 35 percent occur in the range from Gr of zero to 10^6. Heat transfer is much more sensitive to rotation than pressure drop. At a Grashof number of 10^6, the Nusselt number is approximately twice the value of that in a stationary duct.

There has been speculation in the literature concerning the effects of rotation on transition to turbulent flow. Johnson and Morris [9] performed isothermal experiments in a rotating circular tube and obtained pressure drop data which seem to show a continuous transition from laminar to turbulent flow. Similarly, Kadambi [14] presented results on pressure drop in a stationary curved rectangular duct which show transition beginning at Reynolds numbers below 1000 and extending smoothly and continuously to $\mathrm{Re} \sim 10{,}000$. Recent results by Garimella et al. [15] for stationary curved annular ducts also show the same trend.

Such effects were not found in the experiments carried out here. The data shown in Figs. 9-13 cover a range of Reynolds numbers from 1500 to 2370 and appear to be in agreement with the laminar theory over the entire range.

Acknowledgments

This study was supported by the National Science Foundation under Grant No. MEA 7923751.

References

1 Neti, S., Warnock, A., Levy, E., and Kannan, K., "Computation of Laminar Heat Transfer in Rotating Rectangular Ducts," ASME Journal of Heat Transfer, Vol. 107, Aug. 1985, pp. 575-582.

2 Morris, W. D., "Laminar Convection in a Heated Vertical Tube Rotating About a Parallel Axis," *Journal Fluid Mechanics*, Vol. 21, Part 3, 1965, p. 453.

3 Mori, Y., and Nakayama, W., "Forced Convective Heat Transfer in a Straight Pipe Rotating About a Parallel Axis (Laminar Region)," *Int. J. Heat Mass Transfer*, Vol. 10, 1967, p. 1179.

4 Woods, J. L., and Morris, W. D., "An Investigation of Laminar Flow in the Rotor Windings of Directly Cooled Electrical Machines," *J. Mech. Eng. Sci.*, Vol. 16, 1974, p. 408.

5 Skiadaressis, D., and Spalding, D. B., "Laminar Heat Transfer in a Pipe Rotating About a Parallel Axis," Imperial Coll. Science and Tech. Mech. Eng. Report, No. HTS/76/23, 1976.

6 Morris, W. D., and Woods, J. L., "Heat Transfer in the Entrance Region of Tubes That Rotate About a Parallel Axis," *J. Mech. Engineering Science*, Vol. 20, No. 6, 1978, p. 319.

7 Woods, J. L., "Heat Transfer and Flow Resistance in a Rotating Duct System," D. Phil. Thesis, University of Sussex, Falmer, England, 1975.

8 Woods, J. L., and Morris, W. D., "An Investigation of Laminar Flow in the Windings of Directly Cooled Electrical Machines," *J. Mech. Eng. Sci.*, Vol. 16, 1974, p. 408.

9 Johnson, A. R., and Morris, W. D., "Pressure Loss Measurements in Circular Ducts Which Rotate About a Parallel Axis," *Proceedings XIV ICHMT Symposium, Heat and Mass Transfer in Rotating Machinery*, Yugoslavia, 1982.

10 Morris, W. D., *Heat Transfer and Fluid Flow in Rotating Cooling Channels*, Research Studies Press, 1981.

11 Dias, F. M., "Heat Transfer and Resistance to Flow in Rotating Square Tubes," D. Phil. Thesis, University of Sussex, Falmar, England, 1978.

12 Morris, W. D., and Dias, F. M., "Laminar Heat Transfer in Square-Sectioned Ducts Which Rotate in the Parallel-Mode," *Power Ind. Res.*, Vol. 1, 1981.

13 Power Test Codes (PTC 19.5;4): *Flow Measurement*, ASME, New York.

14 Kadambi, V., "Heat Transfer and Pressure Drop in a Helically Coiled Rectangular Duct," ASME Paper No. 83-WA/HT-1, 1983.

15 Garimella, S., Christensen, R., and Richards, D., "Experimental Investigation of Heat Transfer in Curved Annular Ducts," ASME Paper No. 84-WA/HT-28, 1984.

16 Levy, E., Brown, G., Neti, S., and Kadambi, V., "Laminar Pressure Drop in a Heated Rectangular Duct Rotating About a Parallel Axis," ASME Paper No. 84-WA/HT-59, 1984.

17 Brown, G., "Heat Transfer and Pressure Drop in a Rotating Rectangular Duct," MS Thesis, Lehigh University, May 1984.

Local Heat Transfer From a Rotating Disk in an Impinging Round Jet

C. O. Popiel[1]

L. Boguslawski
Department of Working
Machines and Vehicles,
Technical University,
60965 Poznań,
ul. Piotrowo 3, Poland

The results of an experimental investigation of local convective heat transfer from the surface of a rotating disk in an impinging free round air jet, issuing from a long tube, are reported. Using a transient heat transfer method applied to the ring-shaped h-calorimeter (as a single lumped capacitance element) measurements of convective heat transfer rates were made for five impingement radius (fixed) to tube diameter ratios for a range of rotational and jet Reynolds numbers. In the pure impingement-dominated regime, where the rotation of the disk does not show an effect on heat transfer, the velocity ratio is $u_r/u_j \leq (1-2 \times 10^{-4}\, Re^{2/3})\ (1-0.18 \sqrt{r/d})$, *where* u_r = *tangential velocity of the disk at the jet impingement radius* r, u_j = *average exit velocity of jet, and* d = *jet tube diameter. In this regime, the local heat transfer on the rotating disk can be strongly enhanced by jet impingement. For* $u_r/u_j \gtrsim 5$, *the effect of the jet impingement on heat transfer can be neglected. The discussion of the heat transfer results has been supported by smoke flow visualization.*

Introduction

Jet impingement is very attractive as a means of intensifying convective processes and the heat or mass transfer distribution over a heated, cooled, or drying surface. Impinging jets can be applied to moving surfaces. They can produce very high local heat or mass transfer rates with minimal consumption of fluid.

The rotating disk induces on its surface an axisymmetric wall jet (pumped flow) which interacts with the impinging jet to produce a cross-flow effect, deforming the jet trajectories and consequently deforming the distribution of impingement heat transfer rates. This cross-flow effect is different from those described in, e.g., [1], where the cross flow velocity distribution beyond a stationary impinged plate was uniform, having only a thin boundary layer. On the surface of the rotating disk, the cross flow has a form of the three-dimensional axisymmetric wall jet [2, 3] having a strong circumferential component as well as radial and normal components of the velocity. The thickness of the wall jet can be expressed by formulas [2, 3]

in laminar region

$$\left(\mathrm{Re}_r = \frac{\omega r^2}{\nu} \leq 2 \times 10^5\right): \quad \delta_{\mathrm{lam}} = 3.7(\nu/\omega)^{0.5}$$

in turbulent region

$$(\mathrm{Re}_r \geq 2.5 \times 10^5): \quad \delta_{\mathrm{turb}} = 0.525 r(\nu/\omega r^2)^{0.2}$$

This means that the wall jet on the rotating disk is confined to a rather thin layer in comparison to the sizes of the most impingement jet geometries (see Fig. 1) which can be applied in practice (e.g., at the ratios of jet nozzle diameter to radius of gas turbine disk of roughly 0.02–0.04 and nozzle-to-disk spacing of 4–8).

In addition it is necessary to realize that a stationary jet impinging on the rotating disk at some radius produces, on its movable surface, periodic pulsations of the instantaneous heat transfer rates. For thick turbine disks, however, such variations do not have major practical significance and it is more interesting to study the mean heat transfer rates averaged over a circumference at given radius.

The heat or mass transfer data base related to jet impingement on stationary surfaces has quite a large literature, for instance reviewed by Martin [4], Udaev et al. [5], and recently by Dyban and Mazur [6]. Concerning moving surfaces, only a rotating disk in an impinging round jet has gained sufficient attention [7-13] because of its application in gas turbine cooling systems. The jet impingement of coolant is usually realized as a single or multiple jet directed normal to the surface of the rotating disk.

The early papers of Kuznetzov [7, 8] and Devyatov [9] present the effect of multiple jet impingement on convective heat transfer for a nonisothermal rotating disk which was shrouded with an insulated wall. The single round jets were distributed along one circle in the vicinity of a hub or at the disk rim. In all these experiments the heat transfer was strongly affected by jet impingement (for velocity ratios $u_r/u_j = 0.002$–1 in [7, 8] and $u_r/u_j = 0.3$–1.65 in [9]).

The study done by Metzger and Grochowsky [11] concerns measurements of the average convective heat transfer characteristics on the jet-side disk face. The transient heat transfer method was applied to the overall disk, correcting for effects of back-side convection and conduction losses through the disk shaft. The measurements were conducted with three

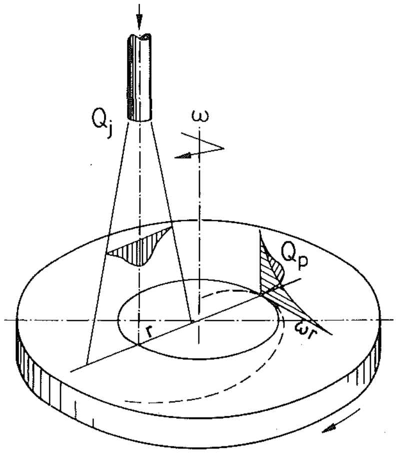

Fig. 1 Impinging jet on a rotating disk

---

[1] Present address: Heat Transfer Section, Institute of Environmental Engineering, Technical University, 60965 Poznań, ul. Piotrowo 3, Poland.

Contributed by the Heat Transfer Division for publication in the JOURNAL OF HEAT TRANSFER. Manuscript received by the Heat Transfer Division June 5, 1984.

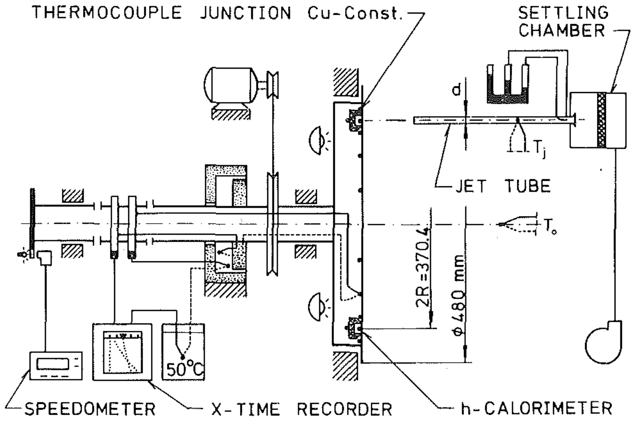

Fig. 2 Schematic diagram of apparatus

jet sizes and three disk diameters, while changing the jet flow rate, the radial impingement location, and the rotational disk speed. The uncertainty in the average Nusselt numbers was estimated to be ±12 percent. The heat transfer results were supported by smoke flow visualization showing points of flow regime transition which ought to be interpreted as the end of the rotation-dominated heat transfer zone. A graphic correlation of observed transition conditions was attained by utilizing the calculated values of rotationally induced wall jet (pumping) flow Q_p passing the impingement radius. This correlation, shown in terms of the ratio Q_j/Q_p versus Re_r, appears to be in the form of a rather wide band of points; for example, for the ratio $Q_j/Q_{p\text{-lam}} = 0.4$ the transition can occur in the range of Re_r from 10^4 to 10^5. All heat transfer measurements were done at laminar rotational Reynolds numbers. The subsequent paper of Metzger et al. [12] deals with the heat transfer behavior in the vicinity of the rotating disk rim convectively cooled by two round impinging jets. The authors notice that the disk face contour has little effect on heat transfer, either with or without impingement. The heat transfer rates are found to be relatively unaffected by impingement for single jet flowrates less than the order of 1/10 the disk turbulent pumping flow capability.

The measurements of local heat transfer were done by Bogdan [13] using the transient technique described in [14]. He found that the augmentation of the cooling process of the rotating disk with the impinging jet is due to two effects: free jet introduction of new amount of air of lower temperature into the disk-induced wall jet; and free jet promotion of turbulence in the disk induced laminar wall jet. His proposed correlation equations for the local Nusselt number in laminar and turbulent regions, however, do not show the effect of a ratio of the radius of impingement to the jet diameter which has been suggested in, e.g., [10] and the presence of which seems to be obvious. Moreover, his results were obtained on the nonisothermal surface of the disk; therefore, the uncertainty of these results must be high, even though the recorded data were corrected.

The main aim of this communication is to provide more detailed experimental results concerning local heat transfer on the isothermal surface of the rotating disk in an impinging round air jet. Some insight into the flow pattern was also achieved using smoke flow visualization.

Apparatus

A transient heat transfer method was used and the experimental procedure as well as test disk were identical to that described in [14]. A brief summary of the experimental procedure and apparatus will be repeated here.

Figure 2 shows schematically the main parts of the experimental equipment employed in the investigation. The test disk was attached to the end of a horizontal shaft and driven by a direct-current electric motor through a belt transmission. Continuous control of the disk speed was provided by the fine resistor in the thyristor motor power supply. The disk speed was monitored with a photoelectric transducer and digital speedometer. On the disk body, 480 mm in diameter, a ring-shaped h-calorimeter of 185.2 mm average radius and 20 mm width was mounted, with a 5 mm gap between them. The gap was filled with glass wool. The face surface of the disk and ring created a flat uniform surface having only a 0.4 mm gap, filled with dentist's cement. Both the disk and h-calorimeter were made of aluminum and their face surfaces were polished to reduce heat radiation.

A set of infrared lamps and a removable electric fan-heater were used to heat the disk to about 120°C. Copper-constantan thermocouples, 0.2 mm in diameter, were applied to measure the temperatures of the disk and the h-calorimeter. Impulses from the rotating thermocouple junctions were transmitted to a multichannel recorder via slip rings and a special compensation box.

The air jet issued from a tube having a minimum 20 d length. Five jet tubes, 9.65, 20.0, 36.8, 68.6, and 105.6 mm i.d., were used. The air jet mean velocity was measured at the bell-shaped tube inlet by means of a Pitot pipe, 1.3 mm o.d. The tube inlet was situated in a settling chamber to which air was supplied with a radial blower. The temperatures of the ambient and jet air during each run were equal and kept constant.

The disk body and the h-calorimeter were heated to approximately 100°C. Then the h-calorimeter was heated or cooled by a few degrees from the disk body temperature. Afterward the disk face was cooled down under the required flow conditions, i.e., rotating speed and jet parameters. Based on the recorded changes of the disk body and h-calorimeter temperatures, the measurement period was determined in

Nomenclature

A = h-calorimeter face area
c = specific heat
d = jet tube diameter
G = mass of h-calorimeter
h = local heat transfer coefficient
H = jet tube-to-disk spacing
k = fluid thermal conductivity
Nu_r = local Nusselt number = hr/k
Q_j = jet volumetric flow rate = $0.25\pi d^2 u_j$
Q_p = rotationally induced laminar wall jet flow (pumping flow) as given in [2] = $0.886\pi r\nu \mathrm{Re}_r^{1/2}$
r = impingement radial position
R = mean radius of the h-calorimeter
Re_j = jet Reynolds number = $u_j d/\nu$
Re_r = rotational Reynolds number = $\omega r^2/\nu$
T_0 = jet and ambient air temperature
T_1, T_2 = temperatures of the h-calorimeter at the beginning and end of a measurement period
u_j = average exit velocity of the jet
u_r = tangential velocity of the disk at the jet impingement radius = ωr
x = distance from jet tube centerline
$\Delta\tau$ = measurement period
ν = fluid kinematic viscosity
ω = angular velocity

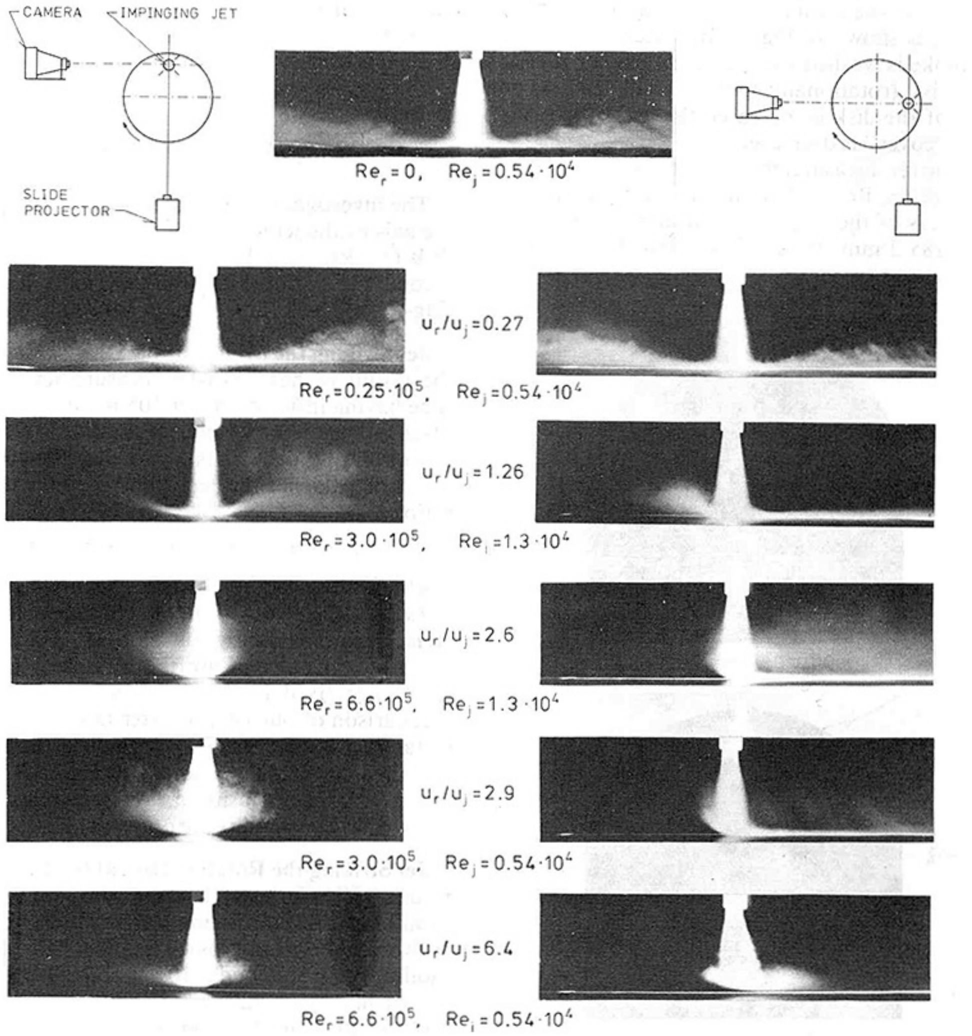

Fig. 3 Smoke visualization of a round jet impinging normally onto a rotating disk at $H/d = 5$ and $R/d = 19.2$

which the intersection of the mean temperatures of the disk body and h-calorimeter was contained. Equalization of those two temperatures caused the expected disappearance of heat losses and formed the model of the rotating isothermal disk surface. The heat-transfer coefficient could then be calculated from the formula

$$h = \frac{Gc}{A}\,\frac{\ln(T_1 - T_0) - \ln(T_2 - T_0)}{\Delta\tau} \qquad (1)$$

where G, A, c = mass, face surface, and specific heat of the h-calorimeter; T_1, T_2 = temperatures of the h-calorimeter at the beginning and at the end of the measurement period $\Delta\tau$.

During the measurement period the temperature of the h-calorimeter usually was reduced approximately from 80 to 70°C at an ambient air temperature of about $T_0 = 23°\mathrm{C}$, which assured high accuracy of the heat transfer measurements [14].

Experimental Results

Flow Visualization. Flow visualization was performed by seeding the air jet with smoke produced by a cigarette smoke generator. The diameter of the jet tube was $d = 9.65$ mm and the tube outlet to disk surface distance was $H/d = 5$. Pictures were taken in the dark while the flow pattern was illuminated by a flat beam of intense light from a slide projector, of approximately 2 mm width. In this way, pictures of flow cross section could be obtained, providing some insight into the normally impinging round single jet flow interaction with the rotating wall jet produced by the rotating disk.

Figure 3 presents the pictures of two flow cross sections for various velocity ratios u_r/u_j and two jet Reynolds numbers. The pictures situated on the left show flow patterns in the plane of the jet axis and the disk rotation axis, and those on the right, in the plane of jet axis and normal to the former. At velocity ratios of $u_r/u_j = 0$ and 0.27, all pictures are almost the same. Only a slight asymmetry in the radial wall jet at $u_r/u_j = 0.27$ can be discerned. At $u_r/u_j = 1.26$, one can observe a strong influence of the rotationally induced wall jet on the round impinging jet, which is intensified at the higher values of u_r/u_j. In particular, for $u_r/u_j = 2.6$ and 2.9 the pictures show the typical flow pattern before the impinging jet is separated from the surface of the rotating disk. The doubling of both Reynolds numbers at almost the same velocity ratios $u_r/u_j = 2.6$–2.9 does not change a basic flow pattern. At $u_r/u_j = 6.4$, the smoke of the jet in an impingement region is already separated from the disk surface by a thin layer of clean air from the rotationally induced wall jet. This separation was observed by Metzger and Grochowsky [11] as the transition to the rotationally dominated regime.

The general view of the smoke jet impinging on a rotating black painted disk is shown in Fig. 4. It is seen that the impingement jet smoke is washed away by the clean air rejected by the rotating disk (rotationally induced wall jet). As the rotational speed of the disk is increased the area of the disk under the smoke "cover" is decreased.

Local heat transfer measurements have been completed within the range of jet Reynolds numbers from 10^4 to 7×10^5. Since the radius of the ring-shaped heat flux sensor was constant, $r = R = 185.2$ mm, the dimensionless distance from the rotation axis r/d of the test disk was varied (assuming the geometric similarity) by using jet tubes having different diameters d:

d, mm	105.6	68.6	36.8	20.0	9.65
r/d	1.76	2.70	5.03	9.26	19.2

The investigation was conducted for two cases. In the first, the axis of the jet tube was coincident with the axis of the test disk ($x = R$), i.e., the jet hit the middle of the disk. In the second, the axis of the jet tube was located at the radius of the ring-shaped heat flux sensor ($x = 0$).

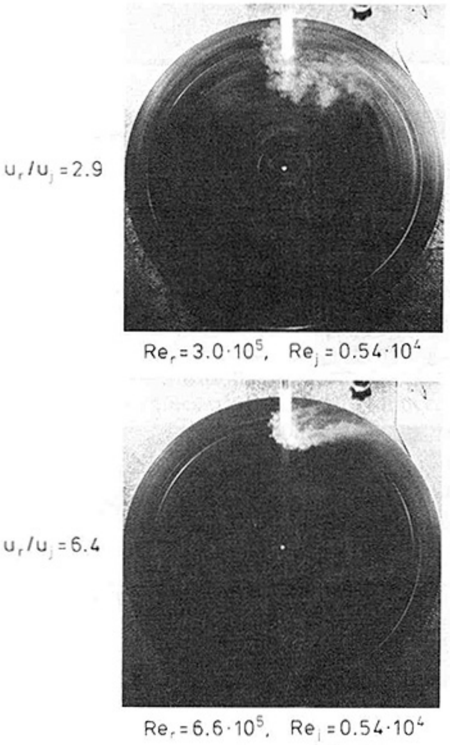

Fig. 4 General view of smoke jet impinging onto a rotating disk (at $H/d = 5$ and $R/d = 19.2$)

Jet Striking the Middle of the Disk ($x = R$). An example of the results of heat transfer measurements done with the jet tube having inside diameter 105.6 mm is shown in Fig. 5. The black points on the left side of the diagram were obtained with a nonrotating disk. It is noted that the rotation of the disk does not influence the heat transfer of the disk for jet velocity ratios

$$u_r/u_j \lesssim 1 - 2 \times 10^{-4}(\mathrm{Re}_j)^{2/3} \tag{2}$$

Furthermore, approximately beyond the velocity ratio $u_r/u_j \gtrsim 5$, the effect of the jet impingement can be neglected. It is clear that for ratios of u_r/u_j below values given by equation (2) one can use the local heat transfer results obtained for fixed flat surfaces in impinging round jets. The comparison of our heat transfer rates presented in Fig. 5, for instance, with the results of local heat transfer measurements obtained by Schlunder and Gnielinski [15], for a Schmidt number Sc = 0.59, using a heat and mass transfer analogy, shows that their results are only 4–11 percent lower.

Jet Striking the Rotating Disk at the Radius R ($x = 0$). The results of five series of measurements are shown in Fig. 6. The local heat transfer distribution is similar to the previous case. However, the local Nusselt numbers for dimensionless disk radii of $r/d = 1.76$ and 2.70 are about 10 percent higher when the jet hits the middle of the disk. The rotation of the disk does not show an effect on heat transfer for velocity ratios

$$u_r/u_j \lesssim (1 - 2 \times 10^{-4}\mathrm{Re}_j^{2/3})(1 - 0.18\sqrt{r/d}) \tag{3}$$

or for rotational Reynolds numbers

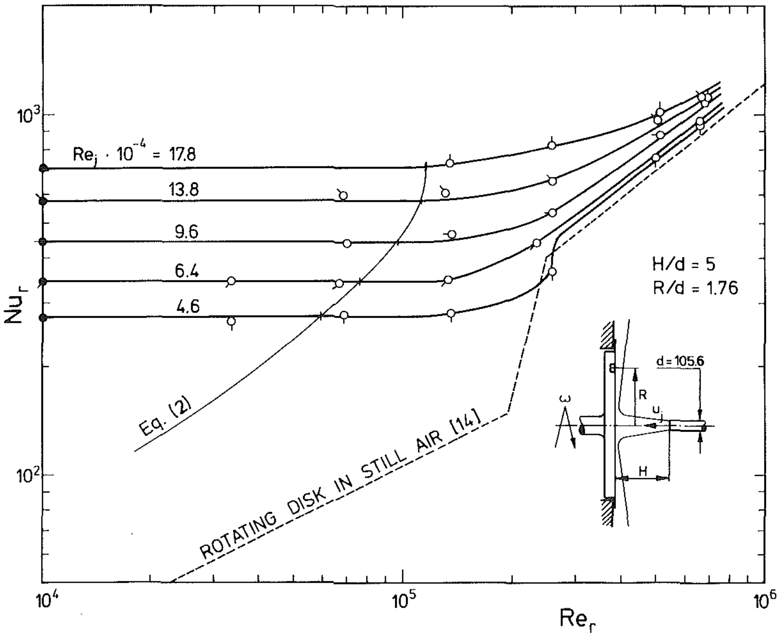

Fig. 5 Local heat transfer on the rotating disk when the jet hits the middle of the disk

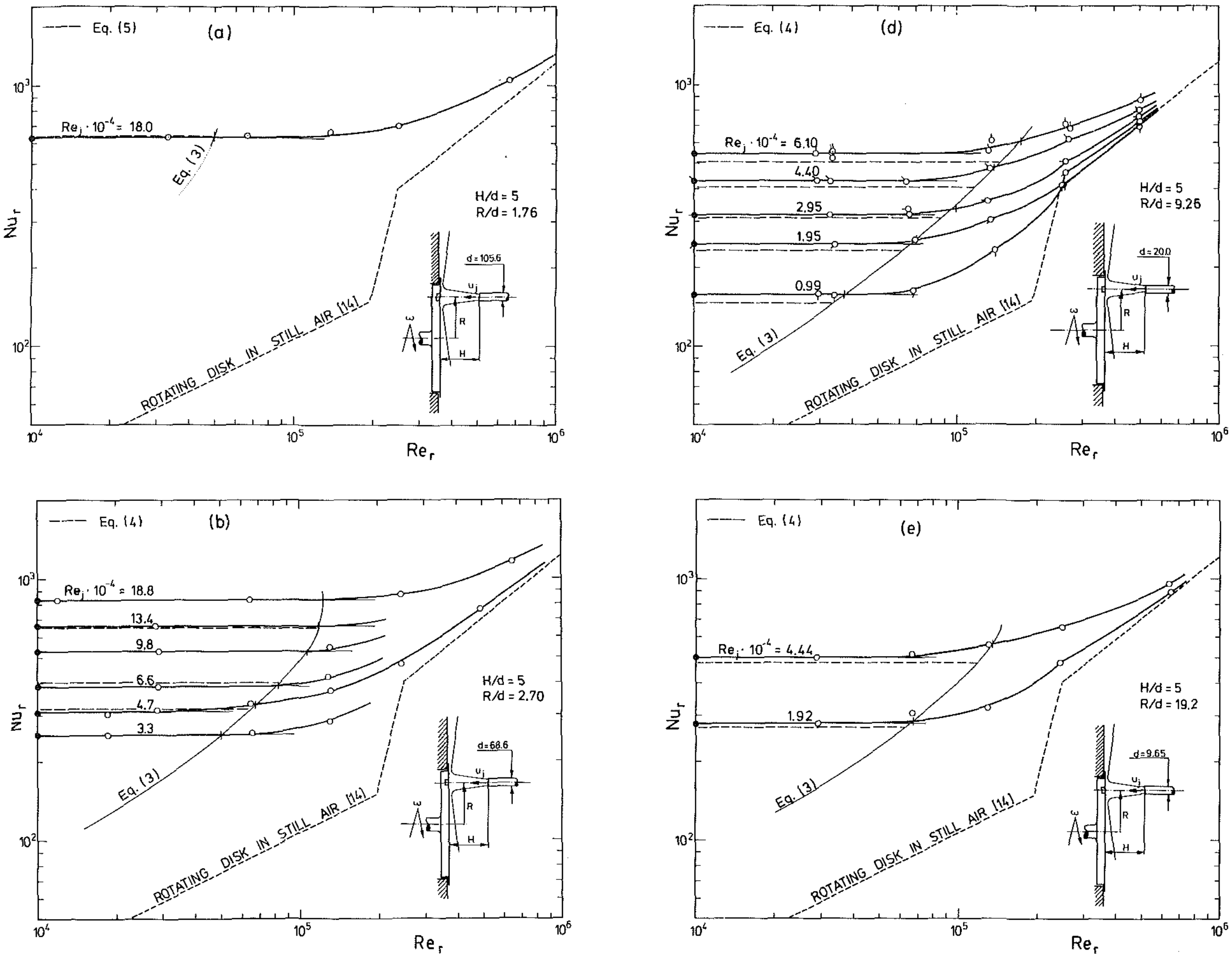

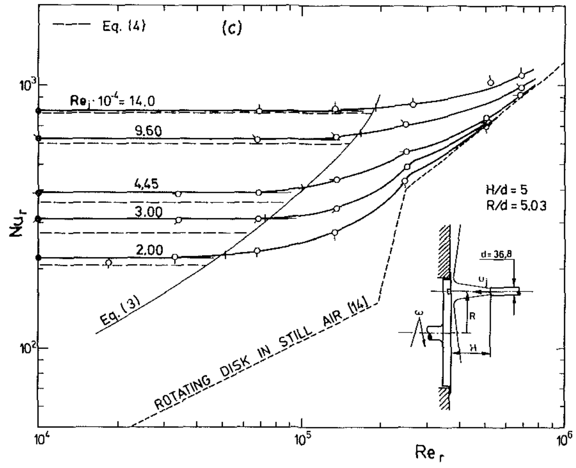

Fig. 6 Local heat transfer on the rotating disk when the jet hits the disk at the radius $R = 185.2$ mm

$$\mathrm{Re}_r \lesssim \mathrm{Re}_j \frac{r}{d}(1-2\times 10^{-4}\mathrm{Re}_j^{2/3})(1-0.18\sqrt{r/d})$$

On the other hand approximately beyond the ratio $u_r/u_j \gtrsim 5$, the effect of the jet impingement can be neglected.

Therefore, from our and Metzger and Grochowsky's [11] results one can distinguish three regimes, as follows:

- jet impingement-dominated regime
- mixed regime
- rotationally dominated regime.

Equation (3) determines the region of the first regime. For the flow visualization conditions (see Fig. 3) this equation gives $u_r/u_j \simeq 0.2$. It means that the pictures taken at $u_r/u_j = 0.27$ approximately refer to the first transition (between the jet impingement-dominated regime and the mixed regime). The pictures for $u_r/u_j = 1.26$, 2.6, and 2.9 are in the mixing region. The last two pictures in Fig. 3, for $u_r/u_j = 6.4$, show a typical rotationally dominated flow pattern.

The convective processes on the rotating disk were strongly enhanced by the impinging jet in the range of velocity ratios determined by equation (3). The effect of the jet Reynolds number in the jet impingement-dominated region is illustrated in Fig. 7. For the dimensionless radii r/d from 2.5 to 19.2, this effect can be expressed by the factor of $\mathrm{Re}_j^{0.68}$ and for the radius $r/d = 1.76$ the same factor has been assumed. The effect of the dimensionless radius has been depicted in Fig. 8. As the radius increases, the local heat transfer coefficient decreases but the Nusselt number based on the radius r increases with the factor of $(r/d)^{0.22}$ for $r/d \gtrsim 2.7$ and of $(r/d)^{0.56}$ for $r/d \lesssim 2.7$. The effect of the dimensionless distance between the outlet of the jet tube and the rotating disk, shown in Fig. 9, appears to be very weak. In previous papers this effect has not been even noticed.

The behavior of the local heat transfer at $r = 9.26\ d$ in the impingement-dominated regime is depicted in Fig. 10 for different radial positions of the jet tube. The effect of inclination angles of the jet tube from the normal direction ($\alpha = \beta = 90$ deg), shown in Fig. 11, indicates that only at the angle $\beta = 120$ deg is observed approximately a 10 percent excess of heat transfer beyond the heat transfer measured at the angle $\alpha = \beta = 90$ deg.

In a view of the practical application of the impinging round jet in cooling or heating systems of rotating disks, a

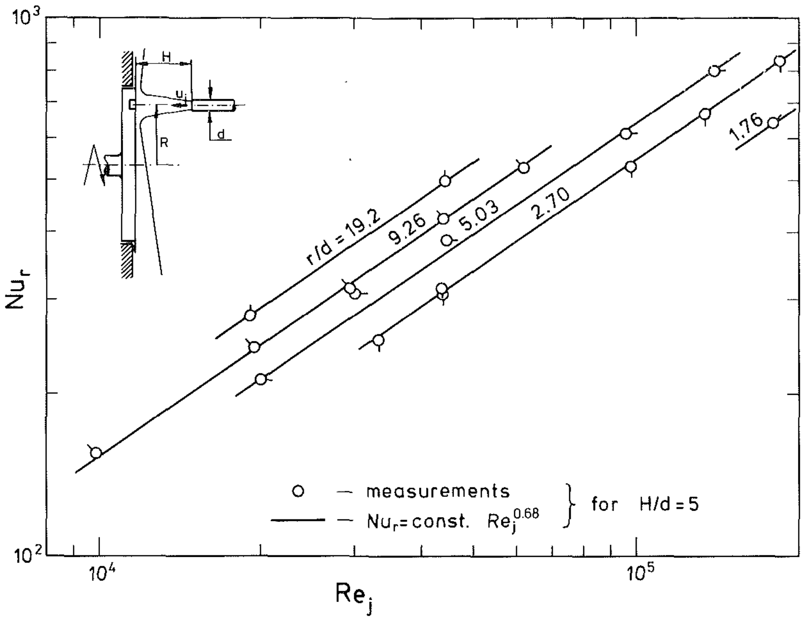

Fig. 7 Effect of jet Reynolds number on the local heat transfer (for jet impingement-dominated region:

$Re_r \leq Re_j \frac{r}{d} (1 - 2 \times 10^{-4} Re_j^{2/3})(1 - 0.18\sqrt{r/d})$)

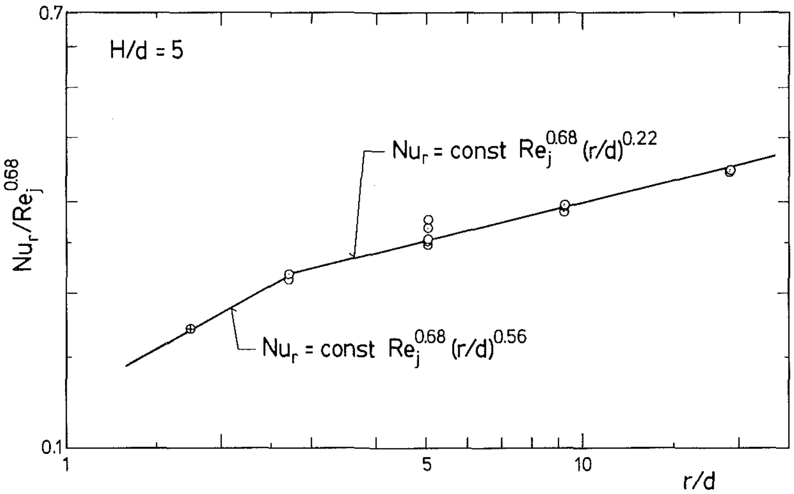

Fig. 8 Effect of dimensionless radius (for jet impingement-dominated region)

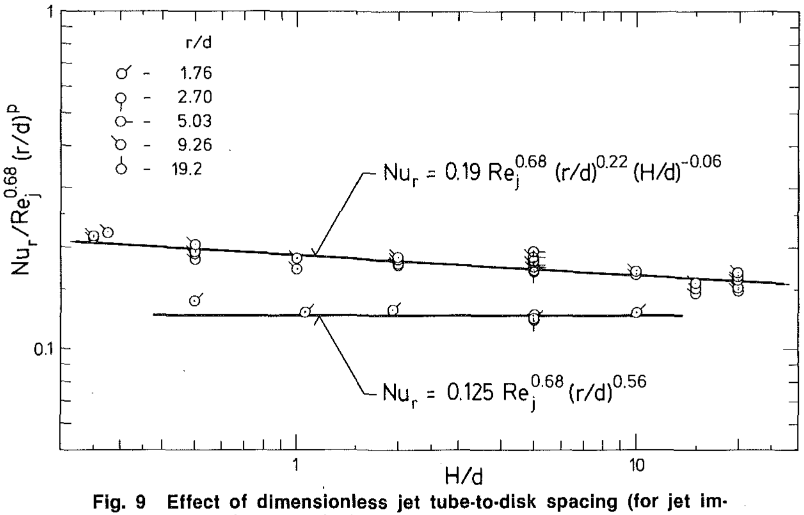

Fig. 9 Effect of dimensionless jet tube-to-disk spacing (for jet impingement-dominated region)

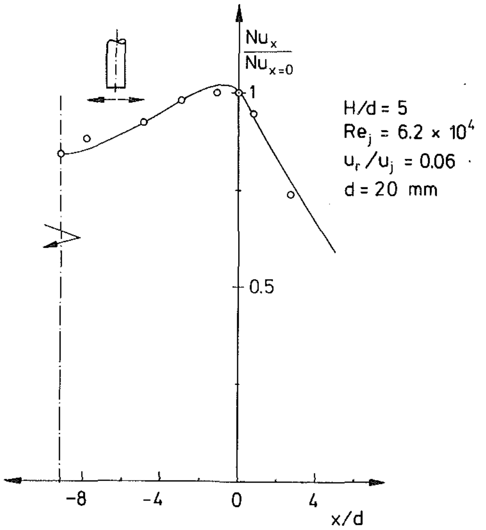

Fig. 10 **The local heat transfer at $R = 9.26\ d$ for different radial positions of the jet tube (for jet impingement-dominated region)**

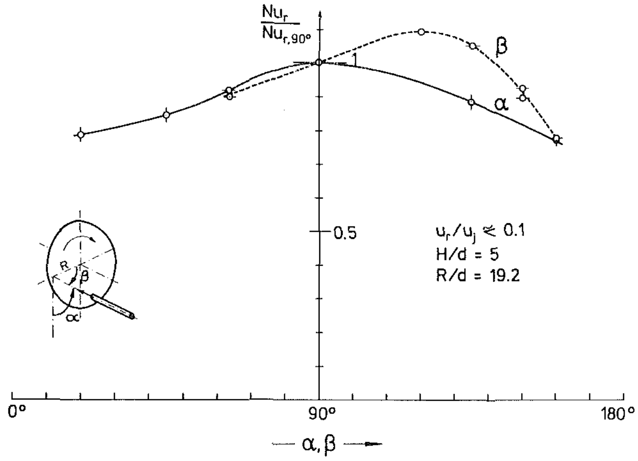

Fig. 11 **Effect of jet inclination on heat transfer (for jet impingement-dominated region)**

correlating equation has been formulated for the local Nusselt numbers

$$\mathrm{Nu}_r = 0.190\mathrm{Re}_j^{0.68}(r/d)^{0.22}(H/d)^{-0.06} \tag{4}$$

for $0.5 \leq H/d \leq 20$ and $2.7 \leq r/d \leq 20$, and

$$\mathrm{Nu}_r = 0.125\mathrm{Re}_j^{0.68}(r/d)^{0.56} \tag{5}$$

for $1 \leqslant H/d \leqslant 10$ and $1.5 \gtrsim r/d \leqslant 2.7$, which are applicable for $u_r/u_j \lessapprox (1 - 2 \times 10^{-4}\ \mathrm{Re}_j^{2/3})(1 - 0.18\sqrt{r/d})$. The correctness of above equations can be examined in Fig. 6. From our local heat transfer data it was possible to determine the pure impingement-dominated region, which has been indicated by equation (3). The transition zone from the pure impingement to the pure rotation-dominated regime, as can be observed in Fig. 6, is smooth and rather wide and can be considered as a region of a mixed regime.

Actually, the correlated data represent the average heat transfer coefficients according to the formula $\bar{h} = 1/2\pi R \int_0^{2\pi R} h\ ds$, where s is the distance along the circle of the rotation radius R and h is a function of a radial distance from the stagnation point of the impinging jet. The average heat or mass transfer data presented in literature are averaged over the surface and can not be compared with our results because of a different averaging procedure. However, it is interesting to note that the effect of the jet Reynolds number in our correlation equations is of the order of that proposed by Schlunder and Gnielinski [15] and is exactly the same as given by Vallis et al. [16].

Metzger and Grochowksy [11] have found, with flow visualization tests, a correlation of all observed transition conditions by utilizing the values of the rotationally induced laminar or turbulent wall jet flow rate Q_p passing the impingement radius as given in [2, 3]. Their data were correlated equally well with the calculated pumping flows for laminar or turbulent wall jets. This correlation is shown in Fig. 12 in terms of the ratio Q_j/Q_p versus Re_r, where Q_p was calculated for the laminar wall jet flow. The tests were conducted by maintaining the jet flow rate and rotational speed constant while slowly increasing the radial impingement location until transition was observed. From the average data presented in [11] one can conclude that these transition conditions determine only the pure rotation-dominated region where changes in impingement jet flow rate do not affect the heat transfer.

It should be noted that all results of the transition conditions shown in Fig. 12 were obtained at practically constant fluid kinematic viscosity ν, i.e., for air at laboratory environment temperatures. We have to realize that for variable viscosity ($\nu = \mathrm{const}$), for instance, the value of Re_r can be increased by a reduction of the viscosity ν. Then, for $r = \mathrm{const}$ and $\omega = \mathrm{const}$ the decrease of Re_r involves a decrease of Q_p (referred to the total circle of radius r) and, at constant ratio of Q_j/Q_r, consequently an identical decrease of Q_j. But the decrease of the flow rate Q_j and momentum of the impinging round jet is much stronger than the decrease of local flow rate and momentum of the rotationally induced disk pumping wall jet because in this case the impinging jet attacks the wall jet only on the fraction of the circle of radius r.

Therefore, for $\nu \neq \mathrm{const}$, $r = \mathrm{const}$, and $\omega = \mathrm{const}$ the increase of Re_r beyond the value of $\mathrm{Re}_{r\text{-transition}}(Q_j/Q_p)$ should not show the mixed regime conditions as we can see in Fig. 12. Then the correlation of the transition conditions from the pure rotation-dominated to mixed regime, proposed by Metzger and Grochowsky [11] and shown in Fig. 12, seems to be valid only for the constant kinematic viscosity for air at laboratory environment temperature and needs further elucidation.

For comparison, our data concerning the transition condition (determined by equation (3)) which were obtained at laminar rotational Reynolds numbers, i.e., below $\mathrm{Re}_{r\text{-crit.}} = 1.9 \times 10^5$ [14], are also presented in Fig. 12. The differences between the results are obvious since they concern two different kinds of transitions and between them the region of the mixed regime is located.

Concluding Remarks

The measured distributions of the local heat transfer coefficient versus the rotational Reynolds number enable the identification of flow conditions at which impinging jets provide effective intensification of convective processes on rotating disks. Three regimes of the impinging round jet and rotationally induced disk pumping flow interaction have been distinguished: pure impingement-dominated regime; mixed regime; and rotation-dominated regime. In the first regime the flow visualization pictures of the impinging round jet on the rotating disk do not shown any significant difference between the flow patterns of the impinging jet on the rotating disk and on a fixed flat plate. In this regime one can determine the heat transfer rates using heat transfer data obtained for a fixed flat surface in an impinging jet. This fact has been proven experimentally for the case where the round air hits the middle of the rotating and almost motionless disk.

In the mixed regime, the impinging jet fluid (smoke) reaches a small area of the rotating disk surface and only a small part of the disk is covered by jet smoke.

The rotation-dominated regime appears at velocity ratios of

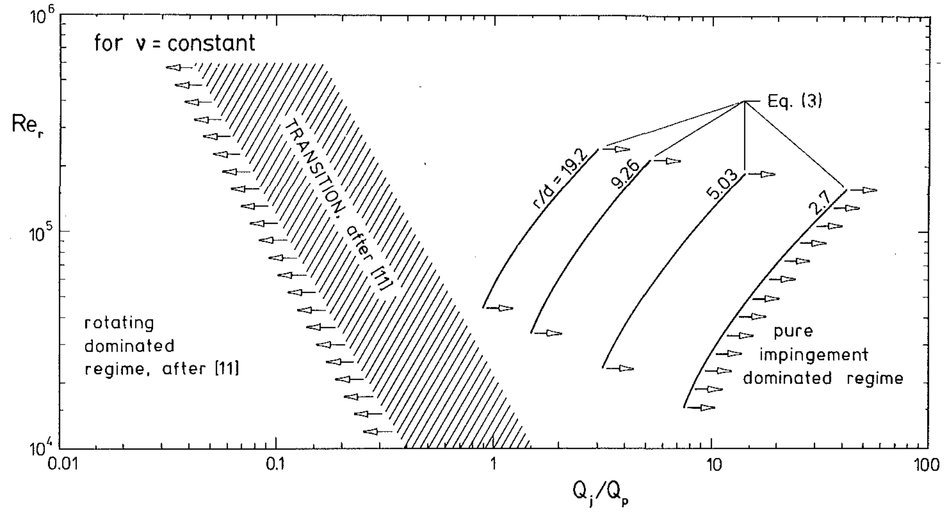

Fig. 12 Regions of dominant regimes (for air)

approximately $u_r/u_j \geq 5$. Then the jet fluid does not reach the rotating disk surface under the jet because the impinging jet starts being underscored by the air rejected by the rotating disk. In this regime, the effect of the jet impingement on the local heat transfer at the impingement location radius is relatively small.

The present data show that when a laminar wall jet is induced by the rotating unshrouded disk (i.e., at $Re_r \lesssim 2 \times 10^5$), the convective heat transfer on a rotating disk can be considerably enhanced with a round impinging jet having a jet Reynolds number $Re_j \geq 10^4$. When the radial wall jet induced by the rotating unshrouded disk is turbulent (i.e., at $Re_r \geq 2.5 \times 10^5$ [14]), it is necessary to use much higher jet Reynolds numbers in order to increase the local heat transfer, e.g., starting with $Re_j \geq 10^5$ at the lowest turbulent rotational Reynolds number.

The free and impinging jet flow structure and the distributions of the local heat transfer coefficients on the impinged surface depend strongly on the shape of the jet nozzle and the initial turbulence of the jet. In principle, the present results are applicable to jets leaving long tubes, producing specific jets [17]. But due to rotation, averaging of the heat transfer takes place on the circumference at any given radius of the disk; therefore, for another jet nozzle, one can expect only a slight departure of the heat transfer from present results.

References

1 Bouchez, J. P., and Goldstein, R. J., "Impingement Cooling From a Circular Jet in a Cross Flow," *Int. J. Heat Mass Transfer*, Vol. 8, 1975, pp. 719-730.

2 Schlichting, H., *Boundary Layer Theory*, McGraw-Hill, New York, 1960, pp. 89 and 548.

3 Dorfman, L. A., *Hydrodynamic Resistance and Heat Transfer of Rotating Bodies* [in Russian], Fizmatgiz, Moscow, 1960, pp. 14-22, 72; English translation by N. Kemmer, Oliver and Boyd Ltd., London, 1963.

4 Martin, M., "Heat and Mass Transfer Between Impinging Gas Jets and Solid Surface," *Advances in Heat Transfer*, J. P. Hartnett and T. F. Irvine, eds., Academic Press, New York, 1977, Vol. 13, pp. 1-60.

5 Udaev, B. N., Mikhailov, M. S., and Savin, W. K., *Heat Transfer at Jet-Obstacle Interaction* [in Russian], Mashinostroenie, Moscow, 1977.

6 Dyban, E. P., and Mazur, H. J., *Convective Heat Transfer at Impinging Flow Around Bodies* [in Russian], Naukova Dumka, Kiev, 1982.

7 Kuznetzov, A. L., "Heat Transfer From a Shrouded Rotating Disk at Air Jet Impingement," *Energomashinostroenie*, Vol. 10, No. 10, 1964, pp. 11-14.

8 Kuznetzov, A. L., "Determination of Local Heat Transfer Coefficients of a Disk Rotating in a Shroud at Air Jet Impingement," *Energomashinostroenie*, Vol. 13, No. 3, 1967, pp. 8-10.

9 Devyatov, V. I., "Investigations of Heat Transfer for Two Versions of Turbine Disk Cooling," *Aviatsionnaya Tekhnika, Izd. VUZ*, Vol. 8, No. 2, 1965, pp. 56-64.

10 Popiel, C. O., Boguslawski, L., and Tuliszka, E., "Heat Transfer From a Rotating Disk in an Impinging Round Air Jet," *Proceedings of the 5th International Heat Transfer Conference*, Tokyo, 1974, Vol. 3, pp. 212-216.

11 Metzger, D. E., and Grochowsky, L. D., "Heat Transfer Between an Impinging Jet and Rotating Disk," ASME JOURNAL OF HEAT TRANSFER, Vol. 99, 1977, pp. 663-667.

12 Metzger, D. E., Mathis, W. J., and Grochowsky, L. D., "Jet Cooling at the Rim of a Rotating Disk," ASME *Journal of Engineering for Power*, Vol. 101, 1979, pp. 68-72.

13 Bogdan, Z., "Cooling of a Rotating Disk by Means of an Impinging Jet," *Proceedings of the 7th International Heat Transfer Conference*, Munich, 1982, Vol. 3, pp. 333-336.

14 Popiel, C. O., and Boguslawski, L., "Local Heat Transfer Coefficients on the Rotating Disk in Still Air," *Int. J. Heat Mass Transfer*, Vol. 18, 1975, pp. 167-170.

15 Schlünder, E. U., and Gnielinski, V., "Wärme- und Stoffübertragung zwischen Gut und aufprallendem Düsenstrahl," *Chemie Ingenieur Technik*, Vol. 39, 1967, pp. 578-584.

16 Vallis, E. A., Patric, M. A., and Wrag, A. A., "Radial Distribution of Convective Heat Transfer Coefficient Between an Axisymmetric Turbulent Jet and a Flat Plate Held Normal to the Flow," *Proceedings of the 6th International Heat Transfer Conference*, Toronto, 1978, Vol. 5, pp. 297-303.

17 Boguslawski, L., and Popiel, C. O., "Flow Structure on the Free Round Turbulent Jet in the Initial Region," *J. Fluid Mech.*, Vol. 90, 1979, pp. 531-539.

Chung-Hsiung Li
Engineering Technologies Department,
Combustion Engineering, Inc.,
Air Preheater Company,
Wellsville, NY 14895
Mem. ASME

Exact Transient Solutions of Parallel-Current Transfer Processes

Exact transient solutions of parallel-current transfer processes are obtained by the use of the Laplace transformation. Solutions are valid for a finite or an infinite transfer zone. The solutions are verified with steady-state solutions. Exact transient solutions of this study are applicable to liquid-to-liquid and liquid-to-gas heat exchangers in which the thermal capacitance of the core is negligible (zero) compared to the thermal capacitance of the stepped liquid contained in the exchanger.

1 Introduction

The purpose of this paper is to present exact solutions for transient parallel-current processes, i.e., for either temperature or mass transfer calculations. In industrial applications, parallel-current transfer processes usually occur only in specialized situations as dictated by mechanical or other reasons; but in fundamental transfer study, the parallel-current transfer process is always discussed along with the countercurrent transfer process [1]. The mathematical analysis of steady-state conditions is relatively simple and well known in all cases. A simple general analytic solution for transient countercurrent transfer processes is not readily obtainable, partly due to the presence of split boundary conditions. The most general analytic solution for the transient transfer process was obtained by Jaswon and Smith [2] and is in a complicated series form. The evaluation of their solution for even relatively simple boundary conditions is difficult and time consuming, requiring lengthy computer calculations as discussed by Tan and Spinner [3]. The simultaneous partial differential equations for nonsteady-state transfer processes have thus been evaluated numerically by many authors in a variety of ways. These include application of finite difference methods and the use of cell or lumped parameter models. Recently, Tan and Spinner [3] applied the method of characteristics proposed by Acrivos [4] to obtain the numerical solution.

Romie [5] presented an exact solution for the transient parallel-flow heat exchanger. His solutions include the effect of the core thermal capacitance but are restricted to exchangers in which the two fluid velocities are equal or, alternatively, to exchangers in which both fluids are gases. Exact solutions of unsteady parallel-current transfer processes of this study are valid for a liquid-to-liquid type parallel-flow heat exchanger in unsteady state or a liquid-to-gas type heat exchanger with a temperature change at the entrance of the liquid phase. In either case the thermal capacitance of the core is assumed to be negligible (zero) compared to the thermal capacitance of the stepped fluid (fluid 1) contained in the exchanger. If the specific heat of water and steel are considered, one can find the specific heat of water is about ten times the specific heat of steel. In the thin partition wall heater, the mass of water per unit length is comparable to the mass of steel per unit length. Hence, the thermal capacitance of the core may not be central to the transient response; in fact, the thermal capacitance of the core may be negligible for liquid-to-liquid heat exchangers. Hence, exact transient solutions of the parallel-current transfer processes can be applied to obtain the transient solutions of the parallel-flow heat exchanger. Also note that the velocities are, in general, not equal.

2 Fundamental Equations

The mechanics underlying parallel-current transfer is illustrated in Fig. 1. The horizontal arrows indicate two parallel-current streams 1 and 2, between which energy or mass is being transferred across the interface AB. If x measures the distance from the entrance of the exchanger, and t is the time after some initial disturbance, usually at $x = 0$, then in general

$$T_1 = T_1(x,\ t),\quad T_2 = T_2(x,\ t)$$

where T_1 and T_2 refer to the temperature or the mass concentration of a particular component in streams 1 and 2, respectively.

The axial diffusion of heat, the internal generation of heat, the axial diffusion of mass and chemical reaction, and the thermal capacitance of the core or partition wall are assumed to be negligible. The physical properties of the flowing streams are assumed to be constant. With these assumptions, the model equations for heat transfer can be stated as

$$\frac{\partial T_1}{\partial t} + v_1 \frac{\partial T_1}{\partial x} = b_1(T_2 - T_1) \tag{1}$$

$$\frac{\partial T_2}{\partial t} + v_2 \frac{\partial T_2}{\partial x} = b_2(T_1 - T_2) \tag{2}$$

where $b_1 = H/M_1c_1$ and $b_2 = H/M_2c_2$. H is the overall heat transfer coefficient which can be computed as

$$\frac{1}{H} = \frac{1}{A_1h_1} + \frac{1}{A_2h_2} \tag{3}$$

The analogous governing equations for mass transfer can be found in [2, 3].

A step temperature change in one fluid of a parallel-current transfer process can be stated as

$$\text{at } t=0,\ T_1 = T_2 = 0 \tag{4}$$

$$\text{at } x=0,\ T_1 = T_{10}U(t),\ T_2 = 0 \tag{5}$$

In this study, the partial differential equations (1) and (2) are analyzed for the cases of $v_1 \neq v_2$ and $v_1 = v_2$ by the technique of Laplace transformations.

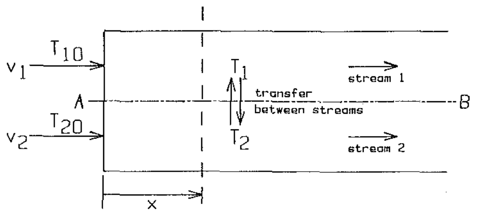

Fig. 1 The model of the two stream parallel-current transfer process

---

Contributed by the Heat Transfer Division for publication in the JOURNAL OF HEAT TRANSFER. Manuscript received by the Heat Transfer Division June 19, 1984.

3 Theoretical Analysis

A **For the Case of $v_1 \neq v_2$.** By applying Laplace transformation to equations (1) and (2), one can obtain

$$\frac{d\bar{T}_1}{dx} = -\frac{s+b_1}{v_1}\bar{T}_1 + \frac{b_1}{v_1}\bar{T}_2 \tag{6}$$

$$\frac{d\bar{T}_2}{dx} = \frac{b_2}{v_2}\bar{T}_1 - \frac{s+b_2}{v_2}\bar{T}_2 \tag{7}$$

where $\bar{T}_1$ and $\bar{T}_2$ are the Laplace transforms of T_1 and T_2.

From equations (6) and (7), one can arrive at

$$\frac{d}{dx}(\bar{T}_1 + \alpha\bar{T}_2) = -\beta(\bar{T}_1 + \alpha\bar{T}_2) \tag{8}$$

where

$$\beta = \frac{s+b_1}{v_1} - \alpha\frac{b_2}{v_2} \tag{9}$$

$$\alpha = -\frac{\dfrac{b_1}{v_1} - \alpha\dfrac{s+b_2}{v_2}}{\dfrac{s+b_1}{v_1} - \alpha\dfrac{b_2}{v_2}} \tag{10}$$

From equation (10), one can arrive at

$$\frac{b_2}{v_2}\alpha^2 - \left(\frac{s+b_1}{v_1} - \frac{s+b_2}{v_2}\right)\alpha - \frac{b_1}{v_1} = 0 \tag{11}$$

The solutions for α in equation (11) are

$$\alpha_{1,2} = \left[\sqrt{\left(\frac{1}{v_1} - \frac{1}{v_2}\right)s + \left(\sqrt{\frac{b_1}{v_1}} + \sqrt{\frac{b_2}{v_2}}\,i\right)^2} \pm\sqrt{\left(\frac{1}{v_1} - \frac{1}{v_2}\right)s + \left(\sqrt{\frac{b_1}{v_1}} - \sqrt{\frac{b_2}{v_2}}\,i\right)^2}\,\right]^2 \Big/ 4\frac{b_2}{v_2} \tag{12}$$

By substituting equation (12) into equation (9), one can obtain

$$\beta_{1,2} = \frac{s+b_1}{v_1} - \left[\sqrt{\left(\frac{1}{v_1} - \frac{1}{v_2}\right)s + \left(\sqrt{\frac{b_1}{v_1}} + \sqrt{\frac{b_2}{v_2}}\,i\right)^2} \pm\sqrt{\left(\frac{1}{v_1} - \frac{1}{v_2}\right)s + \left(\sqrt{\frac{b_1}{v_1}} - \sqrt{\frac{b_2}{v_2}}\,i\right)^2}\,\right]^2 / 4 \tag{13}$$

The solution of equation (8) is

$$\bar{T}_1 + \alpha\bar{T}_2 = Ce^{-\beta x} \tag{14}$$

i.e.,

$$\bar{T}_1 + \alpha_1\bar{T}_2 = C_1 e^{-\beta_1 x} \tag{15}$$

$$\bar{T}_1 + \alpha_2\bar{T}_2 = C_2 e^{-\beta_2 x} \tag{16}$$

where C, C_1, and C_2 are integral constants.

At $x = 0$, $\bar{T}_2 = 0$ and $\bar{T}_1 = T_{10}/s$, so that

$$C_1 = C_2 = \frac{1}{s}T_{10} \tag{17}$$

From equations (15), (16) and (17), one can arrive at

$$\frac{\bar{T}_1}{T_{10}} = \frac{1}{s}\,\frac{\alpha_1 e^{-\beta_2 x} - \alpha_2 e^{-\beta_1 x}}{\alpha_1 - \alpha_2} \tag{18}$$

$$\frac{\bar{T}_2}{T_{10}} = \frac{1}{s}\,\frac{e^{-\beta_1 x} - e^{-\beta_2 x}}{\alpha_1 - \alpha_2} \tag{19}$$

From equation (12), one can arrive at

$$\frac{\alpha_1}{\alpha_1 - \alpha_2} = \frac{1}{2}\left(\frac{1}{v_1} - \frac{1}{v_2}\right)\frac{s}{\sqrt{\Delta}} + \frac{1}{2}\left(\frac{b_1}{v_1} - \frac{b_2}{v_2}\right)\frac{1}{\sqrt{\Delta}} + \frac{1}{2} \tag{20}$$

$$\frac{\alpha_2}{\alpha_1 - \alpha_2} = \frac{1}{2}\left(\frac{1}{v_1} - \frac{1}{v_2}\right)\frac{s}{\sqrt{\Delta}} + \frac{1}{2}\left(\frac{b_1}{v_1} - \frac{b_2}{v_2}\right)\frac{1}{\sqrt{\Delta}} - \frac{1}{2} \tag{21}$$

where

$$\Delta = \left[\left(\frac{1}{v_1} - \frac{1}{v_2}\right)s + \left(\sqrt{\frac{b_1}{v_1}} + \sqrt{\frac{b_2}{v_2}}\,i\right)^2\right] \times \left[\left(\frac{1}{v_1} - \frac{1}{v_2}\right)s + \left(\sqrt{\frac{b_1}{v_1}} - \sqrt{\frac{b_2}{v_2}}\,i\right)^2\right] \tag{22}$$

From equations (18), (20), and (21), one can arrive at

$$\frac{\bar{T}_1}{T_{10}} = \frac{1}{2}\left(\frac{1}{v_1} - \frac{1}{v_2}\right)\left(\frac{e^{-\beta_2 x}}{\sqrt{\Delta}} - \frac{e^{-\beta_1 x}}{\sqrt{\Delta}}\right)$$

Nomenclature

A = dummy, defined in equation (25)
B = dummy, defined in equation (26)
b_1 = defined as H/M_1c_1, 1/s
b_2 = defined as H/M_2c_2, 1/s
C = integral constant
C_1 = integral constant
C_2 = integral constant
c_1 = specific heat of fluid 1, J/(kg•K)
c_2 = specific heat of fluid 2, J/(kg•K)
E = a function, defined in equation (41)
H = the overall coefficient of heat transfer, W/K
h = heat transfer coefficient, W/(m^2•K)
L = the length of a heat exchanger, m
M_1 = mass of liquid contained in exchanger for fluid 1, kg
M_2 = mass of liquid contained in exchanger for fluid 2, kg
$\dot{m}_1$ = the mass flow rate for fluid 1, kg/s
$\dot{m}_2$ = the mass flow rate for fluid 2, kg/s
N_{tu} = number of transfer units, defined in equation (35)
s = the variable of the Laplace transformation, 1/s
T_1 = the temperature change of fluid 1, K
T_2 = the temperature change of fluid 2, K
T_{10} = the inlet step temperature change of fluid 1, K
t = time, s
$t_{\max}$ = defined in equation (34), s
$t_{\min}$ = defined in equation (34), s
$U(t)$ = step function
v_1 = the velocity of fluid 1, m/s
v_2 = the velocity of fluid 2, m/s
x = distance, m
y = dimensionless transfer zone, defined in equation (42)
α = defined in equation (10)
α_1 = defined in equation (12)
α_2 = defined in equation (12)
β = defined in equation (9)
β_1 = defined in equation (13)
β_2 = defined in equation (13)
Δ = defined in equation (22)
θ = dimensionless time, defined in equation (36)

Subscripts

1 = for fluid 1 (the stepped fluid)
2 = for fluid 2

$$+\frac{1}{2}\left(\frac{b_1}{v_1}-\frac{b_2}{v_2}\right)\left(\frac{e^{-\beta_2 x}}{s\sqrt{\Delta}}-\frac{e^{-\beta_1 x}}{s\sqrt{\Delta}}\right)+\frac{1}{2}\left(\frac{e^{-\beta_2 x}}{s}+\frac{e^{-\beta_1 x}}{s}\right) \tag{23}$$

From equations (19) and (12), one can obtain

$$\frac{\bar{T}_2}{T_{10}}=\frac{b_2}{v_2}\left(\frac{e^{-\beta_1 x}}{s\sqrt{\Delta}}-\frac{e^{-\beta_2 x}}{s\sqrt{\Delta}}\right) \tag{24}$$

Define

$$A=\frac{b_1-b_2}{v_1-v_2} \tag{25}$$

and

$$B=\frac{b_2 v_1-b_1 v_2}{v_1-v_2} \tag{26}$$

From the techniques of Laplace transformation and Laplace transform tables as shown in [6, 7], one can obtain the inverse Laplace transformation of equations (23) and (24) and the transient temperature distributions for the parallel-current transfer processes as

$$\begin{aligned}\frac{T_1}{T_{10}}=&\frac{1}{2}\,e^{-Ax-Bt}I_0\left[2\,\frac{\sqrt{b_1 b_2 v_1 v_2}}{v_1-v_2}\left(t-\frac{x}{v_1}\right)^{1/2}\left(\frac{x}{v_2}-t\right)^{1/2}\right]\left[U\left(t-\frac{x}{v_1}\right)-U\left(t-\frac{x}{v_2}\right)\right]\\
&+\frac{B}{2}\,e^{-Ax}\int_0^t e^{-B\tau}I_0\left[2\,\frac{\sqrt{b_1 b_2 v_1 v_2}}{v_1-v_2}\left(\tau-\frac{x}{v_1}\right)^{1/2}\left(\frac{x}{v_2}-\tau\right)^{1/2}\right]\left[U\left(\tau-\frac{x}{v_1}\right)-U\left(\tau-\frac{x}{v_2}\right)\right]d\tau\\
&+\frac{1}{2}\sqrt{\frac{b_1 b_2}{v_1 v_2}}\,x\,e^{-Ax}\int_0^t e^{-B\tau}\frac{I_1\left[2\frac{\sqrt{b_1 b_2 v_1 v_2}}{v_1-v_2}\left(\tau-\frac{x}{v_1}\right)^{1/2}\left(\frac{x}{v_2}-\tau\right)^{1/2}\right]}{\left(\tau-\frac{x}{v_1}\right)^{1/2}\left(\frac{x}{v_2}-\tau\right)^{1/2}}\left[U\left(\tau-\frac{x}{v_1}\right)-U\left(\tau-\frac{x}{v_2}\right)\right]d\tau\\
&+\frac{1}{2}\,U\left(t-\frac{x}{v_1}\right)e^{-\frac{b_1}{v_1}x}+\frac{1}{2}\,U\left(t-\frac{x}{v_2}\right)e^{-\frac{b_2}{v_2}x}\end{aligned} \tag{27}$$

and

$$\frac{T_2}{T_{10}}=\frac{v_1 b_2}{v_1-v_2}\,e^{-Ax}\int_0^t e^{-B\tau}I_0\left[2\,\frac{\sqrt{b_1 b_2 v_1 v_2}}{v_1-v_2}\left(\tau-\frac{x}{v_1}\right)^{1/2}\left(\frac{x}{v_2}-\tau\right)^{1/2}\right]\left[U\left(\tau-\frac{x}{v_1}\right)-U\left(\tau-\frac{x}{v_2}\right)\right]d\tau \tag{28}$$

***B* For the Case of $v_1 = v_2$.** From equation (11), one can obtain

$$b_2\alpha^2-(b_1-b_2)\alpha-b_1=0 \tag{29}$$

To solve equation (29), one can obtain

$$\alpha_1=\frac{b_1}{b_2}\text{ and }\alpha_2=-1 \tag{30}$$

Substituting equation (30) into equation (9), one can obtain

$$\beta_1=\frac{s}{v_1}\text{ and }\beta_2=\frac{s+b_1+b_2}{v_1} \tag{31}$$

From equations (30), (31), (18), and (19), one can obtain the transient temperature distributions in the parallel-flow heat transfer process with equal velocity as

$$\frac{T_1}{T_{10}}=\frac{b_1 e^{-\frac{b_1+b_2}{v_1}x}+b_2}{b_1+b_2}\,U\left(t-\frac{x}{v_1}\right) \tag{32}$$

and

$$\frac{T_2}{T_{10}}=\frac{b_2\left(1-e^{-\frac{b_1+b_2}{v_1}x}\right)}{b_1+b_2}\,U\left(t-\frac{x}{v_1}\right) \tag{33}$$

4 Calculations of Numerical Results

The exact analytical solutions for parallel-current transfer processes shown in equations (27) and (28) can be used to compute transient temperature distributions at the exit of transfer equipment or transfer zones and also to compute transient temperature distributions inside transfer equipment or transfer zones.

The solutions (27) and (28) are verified by steady-state solutions.

***A* Transient Exit Temperatures.** Define

$$t_{\max}=\max\left(\frac{x}{v_1},\ \frac{x}{v_2}\right)\text{ and }t_{\min}=\min\left(\frac{x}{v_1},\ \frac{x}{v_2}\right) \tag{34}$$

and

$$N_{tu,1}=\frac{H}{\dot{m}_1 c_1},\ N_{tu,2}=\frac{H}{\dot{m}_2 c_2} \tag{35}$$

i.e., $t_{\max}$ and $t_{\min}$ are the maximum and minimum of x/v_1 and x/v_2. $N_{tu,1}$ and $N_{tu,2}$ are the number of transfer units for streams 1 and 2, respectively.

One can transform equations (27) and (28) with the variable

$$\theta=\frac{t-t_{\min}}{t_{\max}-t_{\min}} \tag{36}$$

for computing transient temperature distributions at the exit of transfer equipment or transfer zones.

With the new variable θ, exit transient temperature distributions can be stated as

$$\begin{aligned}\frac{T_1}{T_{10}}=&(\text{sign})\frac{1}{2}\,e^{-N_{tu,\theta}}I_0[2\sqrt{N_{tu,1}\ N_{tu,2}}\,\theta^{1/2}(1-\theta)^{1/2}][U(\theta)-U(\theta-1)]\\
&+\frac{1}{2}(N_{tu,2}-N_{tu,1})\int_0^\theta e^{-N_{tu,\bar{\theta}}}I_0[2\sqrt{N_{tu,1}\ N_{tu,2}}\,\bar{\theta}^{1/2}(1-\bar{\theta})^{1/2}]d\bar{\theta}+\frac{1}{2}\sqrt{N_{tu,1}\ N_{tu,2}}\int_0^\theta e^{-N_{tu,\bar{\theta}}}\frac{I_1[2\sqrt{N_{tu,1}\ N_{tu,2}}\,\bar{\theta}^{1/2}(1-\bar{\theta})^{1/2}]}{\bar{\theta}^{1/2}(1-\bar{\theta})^{1/2}}d\bar{\theta}+E(\theta)\end{aligned} \tag{37}$$

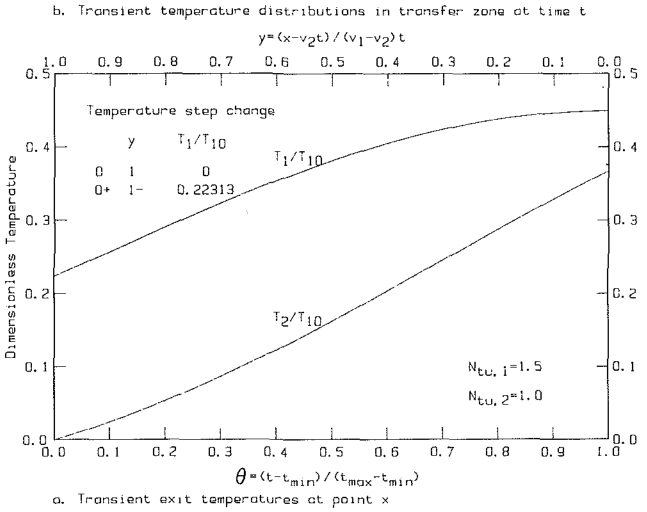

Fig. 2 Transient temperature histories for $N_{tu,1} = 1.5$, $N_{tu,2} = 1$ ($v_1 > v_2$)

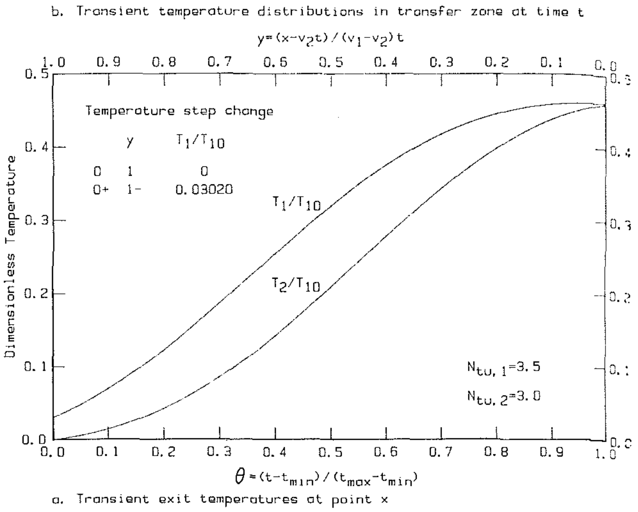

Fig. 4 Transient temperature histories for $N_{tu,1} = 3.5$, $N_{tu,2} = 3$ ($v_1 > v_2$)

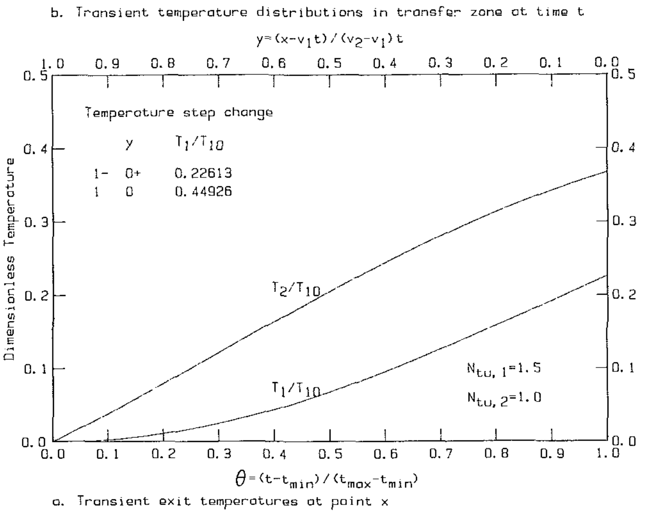

Fig. 3 Transient temperature histories for $N_{tu,1} = 1.5$, $N_{tu,2} = 1$ ($v_1 < v_2$)

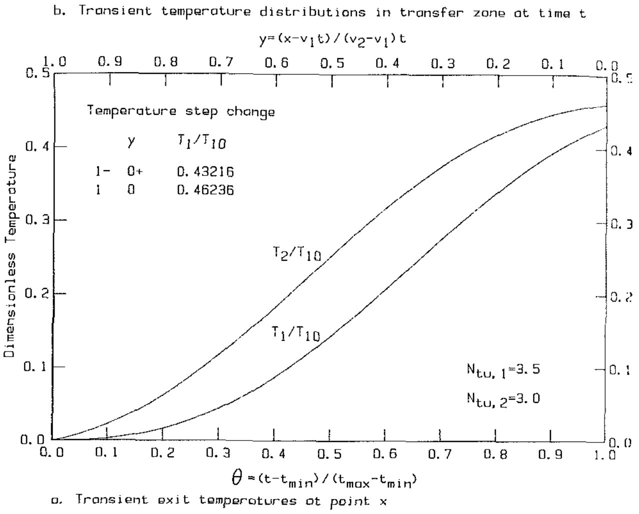

Fig. 5 Transient temperature histories for $N_{tu,1} = 3.5$, $N_{tu,2} = 3$ ($v_1 < v_2$)

and

$$\frac{T_2}{T_{10}} = N_{tu,2}\int_0^{\theta} e^{-N_{tu,\bar\theta}\bar\theta} I_0[2\sqrt{N_{tu,1}N_{tu,2}}\,\bar\theta^{1/2}(1-\bar\theta)^{1/2}]d\bar\theta \qquad (38)$$

where

$$(\text{sign}) = \begin{cases} + & \text{for } v_1 > v_2 \\ - & \text{for } v_1 < v_2 \end{cases} \qquad (39)$$

$$N_{tu,\theta} = \begin{cases} (1-\theta)N_{tu,1} + \theta N_{tu,2} & \text{for } v_1 > v_2 \\ \theta N_{tu,1} + (1-\theta)N_{tu,2} & \text{for } v_1 < v_2 \end{cases} \qquad (40)$$

and

$$E(\theta) = \begin{cases} \frac{1}{2}\, e^{-N_{tu,1}} U(\theta) + \frac{1}{2}\, e^{-N_{tu,2}} U(\theta - 1) & \text{for } v_1 > v_2 \\ \frac{1}{2}\, e^{-N_{tu,1}} U(\theta - 1) + \frac{1}{2}\, e^{-N_{tu,2}} U(\theta) & \text{for } v_1 < v_2 \end{cases} \qquad (41)$$

The numerical results of equations (37) and (38) were computed with three examples where $N_{tu,1} = 1.5$ and $N_{tu,2} = 1.0$ and $N_{tu,1} = 3.5$ and $N_{tu,2} = 3.0$; the results are shown as Case *a* of Figs. 2 to 5.

***B* Transient Temperature Distributions in Equipment or Transfer Zones.** The transient temperature distributions in transfer zones at time *t* can be computed with a new variable as

$$y = \begin{cases} \dfrac{x - v_2 t}{(v_1 - v_2)t} & \text{for } v_1 > v_2 \\[2ex] \dfrac{x - v_1 t}{(v_2 - v_1)t} & \text{for } v_1 < v_2 \end{cases} \qquad (42)$$

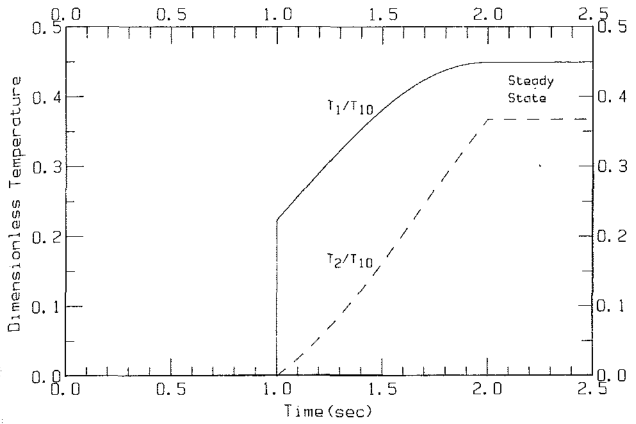

Fig. 6 Transient exit temperature histories for $N_{tu,1} = 1.5$, $N_{tu,2} = 1$ with $L = 4$ m, $v_1 = 4$ m/s, $v_2 = 2$ m/s

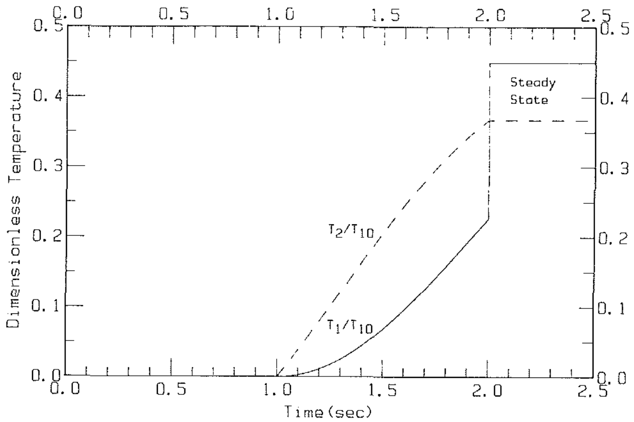

Fig. 7 Transient exit temperature histories for $N_{tu,1} = 1.5$, $N_{tu,2} = 1$ with $L = 4$ m, $v_1 = 2$ m/s, $v_2 = 4$ m/s

One can transform equations (27) and (28) with the variable y defined in equation (42) into two dimensionless equations which are similar to equations (37) and (38). The numerical results are shown as Case b of Figs. 2 to 5.

C **The Validity of Solutions (27) and (28).** The validity of equations (27) and (28) can be seen by comparing solutions of equations (37) and (38) at $\theta = 1$ with steady-state solutions shown as

$$\frac{T_1}{T_{10}} = \frac{N_{tu,2} + N_{tu,1} e^{-(N_{tu,1} + N_{tu,2})}}{N_{tu,1} + N_{tu,2}} \tag{43}$$

$$\frac{T_2}{T_{10}} = \frac{N_{tu,2}}{N_{tu,1} + N_{tu,2}} [1 - e^{-(N_{tu,1} + N_{tu,2})}] \tag{44}$$

The solutions of equations (37) and (38) at $\theta = 1$ should be equal to the steady-state solution, because at $t = t_{\max}$, the transfer processes have attained a steady state.

The numerical results from this comparison are

	Equations (37) and (38) at $\theta = 1$		Steady-state solutions
	$v_1 > v_2$	$v_1 < v_2$	
T_1/T_{10}	0.44924	0.44926	0.44925
T_2/T_{10}	0.36714	0.36719	0.36717

for $N_{tu,1} = 1.5$ and $N_{tu,2} = 1$.

The integrals in equations (37) and (38) were computed with Simpson's 3/8 rule.

D **Solutions With $v_1 = v_2$.** If the step functions are removed from equations (32) and (33), these two equations will be the same as steady-state solutions. The step functions in equations (32) and (33) are transient phenomena. The change from the initial steady state to the final steady state is accompanied by the presence of flow fronts. The temperature distribution at a flow front is discontinuous. This is because of the assumption that there was no axial diffusion of heat or mass. In fact, diffusion always occurs with transfer processes, so the temperature distribution at a flow front should resemble a complementary error function. For $v_1 = v_2$ this analysis is in agreement with the results of [5] when the core thermal capacitance is equal to zero.

5 Discussion

The exact solutions of parallel-current transient transfer processes are obtained in this study with the techniques of Laplace transforms. The validity of exact solutions is verified by comparison to steady-state solutions. $N_{tu,1}$ and $N_{tu,2}$, the number of transfer units for streams 1 and 2, are used as parameters for this study. It should be noted that the velocities are important in the transfer process in a transient situation as shown in Figs. 2–7. When v_1 is larger than v_2 and there is a step temperature change at the entrance of stream 1, the heat flux is always from stream 1 to stream 2 in the transient transfer zone as shown on Figs. 2, 4, and 6. When v_1 is smaller than v_2 and there is a step temperature change at the entrance of stream 1, energy is transferred from stream 1 to stream 2 at the beginning of the transient transfer zone and is carried downstream by stream 2. A part of this energy is then transferred back from stream 2 to stream 1 along the transient transfer zone as shown on Figs. 3, 5, and 7. This is also seen from the fact that the temperature T_2 on Figs. 3, 5, and 7 is always larger than the temperature T_2 on Figs. 2, 4, and 6 and the temperature T_1 on Figs. 3, 5, and 7. One can see that the temperatures T_1 and T_2 shown in Figs. 4 and 5 are closer to a constant asymptotic temperature at the exit of the transient transfer zone than the temperatures shown in Figs. 2 and 3. One can show from equations (43) and (44) that when $N_{tu,1}$ and $N_{tu,2}$ are large, the steady-state solutions of T_1/T_{10} and T_2/T_{20} will approach an asymptotic value.

Figures 6 and 7 show the transient exit temperature distribution in a heat exchanger with length $L = 4$ m, $N_{tu,1} = 1.5$, and $N_{tu,2} = 1.0$. Figure 6 shows the temperatures for the case of $v_1 > v_2$ (i.e., $v_1 = 4$ m/s and $v_2 = 2$ m/s). Figure 7 shows the temperatures for the case of $v_1 < v_2$ (i.e., $v_1 = 2$ m/s and $v_2 = 4$ m/s). On Figs. 6 and 7, for times less than 1 s, the exit temperatures are zero, and for times greater than 2 s, the exit temperatures have reached their steady-state values.

References

1 Hausen, H., *Heat Transfer in Counterflow, Parallel Flow, and Cross Flow*, McGraw-Hill, New York, 1983 (translation edited by A. J. Willmott).

2 Jaswon, M. A., and Smith, W., "Countercurrent Transfer Processes in the Non-Steady State," *Proc. Roy. Soc.*, Series A, Vol. 225, 1954, pp. 226–244.

3 Tan, K. S., and Spinner, I. H., "Numerical Methods of Solution for Continuous Counter-Current Processes in the Nonsteady State," *AIChE Journal*, Vol. 30, 1984, pp. 770–786.

4 Acrivos, A., "Method of Characteristics Technique—Application to Heat and Mass Transfer Problems," *Ind. Eng. Chem.*, Vol. 48, 1956, pp. 703–710.

5 Romie, F. E., "Transient Response of the Parallel-Flow Heat Exchanger," ASME JOURNAL OF HEAT TRANSFER, Vol. 107, No. 3, Aug. 1985, pp. 727–730.

6 Arpaci, V. S., *Conduction Heat Transfer*, Addison-Wesley, Reading, 1966.

7 Carslaw, H. S., and Jaeger, J. C., *Conduction of Heat in Solid*, 2nd ed., Oxford University Press, London, 1959.

A Transient Heat Exchanger Evaluation Test for Arbitrary Fluid Inlet Temperature Variation and Longitudinal Core Conduction

R. S. Mullisen
Mechanical Engineering Department,
California Polytechnic State University,
San Luis Obispo, CA 93407
Mem. ASME

R. I. Loehrke
Mechanical Engineering Department,
Colorado State University,
Fort Collins, CO 80523
Mem. ASME

An improved version of the transient technique is described which utilizes a finite-difference model of the heat exchanger for the evaluation of an average heat transfer coefficient. The model, which can accommodate arbitrary inlet fluid temperature variation as well as longitudinal conduction in the heat exchanger core, is well suited for a computer-based data reduction procedure. The finite-difference model is validated by comparison with the predictions of exact solutions for a step change in inlet temperature. Actual tests on a core of known performance indicate that the overall accuracy of the technique can be within ±2 percent.

Introduction

The transient technique has been used for many years to evaluate average heat transfer coefficients for heat exchangers. In this technique, the heat exchanger is operated as a regenerator. The inlet fluid temperature is varied as a function of time and the resulting exit fluid temperature history is measured. Knowing these two temperature histories, the fluid flow rate and the core physical properties, an average convection coefficient can be determined with the aid of an appropriate theory.

In the past, these theories were applied to well-defined inlet temperature functions of time. The most popular were the step function and the harmonic function. Analytical expressions were obtained linking the inlet and exit fluid temperatures for these two functions. Different evaluation criteria were employed by different investigators to compare theory and experiment for the purpose of picking an appropriate heat transfer coefficient. These include curve matching, maximum slope and initial rise for step function inputs, and amplitude attenuation and phase shift for harmonic inputs. The accuracy of the technique may be strongly dependent on the core parameters, evaluation criteria, and on the precision of the experimental inlet temperature functions. It is often necessary to perform extensive numerical calculations to correct for impurities in the inlet temperature function or to implement a certain evaluation criterion. These corrections to analytical solutions and the evaluation procedure itself may be carried out on a digital computer.

This paper describes an alternative approach in which the entire data reduction scheme including the theoretical prediction is designed from the start to be implemented on a computer. A finite-difference model of the core is used which can accommodate arbitrary inlet temperature functions and longitudinal core conduction. The result is a transient test of improved accuracy and flexibility.

Review of Previous Work

Early work in regenerator theory by Schumann (1929) and others is reviewed by Jakob [1]. Figure 1 shows the dimensionless theoretical regenerator exit fluid temperature response to a step change in the inlet fluid temperature as given by Schumann. It can be seen that there is a unique curve for each NTU value. Furnas [2] in 1932 constructed a test using Schumann's assumptions. He matched his experimental exit fluid temperature with Schumann's curves and thereby was able to determine the average heat transfer coefficient for his test core. This "direct curve matching" technique, as it is now called, required considerable computational effort.

In order to reduce the magnitude of the data reduction effort required by the direct curve matching method, Locke [3] advanced his "maximum slope" technique in 1950. Owing to the uniqueness of the maximum slope of the exit fluid temperature curve, within a given NTU range, Locke was able to give an explicit relationship between NTU and maximum slope. Locke's analysis was restricted, however, to cores with zero longitudinal conduction.

Creswick [4] in 1957 was first to apply a numerical technique for the solution of the governing equations and considered, also for the first time, longitudinal conduction in the core. Howard [5] in 1964 extended the work of Creswick by employing an explicit, finite-difference numerical method to obtain a relationship between NTU, maximum slope, and a longitudinal conduction parameter. However, the uncertainty analysis given by Howard indicates the maximum slope method should not be used below NTU of about 3.5.

In order to test cores in the low NTU range, Kohlmayr [6] advanced an indirect curve matching method in 1968 to cover the range 0.5 < NTU < 5.0. The method involves finding the centroid of the area under the exit fluid temperature curve. The analysis relates the position of this centroid to the core NTU. In addition, Kohlmayr provides an analysis for an arbitrary inlet fluid temperature change. He does not, however, put his centroid method to the test and it appears, from reviewing the literature, that only Wheeler [7] has employed this method and with uncertain conclusions.

Another method to reduce the single blow data from low NTU cores was employed by Mondt and Siegla [8] in 1972. Their "initial rise" procedure makes use of the unique

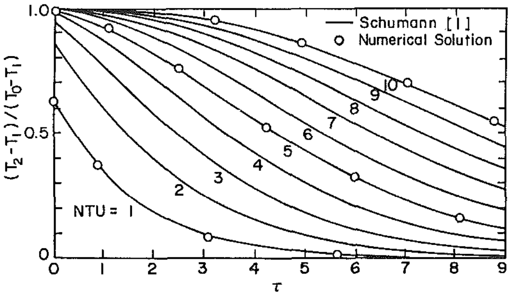

Fig. 1 Regenerator exit fluid temperature response for an inlet step change in fluid temperature.

Contributed by the Heat Transfer Division for publication in the JOURNAL OF HEAT TRANSFER. Manuscript received by the Heat Transfer Division June 19, 1984. Paper No. 83-HT-65.

relation between the step change in the exit fluid temperature at time $t = 0+$ and NTU. This step is quite apparent in Fig. 1 for NTU ≤ 3.

In most of the single blow methods that have been applied, the analysis was based on a step change in inlet fluid temperature. Special efforts have been taken to approximate this step change in experiments. Pucci et al. [9] used a sliding drawer test facility in which the core was moved mechanically from a heated airstream into an ambient airstream. Senshu et al. [10] employed a movable heater that dropped out of the inlet airstream. In practice, however, a true step change is impossible. With the "initial rise" method, data are taken at $t = 0+$; with the "maximum slope" method at low NTU's, the maximum slope occurs near $t = 0+$. Thus, there is considerable sensitivity to the inherent experimental deviation in the inlet fluid temperature step. The result is a convection coefficient value of large uncertainty. To alleviate this large uncertainty in the low NTU range, Liang and Yang [11] in 1975 advanced a single blow analysis based on an experimentally determined inlet fluid temperature response. By experiment, Liang and Yang find the time constant of their heating screen and use this in their analysis to arrive at a theoretical exit air temperature response. By direct curve matching using five points, they determine the average heat transfer convection coefficient of the core.

The "periodic method" was first employed by Bell and Katz [12] in 1949. Their analysis assumed zero longitudinal conduction and sinusoidal inlet fluid temperature variation. Stang and Bush [13] refined the analysis and test technique to accommodate finite longitudinal conduction and arbitrary periodic inlet fluid temperature. In Stang and Bush's work, a Fourier analysis is performed on the data to extract the fundamental components of the inlet and exit fluid temperature waves to accommodate nonharmonic, periodic inlet temperature variations. An average heat transfer coefficient is determined from the measured amplitude attenuation, or phase shift, between the inlet and exit fundamental components. One drawback of the periodic method is that the test period must be selected based on prior knowledge of core NTU to achieve accurate results. This may require multiple testing to arrive at a single data point. Also, for the large NTU cores, test times can be long, since about five periods are required for the startup transients to die out.

In a recent review paper, Shah [14] reports the experimental uncertainty in j for existing transient tests at ±10-15 percent and cites the need for tests with less uncertainty. In addition, it is desirable to have a transient test of short duration with rapid data reduction. A unique test using direct curve matching was thus developed to fulfill these needs.

Data Reduction Procedure

A theoretical prediction for the exit fluid temperature history is obtained by solving a finite-difference model of the heat exchanger with the measured inlet temperature function as input. An initial value problem for conduction in the solid core is coupled to a one-dimensional convection problem in the fluid passages through an average heat transfer coefficient h. In the evaluation procedure, a value for h is guessed and the finite-difference equations are solved to yield an exit fluid temperature history prediction. This prediction is compared with the measured history. If the two curves match within specified limits, then the assumed h is correct. If the curves do not match, h is changed and the process is repeated until an appropriate value is obtained.

This procedure has been used for the evaluation of interrupted-plate surfaces and it is this geometry which will be used to illustrate the details of the method. Figure 2(*a*) shows interrupted wall passages comprised of multiple in-line plates. A pair of plates forming a single passage appears in Fig. 2(*b*). By symmetry, half of this single passage, represented in Fig. 2(*c*), is analyzed with the following idealizations applied:

1 Steady flow
2 Finite wall conduction in flow direction
3 Infinite wall conduction perpendicular to flow direction
4 Zero fluid conduction in flow direction
5 Zero fluid thermal capacity
6 Constant properties
7 Adiabatic side walls

Nomenclature

A = core heat transfer area excluding area of plate edges = number of plates × 2 LW, m^2
A_c = core minimum free flow area, m^2
A_{fr} = core frontal area, m^2
a = half-plate thickness, m
c = wall specific heat, J/kg °C
c_p = air specific heat, J/kg °C
CL = centerline, Fig. 2
f = average friction factor = $(r_h/L_p)\ [\Delta p_c/(G^2/2p)]$ or $(r_h/L^*)\ [\Delta p_t/(G^2/2p) - K_c - K_e]$
G = core mass velocity = $\dot{m}/A_c$, kg/s m^2
h = heat transfer coefficient, W/m^2 °C
i = enthalpy, J/kg
j = Colburn factor = $(h/Gc_p) \cdot \mathrm{Pr}^{2/3}$
K_c = core entrance pressure loss coefficient
K_e = core exit pressure loss coefficient
k = thermal conductivity, W/m°C
L = plate length, Fig. 2, m
L_p = distance between core pressure taps, m
L^* = flow length over heat transfer surface of core, m
m = core mass, kg
$\dot{m}$ = air mass flow rate, kg/s
NTU = number of transfer units = $(hA)/(\dot{m}c_p)$
q = heat transfer rate, W
Re_d = Reynolds number = $4 r_h G/\mu$
r_h = hydraulic radius = $A_c L^*/A$, m
T = temperature, °C
T_0 = initial uniform temperature, °C
T_1 = measured inlet air temperature, °C
T_2 = measured exit air temperature, °C
t = time, s
W = plate span, m
x = axial flow direction coordinate, m
λ = longitudinal conduction parameter = $(kaW)/(\dot{m}c_p L)$
μ = dynamic viscosity of air, Pa s
ρ = density of air, kg/m^3
τ = dimensionless time = $(\dot{m}c_p\ \mathrm{NTU}\ t)/(mc)$
Δp_c = pressure drop between core static pressure taps, Pa
Δp_t = pressure drop between tunnel static pressure taps, Pa

Superscripts

n = time step in finite-difference analysis

Subscripts

d = hydraulic diameter
f = fluid
i = node in finite-difference analysis
m = number of finite-difference nodes in the wall
w = wall
0 = initial conditions
1 = at core entrance
2 = at core exit

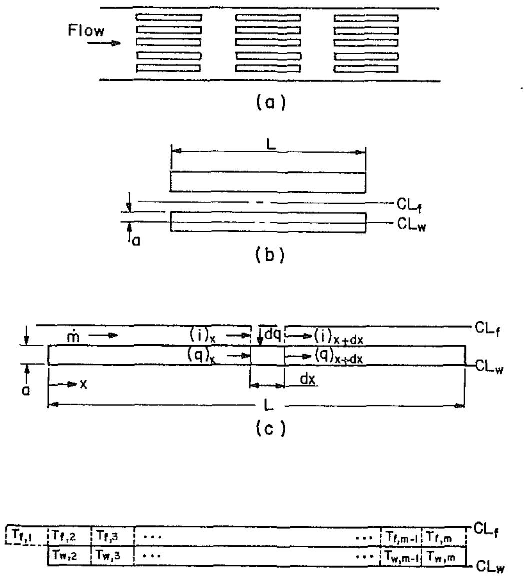

Fig. 2 (*a*) **Multiple, in-line plates; (*b*) a single pair of plates; (*c*) half-flow passage and half-plate; (*d*) the division into finite-difference nodes.**

Under these assumptions the energy equation for the wall is

$$\frac{\partial T_w}{\partial t} = \frac{k}{\rho c}\frac{\partial^2 T_w}{\partial x^2} + \frac{h}{\rho ac}(T_f - T_w) \tag{1}$$

while that for the fluid is

$$\frac{\partial T_f}{\partial x} + \frac{Wh}{\dot{m}c_p}(T_f - T_w) = 0 \tag{2}$$

The governing equations (1) and (2) are subject to the following initial condition

$$T_w(x,\ t=0) = T_f(x,\ t=0) = T_0 \tag{3}$$

This equation expresses thermal equilibrium between the wall and the fluid. The initial temperature T_0 is known from the experiment. The conditions at the heat exchanger inlet and outlet are also known from experiment

$$T_f(x=0,\ t) = T_1(t) \tag{4}$$

$$T_f(x=L,\ t) = T_2(t) \tag{5}$$

where $T_1(t)$ and $T_2(t)$ are the measured inlet and outlet fluid temperatures, respectively. $T_1(t)$ is not restricted to a step or periodic function.

Equations (1) and (2) are converted to finite-difference equations and solved numerically. The fluid and wall in Fig. 2(*c*) are divided into nodes as shown in Fig. 2(*d*). Using an implicit formulation which is second-order accurate in x and first-order in t, equation (1) becomes

$$\frac{T^{n+1}_{w,i} - T^n_{w,i}}{\Delta t} = \frac{k}{2\rho c}\left[\frac{T^{n+1}_{w,i-1} - 2T^{n+1}_{w,i} + T^{n+1}_{w,i+1}}{(\Delta x)^2}\right] + \frac{k}{2\rho c}\left[\frac{T^n_{w,i-1} - 2T^n_{w,i} + T^n_{w,i+1}}{(\Delta x)^2}\right] + \frac{h}{\rho ac}[T^n_{f,i} - T^n_{w,i}] \tag{6}$$

for i = 2 to m. For i = 2 and m, representing left and right end wall nodes respectively, the assumption is made that no heat is conducted out these ends. This assumption is also made for the end nodes in each wall segment of the interrupted-plate geometry. These boundary conditions are satisfied by setting $T^n_{w,1} = T^n_{w,2}$ and $T^n_{w,m+1} = T^n_{w,m}$, where nodes 1 and $m+1$ are fictitious image nodes. These specific boundary conditions were chosen so that the heat transfer coefficients obtained for the interrupted surfaces could be directly compared with those for continuous plates. These conditions force the surface area on which h is based to be the same in both cases. Using these conditions, equation (6) is expressed as a single matrix equation.

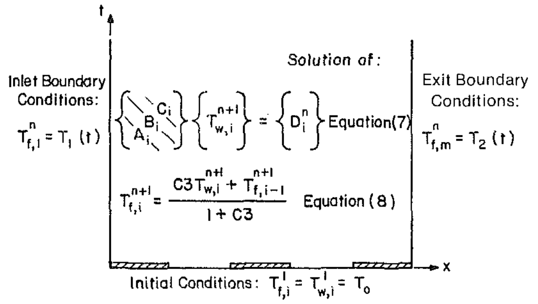

Fig. 3 The direct curve matching solution domain.

$$\begin{Bmatrix} \ddots & & C_i \\ \ddots & B_i & \ddots \\ A_i & \ddots & \end{Bmatrix}\begin{Bmatrix} T^{n+1}_{w,i} \end{Bmatrix} = \begin{Bmatrix} D^n_i \end{Bmatrix} \tag{7}$$

where

$C1 = (k\Delta t)/(2\rho c(\Delta x)^2)$
$A_i = C1$, for $i = 3, m$
$A_2 = 0$
$B_2 = -C1 - 1$
$B_m = B_2$
$B_i = -2C1 - 1$, for $i = 3, m-1$
$C_i = C1$, for $i = 2, m-1$
$C_m = 0$
$D_i = T^n_{w,i}[2C1 + (h\Delta t/\rho ac) - 1] - C1[T^n_{w,i-1} + T^n_{w,i+1}] - [h\Delta t/\rho ac]T^n_{f,i}$, for $i = 2, m$

In equation (7), A_i, B_i, and C_i, are elements of the lower, middle, and upper diagonals of the tridiagonal matrix with all other elements zero. The right-hand side vector D_i is known. Equation (2) is written in backward finite-difference form which gives

$$T^{n+1}_{f,i} = \frac{C3T^{n+1}_{w,i} + T^{n+1}_{f,i-1}}{1+C3} \tag{8}$$

where

$$C3 = \frac{h(\Delta x)W}{\dot{m}c_p}$$

The initial condition specified by equation (3) becomes

$$T^1_{w,i} = T^1_{f,i} = T_0 \tag{9}$$

and boundary conditions of equations (4) and (5) become

$$T^n_{f,1} = T_1(t) \tag{10}$$

$$T^n_{f,m} = T_2(t) \tag{11}$$

The solution domain is depicted in Fig. 3. The objective is to obtain the convection coefficient h, which is tied up in equations (7) and (8). The overall procedure is to guess at h, solve equations (7) and (8) subject to initial condition (9) and inlet boundary condition (10), and arrive at a theoretical exit fluid temperature history $T^n_{f,m}$. These $T^n_{f,m}$ are then compared with the experimental exit fluid temperature history $T_2(t)$. If these two temperature histories match within specific limits (unlikely the first time), then the originally assumed value of h is the correct average heat transfer coefficient of the core. If the histories do not match, h is iteratively changed until agreement, within specified limits, is obtained.

More specifically, the solution proceeds as follows. Equations (7) and (8) are solved in a marching fashion, moving in the direction of time. Moreover, since tests were planned for cores constructed of interrupted-wall passages, the solution of equations (7) and (8), at a given time step, begins with the first upstream passage and then proceeds to subsequent downstream passages. Starting at the second time step ($n = 2$), and the first upstream passage, $T_{w,i}^2$ is obtained by solution of equation (7) using the initial conditions and inlet boundary conditions. At this same time step and same first passage, $T_{f,i}^2$ is obtained next by solving equation (8) with a single sweep starting with the inlet boundary conditions. Still at time $n = 2$, the inlet fluid temperature of the second passage is set equal to the exit fluid temperature of the first passage before equations (7) and (8) are solved in the second passage. This procedure continues through subsequent downstream passages. After all $T_{w,i}^2$ and $T_{f,i}^2$ are calculated, then the temperatures $T_{w,i}^3$ and $T_{f,i}^3$ are obtained in a similar fashion at the third time step, and so the solution advances in time. The procedure is halted after a specified time step is reached. The initial guesses of h and the subsequent iterative adjustment of this parameter, until the theoretical and experimental exit fluid temperatures match within specified limits, follow the method of regula-falsi. The regula-falsi method treats the error between the theoretical and experimental exit fluid temperature histories as a function dependent on h. Two such errors are computed: an average algebraic difference and an average absolute difference between $T_{f,m}^n$ and $T_2(t)$ over the test duration. The average algebraic difference is required by regula-falsi and the value of h is adjusted in an attempt to drive this error to zero. The average absolute difference is used as a convergence criterion.

The numerical method has been used to predict exit fluid temperatures over a range of parameters, $0.1 \leq \text{NTU} \leq 20$ and $0 \leq \lambda \leq 30$. No signs of instability were ever observed. The mesh size is always chosen on the basis of accuracy considerations rather than stability considerations. The method converges to the correct steady-state solution regardless of the size of the time step chosen.

The accuracy of the finite-difference scheme was checked by comparing the numerical solutions of equations (7) and (8) with the available analytical solutions for a step change in inlet fluid temperature. The exit fluid temperature response, for various values of NTU and zero streamwise wall conduction, shows excellent agreement with Schumann's [1] curves in Fig. 1. Typical results, at NTU = 16 for various values of the dimensionless conduction parameter λ, are shown by the solid lines in Fig. 4. Again, the agreement with the exact solution for zero conduction $\lambda = 0$ is good. The response curve for $\lambda = 10$ (and for larger values of λ) is very close to the exact solution for $\lambda = \infty$. There is no exact solution available for comparison for $\lambda = 1$ but there are other published numerical solutions. Handley and Heggs [15] compared their results obtained using an implicit scheme, with those obtained using Creswick's [4] explicit scheme. In general, the present results agree with the results of these investigators when they agree with each other and lie between their results otherwise. The poorest agreement occurs at high NTU. The comparison shown in Fig. 4 is an example of the poorest agreement.

Conservation of energy demands that the energy convected away by the air leaving a hot core be equal to the energy lost by the solid as it cools. When this energy balance is stated in terms of dimensionless variables it yields the condition that the area under the normalized curves in Fig. 4, for $\tau \to \infty$, be equal to NTU regardless of the value of λ. This is a necessary condition for the correctness of a solution. As a further check of the present numerical method, the three curves were numerically integrated out to $\tau = 100$. The resultant areas were within 0.2 percent of NTU. The integral of the exact solution for $\lambda = \infty$ out to $\tau = 100$ gives 0.2 percent closure. An estimate, made by fitting a curve through the solution points of Handley and Heggs, indicates that the energy content of their flow is about 13 percent too low. A similar estimate for the points by Creswick (as quoted in Handley and Heggs) indicates an energy content 6 percent too high. It is critical for the application proposed here that energy conservation errors be minimized since the error in the predicted heat transfer coefficient will be equal to the error in the energy balance. The present finite-difference method is well suited to this application.

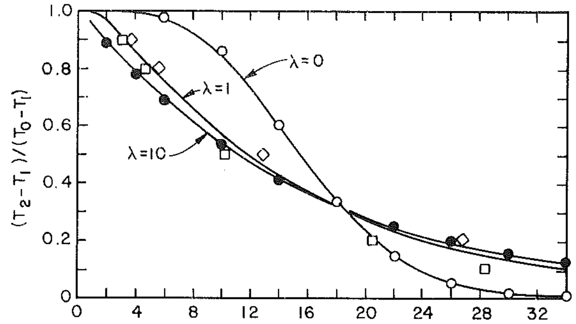

Fig. 4 Evaluation of numerical procedure for step change in inlet temperature with longitudinal conduction at NTU = 16. Solid lines are numerical results with $\Delta\tau = 0.05$ and $\Delta X/L = 0.02$. Symbols: ○ analytical solution, $\lambda = 0$; ● analytical solution, $\lambda = \infty$; □ Handley and Heggs [15], $\lambda = 1$; ◇ Creswick [15], $\lambda = 1$.

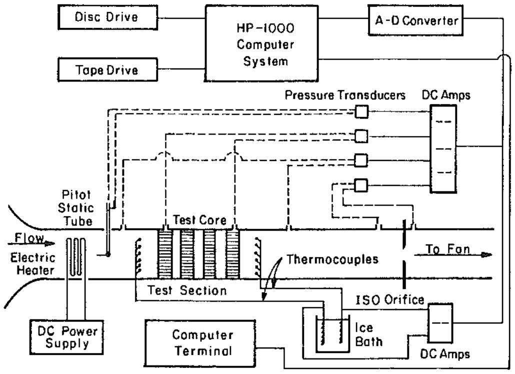

Fig. 5 Instrumentation, data acquisition, and data reduction systems.

The complete data reduction procedure was performed by the FORTRAN program "MATCH." A detailed description of this program is given in [16]. A final test of the method, both experimental and numerical, is discussed following the description of the experimental apparatus.

Experimental Apparatus

Tests employing the data reduction procedure just described were conducted on a parallel-plate array in air. The required inlet and exit air temperature histories were measured, digitized, and entered directly into the computer in which the numerical calculations were performed. The experimental apparatus consisting of the wind tunnel, instrumentation, data acquisition and reduction systems and the test core are described in this section. The test technique and results are presented in the next section.

A schematic diagram of the entire system is shown in Fig. 5. The wind tunnel consists of a nine-to-one square contraction section followed by a four-to-one contraction section, a 15.24 cm by 15.24 cm insulated test section, a 15.24 cm diameter orifice pipe section, and a plenum box containing the fan and motor. An electric resistance heater is located just upstream of the test section. The air temperature at the core inlet is measured by six, 0.076-mm-dia, copper-constantan thermocouples connected in series and strung across the test section just upstream from the core. A similar thermocouple array is located sufficiently far downstream of the core exit to indicate a mixed mean exit air temperature.

The electric heater is constructed of fine wire mesh screens with a relatively large surface area of 760 cm^2 compared to

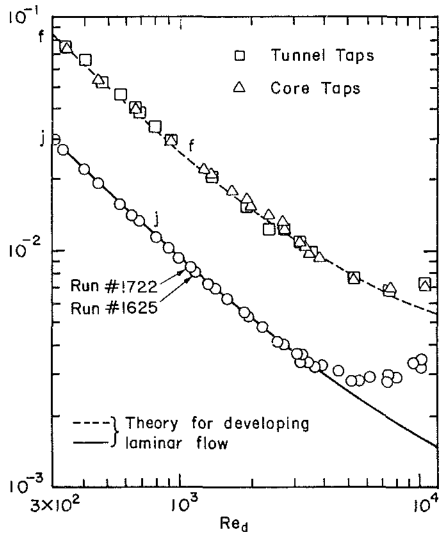

Fig. 6 Heat transfer and friction factors: theories for *j* from Stephan [18] and for *f* from Shah [20].

the flow area of 232 cm^2. This allows the heater to be operated at a low temperature. The upstream thermocouples in direct view of the heater were therefore not required to have radiation shields. This is of critical importance, because the transient test is most sensitive to temperature measurement errors. Shielding the fine wire thermocouples would increase the time response which would adversely affect the transient test.

Special precautions were taken in the design of the test section, heater support structure and the core assembly to ensure that the thermal capacity of the active core surfaces dominates during the test period. The interior surface of the test section is lined with foam and the support structure for the plate arrays is made from balsa wood.

The analog voltage output from the two thermocouple circuits is amplified by 1000 and digitized by a Preston A-D converter. The resulting time series is fed into an HP-1000 system (HP-21MX, E-Series computer) where it is used in the data reduction scheme described earlier.

A test core consisting of equally spaced horizontal parallel plates was constructed for the purpose of checking out the experimental facility. Each of the aluminum plates measures 0.154 cm thick, 15.24 cm wide, and 22.86 cm long. The vertical spacing between the plates is 0.447 cm. The plates were sheared from a single, large sheet selected for uniformity of thickness. The burred edges, due to the shearing process, were removed with a few strokes of a hand file. The plate array was formed by epoxy bonding the plates to balsa wood side walls. The assembly was clamped during curing in a jig specifically designed to maintain dimensional accuracy.

Two static pressure ports were drilled into one of the central plates in the stack. These 0.66-mm-dia ports are located midway between the side supports. One of these ports is 1.9 cm downstream from the leading edge of the plate and the other is 0.32 cm upstream from the trailing edge. The pressure drop measured between these two core taps was used to evaluate an average friction factor for the core according to the definitions provided in the Nomenclature.

The pressure drop between static taps located upstream and downstream of the test core was also measured. Three taps in the wind tunnel wall at each streamwise station were connected together to yield an average static pressure. The measured pressure drop between these tunnel taps was also used to estimate an average friction factor according to the definitions provided in the Nomenclature. The entrance and exit loss coefficients required for this purpose were taken from [17].

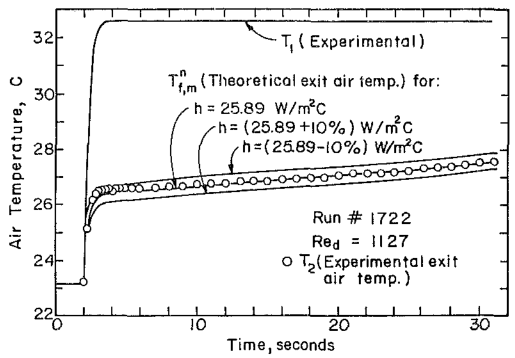

Fig. 7 Curve match for a step rise in T_1, NTU = 1.12.

The mass flow rate through the core was determined, at low flow rates, from the pressure drop across a standard ISO orifice. At high flow rates, the output of a pitot-static tube located upstream of the test core was used, along with a calibration of the tunnel velocity profile, to indicate flow rate. All of the differential pressure signals were converted to electric signals by Validyne Model DP15TL pressure transducers and digitized for computer processing.

Results and Discussion

The parallel-plate geometry was chosen for test since it approximates a geometry for which accepted theoretical predictions for heat transfer and pressure drop are available. The theory is for developing flow between parallel plates of infinite aspect ratio with constant wall temperature. The correlation of Stephan [18] as reported by Shah and London [19] is used here for comparison purposes.

The 26 parallel-plate core was tested over the Reynolds number range 300 to 10,000. The experimental results from the program MATCH, along with the laminar flow theory, are given in Fig. 6. The agreement is excellent up to Re_d = 3000, where transition to turbulence appears to take place. Taking the 23 data points between $296 \leq Re_d \leq 2660$ as lying in the laminar flow region, the average absolute deviation of the *j* data from theory is only 1.7 percent. The uncertainty analysis, summarized in the Appendix, for three of these *j* data points gives an average of 1.2 percent.

The friction factors computed from the measured core and tunnel pressure drops are also plotted in Fig. 6. These are compared with the laminar developing flow theory given by Shah [20]. This theory is also for flow between parallel plates of infinite aspect ratio. The value of *f* calculated from the theory and plotted in Fig. 6 is the average between the core pressure tap locations. For the laminar flow region, $Re_d < 3000$, the average absolute deviation of the core *f* data from theory is 5.3 percent. The uncertainty analysis for three of these *f* data points gives an average of 0.9 percent (see Appendix).

Two *j* data points from Fig. 6 are examined to show details of the curve matching technique. Run number 1722 is at Re_d = 1127 (see Fig. 7) and has the usual step rise in inlet air temperature as required in all previous single blow tests. Run number 1625 is at Re_d = 1152 (see Fig. 8) and has an inlet air temperature rise that is ramplike in appearance and can only be accommodated by the present curve-matching technique. Figure 7 shows the measured inlet (T_1) and measured outlet (T_2) air temperatures plotted against time for run number 1722. For this run, the heater power was first set to give about a 10°C rise in inlet air temperature. At the beginning of the run the main power supply switch was flipped on to achieve a step temperature rise. Notice, however, that T_1 is not a pure step function, a problem discussed earlier. The measured exit air temperature shows an initial rise followed by a gradual increase in temperature. The theoretical exit air temperature,

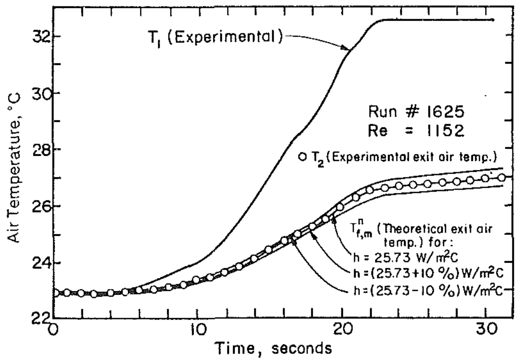

Fig. 8 Curve match for a ramplike rise in T_1, NTU = 1.09.

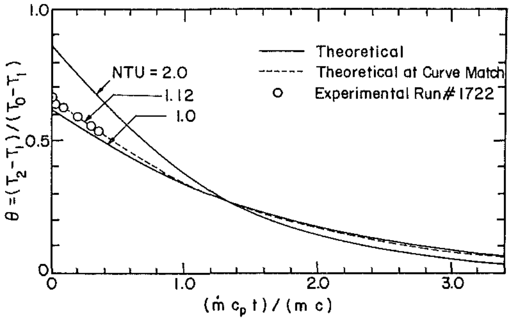

Fig. 9 Curve match for a step change in T_1.

from the program MATCH, best matches the experimental curve at $h = 25.89$ W/m^2 °C. The rms deviation between the theoretical and experimental curves is 0.051°C. The greatest deviation, although slight, occurs during the initial rise. Thermocouple response is a factor and is treated in [16]. The two other theoretical exit air temperature curves plotted in Fig. 7 are for $h = 25.89$ W/m^2 °C ± 10 percent; they show the theoretical curve's sensitivity to h.

For run number 1722, the test time is just over 31 s. A good perspective of this test time, compared to the overall response of the core, can be obtained by viewing Fig. 9. In this figure, the dimensionless theoretical exit air temperature is plotted against dimensionless time for NTU = 1, 2, and 1.12. NTU of 1.12 corresponds to $h = 25.89$ W/m^2 °C, the value at curve match. The dimensionless time used for Fig. 9 is different from that used in Fig. 1 by a factor of NTU and was chosen so that the integral under any theoretical curve from $t = 0$ to ∞ equals unity.

The second j data point to be examined is run number 1625. Figure 8 shows the measured inlet and exit air temperatures for this run. The inlet air temperature rise with a ramplike appearance was obtained by manually increasing the heater power supply output. From the program MATCH, a nearly identical theoretical $T^n_{f,m}$ curve is matched to the experimental T_2 curve at $h = 25.73$ W/m^2 °C or NTU = 1.09. The rms deviation between the two curves is only 0.023°C. Again, two other theoretical curves for $h = 25.73$ W/m^2 °C ± 10 percent are plotted to show the sensitivity of the theoretical curve to h.

While both run numbers 1722 and 1625 give excellent j results, as was shown in Fig. 6, the curve match for run number 1625, with a ramplike inlet air temperature rise, is superior to run number 1722, which has a step inlet air temperature rise. An implication of this result is that an optimum inlet air temperature history might exist for a particular experimental setup, but this possibility was not explored further.

Compared with previously published transient test techniques, the present direct curve matching test incorporated in MATCH appears to give the most accurate results in the shortest period of time. Typical data collection times were 5 to 60 s for NTU ranging from 0.5 to 5.0, with data reduction requiring about 20 s. With a given test core in the test section, experiments were performed over a Reynolds number range of 200 to 10,000. On the average, it took only 10 min to collect, store, retrieve, and reduce the data, print out the information, plot the reduced data for both j and f and bring the core into thermal equilibrium, all set for another Reynolds number run.

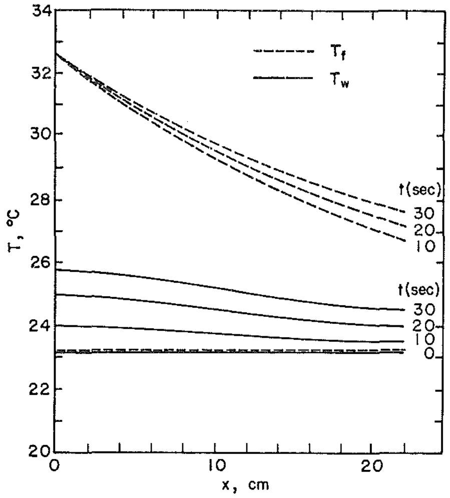

Fig. 10 Theoretical wall and air temperature profiles at curve match for run 1722, NTU = 1.12.

Thermal boundary conditions affect heat transfer coefficients, particularly in the laminar flow region. In the present curve matching test, as in all transient tests except the initial rise test, the thermal boundary conditions are functions of both time and space. Since a finite period of time is required for the curve matching test, it is thus impossible to fix the thermal boundary conditions. However, in the present test, the data are collected over a relatively short period of time, with the result that the constant wall temperature boundary condition is closely approached. For example, theoretical results for a typical test are given in Fig. 10, where wall and air temperatures at curve match are plotted as a function of space and time for run number 1722. The inlet air temperature rise is 9.4°C. After 10 s, the inlet and exit wall temperatures differ by 0.5°C; after 30 s, the test is 1.5 s from termination and the difference is 1.3°C. These relatively small wall temperature differences show that the constant wall temperature thermal boundary condition is approached at NTU = 1.12 in the present curve matching test. However, this condition does depend on NTU and on λ. The wall temperature difference at a particular value of dimensionless time will tend to increase with increasing NTU and decreasing λ.

Summary

A direct curve matching transient heat exchange test was developed for use with a computer-based data acquisition and reduction system. The data reduction procedure involves the numerical solution of finite difference equations describing the heat transfer in the core. This approach has the unique advantage of accommodating any arbitrary inlet fluid temperature history.

Longitudinal conduction within the wall is accounted for in the present formulation. The conduction properties, thermal conductivity or wall thickness, may vary in the streamwise direction as in interrupted surfaces. Infinite transverse wall conduction was assumed in the present formulation but finite transverse conduction could be easily accommodated in the numerical model.

Tests run using the numerical curve matching technique produced accurate results in short times. Because of the short test times, deviations from constant wall temperature boundary conditions are minimized.

Acknowledgments

This research was supported by NSF through grant CME-8009046.

References

1 Jakob, M., *Heat Transfer*, Vol. II, Wiley, 1957.

2 Furnas, C. C., "Heat Transfer From Gas Stream to Bed of Broken Solids," U.S. Bureau of Mines, Bulletin No. 361, 1932.

3 Locke, G. L., "Heat Transfer and Flow Friction Characteristics of Porous Solids," Technical Report No. 10, Department of Mechancial Engineering, Stanford University, Stanford, 1950.

3 Creswick, F. A., "A Digital Computer Solution of the Equations for Transient Heating of a Porous Solid, Including the Effects of Longitudinal Conduction," *Industrial Mathematics*, Vol. 8, 1957, p. 61.

4 Howard, C. P., "The Single-Blow Problem Including the Effects of Longitudinal Conduction," ASME Paper No. 64-GTP-11, March 1964.

5 Kohlmayr, G. F., "An Indirect Curve Matching Method for Transient Matrix Heat-Transfer Testing in the Low NTU Range," *International Journal of Heat and Mass Transfer*, Vol. 11, 1968, pp. 567-581.

6 Wheeler, A. J., "Single-Blow Transient Testing of Matrix-Type Heat Exchanger Surfaces at Low Values of NTU," Technical Report No. 68, Department of Mechanical Engineering, Stanford University, Stanford, 1968.

8 Mondt, J. R., and Siegla, D. C., "Performance of Perforated Heat Exchanger Surfaces," ASME *Journal of Engineering for Power*, Vol. 96, 1974, pp. 81-86.

9 Pucci, P. F., Howard, C. P., and Piersall, C. H., Jr., "The Single-Blow Transient Testing Technique for Compact Heat Exchanger Surfaces," ASME *Journal of Engineering for Power*, Vol. 89, 1967, pp. 29-40.

10 Senshu, T., Hatada, T., and Ishibane, K., "Surface Heat Transfer Coefficients of Fins Used in Air-Cooled Heat Exchangers," *Heat Transfer—Japanese Research*, Vol. 8, No. 4, 1979, pp. 16-26.

11 Liang, C. Y., and Yang, W.-J., "Modified Single-Blow Technique for Performance Evaluation on Heat Transfer Surfaces," ASME JOURNAL OF HEAT TRANSFER, 1975, pp. 16-21.

12 Bell, J. C., and Katz, E. F., "A Method for Measuring Surface Heat Transfer Using Cyclic Temperature Variations," *Proceedings of the Heat Transfer and Fluid Mechanics Institute*, Vol. 2, 1949, pp. 243-254.

13 Stang, J. H., and Bush, J. E., "The Periodic Method for Testing Compact Heat Exchanger Surfaces," ASME *Journal of Engineering for Power*, Vol. 96, 1974, pp. 87-94.

14 Shah, R. K., "Research Needs in Low Reynolds Number Flow Heat Exchangers," *Heat Transfer Engineering*, Vol. 3, No. 2, 1981, pp. 49-61.

15 Handley, D., and Heggs, P. J., "The Effect of Thermal Conductivity of the Packing Material on Transient Heat Transfer in a Fixed Bed," *Int. J. Heat Mass Transfer*, Vol. 12, 1969, pp. 549-570.

16 Mullisen, R. S., "Heat Transfer, Pressure Drop, and Fluid Flow in Interrupted Wall Passages," Ph.D. thesis, Mechanical Engineering Department, Colorado State University, Fort Collins, 1983.

17 Kays, W. M., and London, A. L., *Compact Heat Exchangers*, 2nd ed., McGraw-Hill, New York, 1964.

18 Stephan, K., "Wärmeübergang und druckabfall bei nicht ausgebildeter Laminarströmung in Rohren und in ebenen Spalten," *Chem.-Ing.-Tech.*, Vol. 31, 1959, pp. 773-778.

19 Shah, R. K., and London, A. L., *Laminar Flow Forced Convection in Ducts*, Academic Press, New York, 1978.

20 Shah, R. K., "A Correlation for Laminar Hydrodynamic Entry Length Solutions for Circular and Noncircular Ducts," ASME *Journal of Fluids Engineering*, Vol. 100, 1978, pp. 177-179.

21 Kline, S. J., and McClintock, F. A., "Describing Uncertainties in Single-Sample Experiments," *Mechanical Engineering*, Jan. 1953, pp. 3-8.

22 Moffat, R. J., "Contributions to the Theory of Single-Sample Uncertainty Analysis," ASME *Journal of Fluids Engineering*, Vol. 104, 1982, pp. 250-260.

Table 1 Uncertainty analysis summary

Run No.	Re_d	NTU	T_{step} (°C)	Percent uncertainty		
				j	f	Re_d
1619	296	3.96	10.80	0.33	1.15	0.48
1625	1152	1.09	9.53	1.46	0.87	0.58
1633	2780	0.54	10.72	1.94	0.62	0.58
1634	3386	0.48	9.97	1.57	4.57	2.40
1642	10378	0.45	3.58	8.29	0.84	0.62

APPENDIX

Uncertainty Analysis

The heat transfer and pressure drop experiments described were performed only once at a given operating condition. Kline and McClintock [21] describe such experiments as single sample. The uncertainty bands that may be placed on the reduced data (j, f, and Re_d) are a function of the uncertainties in the measurements made during the experiments. According to Kline and McClintock, if the result R of a single-sample experiment is a function of n independent variables

$$R = f(x_1, x_2, x_3, \ldots, x_n), \tag{12}$$

and if x_i are normally distributed, then the uncertainty in R is

$$\delta R = \left[\left(\frac{\partial R}{\partial x_1} \delta x_1 \right)^2 + \left(\frac{\partial R}{\partial x_2} \delta x_2 \right)^2 + \ldots + \left(\frac{\partial R}{\partial x_n} \delta x_n \right)^2 \right]^{1/2} \tag{13}$$

An additional requirement is that the odds must be the same for each independent variable uncertainty δx_i.

The functional relationships between the dependent variables j, f, and Re_d, and the various independent variables are contained in the data reduction program MATCH. Therefore, the partial derivatives required in equation (13) are obtained through MATCH. This is done, as suggested by Moffat [22], by adding δx_i to x_i as data for the program. Forward finite differences are then used to approximate the partial derivations

$$\frac{\partial R}{\partial x_i} = \frac{(R)_{x_i + \delta x_i} - (R)_{x_i}}{\delta x_i} \tag{14}$$

The results of the analysis performed on runs spanning the range of variables are given in Table 1. The uncertainty in j is seen to be below 2 percent except for run 1642, where it is 8.29 percent. Due to electrical power input limitations and the high flow rate at this run, the air temperature rise was only 3.58°C as compared to the approximately 10°C rise used for the other listed runs. This smaller temperature step makes j more sensitive to the uncertainty in the measured air temperatures.

The uncertainty in f, from Table 1, is about 1 percent, except for run 1634, where the value is 4.57 percent. At this run, the pitot tube used for mass flow measurement was operating at its lower velocity limit. The uncertainty in Re_d is approximately 0.5 percent when the flow is measured using the ISO orifice. When flow measurements are made with the pitot tube, the uncertainty is higher, about 2.5 percent.

A Study of the Flow Mechanisms Responsible for Heat Transfer Enhancement in Interrupted-Plate Heat Exchangers

R. S. Mullisen
Mechanical Engineering Department,
California Polytechnic State University,
San Luis Obispo, CA 93407
Mem. ASME

R. I. Loehrke
Mechanical Engineering Department,
Colorado State University,
Fort Collins, CO 80523
Mem. ASME

Certain compact heat exchanger cores are modeled by assemblies of parallel plates. The heat transfer in these cores may be enhanced if the plate surfaces are interrupted. The results of an experimental study of the mechanisms responsible for enhancement are reported here along with quantitative measures of the magnitude of the enhancement and the pressure drop penalty incurred. The aim of this work is to identify the important parameters and provide guidelines for designers of heat transfer surfaces and to workers attempting to correlate experimental data. Arrays of parallel plates were tested in a wind tunnel. Fluid flow phenomena were identified using the Schlieren visualization technique. Three distinctly different flow regimes are found within cores composed of in-line plates. These are classified as steady, general unsteady, and periodic unsteady flows. The periodic unsteady flow is accompanied by the emission of a strong acoustic tone. The heat transfer performance of these cores was determined using a transient heating technique. The evolution of the enhancement and the associated changes in the flow regimes are documented over a range of Reynolds number as the streamwise spacing between in-line plates is increased from zero. The results of these experiments are used to interpret the measured performance of cores consisting of staggered arrays of parallel plates and of cores formed by assembling parallel-plate arrays so that alternate plates in the streamwise direction are perpendicular to each other.

Introduction

The flat plate is an element in many heat exchanger surfaces. The flow through certain finned surfaces may be modeled by the flow through arrays of parallel plates. One technique that has been used to enhance heat transfer in this geometry is surface interruption as employed, for example, in offset strip-fins and perforated-plate surfaces. Calculations have shown that augmentation may be realized in interrupted surfaces even if the flow remains laminar and steady [1]. Considerable experimental evidence indicates that additional augmentation can be expected over some range of operating conditions due to the unsteady flow induced by the surface interruptions [2–5]. The purpose of the research reported in this paper was to explore the structure of the flow in plate arrays in order to identify flow mechanisms which are important for heat transfer augmentation. An understanding of the flow is essential for the evaluation of analytical models to be used for calculating heat transfer and pressure drop in these arrays. It is also useful as an aid in constructing empirical correlations [6].

In order to realize the objective of this research, experiments were performed which combined flow visualization with heat transfer and pressure drop measurements. Model cores were tested in air in a wind tunnel [7] over the Reynolds number range $10^2 \leq \mathrm{Re}_d \leq 10^4$, important for compact heat exchangers. Three different geometric configurations of interrupted plates were studied. Parallel plates in both in-line and staggered arrangements were selected to model fin surfaces. An arrangement of perpendicular plate arrays was constructed to model a possible regenerator configuration.

Experiment

The experiments were conducted in a wind tunnel with a 15.24-cm-square test section. The test cores are formed by combining arrays of parallel plates in the wind tunnel test section. The leading edges of all of the plates in an array are located at the same streamwise position. Each array consists of a number of aluminum plates bonded to two balsa wood side supports with epoxy glue. The plates were clamped in a special jig during assembly and curing to ensure that the arrays would be dimensionally uniform. The length of each plate between side supports is 15.24 cm. When the arrays are inserted into the test section the balsa wood supports fit into recessed areas and the plates just span the test section opening. All of the plates in an array have the same thickness and length in the flow direction and each test core is formed from arrays of identical plates. The number of plate columns or stages in the streamwise direction is identical to the number of arrays in a test core. Plate thickness, length, and the streamwise spacing between plate arrays were varied from core to core. Arrays were constructed so that three different core arrangements could be formed: in-line and staggered parallel plates, and perpendicular plates. The perpendicular arrangement is formed by rotating every other in-line array 90 deg about the flow axis. In a core formed with 90 deg arrays, the flow passes alternately through horizontal and vertical channels. The three core arrangements are shown schematically in Fig. 1.

The survey by Wieting [8] was used as a guide in selecting the relative dimensions of the test cores. The scale was chosen large enough to ensure that the plates would be straight, flat, and well aligned. A summary of the dimensions and configurations of all the cores tested is presented in Table 1. Only the highlights of this work will be presented here; full details are given in [9]. The definitions used for reducing the data are generally in agreement with those presented in [10]. As pointed out by Patankar and Prakash [11] however, those definitions which yield the best correlation of the data do not

---

Contributed by the Heat Transfer Division for publication in the JOURNAL OF HEAT TRANSFER. Manuscript received by the Heat Transfer Division June 14, 1984.

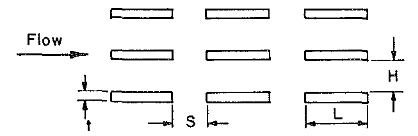

In-line Arrays

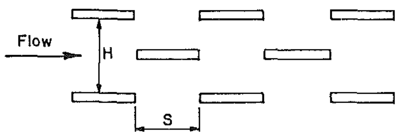

Staggered Arrays

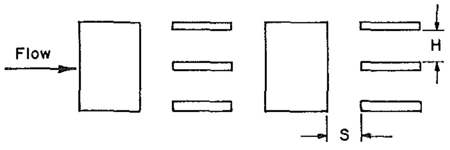

90° Arrays

Fig. 1 Test core configurations.

necessarily reveal the most about the physics. Since the objective of this research was to obtain a better understanding of the relation between the flow phenomena and the heat transfer augmentation and not to test correlations, certain exceptions to the definitions in [10] are noted below.

The experiments reported here concentrated on the in-line geometry. The reason for this was that a core with interrupted plate spacing of zero (i.e., continuous flat plate) could be assembled in this arrangement. This provided a common experimental and theoretical base from which to measure augmentation. It also provided an important check of the experimental technique which lends credence to the data obtained for interrupted surfaces where well-accepted theories are not available. In the experiments on in-line cores both Re_d and S are considered as variables. The evolution of the heat transfer augmentation as these variables are changed can be best illustrated if f and j are constructed so that they reflect only changes in pressure drop and heat transfer rate with changes in S. This same argument applies to the tests of cores constructed from 90 deg arrays. Consequently, for purposes of data reduction, the total heat transfer area was considered to consist only of the total surface area of the exposed sides of the plates and not to include the area of the ends of the plates perpendicular to the mean flow direction. The minimum free-flow area for both the in-line and 90 deg arrays was calculated based on the geometry of a single array and the core length was taken to be the number of arrays in the core times the plate length. The minimum free-flow area and core length for the staggered arrays are calculated at $S = L$. Appropriate adjustments to these definitions are made and identified when the results are compared with other experiments and with correlations.

Two pressure drops were measured at each test point: one between tunnel taps located upstream and downstream of the core and one between two core static taps machined in the aluminum plates. The 0.66-mm-dia core static pressure ports were located 1.9 cm to 2.54 cm from the balsa wood side walls. One of these ports was 1.9 cm downstream from the leading edge of the center plate in the first array and the other

Table 1 Test core dimensions

L (cm)	t (cm)	Number of arrays	L^* (cm)	S (cm)
		In-line arrays H = 0.447 cm		
3.81	0.127	4	15.24	0, 0.318, 0.635, 1.27, 2.54, 3.81
3.81	0.224	4	15.24	0, 0.318, 0.635, 1.27, 2.54, 3.81
3.81	0.318	4	15.24	0, 0.318, 0.635, 1.27, 2.54, 3.81
2.54	0.222	6	15.24	0, 0.318, 0.635, 1.27, 2.54
5.08	0.224	3	15.24	0, 0.318, 0.635, 1.27, 5.08
		Staggered arrays $H = 1.116$ cm		
2.54	0.222	12	30.48	2.54, 3.81
5.08	0.227	6	30.48	5.08, 7.62
		90 deg arrays $H = 0.447$ cm		
3.81	0.222	4	15.24	0, 0.318, 0.635, 1.27, 2.54, 3.81

Nomenclature

A = core heat transfer area excluding area of plate edges = number of plates × $2LW$, m^2
A_c = core minimum free-flow area, m^2
b = plate wake width = plate thickness plus 2 × momentum thickness of boundary layer at the exit of the first plate array, m
c_p = air specific heat, J/kg°C
d = hydraulic diameter = $4r_h$, m
f = Fanning friction factor = $(r_h/L_p)[\Delta p_c/(G^2/2\rho)]$ or $(r_h/L^*)[\Delta p_t/(G^2/2\rho) - K_c - K_e]$
G = core mass velocity = $\dot{m}/A_c$, kg/m^{2}s
h = heat transfer coefficient, W/m^2°C
H = transverse plate spacing, Fig. 1, m
j = Colburn factor = $(h/Gc_p)\mathrm{Pr}^{2/3}$
K_c = core entrance pressure loss coefficient, see [10]
K_e = core exit pressure loss coefficient, see [10]
L = plate length, Fig. 1, m
L_p = distance between core static pressure taps evaluated at $S = 0$ for in-line and 90 deg arrays and at $S = L$ for staggered arrays, m
L^* = flow length over heat transfer surface of core = total core length at $S = 0$ for in-line and 90 deg arrays and at $S = L$ for stagged arrays, m
$\dot{m}$ = air mass flow rate, kg/s
Pr = Prandtl number
Re_b = Reynolds number based on plate wake width = Gb/μ
Re_d = Reynolds number = dG/μ
r_h = hydraulic radius = A_cL^*/A, m
S = longitudinal plate spacing, Fig. 1, m
t = plate thickness, Fig. 1, m
W = plate span, m
β = frequency, Hz
Δp_c = pressure drop between core static pressure taps, Pa
Δp_t = pressure drop between tunnel static pressure taps, Pa
μ = dynamic viscosity of air, Pa s
ρ = density of air, kg/m^3

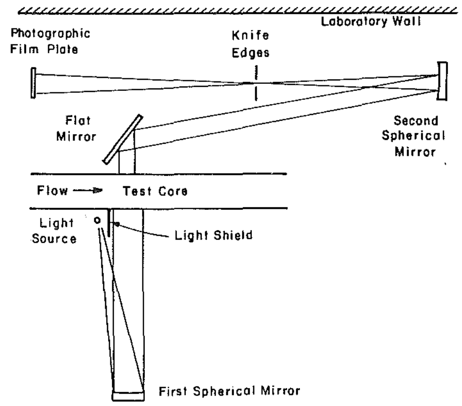

Fig. 2 The Schlieren system used for flow visualization.

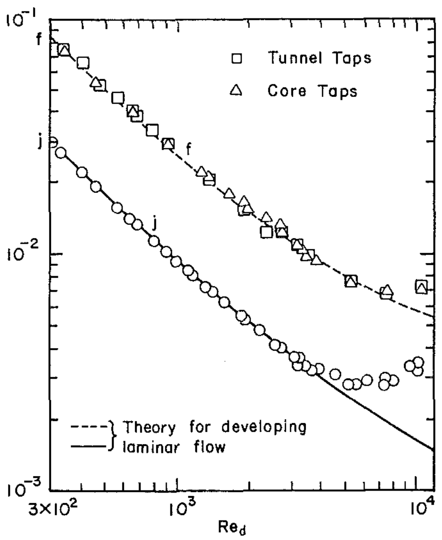

Fig. 3 Heat transfer and friction factors for a continuous plate core; theories of Shah [12] and Stephan [13].

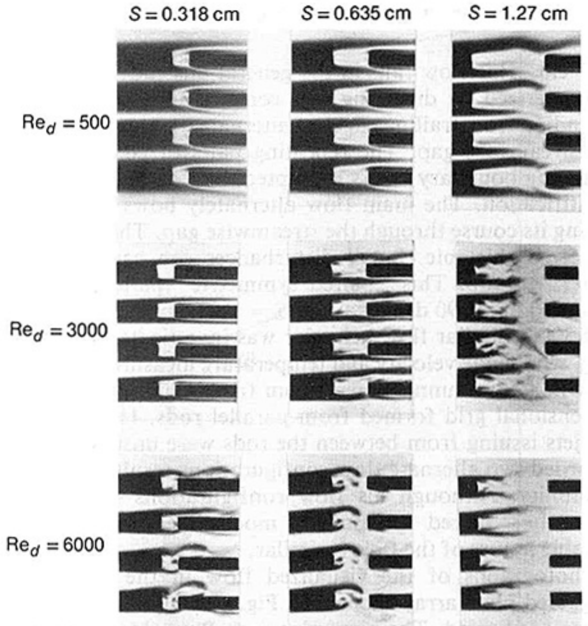

Fig. 4 The effect of Reynolds number and spacing on the flow between in-line arrays, t = 0.222 cm, L = 3.81 cm. Top row, Re_d = 500. Middle row, Re_d = 3000. Bottom row, Re_d = 6000. The view is between the first and second array in a core consisting of six arrays. The flow direction is from left to right.

was 0.32 cm upstream of the trailing edge of the center plate in the last array. The pressure drop measurements are presented in terms of an apparent friction factor. The definitions used to calculate these friction factors are presented in the Nomenclature. The entrance and exit loss coefficients required to reduce the pressure drop between tunnel taps to a friction factor were taken to be the same as those presented in [10] for flow through flat-duct passages.

Flow visualization was performed using a Schlieren technique. During flow visualization, two insulating plugs in the test section side walls are removed and replaced with 3 cm by 5 cm glass viewing ports. Part of the plate array side supports are also cut away to expose a section of the plates. Four of the original plates in one array are replaced with composite plates of identical outside dimensions, but incorporating internal electric resistance heaters. The thermal boundary layers formed over the heated plates are made visible by the Schlieren method. The setup used in this investigation is depicted in plan view in Fig. 2. The light source is the bulb on a General Radio Type 1531-AB Strobotac. The bulb, oriented to form a horizontal line source, produces a flash with a duration of about one microsecond. Two knife edges, also oriented horizontally (but shown vertically in Fig. 2 for illustration), intercept light which has been turned up or down in the test section due to vertical temperature gradients in boundary layers and in the wakes. The image of the core with darkened thermal layers is focused on a viewing screen or photographic film plate.

Average heat transfer coefficients for each test core were determined at various flow rates using a transient technique which is a variant of the so-called single-blow test technique. This accurate and rapid test, utilizing a digital data acquisition system and a curve matching evaluation criterion based on numerical solutions of the core response equations, is described in [7].

Results and Discussion

Facility Calibration. A complete description of the wind tunnel, instrumentation, and test technique is presented in [7]. The results of one experiment run to validate the facility are reproduced here for completeness. In this experiment a core consisting of equally spaced horizontal plates was tested. Each of the aluminum plates measures 0.154 cm thick, 15.24 cm wide, and 22.86 cm long. The vertical spacing between the plates is 0.447 cm. The plates were assembled into a single array by the methods described earlier. This core, with continuous plates, is comparable in size and shape to the interrupted-plate cores to be discussed next.

The test results are summarized in Fig. 3. They are in good agreement with theory for developing flow between parallel plates of infinite aspect ratio with constant wall temperature. Furthermore, the average friction factor determined from the measured pressure drop between the core taps is in good agreement with that calculated from the pressure drop between tunnel taps. The estimates for the uncertainty in the results given in [7] also apply to the work to be described here. The uncertainties depend on the operating point. The maximum uncertainties are estimated to be ± 8 percent for j, ± 5 percent for f, and ± 3 percent for Re_d. The uncertainty in j is less than ± 2 percent for Reynolds number below about 4000.

Flow Visualization. Photographs of the visualized flow in the passages and between in-line arrays appear in Fig. 4. The photos are arranged in columns according to streamwise spacing and in rows according to Reynolds number. The flow is from left to right with the four center upstream plates heated. While both upstream and downstream plates are of identical dimensions, the upstream plates appear thicker due to the attached thermal boundary layers.

Three distinctly different flow regimes can be identified in

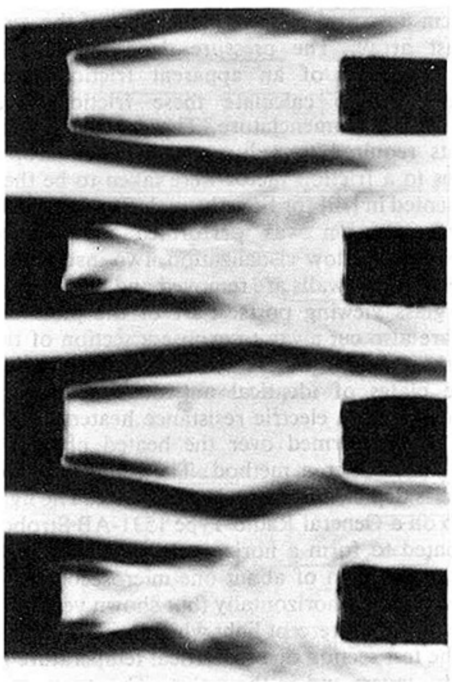

Fig. 5 Paired symmetric flow, t = 0.318 cm, L = 3.81 cm, S = 1.27 cm, and Re_d = 3000; the flow direction is from left to right.

these photographs. They are classified as: steady, general unsteady, and periodic unsteady. The steady flow region is characterized by smooth and straight boundary layers found over the upstream and downstream plates and in the streamwise space between plate arrays. For example, see Fig. 4, $S = 0.318$ cm, $\mathrm{Re}_d = 500$ and 3000. The general unsteady flow region is characterized by boundary layers that undulate after they leave the trailing edge of the upstream plate. The amplitude of the unsteadiness continues to grow as the flow proceeds downstream between the plate arrays. In many cases, the boundary layers appear to develop into turbulentlike flow structures which completely fill the passages in the next downstream array. An example is the flow in Fig. 4 for $S = 1.27$ cm at $\mathrm{Re}_d = 3000$.

The flow in the general unsteady region appears to be more three dimensional than that observed by Roadman and Loehrke [14] for flow between two plates in a water channel. This may be due, in part, to the difference between Roadman and Loehrke's dye visualization which taps a single streakline and the present Schlieren technique which averages over the entire plate span of 15.24 cm. The three-dimensional appearance may be due to slight random transverse wiggles in a nominally two-dimensional vortex. This three-dimensional turbulentlike character was also observed by Loehrke and Lane [4] and Mochizuki and Yagi [16] by dye visualization of water flow through arrays of plates.

The periodic unsteady flow region is characterized by periodic, synchronized vortex shedding from the trailing edges of the upstream plates. One or more vortex may occupy the space between plate arrays. This organized, two-dimensional flow persists in the next downstream passageway. For example, see Fig. 4, $S = 0.635$ cm at $\mathrm{Re}_d = 6000$. An audible tone always accompanies this periodic unsteady flow and is further discussed later.

These three flow regions were observed for both in-line and staggered arrays. No periodic region could be detected for the 90 deg arrays. An additional flow phenomenon was documented for in-line arrays of thick plates and for the 90 deg arrays. A "paired symmetric" flow was discovered and is illustrated in Fig. 5 for thicker plates at $\mathrm{Re}_d = 3000$ and $S =$ 1.27 cm. This flow falls in the general unsteady region. It is characterized by diverging and converging boundary layers extending from trailing edges of alternate upstream plates into the streamwise gap. The repeating pairs of converging and diverging boundary layers prompted the "paired symmetric" identification. The main flow alternately bows out then in, during its course through the streamwise gap. This mean-flow pattern is bistable. Small disturbances can cause the flow pattern to flip. This "paired symmetric" pattern was also observed in the 90 deg arrays at $S = 1.27$ cm and $\mathrm{Re}_d = 1500$ and 3000. Similar flow behavior was investigated by Corrsin [15], who made velocity and temperature measurements in the flow in a wind tunnel downstream from a high-solidity, two-dimensional grid formed from parallel rods. He found that the jets issuing from between the rods were unstable, and he recorded two alternate flow configurations resulting from the instability. Although his flow configurations are different from the "paired symmetric" modes identified here, the bistable nature of the flow is similar.

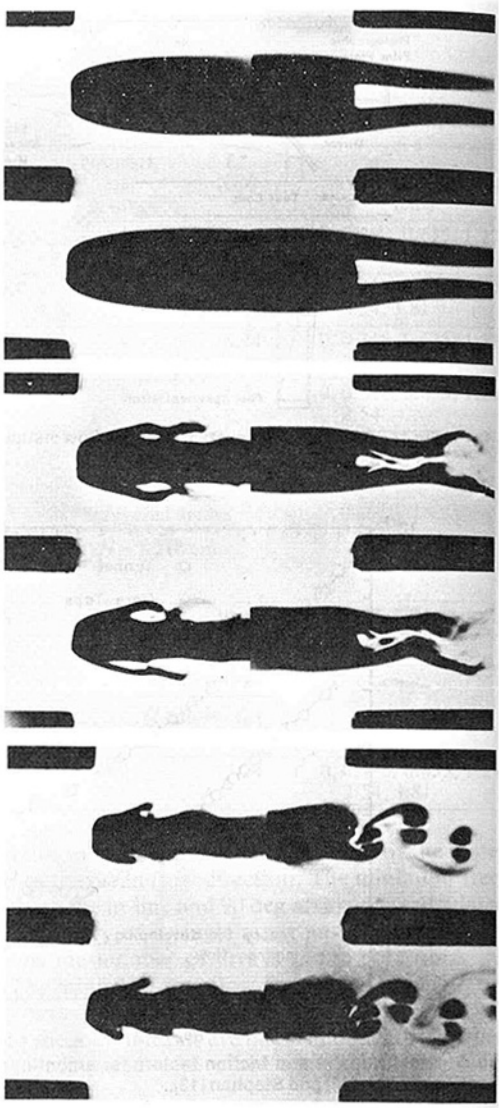

Fig. 6 Flow over plates in a staggered array, t = 0.22 cm, L = 2.54 cm, $S = L$; the flow direction is from left to right.

Photographs of the visualized flow in the passages of staggered plate arrays appear in Fig. 6. Only the central two plates are heated. The picture at each Reynolds number is a composite of two photographs taken at different times: one of the trailing edges and one of the leading edges of the heated plates. The plate support structure partially obstructed the

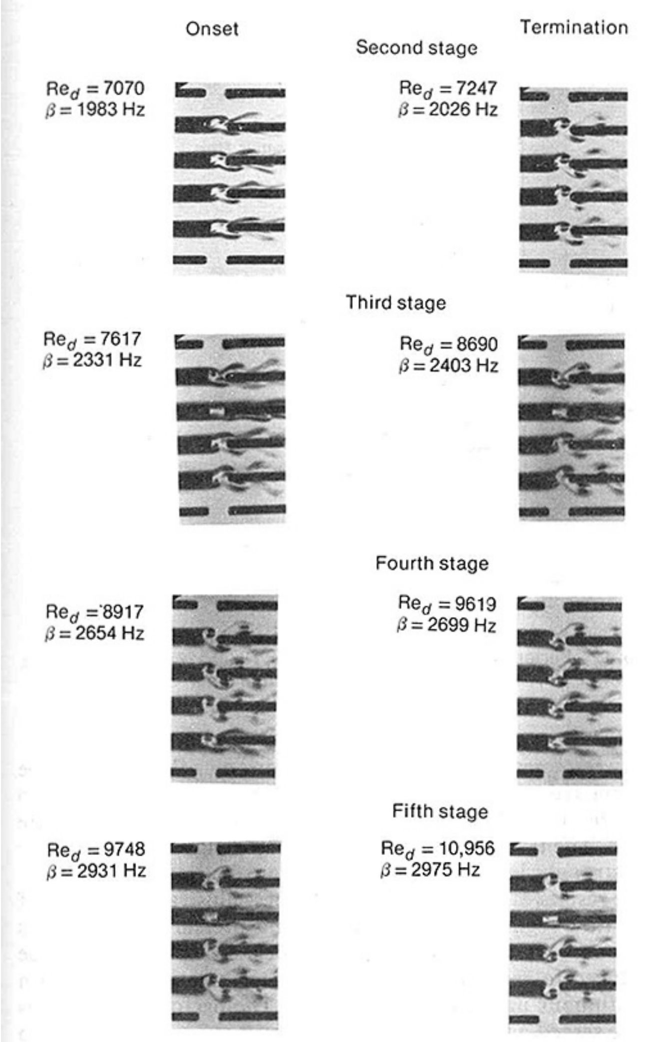

Fig. 7 Vortex shedding patterns in different stages of periodic unsteady flow in in-line arrays, t = 0.127 cm, L = 3.81 cm, S = 0.318 cm; view is between arrays with the flow direction from left to right.

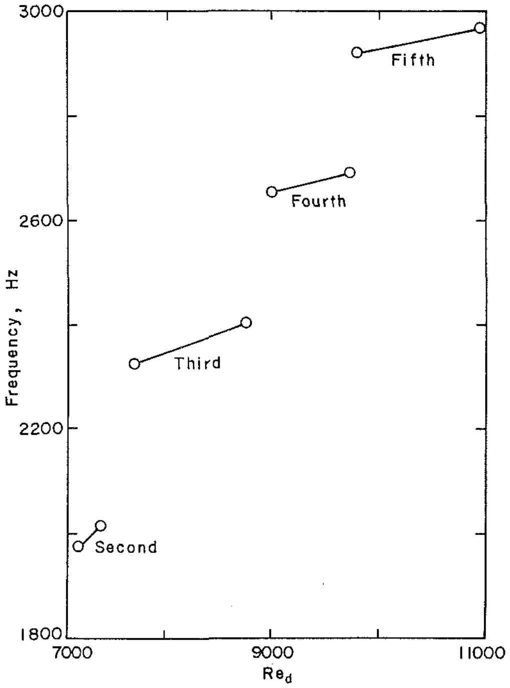

Fig. 8 Frequency staging of the audible tones for two, in-line arrays, L = 3.81 cm, t = 0.127 cm, S = 0.318 cm.

view making it impossible to capture the entire plate at one time. Again, the flow is from left to right with all plates of the same dimensions. The visualized plates are in the second array and there are no plates directly upstream. The two center plates appear thicker due to the attached thermal boundary layers. The three flow regions identified with the in-line arrays are distinctly evident in the staggered arrays. At Re$_d$ = 500, the flow is steady as shown in Fig. 6. The flow is also steady at Re$_d$ = 750 but by Re$_d$ = 1500 unsteady wake motions are detectable. The strong influence of the unsteady wakes of the upstream plate array on the boundary layers on the heated plates is detectable in both the general unsteady and in the periodic regions. In contrast, the flow along the side of the plates in the in-line arrays tested appeared much more tranquil. The boundary layers appeared to be hardly disturbed even though the wakes were unsteady.

The flow between different pairs of plate arrays was observed in in-line arrays at certain fixed values of Reynolds number. These observations indicated that the flow regimes did not depend on streamwise location. This is corroborated by the observations in water by Loehrke and Lane [4] and by the relatively sharp transitions noted in j and f with changes in Reynolds number at small S (see next section). In contrast, Mochizuki and Yagi [16] found that for deep cores with many staggered arrays or stages in the flow direction the Reynolds number at which the transition to unsteady flow occurs near the front of the core may be three times greater than the Reynolds number at the beginning of transition in the downstream sections of the core.

Audible Tones. The periodic unsteady flow region was studied in more detail using the core geometry which produced the strongest audible tones. Sound measurements were made and frequencies recorded over the Reynolds number range in which audible tones occurred. Additionally, photographs of the visualized flow were taken during the occurrence of the tones. The data are given in Fig. 7 and are plotted in Fig. 8. The general behavior of these tones is that they occur in stages. The left column in Fig. 7 shows the conditions at the onset of an audible tone in a particular stage as the wind tunnel velocity is increased from zero. The right column shows conditions just prior to the jump in frequency to the next stage. The first tone was found to be very weak; thus data were taken starting with the second tone and continued through to the fifth tone. A sixth tone was observed at the wind tunnel fan speed limit. The frequencies of the observed tones were well correlated with flow speed but not correlated at all with fan speed which never exceeded 3000 rpm.

Photographs of the visualized flow in Fig. 7 clearly show the periodic unsteady flow structure associated with the audible tones. For all of the tones, a single vortex occupies the streamwise gap and the vortex shedding is synchronized, but not always in phase. The second tone shows all vortices shedding in phase. The third tone shows the bottom two plates shedding vortices in phase and the top plate shedding vortices out of phase with the second from the top plate shedding no distinct vortex street. This nonshedding plate is located on the wind tunnel centerline. With the fourth tone, the top three plates are shedding vortices in phase while the bottom plate is shedding a weakly organized vortex. The fifth tone possesses the same vortex shedding mode as the third tone. The frequency plotted against Reynolds number, in Fig. 8, shows the staging of the four tones.

Loehrke and Lane [4] made amplitude and frequency measurements of audible tones in the same wind tunnel but with different heat exchanger cores. By increasing the wind tunnel velocity, they found a peak in amplitude right after the onset of a given tone. This was followed by a continuous decrease in amplitude up to the termination of the tone.

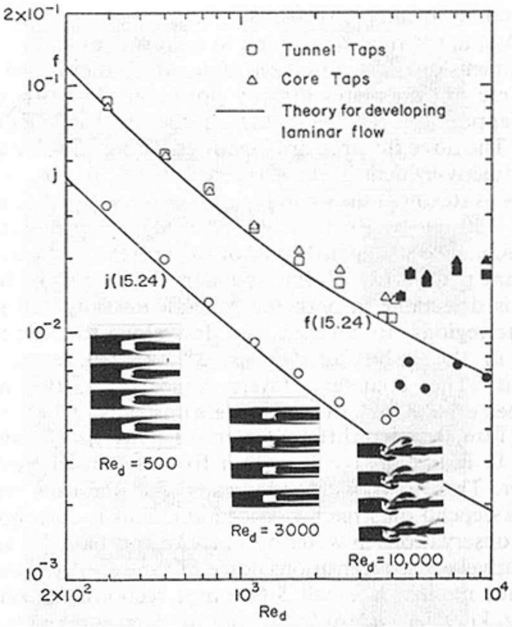

Fig. 9 Performance of four in-line arrays, t = 0.127 cm, L = 3.81 cm, S = 0.318 cm; shaded symbols indicate audible tone.

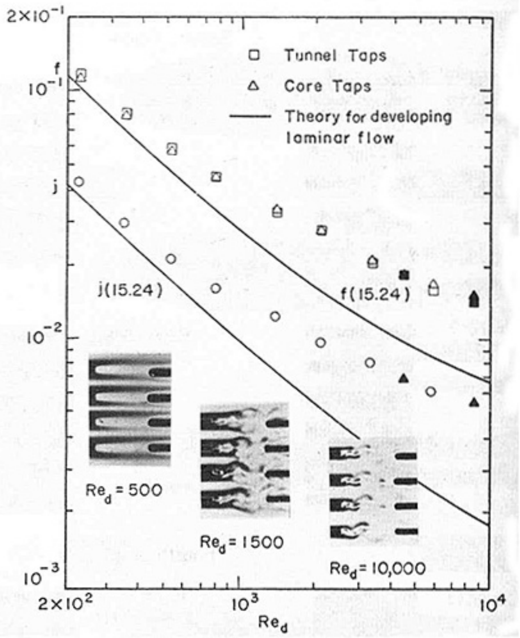

Fig. 11 Performance of four in-line arrays, t = 0.127 cm, L = 3.81 cm, S = 1.27 cm; shaded symbols indicate audible tone.

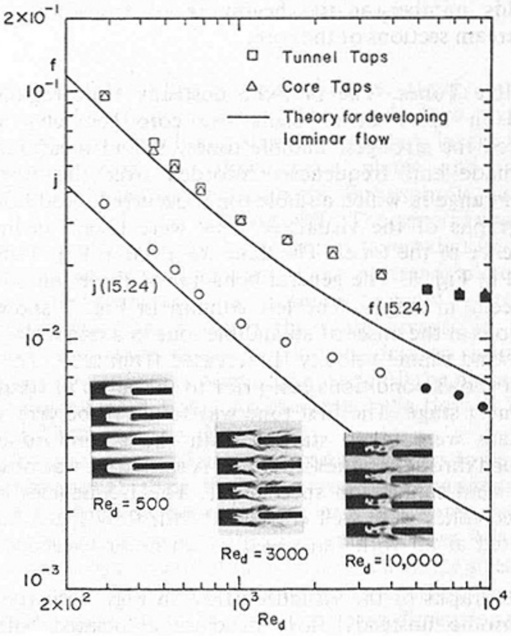

Fig. 10 Performance of four in-line arrays, t = 0.127 cm, L = 3.81 cm, S = 0.635 cm; shaded symbols indicate audible tone.

These observations indicate that the vortex shedding is being synchronized by interaction with resonant acoustic modes. Such modes were first observed and calculated by Parker [17, 18] for a single plate array or cascade. Related flow visualization has recently been reported [19]. The transverse dimensions of the wind tunnel test section or heat exchanger core are important in establishing the resonant frequencies while the plate dimensions and flow velocity set the shedding frequency. When these frequencies are comparable, periodic flow and noise emission should occur. Fundamental research on this important resonance phenomenon continues [20] but it remains to be shown how the resonant modes for in-line and staggered plate arrays relate to those calculated for a single plate cascade.

Heat Transfer and Pressure Drop. In general the transitions between steady, unsteady, and periodic flows could be correlated with transitions in heat transfer and pressure drop for the parallel plate cores but not for the perpendicular plate core. The transition to paired symmetric flow did not appear to strongly influence either heat transfer or pressure drop. The results of test on in-line arrays best illustrate the effect of the flow regimes on heat transfer and pressure drop. This is because the streamwise spacing between plates could be reduced to zero in the in-line geometry creating a core with continuous uninterrupted passages. The performance of this core served as a benchmark from which augmentation due to interruption could be measured. The heat transfer and pressure drop measured at zero spacing agree well with the predictions for laminar developing flow in a rectangular duct of infinite aspect ratio and constant wall temperature as given by Stephan [13] and Shah [12] up to Re_d = 3000. At higher Reynolds numbers a gradual transition to turbulent flow is evident. The augmented peformance can be observed to evolve as the spacing between arrays is increased from zero. Three stages in this evolution are pictured in Figs. 9–11. At the smallest spacing, Fig. 9, the performance of the core is almost identical to that for S = 0 up to Re_d = 4000. The solid lines in these figures represent the laminar duct flow theory for a channel 15.24 cm long, the total plate length in the flow direction for these four-array cores. The photo insets confirm that the flow is steady at Re_d = 500 and 3000. Above Re_d = 4000, j and f jump up in value and an audible tone is heard indicating transition to periodic unsteady flow. At larger spacings, Figs. 10 and 11, transitions in j and f take place at lower values of Re_d. Flow visualization indicates that these transitions represent the effects of changes from steady to general unsteady flows. Periodic unsteady flow may still occur at the higher Reynolds numbers and a further change in the slopes of j and f curves may be observed.

Yang [21] reports three kinds of heat transfer augmentation in perforated surfaces based on transitions observed in the variations of j and f with Reynolds number. He identified the low Reynolds number region as laminar, the medium Reynolds number region as second laminar or transitional, and the third region as turbulent. The transitions which he observed may be related to those identified in this study, but the flow visualization results clearly indicate that the

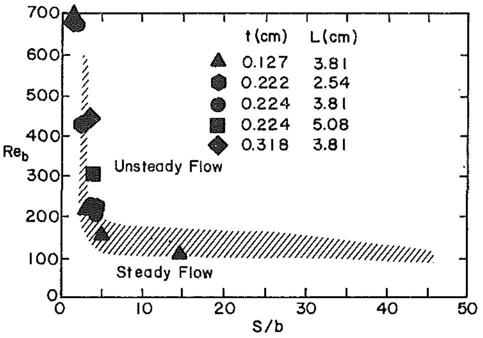

Fig. 12 Transition from steady to unsteady flow in in-line arrays as indicated by *j* and *f*; the shaded region bounds the data in [14].

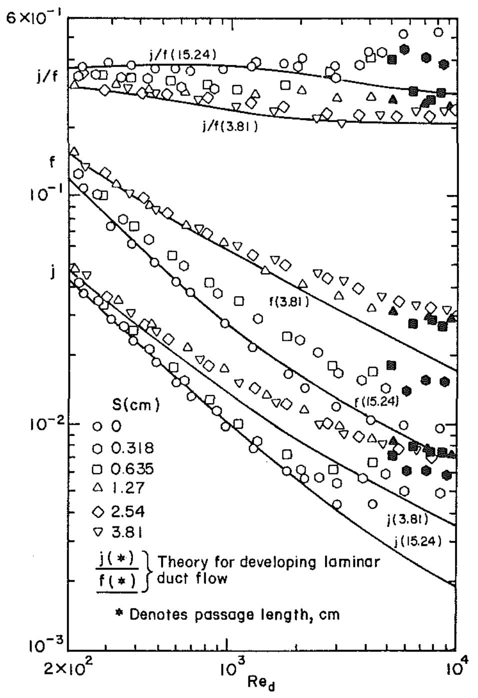

Fig. 13 Performance of four in-line arrays, t = 0.318 cm, L = 3.81 cm; shaded symbols indicate audible tone.

mechanisms responsible for the transitions observed here are different from those implied by his classification.

Unsteady flow may be the rule rather than the exception at large values of plate spacing. At the practically important spacing $S = L$, transition to unsteady flow occurs at Re_d = 380, for the arrays described in Figs. 9–11. Roadman and Loehrke [14] found that the boundary between steady and unsteady flow between two plates scaled with the plate wake width b and that the flow will be unstable for $\mathrm{Re}_b \gtrsim 150$ for large plate spacing. The relationship between Reynolds number based on plate wake width and Reynolds number based on hydraulic diameter depends on the core geometry. For the in-line arrays of thick plates, the two Reynolds numbers are of the same order and transition from steady to unsteady flow at large S takes place near the lower end of the Reynolds number range tested. In this case, the transition point is not obvious in the j and f curves. Transition in the in-line arrays of thin plates and in the staggered arrays takes place at higher values of Reynolds number based on hydraulic diameter but still at values of Reynolds number based on plate wake width comparable to those reported in [14]. Data from those present tests of in-line arrays in which a distinct transition in j and f could be identified are compared with the results of [14] in Fig. 12.

A composite plot of j and f as a function of Reynolds number for a number of plate spacings is shown in Fig. 13 for a different in-line core. Also shown are theoretical lines for developing laminar duct flow. The number in parentheses behind j and f indicates the length in centimeters of the duct. Thus, the line marked j (15.24) represents the average heat transfer factor in a duct of height H and length 15.24 cm. This length corresponds to the sum of the plate lengths in this four-array core and also to the total core length when S = 0. The curve marked f (15.24) represents the average friction factor in developing duct flow over the distance between the two core taps when S = 0. As mentioned earlier this theoretical limit describes well the measured core performance when S = 0 up to the Reynolds number where transition to turbulence is noted.

Also shown in Fig. 13 are two lines marked j (3.81) and f (3.81). These are for developing flow in a duct of length equal to the individual plate length L. They provide an indication of the expected performance of a similar core with zero thickness plates and infinite plate separation in steady flow. They are included for reference only and do not necessarily represent upper limits for j or f in an actual core. At small S and low Re_d, the partially developed channel flow will be passed from one array to the next with little change and thus the experimental data will lie much closer to the lower j and f solid lines than to the upper ones. This is seen at S = 0.318 cm, where nearly theoretical laminar flow behavior is observed in Fig. 13, until transition to unsteady flow occurs, characterized by an abrupt, large rise in j and f values. On the other hand, heat transfer from the exposed ends of the plates and thickness-related pressure drop would tend to yield larger apparent j and f. Likewise, especially at large S and high Re_d, turbulence induced by flow over the interrupted segments should augment the laminar heat transfer and friction. This is seen at the larger streamwise spacings in Fig. 13, where transition from steady flow occurs at lower Reynolds numbers.

The behavior of all of the in-line test cores was qualitatively similar to that shown in Fig. 13. For spacings of $S \geq 1.27$ cm, the j and f data are seen to congregate along narrow bands. These narrow bands form upper boundaries for the j and f data and include the $S = L$ or natural spacing case. The heat transfer augmentation, defined as the ratio of the heat transfer rate at a given flow rate in an interrupted channel to that in a channel with continuous walls of the same material length, can be inferred directly from the j values in Fig. 13. This augmentation depends on Reynolds number. For Reynolds numbers around 1000, this ratio is about 2 for the data shown in Fig. 13. The augmentation will also depend on the overall core length. For the relatively short core for which these data were taken, the laminar flow is in development over much of the length of the continuous passage. For a longer core, the baseline j for laminar flow would be lower. The development length of the unsteady flow in interrupted passages is much shorter. Pressure profiles measured through staggered arrays at Reynolds numbers of 1000 and 4000 show a constant gradient beyond the first array. The experiments of Sparrow and Hajiloo [22] indicate that the flow development is very rapid in the unsteady flow regime. Their per-plate heat transfer coefficients, measured in a staggered plate array, were the same for the second and all subsequent rows. Consequently, the augmentation in deeper cores should be even larger.

For clarity of presentation only, the friction factor based on the pressure drop between core taps is shown in Fig. 13. The agreement between the friction factor based core and tunnel pressure drops which are shown in Figs. 9–11 is typical for the interrupted-plate cores tested. The friction factors shown in Fig. 13 change roughly the same way as the heat transfer factor in response to changes in Reynolds number and plate

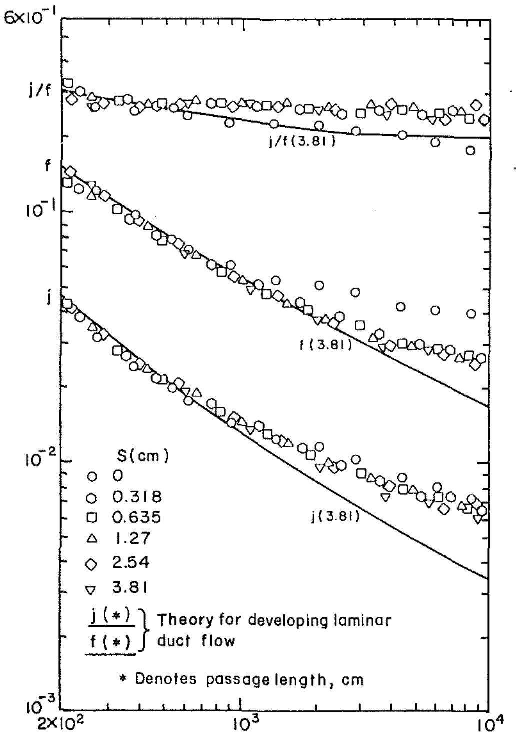

Fig. 14 Performance of four 90 deg arrays, t = 0.222 cm, L = 3.81 cm.

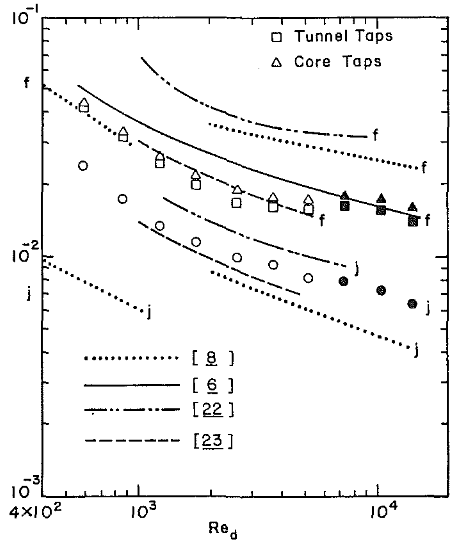

Fig. 15 Performance of six staggered arrays, t = 0.222 cm, L = 5.08 cm, S = L, compared with the literature; shaded symbols indicate audible tones.

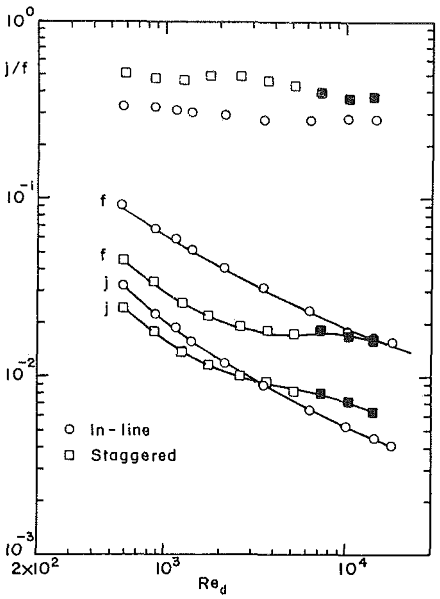

Fig. 16 Comparative performance of equal number of plates, t = 0.222 cm, L = 5.08 cm, S = L in three in-line arrays and in six staggered arrays; shaded symbols indicate audible tone.

spacing. As a result, the ratio j/f remains higher for this technique of augmentation than for many others. The augmentation noted in Fig. 13 is due, in part, to the mixing which keeps the hot upstream boundary layers from bathing downstream plate segments and, in part, to enhance heat transfer at the plate surface itself caused by turbulence generated in the space between plates and at the leading edge. The boundary layer development may also be interrupted by rotating every other array in the streamwise direction by 90 deg. The performance of such an arrangement is summarized in Fig. 14. The heat transfer augmentation is comparable to the maximum shown in Fig. 13 for in-line arrays. The performance of the 90 deg arrays is much less sensitive to streamwise spacing than that of the in-line arrays. Except for $S = 0$, all of the data in Fig. 14 are contained within narrow bounds. The transition from steady to unsteady flow between arrays observed in flow visualization tests is not reflected in transitions in j or f. No periodic flow regime was observed for this arrangement. The friction factor plotted in Fig. 14 is based on the pressure drop between core taps. The flow area A_c used for reducing the data for the 90 deg arrays was based on the unblocked area between parallel plates.

A limited amount of data were obtained for staggered plate arrays. The support structure for these arrays limited the smallest spacing which could be obtained between plates to $S=L$. Very little difference in performance was observed between cores with $S = L$ and $S = 1.5L$. Measured data from one core with $S = L$ will be presented here. Because of the similarity between this geometry and that of the offset-fin heat exchanger surface, there is considerable opportunity for comparison, with related data in the literature. In order to facilitate this comparison a slight change in the definitions used to reduce the data will be made for those data presented in the last two figures of this paper. Specifically, A will be taken to be the entire surface area of the core including the area of the leading and trailing edges of the plates. With this change the definitions given in the Nomenclature for staggered plates with $S = L$ are in agreement with those employed by Webb and Joshi [6].

The data for one core with staggered arrays are shown in Fig. 15. Also shown are lines representing data from other sources or correlations for offset-fin cores. The data of Sparrow and Hajiloo [22] are for a core of parallel plates with nearly the same thickness ratio, $t/L = 0.042$, and aspect ratio W/H as the core tested here but with a length ratio, $L/H = 1.0$, compared with $L/H = 4.6$ for the present core. The comparison shows an increase in j and f, as expected, with a decrease in L/H. The data of Mochizuki and Yagi [23] for strip fins of nearly the same length ratio, $L/H = 5.0$, but smaller thickness ratio, $t/L = 0.02$, and smaller aspect ratio show closer agreement with the present results. The measured friction factors are within about 20 percent of the values predicted for this core using the correlation of Webb and Joshi [6]. The two-part correlations of Wieting [8] agree well with the measurements in some regions and very poorly in others.

Some insight into the behavior of the staggered arrays can be obtained by comparing the performance with that of a similar core of in-line arrays. Two such cores with equal numbers of plates are compared in Fig. 16. These cores also have the same frontal area and total length. (In reducing the data, for this comparison only, the in-line core length L^* was taken to be the number of arrays times $(L + S)$.) The dimensions of the plates are $t = 0.222$ cm and $L = 5.08$ cm. The hydraulic diameters of the two cores and the minimum free-flow areas are the same, so the mass flow rate through each core is identical at the same Reynolds number and the pressure drops and heat transfer rates are identical at equal values of f and j, respectively. The lines connecting the data points in Fig. 16 are sketched to aid in illustrating trends.

The trends indicate that the flow in the staggered arrays is undergoing a transition from steady to unsteady over a broad Reynolds number range. Over this same range the flow between in-line plates at $S = L$ is unsteady. Flow visualization confirms that the transition from steady to unsteady in the staggered array takes place at around a Reynolds number of 1000. In this sense the flow in staggered arrays seems to be more stable than that in in-line arrays. Throughout the range of Reynolds number shown in Fig. 16 the ratio j/f is higher for the staggered arrays than for the in-line arrays.

The relative behavior is qualitatively consistent with the picture one obtains by viewing the staggered core as a configuration obtained by moving every other plate in the in-line core downstream one plate length. Instead of high velocity jets expanding into relatively large void regions between widely spaced arrays of in-line plates one has a more uniform velocity distribution throughout the staggered core with relatively moderate, localized acceleration and deceleration as the fluid passes from one array to the next. Thus, the smooth flow through the staggered arrays at low Reynolds numbers, as seen for example in Fig. 6 at Re = 500, is substituted for turbulent flow through the in-line arrays which, for example, is evident in Fig. 4 at large S even at Re = 500.

Conclusions

Three regimes are identified in the flow through arrays of parallel plates. Steady, general unsteady, and periodic unsteady flow are observed in cores composed of in-line and staggered parallel plates. No periodic regime is detected in the flow in cores composed of 90 deg arrays of parallel plates.

An enhancement of over 100 percent in the average heat transfer coefficient in a parallel-plate core may be realized by interrupting the surface. In interrupted surfaces modeled by arrays of in-line and staggered parallel plates this enhancement occurs, in a large part, because the flow becomes unsteady in the wake of plate segments. The wake unsteadiness promotes mixing of the separated boundary layers and, at least for staggered arrays, disrupts the boundary layers growing on the subsequent downstream plates. These mechanisms do not seem important for the enhancement noted in 90 deg arrays.

The transition from steady to unsteady flow occurs at a critical value of Reynolds number. This critical value decreases with increasing streamwise spacing between plates and with increasing plate thickness. The transition is better correlated by a Reynolds number based on plate wake width than by a Reynolds number based on passage hydraulic diameter. The transition boundary indicated by sudden changes in j and f with changes in Reynolds number for in-line arrays closely follows that measured for the flow between two separated plates. The transition in staggered arrays appears to take place at a slightly higher Reynolds number than in in-line arrays.

A strong acoustic emission is noted in the periodic flow regime. The flow character observed under conditions of acoustic emission indicates that this emission is associated with a resonance which depends on the transverse dimensions of the entire core. The modes observed by flow visualization are similar to those described by Parker [17] for flow through a cascade of parallel plates.

Acknowledgments

This research was supported by NSF through grant CME-8009046.

References

1 Sparrow, E. M., and Liu, L. H., "Heat Transfer, Pressure Drop and Performance Relationships for In-line, Staggered, and Continuous Plate Heat Exchangers," *Int. J. Heat and Mass Transfer*, Vol. 22, 1979, pp. 1613-1625.

2 Adarkar, D. B., and Kays, W. M., "Heat Transfer in Wakes," Technical Report No. 55, Department of Mechanical Engineering, Stanford University, 1963.

3 Zelenka, R. L., and Loehrke, R. I., "Heat Transfer From Interrupted Plates," ASME JOURNAL OF HEAT TRANSFER, Vol. 105, 1983, pp. 172-177.

4 Loehrke, R. I., and Lane, J. C., "Flow Through an Array of Interrupted, Parallel Plates," *Heat Transfer 1982*, Vol. 3, Hemisphere, 1983, pp. 81-86.

5 Webb, R. L., and Joshi, H. M., "A Friction Factor Correlation for the Offset Strip-Fin Matrix," *Heat Transfer 1982*, Vol. 6, Hemisphere, 1982, pp. 251-262.

6 Webb, R. L., and Joshi, H. M., "Prediction of the Friction Factor for the Offset Strip-Fin Matrix," *Proc. ASME/JSME Joint Thermal Engineering Conference*, Vol. 1, ASME, New York, 1983, pp. 461-469.

7 Mullisen, R. S., and Loehrke, R. I., "A Transient Heat Exchanger Evaluation Test for Arbitrary Fluid Inlet Temperature Variation and Longitudinal Core Conduction," ASME JOURNAL OF HEAT TRANSFER, this issue.

8 Wieting, A. R., "Empirical Correlations for Heat Transfer and Flow Friction Characteristics of Rectangular Offset-Fin Plate-Fin Heat Exchangers," ASME JOURNAL OF HEAT TRANSFER, Vol. 97, 1975, pp. 488-490.

9 Mullisen, R. S., "Heat Transfer, Pressure Drop, and Fluid Flow in Interrupted Wall Passages," Ph.D. Thesis, Mechanical Engineering Department, Colorado State University, 1983.

10 Kays, W. M., and London, A. L., *Compact Heat Exchangers*, 2nd ed., McGraw-Hill, New York, 1964.

11 Patankar, S. V., and Prakash, C., "An Analysis of the Effect of Plate Thickness on Laminar Flow and Heat Transfer in Interrupted-Plate Passages," *Int. J. Heat Mass Transfer*, Vol. 24, 1981, pp. 1801-1810.

12 Shah, R. K., "A Correlation for Laminar Hydrodynamic Entry Length Solutions for Circular and Noncircular Ducts," *Journal of Fluids Engineering*, Vol. 100, 1978, pp. 177-179.

13 Stephen, K., "Wärmeübergang und druckabfall bei nicht ausgebildeter Laminarströmung in Rohren und in ebenen Spalten," *Chem.-Ing. Tech.*, Vol. 31, 1959, pp. 773-778.

14 Roadman, R. E., and Loehrke, R. I., "Low-Reynolds Number Flow Between Interrupted Flat Plates," ASME JOURNAL OF HEAT TRANSFER, Vol. 105, 1983, pp. 166-171.

15 Corrsin, S., "Investigation of the Behavior of Parallel Two-Dimensional Air Jets," National Advisory Committee for Aeronautics, NACA ARC Bi, 4G24m, 1944.

16 Mochizuki, S., and Yagi, Y., "Characteristics of Vortex Shedding in Plate Arrays," *Flow Visualization II*, W. Merzkirch, ed., Hemisphere, Washington, 1982, pp. 165-169.

17 Parker, R., "Resonance Effects in Wake Shedding From Parallel Plates: Some Experimental Observations," *J. Sound Vib.*, Vol. 4, No. 1, 1966, pp. 62-72.

18 Parker, R., "Resonance Effects in Wake Shedding From Parallel Plates: Calculation of Resonant Frequencies," *J. Sound Vib.*, Vol. 5, No. 2, 1967, pp. 330-343.

19 Tanida, Y., and Nagashima, T., "Visualization of Vortex Sound in Cascade Plates," *Flow Visualization II*, W. Merzkirch, ed., Hemisphere, Washington, 1982.

20 Welsh, M. C., Stokes, A. N., and Parker, R., "Flow-Resonant Sound Interaction in a Duct Containing a Plate, Part I: Semi-circular Leading Edge," *J. Sound Vib.*, Vol. 95, No. 3, 1984, pp. 305-323.

21 Yang, W.-J., "Three Kinds of Heat Transfer Augmentation in Perforated Surfaces," *Letters in Heat and Mass Transfer*, Vol. 5, 1978, pp. 1-10.

22 Sparrow, E. M., and Hajiloo, A., "Measurements of Heat Transfer and Pressure Drop for an Array of Staggered Plates Aligned Parallel to an Air Flow," ASME JOURNAL OF HEAT TRANSFER, Vol. 102, 1980, pp. 426-432.

23 Mochizuki, S., and Yagi, Y., "Heat Transfer and Friction Characteristics of Strip Fins," Heat Transfer—Japanese Research, Vol. 6, No. 3, 1977, pp. 36-59.

J. W. Baughn[1]
Professor.
Mem. ASME

M. J. Elderkin[1]
Graduate Student.

A. A. McKillop[1]
Professor.
Mem. ASME

Department of Mechanical Engineering,
University of California,
Davis, CA 95616

Heat Transfer From a Single Cylinder, Cylinders in Tandem, and Cylinders in the Entrance Region of a Tube Bank With a Uniform Heat Flux

An experimental technique for obtaining a uniform wall heat flux has been used to determine the local heat transfer coefficients around a cylinder. Data are presented for a single cylinder, for cylinders in tandem, and cylinders located in the entrance of a tube bank. Results are compared to those of other studies with uniform wall heat flux. For the single cylinder, these are found to depend upon blockage, aspect ratio, and free-stream turbulence. For both inline and staggered tube arrangements, the heat transfer coefficient distribution depends on row location but appears to be nearly established by the third row.

Introduction

An experimental technique has been developed for obtaining heat transfer measurements from a surface to a fluid for the wall condition of uniform heat flux [1]. The method employs a thin gold-coated plastic sheet mounted on a rigid, low thermal conductivity surface of a desired shape. One particular application has been the measurement of local heat transfer coefficients from circular cylinders in external flow situations. Baughn et al. [1] have shown that accurate uniform wall heat flux measurements can be obtained with minimal internal conduction effects.

In this paper, we report results of a study using the instrumented cylinder described in [1] for three different geometric arrangements: a single cylinder, cylinders in tandem, and cylinders in the entrance region of tube banks. The study was limited to a single set of pitch ratios for each arrangement and to two subcritical Reynolds numbers.

Our objectives are (1) to establish a reliable set of data with a well-established boundary condition of a uniform heat flux surface, and (2) to compare results with previous studies.

The importance of specifying the thermal boundary condition has been stressed by Žukauskas [2] and Papell [3]. Most studies either have presented data without specifying the boundary condition or have failed to differentiate clearly between them when comparing results. The constant wall temperature and the uniform wall heat flux have been the most commonly studied cases, although perhaps not the most practical. For the single cylinder, the studies of Achenbach [4] and Kraabel et al. [5] have shown that reliable measurements can be obtained for a constant wall temperature.

A uniform heat flux surface cylinder appears deceptively simple to construct, yet results for the single cylinder show much divergence, especially over the rear portion of the cylinder [6, 8-10]. A key problem is that internal conduction can occur due to the surface temperature variation. The particular methods employed to handle this problem may account, in part, for the different results obtained. Since all but one of the cylinders listed in the above studies were used in subsequent tests in either the tandem or tube bank arrangements, with which we compare our results, it is important to examine the heat transfer characteristics of each cylinder design first.

Most studies present and discuss local and mean heat transfer coefficient data. While the mean value has a physical significance for constant wall temperature, it lacks one for uniform wall heat flux. Therefore, it is not useful and is not part of our discussion.

Single Cylinder. Interpretation of the heat transfer coefficient distribution requires a knowledge of the flow, particularly in the separated region. A recent laser anemometry study [11] has examined this flow and presents data of the time-averaged flow properties. In the subcritical Reynolds number range three distinct regions are shown to exist: (1) a laminar boundary layer development up to separation – which is between 80 and 85 deg – depending upon the Reynolds number; (2) a free shear layer which can be either laminar or turbulent depending on the Reynolds number and which flaps near the vortex shedding frequency; and (3) an area of complete turbulence – called the formation region – which persists until a periodic wake forms downstream. This last region consists of two parts: the separated turbulent shear layer and a recirculation bubble. The recirculation bubble length is indicative of the strength of mixing in this region; the shorter the length the stronger the process. The formation length is important in all multiple-tube geometries as it determines whether the turbulent separated shear layer impinges directly on downstream tubes or forms a periodic wake first.

The variation in the heat transfer coefficient distribution can be explained in terms of these regions. In the laminar boundary layer, theory and experiment agree. Since in this region the Nusselt number is proportional to $\sqrt{\mathrm{Re}}$, it is common to define a Frössling number Fg as $\mathrm{Nu}/\sqrt{\mathrm{Re}}$. The Frössling number is a normalized Nusselt number. Both constant wall temperature and uniform heat flux boundary conditions yield a Frössling number at stagnation ($\theta = 0$ deg) of 0.95 for air, but the latter boundary condition gives higher values in the rest of the region. After separation, the results depend on the Reynolds number. At high values of the Reynolds number the transition to turbulence takes place at separation and the turbulent shear layer flaps; this yields strong mixing with an associated increase in the heat transfer coefficient, a process which increases with the Strouhal frequency. In contrast, at low values a laminar free shear layer exists for a short distance. Mixing is still present but its strength is much reduced which accounts for a less rapid increase or even a

---

[1] Authors are listed in alphabetical order.

Contributed by the Heat Transfer Division for publication in the JOURNAL OF HEAT TRANSFER. Manuscript received by the Heat Transfer Division November 14, 1985.

constant heat transfer coefficient before transition to turbulence. Over the rear portion of the cylinder surface, the heat transfer coefficient is directly related to the strength of the mixing process described above. As the Reynolds number increases, the bubble size decreases and a more vigorous heat transfer process takes place.

An important feature of this flow is the free-stream turbulence and its effect on the heat transfer coefficient. Its largest influence appears to be in the laminar region [9, 10, 12, 13]. However, these studies are inconclusive as to its effects in the separated region, if at all. Studies [12, 13] show that its effect on the heat transfer coefficient in the laminar region depends upon the turbulent intensity and the integral length scale; correlations for the increase of the heat transfer coefficient are presented in terms of these two parameters. They show that values as low as 0.7 percent turbulence will cause an increase in the heat transfer coefficient. This feature will be important when comparisons are made for single cylinders. The real importance, however, will be when the separated shear layer from an upstream cylinder impinges on a cylinder where it has dramatic effects on the laminar region. The correlations presented in [12, 13] will be used to estimate the increase in the heat transfer coefficient for this latter case and will be shown to agree with measured values. Šikmanović et al. [9] demonstrated that if sufficient free-stream turbulence is present, the heat transfer coefficient distribution shows two minimums which are attributed to a laminar separation, a turbulent reattachment, and a final turbulent separation.

Tandem Cylinders. For the heat transfer process, the critical spacing of cylinders seems to be the length of the formation region. For closer spacings, the upstream free shear layer impinges on the cylinder and a closed recirculation region forms between the cylinders [6, 8, 14–16]. The longitudinal pitch ratio of 2 used in this study falls marginally within this condition.

The impingement angle depends on the angle at which the shear layer separates from the upstream cylinder. For a pitch ratio of 2, separation from the first cylinder is around 85 deg; reattachment and separation for the second cylinder are 60 and 115 deg, respectively; and reattachment and separation for the third cylinder are 28 and 115 deg, respectively. Eastop and Turner [15] show a slight dependency of these values on Reynolds number and a pattern which repeats itself after the third cylinder. The angle of reattachment corresponds to the point of maximum pressure. The data from several studies show conflicting evidence on the location of $\mathrm{Fg}_{\max}$ for cylinder 2; one study [8] shows it to coincide with θ_a while other studies indicated θ_a to be on either side of it [6, 7]. For cylinder 3, θ_a is considerably forward of $\mathrm{Fg}_{\max}$ [8].

A laminar boundary layer develops downstream from $\mathrm{Fg}_{\max}$ on the second and on the third cylinders [7, 8]; the heat transfer coefficient is enhanced due to the turbulence in the impinging free shear layer. A difference of opinion exists as to what happens at the end of the laminar boundary layer. One suggestion is that separation occurs with a turbulent reattachment and then a second separation [8], while another suggestion is that the boundary layer makes a transition to turbulence before separation [6, 7].

Upstream of $\mathrm{Fg}_{\max}$ in the recirculation region between cylinders, the heat transfer coefficients are similar to the distribution for a single cylinder from the rear stagnation point forward. It is doubtful that a laminar boundary layer exists forward of θ_a as is reported by one study [7], that is the Frössling number is dependent on the Reynolds number [15].

Tube Banks. Heat transfer within tube banks depends upon four parameters: (1) the tube arrangement (inline or staggered), pitch ratios, and location of the row; (2) the Reynolds number; (3) thermal boundary conditions; and (4) surface roughness. Several studies have examined these parameters [2, 8, 14, 17, 18]. Our study is concerned with smooth tubes only. For both staggered and inline arrangements, the first row acts much like a single tube but with mild blockage, that is acceleration delays the separation; therefore, the point of minimum heat transfer moves rearward.

In staggered tube arrangements, the Frössling number distribution over the second row surprisingly shows no effect of turbulence in the boundary layer region. The combination of blockage and turbulence causes the laminar separation point to move rearward apparently with no reattachment after separation.

The strong turbulence generated within the separated shear layers in the first two rows becomes established by the third row with the result that the flow pattern and heat transfer coefficient distribution change little in subsequent rows [18, 19]. Although a laminar boundary layer develops from the stagnation point ($\theta = 0$), it is influenced by the high turbulence and, in fact, becomes turbulent itself before separation [18]. The transition may be discerned in the Frössling number distribution by the appearance of two local minimums corresponding to the transition and turbulent separation. The transition moves forward with an increase in Re_c.

For inline tube bank arrangements, the flow field and heat transfer coefficient patterns are similar to those of tandem

Nomenclature

D = tube outside diameter, m
D/H = blockage
F = calibration factor
Fg = Frössling number = $\mathrm{Nu}/\sqrt{\mathrm{Re}}$
Fg_c = Frössling number = $\mathrm{Nu}/\sqrt{\mathrm{Re}_c}$
$\mathrm{Fg}_{\max}$ = maximum Frössling number
H = height of test section, m
h = heat transfer coefficient, $\mathrm{W/m^2\,°C}$
k = thermal conductivity, $\mathrm{W/m\,°C}$
L = length of tube, m
L/D = aspect ratio
Nu = Nusselt number = hD/k
q'' = heat flux, $\mathrm{W/m^2}$
R_o = tube resistance at T_R
Re = Reynolds number = $U_\infty D/\nu$
Re_c = Reynolds number = $U_c D/\nu$
S_D = longitudinal tube spacing, m
S_L/D = longitudinal pitch ratio
S_T = transverse tube spacing, m
S_T/D = transverse pitch ratio
T = temperature, °C
T_R = reference temperature, °C
T_{aw} = adiabatic wall temperature, °C
T_0 = measured free-stream air temperature, °C
T_w = wall temperature, °C
ΔT_{aw} = $T_{aw} - T_0$, °C
U_∞ = free-stream air velocity, m/s
U_c = maximum velocity in tube banks at minimum free flow area, m/s
V = voltage, volts
β = temperature coefficient of gold resistance, $(\mathrm{°C})^{-1}$
θ = circumferential angle, rad
θ_a = angle of reattachment, rad
ν = fluid kinematic viscosity, $\mathrm{m^2/s}$

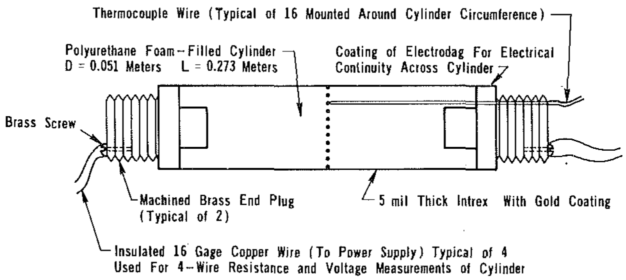

Fig. 1 Diagram of instrumented cylinder

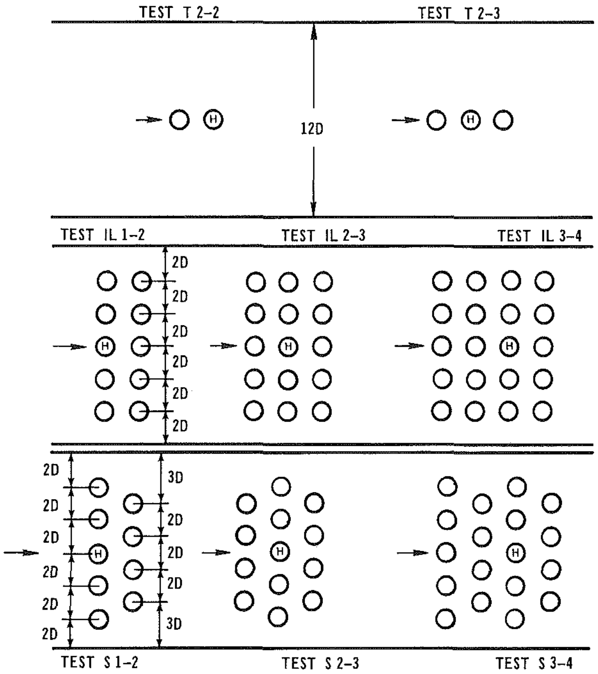

Fig. 2 Tube arrangements: H represents the heated tube

cylinders with a modification due to blockage. The blockage alters the angle of reattachment and the location of the laminar boundary layer separation, and possibly causes a turbulent reattachment and a second separation. As in the case of staggered tubes, the third or fourth row represents an established pattern for succeeding rows [8]. For a pitch ratio less than 2, the vortex shedding is suppressed [20]. Lack of shedding should result in a decrease in the heat transfer coefficient.

Experimental Procedures

A diagram of the instrumented cylinder is reproduced in Fig. 1. Its details of construction, calibration, and measurement reproducibility are given in [1], where also effects of internal conduction are shown to be negligible. As shown in [1] the heat flux is given by

$$q'' = \frac{V^2 F}{R_0[1+\beta(T-T_R)]\pi DL} \tag{1}$$

Once the heat flux is determined, the Frössling number can be calculated from

$$\mathrm{Fg} = \frac{q'' D}{k(T_w - T_0 - \Delta T_{aw})\mathrm{Re}} \tag{2}$$

where $\Delta T_{aw} = T_{aw} - T_0$ is a small correction for the adiabatic wall temperature [5] and is a function of the Reynolds number and the circumferential location. This correction was determined in a separate series of runs where the tube wall was not heated; it did not exceed a value of 0.15 K at any position on the cylinder surface. The heat flux was adjusted to maintain a $T_w - T_{aw}$ of approximately 5 to 15 K so that fluid thermal properties could be taken as constant.

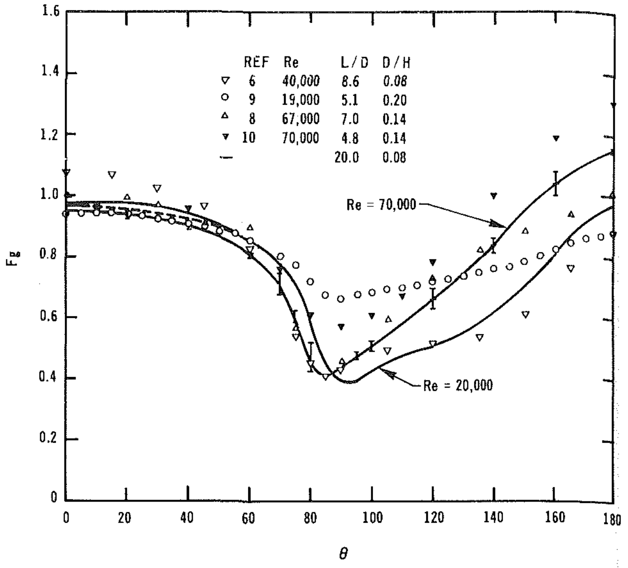

Fig. 3 Frössling number distribution for single cylinder with uniform heat flux

The estimated uncertainties with odds of 20:1, using standard techniques, are as follows [1, 21]: 2 percent for the Nusselt number, 1 percent for the Reynolds number, and 2 to 3 percent for the Frössling number.

All tests were run in a 0.6 m × 1.0 m test section of an open-jet wind tunnel. The free-stream velocity distribution upstream was uniform within 1 percent. The free-stream turbulence was 0.3 percent at a single cylinder Reynolds number of 100,000. For all tests, the aspect ratio was 20; for the single and tandem cylinder tests blockage was 0.083. All dummy (i.e., noninstrumented) tubes were aluminum, 50.8 mm in diameter. Only the test cylinder was heated, as was the case for other studies compared in this paper. Aiba and Yamazaki [6] found that heating all cylinders had little effect on their results. A complete description of the experimental procedures can be found in Elderkin [21].

Results and Discussion

Figure 2 shows a diagram of the tube arrangements studied in our experimental program. All tests were performed with pitch ratios of 2, that is a tube spacing of two diameters. Arrangements were selected so that test rows contained five tubes with a single row behind. In tube bank tests, the clearance between the tube set and the tunnel wall was 1.5 diameters while the clearance between tubes was 1.0 diameters. This may result in some bypass effect.

All results are presented in terms of the local Frössling number. For the single cylinder, tandem cylinders, and the first row of tube banks, this number is defined based on the free-stream velocity. For the interior rows of tube banks, it is defined in terms of the velocity determined by the minimum flow area for a five-tube row, that is $U_c = 1.71\ U_\infty$. By using these two definitions we were able to make comparisons in the laminar boundary layer region. For clarity we have connected the experimental points but in doing so we do not imply that this characterizes distribution between the points.

Single Cylinder. Our results are shown in Fig. 3. The dashed line represents the analytical solution for uniform heat flux at a Reynolds number of 19,000; the agreement with experimental results is excellent up to 80 deg. We attribute the slightly higher results near stagnation at the lower Reynolds number to a small increase in tunnel turbulence for the lower

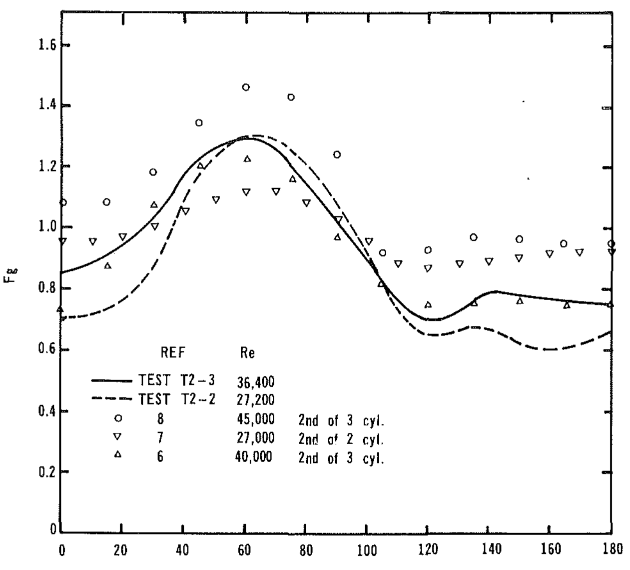

Fig. 4 Frössling number distribution for tandem cylinders

flow rate, a characteristic of many tunnels. At the higher Reynolds number, we rotated the cylinder so as to achieve repeated measurements at each angle. The vertical bars indicate the range of values obtained. Since the uncertainty in Fg is within 2-3 percent, the spread represents a lack of reproducibility at some locations around the cylinder.

The angle at which minimum heat transfer occurs moves rearward at the lower Reynolds number; this same dependency was found for the constant wall temperature case [5]. The delay in recovery of the Frössling number immediately after minimum heat transfer at the lower Reynolds number, as discussed above, is attributed to the initial laminar free shear layer and to the less vigorous mixing in the recirculation region.

Also in Fig. 3, data from other single cylinder tests for a uniform wall heat flux surface are shown together with their corresponding values of the aspect ratio and the blockage. The agreement among all data, including ours, in the boundary layer region before separation is good. The higher results of Aiba and Yamazaki [6] – with a free-stream turbulence of 0.7 percent – are within the range predicted using the correlations from [12].

The studies of Seban [10] and Šikmanović et al. [9] involved blockage, low aspect ratio, and internal conduction, all of which affect the Frössling number. Apelt and West [22] show that blockage and low aspect ratio fortify each other to produce a pressure distribution that would yield Frössling number distributions consistent with the results of these two studies. It is difficult to assess the role of internal conduction for the data of Šikmanović et al. [9]. The construction of their heated test section which averages results over an 11 deg arc also affects their results.

The divergence of results over the rear 40 deg is puzzling. If free-stream turbulence accounts for this, then there should be a significant increase in the Frössling number in the laminar boundary layer portion, which there is not. We could not assess internal conduction effects. The interplay of blockage, aspect ratio, and conduction needs further study.

Tandem Cylinders. Figure 4 shows the results for tests T 2-2 and T 2-3 at Reynolds numbers of 27,000 and 36,000, respectively. The following features can be noted: (1) The maximum Frössling number occurs at 62 deg which corresponds to θ_a for a pitch ratio of 2 [7, 8]; (2) a laminar boundary layer develops downstream of θ_a; (3) a laminar separation takes place at 120 deg; (4) the nearly constant values of the Frössling number after separation are not indicative of turbulent reattachment and separation, as suggested in earlier studies [7, 8], but rather are similar to the distribution for a single cylinder at low subcritical Reynolds numbers; (5) a Reynolds number dependency of the Frössling number forward of θ_a precludes a laminar development as suggested in an earlier study [7]; (6) the Frössling number distribution over the forward surface is similar to that for a single cylinder from the rear stagnation point forward; (7) the effect, if any, of the presence of the third cylinder is restricted to the wake region.

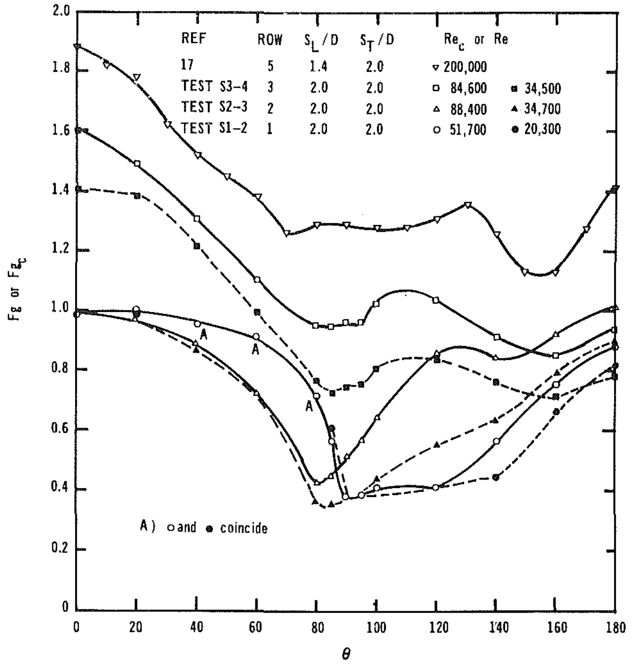

Fig. 5 Frössling number distributions for entrance region of staggered tube bank

The large values of Fg_{max} can be attributed to the interaction of the turbulence contained in the impinging free shear layer and of the laminar boundary layer. If we estimate the turbulence at impact to be 0.14 (from the data in [6]) and if we take a Reynolds number of 30,000, the Frössling number would be 1.4 based on the correlation in [13]; this agrees well with our value shown in Fig. 4.

The flat profile from the measurements of Kostić and Oka [7] may be attributable to the combined effects of blockage, low aspect ratio, and internal conduction as we noted in the discussion of their single cylinder test.

The results of test 2-3 compare well with those of Aiba and Yamazaki [6] and Turner [8]. The maximum value of the Frössling number for Turner is 1.46; the correlation in [12] gives a value of 1.5 for a Reynolds number of 45,000 and a turbulent intensity of 0.14. We agree with Turner that Fg_{max} and θ_a coincide. As in the case of the single cylinder, it is difficult to assess if thermal boundary conditions played any part in the results.

Tube Banks. Runs were made at Reynolds numbers of 20,000 and 50,000 for each tube arrangement shown in Fig. 2. Tests showed that the Frössling number distribution was symmetric with respect to the upper and lower half of the cylinder. The results were compared to Achenbach's [17] for the fifth row at pitch ratios of 2 × 1.4 with constant wall temperature and to Turner's [8] for the second and third rows at pitch ratios of 2 × 2 with uniform wall heat flux.

Staggered Tubes. Figure 5 contains the results of the staggered tube bank tests. Several observations are noteworthy.

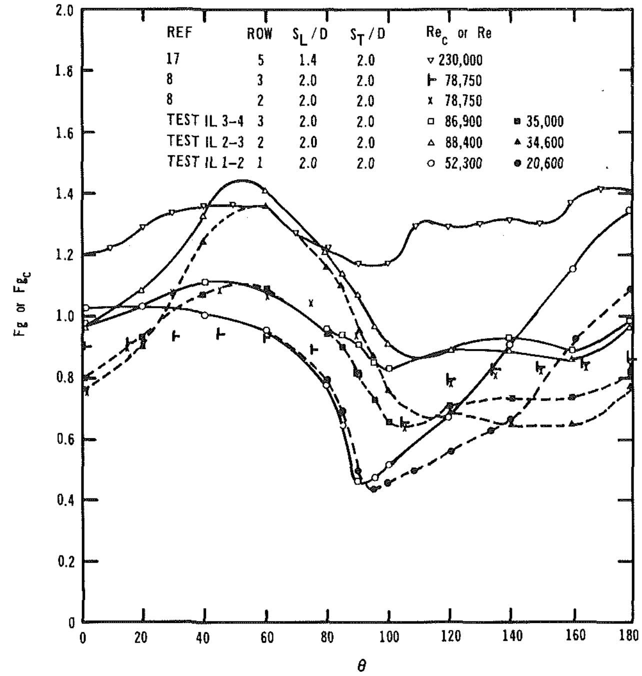

Fig. 6 Frössling number distribution for entrance region of inline tube banks

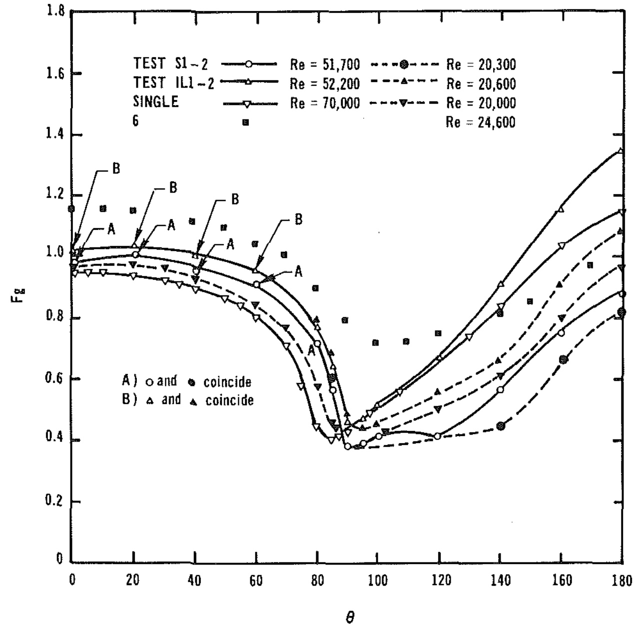

Fig. 7 Comparison of Frössling number distribution for a single cylinder and the first row of inline and staggered tube banks

1 The stagnation Frössling numbers for rows 1 and 2 show the effect of blockage – a 4 percent increase – but not of turbulence.

2 The lack of recovery of the Frössling number on the rear surface of the first tube is surprising.

3 In the second row, laminar separation takes place with no reattachment apparent, that is the distribution is similar to that for a single tube.

4 Laminar heat transfer takes place over the forward portion of the tube for all three rows. When comparison is made to a single cylinder, the first row shows higher Frössling numbers due to acceleration from blockage and the second row shows lower values. The latter could be indicative of bypassing of air around the main core. By the third row, the influence of turbulence is prominent. The stagnation Frössling numbers of 1.4 and 1.6 are consistent with the values shown in [13].

5 The distribution in the third row (Test S 3-4) bears a striking similarity to Achenbach's [17] for the fifth row. His high values might be attributed to a combination of higher Reynolds numbers and a smaller longitudinal pitch ratio. The effect of the different thermal boundary conditions cannot be determined from comparison of the two sets of data, if indeed there is one. Apparently, a repeated pattern is nearly established by the third row.

6 In the third row, two local minimums occur at 80 and 160 deg. Turbulence must certainly play a role, but whether it is transition to turbulence of the laminar boundary layer as suggested by Achenbach [18] or is laminar separation followed by turbulent reattachment and separation as suggested by Žukauskas [2] cannot be determined.

Inline Tubes. Figure 6 shows the results of the inline tube bank tests. The arguments put forth in the discussion of tandem cylinders are applicable. An additional factor is the blockage caused by the presence of the neighboring transverse tubes.

Characteristics similar to tandem cylinders are: (1) the development of a laminar boundary layer rearward from Fg_{max}, although there appears to be some effect of turbulence at the high Reynolds number in row 2; (2) a laminar separation with little change in the Frössling number thereafter. Fg_{max} is dependent upon the Reynolds number; at the higher Reynolds number in row 2, it moves forward to 55 deg, while in row 3 it occurs at 42 deg. As a result there is a delay in separation as compared to row 1.

The major difference between rows 2 and 3 is the reduction in the Frössling number in the laminar boundary layer region. We attribute this difference to the turbulence contained in the free shear layers that impinge on the second row. McKillop et al. [11] show that the turbulent intensity contained in the free shear layer is related to the Strouhal frequency, that is the higher the frequency the higher the turbulence intensity. Eastop and Turner [15] show that the Strouhal frequency from the first row is 50 percent greater than from a single tube, a fact which should mean a higher turbulence impinging on the second cylinder, and as a consequence a larger Frössling number. Heinecke and von der Decken [20], on the other hand, show that shedding is suppressed downstream for an inline tube bank, a fact which should mean a lower Frössling number.

Comparison of our findings with previous ones shows the following: (1) There is a similarity between Achenbach's fifth row and our third row, any difference being attributable to the different Reynolds numbers and pitch ratio, and the distribution pattern is, therefore, nearly established by the third row; (2) a marked difference exists between our tests and those of Turner [8] in the laminar boundary layer region, 30 deg $< \theta <$ 90 deg. We can offer no reason for this difference. Certainly comparison to the single cylinder tests would not offer any explanation.

Single Row. In Fig. 7, we compare our results for a tube in the first row with those for a single cylinder. Blockage effects account for the higher Frössling numbers at the stagnation point and in the boundary layer; it is also responsible for the shifting of the minimum Frössling number (and presumably the separation point) rearward. In the separated region, the large values for the inline arrangement might be attributable to the greater mixing associated with the larger Strouhal frequency, as noted earlier. The low values for the staggered arrangements might be caused by the channeling of the air around the main core (see Fig. 2). Finally we observed the effect of smaller pitch ratios found by Aiba and Yamazaki [6]. The lower values in the recirculation region on the rear surface are consistent with their results for a single cylinder (see Fig. 3).

Summary

We have applied a new experimental technique with a uniform heat flux boundary condition to measurements of the Frössling number for a circular cylinder in air. Comparison of test results for a single cylinder indicate the importance of blockage, aspect ratio, and free-stream turbulence on the Frössling number distribution for a given Reynolds number. We could not assess internal conduction effects which would cause a change in the thermal boundary condition.

Well-documented results are presented for cylinders in tandem and in the entrance region of tube banks. Comparison with the few available published results show that the Frössling number distribution approaches a pattern by the third row that would occur for tube rows further downstream.

References

1 Baughn, J. W., Takahashi, R. K., Hoffman, M. A., and McKillop, A. A., "Local Heat Transfer Measurements Using an Electrically Heated Thin Gold-Coated Plastic Sheet," ASME Journal of Heat Transfer, Vol. 107, No. 4, Nov. 1985.

2 Žukauskas, A. A., "Heat Transfer of Banks of Tubes in Crossflow at High Reynolds Numbers," in: *Heat Exchangers: Design and Theory Source Book*, W. H. Afgan and E. U. Schlünder, eds., McGraw-Hill, New York, 1974, pp. 75–100.

3 Papell, S. S., "Influence of Thermal Boundary Conditions on Heat Transfer From a Cylinder in Crossflow," NASA Technical Paper 1894, Lewis Research Center, 1981.

4 Achenbach, E., "Total and Local Heat Transfer From a Smooth Circular Cylinder in Crossflow at High Reynolds Numbers," *International Journal of Heat and Mass Transfer*, Vol. 18, 1975, pp. 1387–1396.

5 Kraabel, J. S., McKillop, A. A., and Baughn, J. W., "Heat Transfer to Air From a Yawed Cylinder," *International Journal of Heat and Mass Transfer*, Vol. 25, 1982, pp. 409–418.

6 Aiba, S., and Yamazaki, K., "An Experimental Investigation of Heat Transfer Around a Tube in a Bank," ASME Journal of Heat Transfer, Vol. 98, 1976, pp. 503–508.

7 Kostić, Ž. G., and Oka, S. N., "Fluid Flow and Heat Transfer With Two Cylinders in Crossflow," *International Journal of Heat and Mass Transfer*, Vol. 15, 1972, pp. 279–299.

8 Turner, J. R., "Heat Transfer and Pressure Distribution Within Tube Banks," Ph.D. thesis, The Polytechnic, Wolverhampton, 1978.

9 Sikmanović, S., Oka, S., and Končar-Djurajević, S., "Influence of the Structure of Turbulent Flow on Heat Transfer From a Single Cylinder in a Crossflow," *Proceedings of the Fifth International Heat Transfer Conference*, Tokyo, Vol. 2, 1974, pp. 320–342.

10 Seban, R. A., "The Influence of Free Stream Turbulence on the Local Heat Transfer From Cylinders," ASME Journal of Heat Transfer, Vol. 82, 1960, pp. 101–107.

11 McKillop, A. A., and Durst, F., "LDA Experiments of Separated Flow Behind a Circular Cylinder," *Proceedings of the Second Symposium on the Application of Laser Anemometry to Fluid Mechanics*, Lisbon, 1984, pp. 14.4, 1–6.

12 Yardi, N. R., and Sukhatme, S. P., "Effects of Turbulence Intensity and Integral Length Scale of a Turbulent Free Stream on Forced Convection Heat Transfer From a Circular Cylinder in Crossflow," *Proceedings of the Sixth International Heat Transfer Conference*, Toronto, Vol. 5, pp. 347–352.

13 Lowery, G. W., and Vachon, R. I., "The Effect of Turbulence on Heat Transfer From Heated Cylinders," *International Journal of Heat and Mass Transfer*, Vol. 18, 1975, pp. 1229–1242.

14 Aiba, S., Ota, T., and Tsuchida, A., "A Note on an Improvement of Heat Transfer of Tube Banks," *Wärme- und Stoffübertragung*, Vol. 17, 1982, pp. 59–64.

15 Eastop, T. D., and Turner, J. R., "Air Flow Around Three Cylinders at Various Pitch-to-Diameter Ratios for Both a Longitudinal and a Transverse Arrangement," *Transactions of the Institute of Chemical Engineers*, Vol. 60, 1982, pp. 359–363.

16 Zdravkovich, M. M., and Pridden, D. L., "Interference Between Two Circular Cylinders; Series of Unexpected Discontinuities," *Journal of Industrial Aerodynamics*, Vol. 2, 1977, pp. 255–270.

17 Achenbach, E., "Total and Local Heat Transfer and Pressure Drop of Staggered and In-Line Tube Bundles," in: *Heat Exchangers: Thermal-Hydraulic Fundamentals and Design*, S. Kakac, A. E. Bergles, and F. Mayinger, eds., McGraw-Hill, New York, 1981, pp. 85–96.

18 Achenbach, E., "Investigations on the Flow Through a Staggered Tube Bundle at Reynolds Numbers up to Re = 10^7," *Wärme- und Stoffübertragung*, Vol. 2, 1969, pp. 47–62.

19 Varty, R. L., and Currie, I. G., "Index-Matched Laser-Anemometry Measurements of Crossflow in Tube Bundles," *Second International Symposium on Application of Laser Anemometry to Fluid Mechanics*, Lisbon, 1984, pp. 5.4, 1–6.

20 Heinecke, E., and von der Decken, C. B., "Steady and Unsteady Flow Phenomena in and Behind Staggered and In-line Tube Banks," in: *Heat Exchangers: Design and Theory Source Book*, N. H. Afgan and E. U. Schlünder, eds., McGraw-Hill, New York, 1974, pp. 663–671.

21 Elderkin, M. J., "Measurements of Local Heat Transfer Coefficients in Air for Staggered and In-line Tube Banks," M.S. Thesis, University of California, Davis, 1983.

22 West, G. S., and Apelt, C. J., "The Effects of Tunnel Blockage and Aspect Ratio on the Mean Flow Past a Circular Cylinder With Reynolds Numbers Between 10^4 and 10^5," *Journal of Fluid Mechanics*, Vol. 114, 1982, pp. 361–377.

Laminar Combined Convection in a Horizontal Annulus Subject to Constant Heat Flux Inner Wall and Adiabatic Outer Wall

M. Kaviany
Department of Mechanical Engineering
and Applied Mechanics,
University of Michigan,
Ann Arbor, MI 48109
Mem. ASME

Steady-state, fully developed velocity and temperature fields in mixed convection through a horizontal annulus (ratio of outside to inside radii of 1.25), with a prescribed constant heat flux on the inner cylinder and an adiabatic outside cylinder, are analyzed using finite difference approximations. The effects of the buoyancy-driven lateral flow on the temperature of the inner surface are studied in detail. The results show that, as the buoyancy potential (Rayleigh number) increases, the lateral flow structure changes from one cell (on each side) to two cells. The consequence of these flow regimes is that as Rayleigh number increases the temperature of the upper portion of the inner cylinder first increases significantly above its value for pure forced convection and then decreases significantly as the number of cells increases. The average temperature of the inner cylinder decreases monotonically as the Rayleigh number increases.

1 Introduction

Significant buoyancy-driven secondary flows can develop in heated horizontal ducts under forced flows [1-5]. This can cause excessively high temperatures in the upper portion of the duct.

For a horizontal cylinder, the superposed buoyancy on external [1] and internal flows [1-4], as well as nonuniform peripheral heating [5], has been studied (mostly for isothermal surfaces), and the effects of buoyancy on the temperature and velocity fields have been determined. Natural convection in horizontal annuli has been studied both experimentally (cf. [6]) and analytically [7-9] for isothermal surfaces, and empirical correlations are available [6]. The entrance effects for forced convection in annuli have been studied both experimentally and analytically [10, 11]. Fully developed mixed convection in annuli with isothermal surfaces (in [12] one surface was adiabatic) has been investigated for fluids with linear equations of state [12, 13] as well as for water near 4°C [12, 14].

In forced convection through horizontal annuli, for some situations of practical interest the heat fluxes on the surfaces, rather than temperature, are prescribed. As a result of the lateral motion induced by buoyancy, the surface temperatures in the upper portion of the annulus can become undesirably high. For the isothermal boundaries, the structure of the lateral motion changes with the effectiveness of the buoyancy force [12-14], i.e., the Rayleigh number. As the Rayleigh number increases, the structure of the cellular motion changes from one cell on each side of the annulus to two and gradually into a multicell structure. When this happens (while at the same time the lateral mixing intensifies), the fluid heated at the bottom portion of the annulus will not reach the top. This may result in lower temperatures in the upper portion than those for a single-cell structure.

In this study[1] such changes in the structure of the lateral motion and the associated temperature field are studied for a case when the inner surface is heated with a constant and prescribed heat flux and the outer surface is maintained as adiabatic. This situation arises when the heat source is located inside the inner cylinder. The generated heat may be due to a chemical reaction or thermal radiation from an electrically heated target. The variations in temperature of the upper surface (which has the highest temperature in the annulus) with respect to Rayleigh and Prandtl numbers are studied in detail. The ratio of the outside to inside radii is taken as 1.25 for its application to certain compact and high heat flux exchangers. The flow and temperature fields are assumed to be longitudinally fully developed. This makes the velocity and temperature profiles invariant with longitudinal position. In addition, it is required that the pressure gradient not be affected by the lateral motion induced by buoyancy while at the same time the lateral distribution and the average value of the longitudinal velocity are allowed to change. The entrance length for simultaneous development of velocity and temperature fields for pure forced convection is given in [10] and the results for Prandtl numbers near and above unity give the nondimensional entrance length as

$$z \simeq 0.1(R-1)\mathrm{Re}\,\mathrm{Pr}$$

These characters are defined in the nomenclature. Due to the added resistance to the flow caused by the lateral motion, the average longitudinal velocity decreases (as will be shown). This reaction and any measurable decrease in the kinematic viscosity associated with heating must both be accounted for in determining the Reynolds number.

Although the assumption of fully developed fields is, in general, rather restrictive, it simplifies the problem notably, since the magnitude of the average longitudinal velocity (or Reynolds number) does not influence the buoyancy-induced lateral motion [5]. Making this assumption enables us to understand some of the consequences of the lateral motion such as (*i*) the extent of lateral mixing, (*ii*) the temperature difference between the upper portion of the inner cylinder (i.e., the area of the highest temperature) and the bulk mean temperature, and (*iii*) the effects of the Rayleigh number on the flow regimes. When the annulus is not long enough for the entrance effects to be important, the results presented here should only be used as a general guide.

---

[1] This study was originated by an attempt to understand the extent of lateral mixing in the flow of an oil over a cylinder, where the prescribed lateral heat flow rates to the oil were relatively high. In these problems the lateral and longitudinal variations in the viscosity, with temperature, are significant and the boundary conditions on the outer cylinder are neither of prescribed temperature nor heat flux. However, assumptions of adiabatic outer boundary and constant viscosity were considered valid first-order approximations for this problem.

Contributed by the Heat Transfer Division for publication in the JOURNAL OF HEAT TRANSFER. Manuscript received by the Heat Transfer Division May 3, 1984.

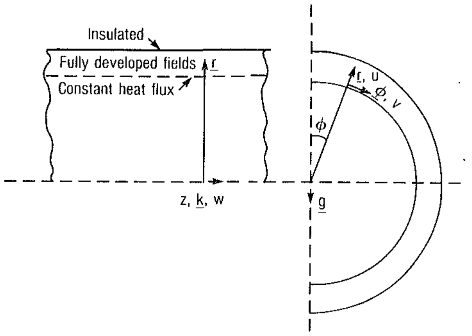

Fig. 1 Schematic of the problem considered

2 Analysis

A schematic of the problem considered is given in Fig. 1. The fluid flows between two horizontal, concentric cylinders where the inner cylinder is heated at a steady and uniform rate q and the outer cylinder is adiabatic. It is assumed that the velocity and temperature fields are fully developed and the Boussinesq approximation[2] holds. A linear equation of state is also assumed. The governing equations which are expressions of conservation of mass, momentum, and thermal energy are nondimensionalized using r_i, $r_i^2\,\alpha^{-1}$, $\bar{w}_0$, αr_i^{-1}, and $q\,r_i k^{-1}$ to scale length, time, longitudinal velocity, lateral velocities, and temperature. Following [14] the vorticity-stream function formulation is applied in order to avoid direct determination of the lateral variations of pressure. The conservation equations then become

Vorticity:

$$\omega_t + r^{-1}(ru\omega)_r + r^{-1}(v\omega)_\phi = \Pr\nabla_1^2\omega - \Pr\,\mathrm{Ra}(r^{-1}T_\phi\cos\phi + T_r\sin\phi) \qquad (1)$$

Temperature:

$$T_t + r^{-1}(ruT)_r + r^{-1}(vT)_\phi + 2(R^2-1)^{-1}\bar{w}^{-1}w = \nabla_1^2 T \qquad (2)$$

Longitudinal velocity:

$$w_t + r^{-1}(ruw)_r + r^{-1}(vw)_\phi = 8\Pr[R^2+1-(R^2-1)\ln^{-1}R]^{-1} + \Pr\nabla_1^2 w \qquad (3)$$

Stream function:

$$\nabla_1^2\psi = -\omega \qquad (4)$$

from which the lateral velocities are

$$u = r^{-1}\psi_\phi, \qquad v = -\psi_r \qquad (5)$$

where $\nabla_1^2 = \partial_{rr} + r^{-1}\partial r + r^{-2}\partial_{\phi\phi}$. When Ra = 0, the distribution of the longitudinal velocity (normalized with respect to mean velocity $\bar{w}_0$) is given as [10]

$$w_0 = [1 - r^2 + (R^2-1)\ln^{-1}R\ln r][R^2+1 - (R^2-1)\ln^{-1}R]^{-1} \qquad (6)$$

It is assumed that the average longitudinal pressure drop is prescribed, i.e., it is not altered by the onset of lateral motions. Note that $w_z = u_z = v_z = 0$, and $T_z = (T_b)_z$. The dimensionless temperature is $(T - T_b)\,q^{-1}r_i^{-1}k$, where T_b is the dimensional bulk mean temperature and its gradient (in the z direction) is a constant and is equal to $2r_i\,q[\rho c_p w(r_0^2 - r_i^2)]^{-1}$. With this definition for dimensionless temperature, the dimensionless bulk mean temperature is zero.

The Nusselt number is defined as

$$\overline{\mathrm{Nu}} = 2(R-1)\bar{T}_w^{-1}$$

where $\bar{T}_w$ is the average inner wall temperature.

Although steady-state solutions to equations (1)–(6) are sought, these equations are solved in their time-dependent forms. The initial and boundary conditions are

$$t=0: \quad \psi = \omega = T = 0,\ w = w_0 \qquad (7a)$$

$$t>0: \quad \text{at}\ \phi = 0,\pi,\ \psi = w_\phi = T_\phi = \omega = 0 \qquad (7b)$$

$$r=1 \quad \psi = w = 0,\ T_r = -1,\ \omega = -\psi_{rr} \qquad (7c)$$

$$r=R \quad \psi = w = T_r = 0,\ \omega = -\psi_{rr} \qquad (7d)$$

Due to the presence of symmetry, only the domain $0 \le \phi \le \pi$ is considered.

3 Solution

The governing equations were converted to the appropriate approximate finite-difference forms (all except time derivatives were written in second-order approximation form) as described and successfully applied in [15–17].

The calculation procedure was as follows:

1 The time step was limited by the stability requirement which was determined by the grid spacing, maximum velocities and the Prandtl number. This was taken as

$$\Delta t < \left(\frac{2}{\Pr^* r_i{}^2\Delta\phi^2} + \frac{2}{\Pr^*\Delta r^2} + \frac{u_{\max}}{r_i} + \frac{u_{\max}}{\Delta r} + \frac{v_{\max}}{r\Delta c}\right)^{-1} \qquad (8)$$

---

[2] For small ratios of outside to inside diameter, the heat fluxes and consequent rise in fluid temperature required to produce a significant lateral motion are relatively large. Therefore, especially for liquids, variations in viscosity and thermal expansion coefficient with temperature must be included as done in [1]. In general, these variations cause (at the heated surface) thinning of the boundary layer and acceleration within it. These effects are not included here.

Nomenclature

c_p = specific heat capacity, J•kg^{-1}°C^{-1}
D_h = $2(r_o - r_i) = 2r_i(R-1)$ = hydraulic diameter
k = thermal conductivity, W•m^{-1}°C^{-1}
$\overline{\mathrm{Nu}}$ = $2(R-1)T_w^{-1}$ = average Nusselt number
Pr = $\nu\alpha^{-1}$ = Prandtl number
q = prescribed heat flux on the inner cylinder, W•m^{-2}
r = radial coordinate, m
r_i = inside radius, m
r_o = outside radius, m
R = $r_o r_i^{-1}$
Ra = $g\beta q r_i^4\ k^{-1}\nu^{-1}\alpha^{-1}$ = Rayleigh number
Re = $\bar{w}\ D_h\nu^{-1}$ = Reynolds number
t = time, s
T = temperature, °C
T_b = $2[\pi(R^2-1)\bar{w}]^{-1}\int_0^\pi\int_1^R Tw\,{\bullet}\,r dr d\phi$ = bulk mean temperature, °C
u, v, w = velocity components, m•s^{-1}
$\bar{w}$ = $2[\pi(R^2-1)]^{-1}\int_0^\pi\int_1^R w\,{\bullet}\,r dr d\phi$ = mean longitudinal velocity, ms^{-1}
z = horizontal coordinate axis, m
α = thermal diffusivity, m^2•s^{-1}
β = thermal expansion coefficient, C^{-1}
ν = kinematic viscosity, m^2•s^{-1}
ϕ = azimuth angle, rad
ψ = stream function
ω = vorticity

Subscripts

0 = for Ra = 0
w = at the inner surface
max = maximum value
min = minimum value

Superscripts

= average over the lateral plane
r, t, z, d = derivatives

Table 1 Predicted value of various variables for several Rayleigh and Prandtl numbers; $R = 1.25$, the inner wall is heated with constant and specified heat flux and the outer wall is adiabatic; the results are for a mesh net of 16 × 61

	Pr = 0.7				Pr = 7					Pr = 70				
Ra	10^5	10^6	10^7	10^8	10^5	10^6	10^7	10^8	10^9	10^5	10^6	10^7	10^8	10^9
T_{max}	0.200	0.380	0.300	0.283	0.124	0.330	0.232	0.164	0.115	0.0908	0.268	0.205	0.142	0.091
$\bar{T}_w$	0.0878	0.0696	0.0571	0.0538	0.0889	0.0697	0.0507	0.0378	0.0317	0.0893	0.0730	0.0500	0.0359	0.028
$\overline{Nu}$	5.69	7.18	8.76	9.29	5.62	7.18	9.87	13.24	15.76	5.60	6.85	10.00	13.92	17.48
$\bar{w}$	0.995	0.995	0.974	0.929	0.996	0.995	0.994	0.989	0.975	0.995	0.995	0.995	0.995	0.994
ψ_{max}	0.451	2.33	8.77	24.40	0.465	2.43	9.11	31.82	96.52	0.472	2.78	9.10	32.70	108.4
ψ_{min}	0.0	0.0	-0.864	-2.37	0.0	0.0	-0.634	-2.23	-3.36	0.0	0.0	-0.497	-2.15	-3.32

$$\text{where } \mathrm{Pr}^* = \begin{cases} 1, & \text{for } \mathrm{Pr} < 1 \\ \mathrm{Pr}, & \text{for } \mathrm{Pr} > 1 \end{cases}$$

The field of grid points was searched in order to find the maximum velocities. Then the time step was determined for the next time advancement.

2 Temperature at all the interior grid points was advanced with an explicit difference form that uses the second-order upwind finite-difference form for the convective terms, the second-order central finite-difference form for the diffusive terms, and the first-order forward finite-difference form for the time derivative.

3 Vorticity at all interior grid points was similarly advanced with the buoyancy term written in a second-order central finite-difference form using the updated temperature field.

4 Stream function at all interior grid points was updated with the updated vorticity field. The second-order central finite-difference form was used and the method of successive overrelaxation was employed to obtain the new stream function at each grid point. Convergence was assumed whenever the maximum normalized change in the value of ψ between any two successive iterations was less than 10^{-4}.

5 Temperatures at the inner and outer surfaces were calculated using the second-order backward finite-difference form.

6 Vorticity at boundary grid points was calculated using the second-order backward finite-difference form.

7 Velocities and their mean values, which were needed for determining the time step and the convective terms in the next iteration, were calculated.

Steps 1-7 were repeated until the magnitude of $\bar{T}_w$ did not change by more than 10^{-5}. In addition, since (*a*) the equations (except for equation (4)) were written in explicit form, and (*b*) the approximations were second order, the dimensionless T_b was slightly different from zero. Therefore, after each time step T_b was calculated (using the trapezoidal rule) and subtracted from the newly computed temperature field.

For equation (4) a relaxation factor of 1.81 was used for the 16 × 61 grid net and $R = 1.25$. Fewer than 100 iterations were needed for convergence in each time step. As an example of the number of time steps required, for $\mathrm{Ra} = 10^7$ and $\mathrm{Pr} = 0.7$, a total of 12,000 time steps were taken before steady state was obtained. The time steps were about 10^{-4}. Therefore, the accumulated nondimensional time (for steady state) for this run was about unity.

The available literature results are for $\mathrm{Ra} = 0$. For $R = 1.25$ the average Nusselt number is 5.58 as given in [10] which uses other solution and computational methods not used in this study. Due to the rather excessive computational time associated with very fine grid nets, a compromise had to be made between accuracy and economy. Through trials it was found that a 16 × 61 grid net gives nearly accurate results and was also economical. For this grid net the results give $\overline{\mathrm{Nu}} = 5.5905$ for $\mathrm{Ra} = 0$, which is in agreement with the value given in [10]. All the results to be reported are for $R = 1.25$ with a uniform grid net of 16 × 61. It is expected that for flow regimes with thick boundary layers, this grid net should suffice, while for large values of Ra the results may depend on grid size. However, according to the results reported in [14], this mesh net should be adequate. No attempt was made to use a nonuniform grid net [5] or extrapolation [18].

For $\mathrm{Ra} = 0$, further comparisons of the detailed velocity and temperature distributions were made with those reported in [10] and complete agreement was found (e.g., equation (5) and Fig. 4 in [10]). For $\mathrm{Ra} \neq 0$, only a general comparison was made with the results of [5, 12-14] and agreement was found with Fig. 8 of [5], Fig. 4 of [12], Fig. 2 of [13] (for $R = 2$), and Fig. 6 of [14].

4 Results and Discussion

The results are for $\mathrm{Pr} = 0.7$, 7, and 70 and for various magnitudes of the Rayleigh number. Table 1 gives the values for $T_{\max}$ (which takes place on the inner wall at $\phi = 0$), $\bar{T}_w$, $\overline{\mathrm{Nu}}$, $\bar{w}$, $\psi_{\max}$, and $\psi_{\min}$. For very large Rayleigh numbers no steady-state solution was found. However, since in the combined mode studied here any unsteady motion must be three dimensional, no physical significance can be given to these results for high Rayleigh numbers. Therefore, only the results for the cases where the steady-state solutions were obtained are given. Note that for $\mathrm{Ra} = 0$, $\overline{\mathrm{Nu}} = 5.58$ and $\bar{T}_w = 0.0896$. The results given in Table 1 are also shown graphically in Figs. 2-9. As will be shown later, in general as the Rayleigh number increases, the average longitudinal velocity decreases, the average inner wall temperature decreases, and the lateral mixing increases.

Figures 2-4 show the effects of buoyancy on the velocity and temperature fields when the fluid is a gas ($\mathrm{Pr} = 0.7$) and $\mathrm{Ra} = 10^7$. Figure 5 shows the patterns of lateral motion and the temperature fields for $\mathrm{Pr} = 70$ (for some oils) and $\mathrm{Ra} = 10^9$. Figures 6-9 show the variations of the inner cylinder temperature distributions and the flow regimes for various values of Pr and Ra.

For $\mathrm{Ra} > 10^7$ (and for the range of Pr considered here) there are two cells on each side of the annulus. The stronger cell extends to the top while the weaker cell remains at the bottom and extends slightly further upward as Ra increases (see Fig. 2). The shorter path length (resulting from the presence of more than one cell), for the cellular convection, means that the fluid reaching the top may have a lower temperature than would have been expected if there was only one cell (on each side). However, this depends on the lateral mass flow rate and the extent of lateral mixing.

Figure 3 shows the profiles of the longitudinal velocity for several azimuthal angles for $\mathrm{Pr} = 0.7$ and $\mathrm{Ra} = 10^7$. As was

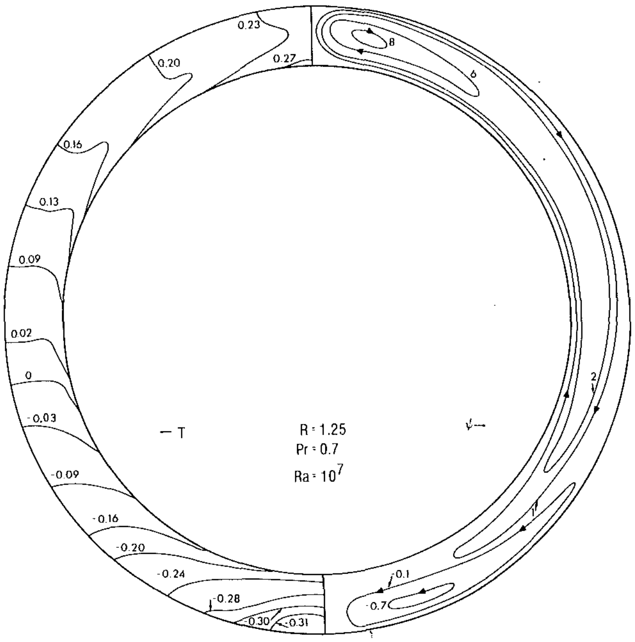

Fig. 2 Constant stream-function lines and constant temperature lines for R = 1.25, Pr = 0.7, and Ra = 10^7

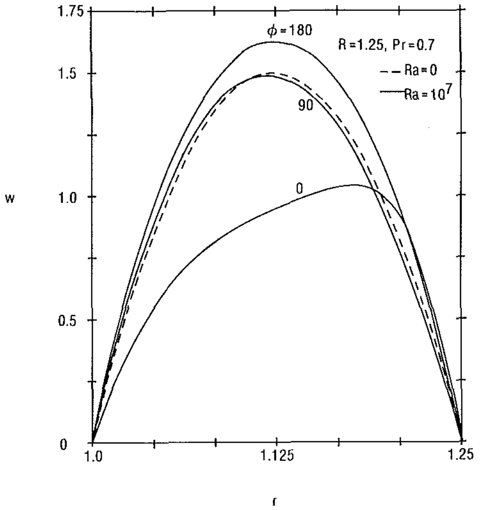

Fig. 3 Effect of buoyancy-driven lateral motion on the radial distribution of the longitudinal velocity. The results are for R = 1.25, Pr = 0.7, Ra = 10^7, and various azimuthal angles.

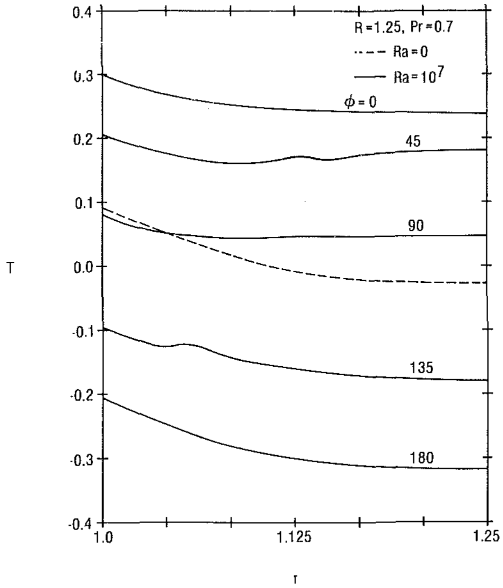

Fig. 4 Effect of buoyancy-driven lateral motion on the radial temperature distribution. The results are for R = 1.25, Pr = 0.7, Ra = 10^7, and various azimuthal angles.

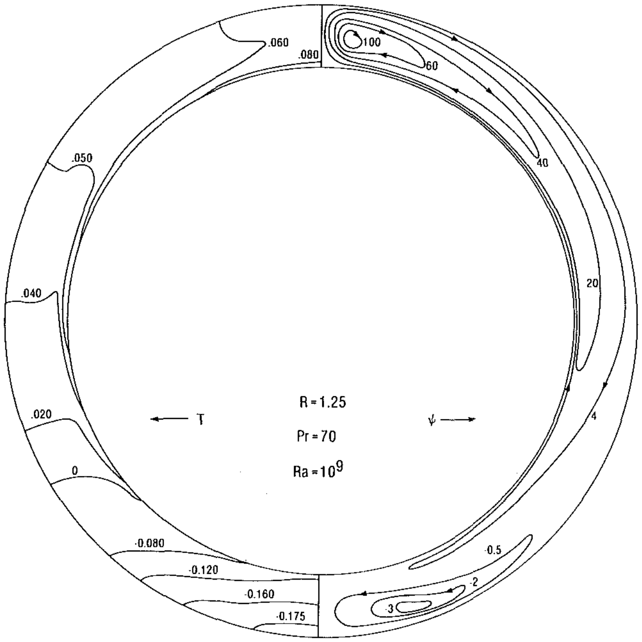

Fig. 5 Constant stream-function lines and constant temperature lines for R = 1.25, Pr = 70, and Ra = 10^9

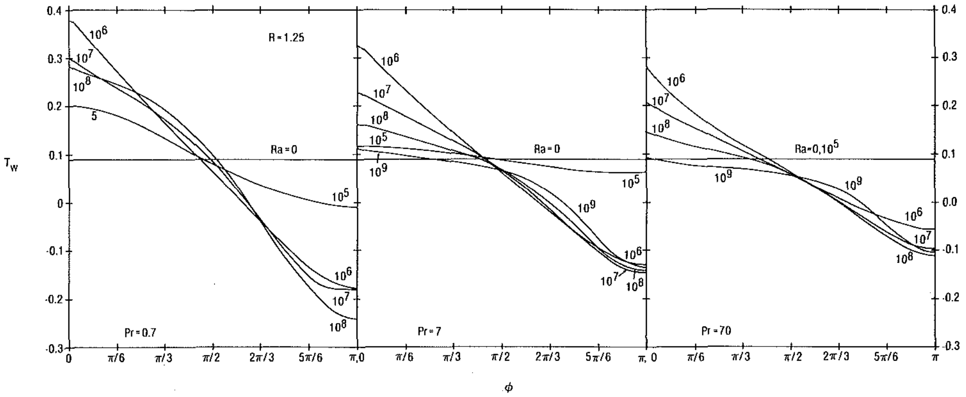

Fig. 6 The inner surface temperature distributions for R = 1.25, Pr = 0.7, 7, and 70, and various Rayleigh numbers

noted, the pressure drop is prescribed and not altered by the onset of lateral motion. On the average, the lateral buoyancy-driven convection decreases the longitudinal flow rate in the upper portion of the annulus and increases it in the lower portion. This is due to the higher circulation strength associated with the upper cell which causes higher resistance to the longitudinal flow. These results are similar to those reported in [12-14] for prescribed surface temperatures.

Figure 4 shows the radial variations in temperature for several azimuthal angles for Pr = 0.7 and Ra = 10^7. Due to the presence of the upper cell ($\phi \approx 45$), the minimum temperature, which takes place at the outer wall for Ra = 0, occurs at R = 1.1. The results also show that the upper cell causes a more uniform temperature than the lower one.

Similar trends are expected for other Prandtl numbers as shown in Fig. 5 for Pr = 70 and Ra = 10^9.

The variations of the abovementioned characteristics with respect to Ra are now discussed in Figs. 6-9. The temperature distribution in the annulus is affected by (*a*) the lateral mass flow rate and (*b*) the extent of local mixing. The maximum temperature will always be at R = 1 and ϕ = 0, i.e., T_w ($R=1$, $\phi=0$) = $T_{\max}$. Figure 6 shows the temperature distribution along the inner cylinder for various Rayleigh numbers and for Pr = 0.7, 7, and 70. For Ra < 10^7 there exists only one cell on each side. Therefore, with increases in Ra, the energy transported upward by the cellular motion also increases. For Ra ≥ 10^7, there is more than one cell on each side; therefore, the net upward transport is not as effective but the local mixing is more extensive. Thus, due to the transition from a single cell to a double-cell structure, $T_{\max}$ first increases[3] and reaches a maximum and then begins to decrease. At the same time, because of the mixing, the temperature of the entire inner surface is continuously lowered as Ra increases. The interplay between these two processes determines the temperature distribution for a given Ra. As the Prandtl number increases, the variation in the inner surface temperature becomes less drastic but is still significant even for Pr = 70.

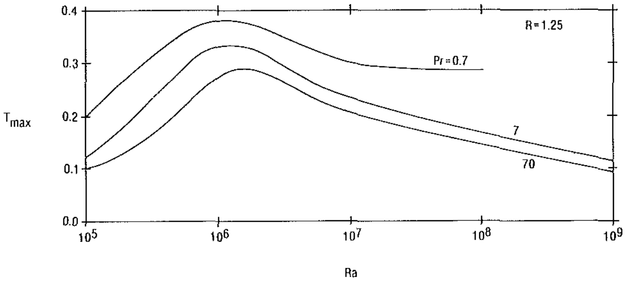

Fig. 7 Variations in the maximum temperature of the inner surface with respect to Rayleigh number for several values of Prandtl number

Figure 7 shows the variation of $T_{\max}$ with respect to Rayleigh number for several Prandtl numbers. The Rayleigh number corresponding to the maximum of $T_{\max}$ is the transition Rayleigh number that separates the single-cell and double-cell regimes. Figure 7 shows that this transition Rayleigh number increases with increases in Prandtl number.

Figure 8 shows the variations in the normalized average longitudinal velocity, the normalized average inner wall temperature, and the maximum values of the stream function with respect to Rayleigh number for Pr = 0.7, 7, and 70. As the Prandtl number increases the average longitudinal velocity is less affected by the lateral motion, while the average inner wall temperature decreases more as Prandtl number increases.[4] The lateral mass flow rate, as indicated by $\psi_{\max}$, increases as Rayleigh number increases and also increases slightly as Prandtl number increases. Note that ψ is scaled with respect to αr_i^{-2}.

Figure 9 shows the flow regimes found for R = 1.25. The boundaries are drawn by interpolation and are intended to be approximations. Due to the rather small radii ratio, the lateral buoyancy-driven motion is insignificant for Ra < 10^4. The single-cell structure persists for nearly two orders of magnitude of Ra and is followed by the double-cell regime that spans nearly three orders of magnitude. For all the transitions, as the Prandtl number increases, the transition Rayleigh number also increases. Due to the assumption of a fully developed field, no description can be made of the regime that follows the double-cell regime.

5 Summary

The effects of buoyancy-driven lateral convection on forced convection between horizontal concentric cylinders, where the

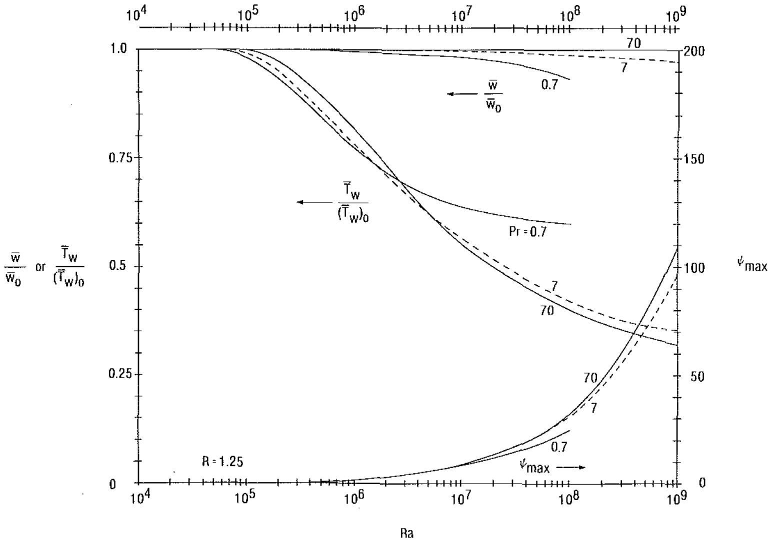

Fig. 8 Variations in the normalized average longitudinal velocity, the normalized average inner surface temperature, and maximum value of the stream function with respect to Rayleigh number for various Prandtl numbers

---

[3] Note that T is normalized with respect to q.

[4] Note that Ra is proportional to $(\nu\alpha)^{-1}$. Therefore, in order to keep Ra and q the same while increasing Pr, the viscosity must change in proportion to $\mathrm{Pr}^{1/2}$.

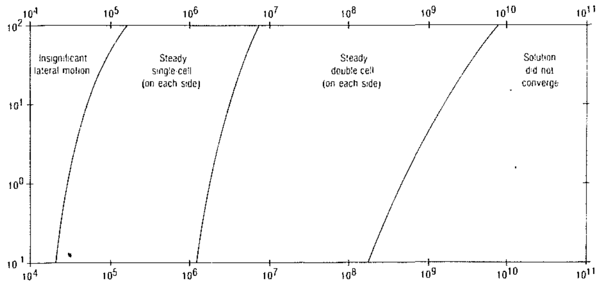

Fig. 9 Flow regime diagram for $R = 1.25$

inner cylinder is heated at a constant and prescribed heat flux and the outer cylinder is adiabatic, are considered. Although two restrictive assumptions of Boussinesq fluid and longitudinally fully developed fields are made, the results obtained should adequately describe the general characteristics of these flows. The solutions are found by finite difference approximations and validation is made only for $\mathrm{Ra} = 0$, for which the results are available in the literature.

While the average inner surface temperature decreases as the Rayleigh number based on heat flux increases, the maximum temperature on this surface first increases with Rayleigh number and then decreases. This occurs when the transition from a single-cell (on each side) regime to a double-cell regime takes place. The average inner surface temperature and the maximum temperature at this surface both decrease as the Prandtl number increases. The flow regimes, namely the regimes of (*i*) insignificant lateral motion, (*ii*) single-cell, and (*iii*) double-cell, are separated by transition Rayleigh numbers with an order of magnitude (for $\mathrm{Pr} = 0.7$) of 10^4 and 10^6, while the last regime appears to extend up to 10^8 with these values increasing with Prandtl number.

6 Acknowledgments

This work was performed while the author was at the Department of Mechanical Engineering of the University of Wisconsin – Milwaukee. The support of the General Electric Company – Medical Systems Group, through Grant #133G395, is greatly appreciated, as is that of the State of Wisconsin Department of Development.

References

1 Yao, L. S., Catton, I., and McDonough, J. M., "Buoyancy-Driven Asymmetric Water Boundary Layer Along a Heated Cylinder," *J. Fluid Mech.*, Vol. 98, 1980, pp. 417–434.

2 Prusa, J., and Yao, L. S., "Numerical Solution for Fully Developed Flow in Heated Curved Tubes," *J. Fluid Mech.*, Vol. 123, 1982, pp. 503–522.

3 Yao, L. S., "Entry Flow in a Heated Straight Tube," *J. Fluid Mech.*, Vol. 88, 1978, pp. 465–483.

4 Hishida, M., Nagano, Y., and Motesclaros, M. S., "Combined Forced and Free Convection in the Entrance Region of an Isothermally Heated Horizontal Pipe," ASME JOURNAL OF HEAT TRANSFER, Vol. 104, 1982, pp. 153–159.

5 Patankar, S. V., Ramadhyani, S., and Sparrow, E. M., "Effect of Circumferentially Nonuniform Heating on Laminar Combined Convection in a Horizontal Tube," ASME JOURNAL OF HEAT TRANSFER, Vol. 100, 1978, pp. 63–70.

6 Kuehn, T. H., and Goldstein, R. J., "Correlating Equations for Natural Convection Heat Transfer Between Horizontal Circular Cylinders," *Int. J. Heat Mass Transfer*, Vol. 19, 1976, pp. 1127–1134.

7 Ingham, D. B., "Heat Transfer by Natural Convection Between Spheres and Cylinders," *Numerical Heat Transfer*, Vol. 4, 1981, pp. 53–67.

8 Projahn, V., Rieger, H., and Beer, H., "Numerical Analysis of Laminar Natural Convection Between Concentric and Eccentric Cylinders," *Numerical Heat Transfer*, Vol. 4, 1981, pp. 131–146.

9 Tsai, Y. T., and Tremblay, B., "On Transient Natural Convection Heat Transfer in the Annulus Between Concentric Horizontal Cylinders With Isothermal Surfaces," *Int. J. Heat Mass Transfer*, Vol. 27, 1984, pp. 103–111.

10 Heaton, H. S., Reynolds, W. C., and Kays, W. M., "Heat Transfer in Annular Passages Simultaneous Development of Velocity and Temperature Fields in Laminar Flow," *Int. J. Heat Mass Transfer*, Vol. 7, 1964, pp. 763–781.

11 Kays, W. M., and Crawford, M. E., *Convective Heat and Mass Transfer*, 2nd ed., McGraw-Hill, 1980, pp. 98–101.

12 Hattori, N., "Combined Free and Forced Convection Heat Transfer for Fully Developed Laminar Flow in Horizontal Concentric Annuli (Numerical Analysis)" (in Japanese), *JSME Transactions*, Vol. 45, 1979, pp. 227–240.

13 Mojtabi, A., and Caltagirone, J. P., "Analyse du Transfert de Chaleur en Convection Mixte Laminaire Entre Deux Cylindres Coaxiaux Horizontaux," *Int. J. Heat Mass Transfer*, Vol. 23, 1980, pp. 1369–1375.

14 Nguyen, T. H., Vasseur, P., Robillard, L., and Chandrasekhar, B., "Combined Free and Forced Convection of Water Between Horizontal Concentric Cylinders," ASME JOURNAL OF HEAT TRANSFER, Vol. 105, 1983, pp. 498–504.

15 Torrance, K. E., "Comparison of Finite-Difference Computations of Natural Convection," *Journal of Research of the National Bureau of Standard – B. Mathematical Sciences*, Vol. 72B, 1968, pp. 281–301.

16 de Vahl Davis, G., and Jones, F. P., "Natural Convection in Square Cavity. A Comparison Exercise," *Proceedings of the Second International Conference in Numerical Methods in Thermal Problems*, Lewis, Morgan and Schnefler, eds., Venice, Italy, July 7–10, 1981.

17 Kaviany, M., "Effect of a Protuberance on Thermal Convection in a Square Cavity," ASME JOURNAL OF HEAT TRANSFER, Vol. 106, 1984, pp. 830–834.

18 Churchill, J. W., Chao, P., and Ozoe, H., "Extrapolation of Finite-Difference Calculation of Laminar Natural Convection in Enclosures to Zero Grid Size," *Numerical Heat Transfer*, Vol. 4, 1981, pp. 39–51.

Fue-Sang Lien
Graduate Student.

Cha'o-Kuang Chen
Professor.
Department of Mechanical Engineering,
National Cheng Kung University,
Tainan, Taiwan, Republic of China

J. W. Cleaver
Senior Lecturer,
Department of Mechanical Engineering,
The University of Liverpool,
Liverpool, England, United Kingdom

Mixed and Free Convection Over a Rotating Sphere With Blowing and Suction

An analysis is performed to study the flow and heat transfer characteristics for the case of laminar mixed convection and pure free convection about a rotating permeable sphere. The transformed conservation equations of the nonsimilar boundary layers are solved by an efficient finite difference method. It is found from the numerical results that both the local friction factor and the local Nusselt number increase with increasing rotation parameter and buoyancy force for aiding flow. The agreement of solutions obtained by the present method with others is found to be good.

Introduction

By spinning a vertical axisymmetric body in a mixed convective flow, the fluid near the surface of the spinning body is forced outward in the radial direction due to the action of centrifugal force. This fluid is then replaced by fluid moving in the axial direction and, therefore, the axial velocity of a fluid in the neighborhood of a spinning body has a higher value as compared to that of a nonspinning body. This increase in axial velocity enhances the convective heat transfer rate between the body and the fluid.

The application of the abovementioned idea in order to develop rotating systems for enhancing the heat transfer rate is important in the analysis of the rotary machine design. The *flow field in the vicinity of a rotating sphere in a uniform flow* stream has been investigated by Hoskin [1]. Siekmann [2] utilized Hoskin's results for the flow field to analyze the thermal boundary layer for a similar problem. Both of these authors used the Blasius series technique to solve their governing boundary layer problem. Chao and Greif [3] used a quadratic velocity profile assumption to investigate the laminar forced convection heat transfer over rotating bodies with uniform and nonuniform surface temperature. In general, their solution is very accurate for moderate or high Prandtl numbers and for small values of the rotating parameter. In order to avoid the difficulties encountered by the previous methods, Lee et al. [4] have analyzed the momentum and heat transfer rates through laminar boundary layers over rotating isothermal bodies with revolution of fairly arbitrary shape by employing Merk's series expansion technique.

The flow field in the vicinity of a fixed sphere for pure free convection with various surface thermal conditions has been investigated by Chiang et al. [5].

The problem of mixed forced and free convection about a sphere has received relatively little attention. To the best knowledge of the authors, the only such studies which have been reported are the experimental work of Yuge [6] and Klyachko [7] and the analytical work of Hieber and Gebhart [8] and Chen and Mucoglu [9]. These studies, both experimental and analytical, were carried out only for a stationary sphere without mass transfer.

The present study treats mixed and pure free convective heat transfer around a vertical rotating sphere with blowing and suction. In the analysis, the conservation equations of the boundary layers are transformed such that they can lend themselves to either local nonsimilarity or finite-difference solutions. In the present study, an efficient and very accurate finite-difference method due to Cebeci and Bradshaw [10] is employed to solve the system of transformed equations.

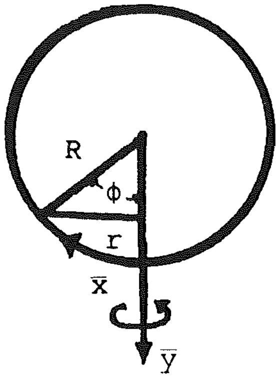

Fig. 1 Coordinate system

Numerical investigations for a rotating sphere were carried out for the case of uniform surface temperature and the case of uniform heat flux. Both of the cases were calculated for various values of the rotation parameter B, the mass transfer parameter B_p (or v_w), the buoyancy parameter Ω (or $\hat{\Omega}$) and the Prandtl number Pr.

Analysis

The steady, laminar, nondissipative, constant-property, incompressible boundary layer flow around a rotating sphere placed in a uniform stream is considered. The axis of rotation of the body is parallel to the free-stream velocity $\bar{u}_\infty$. We choose nonrotating coordinates $\bar{x}$ and $\bar{y}$, with $\bar{x}$ representing the distance measured along a meridian curve from the lower stagnation point and $\bar{y}$ being measured normal to the surface of the rotating body. The quantity $r(x)$ is the radius of the sphere at point $\bar{x}$, $\bar{u}$ and $\bar{v}$ are the $\bar{x}$ and $\bar{y}$ components of the velocity, respectively, and $\bar{\omega}$ is the transverse velocity component due to spin of the sphere. The convective forced flow is assumed to be moving upward, while the gravity $\hat{g}$ acts downward in the opposite direction. The surface of the sphere is maintained at a uniform temperature T_w or a uniform heat flux q_w.

In the analysis, we only consider the boundary condition of heated surface, without loss of generality, for the rotating sphere. The coordinate system is shown in Fig. 1. Under the assumption of Boussinesq approximation, the boundary layer equations are:

Contributed by the Heat Transfer Division for publication in the JOURNAL OF HEAT TRANSFER. Manuscript received by the Heat Transfer Division October 15, 1984.

Continuity:

$$\frac{\partial}{\partial x}(r\bar{u})+\frac{\partial}{\partial y}(r\bar{v})=0 \tag{1}$$

Momentum:

$$\bar{u}\frac{\partial \bar{u}}{\partial \bar{x}}+\bar{v}\frac{\partial \bar{u}}{\partial \bar{y}}-\frac{\bar{\omega}^2}{r}\frac{dr}{d\bar{x}}$$

$$=U_e\frac{dU_e}{d\bar{x}}+\nu\frac{\partial^2 \bar{u}}{\partial \bar{y}^2}+\hat{g}\hat{\beta}(T-T_\infty)\sin \bar{x}/R \tag{2}$$

$$\bar{u}\frac{\partial \bar{\omega}}{\partial \bar{x}}+\bar{v}\frac{\partial \bar{\omega}}{\partial \bar{y}}+\frac{\bar{u}\bar{\omega}}{r}\frac{dr}{d\bar{x}}=\nu\frac{\partial^2 \bar{\omega}}{\partial \bar{y}^2} \tag{3}$$

Energy:

$$\bar{u}\frac{\partial T}{\partial \bar{x}}+\bar{v}\frac{\partial T}{\partial \bar{y}}=\alpha\frac{\partial^2 T}{\partial \bar{y}^2} \tag{4}$$

with the boundary conditions

$$\left.\begin{array}{l}\bar{u}=0,\ \bar{v}=\bar{v}_w,\ \bar{\omega}=r\Omega,\quad T=T_w\\ \qquad\qquad\text{or } -k\dfrac{\partial T}{\partial \bar{y}}=q_w\end{array}\right\}\ \text{for } \bar{y}=0 \tag{5a}$$

$$\bar{u}=U_e,\ \bar{\omega}=0,\ T=T_\infty \qquad \text{for } \bar{y}\to\infty \tag{5b}$$

where U_e is the velocity of the mainstream at the edge of the boundary layer and Ω is the angular velocity of the rotating sphere which is assumed to be constant.

Case 1 Mixed Convection Case With Uniform Surface Thermal Conditions ($U_e \neq 0$). The pseudo-similarity variables (ξ, η) are defined as

$$\xi=\int_0^x \frac{U_e(\bar{x})}{\bar{u}_\infty}\left(\frac{r}{R}\right)^2\frac{d\bar{x}}{R} \tag{6}$$

$$\eta=\left(\frac{\mathrm{Re}_R}{2\xi}\right)^{1/2}\left(\frac{U_e}{\bar{u}_\infty}\right)\left(\frac{r}{R}\right)\frac{\bar{y}}{R} \tag{7}$$

where R is the radius of the sphere and Re_R is the Reynolds number, $\mathrm{Re}_R=\bar{u}_\infty R/\nu$.

The dimensionless stream function $f(\xi, \eta)$, the dimensionless angular velocity function $g(\xi, \eta)$ and the dimensionless temperature of fluid $\theta(\xi, \eta)$ are defined by

$$f(\xi,\eta) = \left[\psi(x, y)+\int_0^x \frac{r}{R}\bar{v}_w dx\right]/\bar{u}_\infty R(2\xi/\mathrm{Re}_R)^{1/2} \tag{8}$$

$$g(\xi, \eta) = \bar{\omega}(x,y)/r\Omega \tag{9}$$

$$\theta(\xi, \eta) = (T-T_\infty)/\Delta\theta \tag{10}$$

where $\Delta\theta=T_w-T_\infty$, for isothermal surface (iso); $\Delta\theta=q_wR/(k\mathrm{Re}_R{}^{1/2})$, for constant-heat-flux surface (chf); and the stream function $\psi(x, y)$ satisfies the continuity equation (1) with

$$\bar{u}=\frac{R}{r}\frac{\partial\psi}{\partial\bar{y}},\ \bar{v}=-\frac{R}{r}\frac{\partial\psi}{\partial\bar{x}} \tag{11}$$

Substituting (6)–(11) into (2)–(4), the transformed governing equations and boundary conditions become

$$f'''+ff''+\Lambda(1-(f')^2)+\frac{2\xi}{r}\frac{dr}{d\xi}\left(\frac{r^2\Omega^2}{U_e{}^2}\right)g^2-\hat{\alpha}(\xi)f''$$

$$+\left(\frac{2\xi\bar{u}_\infty\hat{g}\hat{\beta}\Delta\theta R^3\sin x/R}{U_e{}^3r^2}\right)\theta=2\xi\left(f'\frac{\partial f'}{\partial\xi}-f''\frac{\partial f}{\partial\xi}\right) \tag{12}$$

$$g''+fg'-fg'\left(\frac{4\xi}{r}\right)\frac{dr}{d\xi}-\hat{\alpha}(\xi)g'=2\xi\left(f'\frac{\partial g}{\partial\xi}-g'\frac{\partial f}{\partial\xi}\right) \tag{13}$$

$$\mathrm{Pr}^{-1}\theta''+f\theta'-\hat{\alpha}(\xi)\theta'=2\xi\left(f'\frac{\partial\theta}{\partial\xi}-\theta'\frac{\partial f}{\partial\xi}\right) \tag{14}$$

with the boundary conditions

$$\left.\begin{array}{lll}f=f'=0, & g=1, & \theta = 1\ (\text{iso})\\ & \text{or} & \theta' = -\sqrt{2\xi}/(rU_e/Ru_\infty)\ (\text{chf})\end{array}\right\}\ \text{at } \eta=0$$

$$f'=1,\quad g=0,\quad \theta = 0 \qquad \text{as } \eta\to\infty \tag{15}$$

where

$$\hat{\alpha}(\xi)=\frac{\bar{v}_wR}{U_er}\sqrt{2\xi}\mathrm{Re}_R{}^{1/2}$$

For a spherical body, it is known from the potential flow theory that $U_e/\bar{u}_\infty=1.5\sin\bar{x}/R$ and from the geometry, $r/R=\sin\bar{x}/R$. So we may find

$$\frac{r^2\Omega^2}{U_e{}^2}\frac{2\xi}{r}\frac{dr}{d\xi}=\frac{4}{9}\left(\frac{R\Omega}{\bar{u}_\infty}\right)^2\Lambda=B\Lambda \tag{16}$$

$$\frac{4\xi}{r}\frac{dr}{d\xi}=2\Lambda \tag{17}$$

$$\hat{\alpha}(\xi)=B_p\frac{\sqrt{2\xi}}{1.5\sin^2\beta} \tag{18}$$

$$\frac{2\xi\bar{u}_\infty\hat{g}\hat{\beta}\Delta\theta R^3\sin\bar{x}/R}{U_e{}^3r^2}=\begin{cases}0.5926\ \Omega\xi/\sin^4\beta\ (\text{iso})\\ 0.5926\ \bar{\Omega}\xi/\sin^4\beta\ (\text{chf})\end{cases} \tag{19}$$

where

$$\xi = 1-1.5\cos\beta+0.5\cos^3\beta \tag{20a}$$

$$\Lambda = \frac{4\cos\beta-6\cos^2\beta+2\cos^4\beta}{3\sin^4\beta} \tag{20b}$$

$$B_p = \frac{\bar{v}_w\mathrm{Re}_R{}^{1/2}}{\bar{u}_\infty} \tag{20c}$$

$$\left.\begin{array}{rl}\Omega = & \mathrm{Gr}_R/\mathrm{Re}_R{}^2\ (\text{iso})\\ \text{or}\quad \bar{\Omega} = & \bar{\mathrm{G}}\mathrm{r}_R/\mathrm{Re}_R{}^{5/2}\ (\text{chf})\end{array}\right\} \tag{20d}$$

in which the Grashof numbers Gr_R, $\bar{\mathrm{G}}\mathrm{r}_R$, and β are defined as follows

$$\left.\begin{array}{l}\mathrm{Gr}_R = \dfrac{\hat{g}\hat{\beta}(T_w-T_\infty)R^3}{\nu^2}\ (\text{iso})\\[2ex] \overline{\mathrm{Gr}}_R = \dfrac{\hat{g}\hat{\beta}R^4q_w}{\nu^2k}\ (\text{chf})\end{array}\right\} \tag{21a}$$

$$\beta = \bar{x}/R \tag{21b}$$

The physical quantities of interest are the local friction factor C_f and the local Nusselt number Nu which are expressed as follows

$$\tfrac{1}{2}C_f\mathrm{Re}_R{}^{1/2} = 2.25\sin^3\beta(2\xi)^{-1/2}f''(\xi,0) \tag{22}$$

$$\mathrm{NuRe}_R{}^{-1/2} = 1.5\sin^2\beta(2\xi)^{-1/2}\theta'(\xi,0)\ (\text{iso}) \tag{23a}$$

$$\mathrm{NuRe}_R{}^{-1/2} = 1/\theta(\xi,0)\ (\text{chf}) \tag{23b}$$

Case 2 Pure Free Convection Case With Nonuniform Surface Thermal Conditions ($U_e=0$). To transform equations (1)–(5) into dimensionless form, we introduce the dimensionless variables as follows: for the prescribed surface-temperature case

$$x=\bar{x}/R,\ y=\bar{y}\ \mathrm{Gr}^{1/4}/R,\ u=\bar{u}/\left(\frac{\nu}{R}\right)\mathrm{Gr}^{1/2},\ \omega=\bar{\omega}/\left(\frac{\nu}{R}\right)\mathrm{Gr}^{1/2},$$

$$v=\bar{v}/\left(\frac{\nu}{R}\right)\mathrm{Gr}^{1/4},\ \theta=(T-T_\infty)/(T_{w0}-T_\infty)F(\bar{x}) \tag{24}$$

where T_{w0} is the temperature of the stagnation point, $F(\bar{x})$ is the dimensionless surface temperature function, $F(\bar{x})=(T_w(\bar{x})-T_\infty)/(T_{w0}-T_\infty)$, and Gr is the Grashof number, $\mathrm{Gr}=\hat{g}\hat{\beta}(T_{w0}-T_\infty)R^3/\nu^2$.

For the prescribed surface-heat-flux case

$$x=\bar{x}/R,\ y=\bar{y}\overline{\mathrm{Gr}}^{1/5}/R,\ u=\bar{u}/\left(\frac{\nu}{R}\right)\overline{\mathrm{Gr}}^{2/5},\ \omega=\bar{\omega}/\left(\frac{\nu}{R}\right)\overline{\mathrm{Gr}}^{2/5},$$

$$v=\bar{v}/\left(\frac{\nu}{R}\right)\mathrm{Gr}^{1/5},\ \theta=\overline{\mathrm{Gr}}^{1/5}k(T-T_\infty)/q_{w0}RF(\bar{x}) \tag{25}$$

where q_{w0} is the heat flux of the stagnation point, $F(\bar{x})$ is the dimensionless surface heat flux function, $F(\bar{x})=q_w(\bar{x})/q_{w0}$, and $\overline{\mathrm{Gr}}$ is the Grashof number, $\overline{\mathrm{Gr}}=\hat{g}\hat{\beta}q_{w0}R^4/\nu^2k$. Substituting equation (24) or equation (25) into equations (1)–(5) and recasting into dimensionless form

$$\frac{\partial}{\partial x}(ru)+\frac{\partial}{\partial y}(rv)=0 \tag{26}$$

$$u\frac{\partial u}{\partial x}+v\frac{\partial u}{\partial y}-\frac{\omega^2\cos(x)}{\sin(x)}=F(x)\theta\sin(x)+\frac{\partial^2 u}{\partial y^2} \tag{27}$$

$$u\frac{\partial\omega}{\partial x}+v\frac{\partial\omega}{\partial y}+\frac{u\omega\cos(x)}{\sin(x)}=\frac{\partial^2\omega}{\partial y^2} \tag{28}$$

$$u\frac{\partial\theta}{\partial x}+v\frac{\partial\theta}{\partial y}+\frac{u\theta}{F(x)}\frac{dF(x)}{dx}=\mathrm{Pr}^{-1}\frac{\partial^2\theta}{\partial y^2} \tag{29}$$

$$\left.\begin{array}{l}u=0,\ v=v_w,\quad \omega=r\Omega/\left(\frac{\nu}{R}\right)\mathrm{Gr}^{1/2},\quad \theta=1\ (*)\\ \qquad\text{or}\quad \omega=r\Omega/\left(\frac{\nu}{R}\right)\bar{\mathrm{G}}\mathrm{r}^{5/2},\quad \frac{\partial\theta}{\partial y}=-1\ (**)\end{array}\right\}\ \text{at } y=0$$

$$u=0,\ T=T_\infty,\ \omega=0,\qquad \text{as } y\to\infty \tag{30}$$

(* = prescribed surface temperature; ** = prescribed surface heat flux). Equations (26)–(30) do not admit similarity solutions; we introduce the other pseudo-similarity variables (ξ,η)

$$\xi=\int_0^x F(x)\,dx \tag{31}$$

$$\eta=yF(x)^{1/2} \tag{32}$$

and the dimensionless stream function $f(\xi,\eta)$

$$\psi=-\frac{1}{r}\int_0^x rv_w(x)\,dx+f(\xi,\eta)\xi/F(x)^{1/2} \tag{33}$$

where the stream function $\psi(x,y)$ satisfies the continuity equation with

$$ru=\partial r\psi/\partial y\qquad rv=-\partial r\psi/\partial x \tag{34}$$

We also defined a dimensionless rotating velocity function $g(\xi,\eta)$ by

$$\omega(x,y)=\sin(x)\,B^{1/2}g(\xi,\eta) \tag{35a}$$

where

$$B^{1/2}=R^2\Omega/\mathrm{Gr}^{1/2}\nu\ (*) \tag{35b}$$

or

$$B^{1/2}=R^2\Omega/\overline{\mathrm{Gr}}^{2/5}\nu\ (**) \tag{35c}$$

By introducing equations (31)–(35) into equations (26)–(30), we obtain

$$f'''+ff''[1+\alpha1(x)-\alpha2(x)]-f''\alpha3(x)+B\alpha4(x)g^2$$
$$+\alpha5(x)\theta-(f')^2=\xi\left(f'\frac{\partial f'}{\partial\xi}-f''\frac{\partial f}{\partial\xi}\right) \tag{36}$$

$$g''+fg'[1+\alpha1(x)-\alpha2(x)]-2\alpha1(x)f'g-\alpha3(x)g'$$
$$=\xi\left(f'\frac{\partial g}{\partial\xi}-g'\frac{\partial f}{\partial\xi}\right) \tag{37}$$

$$\mathrm{Pr}^{-1}\theta''+f\theta'[1+\alpha1(x)-\alpha2(x)]-2\alpha2(x)f'\theta$$
$$-\alpha3(x)\theta'=\xi\left(f'\frac{\partial\theta}{\partial\xi}-\theta'\frac{\partial f}{\partial\xi}\right) \tag{38}$$

and

$$\left.\begin{array}{lr}f=f'=0,\ g=1,\quad \theta=1 & (*)\\ \qquad\text{or}\quad \theta'=-F(x)^{-1/2} & (**)\end{array}\right\}\ \text{at } \eta=0$$

$$f'=0,\ \theta=0,\ g=0\qquad \text{as } \eta\to\infty \tag{39}$$

where

$$\alpha1(x)=\cos(x)\xi/\sin(x)F(x) \tag{40a}$$

$$\alpha2(x)=\xi\frac{dF(x)}{dx}/2F(x)^2 \tag{40b}$$

$$\alpha3(x)=v_w(x)F(x)^{-1/2} \tag{40c}$$

$$\alpha4(x)=\sin(2x)/2\xi F(x) \tag{40d}$$

$$\alpha5(x)=\sin(x)/\xi \tag{40e}$$

In the foregoing equations, the primes stand for partial derivatives with respect to η. If $\alpha2(x)=\alpha3(x)=0$, equations (36)–(39) can be reduced to the case of uniform surface conditions and mass transfer. For comparison of our results with others, we take $F(x)=1$ for the special cases of uniform surface temperature and uniform surface heat flux to calculate the numerical solutions over a wide range of v_w and B at a Prandtl number of 0.7. The physical quantities of interest are the local friction factor C_f and local Nusselt number Nu. They can be expressed as follows. For the prescribed surface-temperature case

$$\mathrm{NuGr}^{-1/4}=-F(x)^{1/2}\theta'(\xi,0) \tag{41}$$

$$\tau_w/\rho\left(\frac{\nu}{R}\right)^2\mathrm{Gr}^{3/4}=\xi F(x)^{1/2}f''(\xi,0) \tag{42}$$

For the prescribed surface-heat-flux case

$$(T_w-T_\infty)\overline{\mathrm{Gr}}^{1/5}/(q_{w0}R/k)=F(x)\theta(\xi,0) \tag{43}$$

$$\tau_w/\rho\left(\frac{\nu}{R}\right)^2\overline{\mathrm{Gr}}^{3/5}=\xi F(x)^{1/2}f''(\xi,0) \tag{44}$$

Numerical Procedure

We use a two-point finite-difference method to solve the systems (11)–(14) and (36)–(39). This is a very efficient numerical method developed by Cebeci and Bradshaw [10].

According to this method, the transformed equations are first written in the form of a first-order system by introducing new unknown functions of η-derivatives. The functions and their derivatives in the first-order equations are then approximated by centered difference quotients and averaged at the midpoints of net rectangles in the (ξ,η) domain or net segments in the ξ and η coordinates, as required, to yield finite-difference equations with the order of $(\Delta\xi)^2$ and $(\Delta\eta)^2$. The resulting nonlinear difference equations, along with the corresponding expressions for the boundary conditions, are

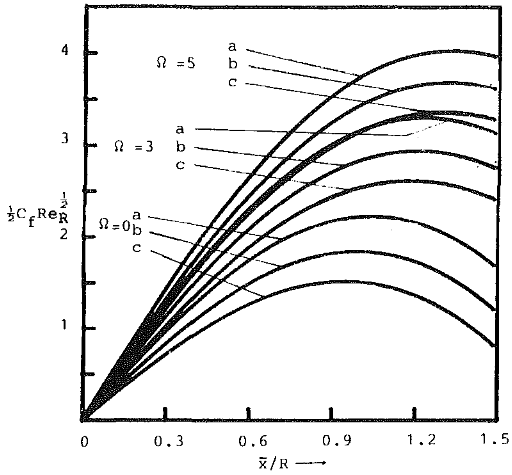

Fig. 2 Angular distributions of the local friction factor for an isothermal rotating sphere; Pr = 1; $B = 1$; (a) $B_p = -0.5$; (b) $B_p = 0$, (c) $B_p = 0.5$

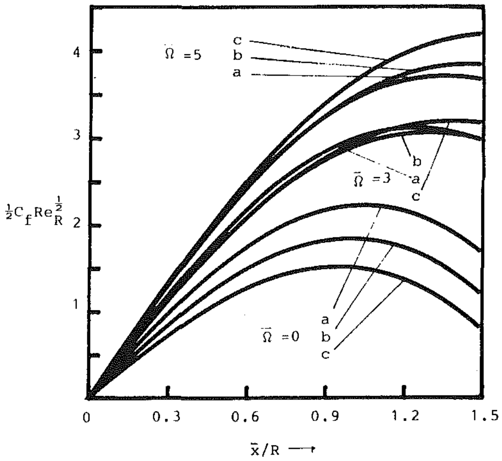

Fig. 3 Angular distributions of the local friction factor for a constant-heat-flux rotating sphere; Pr = 1; $B = 1$; (a) $B_p = -0.5$, (b) $B_p = 0$, (c) $B_p = 0.5$

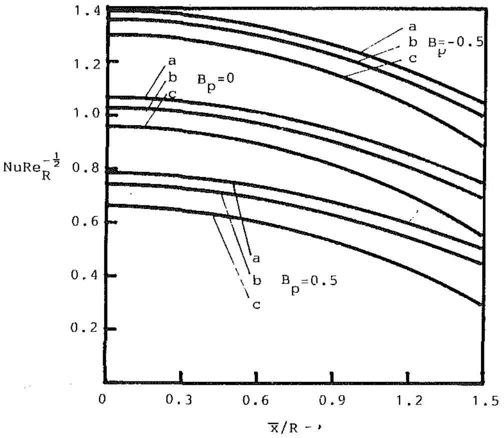

Fig. 4 Angular distributions of the local Nusselt number for an isothermal rotating sphere; Pr = 1; $B = 1$; (a) $\Omega = 5$, (b) $\Omega = 3$, (c) $\Omega = 0$

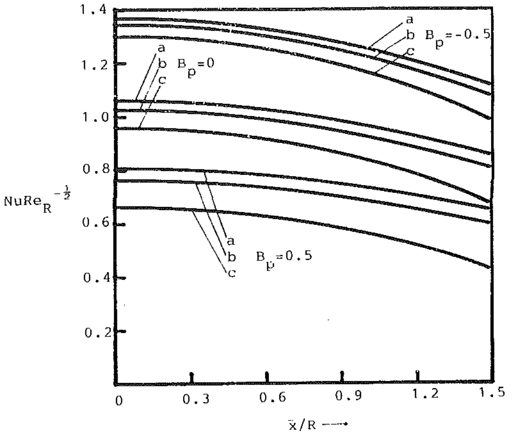

Fig. 5 Angular distributions of the local Nusselt number for a constant-heat-flux rotating sphere; Pr = 1; $B = 1$; (a) $\bar{\Omega} = 5$, (b) $\bar{\Omega} = 3$, (c) $\bar{\Omega} = 0$

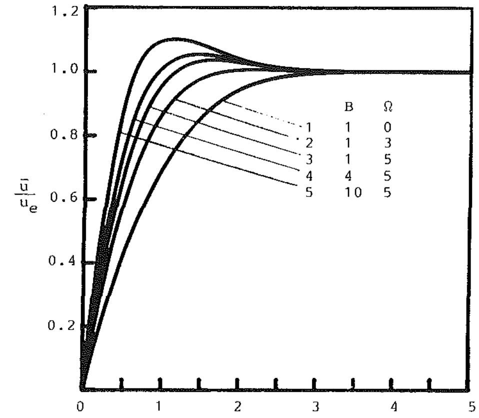

Fig. 6 Representative velocity profiles of an isothermal rotating sphere for Pr = 1, $B_p = 0$, and $\bar{x}/R = 0.951$

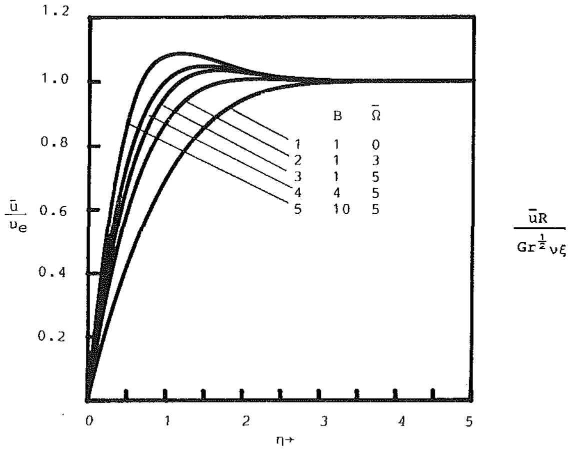

Fig. 7 Representative velocity profiles of a constant-heat-flux rotating sphere for Pr = 1, $B_p = 0$, and $\bar{x}/R = 0.951$

finally solved iteratively by using Newton's method. At $\xi = 0$, the transformed equations have only η-derivatives. We take the arbitrary velocity and temperature or heat-flux distributions which satisfy the boundary conditions to be used as initial iterative values.

The details of the solution method can be found in [10] and are omitted here. Most importantly, the scheme is simple and numerically stable and thus allows computations to be carried out extremely close to the flow separation point.

Results and Discussion

Numerical results were obtained for the cases of mixed and pure free convection over a heated rotating sphere. They cover the local friction factor, the local Nusselt number, and the velocity distributions for aiding flow. The buoyancy force parameter Ω (iso) and $\bar{\Omega}$ (chf) for mixed convection in the computations ranged from 0 to 5.

Table 1 Local friction $\frac{1}{2}C_f\mathrm{Re}_R^{1/2}$ for a rotating sphere with $\Omega = 0$ and $B_p = 0$

		$B=1$			$B=4$		
Λ	$\frac{x}{R}$	Lee [4]	Hoskin [1]	Present method	Lee [4]	Hoskin [1]	Present method
0.48	0.474	1.2496	1.2497	1.2499	1.8170	1.8170	1.8182
0.40	0.951	1.8403	1.8402	1.8400	2.6362	2.6359	2.6366
0.30	1.215	1.7207	1.7203	1.7185	2.4023	2.4031	2.3990
0.20	1.374	1.4780	1.4783	1.4732	1.9892	1.9953	1.9786
0.10	1.486	1.2269	1.2336	1.2173	1.5644	1.5876	1.5373

Table 2 Values of $\mathrm{NuRe}_R^{-1/2}$ for an isothermal rotating sphere with $\mathrm{Pr}=1$, $B_p=0$, and $\Omega=0$

		$B=1$			$B=4$		
Λ	$\frac{x}{R}$	Lee [4]	Chao [11]	Present method	Lee [4]	Chao [11]	Present method
0.5	0.	0.9588	0.9589	0.9586	1.0214	1.0214	1.0213
0.4	0.951	0.7998	0.7992	0.7993	0.8484	0.8485	0.8480
0.3	1.215	0.6961	0.7064	0.6966	0.7328	0.7362	0.7339
0.2	1.374	0.6171	0.6275	0.6195	0.6414	0.6528	0.6459
0.1	1.486	0.5510	0.5557	0.5559	0.5593	0.5868	0.5698

Table 3 Values of Nusselt number for a fixed sphere without blowing and suction

	$\mathrm{NuGr}^{-1/4}$		$(T_w - T_\infty)\bar{\mathrm{Gr}}^{1/5}/\left(\frac{q_{w0}R}{k}\right)$	
ϕ	*	**	*	**
0	0.4573	0.4576	1.8700	1.8691
10	0.4562	0.4565	1.8731	1.8715
20	0.4531	0.4534	1.8804	1.8790
30	0.4479	0.4482	1.8931	1.8913
40	0.4406	0.4410	1.9112	1.9087
50	0.4310	0.4316	1.9350	1.9309
60	0.4193	0.4209	1.9653	1.9582
70	0.4051	0.4068	2.0026	1.9904
80	0.3885	0.3912	2.0479	2.0275
90	0.3692	0.3736	2.1026	2.0696

* = present method for $B=0$, $v_w=0$, $\mathrm{Pr}=0.7$.
** = Chiang [5].

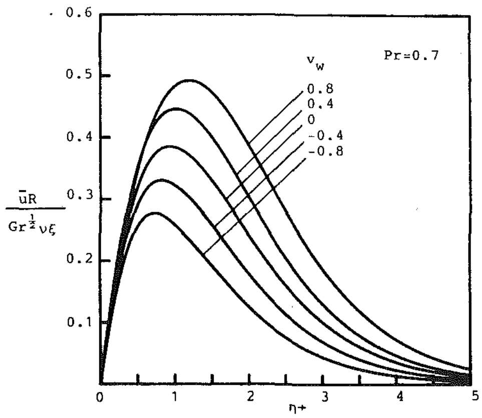

Fig. 8 Dimensionless x-direction velocity profiles for $B=1$, $\phi=30$ deg; uniform surface-temperature case

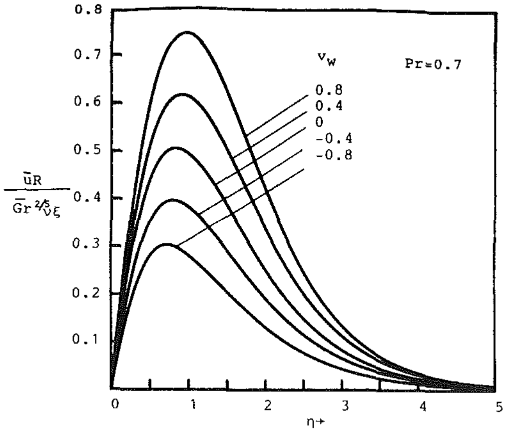

Fig. 9 Dimensionless x-direction velocity profiles for $B=1$, $\phi=30$ deg; uniform surface-heat-flux case

Mixed Forced and Free Convection Case. Figure 2 and 3 illustrate the angular distributions of the local friction factor $\frac{1}{2}C_f\mathrm{Re}_R^{1/2}$ for the cases of isothermal surface and constant-heat-flux surface with mass transfer. It can be seen from the two figures that the local friction factor increases with increasing buoyancy force parameter Ω (or $\bar{\Omega}$). From Fig. 2 we may find that the local friction factor increases with increasing suction and decreases with increasing blowing for the isothermal surface case. However, Fig. 3 shows that the local friction factor of the sphere with blowing is larger than that with suction for constant-heat-flux surface case and $\bar{\Omega}>0$. The phenomenon described above is strongly felt for larger buoyancy force for aiding flow, particularly at large angles away from the stagnation point. This is because the surface temperature of the sphere with blowing is higher than that with suction for large angular position, and the effect of

Table 4 Angular distributions of the local friction factor $\tau_w/\rho\left(\frac{\nu}{R}\right)^2 \mathrm{Gr}^{3/4}$ for an isothermal rotating sphere; $\mathrm{Pr}=0.7$

	$B=1$			$B=4$			$B=10$		
ϕ	$v_w=-0.8$	$v_w=0$	$v_w=0.8$	$v_w=-0.8$	$v_w=0$	$v_w=0.8$	$v_w=-0.8$	$v_w=0$	$v_w=0.8$
10	0.1808	0.1867	0.1741	0.3075	0.3246	0.3179	0.5267	0.5560	0.5555
30	0.5149	0.5304	0.4911	0.8493	0.8961	0.8731	1.4325	1.5141	1.5078
60	0.8630	0.8799	0.7907	1.2578	1.3201	1.2524	1.9708	2.0875	2.0421
90	0.9610	0.9472	0.7880	1.0185	1.0101	0.8465	1.1286	1.1302	0.9598

Table 5 Angular distributions of the local friction factor $\tau_w/\rho\left(\frac{\nu}{R}\right)^2 \bar{\mathrm{G}}\mathrm{r}^{3/5}$ for a constant-heat-flux rotating sphere; $\mathrm{Pr}=0.7$

	$B=1$			$B=4$			$B=10$		
ϕ	$V_w=-0.8$	$v_w=0$	$v_w=0.8$	$v_w=-0.8$	$v_w=0$	$v_w=0.8$	$v_w=-0.8$	$v_w=0$	$v_w=0.8$
10	0.1987	0.2560	0.3109	0.3181	0.3746	0.4218	0.5303	0.5881	0.6273
30	0.5706	0.7396	0.9005	0.8841	1.0503	1.1890	1.4465	1.6152	1.7295
60	0.9886	1.3046	1.5997	1.3498	1.6590	1.9157	2.0246	2.3288	2.5356
90	1.1700	1.5891	1.9586	1.2177	1.6106	1.9405	1.3070	1.6615	1.9288

Table 6 Angular distributions of the Nusselt number $\mathrm{NuGr}^{-1/4}$ for an isothermal rotating sphere; $\mathrm{Pr}=0.7$

	$B=1$			$B=4$			$B=10$		
ϕ	$v_w=-0.8$	$v_w=0$	$v_w=0.8$	$v_w=-0.8$	$v_w=0$	$v_w=0.8$	$v_w=-0.8$	$v_w=0$	$v_w=0.8$
0	0.8225	0.4869	0.2469	0.8756	0.5502	0.3100	0.9494	0.6324	0.3896
30	0.8091	0.4732	0.2354	0.8545	0.5294	0.2923	0.9201	0.6044	0.3656
60	0.7691	0.4326	0.2021	0.7913	0.4671	0.2403	0.8304	0.5190	0.2938
90	0.7025	0.3649	0.1490	0.6835	0.3575	0.1520	0.6591	0.3539	0.1608

Table 7 Angular distributions of the surface temperature $(T_w - T_\infty)\bar{\mathrm{G}}\mathrm{r}^{1/5}/(q_{w0}R/k)$ for a constant-heat-flux rotating sphere; $\mathrm{Pr}=0.7$

	$B=1$			$B=4$			$B=10$		
ϕ	$v_w=-0.8$	$v_w=0$	$v_w=0.8$	$v_w=-0.8$	$v_w=0$	$v_w=0.8$	$v_w=-0.8$	$v_w=0$	$v_w=0.8$
0	1.1922	1.8159	2.8182	1.1310	1.6898	2.5943	1.0507	1.5256	2.2910
30	1.2067	1.8438	2.8659	1.1515	1.7254	2.6516	1.0754	1.5660	2.3536
60	1.2516	1.9302	3.0123	1.2161	1.8381	2.8304	1.1572	1.6986	2.5558
90	1.3336	2.0919	3.2862	1.3394	2.0591	3.1793	1.3390	1.9949	2.9989

buoyancy force to the skin friction is stronger than that of mass transfer to the skin friction.

The angular distributions of the local Nusselt number $\mathrm{NuRe}_R^{-1/2}$ are shown in Figs. 4 and 5 with two different thermal boundary conditions. As shown in these figures, the local surface heat transfer rate increases as the buoyancy force increases for fixed mass transfer. Also, for given buoyancy force and mass transfer parameters, the local Nusselt number of Fig. 4 or 5 is seen to decrease with increasing angle from the stagnation point. Figures 4 and 5 also show that an increasing suction yields an increase in the local Nusselt number $\mathrm{NuRe}_R^{-1/2}$, but increasing blowing yields a decrease in $\mathrm{NuRe}_R^{-1/2}$.

To illustrate how the buoyancy force and the centrifugal force affect the velocity field in the boundary layer, representative velocity profiles at $x/R=0.951$ for several buoyancy parameters and rotation parameters are shown in Figs. 6–7 for both isothermal and constant-heat-flux surface conditions. It is noted that in the figures the dimensionless coordinate η is used as the boundary-layer thickness. It is evident from Figs. 6 and 7 that for aiding flow the velocity gradient at the wall increases as the buoyancy force increases, with an accompanying increase in the velocity near the wall region and an overshooting of the velocity beyond its local free-stream value.

For comparison of our skin friction and heat transfer results, Hoskin's [1], Siekmann's [2], Chao's [11] and Lee's [4] results were used. The results are included in Tables 1 and 2 and show excellent agreement with our results.

Pure Free Convection Case. To illustrate the accuracy of the solutions by the present method, the local heat transfer results of Nusselt number and surface temperature from the present implicit finite-difference technique and the series expansion method [5] are compared in Table 3. It is seen from the table that the results of this paper are in good agreement with [5]. The largest deviation between the two methods is at large angular positions.

The effects of the angular velocity and mass transfer on the local friction factor for prescribed surface conditions are shown in Tables 4 and 5. For both the uniform surface-temperature case and the uniform surface-heat-flux case, the local friction factor increases with increasing value of B. It is seen from Table 5 that the local friction factor increases with increasing blowing and decreases with increasing suction for uniform surface-heat-flux case.

The heat transfer results for various values of B and v_w are brought together in Tables 6 and 7. For an isothermal surface, $\mathrm{NuGr}^{-1/4}$ increases with increasing suction and an increase in B, but decreases with increasing blowing and an increase in ϕ. For a constant-heat-flux surface, the local surface temperature $(T_w - T_\infty)\bar{\mathrm{G}}\mathrm{r}^{-1/5}/(q_{w0}R/k)$ increases with increasing blowing and an increase in ϕ, but decreases with increasing suction and an increase in B.

Representative x-direction velocity profiles at $\phi=30$ deg of a permeable sphere for various values of v_w are illustrated in Figs. 8 and 9 in which $\bar{u}R/\mathrm{Gr}^{1/2}\nu\xi$ and $\bar{u}R/\bar{\mathrm{G}}\mathrm{r}^{2/5}\nu\xi$ are plotted against η. It is seen from Figs. 8 and 9 that the x-direction velocity increases with increasing blowing, but decreases with increasing suction for a fixed value of B.

Conclusion

A numerical method is presented for calculating the heat transfer rate and skin friction from a rotating permeable sphere. Both the cases of mixed convective flow and pure free convective flow over the sphere are considered. A great advantage of the present method is that this scheme is very efficient, unconditionally stable, and easily modified for the cases of nonuniform thermal boundary conditions. From the results of the present analysis, it is found that the local friction factor and local Nusselt number results exhibit a strong dependence on the variation of the mass transfer rate and buoyancy force for various values of B and Pr, particularly at large angular positions away from the stagnation point.

References

1 Hoskin, N. E., "The Laminar Boundary Layer on a Rotating Sphere," in: *50 Jahre Grenzschichtforchung*, H. Gortler and W. Tollmien, eds., 1955, pp. 127-131.

2 Siekmann, J., "The Calculation of the Thermal Laminar Boundary on a Rotating Sphere," *Z. Angew. Math. Phys.*, Vol. 13, 1962, p. 468.

3 Chao, B. T., and Greif, R., "Laminar Forced Convection Over Rotating Bodies," ASME JOURNAL OF HEAT TRANSFER, Vol. 96, 1974, pp. 463-466.

4 Lee, M. H., Jeng, D. R., and Dewitt, K. J., "Laminar Boundary Layer Transfer Over Rotating Bodies in Forced Flow," ASME JOURNAL OF HEAT TRANSFER, Vol. 100, 1978, pp. 496-502.

5 Chiang, T., Ossin, A., and Tien, C. L., "Laminar Free Convection From a Sphere," ASME JOURNAL OF HEAT TRANSFER, Vol. 86, 1964, pp. 537-542.

6 Yuge, T., "Experiments on Heat Transfer From Spheres Including Combined Natural and Forced Convection," ASME JOURNAL OF HEAT TRANSFER, Vol. 82, 1960, pp. 214-220.

7 Klyachko, L. S., "Heat Transfer Between a Gas and a Spherical Surface With the Combined Action of Free and Forced Convection," ASME JOURNAL OF HEAT TRANSFER, Vol. 85, 1963, pp. 355-357.

8 Hieber, C. A., and Gebhart, B., "Mixed Convection From a Sphere at Small Reynolds and Grashof Numbers," *J. Fluid Mech.*, Vol. 38, 1969, pp. 137-159.

9 Chen, T. S., and Mucoglu, A., "Analysis of Mixed Forced and Free Convection About a Sphere," *Int. J. Heat Mass Transfer*, Vol. 20, 1977, pp. 867-875.

10 Cebeci, T., and Bradshaw, P., "Momentum Transfer in Boundary Layers," Hemisphere, Washington, D.C., 1977.

11 Chao, B. T., "An Analysis of Forced Convection Over Nonisothermal Surface via Universal Functions," *Recent Advances in Engineering Science—Proceedings of 14th Annual Meeting of the Society of Engineering Science,* Lehigh University, 1977, pp. 471-483.

ERRATA

Corrections to "Augmentation of Laminar Flow Heat Transfer by Means of Wire Coil Inserts," by S. B. Uttarwar and M. Raja Rao, published in the November 1985 issue of the ASME Journal of Heat Transfer, pp. 930–935.

Error	*Correction*
$\frac{A_a}{A_o}=\frac{hi_o}{hi_a}=\frac{\text{Nu}_o}{\text{Nu}_a}=2.(\text{Gz})^{1/3}(\mu_b/\mu_w)^{0.14}$ (17)	$\frac{A_a}{A_o}=\frac{hi_o}{hi_a}=\frac{\text{Nu}_o}{\text{Nu}_a}=\frac{2.(\text{Gz})^{1/3}(\mu_b/\mu_w)^{0.14}}{\text{Nu}_a}$ (17)
$\frac{16}{\text{Re}_o}\bullet\frac{\text{Re}_o^3 D_i}{f_a \text{Re}_a^3 D_e}=2(\text{Re}_o)^{1/3}\text{Pr}^{1/3}\left(\frac{\pi}{4}\right)^{1/3}\left(\frac{D_i}{L}\right)^{1/3}\frac{(\mu_b)^{0.14}}{\mu_w}$ (18)	$\frac{16}{\text{Re}_o}\bullet\frac{\text{Re}_o^3 D_i}{f_a \text{Re}_a^3 D_e}=\frac{2(\text{Re}_o)^{1/3}\text{Pr}^{1/3}\left(\frac{\pi}{4}\right)^{1/3}\left(\frac{D_i}{L}\right)^{1/3}}{\text{Nu}_a}\left(\frac{\mu_b}{\mu_w}\right)^{0.14}$ (18)

Use of a Cubic Equation to Predict Surface Tension and Spinodal Limits

P. O. Biney[1]

Wei-guo Dong[2]

J. H. Lienhard
Fellow ASME

Heat Transfer and Phase-Change Laboratory,
Mechanical Engineering Department,
University of Houston,
Houston, TX 77004

The very general Shamsundar-Murali cubic equation is used to interpolate p-v-T *data into the metastable and unstable regions. This yields a spinodal line that closely matches the homogeneous nucleation limit predicted by an improved kinetic theory. Only the pressure, the saturated liquid and vapor volumes, and the liquid compressibility at saturation, as well as one compressed liquid data point, are needed to use the cubic equation for the interpolation process. The equation also yields an accurate prediction of the temperature dependence of surface tension when it is substituted in van der Waals' surface tension formula. Thus, by capitalizing on the inherent relation among the* p-v-T *equation, the spinodal prediction, and the surface tension – all three – it is possible to obtain each with high accuracy and minimal experimental data.*

Introduction

Surface tension is intimately related to the metastable and unstable fluid states, and to the *p-v-T* equation that describes these states. The aim of this study is to use this interrelation to assist in the development of means for estimating and predicting both *p-v-T* and surface tension data. We therefore begin by reviewing the character of this relationship.

Surface Tension and the Equation of State. It was shown in 1894 by van der Waals [1] that the temperature dependence of surface tension could be predicted precisely by the expression

$$\frac{\sigma}{\sigma_0}=f(T_r)=\int_{v_{r_f}}^{v_{r_g}} \frac{1}{v_r^{5/2}}\left[p_{r,\mathrm{sat}}(v_r-v_{r_f})-\int_{v_{r_f}}^{v_r} p_r dv_r\right]^{1/2} dv_r \quad (1)$$

where σ is the surface tension; T_r, p_r, and v_r are the reduced[3] temperature, pressure, and volume; and where g and f denote saturated vapor and liquid values. The constant σ_0 is a reference value of the surface tension which van der Waals showed how to evaluate in terms of molecular properties. (No one to date has managed to make accurate evaluations of σ_0.)

Little has been done with equation (1) because its use requires a full knowledge of *p-v-T* information throughout the metastable and unstable fluid regimes (see Fig. 1). van der Waals used his own famous equation of state in equation (1) and – without the aid of a computer – succeeded in making an approximation valid only near the critical point:

$$\lim_{T_r\to 1}\sigma=\frac{16}{\sqrt{6}}\sigma_0(1-T_r)^{3/2} \quad (2)$$

Recent studies (see, e.g., [2]) of the variation of σ with T_r near the critical point suggest that

$$\lim_{T_r\to 1}\sigma\propto(1-T_r)^{1.28\text{ or }1.29} \quad (3)$$

gives a more plausible temperature dependence for real fluids than equation (2). It is also known that a form of equation (2) with an exponent of 11/9, or 1.22, represents a wide variety of fluids pretty well at lower temperatures.

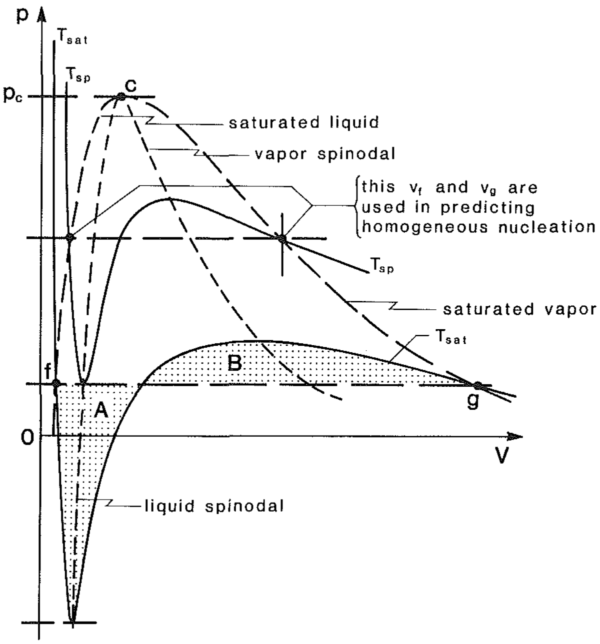

Fig. 1 Typical real-fluid isotherms

On Locating the Spinodal Line. A knowledge of the location of the liquid and/or vapor spinodal lines can be particularly helpful in the process of developing the *p-v-T* equation of state that is needed to complete the integration of equation (1). In 1981, Lienhard and Karimi [3] provided molecular arguments that showed that the liquid spinodal limit[4] could be predicted quite accurately by homogeneous nucleation theory. They also showed that this was not true for the vapor spinodal limit [3, 4]. Vapor spinodal lines lie nowhere near the limit of homogeneous nucleation for vapors.

In the course of their work, Lienhard and Karimi used the conventional homogeneous nucleation expression

$$j\,\frac{\text{nucleation events}}{\text{molecule collisions}}=e^{-\mathrm{Gb}} \quad (4)$$

---

[1] Present address: Mechanical Engineering Department, Prairie View A. and M. University, Prairie View, TX 77445.

[2] On leave from the Thermal Power Engineering Research Institute, Xi-an, People's Republic of China.

[3] A "reduced" property is one divided by its thermodynamic critical value.

[4] The spinodal limit is the locus of points at which $(\partial p/\partial v)_T$ is zero (see Fig. 1).

Contributed by the Heat Transfer Division and presented at the 23rd National Heat Transfer Conference, Denver, CO, August 1985. Manuscript received by the Heat Transfer Division November 8, 1984.

where[5]
$j \equiv$ probability of nucleating a bubble in a given collision (5)
and

$$\mathrm{Gb} \equiv Wk_{\mathrm{crit}}/(kT \text{ or } kT_c) \tag{6}$$

and (see e.g. [5])

$$Wk_{\mathrm{crit}} = \frac{16\pi\sigma^3}{3[p_{\mathrm{sat}}(T_{sp})-p]^2(1-v_f/v_g)^2} \tag{7}$$

Notice that in equation (6) we suggest that the Gibbs number Gb should be a ratio of the critical work required to form a nucleus to either kT or kT_c. The conventional nucleation theory is based on the average kinetic energy of the surrounding molecules, which is on the order of kT. However, it was noted in [3] that the energy required to separate molecules from one another is on the order of kT_c. This seemed to be an equally plausible candidate for the characteristic energy of the system.

When equations (4), (6), and (7) are combined, we obtain the following expression for the homogeneous nucleation pressure p corresponding with a given temperature T_{sp}

$$-\ln j = \frac{16\pi\sigma^3}{3(kT \text{ or } kT_c)[p_{\mathrm{sat}}(T_{sp})-p]^2(1-v_f/v_g)^2} \tag{8}$$

where v_f and v_g are to be evaluated at T_{sp}. Two issues remained: identifying the value of j that will give the spinodal limit, and deciding whether to use kT or kT_c.

Lienhard and Karimi next curve-fit cubic equations to the well-documented stable equilibrium states of water, constraining them to satisfy the "Gibbs-Maxwell" requirement that

$$\int_f^g v\,dp = 0 \tag{9}$$

which stipulates that the two regions between an isotherm and a horizontal line connecting f and g must be equal to one another in area (e.g., Area A in Fig. 1 equals area B). They chose the Himpan form [8] of cubic equation

$$p_r = \frac{A}{v_r-b} - \frac{a}{(v_r-c)(v_r+d)} \tag{10}$$

and evaluated all five constants using least squares fit. They re-evaluated the constants for each of many isotherms.

There were two weaknesses in this curve-fit procedure. The first is that equation (10) was not forced to fit the ideal gas law precisely at high temperatures. The second is that the Himpan form turns out to be slightly restrictive. We remedy these features subsequently.

Equation (10) with the five statistically fitted constants gave interpolated liquid spinodal pressures that showed some numerical data scatter. These pressures corresponded very closely to the homogeneous nucleation pressures given by equation (8) with $j = 10^{-5}$ and with kT_c used as the characteristic energy. The interpolations *did not* come close to equation (8) when the conventional energy kT was used. (The minimal value of $j = 10^{-5}$ was not purely empirical. Molecular arguments in [3] fixed it within an order of magnitude or so.)

It is important to note that when these arguments are applied to the vapor spinodal [3] they show that the limit of homogeneous nucleation of droplets is far from the vapor spinodal limit.

A New Form of Cubic Equation for Fitting p-v-T Data. Shamsundar and Murali [9, 10] have recently made effective use of the following general form of cubic equation in fitting individual isotherms

$$\frac{p}{p_{\mathrm{sat}}} = 1 - \frac{(v-v_f)(v-v_m)(v-v_g)}{(v+b)(v+c)(v+d)} \tag{11}$$

The quantities p_{sat}, v_f, v_m, v_g, b, c, and d all vary with temperature. This form has the advantage that it automatically satisfies critical point criteria, but it need not be tied to them. It is also prefactored to simplify fitting the constants.

Three of the coefficients in equation (11) are the known temperature-dependent properties: p_{sat}, v_f, and v_g. Thus the most straightforward use of the equation is one in which it is fit to one isotherm at a time.

Murali simplified equation (11) by setting $c = d$ and thereby reducing the number of unknown coefficients to three. These three coefficients were determined by imposing the following three conditions on the equation: the ideal gas limit at low pressures, the Gibbs-Maxwell condition, and the measured isothermal compressibility of saturated liquid. He thus evaluated the coefficients of the equation directly (rather than statistically) using very few data.

The condition under which equation (11) reduces to the ideal gas law, by the way, is

$$\frac{RT}{p_{\mathrm{sat}}} = b + c + d + v_f + v_m + v_g \tag{12}$$

This kind of temperature-by-temperature application of equation (11) yielded far higher accuracies [10] than any existing cubic equation, particularly in the liquid range. The equation also performs extremely well in the stable superheated vapor range. The key to this success is, of course, the fact that the coefficients do not have to obey any predetermined dependence on temperature.

An Illustrative Application of the Preceding Ideas. Information of the kind we have been describing can be used to expand existing knowledge. Karimi, for example, developed a new fundamental equation [11] for water, based in part on his interpolations. When this fundamental equation was used to generate p-v-T data for use in equation (1), the resulting values of σ/σ_0 lay within 4.3 percent of measured values over all but the lowest range of saturation temperatures. This was

---

[5] Actually, it is more common (see Skripov [5, 6] and Avedisian [7]) to use J instead of j. J is equal to j multiplied by the rate of molecular collisions per cubic centimeter. For water, J is about 10^{39} times j in these units.

Nomenclature

A, a, b, c, d = undetermined constants in the various cubic equations
Gb = Gibbs number (see equation (6))
j = nucleation probability, equation (5)
J = j expressed as a rate per unit volume
k = Boltzmann's constant
p = pressure
T = temperature
v, v_f, v_g = specific volume, saturated liquid volume, saturated vapor volume
v_m = v at the root of a cubic p-v-T equation between v_f and v_g
σ, σ_0 = surface tension, undetermined reference value of σ
ω = the Pitzer acentric factor, $-1-\log_{10}p_{r,\mathrm{sat}}$ $(T_r = 0.7)$

Superscripts and Subscripts

c = a property at the critical point
f, g = saturated liquid or vapor properties
r = a "reduced" property ($X_r \equiv X/X_c$)
sat = a property at a saturation condition
sp = a property at a spinodal point

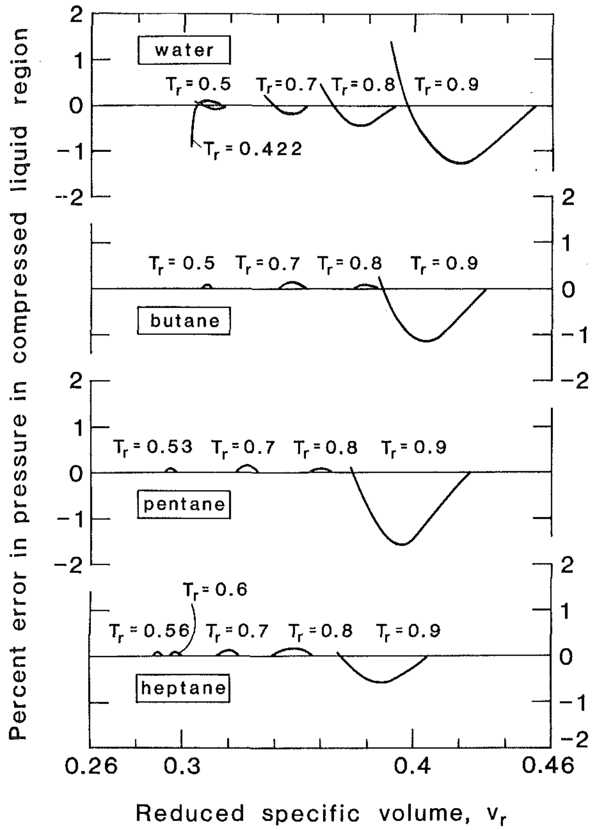

Fig. 2 Typical values of the error in pressure as predicted by cubic *p-v-T* equation curve-fitted to four data points

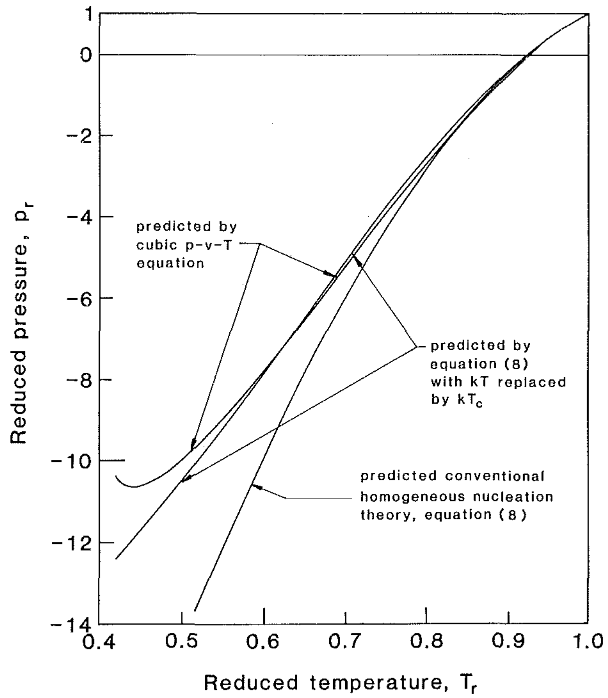

Fig. 3 Comparison of the spinodal limit of water as predicted by homogeneous nucleation theory and by the general cubic equation

the first and only such use of the van der Waals surface tension theory to verify *p-v-T* information, to our knowledge, and it displays the potential interaction of σ and *p-v-T* information.

Present Objectives. The availability of Shamsundar and Murali's new method for interpolating isotherms gives means for substantially improving upon the work in [3] and for reopening the two questions: (1) "Is kT_c a better characteristic energy than kT?" (2) "What minimum value of j gives the spinodal limit when it is used in equation (8)?"

We therefore address these matters using van der Waals' surface tension prediction as a hitherto little-used validity check.

Isothermal Curve Fits

We altered two of Murali's assumptions: We did not use the assumption that $c = d$. This increased the number of unknown coefficients by one, but stood to improve the accuracy of the resulting equation. The second alteration dealt with the restrictive form of the denominator of equation (11) $(v+b) \cdot (v+c)\ (v+d)$. In this form the equation is restrictive if b, c, and d are to be real. This implication was relaxed by writing the denominator in the form $(v+a)\ (v^2+fv+g)$ where $f=b+c$ and $g=bc$ [9]. This form allows b and c to be complex without using complex numbers explicitly.

To complete the curve fit we needed one more condition than Murali did since we chose not to set $c = d$. For this we selected a high-pressure liquid point. We identified the pressure that made the isotherm best fit the available data for stable liquid and vapor states by trying several pressures until we found the one that worked best. For water this pressure proved to be about 800 bars, or a reduced pressure of about 3.7, although substantially higher or lower values worked almost as well. Data from the IFC Formulation for Scientific Use [12] were used to do this.

When the four conditions were applied to the cubic equation (11) they yielded four nonlinear equations which we solved using the method of successive substitutions and linear interpolation.

We made sets of isothermal curve fits for water and for several straight-chain hydrocarbons. For the straight-chain hydrocarbons, we used the data of Starling [13] as curve-fitted by Reynolds [14], where we could. (However, in a few cases the Starling data for liquids disagreed with API data [15] or the data of Vargaftik [16].) These were the only substances for which we could readily obtain reliable *p-v-T* and surface tension data [15, 16, 17] over broad ranges of temperature. In all cases, the high-pressure *p-v-T* data point used in the curve fit was the value at $p_r = 5$.

We also looked at ammonia, argon, benzene, carbon dioxide, methane, hydrogen, oxygen, and nitrogen for which we did not have complete data over large ranges. In these cases curve fits were only made at one temperature each. The data sources for these cases were [16, 17, 18].

The fluids considered here resolve roughly into two classifications: those for which we are confident of the accuracy (water, oxygen, hydrogen, nitrogen, butane, heptane, pentane, and propane) and those for which we found some level of unresolvable disagreement in the relevant properties (ammonia, argon, benzene, carbon dioxide, ethane, hexane, methane, and octane). In the subsequent discussions we take care to base our conclusions only on the results obtained in the former fluids.

Figure 2 shows the resulting errors of the cubic interpolations for several typical fluids. These plots of error in the predicted pressure, at selected values of T_r in the liquid range, reflect a very severe test of the curve fits. They consistently show errors substantially less than one percent, at reduced temperatures below 0.9.

Liquid Spinodal Limits

Figure 3 compares the spinodal limit of water as predicted by our cubic equation with the predicted spinodal limit based on equation (8). The NBS surface tension recommendation [19] was used in this calculation. (The value of j used in Fig. 3

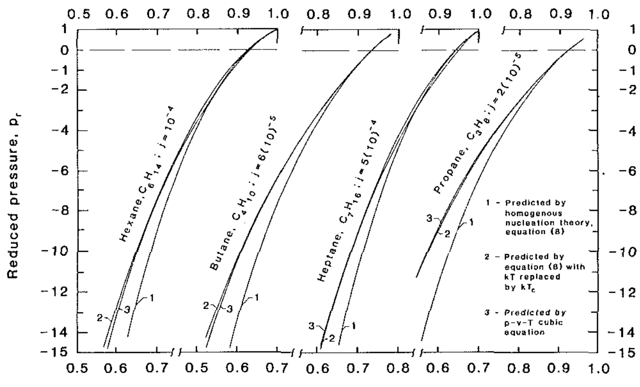

Fig. 4 Comparison of the spinodal limit of several fluids as predicted by homogeneous nucleation theory and by the general cubic equation

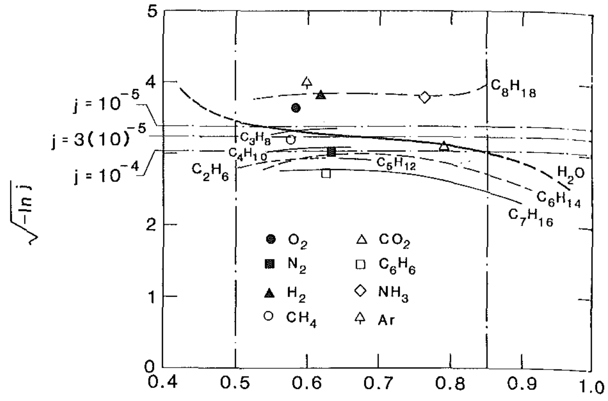

Fig. 5 Comparison of the values of $\sqrt{-\ln(j)}$ for which equations (8) and (11) agree exactly

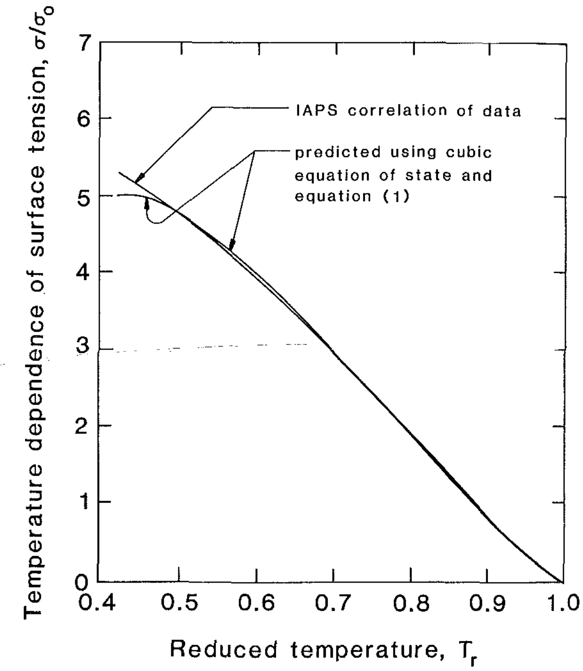

Fig. 6 Predicted and measured temperature dependence of the surface tension of water

was 2×10^{-5}. We return to the question of specifying j below.) The agreement is very good when kT_c is used in place of kT in the equation, except at such low temperatures and high liquid tensile stresses that both theories are being pushed to the edge of their limits of applicability. The choice between kT and kT_c makes little difference in the region of positive pressure, and this is the only region in which nucleation experiments have ever been made for large j. At lower pressures the two diverge very strongly.

Our suggestion that kT be replaced with kT_c is largely based on this kind of extrapolation. This kind of demonstration was made less conclusively (with the less flexible Himpan equation) in [3]. The present evidence is very compelling indeed.

Several other such comparisons are given in Fig. 4 for butane, heptane, hexane, and propane. (Since surface tension data were not available for butane and propane over the entire range of temperature, the missing values had to be filled in with the help of equation (1) in these cases.) In each case, we have used a limiting value of j that best fits the extrapolation. These j's do not all match the value of 2×10^{-5} used for water.

The four fluids selected for display in Fig. 4 were chosen because they embrace a wide range of j values. By the same token, the four fluids shown in Fig. 2 were selected because they typified the error of the many fluids that have been fitted.

The results of an inverse kind of calculation are shown in Fig. 5. Values of $\sqrt{-\ln(j)}$, which is inversely proportional to the pressure difference between saturation and the liquid spinodal line, were calculated at each point using equation (8), with kT_c, and the pressure difference predicted by equation (11).

Figure 5 strongly suggests that a "best value" of j for the spinodal limit – if one truly exists – is one slightly in excess of 10^{-5}, in preference to 10^{-5} which was previously suggested [3]. It is clear that these j limits are fairly sensitive to the accuracy of the data upon which they are based. Thus, in choosing the appropriate limiting value, one must be guided strongly by water and the other very well-documented fluids.

One must also consider whether or not these j values were obtained in regimes in which the cubic equation is truly very accurate. Figure 2 makes it clear that the general cubic equation interpolations begin to lose precision at very high temperatures – typically before $T_r = 0.9$. It also becomes apparent in the subsequent section that, although it interpolates stable properties very accurately at low temperatures, equation (11) probably fails to represent metastable and unstable properties with very high accuracy at low temperatures. This is evident in its failure to predict the temperature dependence of surface tension with high accuracy below $T_r \cong 0.5$.

We accordingly restrict the plots in Fig. 5 to the range $0.5 < T_r < 0.85$, or to a smaller range in which reliable data are available. Furthermore, we suggest that the middle temperature range in Fig. 5 is the most reliable. We have averaged the ordinate values of the more reliable data in Fig. 5, giving water double weight, to obtain the recommendation that

$$j_{\text{spinodal}} \cong 3 \times 10^{-5}$$

This is just a little higher than the values of $(1 \text{ or } 2) \times 10^{-5}$, used previously. However this must be accompanied by the warning that we might eventually have to admit some dependence of the limiting j on T_r and the fluid. (Of course 3×10^{-5} is an approximation that one would only want to use if better information about j were unavailable.)

Notice, too, that replacing kT with kT_c was a pretty revolutionary suggestion. The modification of j by even so much as an order of magnitude, on the other hand, is far less important because most calculations based on j are very insensitive to its value.

Prediction of Surface Tension

The acid test of any p-v-T equation that purports to predict

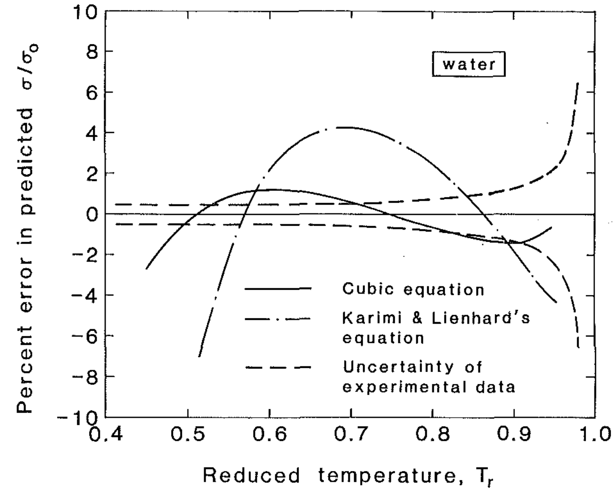

Fig. 7 Accuracy of the predicted temperature dependence of the surface tension of water, based on the present cubic interpolations of p-v-T data, and upon Karimi's fundamental equation

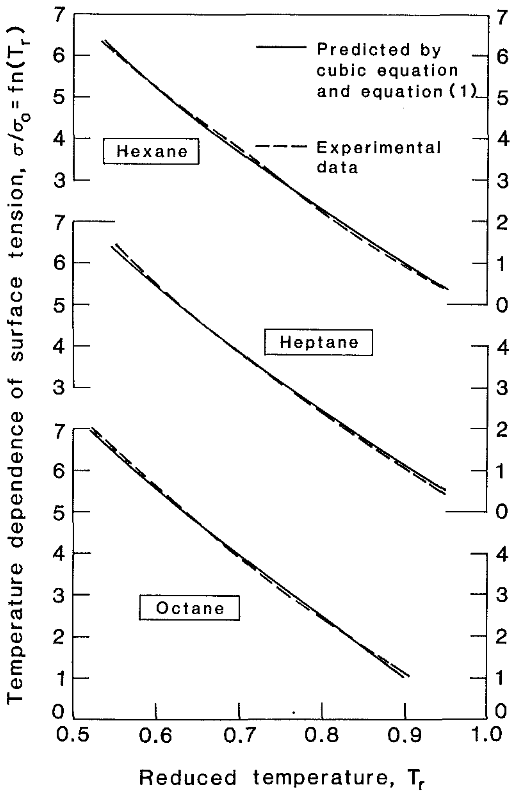

Fig. 8 Predicted and measured temperature dependence of the surface tension of three fluids

metastable and unstable properties is whether or not it correctly predicts the temperature dependence of surface tension when it is used in van der Waals' equation (1). We have subjected our cubic equations for water to this test at each temperature, and the results are shown in Fig. 6.

Figure 6 makes it quite clear that, except at the very lowest temperatures, this prediction has been extraordinarily successful. Nevertheless, it is this evidence that suggests that, while the cubic fits the low-temperature stable points with great accuracy, it is probably less accurate than we would wish in the metastable-unstable range. Of course, this observation is based on water – the only substance for which we had full data below $T_r = 0.5$, but one which is also known for its strange behavior at low temperatures.

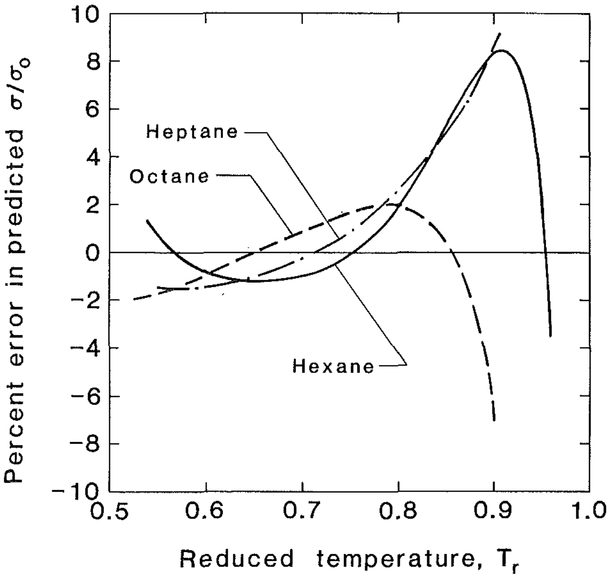

Fig. 9 Accuracy of the predicted temperature dependence of the surface tension of three fluids, based upon the present cubic interpolations of p-v-T data

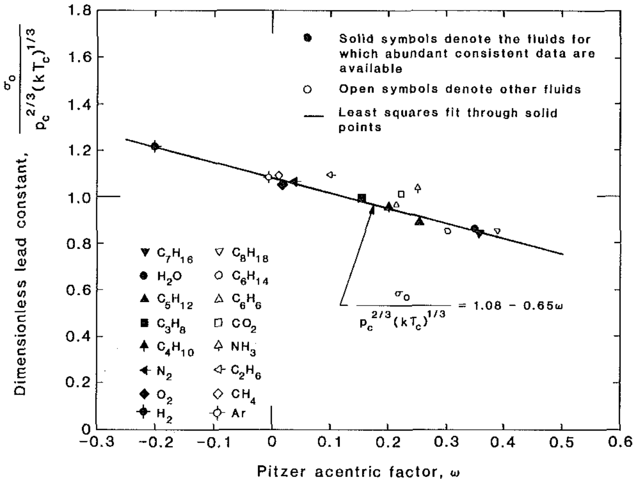

Fig. 10 Corresponding states correlation of the surface tension lead constant

Figure 7 shows the error in the predicted temperature dependence of surface tension, for water. The prediction is very nearly within the reported accuracy of the NBS surface tension data [19] for $T_r \geq 0.5$. The accuracy of Karimi's prediction is also included for comparison.

Figure 8 includes a comparable set of curves for heptane, hexane, and octane, the only fluids besides water for which convincing surface tension data were available over a wide range of temperature [16]. These curves again show that the cubic interpolations give very good predictions of the temperature dependence of surface tension when they are substituted in equation (1). Figure 9 shows the percent error in σ/σ_0 for these fluids. Once again the results are very accurate for $T_r \leq 0.85$.

While equation (1) only predicts σ/σ_0, we would like to be able to predict σ_0 as well. To make the comparisons in Figs. 6 and 8, it was necessary to calculate the average value of σ_0 for each substance, based on the surface tension data. We also computed some values of σ_0 at single points for fluids for which reliable p-v-T and σ data were not available over ranges of temperature.

In 1955, Brock and Bird [20] showed that the appropriate corresponding states nondimensionalization of σ was

$\sigma_0/p_c^{2/3}(kT_c)^{1/3}$. Figure 10 presents the correlation of our σ_0 values as a function of the Pitzer factor ω using this nondimensionalization.[6] The points based upon the data in which we have high confidence are presented as solid symbols. They define the following correlation

$$\sigma_0/p_c^{2/3}(kT_c)^{1/3} = 1.08 - 0.65\omega \tag{13}$$

with a correlation coefficient of 0.995. The remaining data are somewhat more widely scattered, but they do not significantly alter the correlation.

Others, starting with Hakim et al. [23], have formed corresponding states correlations for σ that include expressions for σ_0. These can be very useful, but they are normally based on assumed forms of the temperature dependence of σ/σ_0, that differ from that given by van der Waals' integral. Yet, even though these σ_0 expressions might also be linear in ω (as is true in [23]), they do not and should not match equation (13). Equation (13) gives the lead constant specifically for the van der Waals integral.

One can thus predict surface tension with acceptable accuracy for many applications, using p-v-T data alone, with the help of equations (1) and (13). As a matter of academic interest, we can predict a dimensionless σ_0 for the van der Waals equations (for which $\omega = -0.302$). The value is 1.276.

Conclusions

1 It appears possible to interpolate p-v-T data with great accuracy and a minimum of experimental data, using equation (11). The accuracy of such predictions has proven to be best (for the 16 fluids studied) in the range $0.5 < T_r < 0.85$.

2 The limiting value of j for which the homogeneous nucleation theory, equation (8), gives the spinodal limit, is on the order of 3×10^{-5}. However, it might ultimately show some variation from fluid to fluid, or from one saturation condition to another.

3 Further compelling support is provided for the idea (suggested in [3]) that kT_c should be used in equation (8) in place of kT.

4 Equation (1) provides convincing support for the present predictions of metastable and unstable p-v-T data.

5 The lead constant σ_0 in equation (1) is given by equation (13).

6 The Shamsundar-Murali cubic equation has only been used for individual isotherms here. We strongly recommend that the problem of developing general corresponding states correlations to represent the temperature dependence of its coefficients be undertaken in the future.

Acknowledgments

We are particularly grateful to Prof. N. Shamsundar for his very helpful counsel in all aspects of this work. This work has received support from the Electric Power Research Institute with Dr. G. Srikantiah as Project Manager, and the University of Houston Energy Laboratory.

References

1 van der Waals, J. D., "Thermodynamische Theorie der Kapillarität unter Voraussetzung stetiger Dichteänderung," *Zeit. Phys. Chemie*, Vol. 13, 1894, pp. 657-725; also published as "The Thermodynamic Theory of Capillary Under the Hpothesis of a Continuous Variation of Density," tr. by J. S. Rowlinson, *J. Stat. Phys.*, Vol. 20, No. 2, 1979, pp. 197-244.

2 Fisk, S., and Widom, B., "Structure and Free Energy of the Interface Between Fluid Phases in Equilibrium Near the Critical Point," *J. Chem. Phys.*, Vol. 50, No. 8, 1969, p. 3219.

3 Lienhard, J. H., and Karimi, A., "Homogeneous Nucleation and the Spinodal Line," ASME JOURNAL OF HEAT TRANSFER, Vol. 102, No. 3, 1980, pp. 457-460.

4 Lienhard, J. H., and Karimi, A., "Corresponding States Correlations of the Extreme Liquid Superheat and Vapor Subcooling," ASME JOURNAL OF HEAT TRANSFER, Vol. 100, No. 3, 1978, pp. 492-495.

5 Skripov, V. P., *Metastable Liquids*, Wiley, New York, 1974.

6 Skripov, V. P., Sinitsin, E. N., Pavlov, P. A., Ermakov, G. V., Muratov, G. N., Bulanov, N. V., and Baidakov, V. G., *Thermophysical Properties of Liquids in the Metastable State* [in Russian], Atomizdat, USSR, 1980.

7 Avedisian, C. T., "The Homogeneous Nucleation Limits of Liquids," *J. Chem. Phys. Ref. Data* (in press).

8 Himpan, J., "Die definitive Form der neuen thermischen Zustandgleichung nest ihren Stoffkonstanten von über 100 verschiedenen Stoffen," *Monatschefte für Chemie*, Vol. 86, 1955, pp. 259-268.

9 Shamsundar, N., private communication, 1984.

10 Murali, C. S., "Improved Cubic Equations of State for Polar and Nonpolar Fluids," MSME thesis, Dept. of Mech. Engr., University of Houston, 1983.

11 Karimi, A., and Lienhard, J. H., "A Fundamental Equation Representing Water in the Stable, Metastable, and Unstable States," EPRI Report NP-3328, Dec. 1983.

12 International Formulation Committee, "The 1968 IFC Formulation for Scientific and General Use. A Formulation of the Thermodynamic Properties of Ordinary Water Substance," ASME, New York, 1968.

13 Starling, K. B., *Fluid Thermodynamic Properties for Light Petroleum Systems*, Gulf Publishing Company, Houston, 1973.

14 Reynolds, W. C., *Thermodynamic Properties in SI*, Department of Mechanical Engineering, Stanford University, 1979.

15 API Research Project No. 44, "Selected Values of Physical and Thermodynamic Properties of Hydrocarbons and Related Compounds," Texas A. and M. University (various dates and authors).

16 Vargaftik, N. B., *Tables on the Thermophysical Properties of Liquids and Gases*, 2nd ed., Hemisphere, Washington, D.C., 1975.

17 Jaspar, J. J., "The Surface Tension of Pure Liquid Compounds," *J. Phys. and Chem. Ref. Data*, Vol. 1, No. 4, 1972, pp. 841-1010.

18 *Heat Exchanger Design Handbook*, Vol. 5, Hemisphere, Washington, D.C., 1983, Section 5.5.1.

19 The International Association for the Properties of Steam, "Release of Surface Tension of Water Substance," National Bureau of Standards, Dec. 1976.

20 Brock, J. R., and Bird, R. B., "Surface Tension and the Principle of Corresponding States," *AIChE Jour.*, Vol. 1, 1955, p. 174.

21 Pitzer, K. S., Lippman, D. Z., Curl, R. F., Huggins, C. M., and Peterson, D. E., "The Volumetric and Thermodynamic Properties of Fluids. II. Compressibility Factor, Vapor Pressure and Entropy of Vaporization," *J. Am. Chem. Soc.*, Vol. 77, 1955, pp. 3433-3440.

22 Lienhard, J. H., Shamsundar, N., and Biney, P. O., "Spinodal Lines and Equations of State – A Review," *J. Nuclear Engr. and Design* (in press).

23 Hakim, D. I., Steinberg, D., and Stiel, L. I., "Generalized Relationship for the Surface Tension of Polar Fluids," *Ind. Eng. Chem. Fundam.*, Vol. 10, No. 1, 1971, pp. 174-175.

---

[6] The Pitzer acentric factor [21], $\omega \equiv -1 - \log_{10} p_{r,\mathrm{sat}}$ $(T_r = 0.7)$, is probably the best choice of molecular parameter available for correcting Corresponding States correlations. See, e.g., [22] for a further discussion of recent applications.

Evaporation at a Liquid Surface Due to Jet Impingement

E. M. Sparrow
Fellow ASME

S. W. Celere

L. F. A. Azevedo

Department of Mechanical Engineering,
University of Minnesota,
Minneapolis, MN 55455

Experiments were performed to determine mass transfer coefficients for evaporation from a water surface on which an air jet impinged. During the course of the experiments, parametric variations were made of the jet velocity and diameter, the separation distance between the jet origin and the water surface, the diameter of the water surface, and the degree of insulation of the water containment pan. It was found that for all of the investigated operating conditions, the dimensionless mass transfer coefficient varied with the 0.8 power of the jet Reynolds number. Furthermore, the transfer coefficient decreased linearly as the separation distance between the jet origin and the water surface increased, with the most significant decreases occurring at relatively small values of the surface-to-jet diameter ratio. At larger diameter ratios, the transfer coefficient was relatively insensitive to the separation. In general, the larger the diameter of the water surface, the lower the transfer coefficient. Comparisons with the literature showed that the dimensionless mass transfer coefficients for impingement on a liquid surface are lower than those for impingement on a solid surface.

Introduction

Jet impingement provides heat transfer coefficients that are among the highest available in any forced convection flow. This characteristic has motivated experimental study of a variety of jet/impingement-surface configurations, involving both heat transfer and mass transfer. The mass transfer work was limited to jet impingement on solid surfaces, and the resulting mass transfer coefficients were transformed to heat transfer coefficients by employing the well-established analogy between the two transport processes. A survey of the available heat and mass transfer literature on jet impingement has been provided by Martin [1].

The present work is concerned with evaporation mass transfer which occurs due to jet impingement on a liquid surface. The capability of the liquid surface to deform and to move in response to both the impinging jet and the ensuing wall jet gives rise to a pattern of fluid flow which differs from that existing adjacent to a solid surface. The response of the mass transfer coefficient to such an altered flow pattern will be investigated here by experiment.

The physical situation to be studied is the normal impingement of an air jet on a water surface. The jet is of circular cross section and impinges at the center of the water surface, which is also of circular planform. Measurement of the rate of evaporation and evaluation of the density of the water vapor at the liquid surface and in the jet from temperature and pressure measurements enabled the mass transfer coefficient and the Sherwood number to be determined.

The experiments encompassed systematic variations of four relevant physical parameters. These included the jet velocity, the diameters D_j and D_w of the jet and the water surface, and the separation distance S between the origin of the jet and the surface. In dimensionless terms, the parameters can be represented by the jet-origin Reynolds number Re and the dimension ratios D_w/D_j and S/D_j. The D_w/D_j ratio extended from 7.7 to 23.5 in six steps, with one of the D_w/D_j values being attained using two different combinations of D_w and D_j. This duplication was employed with a view to verifying the universality of D_w/D_j as a correlating parameter. The S/D_j ratio ranged from 5 to 15 in three steps. For each D_w/D_j, S/D_j combination, the jet Reynolds number covered the range from about 3800 to 15,000. The presentation of results will be structured so as to highlight the effect of each of the dimensionless parameters on the Sherwood number.

The densities of the water vapor at the liquid surface and in the jet were constant during a given data run but varied appreciably during the duration of the experimental work. Such variations were useful in that they provided the opportunity to demonstrate that the mass transfer coefficients were universal, i.e., independent of the densities of the water vapor. To vary the vapor density at the liquid surface, different degrees of insulation of the water containment pan were used. The response of the Sherwood number to the thus-achieved changes in vapor density will be highlighted. Density changes also occurred in response to climatic changes, i.e., changes in the relative humidity of the air.

Experimental Apparatus and Procedure

Apparatus. To achieve the well-defined thermal, vapor concentration, and hydrodynamic conditions necessary for the attainment of accurate and reproducible data, the experiments were performed in an environment chamber and in the suction mode. In this mode of operation, air from the temperature-controlled laboratory room was drawn into and through the chamber by a downstream-positioned blower, the discharge of which was vented outside the building. This arrangement avoided the uncontrolled compression-related preheating of the air and the hydrodynamic disturbances which would have occurred had the system been operated in the blowing mode, i.e., with an upstream-positioned blower.

The description of the experimental apparatus is facilitated by reference to Fig. 1. The environment chamber was a large, rectangular, metal-walled enclosure, completely airtight except for a vertically oriented jet delivery tube that pierced its upper wall and an air exit port that was centered in its lower wall. The chamber was 1.52 m in height, with a square horizontal cross section of dimensions 0.61 × 0.61 m. Only the upper portion of the chamber is depicted in Fig. 1.

The water to be evaporated was contained in a specially fabricated, straight-sided circular pan supported from below by a cylindrical column. Two such pans were employed during the course of the experiments, with respective water-surface diameters D_w of 16.34 and 22.30 cm (surface area ratio = 1.84) and a sidewall height of 2.54 cm. The pans were fabricated from 0.0635-cm-thick galvanized steel. Distilled water was used in all of the experiments.

The actual support of the pan was accomplished by three

Contributed by the Heat Transfer Division for publication in the JOURNAL OF HEAT TRANSFER. Manuscript received by the Heat Transfer Division July 5, 1985.

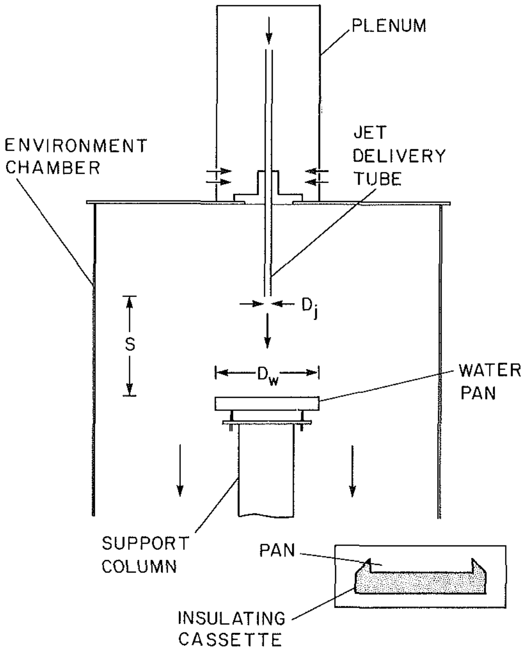

Fig. 1 Main features of the experimental apparatus

sharp-tipped Teflon screws threaded into a plexiglass flange at the top of the support column. Adjustment of the screws facilitated the leveling of the pan. The support column was a thin-walled 10.16-cm-dia pvc tube. Note that all the components of the support system were made of low-conductivity materials which, coupled with the point contact between the screw tips and the bottom of the pan, served to minimize extraneous heat conduction.

In a supplementary set of experiments, the water containment pan was enveloped at the sides and from below by an insulating cassette as pictured schematically in the inset at the lower right in Fig. 1. The presence of the insulation gave rise to lower temperatures of the evaporating water surface and to lower vapor pressures at the surface. The cassette was fabricated from closed-pore polystyrene insulation (Styrofoam) and covered with plasticized contact paper. Its outboard, upfacing surfaces were beveled downward at 45 deg in order to avoid altering the pattern of fluid flow adjacent to the water surface. Support of the cassette-enveloped pan was by the sharp-tipped Teflon screws as before.

The jet which impinged on the water surface originated at the exit cross section of a circular tube (i.e., the jet delivery tube). As seen in the figure, the delivery tube was supported and positioned by a sleevelike guide which rested in a lap in the upper wall of the environment chamber. The tube could be moved vertically within the guide, so that its exit could be positioned at any desired distance S from the water surface. At the lower end of the tube, the outer wall was beveled back from the exit cross section at 45 deg to minimize possible effects of the finite wall thickness.

Three jet delivery tubes were used throughout the course of the experiments, with respective internal diameters D_j equal to 0.950, 1.572, and 2.129 cm. A different custom-fitted guide was used with each tube. The lengths of the tubes were selected to ensure the attainment of hydrodynamically developed flow at the exit, and the respective length-diameter ratios of the tubes were 80, 60, and 50. The motivation for the attainment of developed flow is that such flows are characterized by well-defined and reproducible velocity distributions and turbulence levels.

The portion of the jet delivery tube which protruded above the upper wall of the environment chamber was enclosed in a cylindrical plenum chamber. The wall of the plenum was pierced near its lower end by an array of holes, and it was through these holes that air was drawn into the system. This plenum arrangement was adopted to ensure the accurate measurement of the initial state of the airflow by a psychrometric unit situated atop the upper wall of the environment chamber.

In the lower portion of the environment chamber (not shown in Fig. 1) was situated a balance for mass measurement and a platform. Immediately preceding and immediately following each data run, when measurements were made of the mass of the pan and its contents, the lower end of the support column rested on the weighing surface of the balance. During the data run proper and at all other times, the column rested on the platform. In the transfer of the support function from the balance to the platform, both the column and the balance remained stationary while the platform was slid under the flanged lower end of the column. The balance and the platform were positioned so as to avoid blocking the air exit port situated at the center of the lower wall of the environment chamber.

The environment chamber was equipped with two leakproof access windows. One of these was situated in the upper portion of the chamber and was used for filling and emptying the water pan and for positioning the pan and the jet delivery tube. The second window, situated in the lower part of the chamber, was used to facilitate the mass measurement operations and in transferring the support function from the platform to the balance and vice versa.

The upstream plenum, the jet delivery tube, and the environment chamber were part of an open-loop flow circuit. The air exiting the environment chamber was ducted through a flowmeter (a calibrated orifice plate) and a control valve to the blower, which was situated in a service corridor outside the laboratory.

Instrumentation. The humidity of the air entering the environment chamber was measured by a specially designed psychrometric unit. It consisted of a 76-cm length of 7.6-cm-dia plexiglass tube equipped at its downstream end with a fan which operated in the suction mode. The fan and the tube

Nomenclature

A = area of water surface $= \pi D_w^2/4$
D_j = diameter of jet at origin (i.d. of delivery tube)
D_w = diameter of water surface
$\mathfrak{D}$ = mass diffusion coefficient
h = enthalpy per unit mass
K = average mass transfer coefficient, equation (1)
ΔM = change of mass
$\dot{m}_j$ = rate of mass flow in jet delivery tube
p = pressure
Re = jet-origin Reynolds number $= 4\dot{m}_j/\mu\pi D_j$
S = separation distance between jet origin and water surface
Sc = Schmidt number
Sh = Sherwood number $= KD_w/\mathfrak{D}$
T_{db} = dry-bulb temperature
T_{wb} = wet-bulb temperature
T_{wtr} = water temperature
W = specific humidity
μ = viscosity
ν = kinematic viscosity
ρ = density
$\rho_{wv,j}$ = water vapor density in jet
$\rho_{wv,s}$ = water vapor density at liquid surface
τ = duration of data run

cross-sectional area were chosen to yield an airflow velocity which provides near equality of the psychrometric wet-bulb temperature and the thermodynamic wet-bulb temperature. Wet- and dry-bulb thermometers, which could be read to 0.1°F or better, were inserted radially into the tube through cork apertures in the cylindrical wall. The thermometer bulbs were positioned at the tube centerline, with the dry-bulb thermometer upstream of the wet-bulb thermometer (the separation distance was 30 thermometer diameters). Radiation shielding was provided by aluminum foil which completely covered the outside wall of the plexiglass tube.

The air temperature in the environment chamber was sensed by a thermocouple situated at a distance of $\frac{1}{2}S$ above the water surface and displaced to the side of the jet by a distance of $\frac{1}{4}D_w$ from the jet centerline. The thermocouple reading was virtually indistinguishable from that of the dry-bulb thermometer of the psychrometric unit.

Four thermocouples were used to measure the temperature of the evaporating water. One of these was situated at the centerline, and a second was positioned adjacent to the outer rim (about 0.3–0.4 cm from the rim). The other two thermocouples were installed so as to give a uniform radial spacing for the four thermocouples. Owing to the presence of surface motions which occurred for certain operating conditions, the thermocouple junctions were located about 0.6 cm below the nominal surface plane of the water. That placement ensured that the junctions were not exposed to the airflow. All thermocouples were made from precalibrated, Teflon-coated, 30-gage chromel and constantan wire.

Mass measurements were made with an Ohaus triple-beam balance having a capacity of 2610 g and which could be read to *0.05 g. The mass evaporated during a data run typically fell in* the range of 20–50 g.

The pressure in the environment chamber was read relative to ambient by a Baratron solid-state, capacitance-type pressure meter having a resolution of 10^{-3} Torr. The same meter was used for the pressure measurements relevant to the orifice flowmeter. A barometer situated adjacent to the environment chamber provided the ambient pressure.

Procedure. It is well established that the temperature of an evaporating water surface is lower than that of the ambient air into which the evaporation takes place. Furthermore, if the water is initially at ambient temperature, a waiting period must be allowed for the water temperature to decrease to its equilibrium value for steady-state evaporation. In the present experiments, it was determined from preliminary data runs that equilibration periods of 1 and 1½ hours, respectively, for the smaller and larger pans, were more than sufficient to yield steady-state evaporation. Prior to the initiation of the equilibration period, the pan was overfilled to compensate for the expected loss of mass due to evaporation. During the period, the jet velocity and separation distance were those of the upcoming data run.

At the conclusion of the equilibration period, the pan remained slightly overfilled (an elevation of the surface of 0.05–0.1 cm at the center). This degree of overfilling ensured that the water level did not drop perceptibly below the upper edge of the pan sidewall during the ensuing data run. The termination of the equilibration period was immediately followed by the measurement of the mass of the pan and its contents, after which the data run proper was initiated.

During the run, the four thermocouples situated in the pan were read periodically – a total of twenty times. The wet- and dry-bulb thermometers, the environment chamber thermocouple, and the pressures were read four times at equal intervals. The duration of the run was chosen to yield evaporation-induced changes of mass in the 20 and 40 g ranges, respectively, for the smaller and larger pans. The mass was measured immediately after the termination of the run.

Data Reduction

The mass transfer coefficient K for the evaporation process was evaluated from the definition

$$K = (\Delta M/\tau A)/(\rho_{wv,s} - \rho_{wv,j}) \tag{1}$$

In this equation, ΔM is the measured change of mass which occurred during a time interval τ, while A is the area of the circular planform of the water surface (i.e., $A = \pi D_w^2/4$). The denominator is the difference between the densities of the water vapor at the water surface and in the jet, $\rho_{wv,s}$ and $\rho_{wv,j}$, respectively. Note that for the conditions of the experiments,

$$\rho_{wv,j} = \rho_{wv,\infty} \tag{2}$$

where $\rho_{wv,\infty}$ is the vapor density in the ambient within the environment chamber. From the standpoint of practice, $\rho_{wv,\infty}$ is the most convenient representation of $\rho_{wv,j}$, since it is well defined and can be readily determined.

For the evaluation of $\rho_{wv,s}$, it was assumed that phase equilibrium prevailed at the liquid–vapor interface (i.e., at the surface of the liquid), so that the vapor was saturated vapor corresponding to the water temperature T_{wtr}. The value of T_{wtr} was obtained by averaging the thermocouple readings both radially and temporally. Owing to the virtual uniformity of the radial temperature distribution, it was not necessary to weight the individual thermocouple readings. Then, in terms of standard notation (g = saturated vapor)

$$\rho_{wv,s} = \rho_g(T_{wtr}) \tag{3}$$

The evaluation of $\rho_{wv,j}$ begins with the determination of the specific humidity W of the air entering the upstream plenum from the laboratory. From any standard thermodynamics text,

$$W = [W_{wb} h_{fg}(T_{wb}) + c_{pa}(T_{wb} - T_{db})]/[h_g(T_{db}) - h_f(T_{wb})] \tag{4}$$

Here, h_f and h_g denote the enthalpies of saturated liquid and saturated vapor, and h_{fg} is the latent heat, each evaluated at the indicated temperature, where T_{db} and T_{wb} respectively denote the dry-bulb and wet-bulb temperatures measured by the psychrometric unit. In addition, c_{pa} is the specific heat of dry air (taken as 1.006 kJ/kg – °C) and W_{wb} is the specific humidity corresponding to the wet-bulb saturation condition, i.e.,

$$W_{wb} = 0.622 p_{\text{sat}}(T_{wb})/[p_{\text{bar}} - p_{\text{sat}}(T_{wb})] \tag{5}$$

in which p_{bar} and p_{sat} are, respectively, the barometric pressure in the laboratory and the saturation pressure of water vapor.

In the impinging jet, the specific humidity is equal to the value obtained from equation (4), but the pressure is no longer equal to p_{bar}. If Δp is the pressure drop between the laboratory and the environment chamber, the pressure in the jet can be expressed as $p_j = (p_{\text{bar}} - \Delta p)$. Then, in the jet,

$$W = 0.622 p_{wv,j}/(p_j - p_{wv,j}) \tag{6}$$

or

$$p_{wv,j} = W p_j/(0.622 + W) \tag{7}$$

from which the numerical value of $p_{wv,j}$ follows directly. Finally, from the definition of the relative humidity ϕ

$$\phi = p_{wv,j}/p_{\text{sat}}(T_j) = \rho_{wv,j}/\rho_g(T_j) \tag{8}$$

where the temperature T_j is the measured temperature in the environment chamber, which was virtually identical to the dry-bulb temperature at the psychrometric unit. Equation (8) can be solved for the numerical value of $\rho_{wv,j}$, which is then introduced into equation (1), thereby completing its evaluation.

All of the thermodynamic properties needed in the foregoing calculations were taken from the ASHRAE Handbook [2].

The mass transfer coefficients determined from equation (1) were recast in dimensionless form in terms of the Sherwood number

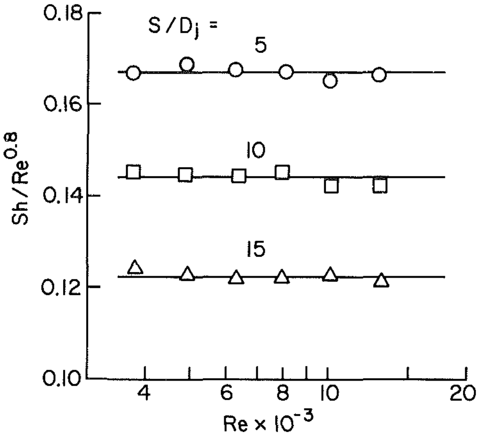

Fig. 2 Sherwood number results for $D_w/D_j = 7.68$

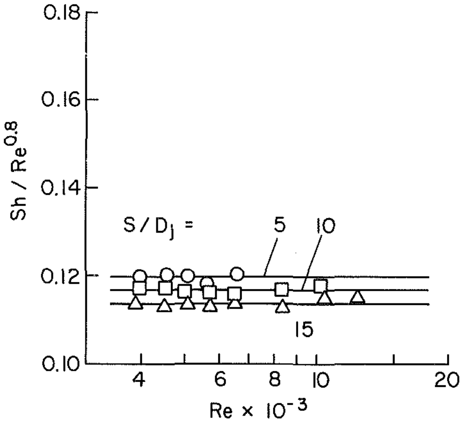

Fig. 5 Sherwood number results for $D_w/D_j = 17.20$

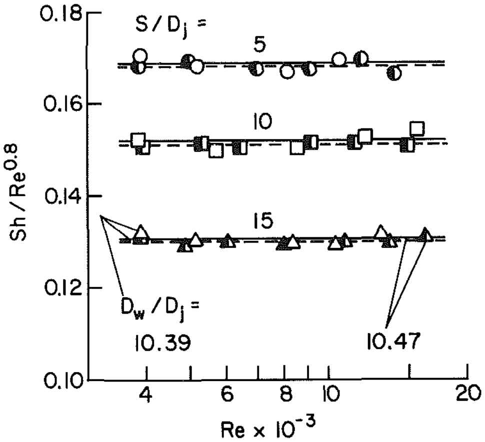

Fig. 3 Sherwood number results for $D_w/D_j = 10.4$

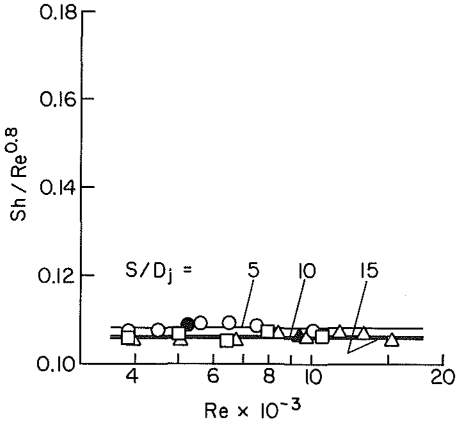

Fig. 6 Sherwood number results for $D_w/D_j = 23.47$

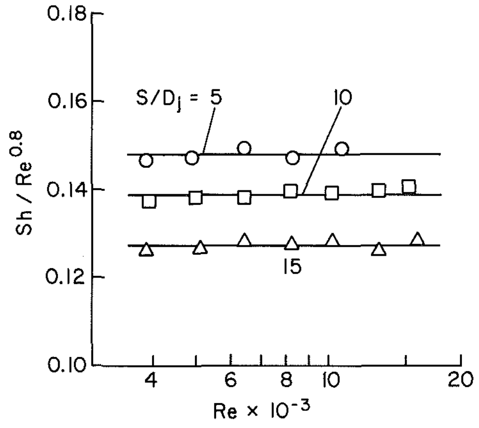

Fig. 4 Sherwood number results for $D_w/D_j = 14.18$

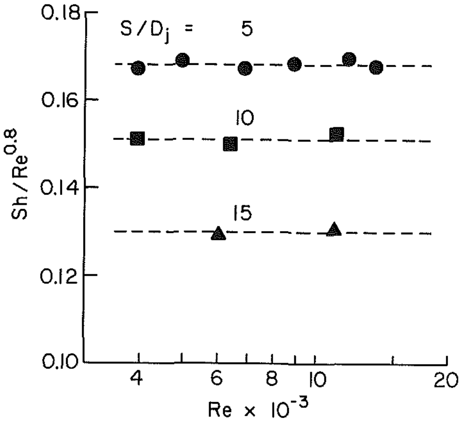

Fig. 7 Sherwood number results for the insulated water containment pan, $D_w/D_j = 10.47$

$$\mathrm{Sh} = KD_w/\mathfrak{D} \tag{9}$$

By introducing the Schmidt number $\mathrm{Sc} = \nu/\mathfrak{D}$, the mass diffusion coefficient $\mathfrak{D}$ can be eliminated from equation (9), so that

$$\mathrm{Sh} = (KD_w/\nu)\mathrm{Sc} \tag{10}$$

For the air/water vapor system, $\mathrm{Sc} = 0.6$ (Table 10.1 of [3] and Table 7 of [4]).

The kinematic viscosity ν ($= \mu/\rho$) appearing in equation (10) was evaluated at jet conditions. The viscosity μ of mixtures of air and water vapor is not known to high precision, but for the jet temperatures and vapor concentrations of the present experiments, it did not differ by more than 0.2 percent from that for dry air [4]. In view of this, dry-air viscosities were used. The density of the air/water vapor mixture comprising the jet is given by

$$\rho_j = \rho_{wv,j} + \rho_{a,j} \tag{11}$$

where $\rho_{wv,j}$ is known from equation (8) and $\rho_{a,j}$ is determined by using the perfect gas law with T_j and $p_{a,j}$ ($= p_j - p_{wv,j}$) as inputs.

The Sherwood number results were parameterized by the Reynolds number Re at the jet origin (i.e., at the exit of the jet delivery tube)

$$\mathrm{Re} = 4\dot{m}_j/\mu\pi D_j \tag{12}$$

in which $\dot{m}_j$ is the rate of mass flow through the delivery tube. The value of $\dot{m}_j$ was obtained from the measured flow rate at the orifice meter by subtracting the rate of evaporation at the water surface.

Results and Discussion

An analysis of the data indicated that for a given geometric configuration characterized by fixed values of D_w/D_j and S/D_j, the Sherwood number varied with the 0.8 power of the Reynolds number. This suggests a generalized presentation of results in terms of $\mathrm{Sh}/\mathrm{Re}^{0.8}$ rather than a presentation of Sh itself.

The $\mathrm{Sh}/\mathrm{Re}^{0.8}$ data for all of the investigated operating conditions are plotted in Figs. 2-7. Each figure pertains to a specific value of the diameter ratio D_w/D_j of the water surface and the jet, starting with $D_w/D_j = 7.68$ in Fig. 2 and increasing from figure to figure to $D_w/D_j = 23.47$ in Fig. 6. Among the six values of D_w/D_j that were employed to parameterize the experiments, two were nearly identical, namely, 10.39 and 10.47. The results for both these cases are presented in Fig. 3 to facilitate their direct comparison. In addition, results from supplementary experiments in which the water containment pan was insulated are presented in Fig. 7.

In each of Figs. 2-7, the $\mathrm{Sh}/\mathrm{Re}^{0.8}$ ratio is plotted as a function of the Reynolds number Re for three parametric values of the dimensionless separation distance S/D_j between the jet origin and the water surface, namely, $S/D_j = 5$, 10, and 15. The horizontal lines that pass through the data for each S/D_j are least-squares fits. To facilitate figure-to-figure comparisons, the ordinate scales for all of the figures were made identical.

An overall inspection of Figs. 2-7 indicates that the deviations of the data from the $\mathrm{Sh} \sim \mathrm{Re}^{0.8}$ correlation do not exceed about two percent, and there is no evidence of systematic deviations with either D_w/D_j or S/D_j. The 0.8 power strongly suggests that the airflow passing over the water surface is turbulent, and the early onset of turbulence is believed due to the presence of roughnesslike disturbances and waves on the surface. This matter will be elaborated later when comparisons are made with the literature on jet impingement on solid surfaces.

In general, for fixed values of the water surface diameter and the jet diameter (i.e., fixed D_w/D_j), the mass transfer coefficient decreases as the separation between the jet origin and the water surface increases. From a comparison of the successive figures, it is seen that the sensitivity of the transfer coefficient to the separation distance is markedly affected by the D_w/D_j ratio. Over all, there is a trend for the coefficient to become less and less dependent on the separation distance as D_w/D_j increases. This is especially strongly manifested for the three largest investigated D_w/D_j (14.18, 17.20, and 23.47). In particular, at $D_w/D_j = 23.47$, the effect of S/D_j is only 2-3 percent throughout its entire range. This insensitivity is physically plausible since the details of the impingement which are affected by the separation distance (i.e., impingement velocity and size of impingement zone) are relatively unimportant when the impingement zone is very much smaller than the overall area of the surface.

Further comparisons of the successive figures reveal an initial increase of $\mathrm{Sh}/\mathrm{Re}^{0.8}$ with D_w/D_j (compare Figs. 2 and 3), followed by a marked decrease at still larger values of D_w/D_j. In rationalizing these results, it is convenient to think in terms of a fixed jet diameter and, thereby, to associate increases in D_w/D_j with increases in the diameter of the water surface. Thus, the wall jet which is spawned by the impinging jet traverses a longer radial distance along the water surface as D_w/D_j increases, with related increases in the thicknesses of the velocity and vapor-concentration boundary layers. These thicker boundary layers give rise to lower mass transfer coefficients for larger D_w/D_j. The Sherwood number, however, contains the product of the mass transfer coefficient and the diameter of the water surface, which vary oppositely with D_w/D_j. At smaller D_w/D_j, the two opposing factors are competitive, leading to the initial increase of the Sherwood number, while at larger D_w/D_j, the decrease of the mass transfer coefficient dominates.

Attention will now be turned to Fig. 3 and to the comparison of results for two cases having virtually identical values of the D_w/D_j ratio but for which the individual values of D_w and of D_j differed. These cases were investigated with a view to exploring the universality of D_w/D_j as a correlation parameter. The data corresponding to $D_w/D_j = 16.34/1.572 = 10.39$ are represented by the half-black symbols and the dashed least-squares lines, while those for $D_w/D_j = 22.30/2.129 = 10.47$ are represented by the open symbols and the solid least-squares lines.

As seen in the figure, the data for the two cases are nearly coincident. In fact, the maximum deviation of the corresponding least-squares correlating lines is 0.6 percent. This excellent agreement provides strong testimony in support of the universality of D_w/D_j as a correlation parameter.

As noted earlier, auxiliary experiments were undertaken to demonstrate that the Sherwood number results are independent of the densities of the water vapor. To supplement the naturally occurring changes in vapor density which accompanied climatic changes (i.e., changes in the relative humidity of the ambient air), more controlled changes of the vapor density at the liquid surface were achieved by the use of the insulating cassette described earlier. The presence of the insulation brought about a decrease in the water temperature which, in turn, decreased the vapor pressure and vapor density at the surface. For instance, for one set of operating conditions, the values of $(T_{wtr} - T_{wb})/(T_{db} - T_{wb})$ were 0.321 and 0.243, respectively, without and with the insulation. The corresponding values for another case were 0.208 and 0.134.

The Sherwood number data obtained with the insulating cassette in place are represented by the black data symbols in Fig. 7 and by the pair of black data points in Fig. 6. In Fig. 7, the dashed lines are the least-squares lines corresponding to the uninsulated containment pan, i.e., the same dashed lines that are plotted in Fig. 3. Both Figs. 7 and 6 display excellent agreement between the Sherwood numbers for the uninsulated and insulated pans. Since the two sets of results correspond to different vapor densities at the liquid surface, it may be concluded that the Sherwood numbers are universal with respect to this parameter. Furthermore, from the fact that the Sherwood numbers were also independent of the vapor densities in the jet, it follows that they are universal with respect to both the vapor densities at the surface and in the jet.

Consideration will now be given to quantifying the variations of $\mathrm{Sh}/\mathrm{Re}^{0.8}$ with D_w/D_j and S/D_j. These variations have been discussed qualitatively in connection with Figs. 2-6, but in those figures both D_w/D_j and S/D_j served as discrete parameters rather than as continuous independent variables, so that their quantitative influences were not readily discernible.

In Fig. 8, $\mathrm{Sh}/\mathrm{Re}^{0.8}$ is plotted as a function of D_w/D_j for parametric values of S/D_j. The data points shown in the figure correspond to the least-squares horizontal lines in Figs. 2-6 and are, therefore, representative of the entire investigated Reynolds number range. Smooth curves have been passed through the data for continuity.

The figure shows that the overall variation of the Sherwood number with D_w/D_j at a fixed Reynolds number is substantial

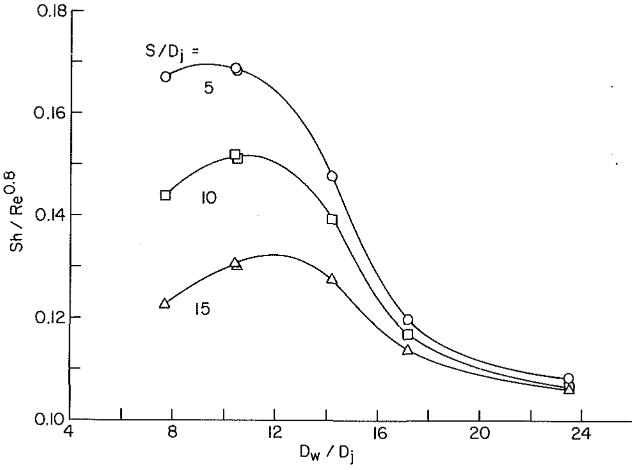

Fig. 8 Variation of the Sherwood number with D_w/D_j

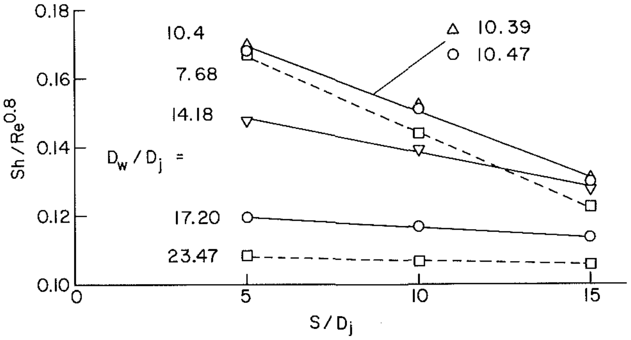

Fig. 9 Variation of the Sherwood number with S/D_j

when the separation distance between the jet origin and the water surface is relatively small. For example, for $S/D_j = 5$, the minimum and maximum values of $\mathrm{Sh}/\mathrm{Re}^{0.8}$ are 1.083 and 1.695. As the separation distance increases, there is a marked decrease in the variation of $\mathrm{Sh}/\mathrm{Re}^{0.8}$ with D_w/D_j, so that for $S/D_j = 15$, $\mathrm{Sh}/\mathrm{Re}^{0.8}$ is confined to the range between 1.058 and 1.323. Notwithstanding the just-documented fact that the overall variation of Sh with D_w/D_j is quite sensitive to S/D_j, the sensitivity dies away at larger D_w/D_j, where all the results tend to merge.

All of the curves in Fig. 8 are characterized by a common shape, which includes an initial rise, the attainment of a maximum, and a sharp dropoff which becomes increasingly more gradual at larger D_w/D_j. As noted earlier, the maximum in the Sh versus D_w/D_j distribution should not be regarded as indicating a maximum value of the mass transfer coefficient. Rather, the maximum in Sh is due to the conflict between K and D_w. Indeed, it is readily shown that the mass transfer coefficient decreases monotonically with D_w/D_j over the investigated range.

Figure 9 presents the variation of $\mathrm{Sh}/\mathrm{Re}^{0.8}$ with S/D_j, with D_w/D_j as the curve parameter. Again, the data points appearing in the figure correspond to the least-squares horizontal lines in Figs. 2-6. As expected, the mass transfer coefficient drops off as the separation distance increases.

The figure shows that the variation of $\mathrm{Sh}/\mathrm{Re}^{0.8}$ with S/D_j at a fixed value of D_w/D_j is well represented by a straight line. The slope of the straight line is markedly affected by the D_w/D_j ratio. At small values of D_w/D_j, the transfer coefficient is quite sensitive to the separation distance, while at large D_w/D_j, it is virtually independent of the separation distance.

With regard to comparisons with the literature, it was already noted in the Introduction that prior jet-related mass transfer experiments appear to be limited to impingement on solid surfaces. In the absence of prior liquid-surface impingement results, the present Sherwood numbers will be compared with those for impingement on a solid surface.

An empirical correlation of Sherwood number data for jet impingement on solid surfaces was presented in [1]. That correlation, when rephrased in terms of the present notation and evaluated for $\mathrm{Sc} = 0.6$, is

$$\mathrm{Sh} = 1.614F(\mathrm{Re})[(D_w/D_j) - 2.2]/[(D_w/D_j) + 0.2((S/D_j) - 6)] \tag{13}$$

where $D_w/D_j > 5$. For the Reynolds number range between 2000 and 30,000, which includes the range investigated here,

$$F(\mathrm{Re}) = 1.36\mathrm{Re}^{0.574} \tag{14}$$

At higher Reynolds numbers, the exponent increases, attaining a value of 0.775 for Re between 120,000 and 400,000.

The $\mathrm{Re}^{0.574}$ and $\mathrm{Re}^{0.8}$ dependences of the Sherwood number, respectively, for solid-surface impingement and liquid-surface impingement, provide clear evidence of the major differences in the transfer processes which prevail in the two situations. The solid-surface case is characterized by laminar flow over a smooth, flat surface. On the other hand, the liquid-surface case corresponds to turbulent flow over a compliant surface which deforms in response to the airflow and whose deformation, in turn, affects the airflow pattern. Careful visual observations made during the course of the experiments revealed a depression of the water surface in the impingement zone, with the size and depth of the depression depending on the Reynolds number and on the separation distance. In the region away from the impingement zone, surface waves were in evidence. From the standpoint of the airflow, these waves acted like major roughness elements, in all likelihood causing flow separation. At Reynolds numbers higher than those for which data were collected, the relatively deep depression caused by the impinging jet tended to be unstable, and the surface waves were large and irregular.

It is believed that both the surface depression in the impingement zone and the waves situated in the region away from the impingement zone contribute to diminished rates of mass transfer. This conjecture is substantiated by comparisons between the present data and equations (13)-(14). Such comparisons show that the Sherwood numbers for impingement on a liquid surface are consistently lower than those for impingement on a solid surface.

Concluding Remarks

The experimental work reported here is, seemingly, the first study of evaporation from a liquid surface due to jet impingement. With water as the evaporating liquid and ambient air as the impinging jet, parametric variations were made of the jet velocity and diameter, the separation distance between the jet origin and the water surface, and the diameter of the water surface. In dimensionless terms, these parameters can be represented by S/D_j, D_w/D_j, and Re, where S is the separation distance, D_w and D_j are the water surface and jet diameters, and Re is the jet-origin Reynolds number. The investigated ranges of these groups extended from 5 to 15 for S/D_j, from 7.68 to 23.47 for D_w/D_j, and from 3800 to 15,000 for Re. The experiments yielded mass transfer coefficients, which were presented in terms of the Sherwood number Sh based on the water surface diameter.

It was found that for all of the investigated operating conditions, the Sherwood number varied with the 0.8 power of the Reynolds number. Furthermore, at a fixed Reynolds number and D_w/D_j ratio, the Sherwood number decreased linearly as the separation distance between the jet origin and the water surface increased. The decrease was significant at small values of D_w/D_j, but, at large values of D_w/D_j, the Sherwood number was virtually independent of the separation distance.

The mass transfer coefficient decreased monotonically with increases in the diameter of the water surface (although the Sherwood number displayed a local maximum). The overall change of the coefficient in response to changes in the water surface diameter was greatest at small separation distances.

Supplementary experiments involving different jet diameters and different water surface diameters, but with a common value of D_w/D_j, affirmed the universality of the D_w/D_j ratio as a correlation parameter. Other experiments demonstrated that the Sherwood number results were independent of the densities of the water vapor at the liquid surface and in the impinging jet.

Comparisons with the literature showed that the Sherwood numbers for jet impingement on the liquid surface are lower than those for jet impingement on a solid surface.

References

1 Martin, H., "Heat and Mass Transfer Between Impinging Gas Jets and Solid Surfaces," *Advances in Heat Transfer*, Vol. 13, 1977, pp. 1-60.

2 ASHRAE Handbook – 1981 Fundamentals, American Society of Heating, Refrigerating, and Air Conditioning Engineers, Atlanta, GA, 1981.

3 Threlkeld, J. L., *Thermal Environmental Engineering*, Prentice-Hall, Englewood Cliffs, NJ, 1970.

4 Mason, E. A., and Monchick, L., "Survey of the Equation of State and Properties of Moist Air," in: *Humidity and Moisture*, A. Wexler, ed., Vol. 3, Reinhold, New York, 1965.

Effects of Ambient Pressure on the Instability of a Liquid Boiling Explosively at the Superheat Limit

D. Frost

B. Sturtevant

Graduate Aeronautical Laboratories,
California Institute of Technology,
Pasadena, CA 91125

The effect of ambient pressure on the intrinsic instability of rapid vaporization in single droplets boiling explosively at the limit of superheat has been studied experimentally and theoretically. The instability that distorts the evaporating interface and substantially enhances the mass flux at atmospheric pressure is suppressed at high pressure. The radiated pressure field is two orders of magnitude smaller from stabilized bubbles than from unstable. At intermediate pressures bubble growth occurs in two stages, first stable, then unstable. The Landau-Darrieus instability theory predicts absolute stability at atmospheric pressure for a spherical bubble, whereas the theory for planar interfaces yields results in general agreement with observation. The sensitivity of the instability to temperature suggests that small temperature nonuniformities may be responsible for quantitative departures of the behavior from predictions.

1 Introduction

Among the most rapid vaporization rates observable are those that occur when a liquid boils near its limit of mechanical stability; that is, at its so-called limit of superheat. Several interesting phenomena which provide important insight into the behavior of metastable liquids occur under the extreme conditions of superheat-limit vaporization. In particular, the rapid vaporization drives a dynamic instability to which is attributed the destructiveness of boiling at the superheat limit, when it occurs at large scale in vapor explosions. The explosive effects observed at the superheat limit are consequences of a baroclinic interfacial instability similar to the Landau mechanism for the instability of laminar flames [1, 2]. The instability mechanism was developed independently in France by Darrieus [3, 4], also in the context of the stability of a propagating flame front. The instability was discovered in the context of evaporation at the superheat limit by Shepherd and Sturtevant [5]. They observed that the instability distorts and roughens the liquid-vapor interface, and they inferred from their measurements that, in fact, it tears the interface, producing a substantial increase in the surface area available for evaporation and a high-velocity two-phase flow away from the interface. The instability-driven mass flux generates a jet which impinges upon the surrounding fluid [5]. The combined effect of the instability and the impact of the resulting jet on, for example, the fuel in a fuel-coolant interaction are sufficient to provide the long-sought-after mechanism of "fragmentation" in explosive interactions caused by spills. In any case, the vaporization rates observed in the unstable configuration are sufficient to explain the destructiveness of vapor explosions without invoking any other processes. It is important that the instability occurs during the *growth* phase of vapor bubbles, while, for example, the Rayleigh-Taylor instability, which is another mechanism for jetting but which occurs only upon bubble *collapse*, plays no role. No existing theoretical model of fuel-coolant interactions treats the significant effects of the intrinsic instability. In order that the physical processes of the instability may properly be incorporated into future theories it is first necessary to conduct exploratory experiments in simple systems at small scale so the basic phenomena may be discovered and exhibited in detail.

This paper reports experiments that have been carried out to examine the effect of ambient pressure on the dynamics of the decomposition of metastable superheated liquids. Single droplets are heated until they vaporize explosively at the superheat limit. Heterogeneous nucleation and ordinary boiling are suppressed by immersing the droplets in a hot nonvolatile liquid, thus isolating them from solid surfaces containing gas nuclei. When the superheat limit is reached, boiling begins spontaneously by homogeneous nucleation, and the subsequent evaporative fluxes, fluid accelerations, and departures from thermodynamic equilibrium are orders of magnitude greater than in ordinary boiling. The results reported here show that it is possible to suppress the Landau instability, and, therefore, the explosive nature of a liquid vaporizing at the superheat limit, by controlling the ambient pressure. Increasing the ambient pressure lowers the susceptibility of the liquid to the instability by decreasing the pre-instability mass transfer rate. In fact, by controlling the ambient pressure, it is possible to inhibit the instability altogether and change the nature of the vaporization from an explosive event to that of stable growth of a smooth vapor bubble. The theory of the Landau instability is discussed in light of the experimental observations.

The role of ambient pressure may be understood by examining the p–T diagram shown in Fig. 1. The limit of superheat is observed to occur close to the liquid spinodal [6], the locus of points of neutral mechanical stability of the liquid, i.e., $(\partial p/\partial v)_T = 0$. It is well known [7-9] that the limit of superheat is relatively insensitive to ambient pressure. However, experiments reported by Avedisian [10] have shown that the substantial reduction of superheat at the liquid

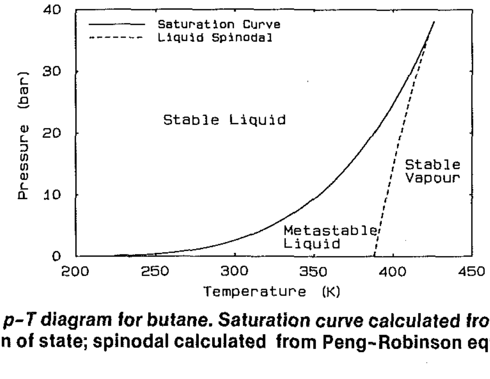

Fig. 1 *p*–*T* diagram for butane. Saturation curve calculated from Reidel equation of state; spinodal calculated from Peng-Robinson equation of state.

Contributed by the Heat Transfer Division for publication in the JOURNAL OF HEAT TRANSFER. Manuscript received by the Heat Transfer Division October 4, 1984.

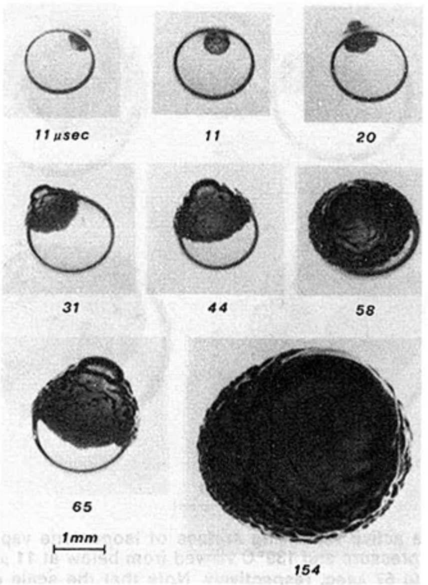

Fig. 2 Photographs of bubble growth in ether droplets at atmospheric pressure and 147°C. Each picture is taken during a different explosion.

spinodal (i.e., $T_{sl} - T_{\text{sat}}$, the difference between the superheat limit temperature and the saturation temperature) as the critical point is approached has a strong effect on the rate of vaporization of droplets after nucleation occurs. Moreover, the moderating effect of superheat reduction due to an increase in the external pressure has been noted by a number of authors in the context of models for large-scale vapor explosions [11-13], and it has been observed that only a modest increase in ambient pressure is needed to suppress the onset of vapor explosions in some fuel-coolant interaction systems [14].

In this paper the experimental apparatus and technique are described and the results illustrating the effect of ambient pressure on the vaporization process are presented. This is followed by a discussion of the Landau instability in both planar and spherical geometry, and of its relevance to the present experimental results.

2 Experimental

The apparatus in the present experiments is a modified version of the bubble-column apparatus of Shepherd and Sturtevant [5], redesigned for operation at elevated pressures and temperatures. A small drop of the test liquid is injected into the bottom of a vertical tube filled with an immiscible host liquid. The host fluid must be more dense than the test fluid, have a surface tension sufficiently high to insure homogeneous nucleation, and have a boiling point higher than the superheat limit of the drop. A heater at the top of the column and a cooling coil at the bottom produce a stable temperature gradient in the host liquid. The temperature in the test section at the top of the column is monitored and maintained at the superheat limit of the test liquid. The test drop slowly rises up the column and is heated by the transfer of heat from the surrounding host. When the drop reaches the test section, homogeneous nucleation occurs and the drop evaporates with an explosive pop. In the present experiments the explosion process is examined with high-speed high-resolution microphotography and fast-response pressure measurements.

The choice of host and test fluids was dictated largely by convenience and the experience of previous investigators. Glycerol was used as the host fluid. Three volatile hydrocarbons were used as test fluids: pentane, isopentane, and ethyl ether. All three are liquid at room temperature and have superheat limits (148°C, 139°C, 147°C, respectively, at atmospheric pressure) low enough to allow the use of conventional piezoelectric transducers immersed in the test section. At the superheat limit superheats of typically 112°C are attained, slightly higher than the 105°C achieved using butane at atmospheric pressure in the previous experiments by Shepherd and Sturtevant [5], and much higher than most early experiments [15-19]. Tests have been carried out for ambient pressures up to 4.2 bar. The saturation temperature increases more rapidly than the superheat limit with increasing ambient pressure. As a result, for example, in ether the superheat at the superheat limit decreases from 112.3°C at atmospheric pressure to 70.5°C at 4 bar.

A fast-response piezoelectric pressure transducer mounted in a large baffle near the point at which the drops exploded is used to record the blast-generated pressure field. A short-duration spark-gap light source facilitates the photography of the vaporization process. The spark-gap is triggered from the pressure signal after a variable delay time. By varying the delay, a series of photographs is obtained documenting the entire explosion process. As described below, at high ambient pressures the signal from the growing bubble is very small. However, under all circumstances a pressure spike is observed when the bubble first nucleates, typically of about 40 mbar amplitude at an ambient pressure of 3 bar (at a distance of ~5 mm from the bubble). With proper amplification this signal is sufficient for triggering.

3 Results

Figure 2 shows a series of photographs taken at various times during the explosive vaporization of ether at at-

Nomenclature

b = coefficient in dispersion relation (8), defined in equation (9)
c = coefficient in dispersion relation (8), defined in equation (10)
F = nondimensional "figure of merit" defined in equation (11)
K = nondimensional wavenumber $= kR$
k = wavenumber
N_I = inertia number defined in equation (3)
N_W = Weber number defined in equation (4)
n = spherical harmonic index
p = pressure
R = vapor bubble radius
$\dot{R}$ = radial velocity
$\ddot{R}$ = radial acceleration
T = temperature
t = time
U = radial bubble velocity
α = density ratio $= \rho_v/\rho_l$
ϵ = perturbation amplitude
κ = curvature
λ = perturbation wavelength
ρ = density
τ = time interval during which a growing bubble is predicted to be linearly unstable
Ω = nondimensional growth rate in the planar instability theory defined in equation (2)
ω' = nondimensional growth rate in the spherical instability theory
ω = dimensional growth rate

Subscripts

l = liquid
max = maximum value
sat = saturation conditions
sl = superheat limit conditions
v = vapor

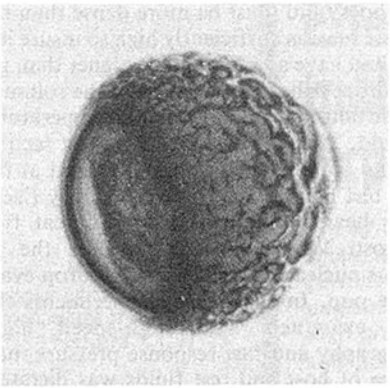

Fig. 3 2.4-mm-dia isopentane drop at atmospheric pressure nearly completely vaporized. Note that the vaporizing liquid-vapor interface can be viewed inside the drop from below.

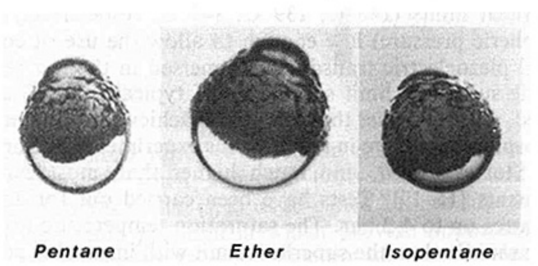

Pentane *Ether* *Isopentane*

Fig. 4 Views of the smooth cap produced by all three substances studied in this work exploding at atmospheric pressure. Drop diameters: pentane, 2.0 mm; ether, 2.0 mm; isopentane, 2.5 mm.

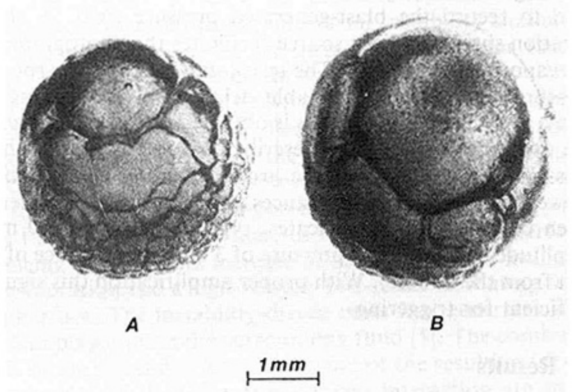

Fig. 5 Remnant caps on fully vaporized drops of ether at atmospheric pressure. The scale of the disturbances on the bubble surface decreases monotonically away from the cap. Bubble diameters: 3.3 mm, 3.7 mm.

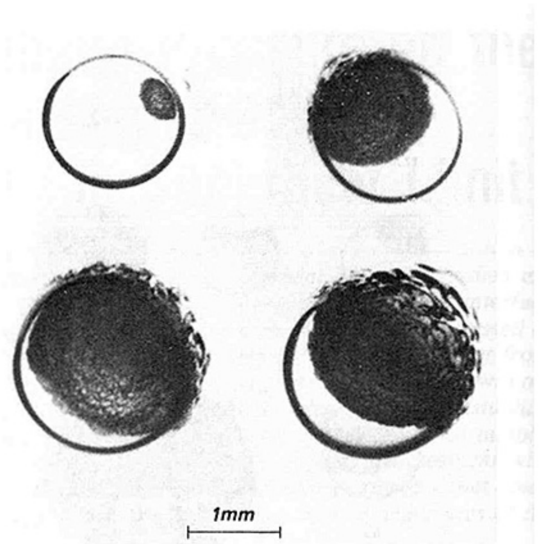

Fig. 6 The active vaporizing surface of isopentane vaporizing at atmospheric pressure and 139°C viewed from below at 11 μsec, 43 μsec, 67 μsec, and 67 μsec, respectively. Note that the scale of the disturbances on the vaporizing interface is the same on all pictures.

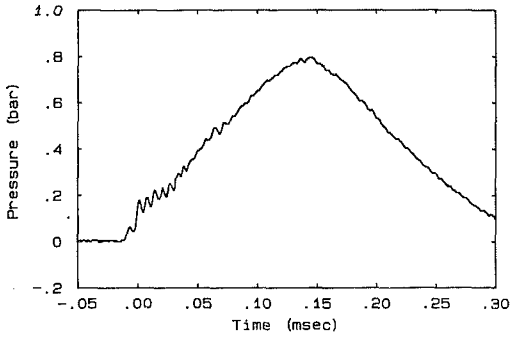

Fig. 7 Early time behavior of radiated pressure field. Ether at atmospheric pressure; 1.3-mm-dia drop; baffled pressure transducer 9 mm from drop.

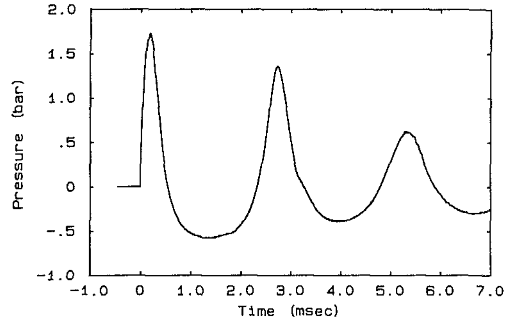

Fig. 8 Long time behavior of pressure radiated from exploding and oscillating drop of ether, atmospheric pressure. Baffled pressure transducer 6 mm from bubble center.

mospheric pressure. The drops are shown immersed in host fluid, which appears light grey in the photographs. The time listed below each drop is the elapsed time since the pressure wave first left the drop. Each picture depicts the vaporization of a different drop; the nucleation of the vapor bubble within the drop occurs at random asymmetric locations within the drops, always rather close to the drop boundary.

A number of repeatable features are evident from these photographs, the most important of which is the small-scale roughness evident on the evaporative liquid–vapor interface. The roughness on the bubble causes it to appear opaque in the photographs, the most important of which is the small-scale roughness evident on the evaporative liquid-vapor interface. The roughness on the bubble causes it to appear opaque in the evaporating surface is only visible in certain photographs, depending on the orientation of the initial nucleation. Figure 3 shows a drop of isopentane that is nearly completely vaporized. Only the lower portion of the drop remains liquid. Subject to the "fish-eye" lensing effect of the remaining liquid, it is possible to see up inside the drop and view the perturbations on the evaporating surface. This behavior is quite different from that observed on vapor bubbles growing in boiling liquids at lower superheats, where the bubble surface usually has a smooth, glassy appearance.

A second feature is a characteristic bulging into the host fluid that is observed in each case when the initial bubble has grown large enough to contact the boundary of the drop. This feature was first observed in butane by Shepherd and Sturte-

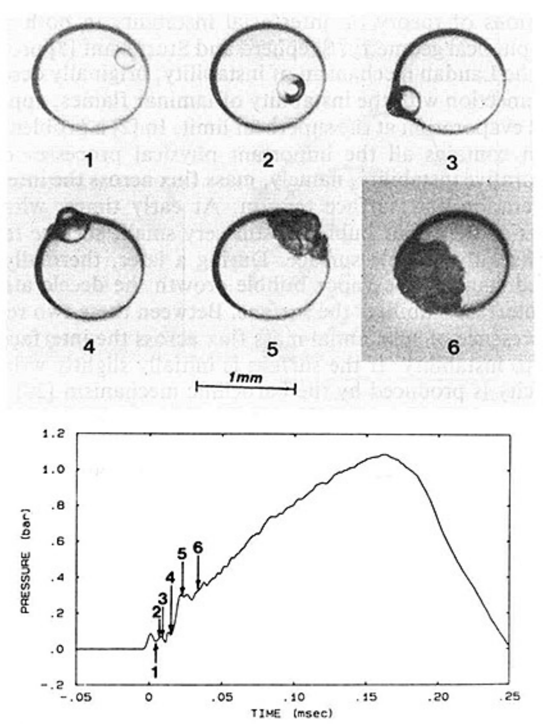

Fig. 9 Photographs and pressure trace of ether droplets exploding at 2 bar ambient pressure. Before the onset of instability (1, 2, 3, and 4) the radiated pressure is at a lower level than afterward (5, 6). Baffled pressure transducer 5 mm from drops.

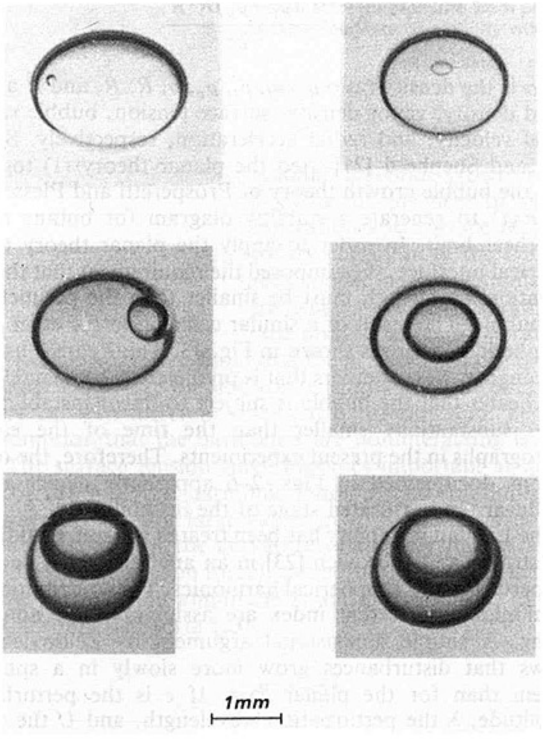

Fig. 10 Ether droplets exploding at 4.2 bar ambient pressure. Times for the first five photographs at 20 μsec, 80 μsec, 240 μsec, 1.22 msec, and 1.42 msec, respectively.

vant [5] and occurs in all three liquids in the present experiments (see Fig. 4). Figure 5 shows that the bulge persists in the form of a smooth caplike structure even after the drop has completely vaporized.

Figure 6 shows a series of photographs of isopentane in which the initial vapor bubble and subsequent caplike structure had formed on the side of the drop *away* from the viewer. As a result, the scale of the perturbations on the evaporating surface may be observed. Although the roughening appears random in orientation and many length scales are present, the length scale of the smallest perturbations appears to remain roughly constant at a value of about 100 μm throughout the evaporation process. This observation will be relevant below in the discussion of the theoretical models for the instability.

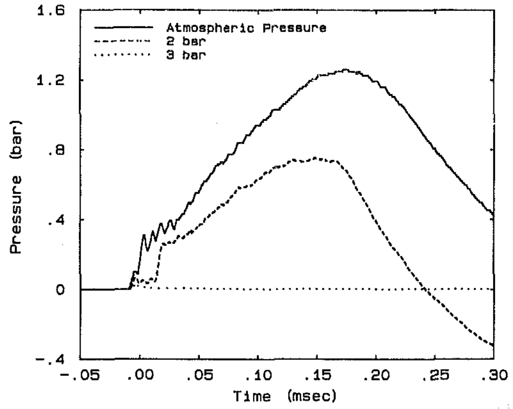

Fig. 11 Superposition of pressure signals radiated from ether droplets. Pressure, drop diameter, and distance from baffled pressure transducer: bottom, 3 bar, 1.6 mm, 4.4 mm; middle, 2 bar, 1.3 mm, 6 mm; top, atmospheric pressure, 1.2 mm, 6 mm.

Figures 7 and 8 are representative pressure traces for the explosion of two different drops of ether at atmospheric pressure. Figure 7 shows the typical early-time behavior during the vaporization process. The small-scale pressure oscillations in the first 40 μsec are probably due to the reverberations within the drop of the initial blast wave produced by the nucleation. The pressure reaches a maximum after about 150 μsec when the evaporation is complete. The overpressure in the bubble and the kinetic energy in the surrounding fluid cause the vapor bubble to continue to expand and overshoot the equilibrium radius. As a consequence, it subsequently collapses violently and oscillates on a millisecond time scale, producing the pressure oscillations shown in Fig. 8. During the oscillations the acceleration of the bubble surface is large and the surface breaks up due to Rayleigh–Taylor instability [5].

By increasing the ambient pressure to 2 bar it is possible to observe the onset of the instability during the vaporization of ether. Figure 9 shows a sequence of photographs of drops all of approximately 1 mm diameter at various stages of vaporization. Note that at early times (especially picture 1) the surface of the vapor bubble appears smooth. Then after about 25 μsec (*picture 5) considerable roughness has developed and the* vapor region appears opaque. The distortion of the interface corresponds to a dramatic increase of the far-field pressure by as much as a factor of 5, indicating a jump in the vaporization rate.

If the ambient pressure is increased above 3 bar it is possible to suppress the instability altogether. Figure 10 shows the vaporization of ether at 4.2 bar. In each case the instability is no longer present and the growing vapor bubble is smooth. As has been noted by other authors (e.g., [9, 10]), the characteristic popping sound accompanying the explosion of a drop at atmospheric pressure is no longer evident at high pressure.

Figure 11 shows a superposition of three pressure traces for drops of ether, all of approximately the same size (typically 1.4 mm), at ambient pressures of 1, 2, and 3 bar. The pressure recorded when the instability is suppressed at 3 bar is several orders of magnitude less than at atmospheric pressure. Also, the time for the drop to completely evaporate is substantially increased. For example, a 1.5-mm-dia drop typically takes about 170 μsec to vaporize at atmospheric pressure. This time

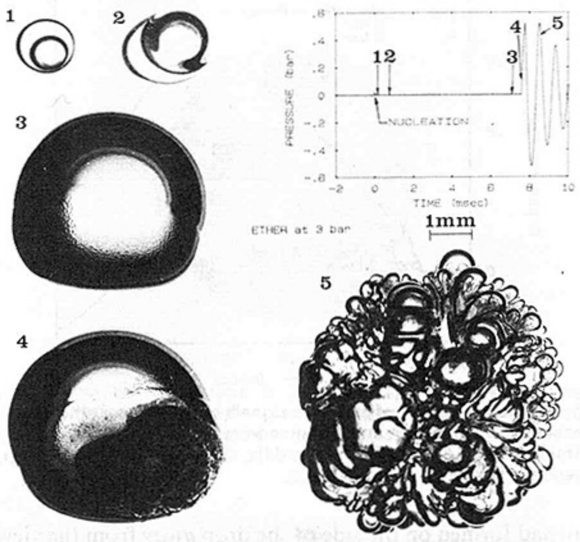

Fig. 12 Ether at 3 bar ambient pressure. Demonstration of low pressure radiated during bubble growth compared to large pressures after the explosion and during subsequent oscillation. In picture 3 the liquid cap with the orange-peel disturbance is in the lower portion of the photograph. Pressure transducer 6 mm from drops.

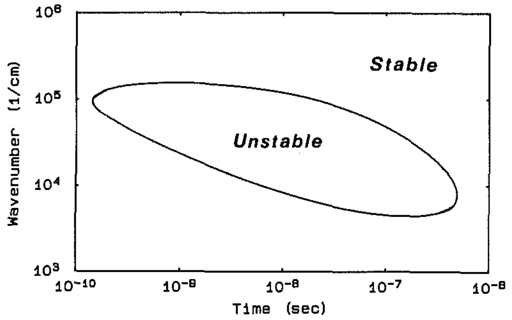

Fig. 13 Neutral stability curve from planar theory for ether at atmospheric pressure

is increased by roughly a factor of 30 to about 5 msec at 3 bar.

The range of ambient pressures between violently unstable boiling and stabilized boiling (in particular, at about 3 bar in ether) in which a kind of metastable or transitional stability is found, provides an important opportunity for documenting the detailed behavior of explosive boiling. The pressure trace of Fig. 12 shows a remarkable behavior, in which for about 7 msec, while the droplet is evaporating stably, the overpressure measured 5 mm away is less than 0.005 bar, whereupon a sudden impulse causes the bubble to grow rapidly and then oscillate violently, as with unstable boiling. The photographs in Fig. 12 show that during the early stages of vaporization at these conditions the bubble surface is completely smooth, but later, when the remaining liquid forms only a thin cap at the end of the bubble, the liquid–vapor interface of the "stably" vaporizing liquid develops small-amplitude short-wavelength disturbances (giving the appearance of "orange peel"). Finally (picture 4), the violent instability is triggered at some point near the edge of the liquid cap, rapidly spreads out radially, and the remaining liquid boils explosively. Picture 5 in Fig. 12 shows the consequences of the Rayleigh–Taylor instability of the bubble after only one rebound. A detailed study of the evaporative behavior in this transitional regime will be the subject of a forthcoming publication.

4 Discussion

4.1 Instability Theory. In this section we consider the implications of theory on interfacial instability in both planar and spherical geometry. Shepherd and Sturtevant [5] proposed that the Landau mechanism of instability, originally described in connection with the instability of laminar flames, applies to rapid evaporation at the superheat limit. In [2] a problem is set which contains all the important physical processes of the evaporative instability, namely, mass flux across the interface, acceleration and surface tension. At early times, when the radius of the vapor bubble is still very small, surface tension stabilizes the bubble surface. During a later, thermally controlled stage of the vapor bubble growth the deceleration of the interface stabilizes the surface. Between these two regimes the presence of substantial mass flux across the interface may lead to instability. If the surface is initially slightly wrinkled, vorticity is produced by the baroclinic mechanism [20] in the flow transition at the interface and appears in the vapor phase. For a planar interface the Landau theory yields a dispersion relation between the nondimensional growth rate Ω and wave number K [2].

$$\Omega^2+\frac{2\alpha}{\alpha+1}\Omega K+\frac{1}{\alpha+1}\left[\alpha(\alpha-1)K^2+\frac{2N_W K+K^3}{2N_I}\right]=0 \qquad (1)$$

where Ω and K are related to the corresponding dimensional quantities (ω, k) by

$$\Omega=\omega\frac{R}{\dot{R}} \qquad K=kR \qquad (2)$$

In equation (1) the effects of surface tension and acceleration are contained in the "inertia number" and the Weber number

$$N_I=\frac{\rho_l R\dot{R}^2}{2\sigma} \qquad (3)$$

$$N_W=\frac{(\rho_l-\rho_v)R^2\ddot{R}}{2\sigma} \qquad (4)$$

and α is the density ratio ρ_v/ρ_l. ρ_l, ρ_v, σ, R, $\dot{R}$, and $\ddot{R}$ are the liquid density, vapor density, surface tension, bubble radius, radial velocity, and radial acceleration, respectively. Sturtevant and Shepherd [21] used the planar theory (1) together with the bubble growth theory of Prosperetti and Plesset [22] for $R(t)$ to generate a stability diagram for butane at the superheat limit. In order to apply the planar theory to the spherical interface, they imposed the requirement that the perturbation wavelength must be smaller than the perimeter of the bubble. The result of a similar calculation for ether at atmospheric pressure is shown in Fig. 13. The figure illustrates the range of wavenumbers that is predicted to be unstable and it indicates that the bubble is subject to linear instability for times substantially smaller than the time of the earliest photographs in the present experiments. Therefore, the observations documented in Figs. 2–6 apparently depict a late, nonlinear, and saturated stage of the instability.

The Landau instability has been treated for spherical flames by Istratov and Librovich [23] in an analysis which develops the perturbations in spherical harmonics. The contributions of harmonics of different index are assumed to be noninteracting. A simple dimensional argument by Zeldovich [24] shows that disturbances grow more slowly in a spherical system than for the planar case. If ϵ is the perturbation amplitude, λ the perturbation wavelength, and U the radial velocity of the bubble, then

$$\frac{d\epsilon}{dt}\sim\frac{\epsilon U}{\lambda} \qquad (5)$$

For a plane interface λ is constant and (5) leads to exponential growth (with growth parameter $\omega \sim U/\lambda$) for ϵ. However for a spherical bubble, if there is no energy transfer between modes the wavelength of a given spherical harmonic grows like the radius and (5) leads to algebraic growth in time for ϵ, i.e.,

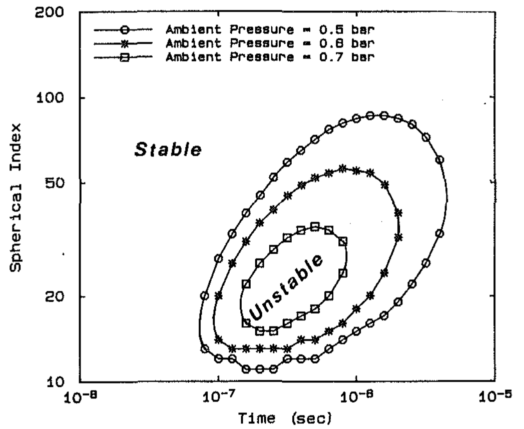

Fig. 14 Neutral stability curves from spherical theory for ether at ambient pressures of 0.5, 0.6, and 0.7 bar absolute

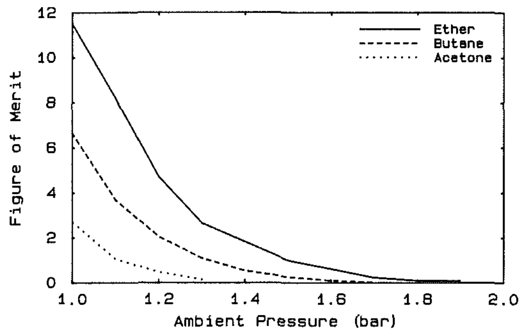

Fig. 15 Variation of figure of merit with ambient pressure from planar theory for three different liquids showing increase of stability with increasing pressure

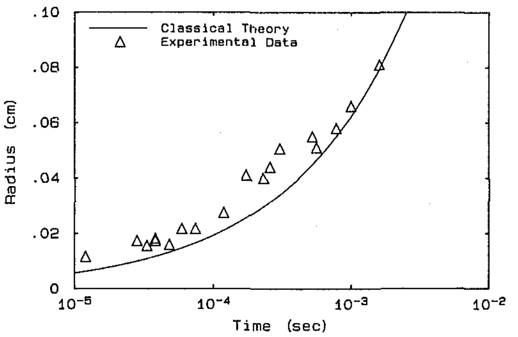

Fig. 16 Comparison between theory and experiment for stable bubble growth in ether at 3 bar (T_{sat} = 342.7 K, T_{sl} = 422.7 K)

$$\epsilon \sim t^{\omega'} \tag{6}$$

where ω' is now the (nondimensional) algebraic growth rate.

To apply the spherical analysis to the problem of rapid vaporization, the effects of acceleration and surface tension have been included in the boundary condition at the bubble surface. In this way a quasi-steady model may be formulated for bubbles that are growing with arbitrary velocity, assuming that the instability responds to the instantaneous acceleration and surface tension forces and that the previous history is not important. However, the surface tension terms introduce a coupling between different spherical harmonics and, hence, the assumption that the harmonics are noninteracting is not valid. The surface tension force becomes important at large values of the spherical harmonic index n, corresponding to small wavelengths. For large values of n, if one nevertheless neglects the coupling, the curvature of the interface κ (and, hence, the surface tension force), can be modeled as a function of n, the perturbation amplitude ϵ, and the radius R, in the following simplified form [23]

$$\kappa = -\epsilon \frac{n(n+1)}{R^2} \tag{7}$$

The resulting dispersion relation between ω' and n is

$$\omega'^2 + b\omega' + c = 0 \tag{8}$$

where

$$b = 3 + \frac{n(1+2\alpha n)}{(n+1)\alpha + n} \tag{9}$$

$$c = 3 + \frac{\alpha(\alpha n+1)(n^2-1) - \alpha n^2(n-1)}{(n+1)\alpha + n} - \frac{n(n+1)\left[N_W - \dfrac{n(n+1)}{2}\right]}{[(n+1)\alpha + n]N_I} \tag{10}$$

Figure 14 shows neutral stability contours in ether at various pressures. Kinks appear in the lower sections of the curves because only integral values of the spherical harmonic index n are considered due to the spherical constraint. Positive values of ω' indicate that the perturbation amplitude grows more rapidly than the radius, leading to instability. Note that the unstable region shrinks with increasing pressure and in fact at atmospheric pressure the interface is predicted to be stable at all times. This is in disagreement with the experimental results, from which it is clear that the instability is present at atmospheric pressure. Apparently the instability occurs at such small wavelengths that the spherical constraint does not hold.

The nondimensional number

$$F = \omega_{max}\tau \tag{11}$$

where ω_{max} is the maximum growth rate at a given pressure and τ is the time interval during which a growing bubble is predicted to be linearly unstable, is a useful parameter to measure the effect of ambient pressure on the predictions of planar instability theory. It is a measure of the amount the amplitude of a perturbation is magnified during the time the interface is linearly unstable. Figure 15 shows the effect of ambient pressure on this "figure of merit" for three different liquids. This plot confirms the stabilizing effect of increasing the ambient pressure. In addition, the figure is useful for assessing the *relative* stability of the different liquids, and suggests that acetone is less prone to instability than both butane and ether. When droplets of acetone were heated to the superheat limit it was observed that they vaporized *stably* at *atmospheric* pressure, in sharp contrast to the violent unstable boiling that occurs in butane and ether at this pressure. On the basis of the liquids tested, it is therefore suggested that for practical estimates of the susceptibility to instability, a figure of merit of 3 be taken as a lower limit for instability.

Because bubble growth rate depends strongly on the bubble surface temperature (and therefore on the ambient temperature), due to the temperature dependence of vapor pressure (density), the calculated instability growth rates are also strongly temperature dependent. Therefore, in any real situation where temperature nonuniformities are present, departures from the quantitative predictions of the theory should be expected. In particular, it is likely that in the regime of transitional stability, which might occur very frequently in practice, one of a number of different possible kinds of disturbances could serve to trigger a breakdown to violent instability.

4.2 Classical Bubble Growth Theory. The bubble growth theory of Prosperetti and Plesset [22] shows that in a uniformly superheated liquid, growth proceeds in three stages: first, a stage dominated by surface tension, in which the bubble grows from a critical radius; second, an inertially controlled stage during which the bubble grows at a constant rate; and, finally, an asymptotic stage governed by heat transfer in which the radius grows as $t^{1/2}$. Figure 16 shows the prediction of bubble growth in ether in the thermally dominated stage. The experimental data shown are for ether at 3 bar when the bubble surface is smooth; the bubble radius was estimated from two simultaneous perpendicular views of the bubble. The discrepancy between the theoretical curve and experimental results is not surprising considering the fact that the finite size of the drop and heat transfer from the host fluid to the evaporating surface and to the vapor in the bubble are not accounted for in the theory. In any case, the agreement between theory and experiment is much better than when the instability is present [5].

5 Conclusions

In a series of experiments with pentane, isopentane, and ethyl ether it has been shown that the instability of rapid vaporization may be suppressed by increasing the ambient pressure. At atmospheric pressure, the instability of vapor bubbles in liquids boiling at the limit of superheat substantially enhances the vaporization rate. Increasing the ambient pressure stabilizes the liquid-vapor interface and at high pressure the surface of the growing vapor bubble becomes smooth. The pressure field radiated from single exploding droplets of ether is two orders of magnitude smaller when the evaporating surface is stabilized. At intermediate pressures the vaporization occurs in two stages, an initially stable phase during which the radiated pressure is rather small, followed by a sudden transition to the destabilized configuration with an attendant jump of radiated pressure. It is observed that the onset of instability in 1.5-mm-dia drops may be delayed for up to 10 msec and that it can be initiated at very late stages in the vaporization. Similar dynamic effects are observed in each of the three fluids tested; however, the ambient pressure at which a smooth interface is first observed varies with the liquid. It is observed that the predominant spatial scale of the distortions on the (unstable) liquid-vapor interface at atmospheric pressure remains relatively constant and equal to about 100 μm throughout the vaporization process.

Plane and spherical versions of the Landau instability theory have been examined in the context of rapid evaporation at the superheat limit. The theory predicts that a spherical interface is inherently more stable to disturbances than its planar analog. When applied to vaporization at the superheat limit the spherical theory predicts a stable bubble surface at atmospheric pressure, in disagreement with the observations. Apparently, the instability occurs at such large wavenumbers that the spherical constraint does not hold. From planar theory, the product of the maximum growth rate and the time interval the interface is predicted to be linearly unstable measures the susceptibility to instability. For practical estimates it is suggested that a value of 3 for this parameter be taken as a lower limit for instability.

It is widely recognized that the homogeneous nucleation of highly superheated liquids plays an important role in some large-scale vapor explosions [25]. The interfacial instability observed in the present and previous [5] experiments is responsible for the extremely large mass fluxes and heat transfer rates characteristic of vapor explosions. The present results serve to emphasize that a great deal of experimental research at small scale must yet be done before sufficient information is available to properly model vapor explosions and to predict their severity.

6 Acknowledgments

This work was supported by a grant from the United States Department of Energy, project agreement DE-AT03-80ER10634.

References

1 Landau, L. D., "On the Theory of Slow Combustion," *Acta Physiochimica URSS*, Vol. 19, 1944, pp. 77–85.

2 Landau, L. D., and Lifshitz, E. M., *Fluid Mechanics*, Pergamon, 1959, p. 479.

3 Darrieus, G., "La Mécanique des Fluides," *La Technique Moderne*, 1938, pp. 15–16.

4 Darrieus, G., "Propagation d'un Front de Flamme," presented at Le Congrès de Mecanique Appliquée.

5 Shepherd, J. E., and Sturtevant, B., "Rapid Evaporation at the Superheat Limit," *J. Fluid Mech.*, Vol. 121, 1982, pp. 379–402.

6 Skripov, V. P., *Metastable Liquids*, Wiley, New York, 1974.

7 Reid, R. C., "Superheated Liquids," *Amer. Scientist*, Vol. 64, 1976, pp. 146–156.

8 Avedisian, C. T., and Glassman, I., "Superheating and Boiling of Water in Hydrocarbons at High Pressures," *Int. J. Heat Mass Trans.*, Vol. 24, No. 4, 1981, pp. 695–706.

9 Avedisian, C. T., and Glassman, I., "High Pressure Homogeneous Nucleation of Bubbles Within Superheated Binary Liquid Mixtures," ASME JOURNAL OF HEAT TRANSFER, Vol. 103, May 1981, pp. 272–280.

10 Avedisian, C. T., "Effect of Pressure on Bubble Growth Within Liquid Droplets at the Superheat Limit," ASME JOURNAL OF HEAT TRANSFER, Vol. 104, 1982, pp. 750–757.

11 Buchanan, D. J., "A Model for Fuel-Coolant Interactions," *J. Phys. D: Appl. Phys.*, Vol. 7, 1974, pp. 1441–1457.

12 Drumheller, D. S., "The Initiation of Melt Fragmentation in Fuel-Coolant Interactions," *Nucl. Sci. & Eng.*, Vol. 72, 1979, pp. 347–356.

13 Henry, R. E., and Fauske, H. K., "Nucleation Processes in Large Scale Vapor Explosions," ASME JOURNAL OF HEAT TRANSFER, Vol. 101, 1979, pp. 280–287.

14 Nelson, L. S., and Buxton, L. D., "Effects of Pressure on Steam Explosion Triggering in Corium-E Simulants," *Am. Nucl. Soc. Trans.*, Vol. 28, 1978, p. 448.

15 Dergarabedian, P., "The Rate of Growth of Vapor Bubbles in Superheated Water," ASME *Journal of Applied Mechanics*, Vol. 20, 1953, pp. 537–545.

16 Dergarabedian, P., "Observations on Bubble Growth in Various Superheated Liquids," *J. Fluid Mech.*, Vol. 9, 1960, pp. 39–48.

17 Florshuetz, L. W., Henry, C. L., and Khan, A. R., "Growth Rates of Free Vapor Bubbles in Liquid at Uniform Superheats Under Normal and Zero Gravity Conditions," *Int. J. Heat Mass Transfer*, Vol. 12, 1969, pp. 1465–1489.

18 Hewitt, H. C., and Parker, J. D., "Bubble Growth and Collapse in Liquid Nitrogen," ASME JOURNAL OF HEAT TRANSFER, Vol. 90, 1968, pp. 22–26.

19 Kosky, P. G., "Bubble Growth Measurements in Uniformly Superheated Liquids," *Chem. Eng. Sci.*, Vol. 23, 1968, pp. 695–706.

20 Turner, J. S., *Buoyancy Effects in Fluids*, The University Press, Cambridge, 1973.

21 Sturtevant, B., and Shepherd, J. E., "Evaporative Instability at the Superheat Limit," *Appl. Sci. Res.*, Vol. 38, 1982, pp. 85–97.

22 Prosperetti, A., and Plesset, M., "Vapour Bubble Growth in a Superheated Liquid," *J. Fluid Mech.*, Vol. 85, 1978, pp. 349–368.

23 Istratov, A. G., and Librovich, V. B., "On the Stability of Gas Dynamic Discontinuities Associated With Chemical Reactions. The Case of a Spherical Flame," *Astron. Acta.*, Vol. 14, 1969, pp. 453–467.

24 Zeldovich, Y. B., "Stability of Chemical Processes: The Semenov's Theory and Its Progress," in: *Chemical Kinetics and Chain Reactions*, Moscow, 1966, p. 574.

25 Reid, R. C., "Rapid Phase Transitions From Liquid to Vapor," *Advances in Chem. Eng.*, Vol. 12, 1983, pp. 105–208.

M. Khatib-Rahbar
Staff Scientist/Nuclear Engineer.

E. G. Cazzoli
System Analyst.

Department of Nuclear Energy,
Brookhaven National Laboratory,
Upton, NY 11973

Flow Excursion-Induced Dryout at Low Heat Flux Natural Convection Boiling

Flow excursion-induced dryout at low heat flux natural convection boiling, typical of liquid metal fast breeder reactors, is addressed. Steady-state calculations indicate that low-quality boiling is possible up to the point of the Ledinegg instability, leading to flow excursion and subsequent dryout in agreement with experimental data. A flow regime-dependent critical heat flux relationship based upon a saturated boiling criterion is also presented. Transient analyses indicate that premature flow excursion cannot be ruled out and the boiling process is transient dependent. Analysis of a loss-of-flow transient at high heat flux forced convection shows a significantly faster flow excursion leading to dryout, which is in excellent agreement with the results of the two-dimensional THORAX code.

Introduction

The Liquid Metal Cooled Fast Breeder Reactors (LMFBRs) are currently designed so that the maximum coolant temperature during normal operation is about 350 K below the saturation temperature. Nevertheless, despite this large temperature margin, hypothetical accidents must be envisioned that would lead to coolant temperature excursions and boiling.

Among the most serious of the postulated accidents are the primary loss-of-piping integrity accident and the complete loss-of-heat sink accident. Analysis models used to calculate the consequences of such accidents assume that once sodium boiling is initiated, dryout occurs as a result of rapid vapor bubble growth and subsequent subassembly flow stagnation or reversal.

There are many factors, such as transient flow redistribution between subassemblies, that will determine whether flow stagnation and boiling will occur in a particular subassembly in a particular accident [1]. Once boiling is initiated in an assembly, a substantial gravity pressure difference would exist between this assembly and other cooler assemblies in the core, giving rise to natural convection flow boiling accompanied by flow oscillations prior to excursion, often leading to fuel pin dryout.

Of particular interest to LMFBR safety analysis is the prediction of sodium boiling behavior and conditions conducive to the fuel pin dryout phenomenon.

Analytical models to date are based on the slug flow approximations developed mainly to describe sodium boiling behavior under conditions of high heat flux forced convection. Application of these types of models to recent experiments [2, 3] has shown them to be very sensitive to a number of input parameters, such as liquid film thickness at the time of voiding inception, degree of superheat, and wall friction factor [4].

Detailed multidimensional boiling models have also been developed and used to study sodium boiling phenomena in LMFBR rod bundles [5, 6]; however, due to the mathematical and numerical complexity of these methods, their application to long-duration natural convection transients is not very practical.

It is therefore the principal objective of the present work to formulate an analysis method for study of low heat flux sodium boiling; in particular, prediction of fuel pin coolability and dryout limits during natural convection transient events in LMFBRs [7].

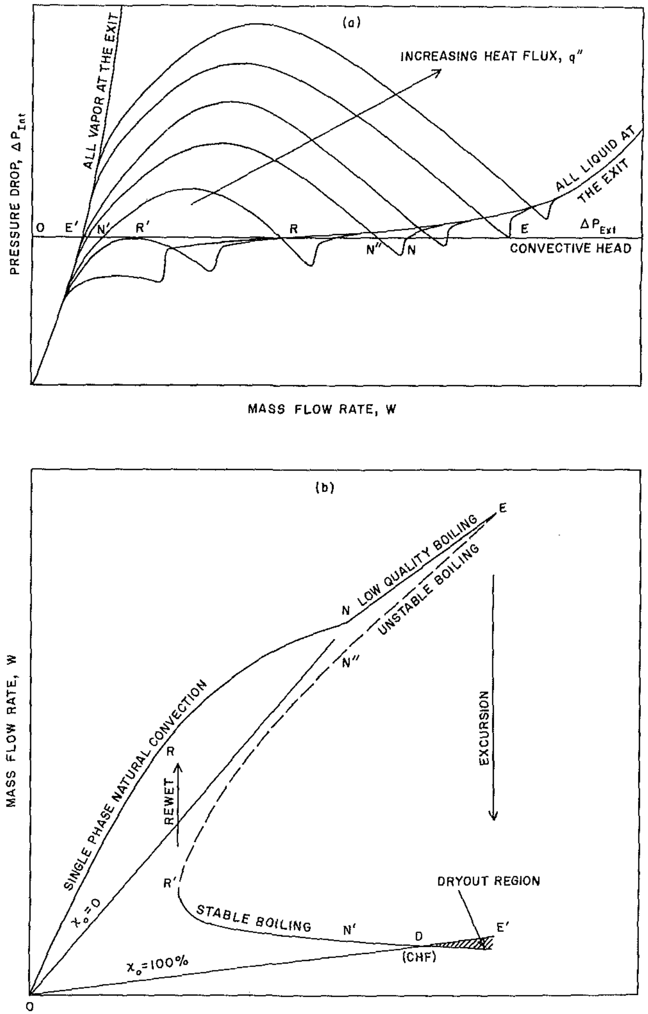

Fig. 1 Illustration of low-pressure natural convection boiling characteristics

---

Contributed by the Heat Transfer Division and presented at the 1983 ASME-JSME Thermal Engineering Conference, Honolulu, Hawaii, March 1983. Manuscript received by the Heat Transfer Division May 2, 1983.

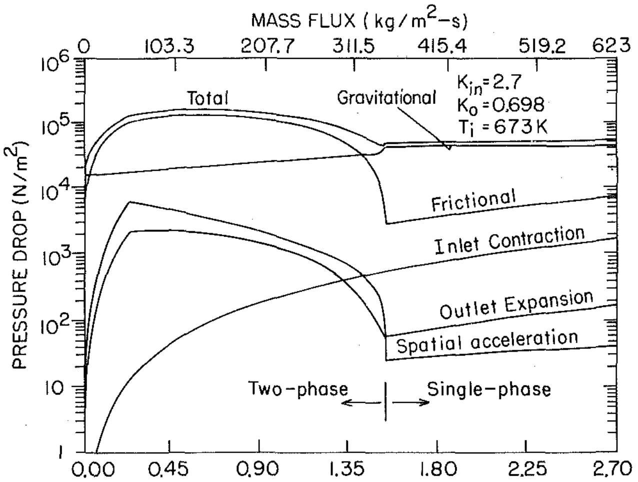

Fig. 2 Pressure drop characteristics of low-pressure sodium system

Sodium Boiling and Flow Excursion Phenomena

The low-pressure operation of sodium cooled fast reactors compared with light water reactors influences the overall pressure drop characteristic during boiling.

At low pressures, the flow rate can be multivalued for certain available pressure characteristics. The increase of the pressure drop as the flow rate is reduced to cause boiling is due to an increase in the frictional component and the requirement of the extra pressure head to produce the necessary acceleration from the single-phase fluid to a two-phase mixture [8–11].

For low-pressure sodium boiling, the implications of these S-shape pressure drop characteristics are that, at the onset of boiling, flow instabilities can develop which may induce a flow excursion possibly causing the Critical Heat Flux (CHF) conditions to be exceeded. The flow excursion instability, also referred to as Ledinegg instability, is explained in detail by Bour'e et al. [9] and Yadigaroglu [10].

A schematic of a typical pressure drop versus flow rate and heat flux characteristics for sodium under natural convection condition is shown in Fig. 1(*a*). It is seen that at high mass flow rates the total ΔP_{int} merges with single-phase liquid pressure drop for a nonboiling system, while for very low mass flow rates, the pressure drop is essentially the same as for single-phase vapor. For the intermediate values of mass flow rate, ΔP_{int} exhibits a local minimum and maximum. It can be seen that this behavior is due to the corresponding trends in the gravitational, frictional, and spatial acceleration and other components of the total internal pressure drop as shown in Fig. 2.

The intersections of the internal pressure drop curves with the external driving head ΔP_{ext} (horizontal line) represent possible operating conditions shown in Fig. 1(*b*). The dashed line indicates the unstable operating points, while the solid lines show the stable conditions. It is therefore evident that for certain values of heat flux, multiple solutions exist for the mass flow rate and thus, the operating condition is strongly dependent upon the operational history.

The boiling regimes identified on Fig. 1(*b*) consist of:

Low-Quality Boiling (*Line NE*). The operating points on this line correspond to the stable low-quality boiling regime. At E, boiling becomes unstable and flow excursion takes place.

Unstable Boiling (*R'N"E*). Operation along this curve is statically unstable and can lead to flow excursion. Also, due to the close proximity of the low-quality boiling (Line NE) and the unstable boiling mode solutions, operation with boiling in this heat flux range is expected to be oscillatory in nature, and can often lead to premature excursion.

Stable High Quality (*R'N'DE'*). Vapor quality along this path is high and the fluid approaches saturated vapor condition at D, at which point CHF takes place. Therefore, stable operation beyond D is considered unsafe, and can cause fuel pin failure. Furthermore at R' the flow is unstable and can recover to high flow natural convection leading to restoration of single-phase flow.

It must be noted that the flow excursion (jump from E to E') is very critical in terms of CHF considerations; if exit quality is greater than or equal to 100 percent following excursion to low flow condition, dryout automatically occurs.

Steady-state single-phase and two-phase natural convection behavior of channel flows can be examined through solution of the steady-state discretized energy and momentum equations of the form

$$h_j = h_{j-1} + \frac{N\pi D\Delta X_j q_j''}{W} \qquad j=2,3,\ \ldots\ ,M \tag{1}$$

and

Nomenclature

A = flow cross-sectional area, m^2
C = constant in the friction factor correlation
D = rod diameter, m
D_e = equivalent hydraulic diameter, m
f = single-phase friction factor
g = gravitational acceleration, m/s^2
h = fluid enthalpy, J/kg
h_f = enthalpy of saturated liquid, J/kg
h_g = enthalpy of saturated vapor, J/kg
h_{fg} = enthalpy of vaporization = $h_g - h_f$, J/kg
i = inlet
j = node number
K_{in} = inlet loss coefficient
K_o = outlet loss coefficient
L = total length, m
L_h = heated length, m
M = total number of nodes
N = number of rods per assembly
n = exponent in the friction factor correlation
o = outlet
P = pressure, N/m^2
P_h = heated perimeter = $N\pi D$, m
q'' = heat flux, W/m^2
T = temperature, K
t = time, s
v_f = specific volume of saturated liquid, m^3/kg
v_g = specific volume of saturated vapor, m^3/kg
v_{fg} = $v_g - v_f$, m^3/kg
W = mass flow rate, kg/s
X_{tt} = Lockhart-Martinelli parameter
X = axial position, m
Z = elevation, m
α = void fraction
Δh_{sc} = inlet subcooling = $h_f - h_i$, J/kg
ΔT_{sc} = inlet subcooling = $T_f - T_i$, K
μ_f = dynamic viscosity of saturated liquid, N-s/m^2
μ_g = dynamic viscosity of saturated vapor, N-s/m^2
μ_{fg} = $\mu_g - \mu_f$, N-s/m^2
$\langle\rho\rangle$ = average density, kg/m^3
ρ^* = momentum-averaged "apparent" density, kg/m^3
ρ_f = density of saturated liquid, kg/m^3
ρ_g = density of saturated vapor, kg/m^3
ϕ = two-phase pressure drop multiplier
ϕ_o = two-phase pressure drop multiplier at the channel outlet
χ = quality

$$\Delta P = \frac{1}{2}\left(\frac{W}{A}\right)^2 \Bigg[\sum_{j=2}^{M} \frac{\phi_j f_j \Delta X_j}{D_e \rho_f} + \Bigg(\frac{(1-\chi_o)^2}{\rho_f(1-\alpha_o)}$$

$$+ \frac{\chi_o^2}{\rho_g \alpha_o} - \frac{1}{\rho_i}\Bigg) + \frac{K_{in}}{\rho_i} + \frac{K_o \phi_o}{\rho_f}\Bigg] + g \sum_{j=2}^{M} \langle \rho_j \rangle \Delta Z_j \qquad (2)$$

A number of two-phase flow multipliers for annular flow regime are available as given by Collier [11] and Wallis [12]; however, at extreme values of the quality they can be highly inaccurate. For the present analysis, the homogeneous flow model based upon the Blasius form of the friction factor and the McAdams definition of the mixture viscosity also recommended by Ishii and Fauske [13] would appear to be the most appropriate choice; that is

$$\phi_j = \left(1 + \chi_j \frac{v_{fg}}{v_f}\right)\left(1 - \chi_j \frac{\mu_{fg}}{\mu_g}\right)^{-0.25} \qquad (3)$$

The two-phase flow multiplier for the outlet orifice region is based upon the empirical modification proposed by James [14] and given in [11, p. 91]

$$\phi_o = 1 + \frac{v_{fg}}{v_f} \chi_o^{1.5} \qquad (4)$$

The void fraction α is determined using the following relation [15]

$$\alpha = \frac{1}{1 + 0.28 X_{tt}^{0.71}} \qquad (5)$$

where the two-phase flow modulus, also known as the Lockhart-Martinelli parameter, is defined as

$$X_{tt} = \left(\frac{1-\chi}{\chi}\right)^{0.9} \left(\frac{\rho_g}{\rho_f}\right)^{0.5} \left(\frac{\mu_f}{\mu_g}\right)^{0.1} \qquad (6)$$

The Lockhart-Martinelli void fraction relation, approximated by equation (5), has been found to be in excellent agreement with the recent liquid metal test data as discussed by Costa [16].

The single-phase friction factor is defined by

$$f = C\,\mathrm{Re}^{-n} \qquad (7)$$

where $n = 1$ for laminar flow and $n = 0.25$ for turbulent flow.

For laminar flow through wire-wrapped fuel assemblies, C is measured to be constant and equal to 84 [17]. On the other hand, for turbulent flow C is a complicated function of the pitch-to-diameter ratio and the spiral wire lead as correlated recently [18, 19].

The operational regimes identified in Fig. 1 illustrate that single-phase natural convection flow exists along the curve ON

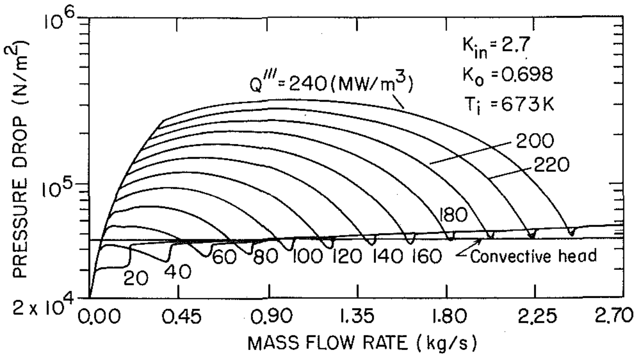

Fig. 3 Typical LMFBR fuel assembly steady-state pressure drop versus flow characteristics at various power densities

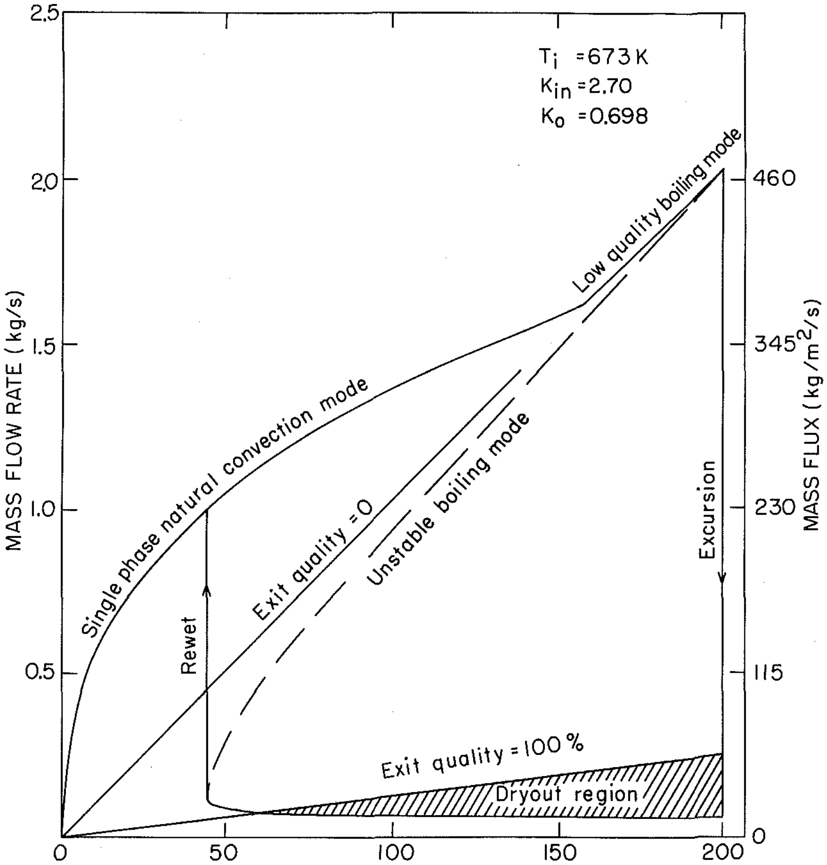

Fig. 4 Typical boiling map at high inlet subcooling

and the flow rate and enthalpy rise can be derived by solving equations (1), (2), and (7) along with an equation of state for density to obtain [20]

$$W \sim q''^{\,1/(3-n)} \tag{8}$$

and

$$\Delta h \sim q''^{\,(2-n)/(3-n)} \tag{9}$$

Equations (8) and (9) indicate the importance of the flow regime change during natural convection cooling, that is, for laminar flow both W and Δh are proportional to $\sqrt{q''}$; while for turbulent flow $W \sim q''^{0.36}$ and $\Delta h \sim q''^{0.64}$. Therefore it is essential to include the Reynolds number dependence for accurate prediction of natural convection behavior [20].

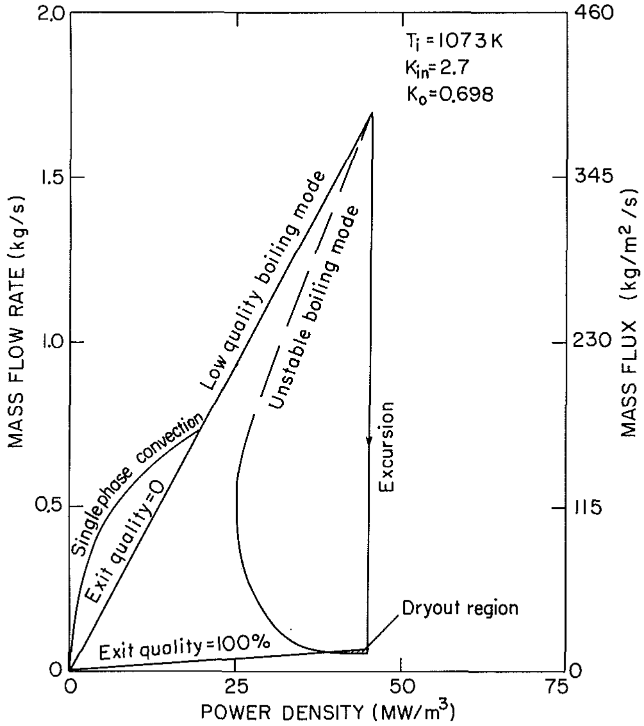

Fig. 5 Typical boiling map at low inlet subcooling

The heat flux corresponding to the intersection of the saturated vapor line (χ_0 = 100 percent) and the high-quality curve is of special significance. An approximate analytical solution for this intersection can be found, assuming that the nonboiling length is much smaller than the total length (very small inlet subcooling). Solving the coolant momentum equation for the condition that exit quality is 100 percent and using an all vapor friction factor, one obtains [7]

$$W \simeq \rho_g A \left[\frac{2g(\rho_f-\rho_g)D_e^{1+n}}{C\mu_g^n \rho_g^{1-n}}\right]^{1/(2-n)} \tag{10}$$

In other words, in order to maintain a dried-out region in the upper part of the rod bundle, the vapor production rate in the lower part of the rod bundle must be sufficient to maintain voiding, and thus prevent re-entry of liquid for rewetting, and therefore, the heat flux corresponding to this vapor production rate is termed the "critical heat flux" and is determined by substituting equation (10) into the energy equation to obtain

$$q''_{\mathrm{CHF}} \geq \left[\frac{2g\rho_g(\rho_f-\rho_g)D_e^{1+n}}{C\mu_g^n}\right]^{1/(2-n)} \times \frac{A}{\pi N D L_h}\,(\Delta h_{sc}+h_{fg}) \tag{11}$$

Again, the influence of flow regime[1] is clearly evident. Equations (10) and (11) are similar to the re-entry criterion proposed by Dunn [21] and later modified by Fauske and Ishii [22]. These equations treat the flow regime explicitly, and as such the vapor production rate and subsequently the heat flux does not depend on the magnitude of the Reynolds number, but only on its range (turbulent, transition, or laminar).

Therefore, for dryout to occur, it is sufficient that the critical heat flux (CHF) point be reached; however, sustained

---

[1] In this context, throughout this paper, "flow regime" refers to turbulent, laminar, and transition flow regimes.

Table 1 Comparison with ORNL-SBT test results

Test No.	Q"'(MW/m^3)	^{G}Experimental (kg/m^2-s)	^{G}Prediction (kg/m^2-s)			Comments		
			Low X	Unstable	High X	Experimental	Present Model	SAS3D[4]
107R2	37	72	102	--	--	Single Phase Natural Convection	Single Phase Natural Convection	Single Phase Natural Convection
109R1	42	205	113	--	--			
108R2	62	93	136	86	21			
100R3	87	103	160	133	18			
100R2	87	93	160	133	18			
100R4	100	113	171	156	17			
131R1	125	--	207	201	17	Chugging	Steady Boiling	Steady Boiling
132R1	137	--	227	222	17			
130R1	162	247	268	265	17			
129R1	162	103	268	265	17	Steady Boiling		
121R1	174	82	287	287	17			
125R1	174	93	287	287	17			
125R2	174	72	287	287	17			
127R1	186	82	--	--	17		Dryout	Rewet
120R1	186	247	--	--	17			
119R1	199	113	--	--	17			
126R2	199	93	--	--	17			
122R1	199	--	--	--	17	Dryout		Dryout
128R1	211	93, 31	--	--	17			
123R1	211	72, 41	--	--	17			
124R1	211	--	--	--	17			
126R1	211	--	--	--	17			

Table 2 Comparison of heat flux limits

T_{in} (K)	ΔT_{sc} (K)	$q''_{Excursion}$ (W/cm^2)	q''_{CHF} (W/cm^2) Model	q''_{CHF} (W/cm^2) Eq. (11)	Error(%)
673	527	25.7	7.30	6.4	14
873	327	15.3	6.15	6.0	3
1073	127	5.8	5.35	5.4	1

dryout requires significant vapor generation to maintain voiding and prevent liquid re-entry for rewetting. Furthermore, the dryout region extends into the entire upper region of the heated section.

Steady-State Analysis

Steady-state analysis of a typical LMFBR fuel assembly [23] is presented along with the examination of the Oak Ridge National Laboratory Sodium Boiling Test (SBT) facility measurements [2] in terms of flow excursion phenomena.

Figure 3 shows the calculated pressure drop versus flow rate characteristics at various power densities. The intersection of these curves with the constant, convective driving head provides the possible operating conditions shown in Fig. 4.

Single-phase natural convection flow exists for steady power densities up to 160 MW/m^3 (5.2 kw/pin). Low-quality stable boiling occurs for power densities greater than 160 MW/m^3 up to the critical power density of 200 MW/m^3 (6.5 kw/pin or 26 W/cm^2), beyond which flow excursion leading to dryout takes place. Recovery from high-quality low-flow conditions is not possible until the power density is reduced to about 44 MW/m^3 (1.43 kw/pin).

Figure 4 also illustrates that the two-phase unstable mode solutions are very close to the stable low-quality mode solutions; thus, premature flow excursions at power densities beyond 57 MW/m^3 (1.83 kw/pin or 7.3 W/cm^2) will lead to dryout and subsequent cladding temperature excursions.

The boiling map exemplified by Fig. 4 demonstrates a very important characteristic, that the sodium boiling phenomenon is strongly path dependent. Let us consider a case where a system is operating at low power, single-phase natural convection; increasing the power level in small quasi-steady steps leads to an increase in the convective flow along the single-phase natural convection curve. However, if the power level is increased in a large step or ramp, the system can easily move to the right of the two-phase unstable operating curve, and thus undergo a premature excursion. A similar situation arises during constant-power, variable-flow conditions, such as flow coastdown at decay power levels or protected loss-of-piping integrity accidents.

The impact of inlet subcooling is demonstrated in Figs. 4 and 5. Higher inlet temperature reduces the margin to boiling inception, and thus reduces the heat flux at which sodium flow excursion occurs. Furthermore, the heat flux interval between the flow excursion point and the rewetting process is also reduced as the inlet temperature is increased.

A similar analysis is performed for the ORNL single-channel sodium boiling experiments.

The geometric characteristics of the SBT test section are approximately equal to those of a full-scale LMFBR fuel assembly [2]. It consists of a radiant furnace heated region, followed by the simulated fission gas plenum region downstream of the heated zone. Table 1 summarizes the test results as compared to the present calculations and those predicted by the SAS3D computer code [4].

Experimentally, single-phase free convection behavior was observed for test section power densities less than 125 MW/m^3. Due to a high degree of wall superheat (100 K), a precise determination of boiling inception was not possible. To circumvent this operational problem, argon bubbles were injected upstream of the heated section to induce boiling; once boiling was established, the argon injection was terminated.

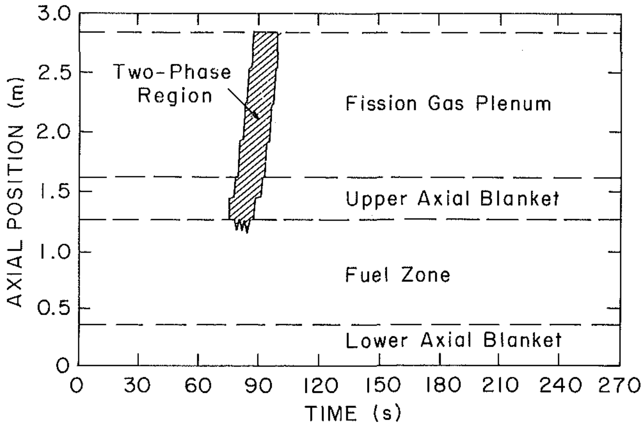

Fig. 6 Axial position of the two-phase region inside an LMFBR fuel assembly

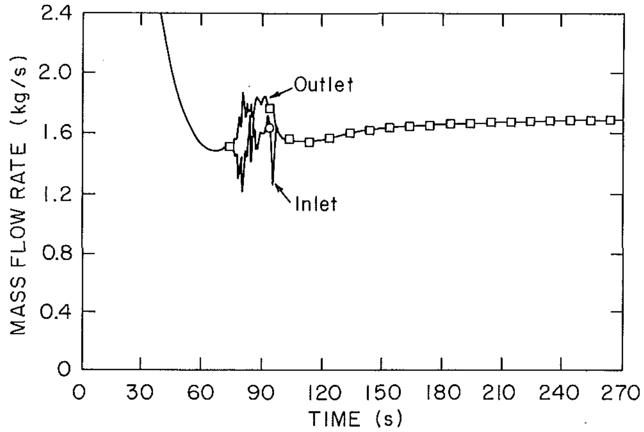

Fig. 7 Assembly inlet and outlet flow during stable natural convection boiling

A chugging instability was observed for test section power densities between 125 to 162 MW/m^3. This is attributed to the high degrees of superheat and associated lack of nucleation sites [2, 9].

A quasi-steady, oscillatory, slug-annular flow boiling behavior was observed for periods up to 45 min at power density between 162 and 200 MW/m^3. Evidence of more than one operating condition for the same test section power density was also observed for power densities near the lower end of the stable boiling regime.

At test section power densities above 200 MW/m^3, intermittent dryout conditions were encountered. Recovery from dryout was frequently observed.

These experimental observations are in direct agreement with analysis of the steady-state model, also summarized in Table 1. The disagreements are in part due to the inaccuracies in the test section power measurement caused by heat losses, which are shown [2] to be about 45 percent at 40 MW/m^3 and decrease to about 18 percent at 200 MW/m^3. Thus, the corrected power density at dryout is about 164 MW/m^3, which is within 6 percent of the predicted value. From these considerations, it can be concluded that CHF was reached as a result of the flow excursion, and somewhat prematurely.

Dryout Criterion

It is evident from the computational results supported by experimental data that dryout is expected to occur following flow excursion for heat flux levels greater than q''_{CHF}.

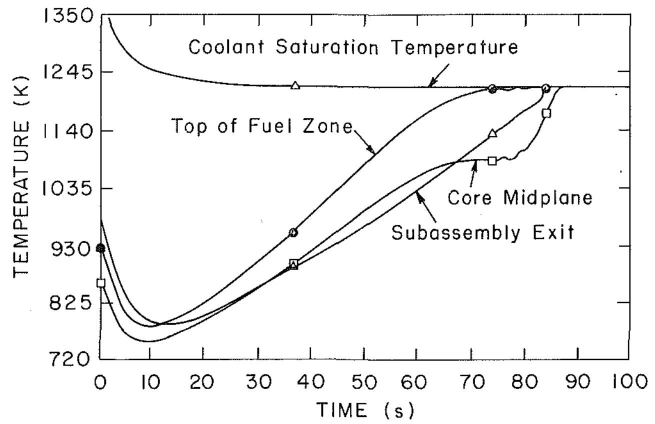

Fig. 8 Subassembly sodium temperature behavior for an unstable natural convection boiling leading to excursion

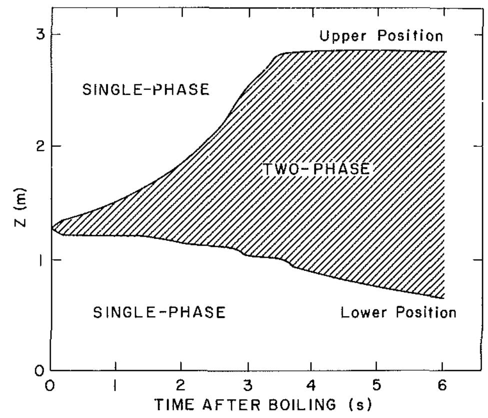

Fig. 9 Axial position of the voided region for a high heat flux forced convection boiling

Following flow excursion, the flow rate reduces to a level corresponding to the laminar-turbulent transition regime where $C \sim 0.4$ and $n = 0.25$ [20]; thus equation (11) becomes

$$q''_{\mathrm{CHF}} \geq \left[\frac{5g\rho_g(\rho_f-\rho_g)D_e^{1.25}}{\mu_g^{0.25}}\right]^{0.57} \frac{A}{\pi N D L_h}(\Delta h_{sc}+h_{fg}) \tag{12}$$

Comparison of the CHF limits given by equation (12) and those obtained from Figs. 4 and 5 and summarized in Table 2 shows excellent agreement.

It is seen that the CHF approaches the heat flux corresponding to the point of flow excursion, in the absence of inlet subcooling. Furthermore, comparison of the detailed numerical results shown in Figs. 4 and 5 with those obtained from equation (12) for CHF shows that the heat flux calculated from the approximate equation is conservative.

These results indicate that the decay heat may be removed via coolant boiling for decay power levels in the range of 3.7 percent (of nominal) at zero inlet subcooling and up to about 5 percent (of nominal) at maximum inlet subcooling of 527 K, somewhat higher than those obtained by Dunn [21] and Perkins and Bari [24] for the FFTF reactor using the SAS3D computer code, but lower than recent calculations reported by Fauske and Ishii [22] using a similar approximate equation and an empirical correlation based on the Katto's low flow convection CHF equation.

Transient Analysis

In order to examine the transient dependence of the Ledinegg instability and subsequent low flow operation, a transient model is developed and used to study this phenomenon.

The model is based on the solution of the conservation of mass, momentum, and energy equations of the form

$$\frac{\partial \rho}{\partial t}+\frac{1}{A}\frac{\partial W}{\partial X}=0 \tag{13}$$

$$\frac{1}{A}\frac{\partial W}{\partial t}+\frac{1}{A^2}\frac{\partial}{\partial X}\left(\frac{W^2}{\rho^*}\right)+\frac{f}{2\rho D_e A^2}W|W|+\rho g+\frac{\partial P}{\partial X}=0 \tag{14}$$

and

$$\rho\frac{\partial h}{\partial t}+\frac{W}{A}\frac{\partial h}{\partial X}=\frac{P_h}{A}q'' \tag{15}$$

The sonic effects associated with the fluid compressibility can be eliminated by assuming that fluid density may be evaluated as a function of fluid enthalpy only [7, 25].

These differential equations are integrated as described in the Appendix using the homogeneous two-phase flow multiplier (equation (7)) and the Lockhart-Martinelli slip flow correlation (equation (5)). At any location in the subassembly where the local average quality reaches unity, dryout is defined to take place.

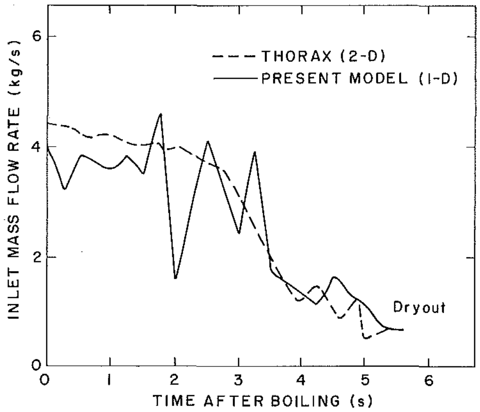

Fig. 10 Comparison of the present model with the ORNL two-dimensional calculations at high heat flux forced convection boiling

The liquid region above the bundle (upper plenum sodium) is in thermal-hydraulic interaction with the subassemblies, and its thermodynamic state is governed by mass and energy conservation for a mixing process. During transients in which sodium boiling occurs, the sodium vapor can condense through this mixing process in the upper plenum liquid sodium, provided the sodium inside the upper plenum is subcooled. It has been shown [26] that for slow loss-of-heat sink scenarios, the upper plenum sodium may approach saturation prior to the core internals.

Application of the present model to a typical LMFBR [23] postulated protected loss-of-flow accident corresponding to a decay heat level of 4.7 kw/pin is illustrated in Figs. 6 and 7. The sodium temperatures increase and reach saturation as a result of power-to-flow mismatch in the subassembly, leading to low-quality boiling at the boundary between the fuel and upper axial blanket regions (Fig. 6). The boiling region propagates upward, causing a significant increase in the fluid buoyancy and thus, improvement in the natural convection flow which sweeps the two-phase front out of the assembly and restores the single-phase natural convection flow. Figure 7 shows the sodium inlet and outlet flow oscillations foreseen by the steady-state analysis.

At 4.7 kw/pin corresponding to 145 MW/m^3, the steady-state boiling map of Fig. 4 yields a single-phase liquid flow of about 1.6 kg/s and an unstable boiling flow of about 1.4 kg/s. These values are in agreement with the transient results of Fig.

7, where as a result of power to flow mismatch in the subassembly, sodium boiling starts at about 75 s when sodium flow reaches a minimum of 1.4 kg/s followed by an increase in thermal buoyancy and thus reestablishment of single-phase natural convection flow of about 1.6 kg/s at about 95 s.

The boiling instability at this heat flux range can be demonstrated if the decay heat level is increased by a very small fraction to about 4.8 kw/pin. Figure 8 illustrates that the system undergoes a premature flow excursion, causing rapid downward propagation of the voided region and subsequent temperature rise as a result of this flow excursion-induced dryout. It also demonstrates that, at low heat flux, the flow excursion process is rather slow; it occurs over a 10 to 20 s time frame, in agreement with the experimental observations reported by Costa [16].

These results indicate that even though the steady-state calculations can predict the boiling existence with the appropriate range of flow and power condition, they cannot adequately quantify the spatial and temporal characteristics of the boiling process. It is seen that premature flow excursion can not be ruled out, particularly for severe transients where the flow rate may be changing quite rapidly; however, there is a possibility of maintaining low-quality oscillatory boiling for an extended period as demonstrated in recent ORNL rod bundle experiments [27].

Therefore, permanent fuel pin dryout can not occur prior to flow excursion. Furthermore, even if flow excursion does take place, the heat flux must be sufficiently high to cause dryout ($q'' \geq q''_{\text{CHF}}$).

High Heat Flux Boiling

The flow excursion process for high heat flux forced circulation systems is also governed by the Ledinegg instability.

In order to demonstrate the validity of the present model, and its applicability to typical LMFBR rod bundles at high heat flux, the model as incorporated into the SSC code [7] is used to simulate a loss-of-flow transient in a 217 pin bundle operating at 15 kw/pin power, 2 M/s sodium inlet velocity and 663 K sodium inlet temperature. Results of these calculations are then compared with a similar calculation performed by Dearing [5] using the THORAX code. THORAX is a two-dimensional porous blockage model, which has been used extensively in support of ORNL sodium boiling experiments, where excellent agreement between experimental and calculated dryout times has been reported [5, 27].

Loss of flow is simulated by changing the driving head in accordance with

$$\Delta P(t) = \begin{cases} [1 - 0.144t]\Delta P(t=0) & 0 \leq t \leq 3.6 \text{ s} \\ 0.48\ \Delta P(t=0) & t > 3.6 \text{ s} \end{cases} \tag{16}$$

Figure 9 shows the axial position of the voiding propagation in the bundle. It is seen that Ledinegg instability begins at the time when a large fraction of the bundle is voided leading to rapid flow excursion as illustrated in Fig. 10. Furthermore, dryout is predicted to occur at about 5.5 s following boiling inception in excellent agreement with the two-dimensional THORAX results [5].

Comparison of the flow excursion process for high and low heat flux boiling clearly indicates that the severity of flow excursion increases with increasing power level as a result of faster propagation of the boiling region inside the bundle. Furthermore, under low heat flux natural convection boiling conditions (generally a much slower process than the high heat flux forced convection boiling), the thermal inertia of the subassembly structural material can significantly influence the propagation of the boiling region through the subassembly.

Summary and Conclusions

Flow excursion-induced dryout at low heat flux natural convection sodium boiling, typical of liquid metal fast breeder reactor following loss of forced cooling with reactor shutdown, was addressed.

Steady-state predictions show that low-quality sodium boiling is possible up to the point of Ledinegg instability leading to flow excursion and subsequent dryout in agreement with ORNL-SBT data.

It was also demonstrated that due to the close proximity of the low-quality and unstable boiling modes, premature flow excursions can limit extended operation up to the point of Ledinegg instability and hence lead to dryout, provided the heat flux level is higher than that corresponding to the saturated boiling (q''_{CHF}).

A flow regime-dependent approximate heat flux relationship corresponding to the limit of safe operation was presented, and comparisons with a more detailed numerical solution at various inlet subcooling demonstrated good agreement in the conservative direction.

Furthermore, results of a transient calculation for a high heat flux-forced convection, loss-of-flow transient scenario was compared with results of a parallel calculation with the two-dimensional THORAX code, and showed a good agreement in predicted dryout time.

Premature flow excursion may preclude operation up to the limit of Ledinegg instability if sodium boiling could be avoided in the first minutes after reactor scram; subsequent boiling could remove sufficient decay heat to prevent cladding failure provided core uncovering has not taken place; this is in agreement with studies concluded recently [26].

Acknowledgments

This work was supported by the United States Nuclear Regulatory Commission (USNRC) and in part by the Power Reactor and Nuclear Fuel Development Corporation (PNC) of Japan.

References

1 Khatib-Rahbar, M., Guppy, J. G., and Agrawal, A. K., "Hypothetical Loss-of-Heat-Sink and In-Vessel Natural Convection: Homogeneous and Heterogeneous Core Designs," in: *Decay Heat Removal and Natural Convection in Fast Breeder Reactors*, A. K. Agrawal and J. G. Guppy, eds., Hemisphere, Washington, 1981.

2 Garrison, P. W., Morris, R. H., and Montgomery, B. H., "Dryout Measurements for Sodium Natural Convection in a Vertical Channel," Oak Ridge National Laboratory, ORNL/TM-7018, 1979.

3 Ribando, R. J., et al., "Sodium Boiling in a Full-Length 19-Pin Simulated Fuel Assembly (THORS Bundle 6A)," Oak Ridge National Laboratory, ORNL/TM-6553, 1979.

4 Klein, G., and Dunn, F., "SAS3D Analysis of Natural-Convection Boiling Behavior in the Sodium Boiling Test Facility," *Trans. Am. Nucl. Soc.*, Vol. 33, 1979, pp. 517-518.

5 Dearing, J. F., "Two-Dimensional Computational Modeling of Sodium Boiling in Simulated LMFBR Fuel Pin Bundles," *Trans. Am. Nucl. Soc.*, Vol. 38, 1981, pp. 755-757.

6 Schor, A. L., and Todreas, N. E., "A Four Equation Two-Phase Flow Model for Sodium Boiling Simulation of LMFBR Fuel Assemblies," *Proceeding of 10th Liquid Metal Boiling Working Group*, H. M. Kottowski and W. Peppler, eds., Karlsruhe, Federal Republic of Germany, 1982.

7 Khatib-Rahbar, M., and Cazzoli, E. G., "Modeling and Analysis of Low Heat Flux Natural Convection Sodium Boiling in LMFBRs," BNL-NUREG-51541, Mar. 1982.

8 Lahey, R. T., Jr., "The Analysis of System Pressure Drop Characteristics During Flow Boiling," *Trans. Am. Nucl. Soc.*, Vol. 38, 1981, pp. 770-771.

9 Bour'e, J. A., et al., "Review of Two-Phase Flow Instabilities," *Nucl. Eng. and Design*, Vol. 25, 1973, pp. 165-192.

10 Yadigaroglu, G., "Two-Phase Instabilities and Propagation Phenomena," in: *Thermohydraulics of Two-Phase Systems for Industrial Design and Nuclear Engineering*, J. M. Delhaye, M. Giot, and M. L. Riethmuller, eds., Hemisphere, Washington, 1981.

11 Collier, J. G., *Convective Boiling and Condensation*, McGraw-Hill, United Kingdom, 1972.

12 Wallis, G. B., *One-Dimensional Two-Phase Flow*, McGraw-Hill, New York, 1969.

13 Ishii, M., and Fauske, H. K., "Boiling and Dryout Behavior in a Liquid Metal Fast Breeder Reactor Subassembly Bundle Under Low Heat Flux and Low Flow Conditions," *Nucl. Sci. and Eng.*, Vol. 84, 1983, pp. 131–146.

14 James, R., "Metering of Steam-Water Two-Phase Flow by Sharp-Edged Orifices," *Proc. Inst. Mech. Engrs.*, Vol. 180, No. 23, 1965–1966, pp. 549–556.

15 Butterworth, D., "A Comparison of Some Void-Fraction Relationships for Co-Current Gas-Liquid Flow," *Int. J. of Multiphase Flow*, Vol. 1, 1975, pp. 845–850.

16 Costa, J., "Contribution to the Study of Sodium Boiling During Slow Pump Coastdown in LMFBR Subassemblies," in: *Symposium on the Thermal and Hydraulic Aspects of Nuclear Reactor Safety*, Vol. 2, O. C. Jones, Jr., and S. G. Bankoff, eds., ASME, New York, 1978.

17 Additon, S. L., and Parziale, E. A., "Natural Circulation in FFTF, A Loop-Type LMFBR," in: *Symposium on the Thermal and Hydraulic Aspects of Nuclear Reactor Safety*, Vol. 2, O. C. Jones, Jr., and S. G. Bankoff, eds., ASME, New York, 1977.

18 Novendstren, E. H., "Turbulent Flow Pressure Drop Model for Fuel Rod Assemblies Utilizing a Helical Wire-Wrap Space System," *Nucl. Eng. and Design*, Vol. 22, 1972, pp. 19–28.

19 Spencer, D. R., and Markley, R. A., "Friction Factor Correlation for 217-Pin Wire-Wrap-Spaced LMFBR Fuel Assemblies," *Trans. Am. Nucl. Soc.*, Vol. 39, 1981, pp. 1014–1015.

20 Agrawal, A. K., Khatib-Rahbar, M., and Madni, I. K., "Prediction of Decay Heat Removal Capabilities for LMFBRs and Comparison With Experiments," *Nucl. Eng. and Design*, Vol. 66, 1981, pp. 437–446.

21 Dunn, F. E., "Severe FFTF Natural Circulation Transients With Boiling," ANL/RAS 76-26, Sept. 1976.

22 Fauske, H. K., and Ishii, M., "Sodium Re-entry and Dryout Criteria Under Decay Power Conditions," *Proceedings of the International Meeting on Liquid Metal Fast Breeder Reactor Safety and Related Design and Operational Aspects*, Lyon-Ecully, France, July 19–23, 1982.

23 Clinch River Breeder Reactor Plant, Preliminary Safety Analysis Report, Project Management Corporation, 1975.

24 Perkins, K. R., and Bari, R. A., "SAS-3D Evaluation of Boiling at Decay-Heat Levels in FFTF," *Trans. Am. Nucl. Soc.*, Vol. 33, 1979, pp. 516–517.

25 Meyer, J. E., "Hydrodynamic Models for the Treatment of Reactor Thermal Transients," *Nucl. Sci. and Eng.*, Vol. 10, 1961, pp. 269–277.

26 Khatib-Rahbar, M., "Core Coolability Following Loss-of-Heat Sink Accidents," *Trans. Am. Nucl. Soc.*, Vol. 45, 1983, pp. 365–366.

27 Rose, S. D., et al., "Analysis of Natural Convection Sodium Boiling in a 61-Pin Simulated LMFBR Fuel Assembly," *Proceedings of 10th Liquid Metal Boiling Working Group*, H. M. Kottowski and W. Peppler, eds., Karlsruhe, Federal Republic of Germany, 1982.

APPENDIX

In order to permit an increase in the integration time step, sonic effects associated with fluid compressibility are eliminated by assuming that fluid density is a function of specific enthalpy only, that is

$$\rho = \rho(h, P^*) \tag{A1}$$

where P^* is a reference pressure.

Therefore, the conservation of momentum equation must be integrated over the entire subassembly (channel) for solution rather than solved in a piecewise manner [25]. For this prupose, we integrate equation (14) from $X=0$ to $X=L$ to obtain

$$\frac{L}{A}\frac{d\hat{W}}{dt} = (P_i - P_o) - \Delta P_{io} \tag{A2}$$

where

$$\hat{W} = \frac{1}{L}\int_0^L W\,dX \tag{A3}$$

and

$$\Delta P_{io} = \frac{1}{2A^2}\left\{\left[\frac{(1-\chi_o)^2}{\rho_f(1-\alpha_o)} + \frac{\chi_o^2}{\rho_g\alpha_o}\right]W_o^2 - \frac{1}{\rho_i}W_i^2\right] + \frac{1}{2}\int_0^L \frac{\phi \bullet f}{D_e\rho_f}\left(\frac{W}{A}\right)^2 dX + g\int_0^L \rho dZ \tag{A4}$$

The variation of mass flow rate along the length of the channel is given by rewriting equation (13) as

$$\frac{\partial W}{\partial X} = -A\frac{\partial \rho}{\partial t} \tag{A5}$$

where ρ is defined by equation of state (A1). The right-hand side of equation (A5) may be obtained after the local time rate of change of enthalpy is determined from

$$\rho_j A\Delta X_j \frac{dh_j}{dt} = W_j(h_{J-1} - h_j) + N\pi D\Delta X_j q_j'' \tag{A6}$$

where q_j'' is the local heat flux rate from the surface of the fuel pin cladding and structural material into the fluid.

Equations (A1)–(A6) can now be solved using the steady-state initial conditions together with boundary conditions T_i, P_i, P_o, and q_j'' as a function of time.

Numerical Solution Procedure

The numerical solution procedure is as follows:

1 Determine T_i, $(P_i - P_o)$, and q_j'' either through transient forcing functions or coupling to a systems transient code.

2 Solve equation (A2) using a fifth-order predictor-corrector method of the Adams type to obtain $\hat{W}^{k+1}$.

3 Calculate the enthalpy distribution using a semi-implicit difference equation of the form:

$$h_j^{k+1} = \frac{W_j^k h_{j-1}^{k+1} + \frac{A\Delta X_j}{\Delta t}\rho_j^k h_j^k + N\pi D\Delta X_j q_j''}{\frac{A\Delta X_j}{\Delta t}\rho_j^k} \tag{A7}$$

4 Calculate the density distribution as a function of the advanced time enthalpy distribution using equation (A1)

$$\rho_j^{k+1} = \rho(h_j^{k+1}, P^{*k+1}) \tag{A8}$$

where P^{*k+1} is calculated as a linear average of inlet and outlet pressures.

5 Determine the mass flow rate distribution using equation (A3)

$$\hat{W}^{k+1} \simeq \frac{1}{2L}\sum_{J=2}^{M}[W_j^{k+1} + W_{j-1}^{k+1}]\Delta X_J \tag{A9}$$

together with equation (A5)

$$W_{j-1}^{k+1} = W_j^{k+1} + \frac{A\Delta X_j}{\Delta t}(\bar{\rho}_j^{k+1} - \bar{\rho}_j^k) \tag{A10}$$

by first solving for the outlet mass flow rate in terms of the average flow rate and then back substituting into equation (A10) and repeating steps 2 through 5 to obtain convergence.

The integration time step is adjusted in order to satisfy a preselected accuracy criterion for local enthalpies.

It must be noted that the present model has been coupled to the system-wide transient code SSC [7] through inlet temperature, $(P_i - P_o)$ and the heat flux q_j'' at the cladding surface.

The surface heat flux q_j'' is calculated using empirical heat transfer coefficients for liquid sodium prior to the occurrence of dryout.

B. S. Johnston
E. I. du Pont de Nemours
and Company,
Savannah River Laboratory,
Aiken, SC

S. G. Bankoff
Walter P. Murphy Professor,
Chemical Engineering and
Mechanical and Nuclear Engineering,
Northwestern University,
Evanston, IL
Fellow ASME

Boiling Heat Transfer in a Narrow Eccentric Annulus: Part III—A Model of Dry Patch Extent and Temperature Distribution

A previous paper, Johnston et al. (1983a), has described the phenomenon of dryout under a condition of line contact in tube support plate crevices. This paper presents the development of a model for the tube wall temperature distribution. The major effort is given to predicting the extent of the dry patch. The results show a satisfactory comparison with experimental data.

1 Introduction

A previous paper (Johnston et al., 1983a) described an experimental study of boiling heat transfer in the narrow annular crevice formed by a tube passing through a drilled tube support plate (TSP) in a PWR steam generator. It was found that a condition of stable dryout exists when the heated tube and plate are in contact. This dryout was shown to result in a characteristic circumferential tube wall temperature distribution. A model of the dryout process should be able to predict this profile.

Baum and Curlee (1980) presented an interesting and quite simple model for predicting the shape of a stable dry patch in a cylindrical TSP crevice. As in their experimental work, the tube was specified to be in line contact with the plate. A number of assumptions were made concerning the prevailing fluid mechanics in the crevice. The fluid was taken to be a saturated liquid in axial laminar flow. The velocity was assumed to be a function only of the angular coordinate. To account for two-phase flow in the crevice, the fluid physical properties were taken to be those of the saturated vapor.

At a given angular position, an energy balance was written on the local axially flowing fluid. For low velocities, as would occur close to the contact line, the liquid would be entirely vaporized within the crevice. Plotting this axial position versus the angular coordinate resulted in a rather steep-sided dry patch over the full axial length of the crevice. Comparisons with the shape of salt deposits from the chemical concentration experiments were strikingly good.

This model, by its nature, could not predict the temperature distribution in the tube wall. Alperi (1978) published an analysis which addressed this question without considering the actual fluid behavior in the TSP crevice. The study is applicable to the condition of a stable dry region on the outer surface of a tube. Alperi solved the steady-state conduction equation for the tube wall in radial and tangential coordinates, with a step change from a low to high outside surface heat transfer coefficient.

The inside boundary condition was taken to be either constant temperature (corresponding to hot water heating) or constant flux (corresponding to electric heating).

In considering the behavior of a dry patch on the tube surface, it seems that the phenomenon might be viewed as the growth or collapse of a confined bubble under the influence of an encroaching liquid. Bankoff (1959) and Marto and Rohsenow (1966) studied such a problem in a simpler geometry. These analyses were concerned with the penetration of liquid into a vapor-filled cylindrical cavity with heated walls. In both cases, despite differing assumptions, the liquid was seen to penetrate the cavity to some maximum depth and then recede. In the TSP crevice problem, the confining geometry is more complicated: curved and converging. The general approach of Bankoff (1959) and Marto and Rohsenow (1966) might still be extended to this situation. In the analysis which follows, a two-dimensional tube wall conduction equation is combined with a two-region heat transfer coefficient. The major effort is given to predicting the extent of the dry patch. Model predictions are then compared with experimental data.

2 Tube Wall Conduction Model

As mentioned above, Alperi (1978) obtained a solution for the two-dimensional temperature distribution in a circular annulus, based on a two-region outer heat transfer coefficient with either a constant flux or temperature inside wall boundary condition. His work will now be extended to provide a more general solution.

Consider a tube of inside radius r_i and outside radius r_o. If axial conduction is neglected, the steady temperature distribution is described by the Laplace equation. At the inside wall, a good approximation is that the heat transfer coefficient is constant for a given primary flow rate and bulk temperature. In view of the tube wall temperature variations described in Johnston et al. (1983a), this is thought to be more realistic than the assumption in Alperi (1978) of a constant wall temperature. In the temperature range of interest, the viscosity of water, and thus the convective heat transfer coefficient, do not vary greatly. At the outer wall the heat transfer coefficient may vary around the periphery in an arbitrary manner. Finally, the solution should be periodic about the circumference, and it is reasonable to require symmetry about the line of contact, $\theta = 0$.

Defining dimensionless coordinates

$$X \equiv \frac{T-T_s}{T_p-T_s} \tag{1}$$

$$\eta \equiv \frac{r}{r_o} \tag{2}$$

the governing equations become

$$0=\frac{1}{\eta}\frac{\partial}{\partial\eta}\left(\eta\frac{\partial X}{\partial\eta}\right)+\frac{1}{\eta^2}\frac{\partial^2 X}{\partial\theta^2} \tag{3}$$

$$\frac{\partial X}{\partial\eta}-N_iX=-N_i \qquad \eta=\eta_i,\quad -\pi\le\theta\le\pi \tag{4}$$

$$\frac{\partial X}{\partial\eta}+N_oX=0 \qquad \eta=1,\quad -\pi\le\theta\le\pi \tag{5}$$

Contributed by the Heat Transfer Division and presented at the Joint ASME/JSME Thermal Engineering Conference, Hawaii, March 1983. Manuscript received by the Heat Transfer Division May 4, 1983.

$$X(\eta,\ \theta)=X(\eta,\ -\theta) \qquad \eta_i \le \eta \le 1 \tag{6}$$

$$X(\eta,\ \theta)=X(\eta,\ \theta+2\pi) \qquad \eta_i \le \eta \le 1 \tag{7}$$

where

$$\eta_i=\frac{r_i}{r_o} \tag{8}$$

$$N_i=\frac{h_i r_o}{k_i} \tag{9}$$

$$N_o=N_o(\theta)=\frac{h_o r_o}{k_i} \tag{10}$$

A solution of equation (3) consistent with equations (6) and (7) is

$$X=a_o+b_o \ln \eta+\sum_{m=1}^{\infty}(a_m \eta^m+b_m \eta^{-m})\cos m\theta \tag{11}$$

Evaluating this expression at the inner wall results in

$$X=a_o+(1-a_o)\alpha_o \ln \eta+\sum_{m=1}^{\infty} a_m(\eta^m-\alpha_m \eta^{-m})\cos m\theta \tag{12}$$

where

$$\alpha_o=\frac{1}{\ln \eta_i-\dfrac{1}{N_i \eta_i}} \tag{13}$$

$$\alpha_m=\eta_i{}^{2m}\,\frac{N_i \eta_i-m}{N_i \eta_i+m} \tag{14}$$

Equation (12) is substituted into equation (5) to obtain

$$\begin{aligned}-\alpha_o&=a_o(N_o-\alpha_o)\\&+\sum_{m=1}^{\infty} a_m[N_o(1-\alpha_m)-m(1+\alpha_m)]\cos m\theta\end{aligned} \tag{15}$$

Equation (15) determines the constants a_m, $m=0, 1, \ldots$. These are obtained by multiplying the equation by $\cos n\theta$ and integrating over the limits $-\pi \le \theta \le \pi$. Advantage is taken of the fact that N_o is an even function of θ. If n is allowed to take successive values 0, 1, 2, . . . , there results an infinite number of linearly independent equations in the constants a_m, $m=0$, 1, 2, ... These may be written in matrix form

$$\mathcal{A}\mathbf{C}=\mathbf{B} \tag{16}$$

$\mathcal{A}$ is an infinite symmetric matrix containing information about the outside heat transfer coefficient. **B** and **C** are infinite column matrices. The elements of these matrices are defined below

$$C_1=a_o$$

$$C_m=a_{m-1}(1-\alpha_{m-1}) \qquad m=2,3,\ \ldots$$

$$B_1=-\pi\alpha_o$$

$$B_m=0 \qquad m=2,3,\ \ldots$$

$$A_{11}=\int_0^{\pi} N_o d\theta-\pi\alpha_o$$

$$A_{mn}=\int_0^{\pi} N_o \cos\,(m-1)\theta \cos\,(n-1)\theta d\theta$$

$$-\frac{(n-1)\pi}{2}\,\frac{1+\alpha_{n-1}}{1-\alpha_{n-1}}\,\delta_{mn} \qquad \begin{array}{l} m=1,2,\ \ldots \\ n=1,2,\ \ldots \\ m=n=1 \text{ excluded}\end{array}$$

The Kronecker delta is defined in the customary manner

$$\delta_{mn}=\begin{cases}0 & m\ne n\\ 1 & m=n\end{cases}$$

Once the outside heat transfer coefficient N_o is known, the matrix elements A_{mn} may be evaluated by analytic or numerical integration. Some finite number of terms may then be obtained for use in equation (12).

3 Crevice Heat Transfer Model

The angular distribution plots of tube surface temperature presented in Johnston et al. (1983a) show several characteristic features. First is the major difference in temperature between

Nomenclature

a_m, a_o = conduction equation solution coefficients
A = dimensionless parameter
$\mathcal{A}$ = square matrix
A_{mn} = matrix element
B = dimensionless parameter
B = column matrix
B_m = matrix element
c = constant
C = dimensionless parameter
C = column matrix
C_m = matrix element
d = distance between centers of tube and drilled hole
D = dimensionless parameter
D_o = tube outside diameter
f = liquid velocity function in wedge
f_2 = center-line liquid velocity function in wedge
h = local heat transfer coefficient
h_i = heat transfer coefficient, tube inside surface
h_o = heat transfer coefficient, tube outside surface
h_1 = heat transfer coefficient, dry surface
h_2 = heat transfer coefficient, wet surface
k_g = thermal conductivity, TSP
k_i = thermal conductivity, tube
k_l = thermal conductivity, liquid
k_v = thermal conductivity, vapor
l = thermal diffusion length in liquid
L = axial length of TSP
m = integer in Fourier series expansion
n = exponent; integer in Fourier series expansion
N_i = dimensionless heat transfer coefficient, tube inside surface
N_o = dimensionless heat transfer coefficient, tube outside surface
p = radial coordinate
p_m = meniscus position in wedge
p_m^* = final meniscus position in wedge
p_2 = initial meniscus position in wedge
P = pressure
P_g = pressure of confined vapor in wedge
P_m = pressure of liquid at meniscus
P_s = saturation pressure at T_s
q = local heat flux
r = radial coordinate
r_h = radius of drilled hole
r_i = tube inside radius

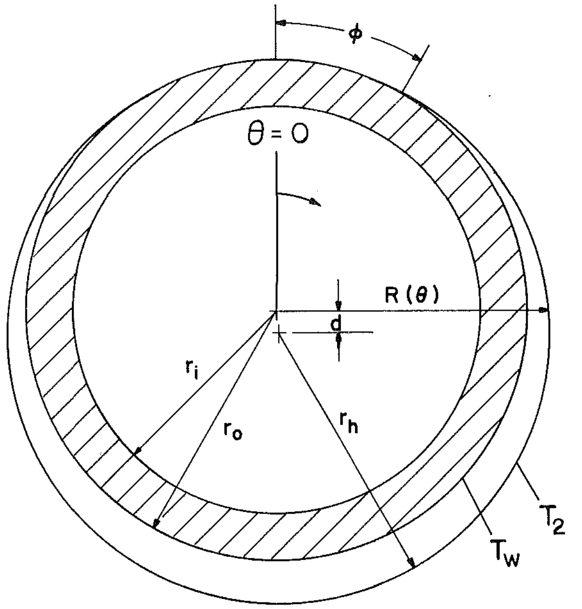

Fig. 1 **Tube support plate crevice geometry with contact at $\theta = 0$ deg**

the wetted and dry portions of the surface. Second is the steepness of the tangential temperature gradient at the dry patch boundary. Third is the **W** shape, the gradual increase in temperature as the crevice widens. This difference in temperature from the patch boundary to 180 deg is much smaller than that between the patch boundary and the contact line ($\theta = 0$ deg).

In an attempt to model the heat transfer processes in the crevice, it seems a reasonable first approximation to ignore the **W** shape and average over the wetted portion of the gap. Furthermore, the steep tangential gradients at the patch boundary suggest that the transition between dry and wet portions is rather abrupt. This leads to a two-region heat transfer coefficient

$0 \leq \theta \leq \phi$	dry patch, poor heat transfer
$\phi < \theta \leq \pi$	wetted surface, good heat transfer

where ϕ is the position of the patch boundary. This model would seem to preserve the more striking of the characteristics of the experimental results.

3.1 Dry Patch Region. Figure 1 illustrates the tube and crevice geometry. In the dry patch region, heat is conducted from the tube surface into the vapor and hence into the tube support plate. There is no experimental information about the motion of the vapor in the patch. As a conservative estimate, the vapor will be presumed to be stagnant, so that heat transfer occurs entirely by conduction. Two-dimensional conduction equations may thus be written for the vapor and TSP. This problem is made difficult by the vapor–TSP interface on which boundary conditions are specified. This is a circular curve whose center of radius does not coincide with the coordinate system origin. A simplification which allows an easy solution is to neglect tangential conduction in the vapor and TSP. A two-dimensional heat conduction solution for the TSP alone indicates that the radial temperature gradient exceeds the tangential gradient by a factor of 10 in the region around the point of tube–TSP contact for a patch half-width of 30 deg.

A steam generator operates over most of its length with saturated secondary fluid. Since only some small fraction of the tubes would be expected to feature a hot spot (Johnston et al., 1983a), a given tube support plate will usually be at the saturation temperature. To describe radial conduction in the TSP, it is necessary to specify a radial distance at which the support plate temperature reaches T_s. Referring again to Fig. 1, and writing one-dimensional conduction relationships,

$$q = \frac{2k_v}{D_o \ln (R/r_o)} (T_w - T_2) \tag{17}$$

$$q = \frac{2k_g}{D_o \ln (1 + t'/R)} (T_2 - T_s) \tag{18}$$

where T_2 is the temperature at $r = R$. However, the outside heat transfer coefficient is defined such that

$$q = h_o (T_w - T_s) \tag{19}$$

Combining these equations, there results

Nomenclature (cont.)

r_o = tube outside radius
R = radial location of drilled hole circumference
R' = dimensionless flow parameter
s = dummy variable
t = time coordinate
t' = effective thermal diffusion distance into TSP
t_o = unspecified time scale
T = temperature
T_p = temperature of primary fluid
T_s = saturation temperature
T_v = temperature of vapor
T_w = temperature of tube outer surface
T_2 = temperature of drilled hole inner surface
ΔT_s = superheat = $T - T_s$
$\bar{u}$ = average velocity of meniscus
U = overall heat transfer coefficient, primary to outer wall
v = velocity
x = dummy variable
X = dimensionless temperature
y = dummy variable; integral time coordinate
z = axial coordinate
α = wedge half-angle
α_l = liquid thermal diffusivity
α_m, α_o = parameters
β = constant
γ = contact angle for liquid–vapor interface
δ_{mn} = Kronecker delta
ζ = dimensionless radial coordinate
$\zeta_0, \zeta_1, \ldots$ = perturbation functions for ζ
ζ_0^* = dimensionless final meniscus position, first approximation
η = dimensionless radial coordinate
η_i = dimensionless tube inside radius
θ = angular coordinate
λ = heat of vaporization
ν = liquid kinematic viscosity
ξ = dimensionless density parameter
ρ = liquid density
ρ_v = vapor density
σ = surface tension
τ = dimensionless time coordinate
ϕ = angular position of dry patch boundary
ϕ_2 = initial position of dry patch boundary
ψ = angular coordinate

$$h_o = \left[\frac{D_o \ln (R/R_o)}{2k_g} + \frac{D_o \ln (1 + t'/R)}{2k_g} \right]^{-1} \qquad 0 \le \theta \le \phi \qquad (20)$$

This equation includes the effect of support plate thermal conductivity. R varies with angular position

$$R = -d \cos \theta + (r_h^2 - d^2 \sin^2 \theta)^{1/2} \qquad (21)$$

where r_h is the radius of the drilled hole and d is one-half the diametral gap. The thermal distance t' is chosen to be about half the distance between adjacent drilled hole perimeters, as suggested by a three-dimensional heat conduction solution in a TSP with surfaces at T_s. The neglect of tangential conduction in the support plate is a conservative assumption and will tend to cause an overprediction of the contact line temperature. This will be more pronounced for narrower dry patches (larger crevices). While it is possible to vary t' with gap size in order to fit the data, it is desired here to choose a physically realistic value and accept the disparities which result.

3.2 Wetted Region. In the wetted region of the tube, the support plate material does not influence the heat transfer (Johnston et al., 1983b). For the first approximation, the effects of flow rate and inlet enthalpy are neglected as well. It is then appropriate to describe the heat transfer by an equation of the form

$$\Delta T_s = cq^n \qquad (22)$$

where c is a function of pressure. For the experiments performed at 0.69 MPa (Johnston et al., 1983b) the data were generally fitted by choosing c to be $0.088\,^\circ\mathrm{C}\ \mathrm{m/W}^{1/2}$ and n to be 0.5.

In the widest part of the gap, the tangential temperature gradients in the tube wall are small, and the conduction of heat may be assumed to be one dimensional. In order to determine the outside surface heat transfer coefficient, the equation for heat conduction from the primary field

$$q = U(T_p - T_w) \qquad (23)$$

is used to eliminate q in equation (22). Making use of equation (19), there results

$$h_o = U \frac{T_p - T_w}{T_w - T_s} \qquad \phi < \theta \le \pi \qquad (24)$$

where T_w is here that value of the outer surface temperature determined by one-dimensional calculation in the wide gap region.

4 Patch Width Model

In order to complete the specification of the crevice heat transfer coefficient h_o, it is necessary to determine the extent of the dry patch, the angle ϕ. As was done in specifying the wide gap region behavior, the influence of flow rate and inlet enthalpy on the dry patch will be neglected. In Johnston et al. (1983b) it was determined that the heat flux and gap size have the greatest effect on patch extent; the model to be developed here will consider these variables.

Figure 2 illustrates the situation under consideration. Liquid in the crevice moves tangentially toward the contact line. The motion results from condensation of the confined vapor, aided by capillary forces. The liquid motion is retarded by viscous shear at the crevice walls, in addition to the increasing pressure of the vapor. This is taken to be the equilibrium vapor pressure associated with the temperature of the liquid meniscus. The temperature rises due to heat transfer from the tube wall, as well as latent heat transport from the condensing vapor. The forces ultimately balance, and the liquid stops at an angular position ϕ, the minimum patch width. Further heat transfer causes the meniscus to vaporize, resulting in rapid expulsion of the liquid. It is desired to analyze this process of liquid inflow to determine the position at which its motion ceases. The equations for heat and momentum transport for a curved converging flow are quite difficult. As the first of several approximations, the crevice of Fig. 2 will be replaced by the narrow straight-sided wedge of Fig. 3. The meniscus position at any time is denoted by p_m. The minimum patch extent ϕ is now associated with the radial position p_m^*.

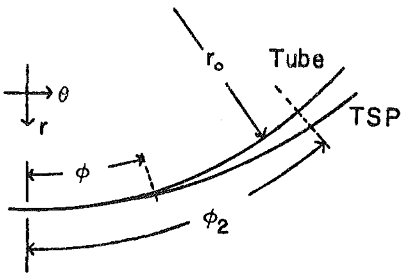

Fig. 2 Liquid motion in crevice

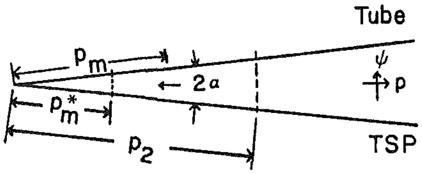

Fig. 3 Liquid motion in wedge

4.1 Fluid Motion. This analysis will not consider the detailed behavior of the interface, but rather will focus on the motion in the bulk of the liquid. The liquid velocity comprises only the radial component and is presumed to be a function of both radial and angular coordinates, p and ψ. The continuity equation gives

$$\frac{\partial}{\partial p} (pv) = 0 \qquad (25)$$

This implies

$$v = \frac{f(\psi, t)}{p} \qquad (26)$$

The liquid flows toward the apex of the wedge; hence

$$f(\psi, t) \le 0$$

The momentum equation is written in terms of equation (26), as

$$\frac{1}{p} \frac{\partial f}{\partial t} - \frac{1}{p^3} f^2 = -\frac{1}{\rho} \frac{\partial P}{\partial p} + \frac{\nu}{p^3} \frac{\partial^2 f}{\partial \psi^2} \qquad (27)$$

As an approximation, this equation will be averaged over the angular coordinate. This ψ average is defined

$$\bar{s}(t) \equiv \frac{\int_0^L \int_{-\alpha}^{\alpha} s(\psi, t) p \, d\psi dz}{\int_0^L \int_{-\alpha}^{\alpha} p \, d\psi dz} = \frac{1}{2\alpha} \int_{-\alpha}^{\alpha} s(\psi, t) d\psi \qquad (28)$$

Applying equation (28) to each term of equation (27), there results

$$\frac{1}{p} \frac{\partial \bar{f}}{\partial t} - \frac{1}{p^3} \overline{f^2} = -\frac{1}{\rho} \frac{\partial \bar{P}}{\partial p} + \frac{\nu}{2\alpha p^3} \left[\frac{\partial f}{\partial \psi} \bigg|_{\alpha} - \frac{\partial f}{\partial \psi} \bigg|_{-\alpha} \right] \qquad (29)$$

The velocity gradient at the wall will be approximated by that for steady converging flow. Goldstein (1938) gives the solution

$$\frac{f}{f_2} = 3 \tanh^2 \left\{ \sqrt{\frac{R'}{2}} (\alpha - |\psi|) + \beta \right\} - 2 \qquad -\alpha \le \psi \le \alpha \qquad (30)$$

where

$$f_2 \equiv f(0) \le f(\psi) \le 0$$

$$R' \equiv -\frac{f_2}{\nu}$$

$$\beta \equiv \tanh^{-1}\sqrt{\frac{2}{3}}$$

Differentiating equation (30), there is obtained

$$\left.\frac{\partial f}{\partial \psi}\right|_{\alpha} = -\left.\frac{\partial f}{\partial \psi}\right|_{-\alpha} = \frac{2}{(3\nu)^{1/2}}(-f_2)^{3/2} \tag{31}$$

The solution given in equation (30) is strictly valid only for large R'. Applying equation (28), it is found that $\bar{f}$ approaches the center-line value f_2. Making this approximation, and using equation (31), equation (29) becomes

$$\frac{1}{p}\frac{df_2}{dt} - \frac{1}{p^3}f_2^2 = -\frac{1}{\rho}\frac{\partial \bar{P}}{\partial p} + \frac{2(3\nu)^{1/2}}{3\alpha p^3}(-f_2)^{3/2} \tag{32}$$

The additional approximation that $\overline{f^2} = \bar{f}^2$ has also been made.

A mass balance on the interface gives

$$\rho(\bar{v} - \bar{u}) - \rho_v(-\bar{u}) = 0 \tag{33}$$

where $\bar{u}$ is the average velocity of the interface, as distinguished from the average liquid velocity $\bar{v}$. In writing this equation, the vapor has been presumed to be stagnant, and the actual shape of the interface has not been considered. Solving for the interface velocity

$$\bar{u} = \frac{1}{\xi}\bar{v} \tag{34}$$

where

$$\xi \equiv \frac{\rho - \rho_v}{\rho} \tag{35}$$

It is seen that the motion of the interface exceeds that of the bulk liquid by an amount dependent on the density ratio of the two phases. For $\rho >> \rho_v$, the vapor condensed produces a negligible volume of liquid, and the liquid flows in the crevice at the same speed as the interface. For the other extreme, $\rho = \rho_v$, condensation of vapor produces an equal volume of liquid, and the interface moves through a stagnant medium. For water at 0.69 MPa, $\xi = 0.995$; at prototypical steam generator conditions, $\xi = 0.95$.

Recognizing that

$$\frac{dp_m}{dt} = \bar{u}$$

and recalling equation (26), equation (34) becomes

$$f_2 = \xi p_m \frac{dp_m}{dt} = \xi p_m \dot{p}_m \tag{36}$$

Using this result in equation (32) and integrating over the radial coordinate from p_m, where $\bar{P} = P_m$, to some p_2, where $\bar{P} = P_s$, there is obtained

$$P_m - P_s = \rho\xi \frac{d}{dt}(p_m\dot{p}_m) \ln \frac{p_2}{p_m} - \rho\xi^2 p_m^2 \dot{p}_m^2 \left(\frac{1}{p_m^2} - \frac{1}{p_2^2}\right)$$
$$- \frac{2\rho\xi^{3/2}(3\nu)^{1/2}}{3\alpha}(-p_m\dot{p}_m)^{3/2}\left(\frac{1}{p_m^2} - \frac{1}{p_2^2}\right) \tag{37}$$

The procedure described above for obtaining equation (37) is analogous to the derivation of the Rayleigh equation for a spherical bubble (Hsu and Graham, 1976). In that case, the saturation pressure P_s is associated with a large value of p_2. The cylindrical geometry of the present case exhibits a logarithmic singularity for large p; therefore, p_2 must be retained as a finite position in the crevice.

Since this analysis excludes a detailed description of the meniscus, a complete interfacial momentum balance will not be written. Instead, a static force balance will be used to relate the pressure difference across the meniscus to the capillary forces. This is written

$$P_m = P_g - \frac{\sigma \cos(\gamma - \alpha)}{p_m \alpha} \tag{38}$$

When this is substituted into the momentum equation

$$P_g - P_s = \rho\xi \frac{d}{dt}(p_m\dot{p}_m) \ln \frac{p_2}{p_m}$$
$$- \rho\xi^2 p_m^2 \dot{p}_m^2 \left(\frac{1}{p_m^2} - \frac{1}{p_2^2}\right) + \frac{\sigma \cos(\gamma - \alpha)}{p_m \alpha}$$
$$- \frac{2\rho\xi^{3/2}(3\nu)^{1/2}}{3\alpha}(-p_m\dot{p}_m)^{3/2}\left(\frac{1}{p_m^2} - \frac{1}{p_2^2}\right) \tag{39}$$

4.2 Heating of Fluid. The pressure difference may be related to the meniscus superheat by the linearized Clapeyron equation

$$P_g - P_s \approx \frac{\rho_v \lambda}{T_s}(T_v - T_s) \tag{40}$$

In order to use equation (39) further it is necessary to consider the energy balance on the moving liquid. As an approximation, the heated fluid is considered to be confined to one relaxation length (Bankoff, 1959) l, where $l = (\alpha_l t)^{1/2}$. With this assumption, a steady-state heat balance gives

$$2\alpha L p_m \rho_v \lambda \left(-\frac{dp_m}{dt}\right) + qL(\alpha_l t)^{1/2}$$
$$= -2\alpha L k_l (p_m + (\alpha_l t)^{1/2}) \frac{T_s - T_m}{(\alpha_l t)^{1/2}} \tag{41}$$

Here L is the axial length of the crevice, which divides out. The left-hand side expresses heat input from the vapor and the tube wall. The TSP is considered to be adiabatic. The right-hand side describes conduction through the liquid. Solving for the meniscus superheat, there is obtained

$$T_m - T_s = \frac{\alpha_l t q - 2\alpha\rho_v\lambda(\alpha_l t)^{1/2} p_m \dot{p}_m}{2\alpha k_l p_m \left(1 + \frac{(\alpha_l t)^{1/2}}{p_m}\right)} \tag{42}$$

Applying a thin thermal boundary assumption implies neglecting $(\alpha_l t)^{1/2}/p_m$ in comparison with 1. Finally, there results

$$T_m - T_s = \frac{\alpha_l q}{2\alpha k_l}\frac{t}{p_m} - \frac{\rho_v \lambda}{k_l}(\alpha_l t)^{1/2}\dot{p}_m \tag{43}$$

This now may be combined with equations (39) and (40) to obtain a single nonlinear ordinary differential equation for the interface position as a function of time. Defining dimensionless parameters

$$\zeta \equiv \frac{p_m}{p_2}$$

$$\tau \equiv \frac{t}{t_o}$$

and rearranging, there results

$$A - B(\zeta^{1/2} - \zeta^{5/2})(-\dot{\zeta})^{3/2} + \alpha C \zeta \ln \zeta \frac{d}{d\tau}(\zeta\dot{\zeta})$$
$$- \alpha\xi C(\zeta - \zeta^3)\dot{\zeta}^2 = \tau - \alpha D \tau^{1/2}\zeta\dot{\zeta} \tag{44}$$

where dimensionless coefficients are defined

$$A \equiv \frac{2\sigma k_l T_s \cos(\gamma - \alpha)}{\rho_v \lambda \alpha q t_o}$$

$$B \equiv \frac{4\rho\xi^{3/2}(3\nu)^{1/2} k_l T_s p_2^2}{3\rho_v \lambda \alpha_1 q t_0^{5/2}}$$

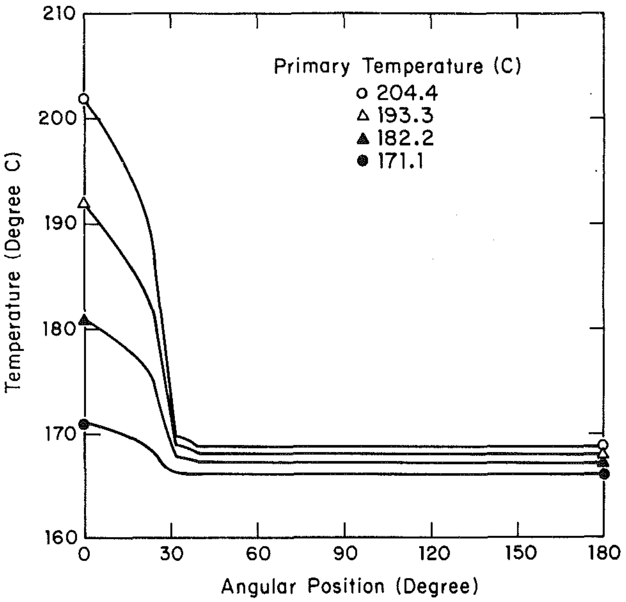

Fig. 4 Predicted wall temperature profile; pressure = 0.69 MPa; diametral gap = 0.38 mm

$$C \equiv \frac{2\rho\xi k_l T_s p_2^3}{\rho_v \lambda \alpha_l q t_o^3}$$

$$D \equiv \frac{2\rho_v \lambda p_2^2}{\alpha_l^{1/2} q t_o^{3/2}}$$

4.3 Solution of Equation. For the narrow crevices under consideration, α is small. It seems reasonable, then, to attempt to express ζ as an asymptotic expansion

$$\zeta = \zeta_0(\tau) + \alpha\zeta_1(\tau) + \alpha^2\zeta_2(\tau) + \ldots \tag{45}$$

In order to approximate the nonlinear terms, use will be made of the logarithmic series

$$\ln(x+y) = \ln x + 2\left(\frac{y}{2x+y} + \frac{1}{3}\left(\frac{y}{2x+y}\right)^3 + \ldots\right) \tag{46}$$

and the binomial series

$$(x+y)^n = x^n + nx^{n-1}y^1 + \frac{n(n-1)}{2!}x^{n-2}y^2 + \ldots \tag{47}$$

In these series, x is to be associated with ζ_0 and y with all terms of $0(\alpha)$. Using equations (45), (46), and (47), and retaining terms of $0(\alpha^0)$, equation (44) becomes

$$A - B(\zeta_0^{1/2} - \zeta_0^{5/2})(-\dot{\zeta}_0)^{3/2} = \tau \tag{48}$$

The surviving terms represent the capillary forces, the viscous wall shear, and heating from the tube wall. Equation (48) is separable and has the solution

$$B^{2/3}\int_{\zeta_0}^{1}(s^{1/2} - s^{5/2})^{2/3}ds = \frac{3}{5}A^{5/3} - \frac{3}{5}(A-\tau)^{5/3} \tag{49}$$

where $\zeta_0 = 1$ at $\tau = 0$. From equation (48) it is apparent that the liquid motion ceases when $\tau = A$. The minimum patch extent ζ_0 is thus given by

$$\int_{\zeta_0^*}^{1}(s^{1/2} - s^{5/2})^{2/3}ds = \frac{3}{5}\left(\frac{A^5}{B^2}\right)^{1/3} \tag{50}$$

where

$$\frac{3}{5}\left(\frac{A^5}{B^2}\right)^{1/3} = \frac{6\sigma k_l T_s \cos(\gamma-\alpha)}{5\rho_v\lambda\alpha_l\xi q}\left[\frac{\sqrt{3}\sigma\cos(\gamma-\alpha)}{2(\rho\mu)^{1/2}p_2^2}\right]^{2/3} \tag{51}$$

The unspecified time scale t_o has disappeared, and the quotient is inversely proportional to the heat flux. For a given value of the right-hand side in equation (50) ζ_0 is easily found by numerical integration. Then, to the first approximation,

$$p_m^* = p_2\zeta_0^* \tag{52}$$

In order to relate p_m^* to the desired result ϕ, it is necessary to specify the initial position p_2, and to choose the wedge angle 2α to approximate the TSP crevice. The first specification may be made on experimental grounds. In Johnston et al. (1983a) it was determined that no stable dry patch formed when the tube and plate were separated more than 0.025 mm. From equation (21), the tube-to-plate separation is expressed as a function of angular position θ

$$\Delta r = -d\cos\theta - r_o + (r_h^2 - d^2\sin^2\theta)^{1/2} \tag{53}$$

Referring to Fig. 2, it is desired to choose $\theta = \phi_2$ such that $\Delta r = 0.025$ mm. Neglecting $d^2\sin^2\theta$, this is given by

$$\phi_2 = \cos^{-1}\left(1 - \frac{0.025}{d}\right) \tag{54}$$

"Unrolling" the crevice, the circular segment represented by ϕ_2 is related to p_2

$$p_2 = r_o\phi_2 \tag{55}$$

The wedge angle 2α may then be chosen such that the tube-to-plate separation in the wedge at p_2 equals that in the crevice at ϕ_2

$$2\alpha \approx \frac{0.025}{p_2} \tag{56}$$

Finally, the heat flux in equation (51) is considered to be that of the wetted tube surface, as given in equation (23). The minimum patch extent ϕ is then

$$\phi = \zeta_0^*\frac{p_2}{r_o} \tag{57}$$

where ζ_0^* and p_2 are determined above. This completes the specification of the outside surface heat transfer coefficient h_o.

5 Predictions and Comparison With Data

The patch width model described above is an approximate solution to a simplified equation describing flow in a straight-sided wedge. Its predictions must be compared to experimental data in order to judge its applicability to the curved geometry in the TSP crevice.

It is possible to obtain a dry patch inception criterion from equations (50) and (51). Taking ζ_0 to be zero, the value of the definite integral in equation (50) is found by numerical integration to be 0.509. Using this result, the heat flux at inception may be calculated from equation (51). For a 0.38-mm diametral gap at 0.69 MPa, this is found to be about 34,700 W/m^2°C, which is certainly comparable to the experimental observations for dryout (Johnston et al., 1983a).

The various parts of the model were combined into a computer program which uses equation (12) to predict the angular distribution of temperature at the outer surface of the tube. Figure 4 shows how the temperature profile is predicted to vary with increasing primary temperature at 0.69 MPa in a 0.38-mm diametral gap. The contact line temperature is close to that of the primary fluid, while the wide gap temperature is little affected. There is a general decrease in temperature with distance from the contact line, reflecting tangential wall conduction. The temperature drops abruptly to the wide gap value at the patch boundary.

Figure 5 features a predicted temperature profile compared with appropriate experimental data. The agreement is quite good. In particular, the data at the 15 and 30 deg positions seem to verify the importance of considering tangential tube wall conduction. In addition, the dry patch extent seems to be close to that observed in the experiment. Good agreement in

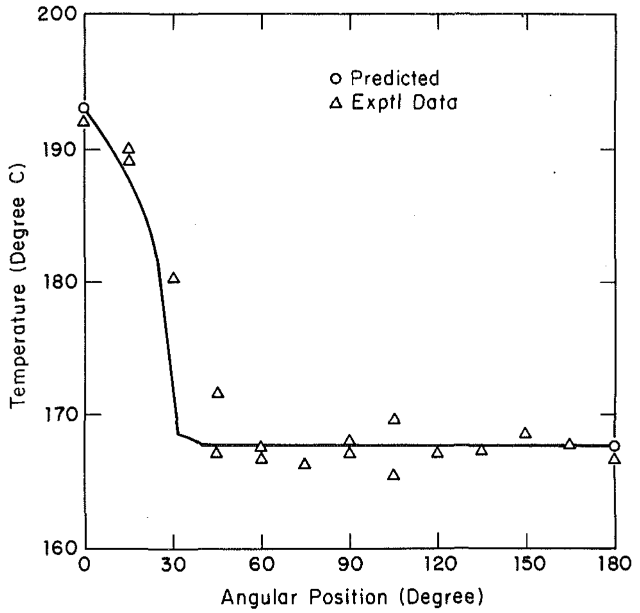

Fig. 5 Predicted wall temperature profile; pressure = 0.69 MPa; diametral gap = 0.38 mm; primary temperature = 195°C; quartz TSP

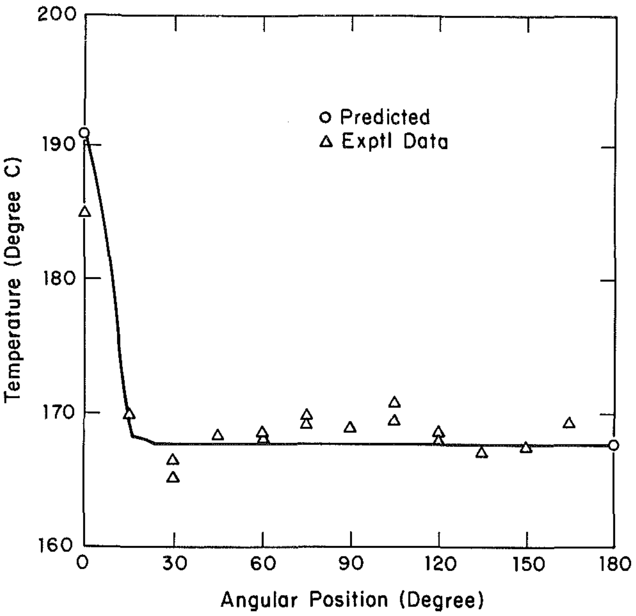

Fig. 7 Predicted wall temperature profile; pressure = 0.69 MPa; diametral gap = 2.03 mm; primary temperature = 199°C; quartz TSP

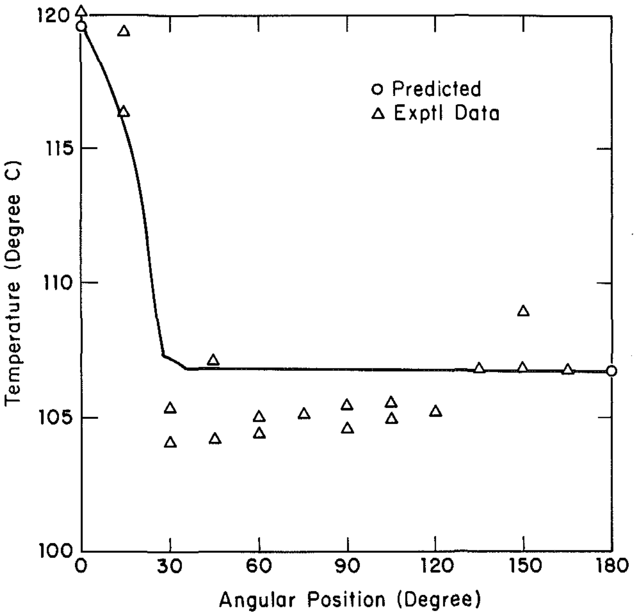

Fig. 6 Predicted wall temperature profile; pressure = 0.12 MPa; diametral gap = 0.38 mm; primary temperature = 121°C; quartz TSP

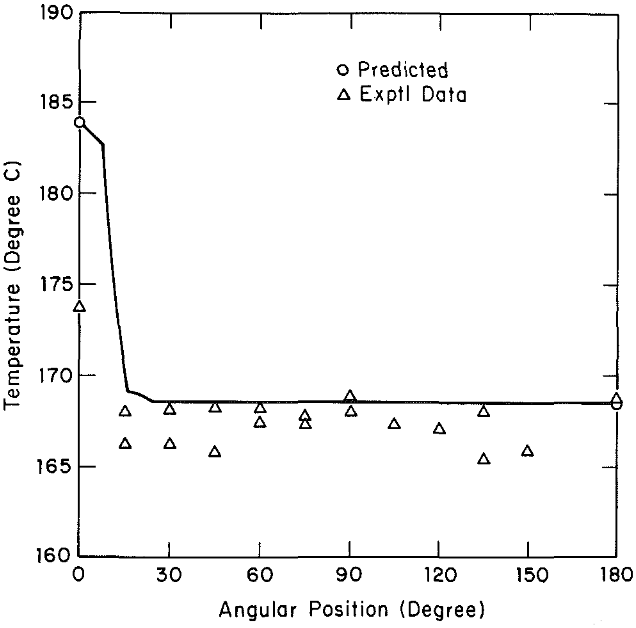

Fig. 8 Predicted wall temperature profile; pressure = 0.69 MPa; diametral gap = 2.03 mm; primary temperature = 199°C; steel TSP

the prediction of dry patch width is also evident in Fig. 6, this experiment being run at atmospheric pressure. A deficiency of the model is also illustrated, as the data exhibit the characteristic **W** shape. Since the effect of flow rate was not considered, the model merely predicts a wide gas temperature in the range of the experimental values.

Figures 5 and 6 have featured excellent predictions of the measured contact line temperatures. Earlier it was anticipated that the neglect of tangential conduction in the support plate would lead to greater errors for narrower dry patches. This is borne out in Fig. 7, which shows data and prediction for a 2.03-mm diametral gap at 0.69 MPa. The predicted contact line temperature exceeds the experimental value by 6°C, which is conservative for design purposes. However, the model does predict that the difference between the primary and contact line temperatures will be greater for the narrower patch. This difference is 8°C compared to 2°C in Fig. 5. This is due to tangential conduction in the tube wall, and not to any increase in the dry patch heat transfer coefficient. It is evident from the low temperatures at the 15 deg position that the dry patch width prediction is satisfactory.

For a steel TSP, the prediction of contact line temperature is even more conservative. In Fig. 8 the prediction exceeds the measured value by 10°C. The model does show the effect of increased support plate thermal conductivity, in that the predicted primary to contact line temperature difference is 15°C. This is nearly twice that for the similar conditions of Fig. 7. Once again the prediction of patch width is satisfactory.

In conclusion, the model does a creditable job of predicting experimental data. Its weaknesses are the neglect of the **W** shape and overprediction of the contact line temperature. In spite of these, it seems to follow the trends of gap size, primary temperature, and TSP thermal conductivity. In particular, the patch width prediction is quite satisfactory.

Acknowledgments

This work was supported under Contract No. S133-1 by the Electric Power Research Institute, Palo Alto, CA. Project managers were G. Hetsroni and C. L. Williams. To these individuals, as well as R. S. Tankin and M. C. Yuen, Department of Mechanical and Nuclear Engineering, Northwestern University, we are indebted for helpful comments.

References

Alperi, R. W., 1978, "Tube Wall Temperatures of an Eccentrically Located Horizontal Tube Within a Narrow Annulus," ASME JOURNAL OF HEAT TRANSFER, Vol. 100, pp. 548-552.

Baum, A. J., and Curlee, N. J., Jr., 1980, "An Experimental and Analytical Investigation of Dryout and Chemical Concentration in Confined Geometries," ASME Century 2 Nuclear Engineering Conference, San Francisco, CA.

Bankoff, S. G., 1959, "Prediction of Surface Temperatures at Incipient Boiling," *Chemical Engineering Progress Symposium Series*, Chicago, IL, No. 29, Vol. 55, pp. 87-94.

Goldstein, S., ed., 1938, *Modern Developments in Fluid Dynamics*, Oxford University Press, England, Vol. 1.

Hsu, Y.-Y., and Graham, R. W., 1976, *Transport Processes in Boiling and Two-Phase Systems*, McGraw-Hill, New York, pp. 18-21.

Johnston, B. S., Sharon, A., Kozawa, Y., and Bankoff, S. G., 1983a, "Boiling Heat Transfer in a Narrow Eccentric Annulus, Part I: Dryout," ASME *Journal of Engineering for Power*, Vol. 105, pp. 742-747.

Johnston, B. S., Sharon, A., and Bankoff, S. G., 1983b, "Boiling Heat Transfer in a Narrow Eccentric Annulus, Part II: Heat Transfer," ASME *Journal of Engineering for Power*, Vol. 105, pp. 748-754.

Marto, P. J., and Rohsenow, W. M., 1966, "Nucleate Boiling Instability of Alkali Metals," ASME JOURNAL OF HEAT TRANSFER, Vol. 88, pp. 183-189.

M. K. Jensen
Associate Professor.
Mem. ASME

M. Pourdashti
Graduate Student.

Department of Mechanical Engineering,
University of Wisconsin—Milwaukee,
Milwaukee, WI 53201

Critical Heat Flux on a Horizontal Cylinder in an Upward Subcooled and Low-Quality Two-Phase Crossflow

An experimental investigation has been conducted to determine the low-velocity critical heat flux (CHF) behavior on a single horizontal tube in a subcooled and low-quality two-phase crossflow of R-113. Data were obtained over a range of velocities (up to 0.3 m/s), subcooling (0 to 14 K), and qualities ($0 < x < +30$ *percent) at two pressures. There was a linear decrease in the CHF with increasing quality up to about 10 percent quality; then, due to a flow regime transition, the CHF remained relatively constant. A correlation has been developed which predicted well the subcooled and low-quality region CHF condition in the linearly decreasing portion of the curve. Data from the literature are also predicted well.*

Introduction

In a recent study [1], it was shown that in kettle reboilers much of the recirculating flow is a two-phase mixture flowing vertically upward through the horizontal tube bundle. The velocities were low but had a significant effect on the convective heat transfer coefficients; no critical heat flux (CHF) data were obtained in this investigation. Indeed, the literature on the CHF condition in tube bundles is quite limited. Comley and Abbott [2] (as cited in [3]) found little difference between the CHF in a small tube bundle and on a single tube when boiling water. Kern [4] suggested that because of possible vapor blanketing of tubes higher in a natural circulation bundle, a maximum heat flux of about 38,000 W/m^2 and 95,000 W/m^2 for organics and water, respectively, should be used. Palen and Taborek [5], Palen and Small [6], and Palen et al. [3] have addressed the problem of the overall CHF in reboilers by examining industrial data (in [5, 6]) and by running large-scale laboratory experiments (in [3]). Conservative, overall approaches for estimating the CHF were suggested in [5, 6]. Because of proprietary data, only qualitative design methods could be presented in [3]. However, they noted that the CHF for a bundle is lower than that of a single tube and that the CHF decreases with increasing bundle diameter at constant pitch. It was suggested that the two-phase pressure drop through the bundle plays an important role in determining the CHF condition. In none of these studies has the effect of the local quality or the local mass velocity on the CHF in the higher rows of the bundle been addressed. Only overall data have been examined. Fokin and Goldberg [7] by arguing that the CHF condition in a tube bundle is hydrodynamic in nature modeled the boiling process in a horizontal tube bundle by flashing air through porous pipes which were immersed in water. By analyzing the true volume gas content near the tube wall and relating that to the CHF, they conclude that the CHF in the upper tube rows of a bundle may be much smaller (possibly by an order of magnitude or more) than that obtained with a single tube in a saturated liquid.

Because the flow in kettle reboilers and in once-through crossflow boilers is quite complex, single horizontal tubes (which are the building blocks of heat exchangers) in crossflow have been studied much more extensively than have complete heat exchangers. Both the subcooled and saturated liquid CHF conditions have been investigated. However, no investigation has been performed on a single, horizontal tube in a two-phase crossflow to determine the effects of fluid velocity and quality on the CHF condition.

Several studies have been conducted with subcooled and saturated liquid crossflows over single horizontal tubes. Vliet and Leppert [8] investigated the CHF for nearly saturated water at one atmosphere flowing normal to a cylinder in a 203 by 31.8 mm channel. The water velocity varied from 0.365 to 2.895 m/s. The test sections were stainless-steel wires and tubes 0.254 to 4.800 mm in diameter. Within these ranges of variables, the CHF was found to increase with the square root of the velocity. Only a weak dependence on the test-section diameter was observed; the tendency was for the peak heat flux to decrease for larger tubes. In a related study, Vliet and Leppert [9] investigated the CHF for subcooled (1.6 to 55.5 K) water at atmospheric pressure with a velocity of 0.152 to 3.352 m/s. The test-section diameters were from 0.254 to 4.800 mm. The experimental results indicated that the CHF in the subcooled region varied directly with the water velocity and subcooling and inversely to a fractional power of the test-section diameter. The exponent which described the diameter dependence was itself a function of both velocity and subcooling. Another subcooled water CHF study was conducted by Ornatskiy et al. [10] for flow velocities of 4 to 20 m/s, pressures of 0.2 and 0.8 MN/m^2, and the degree of subcooling of 40 to 120 K. However, because the flow around the test section was through curvilinear channels, this was not a true crossflow experiment and the results were difficult to interpret.

In the most recent study on crossflow boiling, Yilmaz and Westwater [11] experimentally determined the complete boiling curve for saturated R-113 at 1 atm for high-velocity flows (up to 6.8 m/s). A horizontal, steam-heated 6.5-mm-dia copper tube was used in a 38 × 127 mm channel. They found that with an increase in velocity the complete boiling curve was shifted upward. The CHF was proportional to the square root of velocity. This agreed with the dependence found by Vliet and Leppert [8] but disagreed with that determined by Lienhard and Eichhorn [12].

Lienhard and Eichhorn [12] performed a study of CHF on horizontal cylinders in a vertical crossflow in an infinite flow field to show the relationship of the saturated liquid CHF in flow boiling to that in pool boiling. It was concluded that at very low flow velocities the structure of escaping vapor jets changed from a three- to a two-dimensional pattern. The transition point between these two flow structures was correlated empirically. Sun and Lienhard's [13] pool boiling CHF model could be used to predict the low-velocity CHF before this tran-

---

Contributed by the Heat Transfer Division for publication in the JOURNAL OF HEAT TRANSFER. Manuscript received by the Heat Transfer Division December 7, 1984.

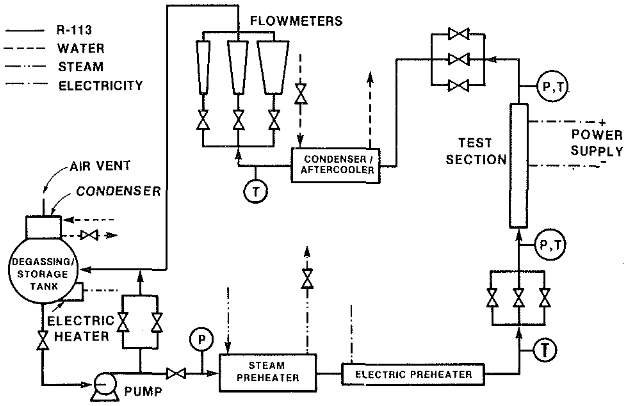

Fig. 1 Schematic of test loop

sition occurs. From an analysis using a mechanical energy stability criterion, an equation was developed to predict the low-to-moderate velocity CHF after this transition occurred. At an increased liquid velocity a second transition occurred. The two-dimensional vapor sheet appeared to narrow and a second predictive correlation involving a constant which characterizes the sheet width was developed. In a subsequent study Hasan et al. [14] extended and refined the analysis of saturated CHF in crossflow boiling for the case where the influence of gravity is negligible.

Hasan et al. [15] also investigated the CHF condition on a small cylinder in crossflow of methanol and isopropanol at one atmosphere in small tube arrays of two and three unheated cylinders placed to create interference in the liquid flow field and the vapor removal path. A single heated cylinder was placed adjacent to one or two parallel unheated cylinders in six different configurations. At low velocities ($< \sim 0.3$ m/s), the peak heat flux on all the arrays was nearly that for a single cylinder. At high velocities, neighboring cylinders had an effect only when the heated cylinder was directly in the wake of an unheated cylinder. For this case, the CHF condition was initiated when a vapor bubble or mass was trapped in the intertube space and blanketed the heated tube with an insulating layer of vapor. An unheated cylinder, four diameters or less upstream of a heated cylinder, reduced the CHF by as much as 90 percent compared to that for a single cylinder. The CHF increased as the ratio of the heater spacing to the tube diameter increased.

An analytical study of the CHF condition in an upward crossflow of saturated liquid also was conducted by Katto and Haramura [16]. The same two vapor escape flow patterns analyzed by Lienhard and Eichhorn [12] were taken into account. A hydrodynamic instability model of CHF proposed by the same researchers [17] was employed in the development of predictive correlations for the two flow regions. However, no criterion was suggested for the transition between the two regimes. The main difference between these two studies [12, 16] is that Lienhard and Eichhorn considered hydrodynamic instability between the gross liquid flow and the vapor wake from the cylinder while Katto and Haramura considered hydrodynamic instability between the liquid in the film on the heated surface and vapor columns through the liquid film.

From this brief review of some of the recent literature, it is evident that the characteristics of the saturated liquid CHF condition are relatively well understood. However, the effect of a two-phase crossflow on the CHF condition has not been investigated. Since much of the bundle in a two-phase heat exchanger is exposed to a two-phase crossflow, it is necessary to determine the effects of such a flow on the CHF condition so that better heat exchanger designs can be developed. Therefore, the present study was undertaken to examine the effect of flow velocity, pressure, and quality (both in the subcooled liquid and low-quality two-phase region) on the CHF condition on a single horizontal cylinder in a low-velocity crossflow.

Experimental Apparatus

In order to accomplish the objectives set forth in the preceding section, an experimental test section was designed for installation in an existing flow loop (see Fig. 1) which uses refrigerant R-113 as the working fluid. The selection of this refrigerant as the working fluid was due to its good modeling characteristics: Water at high pressure can be modeled with low-pressure R-113. In addition, lower test-section power is required when a refrigerant is used compared to water.

The refrigerant was kept in a storage/degassing tank provided with a 1.5 kW electric heater and a cold water condenser. Circulation of the refrigerant from the tank through the loop was done by a positive displacement pump. Liquid R-113 was first pumped through a steam-heated preheater and then through three variable-power electrical heaters, each having a maximum of 4.8 kW power. In these, the temperature of the refrigerant was raised to a level so that the desired test-section quality could be obtained after reducing the refrigerant pressure by passing the liquid through a set of three flashing valves.

A pressure gage mounted just before the flashing valves indicated the pressure of the fluid before flashing. This pressure was always kept at sufficiently high level to prevent the formation of vapor around the heaters and to ensure that the flow was single phase prior to flashing. This was done for two reasons. First, since the refrigerant was single phase, its enthalpy could be determined from the fluid pressure and temperature. Since the flashing across the flashing valves is a constant enthalpy process, by making an enthalpy balance across the flashing valves, the test-section quality could be calculated. Second, the presence of vapor in the electric heaters would lower the CHF which, if experienced, would damage the heaters and thermally decompose the refrigerant. A thermopile consisting of three thermocouples was located immediately upstream of the flashing valves to measure the fluid temperature.

After the refrigerant passed through the flashing valves, it flowed vertically upward through the test-section channel. A thermocouple located upstream of the test-section channel, far

Nomenclature

d = diameter, m
G = mass velocity, kg/m^{2}s
g = acceleration due to gravity, m/s^2
h = enthalpy, J/kg
h_{fg} = enthalpy of evaporation, J/kg
q_c = critical heat flux, W/m^2
$q_{c\,0,k}$ = critical heat flux in saturated boiling predicted by Katto equations (1) and (2), W/m^2
$q_{c\,0,z}$ = critical heat flux predicted by Zuber equation, W/m^2
R' = dimensionless radius of cylinder
u = velocity of bulk liquid flow, m/s
u' = dimensionless velocity of bulk liquid flow
w = channel depth, m
x = quality
ρ_l = density of liquid, kg/m^3
ρ_v = density of vapor, kg/m^3
σ = surface tension, N/m

Subscripts

sl = saturated liquid

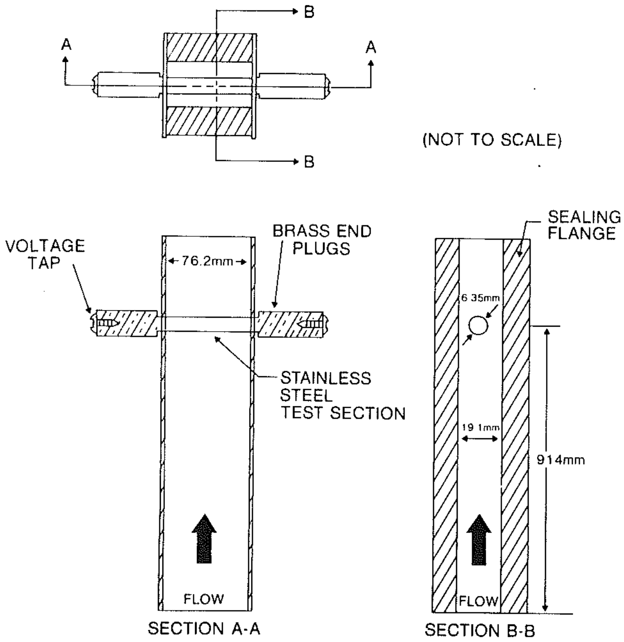

Fig. 2 Schematic of test section

enough from the flashing valves to ensure that the flow was thermally fully developed, measured the temperature of the fluid at the test-section channel inlet. Furthermore, another thermocouple and a pressure tap were located immediately upstream and downstream of the test section, respectively, to monitor the condition of the flow in the channel around the test section. A high-accuracy pressure gage (± 0.7 kPa) was used to measure the test-section pressure. Pressure fluctuations in the channel were less than ± 0.7 kPa.

The two-phase refrigerant then flowed through a set of three test-section pressure control valves and through two water-cooled condensers/aftercoolers in order to liquefy the refrigerant. Single-phase liquid then flowed through one of three rotameters, the choice depending on the flow magnitude. The temperature of the liquid flowing through these rotameters was measured using a thermocouple located downstream of the last condenser. The refrigerant then flowed back to the storage/degassing tank. A bypass line runs from the pump discharge to the return line into the storage tank. This line has two flow control valves and a pressure relief valve.

The flow loop was heavily insulated from the steam heater to the test-section pressure control valves to minimize the heat loss from the loop. This was important since the quality calculations were based on an enthalpy balance which relied on accurate temperature measurement and assumed negligible heat loss.

The test section (see Fig. 2) consisted of two main components: the test section and the channel in which the test section was located. The test section was 5.33/6.35 mm seamless stainless-steel tubing with a heated length of 76.2 mm. Two brass bar end plugs which were silver soldered to the end of the tube were used to conduct electric power to the test section. Each end plug was drilled and tapped to accommodate a small machine screw which served as a voltage tap. Direct current electrical power was supplied to the test-section tube by a 12 kW d-c silicon rectifier (< 1 percent ripple). The test-section tube was positioned horizontally in the middle of an adjustable width rectangular channel. The brass end plugs slipped into two Teflon packing glands attached to the flow channel which, when compressed, electrically insulated and hydraulically sealed the tube. Before each set of test runs, the tube surface was polished with 600 grit emery cloth and flushed with clean R-113.

The flow channel consisted of two U-sections and two stainless-steel plates assembled such that a rectangular channel 1219 mm long, 19.1 mm deep, and 76.2 mm wide was formed (see Fig. 2). A gasket was used to prevent leaks. The test section was centered in this channel 914 mm from the inlet. A pressure tap was located 150 mm downstream of the test section and a small thermocouple (to measure the fluid temperature) was located 610 mm upstream of the test section.

Experimental Procedure

Prior to running any tests, the R-113 in the loop was degassed in the degassing/storage tank. The liquid R-113 was boiled and the R-113 vapor was condensed and returned to the tank. The liberated air was vented to the atmosphere. After degassing the tank was sealed to prevent readmission of air into the system.

The flow rate was set by adjusting the flashing valves just upstream of the test-section channel and the valves located in the bypass line. The test-section quality was varied by changing the amount of energy added to the system through the steam preheater and electric heaters. The test-section pressure was controlled by the valves located immediately downstream of the test section. The heat flux was set by varying the output of the power supply.

Before any data could be taken, the flow loop had to reach a steady-state condition. This was determined by monitoring the temperature of the fluid just downstream of the flashing valves. When this temperature did not change significantly (± 0.5°C) over several minutes, then steady state was assumed. Once the steady-state flow condition was reached, the test-section heat flux was slowly increased by raising the output voltage from the power supply. Power was raised in small increments (~ 1000 W/m^2) in order to prevent premature initiation of the CHF condition.

The initiation of the CHF condition was determined by observing the current flow through the test section. When the CHF condition was reached, the test-section surface temperature would increase drastically because of the breakdown in the heat transfer process. The resistivity (and, thus, the resistance) of the stainless-steel test section increases with an increase in the wall temperature. With a constant applied voltage across the test section, the rising wall temperature results in a sharp drop in the test-section current. Hence, the current flow through the test section was continuously monitored while raising the power to the test section so that the peak heat flux could be determined. In addition, the experimental fluid conditions were continuously monitored and recorded after each change in test-section power.

After the CHF condition was observed, the power to the test section was quickly reduced and the current at the CHF condition, test-section pressure, atmospheric pressure, and the refrigerant flow rate were manually entered into the automatic data acquisition system.

After the CHF data were taken, a new flow condition was set and another set of data was recorded in the same manner as described above. It should be noted that when changing geometries the test section was inspected for both generalized and localized deposit buildup resulting from decomposition of the R-113. A localized deposit would indicate a preferential indication of the CHF condition. No deposits were observed.

The nominal ranges of experimental conditions covered in this experiment were:

Pressure	207 and 414 kPa
Quality	0 to + 30 percent
Subcooling	0 to 14 K
Average fluid approach velocity (assuming total flow is liquid)	0.070 to 0.298 m/s
Critical heat fluxes	200,000 to 360,000 W/m^2

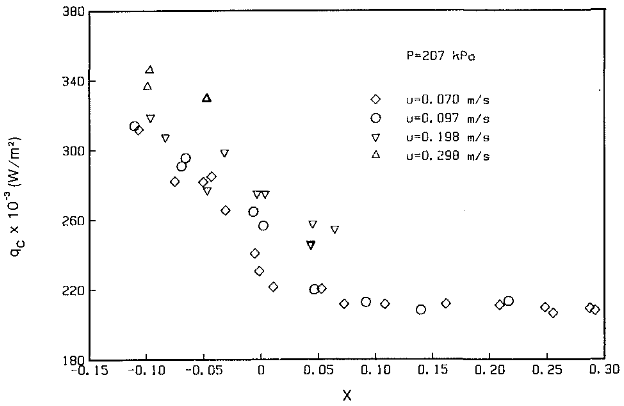

Fig. 3 Effect of quality and velocity on CHF

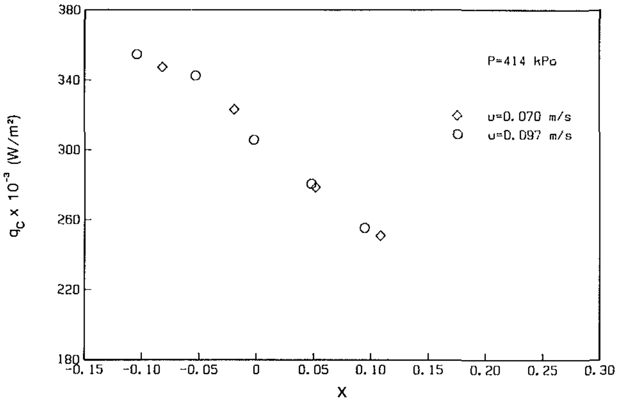

Fig. 4 Effect of quality and velocity on CHF

Uncertainties in the measured data were estimated through a propagation-of-error analysis and are suggested to be: P, ± 0.7 kPa; u, ± 2 percent; q, ± 2 percent. Details of the experimental apparatus, experimental procedure, and tabulated data can be found in [18].

Experimental Results and Discussion

Both subcooled and two-phase forced convection CHF data were taken at the two pressures. However, because of equipment limitations, data taken at the higher pressure covered a smaller range of liquid velocities and qualities compared to those at the lower pressure. At the lower pressure, the fluid velocities in the flow channel were 0.070, 0.097, 0.198, and 0.298 m/s, while only the first two velocities were used at the higher pressure. In the subcooled and saturated liquid flow, the channel flow regime was turbulent with a minimum Reynolds number of about 9000 and increasing to about 45,000 at the higher velocities and fluid temperatures. Note also that a negative quality is used to represent the subcooling and is defined by $x = (h - h_{sl})/h_{fg}$. A quality of − 10 percent represents a subcooling of about 12.1 K and 13.8 K for pressures of 414 kPa and 207 kPa, respectively.

All of the experimental data obtained in this study (Figs. 3 and 4) indicate that the CHF decreases linearly with increasing quality in both the subcooled and low quality (up to ~ 10 percent) regions at fixed pressures and fluid velocities. In this respect, these data are consistent with vertical in-tube flow CHF data (see, for example, Collier [19]) which generally show a linear decrease in the CHF as the test-section exit quality increases from the subcooled to the low-quality regions. The linear decrease in the CHF with decreasing subcooling for a crossflow has also been observed by Vliet and Leppert [9]. From visual observations on their experiment for water at one atmosphere, they concluded that the CHF mechanism for subcooled flows up to about 17 K subcooling is similar to that for saturated flows. From the present data (Figs. 3 and 4) it can be seen that the CHF-quality curve is linear from the subcooled region up to about 10 percent quality. Thus, it appears that the CHF mechanism for low quality flows ($x < \sim 10$ percent) is also similar to that for saturated flows.

However, as shown in Fig. 3, for some conditions above a quality of about 10 percent, the CHF-quality curve levels off and them remains nearly constant. (Equipment limitations prevented determination of the high quality CHF-x curve for higher pressures and flow rates shown on Fig. 4.) An explanation for this behavior possibly could be obtained by an examination of the two-phase flow regimes in the flow channel. Although the actual flow field was not observed, the flow regimes might be determined by using the flow regime maps of Hosler [20]. In that study, Hosler observed the flow regimes in a rectangular channel using water over a wide range of pressures and mass velocities and constructed flow regime maps at several pressures. The ratio of liquid density to vapor density was used to scale the present R-113 data to the water data. According to these flow regime maps, the present two-phase flows tested generally would fall into three different regimes: bubbly, slug, and annular flow. Except at very low qualities the experimental data taken up to approximately 10 percent quality would fall into the slug flow pattern. The experimental data points taken at higher qualities ($x > \sim 10$ percent) where the CHF curve is approximately horizontal would be in the annular flow regime. Thus, while it appears that the transition from slug to annular flow might be responsible for the transition in the present CHF-quality curve (Fig. 3), it does not seem reasonable since the test section would be bathed in a vapor-droplet flow and there could not be any normal CHF. It is apparent that visual observations must be made in the higher quality region ($x > \sim 10$ percent) before any speculation can be made as to the CHF mechanism in this region.

The effects of the fluid velocity in the flow channel and the test-section pressure on the CHF are also shown in Figs. 3 and 4. The CHF increases both with increasing fluid velocity and pressure. On Fig. 3, it is shown that increasing velocity increases the CHF; the velocity levels in Fig. 4 are too close to show any significant increase in CHF with velocity. Comparing data at the same velocities and qualities from Fig. 3 at 207 kPa and from Fig. 4 at 414 kPa, it is evident that the CHF increases with pressure. Both of these trends are consistent with previous saturated liquid CHF data.

In order to confirm the validity of the experimental data taken in this study, the saturated liquid CHF data were tested against two existing correlations developed to predict the CHF of saturated liquids in crossflow. However, before these correlations could be used to predict the present experimental data, the mean liquid velocities in the flow channel were corrected (according to a procedure by Vliet and Leppert [8]) since the average liquid velocity near a cylindrical heater in a finite channel is greater than the mean velocity of the oncoming liquid. The presence of the test section in the middle of the flow channel requires the liquid to accelerate because of the decrease in flow area. Thus, the mean liquid velocity has to be multiplied by a blockage correction factor, defined in [8] as $1/(1 - \pi d/4w)$, in order to give the average velocity of the liquid around the test section. The corrected velocity was used in all calculations. The velocities given for the Vliet and Leppert [9] data (used below) are the corrected values of velocity since they reported only corrected velocities; the Min [21] data did not require correction. The velocities reported for the present investigation are the uncorrected average approach velocities. (These were corrected, as stated above, for all calculations.)

The low and high-velocity correlations of both Katto and Haramura [16] and Lienhard et al. [12, 14] were used to predict the experimental saturated liquid CHF data of this study and those from [9, 21]. Only low-velocity data were used from these two studies so that the velocity levels of all the data were comparable. For the transitions between the two equations given in [12, 14], a transition criterion equation was given. For the transition for the correlations in [16] no correlation was given. However, from examination of the present R-113 data and the curves in [16], it appeared that the transition between the two models in [16] occurs between the 0.198 and 0.298 m/s velocities. Therefore, those data below 0.298 m/s were predicted with the low-velocity model and those above with the high-velocity model. The six saturated liquid CHF data (the 0.298 m/s data at 207 kPa were extrapolated to the saturation condition) were predicted with the Katto equations with an average deviation of −6.8 percent and a maximum deviation of −8.9 percent, but the Lienhard correlations gave an average absolute deviation of 48 percent. The low-velocity equation overpredicted the data and the high-velocity equation underpredicted the data.

There are several possible reasons why the correlations in [16] fit the present data better than those in [12]; in particular, the present data were obtained with a much larger diameter, at higher pressures, and at the low end of the velocity range considered in [12]. Thus, the present data appear to be beyond the range of applicability of the expressions given by Lienhard and Eichhorn. Another possibility is that the hydrodynamic instability model developed in [12] was for a specific flow field that was different from that in the present experiment. That is they considered the hydrodynamic instability between an infinite liquid flow and the vapor wake from a heated tube. The present experimental setup causes an acceleration of the flow due to channel blockage. Because of this, the model developed by Lienhard and Eichhorn [12] may not apply. However, the hydrodynamic instability model used by Katto and Haramura [16] is not tied to a specific flow field nor to the gross interactions between the liquid velocity and vapor wake. Instead, it considers the hydrodynamic instability between the liquid film on the heated surface and vapor columns or stems passing through the liquid film. Therefore, for cases where the flow field approximates an infinite flow field both sets of correlations should predict the CHF equally well; for cases where the flow field does not approximate an infinite flow field then the Katto and Haramura [16] correlations probably will give better predictions. Consequently, because of the better predictions of this data (and the data in [9, 21]) by the Katto and Haramura [16] correlations, the Lienhard and Eichhorn [12] correlations were not used in evaluating either the saturated or nonsaturated liquid CHF data. Katto's [16] correlations are given below:

Low-Velocity Model

$$\begin{aligned}\frac{q_{c\,0,k}}{q_{c\,0,z}} &= \left(\frac{\sqrt{3}}{R'}\right)^{1/16}\left[1+\frac{1}{2(R')^2}\right]^{1/32}\\ &\times\left[1+0.156\left(\frac{\rho_v}{\rho_l}\right)^{0.4}\left(1+\frac{\rho_v}{\rho_l}\right)\frac{1}{R'}\,\frac{1}{(q_{c\,0,k}/q_{c\,0,z})^2}\right]^{5/16}\\ &\times\left[1+1.68\frac{\dfrac{11}{16}+\dfrac{\rho_v}{\rho_l}}{\left(\dfrac{\rho_v}{\rho_l}\right)^{0.4}\left(1+\dfrac{\rho_v}{\rho_l}\right)}\right.\\ &\left.\times\frac{(q_{c\,0,k}/q_{c\,0,z})^3}{1+0.156\left(\dfrac{\rho_v}{\rho_l}\right)^{0.4}\left(1+\dfrac{\rho_v}{\rho_l}\right)\dfrac{1}{R'}\,\dfrac{1}{(q_{c\,0,k}/q_{c\,0,z})^2}}\,u'\right]^{1/16}\end{aligned} \tag{1}$$

where

$$q_{c\,0,z}=0.131\,\rho_v h_{fg}\left[\frac{\sigma g(\rho_l-\rho_v)}{\rho_v^2}\right]^{1/4}$$

$$R'=(d/2)/(\sigma/g(\rho_l-\rho_v))^{1/2}$$

$$u'=u/(\sigma g(\rho_l-\rho_v)/\rho_v^2)^{1/4}$$

High-Velocity Model

$$\frac{q_{c\,0,k}}{Gh_{fg}}=0.151\left(\frac{\rho_v}{\rho_l}\right)^{0.467}\left(1+\frac{\rho_v}{\rho_l}\right)^{1/3}\left(\frac{\sigma\rho_l}{G^2 d}\right)^{1/3} \tag{2}$$

Comparable predictions using the Katto correlations were obtained for the Vliet and Leppert [9] saturated liquid data using approximately the same transition velocity. However, with Min's [21] water data, much better predictions were obtained only using the Katto low-velocity model even for the data at a velocity of 0.38 m/s. Min's data were taken with much smaller diameter test sections than used in the present study or in [9]. The smaller diameter probably affects the transition between the two CHF regimes. Overall, the 14 saturated liquid data points from the three studies were predicted with an average absolute deviation of 10.9 percent. (Note that no data from studies dealing strictly with the saturated liquid CHF were included in the data analysis; it was felt that the saturated liquid CHF condition was adequately addressed with the Katto correlation, the present data, and the data from [9] and [21].) Since the saturated liquid CHF data were predicted well, the nonsaturated liquid CHF data now can be examined.

As can be seen from the subcooled and quality region data, there is a linear relationship between the CHF and quality when other conditions are held constant. The subcooled water data from [9] and [21] show the same behavior but the CHF level is significantly different. Because of the linear relationship it appears that the mechanism for all subcooled and low-quality CHF condition probably is the same (or slightly modified) as that of the saturated liquid condition. Therefore, to scale the different fluids and to help develop a correlation to describe the nonsaturated liquid CHF condition, all of the CHF data were nondimensionalized by dividing the data with the saturated liquid CHF as predicted with either equations (1) or (2). These dimensionless CHF data are plotted versus test-section quality in Figs. 5 and 6.

Three points should be noted in examining these figures. First, the effect of velocity in the subcooled and quality regions is not completely modeled by the saturated liquid CHF correlation. As shown on Figs. 5 and 6, the CHF ratio generally decreases with decreasing velocity at a given pressure and quality. Second, in comparing these three sets of data, note that on a CHF ratio–quality plot the Vliet and Leppert [9] and Min [21] data have a much steeper slope (an order of magnitude larger) than the data from this study, but the Vliet and Leppert [9] data and Min's [21] data have slopes which are comparable. Considering that the data from those two studies were obtained for different sizes of test sections (0.51 to 3.18 mm) while the fluid (water at one atmosphere) used in those experiments was the same and the fluid velocites over the test sections were comparable, it may be concluded that the effect of the test-section diameter is not stong enough to cause a major shift of the slope of the data, but that the diameter effect is accounted for in the saturated liquid correlation. Third, in comparing the experimental results of this study with those of Vliet and Leppert [9] and Min [21], the liquid velocities are comparable. However, the flowing fluid and the size of the test section used in this study differ from those of the other two studies. Since it was concluded above that the effects of the test-section diameter are accounted for in the saturated liquid correlation, then it is a reasonable conclusion that the difference in fluid properties of water and the refrigerant is mainly responsible for shifting of the slope of the CHF ratio–quality curve.

In order to single out the important parameters affecting the

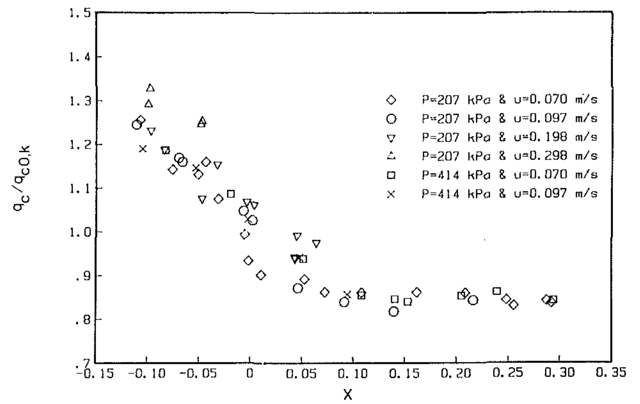

Fig. 5 Variation in the nondimensional CHF with quality and velocity

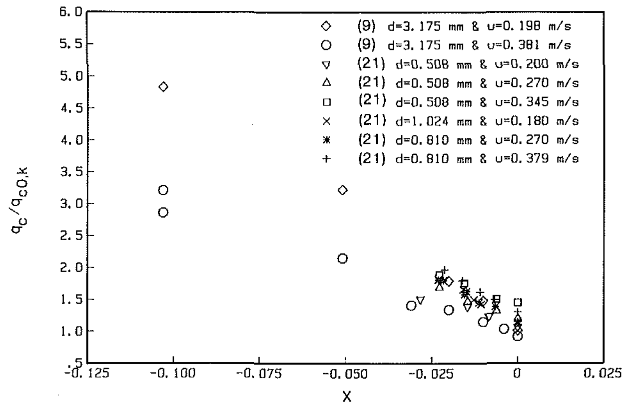

Fig. 6 Variation in the nondimensional CHF with quality and velocity

nonsaturated liquid CHF, a heuristic dimensional analysis was performed and five dimensionless groups were obtained. Since liquid velocity has been shown to be an important parameter, the dimensionless velocity of the bulk fluid u' proposed by Katto and Haramura [16] was taken as a dimensionless term. (For the two-phase region, the velocity used in u' was defined as if the total fluid flow was liquid.) The density ratio ρ_l/ρ_v is a commonly used scaling parameter and was used here. Quality and the CHF ratio were used as two other dimensionless terms since they were already dimensionless. According to Lienhard's [12] CHF model, surface tension is an important parameter governing the CHF behavior. Thus, a Weber number $u^2\rho_l d/\sigma$ was formed using the test-section tube diameter, the fluid density, and the surface tension. Thus, the final dimensionless relationship can be expressed as

$$\frac{q_c}{q_{c\,0,k}}=f\left(\frac{\rho_l}{\rho_v},\ x,\ u',\ \frac{u^2\rho_l d}{\sigma}\right) \tag{3}$$

The form of the above relation may be simplified under two reasonable assumptions: (1) By examination of Figs. 5 and 6, the relationship of the CHF ratio and quality is known to be a linear one; (2) the CHF ratio must be unity at the saturated liquid ($x = 0.0$) condition. These assumptions result in a relation of the form

$$\frac{q_c}{q_{c\,0,k}}=1+g\left(\frac{\rho_l}{\rho_v},\ u',\ \frac{u^2\rho_l d}{\sigma}\right)x \tag{4}$$

A nonlinear regression computer program was used to determine the form of the above functional relation. Numerous functional relationships using the four independent variables were tried. Only the data in the linearly decreasing portion of the CHF-quality curve were used. These data included the 41 data points from this experiment together with 42 subcooled data points from Vliet and Leppert [9] and Min [21]. From this analysis, it was found that a power function relation best approximated the data. Thus, the equation has the form of

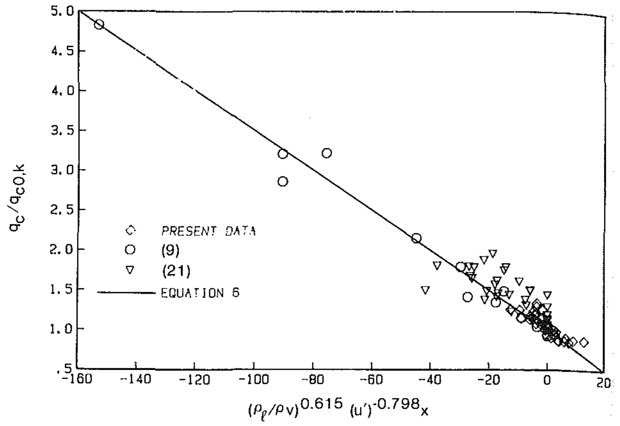

Fig. 7 Predicted data and correlation

$$\frac{q_c}{q_{c\,0,k}}=1+c_1\left(\frac{\rho_l}{\rho_v}\right)^{c_2}(u')^{c_3}\left(\frac{u^2\rho_l d}{\sigma}\right)^{c_4}x \tag{5}$$

By examining the resulting equations and by successively removing each of the dimensionless terms and refitting the resulting equation to the data, it was determined that the term $u^2\rho_l d/\sigma$ had a negligible effect on the CHF ratio. Therefore, this dimensionless group was not used in developing the final correlation

$$\frac{q_c}{q_{c\,0,k}}=1-0.025\left(\frac{\rho_l}{\rho_v}\right)^{0.615}(u')^{-0.798}x \tag{6}$$

The correlation predicted the data from the three studies well. The average ratio of the predicted CHF ratio to the experimental CHF ratio was 0.952 and the average deviation between the predicted and experimental CHF ratios was 8.8 percent. The data from this study had an average deviation of 5.9 percent; from [9] it was 6.6 percent; and from [21] it was 13.8 percent. The correlation and the data are shown in Fig. 7.

Many of the data examined in the present study were in the subcooled region, and, as mentioned previously, because of the linear relationship between CHF and quality in the subcooled and low-quality regions the CHF mechanisms are probably very similar. Hence, the present correlation (equation 6) could be considered more a subcooled correlation that can be extrapolated into the low-quality region rather than a two-phase region correlation.

The CHF predicted by this correlation could be assumed to be an upper limit of the CHF condition for a tube bundle. However, for several reasons it might also be suitable to predict the actual CHF condition in some tube bundles. In the paper by Lienhard et al. [15], an unheated cylinder upstream of the heated cylinder caused a dramatic decrease (up to 90 percent) in the CHF if the velocity was high and the spacing between the cylinders was small. At low saturated liquid velocities (< ~ 0.3 m/s) little degradation in the CHF was evident for any of the tube spacings. Cornwell et al. [1] studied a small slice of a kettle reboiler at a small tube spacing and found that liquid velocities just outside of the bundle ranged from 0.1 to 0.4 m/s depending on the location and heat flux. The CHF condition did not occur on any of the tubes, even though at the top of the bundle there was a high voidage region (quality approaching 3–5 percent) and the heat flux approached the CHF of a single tube under pool boiling conditions [22]. If the velocities measured in that study are comparable to those commonly experienced in actual operating units, then the influence of surrounding tubes might be small, thus permitting the prediction of the CHF condition on each tube with the proposed correlation. The main question, though, is whether or not the two-phase CHF mechanism on a tube in a tube bundle at low velocity is similar to that experienced in [15] for a tube with an unheated tube upstream. This needs to be determined before any quantitative conclusions can be made.

Conclusions

An experimental study has been conducted to investigate the CHF condition in two-phase crossflow over a single horizontal cylinder. The following conclusions can be drawn from this study:

1. In the range of fluid conditions tested the CHF linearly decreases as the quality increases in the subcooled and low-quality two-phase regions. Above a quality of approximately 10 percent in the two-phase regions, the CHF remained constant due to a transition in the two-phase flow pattern.
2. In the range of fluid conditions tested the CHF in the subcooled and two-phase boiling increases directly with an increase in fluid velocity and pressure.
3. A correlation has been developed which predicted well the CHF on a single horizontal cylinder in crossflow boiling in the subcooled and low-quality regions for the range of conditions examined in this study. The correlation should be tested against other data when they become available so that the range of applicability can be determined.

Acknowledgments

Support for this work was provided in part by the Graduate School of the University of Wisconsin—Milwaukee. Mr. Gene Menzel helped to fabricate the test section and flow channel.

References

1 Cornwell, K., Duffin, N. W., and Schuller, R. B., "An Experimental Study of the Effects of Fluid Flow on Boiling Within a Kettle Reboiler Tube Bundle," ASME Paper No. 80-HT-45, 1980.

2 Abbott, M. D., and Comley, W. D., S. M. Thesis, Massachusetts Institute of Technology, Cambridge, MA, 1938.

3 Palen, J. W., Yarden, A., and Taborek, J., "Characteristics of Boiling Outside of Large Scale Horizontal Multitube Bundles." *AIChE Symp. Ser. No. 118*, Vol. 68, 1972, pp. 50-61.

4 Kern, D. Q., *Process Heat Transfer*, McGraw-Hill Kogakusha Ltd., Tokyo, 1950, p. 459.

5 Palen, J. W., and Taborek, J., "Refinery Kettle Reboilers—Proposed Method for Design and Optimization," *Chemical Engineering Progress*, Vol. 58, 1962, pp. 37-46.

6 Palen, J. W., and Small, W. M., "New Way to Design Kettle and Internal Reboilers," *Hydrocarbon Processing and Petroleum Refiner*, Vol. 43, 1964, pp. 199-208.

7 Fokin, B. S., and Goldberg, E. N., "Model of Boiling Crisis Under Conditions of Free Convecton in a Bundle of Horizontal Pipes Flushed With Air," *High Temperature*, Vol. 18, 1980, pp. 806-810.

8 Vliet, G. C., and Leppert, G., "Critical Heat Flux for Nearly Saturated Water Flowing Normal to a Cylinder," ASME JOURNAL OF HEAT TRANSFER, Vol. 86, 1964, pp. 59-67.

9 Vliet, G. C., and Leppert, G., "Critical Heat Flux for Subcooled Water Flowing Normal to a Cylinder," ASME JOURNAL OF HEAT TRANSFER. Vol. 86, 1964, pp. 68-73.

10 Ornatskiy, A. P., Kichigin, A. M., and Kesova, L. A., "Burnout of Cylindrical Surfaces in Transverse Flow," *Heat Transfer—Soviet Research*, Vol. 1, 1969, pp. 110-123.

11 Yilmaz, S., and Westwater, J. W., "Effect of Velocity on Heat Transfer to Boiling Freon-113," ASME JOURNAL OF HEAT TRANSFER, Vol. 102, 1980, pp. 26-31.

12 Lienhard, J. H., and Eichhorn, R., "Peak Boiling Heat Flux on Cylinders in a Crossflow," *International Journal of Heat and Mass Transfer*, Vol. 19, 1976, pp. 1135-1142.

13 Sun, K. H., and Lienhard, J. H., "The Peak Pool Boiling Heat Flux on Horizontal Cylinders," *International Journal of Heat and Mass Transfer*, Vol. 13, 1970, pp. 1425-1439.

14 Hasan, M. Z., Hasan, M. M., Eichhorn, R., and Lienhard, J. H., "Boiling Burnout During Crossflow Over Cylinders Beyond the Influence of Gravity," ASME JOURNAL OF HEAT TRANSFER, Vol. 103, 1981, pp. 478-484.

15 Hasan, M. M., Eichhorn, R., and Lienhard, J. H., "Burnout During Flow Across a Small Cylinder Influenced by Parallel Cylinders," *Proceedings of the Seventh Int. Heat Transfer Conf.*, Hemisphere, Washington, 1982, Vol. 4, pp. 285-290.

16 Katto, Y., and Haramura, Y., "Critical Heat Flux on a Uniformly Heated Horizontal Cylinder in an Upward Crossflow of Saturated Liquid," *International Journal of Heat and Mass Transfer*, Vol. 26, 1983, pp. 1199-1205.

17 Haramura, Y., and Katto, Y., "A New Hydrodynamic Model of Critical Heat Flux, Applicable Widely to Both Pool and Forced Convection Boiling on Submerged Bodies in Saturated Liquid," *International Journal of Heat and Mass Transfer*, Vol. 26, 1983, pp. 389-399.

18 Pourdashti, M. "Critical Heat Flux on a Horizontal Cylinder in an Upward Two-Phase Crossflow," M.S. Thesis, University of Wisconsin—Milwaukee, Milwaukee, WI, 1984.

19 Collier, J. G., *Convective Boiling and Condensation*, McGraw-Hill, London, 1972, p. 243.

20 Hosler, E. R., "Flow Patterns in High Pressure Two-Phase (Steam-Water) Flow With Heat Addition," *Chemical Engineering Progress Symposium Series, No. 82*, Vol. 64, 1968, pp. 58-66.

21 Min, T. K., "Boiling on Cylinders in Crossflow—Low Velocity Peak Heat Flux Measurements for Water and Methanol," M.S. Thesis, University of Kentucky, Lexington, KY, 1975.

22 Leong, L. S., and Cornwell, K., "Heat Transfer Coefficients in a Reboiler Tube Bundle," *The Chemical Engineer*, Apr. 1979, pp. 219-221.

Reflooding With Steady and Oscillatory Coolant Injection: Part 2—Quench Front and Liquid Carryover Behavior

S. Oh
JAYCOR, Inc.,
San Diego, CA

S. Banerjee
Department of Chemical and
Nuclear Engineering,
University of California,
Santa Barbara, CA 93106

G. Yadigaroglu
Institute for Energy Technology,
Swiss Federal Institute of Technology,
ETH-Zentrum,
CH-8092 Zurich, Switzerland

The reflooding of a tubular test section under oscillatory inlet flow conditions has been investigated experimentally for initial wall temperatures from 316°C to 760°C, oscillation periods from 2 to 6 s, and test section liquid level amplitudes up to 0.76 m. Compared to constant-injection reflooding, the oscillations always increase the liquid carryover rate in the early stages of reflooding. As reflooding progresses, the enhancement diminishes and becomes negative. The crossover point roughly coincides with saturation of the liquid at the quench front. The higher initial liquid carryover increases downstream heat transfer and speeds up quench front propagation, but it also reduces the test section mass accumulation rate, and for this reason delays quench front propagation at later stages. These effects are accentuated at higher oscillation amplitude and frequency. Large oscillations change the reflooding behavior substantially. Quantitative comparisons of quench front velocities and heat transfer immediately downstream of the quench front, obtained through the use of empirical local-condition correlations representing the steady-reflooding rate data, are presented.

Introduction

The importance of the reflooding phase of the postulated Loss-of-Coolant Accident (LOCA) in Pressurized Water Reactors (PWR) was outlined in Part 1 of this paper, in which the general features of the experimental and analytical efforts undertaken at the University of California—Berkeley to better understand and model the complex reflooding phenomena were presented.

Following a series of experiments conducted at steady forced-injection reflooding rates [1-3], the forced-oscillation experiments presented in Parts 1 and 2 of this paper were planned and conducted [4, 5]. The flow was oscillated using a piston-cylinder assembly driven by a variable-speed motor. The amplitude of the flow oscillation was varied by adjusting mechanically the linkage between the motor and the oscillating piston.

Realizing the importance of liquid carryover for the correct understanding and analytical description of both fluid flow and heat transfer mechanisms during reflooding, special care was taken in designing a liquid separator, installed at the exit of the test section, making separation of the superheated vapor from the liquid droplets possible with a minimum of phase change [6].

The main results regarding flow regimes, the void fraction, and heat transfer were reported in Part 1. We will concentrate in this second part on the progression of the quench front, on liquid carryover, and on heat transfer immediately downstream of the quench front. Additional information on these topics can be found in [4].

The main emphasis of the experimental program was on providing direct quantitative comparisons of fluid flow and heat transfer with and without oscillations of the inlet flow rate. For this purpose some of the earlier steady-reflooding runs were repeated to verify the reproducibility of the data.

Due to the practical impossibility of obtaining detailed and accurate time-dependent heat transfer and liquid carryover measurements during oscillatory reflooding, the instrumentation and the data reduction techniques were oriented toward the obtainment of time-averaged values.

Since two new dimensions were added to the test matrix, namely the amplitude and the period of the oscillations, the variation of the inlet and boundary conditions had to be restricted. Thus all tests reported in this part of the work were conducted with a unique inlet velocity and subcooling. This data base is, however, complemented by the second set of experiments presented in Part 1 and in [3, 5].

Experimental Setup, Test Plan, and Data Reduction

The general features of the experimental rig were presented in Part 1. Therefore, only the features of the equipment used to separate and meter the exit liquid flow rate will be discussed here.

Exit Mixture Separator. Separate (liquid and vapor) carryover measurements at the channel exit are made difficult by the fact that the phases are generally not in thermodynamic equilibrium at that location. The method for carryover measurements used consisted in separating, collecting, and measuring the liquid carryover rate and in the direct measurement of the exit steam flow rate.

The separator was designed for separating the exit mixture as rapidly as possible, in order to avoid phase changes during separation. It was made up of a 20-cm-dia chamber placed directly at the exit of the channel. The exiting two-phase mixture impinges upon a cone pointing downward. The liquid hits the cone and falls to the bottom of the chamber, which has the form of a funnel, from where it is directed to the liquid metering system. The steam exits from the top of the chamber. Since the evaporation rate is highest when the liquid is finely divided, creation of a liquid film on the cone should reduce the available interfacial surface, and consequently the evaporation of the liquid.

The separator design was optimized and its separating performance tested by a series of preliminary experiments conducted with various separator cone and base designs [6]. Phase changes were minimized by maintaining the separator walls near saturation temperature: An optimal method was devised

---

Contributed by the Heat Transfer Division for publication in the JOURNAL OF HEAT TRANSFER. Manuscript received by the Heat Transfer Division October 2, 1984.

by tape-heating to temperatures somewhat above saturation (105°C) the upper portion of the separator wall where droplets do not impinge. The lower surface where droplets come into contact was heated by blowing hot air into an annular space surrounding the separator chamber.

The actual separator was tested by injecting into it a mixture of superheated steam and droplets. The droplets had diameters in the vicinity of 100 micrometers, while 120-205°C (250-400°F) steam entered the chamber with a velocity of 40 to 120 m/s. Under these conditions the phase changes (generally condensation) amounted to 2-3 percent of the total flow rate at most.

Liquid Collection and Measurement. The liquid collector was a 47.6-mm i.d., 533-mm-long cylinder connected to the separator by a short tube. The height of the water column collected could be continuously measured by a 0.17 bar (2.5 psid) differential pressure transducer. The connecting tube was heated and insulated and the chamber was immersed in a boiling water bath to prevent it from becoming a heat sink. The collector could be drained during a run if its capacity was exceeded. Tests have shown that the delay between the moment that liquid carryover enters the separator and the time it is recorded amounted to only a few seconds [6], and was generally neglected.

Differentiation, after smoothing, of the differential pressure (water level) trace gives the instantaneous water collection rate.

Test Matrix. A total of 75 runs were completed for different initial and boundary conditions, namely:

Exit pressure	Nearly atmospheric
Initial wall temperature	316, 538, and 760°C
Corresponding linear heat generation rate	0.42, 1.3 and 2.7 kW/m
Average inlet injection velocity	7.6 cm/s
Inlet water temperature	23°C
Oscillation amplitude (half wave)	0.15, 0.30, 0.45, 0.61, and 0.76 m
Oscillation period	2, 4, and 6 s

As noted in the introduction, the main goal of the experimental program was to study the effect of the amplitude and period of the oscillations. Thus all the oscillatory experiments presented here were conducted with the same average reflooding velocity and inlet temperature. The effect of the initial wall temperature was, however, studied systematically. For comparison, constant injection reflooding tests without oscillations were also conducted for each value of the initial wall temperature. Detailed information on the experiments and their analysis is presented by Oh [4].

Comparison With Similar Experimental Work. Experiments with forced oscillatory reflooding were also conducted at the Argonne National Laboratory (ANL) [7] and in France [8]. The amplitudes of imposed oscillations in these experiments were, however, significantly smaller than in the UC – Berkeley tests; thus the experimental findings from these experiments are less pronounced. The Berkeley amplitudes cover, however, the range observed during gravity-reflood tests in large installations.

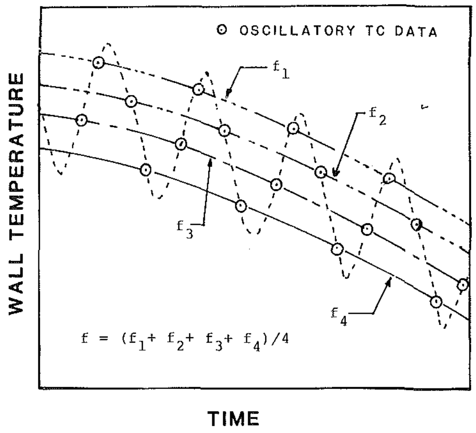

Fig. 1(*a*) Method used for smoothing oscillatory temperature records

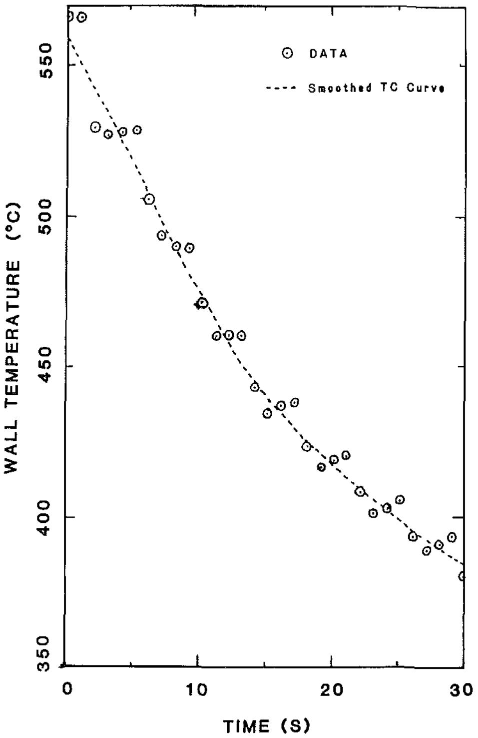

Fig. 1(*b*) Example of smoothed wall temperature

Fig. 1 Thermocouple at 1.4 m elevation; oscillation amplitude: 0.82 m; period: 4 s

Indeed, the ANL tests covered a range of periods extending from 0.3 to 5 s, but the amplitude of the peak-to-peak water level oscillation in the test section was at most in the range of 20 cm, while tests with peak-to-peak amplitudes as high as 150 cm were conducted at Berkeley. The largest differences in quench time observed in the ANL tests did not exceed 25 percent.

Insignificant differences in behavior are reported in [8].

Nomenclature

a = coefficient in equation (1)
B = coefficient in equation (2)
C_w = heat capacity of the wall per unit length, J/m°C
h = heat transfer coefficient (based on saturation temperature)
h_{LG} = latent heat
h_o = coefficient in equation (1)
T = temperature
T_{aq} = wall temperature after quench
T_{bq} = wall temperature before quench
U_q = velocity of quench front
V_{in} = average inlet (reflooding) velocity
w_{in} = average inlet flow rate
x_{eq}^+ = equilibrium quality calculated just above the quench front
x_{eq}^- = equilibrium quality calculated just below the quench front
Δz_q = distance from quench front

Again, the peak-to-peak amplitudes in the French tests were only in the range of 10 to 50 cm.

Data Reduction. As mentioned in Part 1, the wall temperatures were measured with 0.25 mm thermocouples spot welded on the outside surface of the test section, and the heat flux to the fluid was obtained using a simple heat balance involving the rate of change of the wall temperature.

Under oscillatory reflooding conditions, the wall temperatures oscillate with the imposed period. The limitations regarding the scanning rate and the time response of the wall thermocouples make the calculation of the instantaneous value of the heat flux problematic; thus it was decided to locally smooth the temperature traces and use the smoothed records for calculating the heat flux. Since the wall temperatures always oscillated with the imposed period, which was an exact multiple of the scanning time (1 s), the smoothing method [4], illustrated in Fig. 1 for an oscillation period of 4 s, was devised and used: The method consisted in fitting, over a given time interval, cubic spline functions to the data sets obtained by sampling the signal at intervals equal to the period, shifted by one second every time. The sampled data sets were generally much smoother than the original complete data sets. The average spline fit obtained by averaging the coefficients of the spline fits constituted the smoothed temperature record.

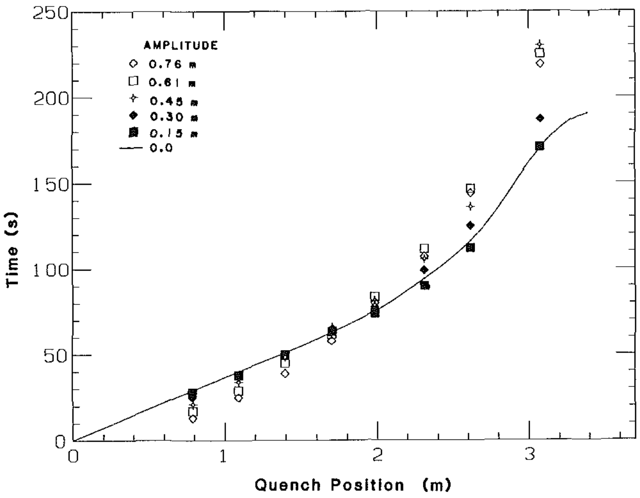

Fig. 2 Effect of oscillation amplitude on quench front propagation; 538°C initial-wall-temperature run, 4-s oscillation period

Reflooding Under Oscillatory Inlet Conditions

When flow oscillations are superimposed on the injection rate, the liquid carryover, heat transfer downstream of the quench front, and the velocity of the quench front are initially increased. However, as reflooding progresses, the oscillations reduce the quench front velocities to values well below those obtained from constant-injection reflooding tests. The increase and subsequent decrease in quench front velocity become more pronounced as the oscillation amplitude and frequency increase. The reasons for this behavior will be explained below in terms of the combined effects of the oscillations and of the liquid inventory in the test section.

Quench Front Behavior

Effects of Initial Wall Temperature and Power Level. The oscillations shorten the quench time for all 316°C initial-wall-temperature runs. However, as the quench front progresses upward to a higher elevation, the difference in quench time gets smaller. No figures are shown to demonstrate this, because the effect becomes clearer at higher initial wall temperatures. For the 538°C initial-wall-temperature runs, the oscillations enhance the quench front progression initially, as shown in Fig. 2. But the difference gets smaller and a crossover occurs about the time the midplane quenches. After the crossover, the oscillations delay quench front propagation.

For 760°C initial-wall-temperature runs, the delay in quenching becomes progressively more important as the quench front advances. The quench times at the 2.5-m elevation between the constant injection runs and the oscillatory runs differ by 100 to 400 s. This is clearly shown in Fig. 3.

Effect of Oscillation Amplitude and Period. For the low initial-wall-temperature (316°C) runs and the early stages of the 538°C runs, higher-amplitude oscillations reduce the quench time. At the later stages of the 538°C runs, and during all stages of the 760°C runs, the quench time becomes longer as the amplitude increases. Similar, but not as pronounced, parametric trends are reported by Cha et al. [7].

As shown in Fig. 4, the effect of shorter periods is similar to that of larger oscillation amplitudes.

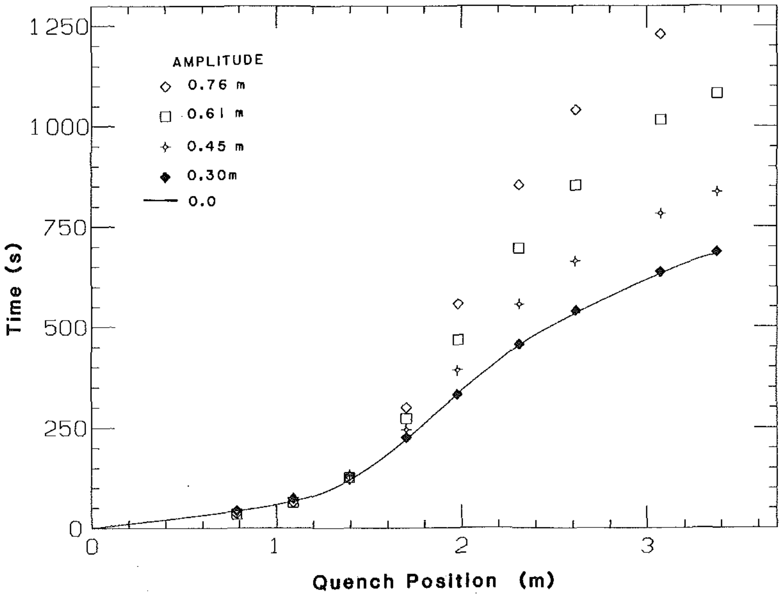

Fig. 3 Effect of oscillation amplitude on quench front propagation; 760°C initial-wall-temperature run, 4-s oscillation period

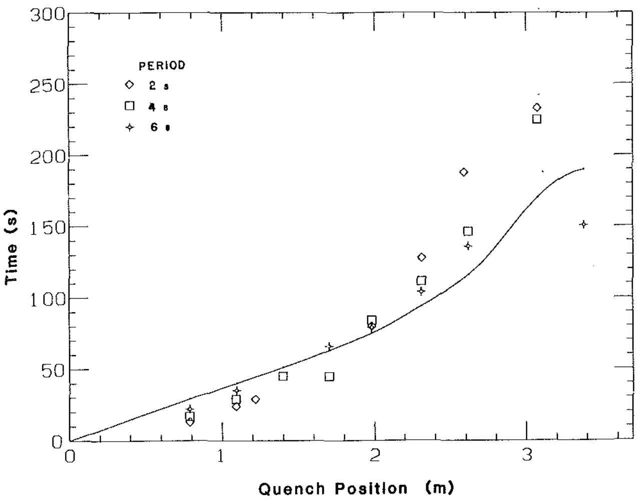

Fig. 4 Effect of oscillation period on propagation of quench front; 538°C initial-wall-temperature run, 0.61 m oscillation amplitude

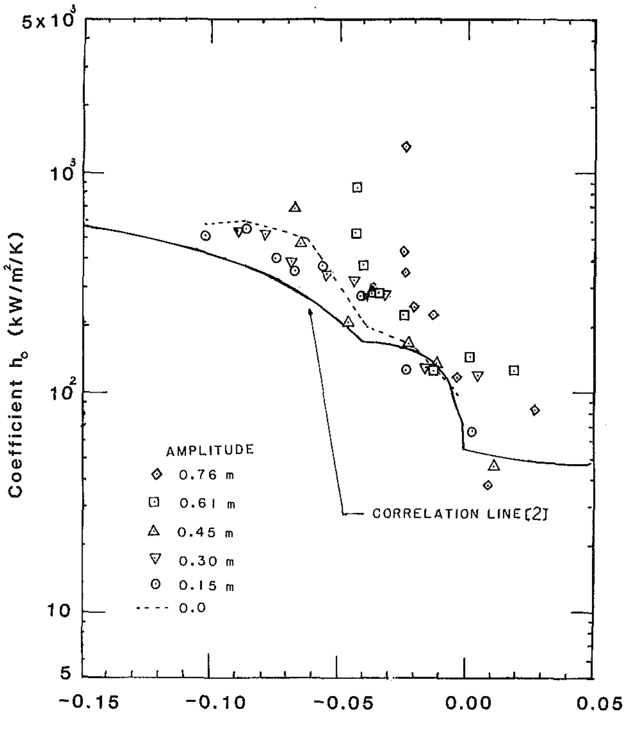

Fig. 5 Variation of the wet-side heat transfer coefficient used in the axial conduction calculation under subcooled flow conditions at the quench front; 538°C initial-wall-temperature runs, 4-s oscillation period

For the 760°C initial-wall-temperature runs, the combined effects of period and amplitude are notable. For the 6-s-period runs the quench time is significantly longer for amplitudes 0.61 m and larger, while amplitudes 0.45 m and smaller produce only small effects. For the 4-s-period runs, amplitudes 0.45 m and larger delay quenching of the higher elevations, while for the 2-s-period runs, amplitudes 0.15 m and larger increase the quench time. Thus we find a synergistic effect of oscillation amplitude and frequency in delaying the quenching of the higher elevations for the high initial-wall-temperature runs. This effect can probably be correlated in terms of the module of the oscillation velocity, which is related to the product of frequency times amplitude.

Comparisons on a Local-Condition Basis. Since conditions anywhere in the channel depend on the entire history of the reflood transient, comparisons based on the initial and boundary conditions have their limitations. On the other hand, it is very difficult to compare a large number of quench front velocities with and without oscillations on the basis of local flow and wall conditions at the location of the quench front, since it is difficult to find identical experimental points, i.e., points for which all the relevant variables have identical average values. Thus a comparison of the oscillatory data with a correlation reproducing well the steady reflooding data becomes necessary. The correlation obtained by Yu [2] using the first series of steady-reflooding-rate UC – Berkeley experiments was used to this effect, essentially as an interpolation tool.

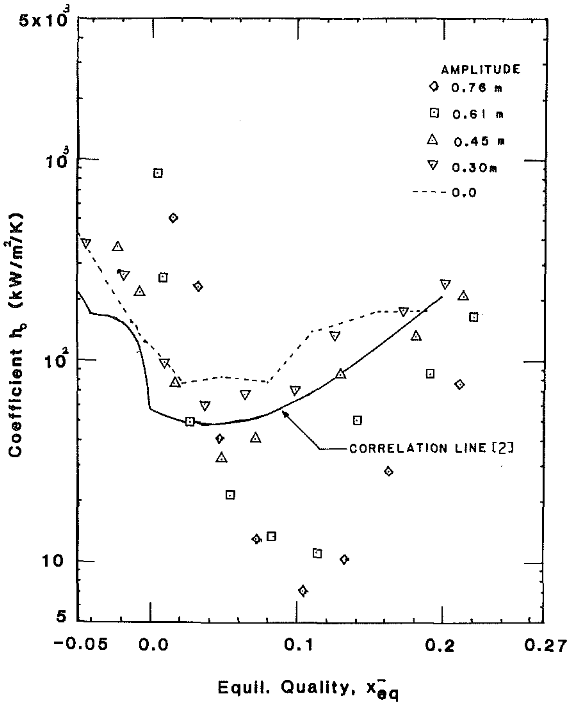

Fig. 6 Variation of the wet-side heat transfer coefficient used in the axial conduction calculation under saturated flow conditions at the quench front; 760°C initial-wall-temperature runs, 4-s oscillation period

Quench front propagation data have been successfully correlated by many investigators assuming that axial conduction with or without precursory cooling of the surface is the controlling mechanism [9]. Yu [2], following the example of Yu et al. [10], utilized a two-dimensional axial conduction model assuming that the heat transfer coefficient is zero above the quench front and high below the quench front (in the wetted region). The method consists of processing the quench front velocity data to obtain this wet-side heat transfer coefficient, which is then correlated in terms of the local flow conditions. Yu [2] used the equilibrium quality (or subcooling) immediately upstream of the quench front and the reflooding velocity as correlating parameters.

The following discussion of the quench front velocity behavior under oscillatory conditions is in terms of the value of this wet-side heat transfer coefficient, which is essentially a measure of the quench front velocity and increases as this velocity increases. Note that the effect of wall temperature before the quench front is taken into consideration in the axial conduction calculation, and does not appear in the wet-side heat transfer coefficient correlation.

As discussed by Oh [4], there exists some ambiguity in determining the average equilibrium quality at the quench front, mainly because of an uncertainty regarding the average channel-inlet temperature during oscillatory reflooding; the latter is affected by the energy stored in the helicoidal inlet piping of the test section which receives the reverse flow during the downstroke. This will not be further discussed here, except to point out that there is an uncertainty regarding the effect of the flow oscillations on the wet-side heat transfer coefficient.

Figure 5 presents data from 538°C initial-wall-temperature runs, which tend to produce quenching under subcooled-flow conditions at the quench front. The figure shows that the oscillations substantially increase the wet-side heat transfer coefficient. The effect is more pronounced as the oscillation amplitude and frequency increase. Note, however, that the values of the heat transfer coefficient approach the Yu correlation line for equilibrium qualities near zero.

Figure 6, in which data from 760°C runs are plotted, shows that for quench front equilibrium qualities between 0.05 and 0.15, increases in oscillation amplitude (and, as revealed by the experiments, also in oscillation period) decrease the wet-side heat transfer coefficient well below the Yu correlation line, i.e., well below the steady-reflooding values. However, for negative or saturation equilibrium quality below the quench front, the values of the wet-side heat transfer coefficient lie again well above the steady-reflooding correlation line.

The lines obtained using the steady-reflooding data from the present series are also shown in Figs. 5 and 6. These do not coincide exactly with the Yu correlation line but are in reasonable agreement, given the overall scatter of the data and experimental uncertainties.

In conclusion, it can be said that the behavior of the wet-side heat transfer coefficient (and hence quench front velocity) depends on whether the equilibrium quality just below the quench front is positive or negative. Oscillations generally have a small effect when their amplitude is less then 0.3 m or if their period is 6 s or longer. Use of the Yu correlation [2], based on the previous steady-reflooding rate experiments, made a systematic evaluation of the effects of large-amplitude or high-frequency oscillations possible.

Heat Transfer Immediately Downstream of the Quench Front

The effect of the oscillations on heat transfer above the quench front was addressed in Part 1. Additional observations regarding heat transfer immediately downstream of the quench front are reported here. Heat transfer in this zone, i.e., in a length extending 10 to 30 cm downstream of the quench front, is important since it provides the precursory cooling that in turn controls the rate of quenching. The flow regime in this zone is either inverted-annular or dispersed-flow (or dispersed-droplet) film boiling (IAFB and DFFB, respectively). IAFB can be associated with the presence of subcooled flow at the quench front, while DFFB occurs under saturated conditions at the quench front [11].

None of the presently available classical film boiling models or correlations can adequately represent heat transfer in this region, especially in relation to reproducing the strong observed effects of mass flux and subcooling (or quality).

Figure 7 shows the variation of the heat transfer coefficients at various axial locations for an oscillatory run and the corresponding steady-reflooding run. For the oscillatory run, we note that the wall at the lower 0.79 cm elevation experiences a very high heat transfer rate from the beginning. Indeed, with a 0.61-m oscillation amplitude and a 4-s period, starting from the lowest point of the cycle, the liquid column has already reached the 0.61 and 1.22 m locations in 2 and 4 s, respectively. Thus the IAFB heat transfer regime is reached rapidly at this location.

The higher elevations also experienced enhanced heat transfer at the beginning of the test, as compared to the steady reflooding run. Indeed, the oscillations produced DFFB rather than simple heat transfer to superheated steam or enhanced the DFFB heat transfer.

Following the DFFB regime, the heat transfer coefficient increases to values between 0.1 and 0.2 kW/m^2. During the upstroke of the oscillations, in this case, a liquid column is present in the tube and the flow regime can be considered, in an average sense, as being analogous to IAFB during steady reflooding.

The experimental data also revealed that after quenching there is little difference in heat transfer between oscillatory and steady reflooding runs. This is consistent with the fact that, in nucleate boiling, the heat transfer coefficient is insensitive to velocity variations. In the forced-convection-to-liquid

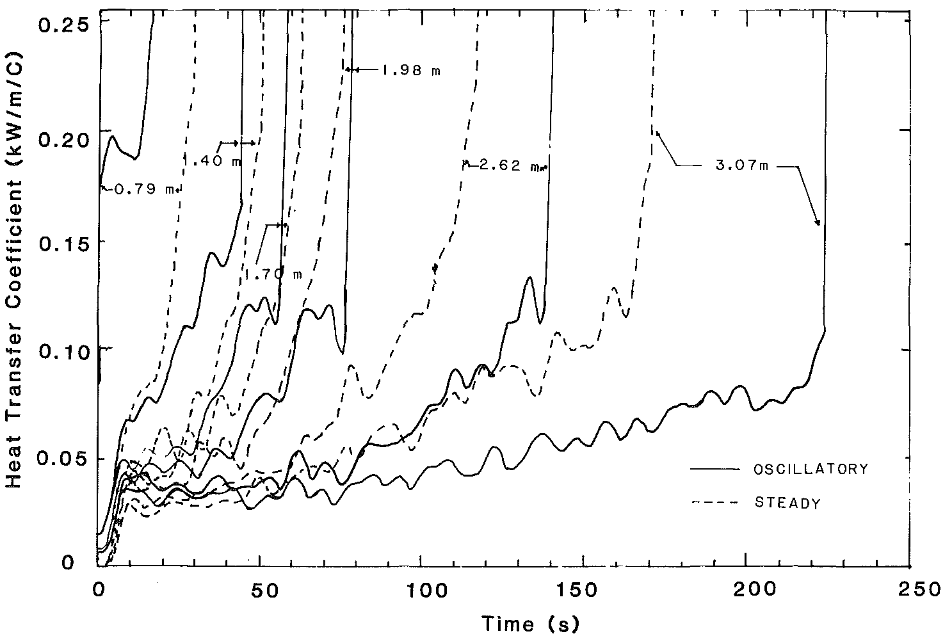

Fig. 7 Comparison of the heat transfer coefficients obtained with and without oscillations; 538°C initial-wall-temperature runs, 4-s period, 0.61 m amplitude (thermocouple axial locations indicated in the figure)

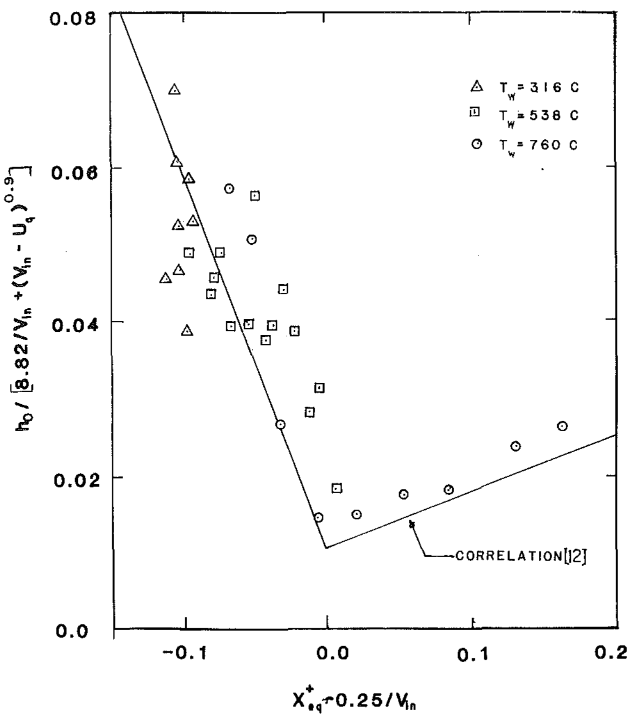

Fig. 8 Comparison of the present constant-reflooding-rate heat transfer data with the Yu and Yadigaroglu [12] correlation line

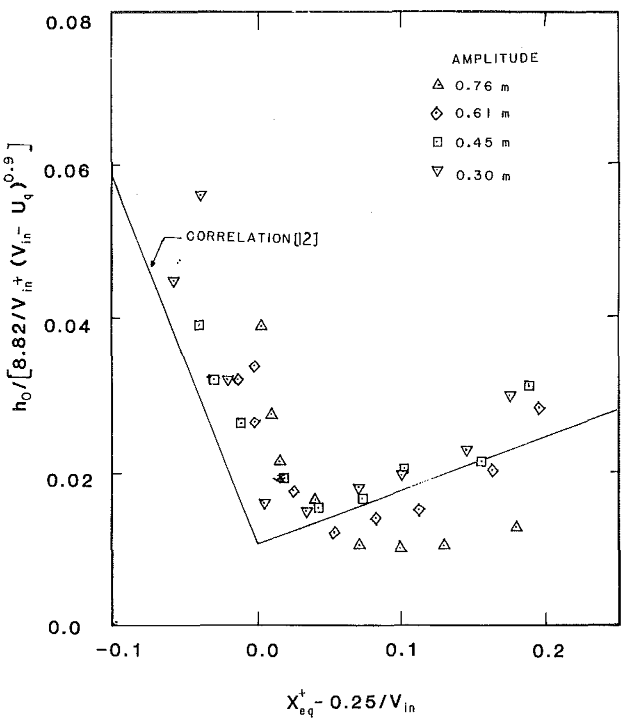

Fig. 9(*a*) Coefficient h_0

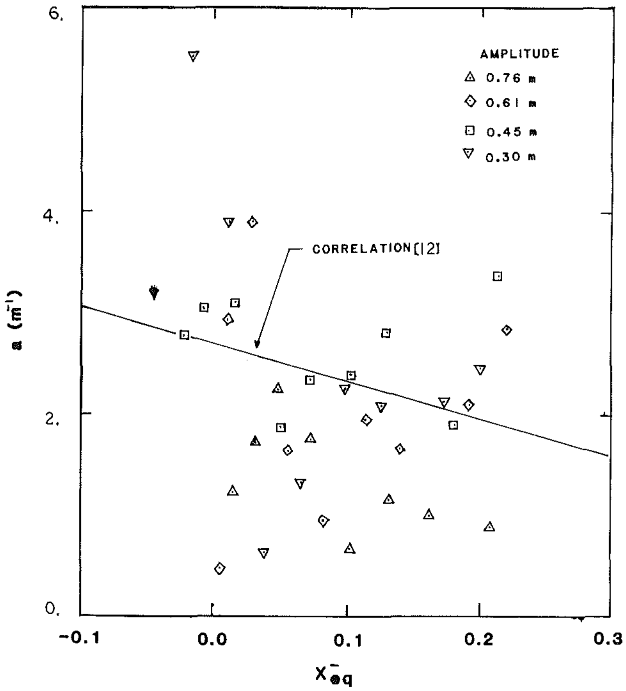

Fig. 9(*b*) Coefficient *a* of Yu and Yadigaroglu [12] correlation

Fig. 9 Effect of amplitude of oscillations on heat transfer immediately downstream of the quench front; high initial-wall-temperature (760°C) run

regime that concludes the runs, the oscillations increase heat transfer again, as expected. The steady-reflooding-rate values were in agreement with the ones predicted by the Dittus-Boelter correlation.

Comparisons on a Local-Condition Basis. The problem mentioned earlier in relation to comparison of quench front velocity under steady and oscillatory conditions also arises, when one tries to assess systematically the effects of the oscillations on heat transfer. Again, the only way to perform these comparisons systematically is through the use of an empirical correlation reproducing the results of the steady-reflooding tests. Such a correlation was proposed by Yu and Yadigaroglu [12], who correlated the heat transfer coefficients immediately downstream of the quench front by the expression

$$h(z)=h_o e^{-a\Delta z_q} \tag{1}$$

where $\Delta z_q = z - z_q$ is the distance measured from the quench front, and h_o and a are coefficients, related to local conditions. The exponential variation of the heat transfer coefficient is suggested by the experimental observations. The spatial variation of the heat transfer coefficient was obtained by transforming the time variation at a fixed thermocouple location to a spatial variation at constant time using the local value of the quench front velocity. This is made possible by the fact that the phenomena downstream of the quench front remain approximately stationary in a frame of reference moving with the velocity of the quench front. Moreover, the quench front propagates rather steadily and, during the time required for the quench front to move over the length of interest, the local conditions do not change appreciably.

The coefficients of equation (1) were correlated as follows [12]

$$\frac{h_o}{\dfrac{8.82}{V_{in}}+(V_{in}-U_q)^{0.9}}=0.0108+B\left[x_{eq}^{+}-\frac{0.25}{V_{in}}\right] \tag{2}$$

with

$$B=-0.506 \qquad \text{for} \left[x_{eq}^{+}-\frac{0.25}{V_{in}}\right]<0$$

$$B=0.0806 \qquad \text{for} \left[x_{eq}^{+}-\frac{0.25}{V_{in}}\right]>0$$

where x_{eq}^{+} denotes the equilibrium quality calculated immediately above the quench front, V_{in} the inlet velocity, and

U_q the quench front velocity. The velocities must be expressed in cm/s, while the value of h_o is returned in kW/m^2°C.

The exponent a (in m^{-1}) is given by [12]

$$a = 4.76\ V_{in}^{-0.277} - 0.0571\, V_{in}^{2.06}\, x_{eq}^{-} \tag{3}$$

where the velocity is again expressed in cm/s and x_{eq}^{-} denotes the equilibrium quality immediately below the quench front. The quality increment at the quench front due to heat release from the wall between temperatures T_{bq} (before quench) and T_{aq} (after quench) is given by

$$\Delta x = \frac{C_w (T_{bq} - T_{aq}) U_q}{h_{LG} w_{in}} \tag{4}$$

where C_w is the heat capacity of the wall per unit length and w_{in} the inlet flow rate.

Figure 8 shows the values of the coefficient h_o obtained during the steady-reflooding runs incorporated in the present series, compared to the Yu and Yadigaroglu correlation line. Fairly good agreement is obtained. The exponent a correlation showed similar results but more scatter. This was the case, however, with the original data also.

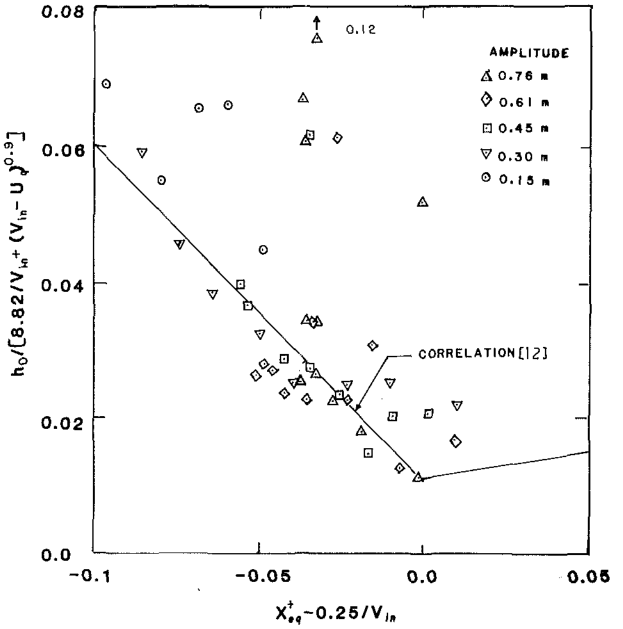

Fig. 10 Effect of amplitude of oscillations on heat transfer immediately downstream of the quench front; medium initial-wall-temperature (538°C) run

Plots of the heat transfer coefficient versus distance from the quench front showed an exponential decay also for the oscillatory reflooding runs, with the exception of the 316°C initial-wall-temperature runs. Details on the 316°C runs, on the behavior of the heat transfer coefficients, and on experimental and data-reduction difficulties are given in [4]. Only the salient features of the comparisons will be summarized here and the parametric effects of oscillation amplitude and period and of the initial wall temperature will be presented.

The data from the high (760°C) initial wall temperature runs were gathered not too far from the Yu and Yadigaroglu h_o correlation line, especially at low frequency and amplitude. As the amplitude or the frequency increased, the values of h_o became larger under subcooled flow conditions at the quench front and lower in the saturated flow range. These effects are evident in Fig. 9(*a*) showing the data of 760°C oscillatory runs with a 4-s period. The values of the exponent a plotted in Fig. 9(*b*) show considerable scatter and are on the average somewhat lower than the correlation line.

Similar trends are observed for the 538°C initial-wall-temperature runs. The departures from the h_o correlation line were, however, more pronounced than for the 760°C runs as the amplitude or the frequency of the oscillations increased, as shown in Fig. 10.

One conclusion from these comparisons is that the exponential decay of the heat transfer coefficient with distance from the quench front is, in most cases, evident, even in the presence of strong oscillations. The oscillations seem to increase the value of the heat transfer coefficient under subcooled conditions, while a reduction in the saturated range is observed. The rate of decay of the heat transfer coefficient with distance from the quench front (as measured by the value of the coefficient a) is on the average lower under oscillatory conditions. This can be explained by the smoothing action that the oscillating flow is exercising. The trends regarding the value of h_o can be qualitatively explained by the considerations regarding flow regimes and liquid inventory of Part 1 and of the following sections.

Liquid Carryover

Parametric Trends. Under oscillatory reflooding, the liq-

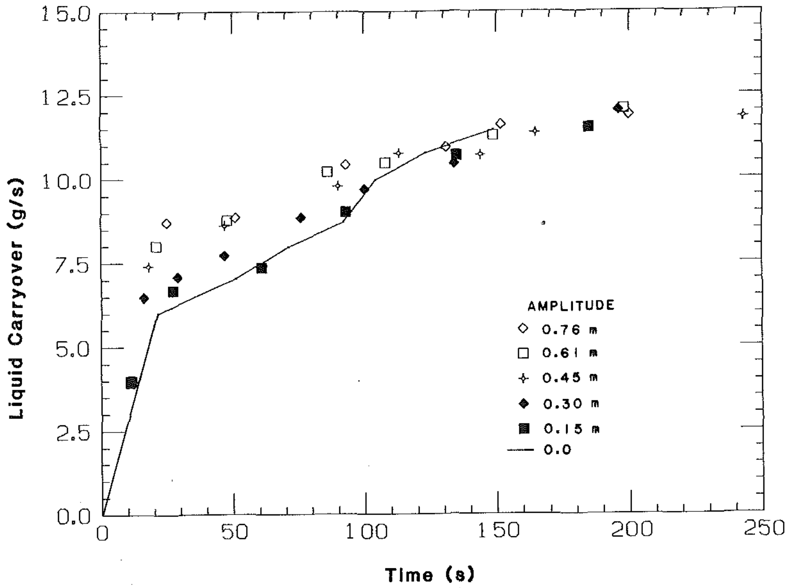

Fig. 11 Effect of the amplitude of the oscillations on liquid carryover rate; 538°C initial-wall-temperature runs, 4-s period

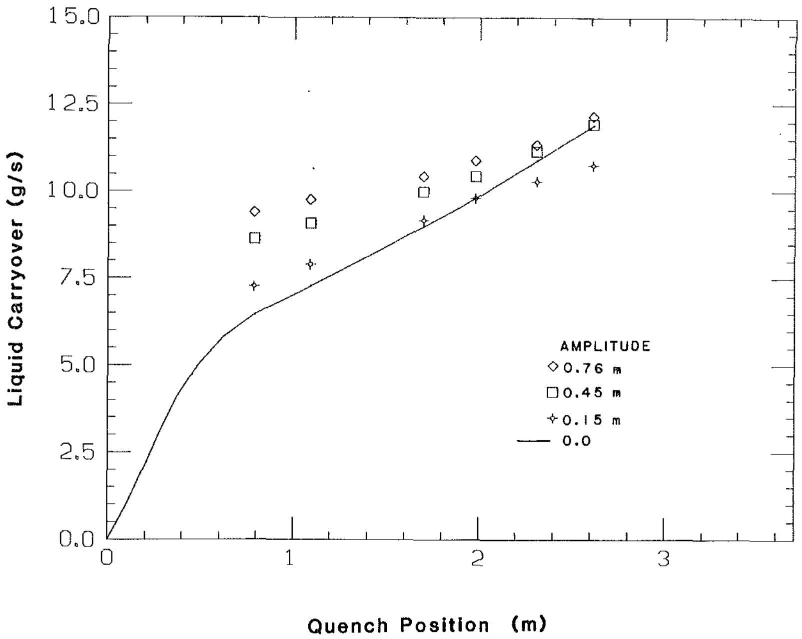

Fig. 12 Effect of the amplitude of the oscillations when compared on the basis of quench front location; same data as for Fig. 11

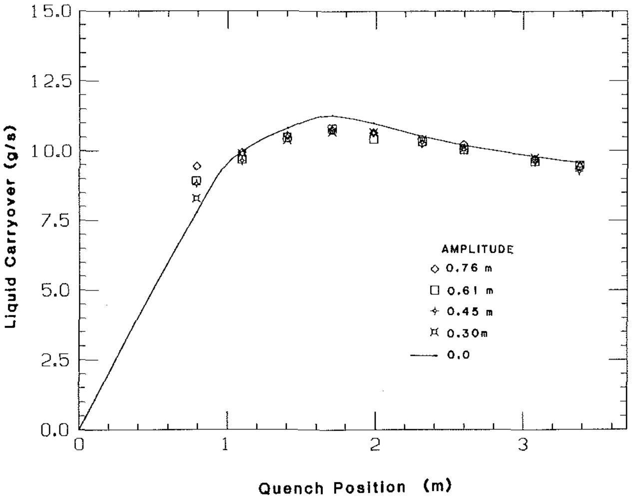

Fig. 13 Effect of the amplitude of the oscillations on liquid carryover when compared on the basis of quench front location; 760°C initial-wall-temperature runs, 4-s oscillation period

uid carryover increases with the oscillation amplitude. For the 316°C initial-wall-temperature runs, no good carryover data could be obtained, due to the short run duration. However, it was clear that the carryover was larger than for the constant-injection runs.

For the 538°C runs, the oscillations enhanced liquid carryover for about 100 s after test initiation. The oscillations had only a minor effect after this time. As shown in Fig. 11, the enhancement increased as the amplitude of the oscillations increased.

For the 760°C initial-wall-temperature runs, similar enhancement was noticed to about 100 s from test initiation. Between 100 and 450 s, the difference in carryover rate between steady and oscillatory injection was negligible, although the constant-injection tests had a slightly higher carryover rate. After about 450 s, the liquid carryover rate decreased somewhat for all cases, but more slowly for the constant-injection runs. The data are not reported here plotted versus time, since quench front position seems to be a better parameter for presenting the carryover data. This is shown in the next section.

Comparison on Quench-Front-Position Basis. When the instantaneous values of the liquid carryover rate are plotted versus the location of the quench front, the oscillations appear to initially increase the carryover rate for the 538°C initial-wall-temperature runs. The difference gets smaller as the quench front moves up the channel, as shown in Fig. 12.

For the 760°C runs, oscillations also increase the carryover at the lowest elevations. However, after the midplane quenches, the difference diminishes and oscillations have only minor effects, as shown in Fig. 13.

Examination of the data reveals that carryover increases when the flow at the quench front is subcooled. Under such conditions, the quench front velocities are also higher than for constant injection. These trends occur for three reasons: First, during the downstroke the liquid column detaches and is left in the form of large liquid chunks which can be relatively easily carried out of the test section. Second, under oscillatory flow conditions, there is better heat transfer to the liquid, causing higher vapor generation, which in turn results in higher droplet carryover. Third, during the upstroke, the vapor velocity is higher due to the piston action of the rising liquid front.

Based on the test data, the ratio of the amount of liquid carried out of the test section to the total mass of the liquid column above the quench front at its peak length was estimated to be about 15 to 20 percent [4]. About 5 to 7 percent of the detached liquid was estimated to be carried over, while the remaining liquid falls back [4].

When the liquid at the quench front reaches saturation, the flow pattern becomes annular with entrained droplets, as suggested by the flow visualization experiments reported in Part 1 and by other evidence [11]. Under saturated conditions at the quench front, i.e., in the presence of DFFB, the flow oscillations were found to have only minor effects.

These observations are further confirmed by the void fraction measurements reported in Part 1: With subcooled liquid at the quench front, the void fraction oscillated between almost zero and one. With saturated flow at the quench front, the void fraction fluctuated only by a small amount around a value of roughly 0.8. No obvious correlation between this

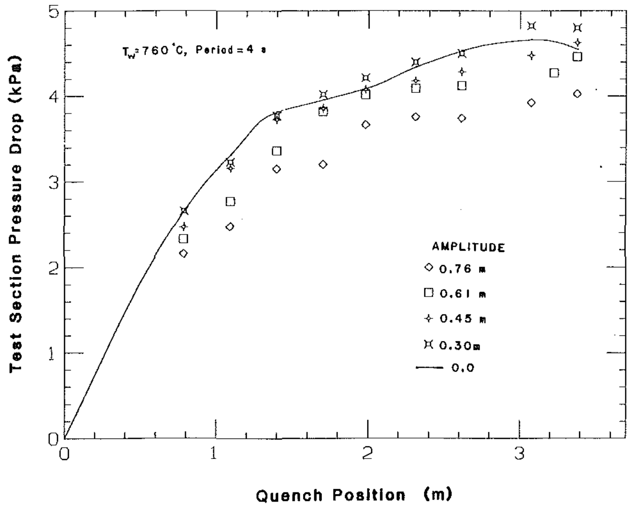

Fig. 14 Test section pressure drop plotted versus quench front position

fluctuation and the inlet oscillations existed. One would not have expected the DFFB regime to be very sensitive to flow rate oscillations.

Conclusions

The reflooding of a vertical channel under oscillatory flow conditions has been investigated experimentally, and a considerable amount of data [4, 5] has been collected under a variety of initial and boundary conditions. These data were compared with the data from constant-reflooding-rate runs mainly through the use of correlations derived from the latter which relate quench front velocity and heat transfer downstream of the quench front to local conditions in the channel. The comparisons show that the oscillations affect the progression of the quench front and heat transfer. The complex oscillatory reflooding behavior can be explained qualitatively as a consequence of the effects of oscillations on liquid carryover.

At the beginning of practically all tests, subcooled conditions prevail at the quench front and liquid carryover is enhanced by the mechanisms described above. There is also a corresponding increase in heat transfer above the quench front due to the oscillatory flow conditions and the interactions of the increased liquid carryover with the hot wall. This effect seems to be responsible for the higher quench front velocities observed during the initial period of the 538°C initial-wall-temperature runs, shown in Figs. 2 and 4.

As reflooding progresses, the liquid at the quench front eventually reaches saturation, and this observed enhancement of heat transfer in the quench region and immediately downstream probably diminishes or vanishes completely. At this stage, the previous period of enhanced carryover has also depleted the test section from part of its liquid inventory (in comparison to a steady-reflooding-rate run). The depletion of the mass inventory then becomes a dominant effect, slowing down the movement of the quench front. This trend is evident in the upper part of the test section during the runs plotted in Figs. 2 to 4.

Indeed, our data show that about the same amount of liquid inventory needs to be accumulated in the test section for a given axial location to be quenched, regardless of whether oscillations are present or not. This is supported, as shown in Fig. 14, by the test section pressure drop measurements, which are a rough indication of the liquid inventory in the tube: When the quench front positions are plotted versus the pressure drop, data from several runs with varying oscillation amplitudes occupy a narrow band.

Particular conclusions regarding quench front behavior and heat transfer immediately downstream of the quench front can be found at the end of the corresponding sections of this paper.

Acknowledgments

This research was supported by the Electric Power Research Institute.

References

1 Seban, R., Greif, R., Yadigaroglu, G., Elias, E., Abdollahian, D., and Peake, W. T., "UC-B Reflood Program: Experimental Data Report," EPRI Report NP-743, Apr. 1978.

2 Yu, K. P., "An Experimental Investigation of the Reflooding of a Bare Tubular Test Section," Ph.D. Thesis, Department of Nuclear Engineering, University of California, Berkeley, CA, 1978.

3 Kawaji, M., and Banerjee, S., "Two-Phase Flow Characteristics During Reflooding of a Hot Vertical Tube," EPRI Report NP-2820, Mar. 1983.

4 Oh, S., "The Effect of Oscillations During the Reflooding of a Tubular Test Section," Ph.D. Thesis, Department of Nuclear Engineering, University of California, Berkeley, CA, 1982.

5 Ng, Y. S., and Banerjee, S., "Two-Phase Flow Characteristics During Controlled Oscillation Reflooding of a Hot Vertical Tube," EPRI Report NP-2821, May 1983.

6 Yu, K. P., Elias, E., Abdollahian, D., Yadigaroglu, G., Peake, W. T., and Greif, R., "UC-B Reflood Experimental Plan," EPRI Report NP-457, Apr. 1977.

7 Cha, Y. S., Henry, R. E., and Lottes, P. A., "An Experimental Investigation of Quench Front Movement During Bottom Reflood of a Vertical Tube Under Forced-Oscillation Conditions," ANL/RAS/LWR 80-1, Jan. 1980.

8 Clement, P., Deruaz, R., and Veteau, J. M., "Reflooding of a PWR Bundle – Effect of Inlet Flow Rate Oscillations and Spacer Grids," European Two-Phase Flow Group Meeting, Paris, June 2–3, 1982.

9 Elias, E., and Yadigaroglu, G., "The Reflooding of the LOCA in PWRs. Part 2: Rewetting and Liquid Entrainment," *Nuclear Safety*, Vol. 19, 1978, pp. 160–175.

10 Yu, S. K. W., Farmer, P. R., and Coney, M. W. E., "Methods and Correlations for the Prediction of Quenching Rates of Hot Surfaces," *Int. J. Multiphase Flow*, Vol. 3, 1977, pp. 415–443.

11 Yadigaroglu, G., and Yu, K. P., "Flow Regimes and Carryover During Reflooding," European Two-Phase Flow Group Meeting, Zurich, June 14–17, 1983.

12 Yu, K. P., and Yadigaroglu, G., "Heat Transfer Immediately Downstream of the Quench Front During Reflooding," ASME Paper No. 79-HT-48, 1979.

Journal of Heat Transfer

Technical Notes

This section contains shorter technical papers. These shorter papers will be subjected to the same review process as that for full papers.

An Exact Solution for the Rate of Heat Transfer From a Rectangular Fin Governed by a Power Law-Type Temperature Dependence

A. K. Sen[1] and S. Trinh[2]

Nomenclature

b = fin thickness
E = emissivity
h = heat transfer coefficient
k = thermal conductivity
l = fin length
m = power law exponent
N = fin parameter
q = heat transfer rate through fin base = $kbd\theta/dz$
Q = dimensionless heat transfer rate = $dT/dx(1) = ql/bk(\theta_b - \theta_a)$
T = dimensionless temperature
x = dimensionless distance (from fin tip)
z = distance from fin tip
θ = temperature at any point in the fin
θ_a = ambient temperature
θ_b = fin base temperature
σ = Stefan-Boltzmann constant

Introduction

Cooling of solid objects by the use of fins has been a common practice for many years. Finned surfaces are widely used, for instance, for cooling electric transformers, the cylinders of air-craft engines, and other heat transfer equipment. For the purely convective fin, the heat lost from its surface to the surrounding fluid is linearly proportional to the temperature difference. This leads to a linear differential equation for the temperature variation in the fin which has an exact analytical solution. An analytical expression for the rate of heat transfer can be easily derived for this linear problem. These results are well established and may be found in textbooks on heat transfer (see, for example, [1]). Recently new parametrizations for the rate of heat transfer in fins and spines have been given by Kraus and Snider [2-4] for the case of purely convective cooling.

In certain applications, however, the heat loss may vary with the local temperature in a nonlinear manner; in particular, the cooling process may be governed by a power law-type temperature dependence. Under these circumstances, the differential equation for temperature becomes strictly nonlinear. Consider, as a concrete example, a rectangular fin of length l and thickness b. The temperature distribution in the fin can be described by the following dimensionless equation

$$\frac{d^2T}{dx^2} - N^2 T^m = 0 \tag{1}$$

(see [5] for details). The exponent m in equation (1) may take the values 1.25, 3, and 4, respectively [6], depending on whether the heat transfer process involves nucleate boiling, natural convection, or radiation into free space. (The case $m = 1$ corresponds to the "linear" cooling situation.) The dimensionless temperature T and the dimensionless parameter N are defined according to the mechanism of the surface heat transfer. For instance

$$N^2 = 2hl^2/bk, \qquad T = (\theta - \theta_a)/(\theta_b - \theta_a) \tag{2}$$

for the convecting fin ($m = 1$), whereas we may write

$$N^2 = 2\sigma E\theta_b^3 l^2/bk, \qquad T = \theta/\theta_b \tag{3}$$

for a fin radiating into free space at zero temperature. The fin length l has been used to scale distance. An appropriate set of boundary conditions for equation (1) is

$$\frac{dT}{dx}(0) = 0 \tag{4a}$$

$$T(1) = 1 \tag{4b}$$

Condition (4*a*) follows from the assumption that the tip of the fin is insulated and the second condition (4*b*) requires that the base temperature be prescribed. To our knowledge, an exact analytical solution to the problem (1)-(4) as it applies to the heat transfer system is not available in the heat transfer literature. The purpose of this note is to present such a solution.

Solution

It is interesting to note that the problem given by equation (1) with appropriate boundary conditions arises in many other applications [7-10]. Mehta and Aris [7, 8] solved similar problems in their study of reactions in porous catalysts. The method of solution presented by these authors has been subsequently used by Kulkarni and Doraiswamy [9] and Kulkarni et al. [10] in the context of gas-liquid reactions. In a recent paper [5], Chang et al. derived an approximate solution of equation (1) subject to the boundary conditions (4), using the so-called optimal linearization approach [11]. Indeed, the exact analytical solution obtained by Mehta and Aris [7] can

---

[1] Associate Professor, Department of Mathematics, Purdue University School of Science, Indianapolis, IN 46223

[2] Graduate Student, Department of Mathematics, Purdue University School of Science, Indianapolis, IN 46223

Contributed by the Heat Transfer Division for publication in the JOURNAL OF HEAT TRANSFER. Manuscript received by the Heat Transfer Division November 14, 1984.

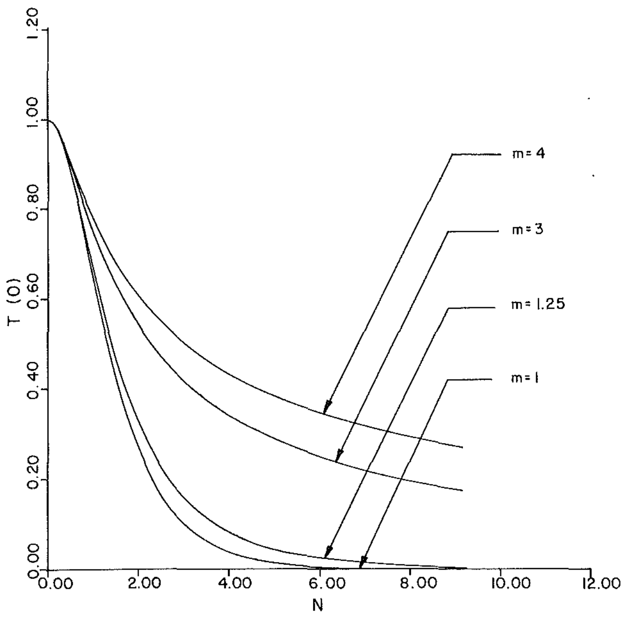

Fig. 1 Variation of dimensionless tip temperature with N

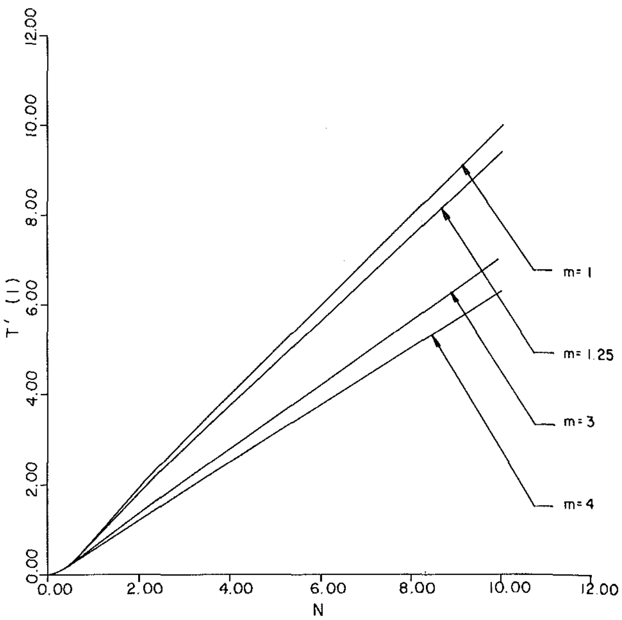

Fig. 2 Variation of dimensionless base heat transfer rate with N

be used directly for the present heat transfer problem. Following [7], we can write the solution of equations (1)–(4), with an appropriate change of notation, as

$$x=\frac{1}{N}\left(\frac{2}{m+1}\right)^{1/2} T_0^{\frac{1-m}{2}}\,\tilde{T}^{1/2}F\left(\frac{1}{2},\frac{m+3}{2(m+1)},\frac{3}{2},\tilde{T}\right) \tag{5}$$

where

$$\tilde{T}=1-(T_0/T)^{m+1} \tag{6}$$

and the tip temperature T_0 has the value given by

$$T_0=T(0)=\left\{\frac{N\left(\dfrac{m+1}{2}\right)^{1/2}}{\psi^{1/2}F\left(\dfrac{1}{2},\dfrac{m+3}{2(m+1)},\dfrac{3}{2},\psi\right)}\right\}^{\frac{2}{1-m}} \tag{7}$$

with

$$\psi=1-T_0^{m+1} \tag{8}$$

In these equations, F represents the hypergeometric function [12]. The solution (5) determines the variation of temperature in the fin with distance, in the form of a quadrature. The dimensionless heat transfer rate from the base of the fin can be easily found to be

$$Q=\frac{dT}{dx}(1)=N\left(\frac{2}{m+1}\right)^{1/2}(1-T_0^{m+1})^{1/2} \tag{9}$$

Discussion of Results

The variation of the tip temperature T_0 with the dimensionless fin parameter N is displayed in Fig. 1 for $m=1$, 1.25, 3, and 4, in accordance with formula (7). The figure shows, as expected, that the dimensionless tip temperature decreases continuously as N increases and approaches the ambient temperature of zero for sufficiently large N. The asymptotic behavior of T_0 for large N can be readily seen from equation (7) as follows. For $m>1$, we find that $N\rightarrow\infty$ as $T_0\rightarrow 0$, since then equation (7) can be approximated as

$$N\sim\left(\frac{2}{m+1}\right)^{1/2}F\left(\frac{1}{2},\frac{m+3}{2(m+1)},\frac{3}{2},1\right)T_0^{-(m-1)/2} \tag{10}$$

Clearly $T_0\rightarrow 0$ corresponds to $N\rightarrow\infty$. In fact, we must have

$$T_0\sim CN^{-2/(m-1)} \tag{11}$$

for large N, where the constant C which depends on m has the value

$$C=\left(\frac{2A^2}{m+1}\right)^{1/(m-1)} \tag{12}$$

with

$$A=F\left(\frac{1}{2},\frac{m+3}{2(m+1)},\frac{3}{2},1\right)=\frac{\sqrt{\pi}}{2}\,\frac{\Gamma\left[\dfrac{m-1}{2(m+1)}\right]}{\Gamma\left[\dfrac{m}{m+1}\right]}, \tag{13}$$

the symbol Γ being used to represent the gamma function [12].

The quantity of most physical interest is the rate of heat transfer from the base of the fin. The dimensionless base heat flux, given by $dT/dx(1)$ is plotted against N in Fig. 2, for the same four values of m used in Fig. 1. It is interesting to note from this figure that for the values of m considered, the base heat flux varies almost linearly with N for $N\geq 2$. The dependence of Q on the dimensionless parameter N for large values of N can be easily established from the use of the results (7) and (9). For $m>1$, we find the following asymptotic relation

$$Q\sim\left(\frac{2}{m+1}\right)^{1/2}N\left\{1-\frac{D}{2}t^{-\frac{2(m+1)}{m-1}}-\frac{D^2}{8}t^{-\frac{4(m+1)}{m-1}}-\ldots\right\} \tag{14}$$

Here

$$t=\left(\frac{m+1}{2}\right)^{1/2}N+\frac{m+1}{m-1} \tag{15}$$

and D is a constant depending on m

$$D=A^{\frac{2(m+1)}{m-1}} \tag{16}$$

where A has the definition (13). It is now apparent from (14) that for large N, the dimensionless heat flux Q is linearly proportional to N, to a first approximation. As a consequence, the physical (i.e., dimensional) heat transfer rate from the fin base which is given by

$$q=kbd\theta/dz \tag{17}$$

would be almost linearly proportional to the parameter group

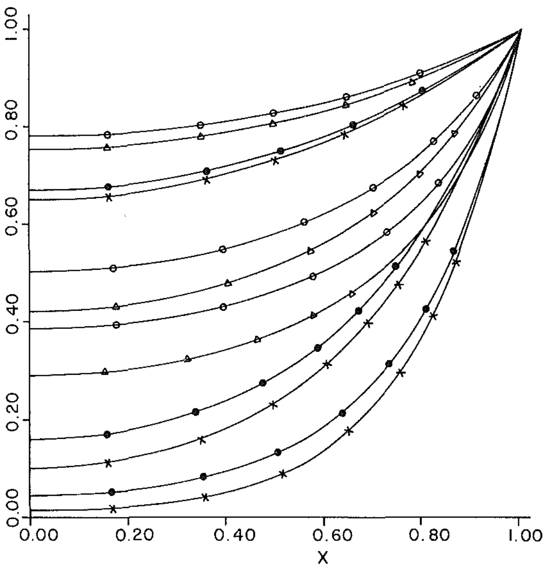

Fig. 3 Dimensionless temperature profiles for $N = 1, 3, 5$ and $m = 1, 1.25, 3$, and 4. The following legends have been used: x for $m = 1$, ● for $m = 1.25$, △ for $m = 3$, and ○ for $m = 4$. For each m, the upper curve corresponds to $N = 1$, the middle curve to $N = 3$, and the lower curve to $N = 5$.

$(kb/l)N(\theta_b - \theta_a)$ when N is large. This means that for a given temperature difference between the fin base and the surroundings, the heat transfer rate q will vary almost linearly as $(2hkb)^{1/2}$ in a convective fin ($m = 1$) and as $(2\sigma E\theta_b^3 kb)^{1/2}$ in a radiating fin ($m = 4$), for sufficiently large N. Note that $N >> 1$ corresponds to the condition

$$\frac{l}{b/2} >> \left(\frac{2k}{hb}\right)^{1/2} \tag{18}$$

for a purely convective fin and the condition

$$\frac{l}{b/2} >> \left(\frac{2k}{\sigma E b\theta_b^3}\right)^{1/2} \tag{19}$$

for a radiating fin.

When N is small ($N << 1$), it can be easily shown from (9) that

$$Q \sim N^2\left\{1 - \frac{m}{3}N^2 + \frac{1}{15}m(3m-1)N^4 - \dots\right\} \tag{20}$$

This trend is also observed in Fig. 2. It is appropriate to point out that for the purely convective fin ($m = 1$), the dimensionless heat flux Q can be obtained as a closed-form analytical expression, for all values of N. We have

$$Q = N \tanh N \tag{21}$$

It follows from equation (21) that for $N >> 1$, $Q \sim N$ since $\tanh N \rightarrow 1$ as $N \rightarrow \infty$. For N small, an expansion of $\tanh N$ shows that (21) is identical to (20) with $m = 1$. For completeness, the temperature profiles for selected values of N, namely $N = 1, 3, 4$, and $m = 1, 1.25, 3$, and 4 are drawn in Fig. 3, using equation (5).

References

1 Myers, G. E., *Analytical Methods in Conduction Heat Transfer*, McGraw-Hill, New York, 1971.

2 Kraus, A. D., and Snider, A. D., "New Parametrizations for Heat Transfer in Fins and Spines," ASME JOURNAL OF HEAT TRANSFER, Vol. 102, 1980, pp. 415-419.

3 Snider, A. D., "Mathematical Techniques in Extended Surface Analysis," *Mathematical Modelling*, Vol. 3, 1982, pp. 191-206.

4 Snider, A. D., and Kraus, A. D., "Recent Developments in the Analysis and Design of Extended Surfaces," ASME JOURNAL OF HEAT TRANSFER, Vol. 105, 1983, pp. 302-306.

5 Chang, Y. M., Chen, C. K., and Cleaver, J. W., "Transient Response of Fins by Optimal Linearization and Variational Imbedding Methods," ASME JOURNAL OF HEAT TRANSFER, Vol. 104, 1982, pp. 813-815.

6 Haley, K. W., and Westward, J. W., "Boiling Heat Transfer From Single Fins," *Proceedings of the Third International Heat Transfer Conference*, Chicago, 1966, Vol. 3, pp. 245-253.

7 Mehta, B. N., and Aris, R., "A Note on a Form of the Emden-Fowler Equation," *Journal of Mathematical Analysis and Applications*, Vol. 36, 1971, pp. 611-621.

8 Mehta, B. N., and Aris, R., "Communications on the Theory of Diffusion and Reaction-VII. The Isothermal p-th Order Reaction," *Chemical Engineering Science*, Vol. 26, 1971, pp. 1699-1712.

9 Kulkarni, B. D., and Doraiswamy, L. K., "Effectiveness Factors in Gas-Liquid Reactions: The General n-th Order Case," *AIChE Journal*, Vol. 22, 1966, pp. 597-600.

10 Kulkarni, B. E., Jayaraman, V. K., and Doraiswamy, L. K., "Effectiveness Factors in Bidispersed Catalysts: The General n-th Order Case," *Chemical Engineering Science*, Vol. 36, 1981, pp. 943-945.

11 Vujanovic, B., "Application of Optimal Linearization Method to the Heat Transfer Problem," *International Journal of Heat and Mass Transfer*, Vol. 16, 1973, pp. 1111-1117.

12 Abramowitz, M., and Stegun, I. A., *Handbook of Mathematical Functions*, Dover, New York, 1972.

Optimum Dimensions of Annular Fin Assemblies

A. Buccini[1] **and H. M. Soliman**[1,2]

Nomenclature

Bi = Biot number = $2h_o r_o/k$
H = ratio of heat transfer coefficients = h_i/h_o
h_i = heat transfer coefficient at inner surface of cylinder
h_o = heat transfer coefficient at outer surface of cylinder, fin sides, and fin tips
k = thermal conductivity of cylinder wall and fins
P = dimensionless pitch = p/r_o
p = half the distance between the midplanes of two adjacent fins
Q = dimensionless heat transfer per computation module = $q/[\pi kp(T_i - T_o)]$
q = rate of heat transfer per computation module
R = dimensionless radial coordinate = r/r_o
R_i = ratio of inner to outer radii of cylinder = r_i/r_o
r = radial coordinate
r_f = radius of fin tips
r_i = inner radius of cylinder
r_o = outer radius of cylinder
T = temperature within cylinder wall and fins
T_i = fluid temperature inside cylinder
T_o = fluid temperature outside cylinder
t = fin thickness
V = dimensionless volume of a single fin = $(r_f^2 - r_o^2)t/r_o^3$
W = dimensionless fin thickness = r_o/t
Z = dimensionless axial coordinate = z/p
z = axial coordinate
ϵ = enhancement factor due to fins defined by equation (7a)
θ = dimensionless temperature = $(T - T_o)/(T_i - T_o)$

---

[1] Department of Mechanical Engineering, University of Manitoba, Winnipeg, Manitoba, Canada R3T 2N2

[2] Mem. ASME

Contributed by the Heat Transfer Division for publication in the JOURNAL OF HEAT TRANSFER. Manuscript received by the Heat Transfer Division November 14, 1984.

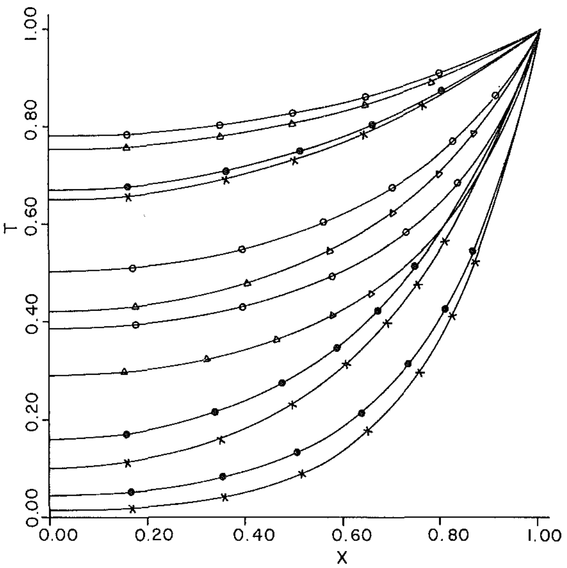

Fig. 3 Dimensionless temperature profiles for $N = 1, 3, 5$ and $m = 1$, 1.25, 3, and 4. The following legends have been used: x for $m = 1$, ● for $m = 1.25$, △ for $m = 3$, and ○ for $m = 4$. For each m, the upper curve corresponds to $N = 1$, the middle curve to $N = 3$, and the lower curve to $N = 5$.

$(kb/l)N(\theta_b - \theta_a)$ when N is large. This means that for a given temperature difference between the fin base and the surroundings, the heat transfer rate q will vary almost linearly as $(2hkb)^{1/2}$ in a convective fin ($m = 1$) and as $(2\sigma E\theta_b^3 kb)^{1/2}$ in a radiating fin ($m = 4$), for sufficiently large N. Note that $N >> 1$ corresponds to the condition

$$\frac{l}{b/2} >> \left(\frac{2k}{hb}\right)^{1/2} \qquad (18)$$

for a purely convective fin and the condition

$$\frac{l}{b/2} >> \left(\frac{2k}{\sigma E b \theta_b^3}\right)^{1/2} \qquad (19)$$

for a radiating fin.

When N is small ($N << 1$), it can be easily shown from (9) that

$$Q \sim N^2\left\{1 - \frac{m}{3}N^2 + \frac{1}{15}m(3m-1)N^4 - \ldots\right\} \qquad (20)$$

This trend is also observed in Fig. 2. It is appropriate to point out that for the purely convective fin ($m = 1$), the dimensionless heat flux Q can be obtained as a closed-form analytical expression, for all values of N. We have

$$Q = N \tanh N \qquad (21)$$

It follows from equation (21) that for $N >> 1$, $Q \sim N$ since $\tanh N \rightarrow 1$ as $N \rightarrow \infty$. For N small, an expansion of $\tanh N$ shows that (21) is identical to (20) with $m = 1$. For completeness, the temperature profiles for selected values of N, namely $N = 1, 3, 4$, and $m = 1, 1.25, 3$, and 4 are drawn in Fig. 3, using equation (5).

References

1 Myers, G. E., *Analytical Methods in Conduction Heat Transfer*, McGraw-Hill, New York, 1971.

2 Kraus, A. D., and Snider, A. D., "New Parametrizations for Heat Transfer in Fins and Spines," ASME JOURNAL OF HEAT TRANSFER, Vol. 102, 1980, pp. 415-419.

3 Snider, A. D., "Mathematical Techniques in Extended Surface Analysis," *Mathematical Modelling*, Vol. 3, 1982, pp. 191-206.

4 Snider, A. D., and Kraus, A. D., "Recent Developments in the Analysis and Design of Extended Surfaces," ASME JOURNAL OF HEAT TRANSFER, Vol. 105, 1983, pp. 302-306.

5 Chang, Y. M., Chen, C. K., and Cleaver, J. W., "Transient Response of Fins by Optimal Linearization and Variational Imbedding Methods," ASME JOURNAL OF HEAT TRANSFER, Vol. 104, 1982, pp. 813-815.

6 Haley, K. W., and Westward, J. W., "Boiling Heat Transfer From Single Fins," *Proceedings of the Third International Heat Transfer Conference*, Chicago, 1966, Vol. 3, pp. 245-253.

7 Mehta, B. N., and Aris, R., "A Note on a Form of the Emden-Fowler Equation," *Journal of Mathematical Analysis and Applications*, Vol. 36, 1971, pp. 611-621.

8 Mehta, B. N., and Aris, R., "Communications on the Theory of Diffusion and Reaction-VII. The Isothermal p-th Order Reaction," *Chemical Engineering Science*, Vol. 26, 1971, pp. 1699-1712.

9 Kulkarni, B. D., and Doraiswamy, L. K., "Effectiveness Factors in Gas-Liquid Reactions: The General n-th Order Case," *AIChE Journal*, Vol. 22, 1966, pp. 597-600.

10 Kulkarni, B. E., Jayaraman, V. K., and Doraiswamy, L. K., "Effectiveness Factors in Bidispersed Catalysts: The General n-th Order Case," *Chemical Engineering Science*, Vol. 36, 1981, pp. 943-945.

11 Vujanovic, B., "Application of Optimal Linearization Method to the Heat Transfer Problem," *International Journal of Heat and Mass Transfer*, Vol. 16, 1973, pp. 1111-1117.

12 Abramowitz, M., and Stegun, I. A., *Handbook of Mathematical Functions*, Dover, New York, 1972.

Optimum Dimensions of Annular Fin Assemblies

A. Buccini[1] and H. M. Soliman[1,2]

Nomenclature

Bi = Biot number = $2h_o r_o/k$
H = ratio of heat transfer coefficients = h_i/h_o
h_i = heat transfer coefficient at inner surface of cylinder
h_o = heat transfer coefficient at outer surface of cylinder, fin sides, and fin tips
k = thermal conductivity of cylinder wall and fins
P = dimensionless pitch = p/r_o
p = half the distance between the midplanes of two adjacent fins
Q = dimensionless heat transfer per computation module = $q/[\pi kp(T_i - T_o)]$
q = rate of heat transfer per computation module
R = dimensionless radial coordinate = r/r_o
R_i = ratio of inner to outer radii of cylinder = r_i/r_o
r = radial coordinate
r_f = radius of fin tips
r_i = inner radius of cylinder
r_o = outer radius of cylinder
T = temperature within cylinder wall and fins
T_i = fluid temperature inside cylinder
T_o = fluid temperature outside cylinder
t = fin thickness
V = dimensionless volume of a single fin = $(r_f^2 - r_o^2)t/r_o^3$
W = dimensionless fin thickness = r_o/t
Z = dimensionless axial coordinate = z/p
z = axial coordinate
ϵ = enhancement factor due to fins defined by equation (7*a*)
θ = dimensionless temperature = $(T - T_o)/(T_i - T_o)$

---

[1] Department of Mechanical Engineering, University of Manitoba, Winnipeg, Manitoba, Canada R3T 2N2.

[2] Mem. ASME

Contributed by the Heat Transfer Division for publication in the JOURNAL OF HEAT TRANSFER. Manuscript received by the Heat Transfer Division November 14, 1984.

Introduction

Fins are known to be a very simple and effective means of enhancing the heat transfer between two fluid mediums separated by a wall [1]. A tremendous amount of literature has been compiled on different aspects of fin design; most of this literature is based on the assumption of one-dimensional heat flow. Since, in actual practice, fins are normally arranged in the form of arrays, a two-dimensional approach to the problem is necessary. The two-dimensional effects on the temperature distribution and heat flow rate were explored in some recent studies (e.g., [2-4]).

One important aspect of fin design is that of optimum dimensions defined as those dimensions which give the greatest amount of heat transfer for a given volume of fin material. Brown [5] developed a solution for a single annular fin of uniform cross section assuming one-dimensional heat flow and insulated tip. Under these conditions, Brown found that for every combination of Biot number Bi and dimensionless fin volume V there is an optimum value for the dimensionless fin thickness W for which the heat transfer from the fin is a maximum. The object of this investigation is to extend the optimization process to the more practical geometry of a fin array (rather than a single fin), treating the problem more precisely as a two-dimensional problem and eliminating the assumption of insulated fin tips.

Analysis

The geometry under consideration (shown in Fig. 1 with the relevant dimensional and heat transfer parameters) is that of a cylinder with an array of circular fins of uniform cross section attached to the outside surface. Due to symmetry, the analysis can be limited to the computation module identified as the hatched area in Fig. 1. Using the dimensionless parameters defined in the Nomenclature, the applicable conduction equation and boundary conditions for two-dimensional heat transfer through the cylinder wall and fin can be written as

$$\frac{1}{R}\frac{\partial}{\partial R}\left(R\frac{\partial \theta}{\partial R}\right)+\frac{1}{P^2}\frac{\partial^2 \theta}{\partial Z^2}=0 \qquad (1)$$

$$\frac{\partial \theta}{\partial R}=\frac{1}{2}H\,\mathrm{Bi}(\theta-1) \quad \text{at } R=R_i,\quad 0\le Z\le 1 \qquad (2)$$

$$\frac{\partial \theta}{\partial R}=-\frac{1}{2}\,\mathrm{Bi}\,\theta \quad \text{at } R=1,\quad 1/(2PW)\le Z\le 1$$

$$\text{and } R=\sqrt{1+VW},\quad 0\le Z\le 1/(2PW) \qquad (3)$$

$$\frac{\partial \theta}{\partial Z}=-\frac{1}{2}P\,\mathrm{Bi}\,\theta \quad \text{at } 1\le R\le\sqrt{1+VW},$$

$$Z=1/(2PW) \qquad (4)$$

$$\frac{\partial \theta}{\partial Z}=0 \quad \text{at } R_i\le R\le 1,\quad Z=1$$

$$\text{and } R_i\le R\le\sqrt{1+VW},\quad Z=0 \qquad (5)$$

After solving for the temperature distribution $\theta(R, Z)$, the total rate of heat transfer per computation module can be evaluated from

$$Q=H\,R_i\,\mathrm{Bi}\int_0^1[1-\theta(R_i, Z)]dZ \qquad (6)$$

Equations (1) to (6) indicate that Q is a function of R_i, H, V, W, P, and Bi. Consequently, if W_{opt} is the optimum fin thickness for which the heat transfer is maximum, then W_{opt} and the corresponding Q_{opt} are both expected to be dependent on R_i, V, P, Bi, and H. A numerical (finite difference) approach was used for solving equations (1) to (6) employing a mesh which insured better than 0.1 percent accuracy in the values of $\theta(R, Z)$ and Q. A computer program was developed to execute the optimization process according to the following procedure: (1) Values of R_i, V, P, Bi, and H were supplied as input data; (2) a number of solutions (minimum of five) were generated corresponding to different specified values of W. It was found that for most cases, Q increases with W up to a point beyond which a further increase in W would cause a decrease in Q. For a range of input data the optimization process failed as will be shown later; (3) using the results of step (2), a fourth-order polynomial was generated giving Q as a function of W. The value of W_{opt} corresponding to $dQ/dW = 0$ was calculated from this polynomial and a new solution was generated for $W = W_{\mathrm{opt}}$ with the resulting heat transfer rate being Q_{opt}.

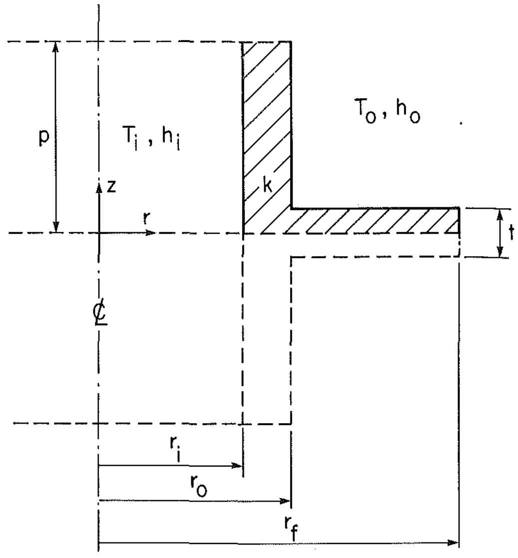

Fig. 1 Schematic of geometry and computation module (hatched area)

Results and Discussion

The following range of parameters was covered in this study:

$\sqrt{\mathrm{Bi}}=0.125$, 0.25, 0.5, 1, 2, and 4
$P = 0.1$, 0.2, 0.4, 0.7, and 1.0
$H = 1$, 10, and 100
$V = 0.01$ to 10

Due to the obviously large volume of computations involved, only one value of R_i was used ($R_i = 0.9$). The results developed for the above range of parameters strongly suggest that H and P do not have significant influences on the value of W_{opt}. Our definition of dimensionless pitch P may not be conventional; however, it was selected because it suited our computation scheme. A more commonly used definition of dimensionless pitch [3, 4] is the ratio of the gap between two successive fins to fin thickness, i.e., $P' = (2p-t)/t$. However, the present definition of P is not the reason for its irrelevance to the value of W_{opt}. For example, at Bi = 0.0625, $V = 0.4$, and $H = 100$, the value of W_{opt} changed from 11.52 at $P = 1$ ($P' = 22$) to 11.51 at $P = 0.1$ ($P' = 1.3$). Also, changing H to 10 and 1 in the previous example resulted in W_{opt} of 11.49 and 11.48, respectively. Consequently, the results of W_{opt} will be presented here using Bi and V as the only independent parameters.

Figure 2 shows the present results (segment corresponding to $P = 0.7$ and $H = 100$ was selected) compared to those of Brown [5], which are labeled W^*_{opt}. Basically, the absolute value of the deviation between the two solutions increases with an increase in Bi and/or V. For Bi < 1, the present solution predicts thicker fins than Brown's, and vice versa for Bi > 1.5. At $\sqrt{\mathrm{Bi}} = 1.25$, the deviation between the two solutions

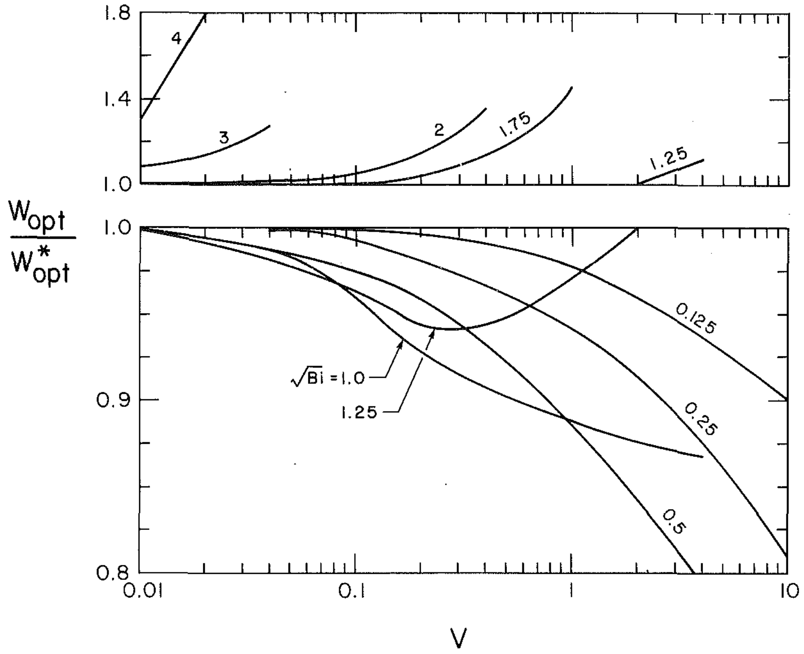

Fig. 2 Comparison between present values of W_{opt} and Brown's solution [5]

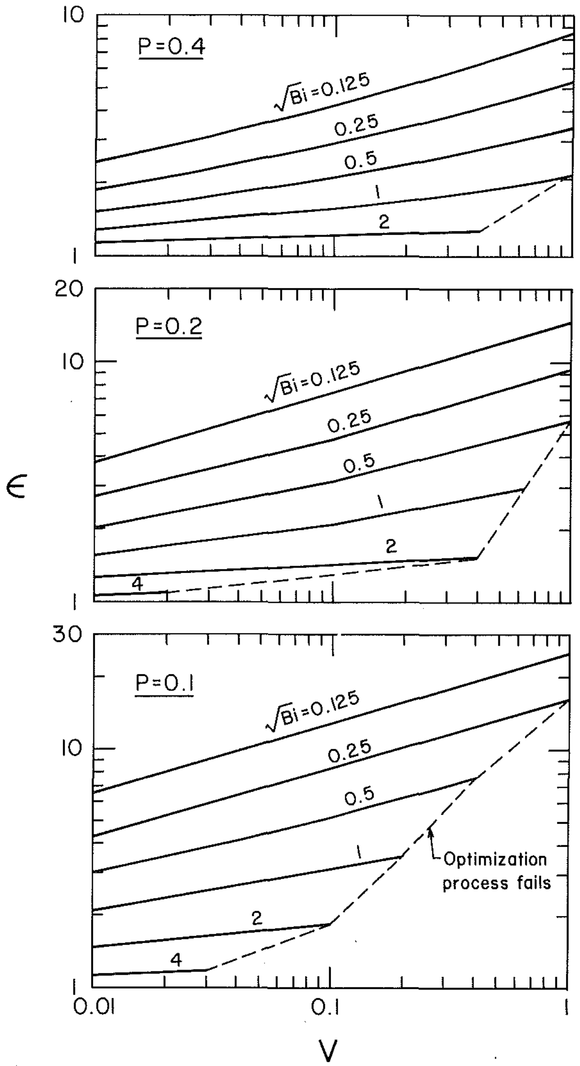

Fig. 3 Enhancement factor for H = 100

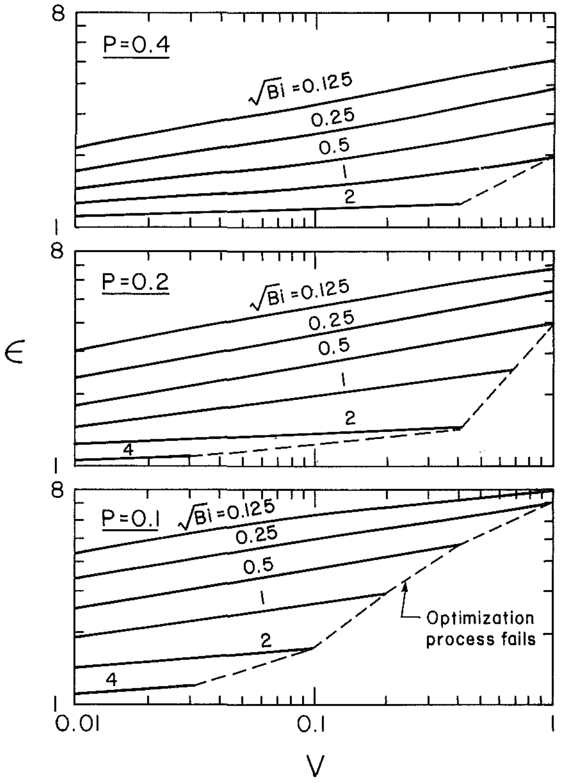

Fig. 4 Enhancement factor for H = 10

starts in one direction and then reverses as V increases, as shown in Fig. 2. For every Bi, the optimization procedure described earlier succeeded in obtaining a solution up to a certain value of V beyond which optimum solutions did not exist. In the domain where the optimization procedure failed it was found that Q increased continuously with W with no reversal in trend. The reason for this behavior is that in the domain of no optimum solution the combination of geometric and heat transfer parameters is such that an increase in W would result in an increase in heat transfer from the unfinned surface (be-

Table 1 Optimum dimensions of an annular fin assembly

P	Number of fins	V (Fig. 3)	W^*_{opt} [5]	W_{opt} (Fig. 2)	t, mm	r_f, cm	Total volume of fins, cm^3
0.1	16	0.019	79.4	79.4	1.26	15.8	955
0.2	8	0.14	22.7	22.4	4.46	20.3	3520
0.4	4	0.95	7.0	6.6	15.2	26.9	11,940

tween two consecutive fins) which exceeds the decrease in heat transfer from the fin sides and tip. The value of V at which the optimization process failed was found to decrease as Bi increased.

While the values of P and H were found insignificant in determining W_{opt}, these parameters strongly influenced Q_{opt}. In presenting our results of optimum heat transfer use was made of the enhancement factor ϵ, defined as

$$\epsilon = Q_{\mathrm{opt}}/Q_u \tag{7a}$$

where Q_u is the dimensionless heat transfer rate per computation module in the absence of the fin, given by

$$Q_u = \frac{H\,R_i\,\mathrm{Bi}}{1 + H\,R_i\left(1 - \frac{1}{2}\mathrm{Bi}\ln R_i\right)} \tag{7b}$$

Values of ϵ as a function of Bi and V at P = 0.1, 0.2, and 0.4 are presented in Fig. 3 for H = 100 and in Fig. 4 for H = 10. The enhancement due to the fins is more pronounced at low Bi, and it increases with increases in V and H, or a decrease in P. The regions in which the optimization process failed are marked in Figs. 3 and 4. Application of the information in Figs. 2, 3, and 4 in actual design can be demonstrated by the following example: Consider an aluminum cylinder (k = 160 W/m•K) with r_i = 9 cm, r_o = 10 cm, and length l = 32 cm. The cylinder is used in an application where T_i = 500°C, T_o = 20°C, $h_i = 5000$ W/m^2•K, $h_o = 50$ W/m^2•K, and it is desired to dissipate a total heat transfer rate of $q = 24$ kW. In order to design the necessary array of fins we first calculate the independent parameters Bi = 0.0625 and H = 100 from their respective definitions. Then, the rate of heat transfer without the fins can be easily evaluated as q_u = 4.757 kW, which means that the required enhancement factor is $\epsilon = q/q_u$ = 5.26. With these values of Bi, H, and ϵ, three possible designs can be made and the results are shown in Table 1. According to these results the lower the P value the better, if overall weight is the major concern. However, there are normally other considerations in design, such as mechanical strength, which may rule out designs with very small values of t. Care should also be taken in avoiding designs with narrow gaps between the fins since the present results are based on the assumption of uniform h_o along the fins and outer surface of the cylinder, which may not apply for closely spaced fin arrays.

Acknowledgments

The financial assistance provided by the Natural Sciences and Engineering Research Council of Canada is gratefully acknowledged.

References

1 Kern, D. Q., and Kraus, A. D., *Extended Surface Heat Transfer*, McGraw-Hill, New York, 1972.

2 Sparrow, E. M., and Lee, L., "Effects of Fin Base-Temperature Depression in a Multifin Array," ASME Journal of Heat Transfer, Vol. 97, 1975, pp. 463-465.

3 Suryanarayana, N. V., "Two-Dimensional Effects on Heat Transfer Rates From an Array of Straight Fins," ASME Journal of Heat Transfer, Vol. 99, 1977, pp. 129-132.

4 Heggs, P. J., and Stones, P. R., "Two-Dimensional Heat Flow Through Fin Assemblies," in: *Heat Exchangers—Theory and Practice*, Hemisphere, Washington, 1983, pp. 917-931.

5 Brown, A., "Optimum Dimensions of Uniform Annular Fins," *International Journal of Heat and Mass Transfer*, Vol. 8, 1965, pp. 655-662.

An Efficient Algorithm for Finite Element Solution to Two-Dimensional Heat Transfer With Melting and Freezing

J. S. Hsiao[1] **and B. T. F. Chung**[2]

Introduction

Heat transfer in materials involving melting and solidification has many practical applications such as casting, welding, and thawing of ice. The inherent nonlinearity of this type of problem has limited the analytical analysis to extremely simplified cases [1-7].

In this study, a new and efficient algorithm is proposed to be incorporated with the equivalent heat capacity model [8, 9] for the finite element analysis of melting and freezing problems. The scheme utilizes the shape function in an isoparametric finite element formulation to properly evaluate the specific heat associated with the melting/freezing element. For demonstration purposes the present algorithm is incorporated into a well-known finite element code, ADIANT (1978 Version) to solve a class of heat transfer problems involving melting and freezing.

Mathematical Formulation

The mathematical formulations for the general phase change problem are usually described in two time periods, namely the pre-phase change and phase change periods. The governing equation for the pre-phase change period is a general heat conduction equation [1]. For the phase change period, one obtains

$$C_l\,\frac{\partial T_l}{\partial t} = \nabla\cdot\mathbf{q}_l \qquad \text{for liquid phase} \tag{1}$$

$$C_s\,\frac{\partial T_s}{\partial t} = \nabla\cdot\mathbf{q}_s \qquad \text{for solid phase} \tag{2}$$

In addition to the normal boundary conditions, there are two coupling conditions have to be satisfied at the moving interface of solid and liquid phases. These are

$$T_s = T_l = T_m \tag{3}$$

and

$$-k_l\,\frac{\partial T_l}{\partial n} + k_s\,\frac{\partial T_s}{\partial n} = HV_n \tag{4}$$

where the subscripts l and s indicate the liquid and solid phases, respectively, T_m the melting temperature, H the latent heat of fusion per unit volume, V_n the speed of the melting front in the normal direction, C the specific heat per unit volume, and k the thermal conductivity.

A common approximation employed in the equivalent heat capacity approach [8, 9] is to include the latent heat effect in the following dirac function

$$C = \begin{cases} C_l & \text{if } T > T_m + \Delta T \\ \dfrac{H}{2\Delta T} + \dfrac{\bar{C}_s + \bar{C}_l}{2} & \text{if } T_m - \Delta T \le T \le T_m + \Delta T \\ C_s & \text{if } T < T_m - \Delta T \end{cases} \tag{5}$$

---

[1] Research Assistant, Department of Mechanical Engineering, The University of Akron, Akron, OH 44325; present address: RCA Laboratories, David Sarnoff Research Center, Princeton, NJ; Assoc. Mem. ASME

[2] Professor, Department of Mechanical Engineering, The University of Akron, Akron, OH 44325; Mem. ASME

Contributed by the Heat Transfer Division for publication in the Journal of Heat Transfer. Manuscript received by the Heat Transfer Division September 25, 1985.

Table 1 Optimum dimensions of an annular fin assembly

P	Number of fins	V (Fig. 3)	W^*_{opt} [5]	W_{opt} (Fig. 2)	t, mm	r_f, cm	Total volume of fins, cm^3
0.1	16	0.019	79.4	79.4	1.26	15.8	955
0.2	8	0.14	22.7	22.4	4.46	20.3	3520
0.4	4	0.95	7.0	6.6	15.2	26.9	11,940

tween two consecutive fins) which exceeds the decrease in heat transfer from the fin sides and tip. The value of V at which the optimization process failed was found to decrease as Bi increased.

While the values of P and H were found insignificant in determining W_{opt}, these parameters strongly influenced Q_{opt}. In presenting our results of optimum heat transfer use was made of the enhancement factor ϵ, defined as

$$\epsilon = Q_{\mathrm{opt}}/Q_u \tag{7a}$$

where Q_u is the dimensionless heat transfer rate per computation module in the absence of the fin, given by

$$Q_u = \frac{H\,R_i\,\mathrm{Bi}}{1 + H\,R_i\left(1 - \frac{1}{2}\mathrm{Bi}\ln R_i\right)} \tag{7b}$$

Values of ϵ as a function of Bi and V at P = 0.1, 0.2, and 0.4 are presented in Fig. 3 for H = 100 and in Fig. 4 for H = 10. The enhancement due to the fins is more pronounced at low Bi, and it increases with increases in V and H, or a decrease in P. The regions in which the optimization process failed are marked in Figs. 3 and 4. Application of the information in Figs. 2, 3, and 4 in actual design can be demonstrated by the following example: Consider an aluminum cylinder (k = 160 W/m•K) with r_i = 9 cm, r_o = 10 cm, and length l = 32 cm. The cylinder is used in an application where T_i = 500°C, T_o = 20°C, $h_i = 5000$ W/m^2•K, $h_o = 50$ W/m^2•K, and it is desired to dissipate a total heat transfer rate of $q = 24$ kW. In order to design the necessary array of fins we first calculate the independent parameters Bi = 0.0625 and H = 100 from their respective definitions. Then, the rate of heat transfer without the fins can be easily evaluated as q_u = 4.757 kW, which means that the required enhancement factor is $\epsilon = q/q_u$ = 5.26. With these values of Bi, H, and ϵ, three possible designs can be made and the results are shown in Table 1. According to these results the lower the P value the better, if overall weight is the major concern. However, there are normally other considerations in design, such as mechanical strength, which may rule out designs with very small values of t. Care should also be taken in avoiding designs with narrow gaps between the fins since the present results are based on the assumption of uniform h_o along the fins and outer surface of the cylinder, which may not apply for closely spaced fin arrays.

Acknowledgments

The financial assistance provided by the Natural Sciences and Engineering Research Council of Canada is gratefully acknowledged.

References

1 Kern, D. Q., and Kraus, A. D., *Extended Surface Heat Transfer*, McGraw-Hill, New York, 1972.

2 Sparrow, E. M., and Lee, L., "Effects of Fin Base-Temperature Depression in a Multifin Array," ASME JOURNAL OF HEAT TRANSFER, Vol. 97, 1975, pp. 463-465.

3 Suryanarayana, N. V., "Two-Dimensional Effects on Heat Transfer Rates From an Array of Straight Fins," ASME JOURNAL OF HEAT TRANSFER, Vol. 99, 1977, pp. 129-132.

4 Heggs, P. J., and Stones, P. R., "Two-Dimensional Heat Flow Through Fin Assemblies," in: *Heat Exchangers—Theory and Practice*, Hemisphere, Washington, 1983, pp. 917-931.

5 Brown, A., "Optimum Dimensions of Uniform Annular Fins," *International Journal of Heat and Mass Transfer*, Vol. 8, 1965, pp. 655-662.

An Efficient Algorithm for Finite Element Solution to Two-Dimensional Heat Transfer With Melting and Freezing

J. S. Hsiao[1] **and B. T. F. Chung**[2]

Introduction

Heat transfer in materials involving melting and solidification has many practical applications such as casting, welding, and thawing of ice. The inherent nonlinearity of this type of problem has limited the analytical analysis to extremely simplified cases [1-7].

In this study, a new and efficient algorithm is proposed to be incorporated with the equivalent heat capacity model [8, 9] for the finite element analysis of melting and freezing problems. The scheme utilizes the shape function in an isoparametric finite element formulation to properly evaluate the specific heat associated with the melting/freezing element. For demonstration purposes the present algorithm is incorporated into a well-known finite element code, ADIANT (1978 Version) to solve a class of heat transfer problems involving melting and freezing.

Mathematical Formulation

The mathematical formulations for the general phase change problem are usually described in two time periods, namely the pre-phase change and phase change periods. The governing equation for the pre-phase change period is a general heat conduction equation [1]. For the phase change period, one obtains

$$C_l\,\frac{\partial T_l}{\partial t} = \nabla \bullet \mathbf{q}_l \qquad \text{for liquid phase} \tag{1}$$

$$C_s\,\frac{\partial T_s}{\partial t} = \nabla \bullet \mathbf{q}_s \qquad \text{for solid phase} \tag{2}$$

In addition to the normal boundary conditions, there are two coupling conditions have to be satisfied at the moving interface of solid and liquid phases. These are

$$T_s = T_l = T_m \tag{3}$$

and

$$-k_l\,\frac{\partial T_l}{\partial n} + k_s\,\frac{\partial T_s}{\partial n} = HV_n \tag{4}$$

where the subscripts l and s indicate the liquid and solid phases, respectively, T_m the melting temperature, H the latent heat of fusion per unit volume, V_n the speed of the melting front in the normal direction, C the specific heat per unit volume, and k the thermal conductivity.

A common approximation employed in the equivalent heat capacity approach [8, 9] is to include the latent heat effect in the following dirac function

$$C = \begin{cases} C_l & \text{if } T > T_m + \Delta T \\ \dfrac{H}{2\Delta T} + \dfrac{\bar{C}_s + \bar{C}_l}{2} & \text{if } T_m - \Delta T \le T \le T_m + \Delta T \\ C_s & \text{if } T < T_m - \Delta T \end{cases} \tag{5}$$

---

[1] Research Assistant, Department of Mechanical Engineering, The University of Akron, Akron, OH 44325; present address: RCA Laboratories, David Sarnoff Research Center, Princeton, NJ; Assoc. Mem. ASME

[2] Professor, Department of Mechanical Engineering, The University of Akron, Akron, OH 44325; Mem. ASME

Contributed by the Heat Transfer Division for publication in the JOURNAL OF HEAT TRANSFER. Manuscript received by the Heat Transfer Division September 25, 1985.

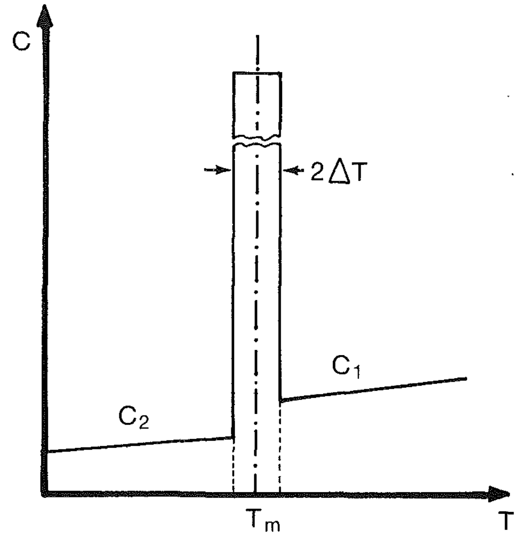

Fig. 1 Approximation of equivalent heat capacity for melting/solidification problem

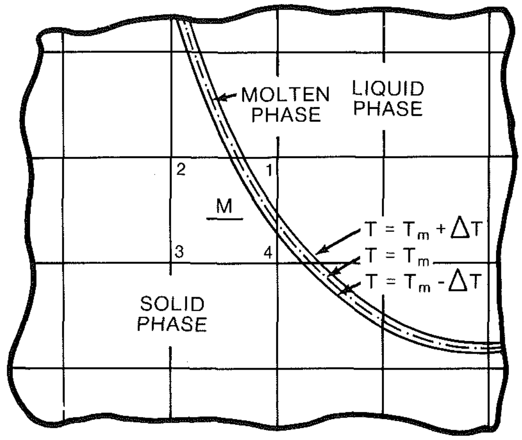

Fig. 2 Portion of the finite element model showing solid, liquid, and molten phases separated by the isothermal lines $T = T_m + \Delta T$ and $T = T_m - \Delta T$

where $H/2\Delta T$ accounts for the latent heat effect and $(\bar{C}_s + \bar{C}_l)/2$ is the averaged sensible heat for the liquid and solid in the temperature range of $T_m - \Delta T$ and $T_m + \Delta T$, and $2\Delta T$ is a small but finite temperature interval assumed for the phase change to take place. Figure 1 depicts the specific heat distribution as a function of temperature given in equation (5).

The finite element formulation for the general heat conduction problem can be found in numerous publications, e.g., [10, 11], and will not be repeated here. The final assembled system of equations for the nodal temperatures is given as follows in a matrix form [11]

$$[C][\dot{T}] + [K][T] = [Q] \tag{6}$$

where $[C]$ is the specific heat matrix, $[K]$ the conductivity matrix, $[T]$ the vector of nodal temperature, and $[Q]$ the vector of external heat flow.

Deficiency of Direct Use of Equivalent Heat Capacity Model

A common practice in a nonlinear finite element analysis is to use the elemental temperature to determine the temperature-dependent material properties such as specific heat. In an isoparametric formulation this elemental temperature is given by

$$\bar{T} = \sum_{i=1}^{n} h_i T_i \tag{7}$$

where n is the total number of nodal points in the element and h_i is the shape function [10].

Consider a typical melting element during a fusion analysis. Unless the element mesh (see Fig. 2) is further refined in such a manner that the nodal temperatures in the melting element are all within the range of $T_m - \Delta T$ and $T_m + \Delta T$, the following numerical errors will arise:

1 The averaged element temperature $\bar{T}$ is either less than $T_m - \Delta T$ or greater than $T_m + \Delta T$. In this case either solid or liquid specific heat will be used. This does not account for the latent heat effect and thereby underestimates the specific heat for the melting element.

2 $\bar{T}$ is within the $2\Delta T$ range across the melting temperature T_m. The specific heat for the element will be $H/2\Delta T + (\bar{C}_l + \bar{C}_s)/2$ given by equation (5), and implies that the whole element is consuming latent heat fusion. This results in an overestimated specific heat for the melting element.

To reduce the above error, finer mesh and smaller time steps are always necessary. Therefore, direct use of the equivalent heat capacity method for the finite element analysis of melting/freezing problem is very expensive and needs further improvement.

New Efficient Algorithm

In this study, a new algorithm is proposed and incorporated with the equivalent heat capacity method for the finite element analysis of the melting and freezing problems.

The method first estimates the mass fractions of solid, liquid and molten (material with temperature within the $2\Delta T$ range across T_m) phases inside the melting/freezing element. The specific heat for the melting/freezing element is then obtained by combining the specific heats of all phases

$$C = C_l m_l + C_s m_s + C_H m_H \tag{8}$$

where m_l, m_s, and m_H are the mass fractions of the liquid, solid, and molten phases respectively.

To calculate the mass fractions m_l, m_s and m_H of the melting element, we use a linear interpolation between the nodal temperature and averaged element temperature. For example, assume the element temperature $\bar{T}$ is greater than $T_m + \Delta T$ and a nodal temperature T_i is less than $T_m - \Delta T$. Then within this temperature interval $\bar{T}$ and T_i all three different phases exist. The mass fractions contributed by this nodal point to the element will be

$$\begin{aligned} m_l^i &= [\bar{T} - (T_m + \Delta T)]/(\bar{T} - T_i) \\ m_s^i &= [(T_m - \Delta T) - T_i]/(\bar{T} - T_i) \\ m_H^i &= 2\Delta T/(\bar{T} - T_i) \end{aligned}$$

Similarly, if $\bar{T}$ and T_i are both greater than $T_m + \Delta T$, this implies that only the liquid phase exists and the mass fractions associated to the node are $m_l^i = 1$ and $m_s^i = m_H^i = 0$, etc.

The total mass fractions for each phase in the element are then obtained by summing up the contributions from all n nodal points with the use of the shape function as a weighting factor. These are given by

$$\begin{aligned} m_l &= \sum_{i=1}^{n} h_i m_l^i \\ m_s &= \sum_{i=1}^{n} h_i m_s^i \\ m_H &= \sum_{i=1}^{n} h_i m_H^i \end{aligned}$$

Once the specific heats for all elements are determined one

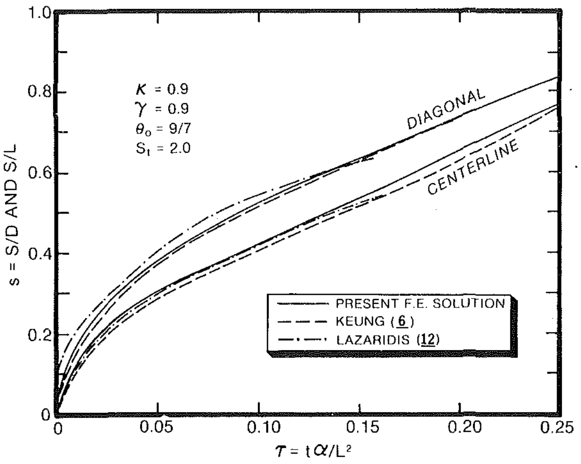

Fig. 3 Interface position along the diagonal and center line for solidification of liquid in a square region with prescribed boundary temperature

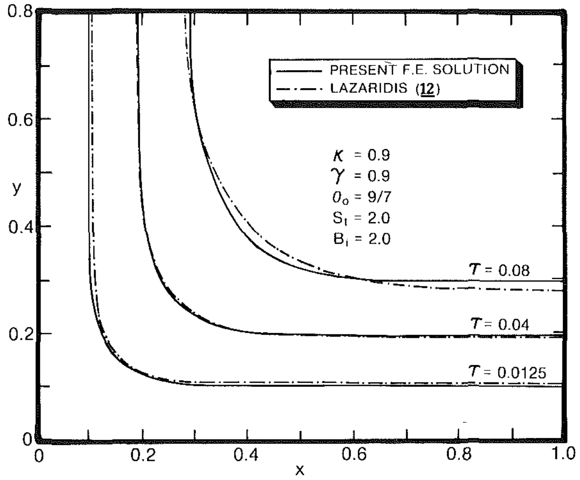

Fig. 4 Comparison of loci of interface obtained from finite element and finite difference methods for liquid in a square region subject to convective cooling

can proceed with the finite element analysis similar to the general nonlinear study. Note that the present algorithm involves only the re-evaluation of the specific heat for the melting/freezing element. It can be easily implemented into any general purpose finite element program for efficient heat transfer analysis with melting and freezing.

Results and Discussion

To demonstrate the present scheme, a freezing problem of liquid in a simple two-dimensional geometry is studied. Both specified wall temperature and convective cooling boundary conditions are examined. The numerical solutions are obtained by implementing the present scheme into a general purpose finite element code ADINAT.

Consider a liquid in an infinitely long square prism with uniform cross section. The liquid is initially at a temperature higher than the melting temperature. The surface is suddenly exposed to a uniform wall temperature below the fusion temperature and solidification takes place immediately. The material properties are so chosen that, in terms of dimensionless form, they are the same as those used by Lazaridis [12]. They are: $\kappa = k_l/k_s = 0.9$, $\gamma = \alpha_l/\alpha_s = 0.9$, $\theta_0 = (T_0 - T_w)/(T_m - T_w) = 9/7$, and Stefan number, $\mathrm{St} = C_s (T_m - T_w)/H = 2$. Figure 3 shows the interface positions as a function of time at the diagonal and center line of the square. Also included in the figure are the results obtained by Keung [6] using the source and sink method and by Lazaridis [12] using the finite difference method. As can be seen, the present finite element solution agrees very well with the other two solutions over the entire time period.

The same problem is solved again for the convective cooling at the boundary. The dimensionless parameters chosen are $\kappa = 0.9$, $\gamma = 0.9$, $\theta_0 = (T_0 - T_a)/(T_m - T_a) = 9/7$, $\mathrm{St} = C_s(T_m - T_a)/H = 2$ and $\mathrm{Bi} = hL/k_s = 2$, with T_a being the ambient temperature. Figure 4 gives the prediction of the freezing front at different values of time. The only available finite difference solution given by Lazaridis [12] is also included. Once again, the present finite element solution agrees well with the finite difference solution.

Although there are no other data available for the direct assessment of the efficiency of the present scheme, it is worth noting that the finite element mesh and time step employed in the above cases are relatively coarse. For example, in the previous convective cooling problem, the finite element model is of 10 × 10 in mesh and the dimensionless time step size is 0.001.

Conclusion

A new simple strategy has been proposed to incorporate the equivalent heat capacity model for the finite element analysis of heat transfer problem with melting/freezing. Accurate results, in comparison with the existing solutions, are obtained efficiently without using a very fine element mesh and/or time step. This scheme can be easily implemented into any general purpose finite element program and is also applicable to three-dimensional cases.

Acknowledgments

This work was partially supported by U.S. Naval Research Laboratory under contract No. ONR N00014-80-C-0888.

References

1 Carslaw, H. S., and Jaeger, J. C., *Conduction of Heat in Solids*, 2nd ed., Clarendon Press, 1959.

2 Goodman, T. R., "The Heat Balance Integral and Its Application to Problems Involving a Change of Phase," *Trans. ASME*, Vol. 80, 1958, pp. 335-342.

3 Yeh, L. T., and Chung, B. T. F., "Integral Method of Freezing and Melting in a Radiating and Convecting Medium With Variable Thermal Properties," ASME Paper No. 82-HT-54.

4 Chung, B. T. F., and Yeh, L. T., "Freezing and Melting of Materials With Variable Properties and Arbitrary Heat Fluxes," *AIAA J.*, Vol. 14, 1976, p. 338.

5 Yeh, L. T., and Chung, B. T. F., "A Variational Analysis of Freezing or Melting in a Finite Medium Subjected to Radiation and Convection," ASME JOURNAL OF HEAT TRANSFER, Vol. 101, 1979, pp. 4-8.

6 Keung, C. S., "The Use of Sources and Sinks in Solving Two-Dimensional Heat Conduction Problems With Change of Phase in Arbitrary Domains," Ph.D dissertation, Columbia University, 1980.

7 Boley, B. A., "The Embedding Technique in Melting and Solidification Problems, Moving Boundary Problems in Heat Flow and Diffusion," *Proceedings of the Conference held at Univ. of Oxford*, March 1974, Ockendon and Hodgkins, eds., pp. 150-172.

8 Shamsunder, N., and Sparrow, E. M., "Analysis of Multi-dimensional Conduction Phase Change via the Enthalpy Model," ASME JOURNAL OF HEAT TRANSFER, Vol. 97, 1975, pp. 333-340.

9 Hsiao, J. S., "Numerical and Analytical Analyses of Heat Transfer With Ablation in a Two-Dimensional Region," Ph.D Dissertation, The University of Akron, 1983.

10 Zienkiewicz, O. C., *The Finite Element Method*, 3rd ed., McGraw-Hill, New York, 1977.

11 Bathe, K. J., and Wilson, E. L., "Numerical Methods in Finite Element Analysis," Prentice-Hall, New York, 1976.

12 Lazaridis, A., "Numerical Solution of the Multidimensional Solidification (or Melting) Problem," *Int. J. Heat Mass Transfer*, Vol. 13, 1970, pp. 1459-1477.

A Short Time Solution for Coupled Conduction and Radiation in a Participating Slab Geometry

W. H. Sutton[1]

Introduction

The analysis of combined conduction and participating radiation heat transfer has been the subject of considerable interest over the past two decades; a convenient catalogue of most of the major works may be found in Sutton [1]. The problem of a gray, constant-property slab with opaque, constant-temperature boundaries is usually the basis for testing the numerical accuracy and computational features of a given solution method. The purposes of the current work are to provide a very accurate picture of the effects of radiation dominated media of "early times" and to illustrate a basic method well suited for such problems.

Short time, here, refers to small Fourier number problems; depending on material properties (insulations, etc.) physical time could be relatively large. The current solution method may be briefly described as a hybrid Galerkin-iterative/finite difference scheme. The unique features of this work, beyond its flexibility, are that no "particular solution" is used for the emission term in the radiative transfer solution and no iteration between conduction and radiation solutions is required.

Analysis

The central difference transient energy balance for the ith interior slab nodal point in terms of dimensionless temperature, $\theta = T/T_{\mathrm{ref}}$, and radiative heat flux, $Q^r = q^r/\sigma T_{\mathrm{ref}}^4$, is

$$\frac{\theta_{i+1}+\theta_{i-1}-2\theta_i}{(\Delta\eta)^2} - \frac{1}{4N}\left(\frac{Q^r_{i+1}-Q^r_{i-1}}{2\Delta\eta}\right) = \frac{\partial\theta_i}{\partial\xi} \tag{1}$$

where $\eta = Z/L$ is the dimensionless spatial coordinate and $\xi = \alpha t/L^2$ is the Fourier number. The conduction to radiation parameter N is taken in the nongray sense as $N = (k/L)/\sigma T_{\mathrm{ref}}^3$. α, k, and L are, respectively, thermal diffusivity, thermal conductivity, and physical thickness of the slab. The boundaries of the slab are assumed to be steady and isothermal and the initial temperature of the slab is assumed to be uniform for comparison purposes. Mathematically, $\theta(0,\xi) = \theta_1 \equiv T_1/T_{\mathrm{ref}}$, $\theta(1,\xi) = \theta_2 \equiv T_2/T_{\mathrm{ref}}$, and $\theta(y, 0) = \theta_0 \equiv T_0/T_{\mathrm{ref}}$. Equation (1) is solved using an explicit finite difference scheme, that is, stepwise marching in stable increments of $\Delta\xi$ away from the given initial condition. The slab is divided into 20 evenly spaced elements (21 nodes); $\Delta\xi$ is taken as approximately 1/80 of the stable increment in order to give benchmark results in all cases tested.

The dimensionless radiative flux at each nodal point in the energy equation is obtained by the hybrid method that follows.

Assuming $\Delta\xi$ large enough so that *direct* $(\partial/\partial\xi = 0)$ transient radiative effects are neglected, the radiative transfer equation in terms of dimensionless intensity, $\psi = I/(\sigma T_{\mathrm{ref}}^4/\pi)$, is

$$\mu\frac{\partial\psi}{\partial\tau} + \psi = (1-\omega)\psi_b + \frac{\omega}{2}\int_{-1}^{1}\psi\, d\mu', \quad 0 \le \tau \le \tau_0, \quad |\mu| \le 1 \tag{2}$$

Gray uniform properties and isotropic scattering are assumed here for illustration purposes. Therefore, $\psi_b = n^2\theta^4$ where the refractive index of the medium is taken as one. ω and τ_0 are the scattering albedo and optical thickness of the medium. The right-hand side of equation (2) is defined as S, the source function. Equation (2) is linear in intensity and this may be superpositioned as illustrated in Özisik and Sutton [2] for general diffuse boundary conditions. The dimensionless intensity is thus written as

$$\psi(\tau,\mu) = \psi_0(\tau,\mu) + (\epsilon_1\theta_1{}^4 + 2\rho_1{}^d K_1)\psi_1(\tau,\mu) + (\epsilon_2\theta_2{}^4 + 2\rho_2{}^d K_2)\psi_2(\tau,\mu) \tag{3}$$

where $K_1 \equiv \int_0^1 \psi(0, -\mu')\mu'\, d\mu'$ and $K_2 \equiv \int_0^1 \psi(\tau_0, \mu')\mu'\, d\mu'$ are simply half-range fluxes for the original problem. ϵ_j and ρ_j are jth surface emittance and reflectance. The solution for each of the subproblems may be formulated ($i = 0, 1, 2$) as

$$\mu\frac{\partial\psi_i}{\partial\tau} + \psi_i = S_i, \quad \psi_i(0,\mu) = \delta_{1i}, \text{ and } \psi_i(\tau_0, -\mu) = \delta_{2i}$$

where

$$S_i = (1-\omega)\delta_{0i}\theta^4 + \frac{\omega}{2}\int_{-1}^{1}\psi_i\, d\mu'$$

and δ_{ij} is the Kröneker delta. The formal solution of each subproblem in terms of S is given as [2]

$$S_i(\tau) = (1-\omega)\delta_{0i}\theta^4 + \frac{\omega}{2}\{\delta_{1i}E_2(\tau) + \delta_{2i}E_2(\tau_0-\tau) + \int_{\tau'=0}^{\tau_0} S_i(\tau')E_1(|\tau-\tau'|)d\tau'\}, \quad i = 0, 1, 2$$

The case for $i = 0$ is solved iteratively in $S_0(\tau)$ for each temperature distribution at a given time. The integral involving S_0 is represented with a ten-point Gaussian quadrature. A comparison to results for certain cases with a 20-point quadrature gave identical results. The case for $i = 1$ or 2 may be solved by assuming a Galerkin power series expansion for S_i as

$$S_i(\tau) = \sum_{n=0}^{N} A_n\tau^n$$

Substituting the expansion and collecting terms yields a matrix equation A_n for the coefficients. The details track Özisik and Yener [3] except that the emission term is omitted and solved here by iteration. A ten-term Galerkin expansion is used in the current work with the various integral terms in the matrix equation performed with 40-point Gaussian quadrature.

Once S_i and ψ_i are known, K_1 and K_2 are obtained by operating on equation (3) with $\int_0^1 \mu' d\mu'$ and an algebraic solution as detailed in [2]. After K_1 and K_2 are found, the net radiative flux at each point in the slab is finally obtained using equation (3) and the definition

$$Q^r \equiv \int_{-1}^{1}\mu'\psi\, d\mu'$$

While the entire process sounds quite complex, in reality it is very efficient because the boundary terms are solved only once for a given problem. Additionally, the time step requirements for the explicit finite difference method force only a small change in the temperature distribution at each step so that the iteration subproblem converges rapidly. The entire process at each time step requires approximately 2 s of CPU time in Fortran G on the IBM 3081.

Results and Conclusion

Recently, it was reported [1, 4] that the results of several previous investigators [6, 7] for the same problem were incorrect due to assumptions made in computation. The current results avoid those problems and compare well to the exact analysis [5]. For illustration of transient effects on temperature, the case of $N = 0.1$ for $\theta_1 = 1$, $\theta_2 = 0$, $\theta_0 = 0$, $\rho_1^d = \rho_2^d = 0$, $\omega = 0.5$, and $\tau_0 = 1$ is plotted in Fig. 1 (Lii and Özisik [6] problem). When the results are carried to steady state, the solutions previously published [6] are obtained; however, the current method is not computationally well suited for longer times.

---

[1] Assistant Professor, School of Aerospace, Mechanical and Nuclear Engineering, University of Oklahoma, Norman, OK 73019; Assoc. Mem. ASME.

Contributed by the Heat Transfer Division for publication in the JOURNAL OF HEAT TRANSFER. Manuscript received by the Heat Transfer Division October 15, 1984.

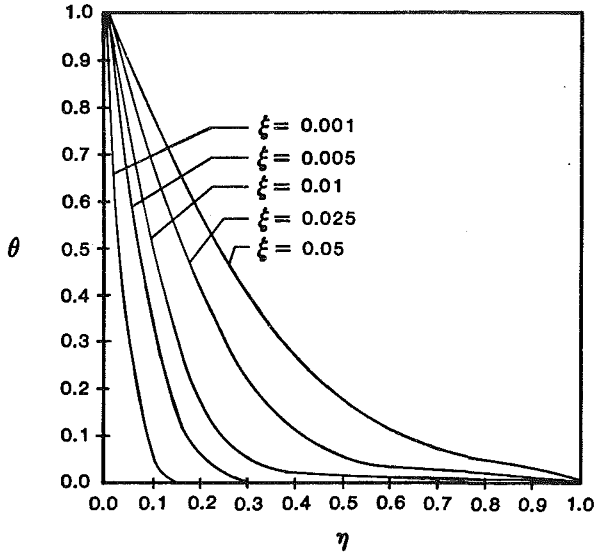

Fig. 1 Temperature distribution during slab heating as a function of time for $N=0.1$ ($\theta_1=1$, $\theta_2=0$, $\theta_0=0$, $\rho_1^d=\rho_2^d=0$, $\omega=0.5$, $\tau_0=1$)

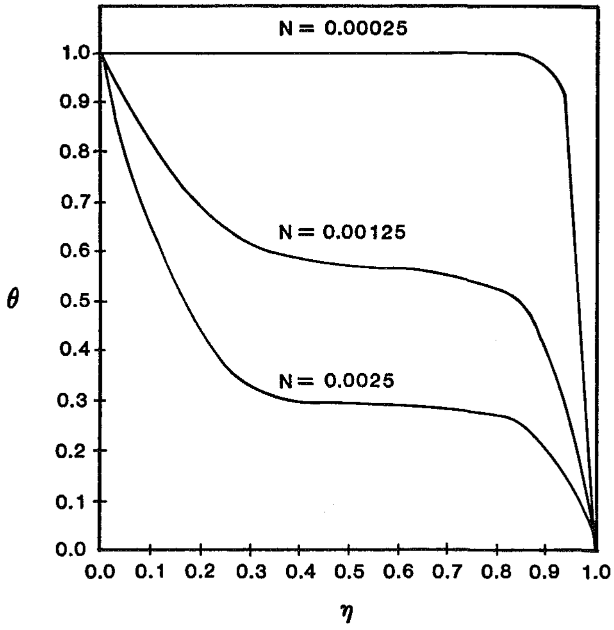

Fig. 2 Temperature distribution as a function of N for $\xi=0.01$ ($\theta_1=1$, $\theta_2=0$, $\theta_0=0$, $\rho_1^d=0$, $\rho_2^d=1$, $\omega=0.9$, $\tau_0=1$)

When N is decreased, holding other parameters fixed for a similar problem ($\rho_2^d=1$, $\omega=0.9$), the radiation clearly affects the entire medium as illustrated in Fig. 2 for the case of $\xi=0.01$. Thus, if radiative effects are ignored for small Fourier number problems, significant errors may be observed in the transient results. This result may be particularly significant in the design of thermal measurement systems involving insulation, ceramics, and other poor thermal conductors.

References

1 Sutton, W. H., "A Short Time Solution for Coupled Conduction and Radiation in a Participating Slab Geometry," ASME Paper No. 84-HT-34.

2 Özisik, M. N., and Sutton, W. H., "A Source Function Expansion in Radiative Transfer," ASME Journal of Heat Transfer, Vol. 102, 1980, pp. 715–718.

3 Özisik, M. N., and Yener, Y., "The Galerkin Method for Solving Radiation Transfer in Plane-Parallel Participating Media," ASME Journal of Heat Transfer, Vol. 104, 1982, pp. 351–354.

4 Sutton, W. H., and Barker, C., "A Systematic Study of Combined Conduction and Radiation Heat Transfer in Semitransparent Slab Geometries," AMNE Research Report 84-11, University of Oklahoma, 1984.

5 Lii, C. C., and Özisik, M. N., "Transient Radiation and Conduction in an Absorbing, Emitting and Scattering Slab With Reflecting Boundaries," *Int. J. Heat Mass Transfer*, Vol. 15, 1972, pp. 1175–1179.

6 Weston, K. C., and Hauth, J. L., "Unsteady, Combined Radiation and Conduction in an Absorbing, Scattering, and Emitting Medium," ASME Journal of Heat Transfer, Vol. 95, 1973, pp. 357–364.

Local Nusselt Numbers for Flowing Packed Particle Beds in Circular Tubes With Constant Wall Heat Flux

K. S. Schnoebelen[1] and S. I. Abdel-Khalik[1]

Nomenclature

a_0, a_1, a_2, a_3 = constants defined in equations (8) and (9)
A_m = constants defined in Table 2
c = specific heat
d = average particle diameter
D = tube diameter
$\mathfrak{F}$ = empirical function defined in equations (7) and (8)
g = gravitational acceleration
h_x = local heat transfer coefficient
k = thermal conductivity
N_{Ar} = Archimedes number $\equiv d^3 g \rho_g(\rho_p-\rho_g)/\mu_g^2$
Nu_x = local Nusselt number defined in equation (1)
$\mathrm{Nu}_{1,x}$ = local Nusselt number for laminar, Newtonian flow in circular tubes with a fully developed velocity profile
$\mathrm{Nu}_{2,x}$ = local Nusselt number for laminar, Newtonian flow in circular tubes with a flat velocity profile
Pe = effective Peclet number defined in equation (2)
x = distance along the tube measured from the beginning of the heated length
x^+ = nondimensional distance (inverse Graetz number) defined in equation (3)
V = average particle bed velocity
β = parameter appearing in equation (6)
γ = parameter appearing in equation (6)

---

[1] Nuclear Engineering Department, University of Wisconsin-Madison, Madison, WI 53706

Contributed by the Heat Transfer Division for publication in the Journal of Heat Transfer. Manuscript received by the Heat Transfer Division September 20, 1984.

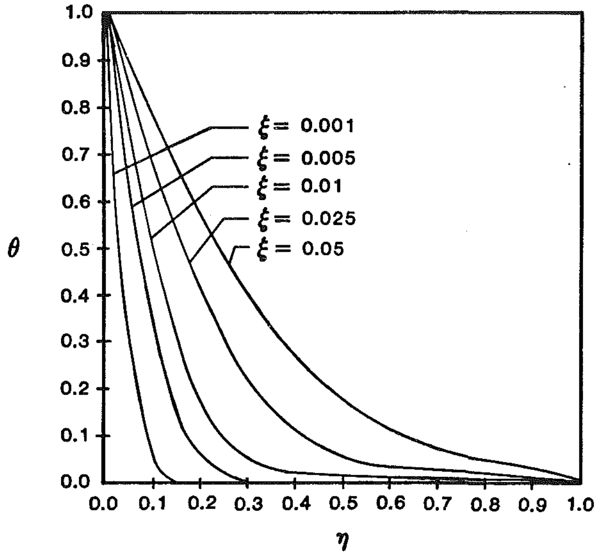

Fig. 1 Temperature distribution during slab heating as a function of time for $N = 0.1$ ($\theta_1 = 1$, $\theta_2 = 0$, $\theta_0 = 0$, $\rho_1^d = \rho_2^d = 0$, $\omega = 0.5$, $\tau_0 = 1$)

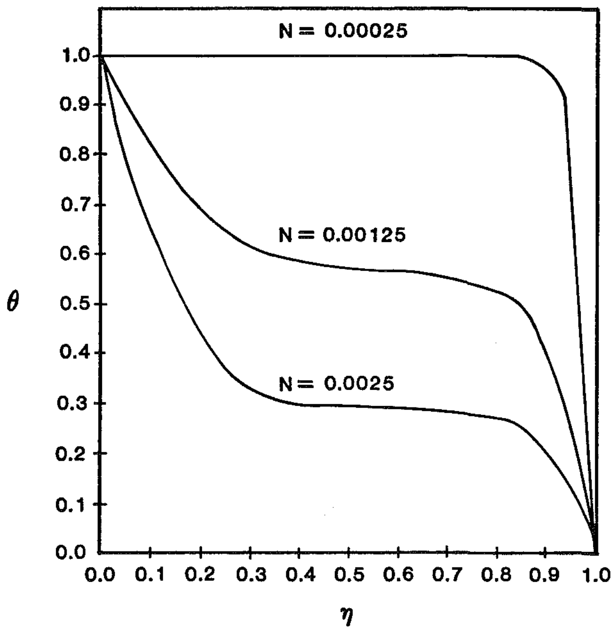

Fig. 2 Temperature distribution as a function of N for $\xi = 0.01$ ($\theta_1 = 1$, $\theta_2 = 0$, $\theta_0 = 0$, $\rho_1^d = 0$, $\rho_2^d = 1$, $\omega = 0.9$, $\tau_0 = 1$)

When N is decreased, holding other parameters fixed for a similar problem ($\rho_2^d = 1$, $\omega = 0.9$), the radiation clearly affects the entire medium as illustrated in Fig. 2 for the case of $\xi = 0.01$. Thus, if radiative effects are ignored for small Fourier number problems, significant errors may be observed in the transient results. This result may be particularly significant in the design of thermal measurement systems involving insulation, ceramics, and other poor thermal conductors.

References

1 Sutton, W. H., "A Short Time Solution for Coupled Conduction and Radiation in a Participating Slab Geometry," ASME Paper No. 84-HT-34.

2 Özisik, M. N., and Sutton, W. H., "A Source Function Expansion in Radiative Transfer," ASME Journal of Heat Transfer, Vol. 102, 1980, pp. 715-718.

3 Özisik, M. N., and Yener, Y., "The Galerkin Method for Solving Radiation Transfer in Plane-Parallel Participating Media," ASME Journal of Heat Transfer, Vol. 104, 1982, pp. 351-354.

4 Sutton, W. H., and Barker, C., "A Systematic Study of Combined Conduction and Radiation Heat Transfer in Semitransparent Slab Geometries," AMNE Research Report 84-11, University of Oklahoma, 1984.

5 Lii, C. C., and Özisik, M. N., "Transient Radiation and Conduction in an Absorbing, Emitting and Scattering Slab With Reflecting Boundaries," *Int. J. Heat Mass Transfer*, Vol. 15, 1972, pp. 1175-1179.

6 Weston, K. C., and Hauth, J. L., "Unsteady, Combined Radiation and Conduction in an Absorbing, Scattering, and Emitting Medium," ASME Journal of Heat Transfer, Vol. 95, 1973, pp. 357-364.

Local Nusselt Numbers for Flowing Packed Particle Beds in Circular Tubes With Constant Wall Heat Flux

K. S. Schnoebelen[1] **and S. I. Abdel-Khalik**[1]

Nomenclature

a_0, a_1, a_2, a_3 = constants defined in equations (8) and (9)
A_m = constants defined in Table 2
c = specific heat
d = average particle diameter
D = tube diameter
$\mathfrak{F}$ = empirical function defined in equations (7) and (8)
g = gravitational acceleration
h_x = local heat transfer coefficient
k = thermal conductivity
N_{Ar} = Archimedes number $\equiv d^3 g \rho_g(\rho_p - \rho_g)/\mu_g^2$
Nu_x = local Nusselt number defined in equation (1)
$\mathrm{Nu}_{1,x}$ = local Nusselt number for laminar, Newtonian flow in circular tubes with a fully developed velocity profile
$\mathrm{Nu}_{2,x}$ = local Nusselt number for laminar, Newtonian flow in circular tubes with a flat velocity profile
Pe = effective Peclet number defined in equation (2)
x = distance along the tube measured from the beginning of the heated length
x^+ = nondimensional distance (inverse Graetz number) defined in equation (3)
V = average particle bed velocity
β = parameter appearing in equation (6)
γ = parameter appearing in equation (6)

---

[1] Nuclear Engineering Department, University of Wisconsin-Madison, Madison, WI 53706

Contributed by the Heat Transfer Division for publication in the Journal of Heat Transfer. Manuscript received by the Heat Transfer Division September 20, 1984.

γ_m = parameter appearing in equation (11), Table 2
ϵ = average bed void fraction
μ = viscosity
ρ = density
ϕ = parameter appearing in equation (6)
ω_m = parameter appearing in equation (12), Table 2

Subscripts

p = particle
g = gas
eff = effective

Introduction

Channel flow of packed particle beds has numerous applications in the chemical industry. Our interest in this area, however, arises from recent advances in fusion reactor designs [1]. In one such design [1], lithium oxide particles 100-200 μm in diameter flow under the influence of gravity through channels in the reactor blanket and serve the dual purpose of tritium breeding and heat transport. Analyses of the performance of these blankets and associated power cycle and tritium recovery systems have been hampered by the lack of convective heat transfer data for channel flow of packed particle beds.

Sullivan and Sabersky [2] obtained a correlation for the average heat transfer coefficient along a flat plate immersed and moving in granular media. Denloye and Botterill [3] examined the problem of heat transfer between a particle bed flowing through a rectangular channel and a flat surface centered in the middle of the channel. A correlation for the average Nusselt number as a function of the Archimedes number N_{Ar} was obtained. More recently, Nietert and Abdel-Khalik [4, 5] conducted an investigation in which the local heat transfer coefficients for gravity flowing packed particle beds in the entrance regions of circular tubes with constant wall heat flux were measured. Data were measured for different particle sizes, tube diameters, wall heat fluxes, and average bed velocities.

The purpose of this investigation is to correlate the voluminous data of Nietert and Abdel-Khalik presented in [4, 5]. A generalized correlation for the local Nusselt numbers for flowing packed particle beds in the entrance regions of circular tubes with constant wall heat flux has been obtained. The local Nusselt number Nu_x is correlated in terms of the inverse Graetz number (nondimensional distance from the inlet x^+), tube-to-particle diameter ratio, and Peclet number.

Experimental Apparatus and Procedure

A schematic diagram of the test loop used by Nietert and Abdel-Khalik is shown in Fig. 1. Soda-lime glass particles of controlled sizes (Table 1) flow by gravity from the upper storage tank through an unheated, 29-cm-long entrance region before entering the test section. The test section is an electrically heated, 54-cm-long, Type 321 stainless steel tube. Tubes of different diameters have been used (Table 1). The particles flow from the test section to the lower collection tank through an unheated, 36-cm-long exit region followed by a sliding cone valve assembly for controlling the particles flow rate. The diameters of the entrance and exit regions are identical to the test section diameter. A suction pump is used to return the particles from the lower collection tank to the upper storage tank continuously via a shell-and-tube heat exchanger.

Electric current from a 50 kW d-c power supply is passed through the test section tube wall which is thermally insulated from the outside. The wall temperature distribution along the test section is measured by chromel-alumel thermocouples spot welded to the outside surface of the test section tube. The particle inlet bulk temperature is also measured using a chromel-alumel thermocouple. Power input, and hence the average heat flux, is determined by measuring the voltage drop and current flow through the test section. The mass flow rate through the test section is determined by collecting and weighing the exiting particles over a measured period of time. A total of 129 experiments have been conducted for three tube diameters, three average particle diameters, and different heat fluxes and average bed velocities. The ranges of experimental variables are listed in Table 1. Variations of the local heat transfer coefficient along the test section have been determined for all the experiments [4]; a total of 1534 data points have been obtained. Additional details regarding the experimental apparatus and procedure, along with a listing of the data, may be found in [4].

Table 1 Ranges of experimental variables

Tube diameter, D mm	7.75, 13.8, 24.8
Average particle diameter d, μm	214, 505, 715
Wall heat flux q, W/cm^2	2.10-4.20
Average bed velocity, V, cm/s	0.9-15.3

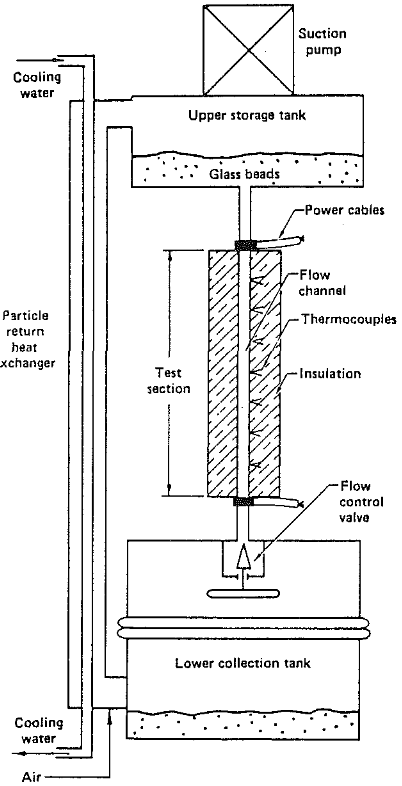

Fig. 1 Schematic diagram of the test loop used by Nietert and Abdel-Khalik [4, 5]

Results

Values of the local Nusselt number Nu_x, Peclet number Pe, and nondimensional distance x^+ were calculated for all the experiments using the relations

$$\mathrm{Nu}_x \equiv \frac{h_x D}{k_{\mathrm{eff}}} \tag{1}$$

$$\mathrm{Pe} \equiv \frac{\rho_{\mathrm{eff}} c_{\mathrm{eff}} V D}{k_{\mathrm{eff}}} \tag{2}$$

and

$$x^+ \equiv \frac{x}{D\,\mathrm{Pe}} \tag{3}$$

Here, D is the tube diameter, x is the distance measured from the beginning of the heated length, and V is the average bed velocity. The effective density and specific heat are given by

$$\rho_{\mathrm{eff}} = \epsilon\rho_g + (1-\epsilon)\rho_p \tag{4}$$

and

$$c_{\mathrm{eff}} = \frac{1}{\rho_{\mathrm{eff}}}[\epsilon\rho_g c_g + (1-\epsilon)\rho_p c_p] \tag{5}$$

The subscripts g and p refer to the gas (air) and particles, respectively, while ϵ is the average void fraction within the bed.

The effective static thermal conductivity k_{eff} was calculated using the model of Specchia et al. [6] which is based on the original model of Kunii and Smith [7]

$$\frac{k_{\mathrm{eff}}}{k_g} = \epsilon + \{\beta(1-\epsilon)/[\phi + (k_g/k_p)\gamma]\} \tag{6}$$

For spherical particles, $\beta = 1$, $\gamma = 2/3$, and $\phi = 0.220\ \epsilon^2$. The Kunii-Smith model accounts for conduction through the voids, radiation between voids, conduction through particle contact points, radiation between particles, conduction through the film, and conduction through the solid particles; these contributions can be represented by a thermal resistance network as described in [4].

In order to obtain a generalized Nusselt-type correlation for the data, attention was first focused on a statistical 2^4 factorial design employing selected runs among the 129 experiments listed in [4]. These runs represent the extremes of the four primitive variables examined, viz., tube diameter, D, average particle diameter d, average bed velocity V, and wall heat flux q. The results of this assay yielded clues as to the relative importance of the nondimensional quantities affecting the local Nusselt number and, also, as to the appropriate form of the local Nusselt number correlation. The basic idea in factorial design is to average out the different experimental results for the selected 2^n combinations representing the extremes for the n independent variables in order to identify their relative impact on the dependent variable. If the independent variables act additively, the factorial does the job with greater precision, whereas if they do not, the factorial can estimate interactions that measure the nonadditivity. This is done through simple arithmatic manipulations of the experimental results as explained by Box et al. [8].

Data for 15 of the selected 16 runs are plotted in Fig. 2. (The sixteenth run was discarded because of an error in the original data.) The "plus" and "minus" signs in the figure key indicate the extreme values for the four primitive variables D, d, q, and V. For example, the data set designated by open circles corresponds to the test run with the largest tube diameter D, the smallest particle diameter d, the lowest heat flux q, and the highest average bed velocity V among the 129 experiments with ranges listed in Table 1. The experimental uncertainty of the measured Nu_x values is estimated to be ±10 percent. The curve labeled $\mathrm{Nu}_{1,x}$ in Fig. 2 is the local Nusselt number in the entrance regions of circular tubes for the case of laminar, Newtonian flow with a fully developed parabolic velocity profile [9, 10]; the curve labeled $\mathrm{Nu}_{2,x}$ is the corresponding case for a flat velocity profile [4]. Infinite series expressions for $\mathrm{Nu}_{1,x}$ and $\mathrm{Nu}_{2,x}$ as functions of the inverse Graetz number (nondimensional) distance x^+) may be found in the literature; they are listed in Table 2 for completeness.

Discussion and Conclusions

The results in Fig. 2 indicate that the Nusselt number data for flowing packed particle beds falls between $\mathrm{Nu}_{1,x}$ and $\mathrm{Nu}_{2,x}$. This fact is physically reasonable and suggests a correlation in the form

$$\mathrm{Nu}_x = \mathrm{Nu}_{1,x} + \mathfrak{F}[\mathrm{Nu}_{2,x} - \mathrm{Nu}_{1,x}] \tag{7}$$

where $\mathfrak{F}$ is a function which varies between zero and nearly unity over the entire range of experimental variables examined.

The data in Fig. 2 show that, as expected, the heat flux has little or no effect on the Nusselt number. Experiments at different heat fluxes have been analyzed to assure consistency between the runs and proper accounting for radiation corrections and the effects of temperature on physical properties [4]. It should be noted, however, that in all the experiments conducted, the temperature did not exceed the range where the effective thermal conductivity models are expected to apply

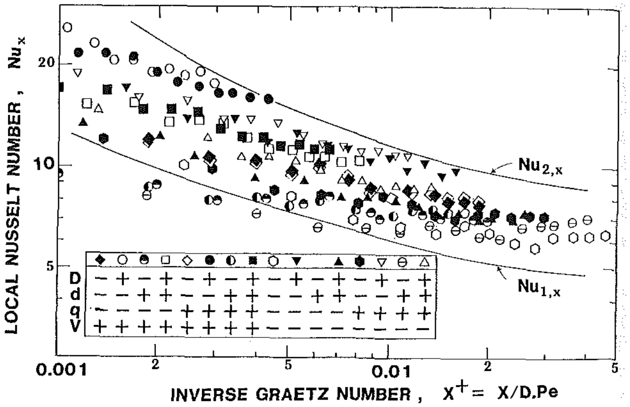

Fig. 2 Variation of the local Nusselt number Nu_x with nondimensional distance x^+ for the different experiments selected in the factorial design

Table 2 Infinite series expressions for $\mathrm{Nu}_{1,x}$ and $\mathrm{Nu}_{2,x}$

(a) Expression for $\mathrm{Nu}_{1,x}$ [9]

$$\mathrm{Nu}_{1,x} = \left[\frac{11}{48} - \frac{1}{2}\sum_m \frac{\exp(-\gamma_m^2 x^+)}{A_m\gamma_m^4}\right]^{-1} \tag{11}$$

m	1	2	3	4	5
γ_m^2	25.68	83.86	174.2	296.5	450.9
A_m	7.630×10^{-3}	2.058×10^{-3}	0.901×10^{-3}	0.487×10^{-3}	0.297×10^{-3}

(For larger m, $\gamma_m = 4m + \dfrac{4}{3}$; $A_m = 0.358\ \gamma_m^{-2.32}$)

(b) Expression for $\mathrm{Nu}_{2,x}$ [4]

$$\mathrm{Nu}_{2,x} = \left[\frac{1}{8} - \sum_m \frac{\exp(-4\omega_m^2 x^+)}{\omega_m}\right]^{-1} \tag{12}$$

where ω_m are the roots for the equation $J_1(\omega_m) = 0$, and J_1 is a Bessel function of the first kind with order one.

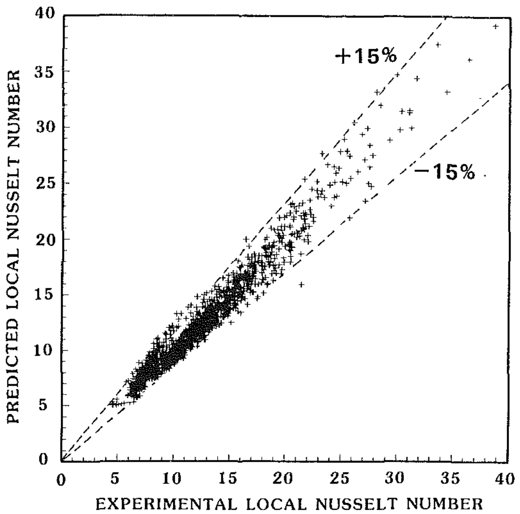

Fig. 3 Comparison between experimental values of Nu_x and those predicted using equations (7)-(9)

($T<950°$C). Figure 2 shows that the function $\mathfrak{F}$ is strongly dependent on the tube-to-particle diameter ratio D/d. For high values of D/d, the Nusselt number values Nu_x approach the $\mathrm{Nu}_{2,x}$ curve for plug flow. This result is consistent with our observations and those of Brinn et al. [11], indicating that the velocity distribution for tube flow of particle beds is uniform across the tube diameter except near the wall where it is about 15 to 20 percent lower. In other words, for large D/d, the bed behavior approaches that of a homogeneous fluid with the same effective physical properties and velocity distribution.

The entire data set (1534 data points) has been used to develop a generalized correlation for $\mathfrak{F}$ as a function of x^+, Pe, and D/d using least-squares fitting. Dependence of $\mathfrak{F}$ on the Archimedes number is not possible to discern since only one gas (air) is used. The following correlation is obtained

$$\mathfrak{F} = \log\{a_0(x^+)^{a_1}(D/d)^{a_2}(\mathrm{Pe})^{a_3}\} \tag{8}$$

where

$$a_0=0.041;\ a_1=0.34;\ a_2=0.63;\ a_3=0.48 \tag{9}$$

Equations (7) through (9) are the main results of this work. They are valid within the following range of variables

$$2.7\times10^{-4}\le x^+\le 0.11,\ 11\le(D/d)\le 115,\ \text{and}\ 550\le \mathrm{Pe}\le 8000 \tag{10}$$

Figure 3 compares the experimental values of Nu_x with those predicted using the above correlation. The vast majority of the 1534 data points falls within ±15 percent of the experimental values. Analysis of the residuals indicates that the standard error in the predicted Nusselt number is 7.6 percent of the observed value. The 95 percent confidence interval for the percent error in the predicted Nusselt number is ±16.9 percent.

Acknowledgments

Financial support by the Lawrence Livermore National Laboratory is acknowledged.

References

1 Conn, R. W., et al., "SOLASE – A Laser Fusion Reactor Study," University of Wisconsin, Report UWFDM-220, Dec. 1977.
2 Sullivan, W. N., and Sabersky, R. H., "Heat Transfer to Flowing Granular Media," *Int. J. Heat Mass Transfer*, Vol. 18, No. 1, 1975, pp. 97-107.
3 Denloye, A. O. O., and Botterill, J. S. M., "Heat Transfer in Flowing Packed Beds," *Chem. Eng. Sci.*, Vol. 32, No. 5, 1977, pp. 461-465.
4 Nietert, R. E., "Heat Transfer Characteristics of Flowing and Stationary Particle Bed Type Fusion Reactor Blankets," Ph.D. thesis, Nuclear Engineering Department, University of Wisconsin-Madison, 1982.
5 Nietert, R. E., and Abdel-Khalik, S. I., "Thermalhydraulics of Flowing Particle-Bed-Type Fusion Reactor Blankets," *Nuclear Eng. Design*, Vol. 68, 1981, pp. 293-300.
6 Specchia, V., Baldi, G., and Sicardi, S., "Heat Transfer in Packed Bed Reactors With One Phase Flow," *Chem. Eng. Commun.*, Vol. 4, Nos. 2-3, 1980, pp. 361-380.
7 Kunii, D., and Smith, J. M., "Heat Transfer Characteristics of Porous Rocks," *AIChE Journal*, Vol. 6, No. 1, 1960, pp. 71-98.
8 Box, G. E., Hunter, W. G., and Hunter, J. S., *Statistics for Experimenters*, Wiley-Interscience, New York, 1978.
9 Siegel, R., Sparrow, E. M., and Hallman, T. M., "Steady Laminar Heat Transfer in a Circular Tube With Prescribed Wall Heat Flux," *Appl. Sci. Res.* (A), Vol. 7, 1958, pp. 386-392.
10 Kays, W. M., *Convective Heat and Mass Transfer*, McGraw-Hill, New York, 1966, p. 127.
11 Brinn, M. S., Friedman, S. J., Gluckert, F. A., and Pigford, R. L., "Heat Transfer to Granular Materials. Settled Beds Moving Downward Through Vertical Tubes," *Ind. Eng. Chem.*, Vol. 40, No. 6, 1948, pp. 1050-1061.

Mixed Convection Flow Over a Horizontal Cylinder or a Sphere Embedded in a Saturated Porous Medium

Ming-Jer Huang,[1] Kuo-Ann Yih,[1] You-Li Chou,[1] and Cha'o-Kuang Chen[2]

Nomenclature

A = constant; $A=2$ for a horizontal cylinder and $A=3/2$ for a sphere
f = dimensionless stream function
F = function defined in equation (5)
g = gravitational acceleration
h = local heat transfer coefficient
K = permeability of the porous medium
k = thermal conductivity of the porous medium
n = constant; $n=0$ for a horizontal cylinder and $n=1$ for a sphere
Nu = local Nusselt number = hR/k
Pe = Peclet number = $U_\infty R/\alpha$
q_w = local surface heat transfer rate per unit area = $-k\left.\dfrac{\partial T}{\partial y}\right|_{y=0}$
R = radius of the horizontal cylinder or the sphere
r = radial distance from symmetric axis to surface = $R\sin(\bar{x}/R)$
Ra = modified local Rayleigh number = $gKq_wR^2\rho_\infty\beta/(Ak\alpha\mu)$
Sn = function defined in equation (9)
T = temperature
T_∞ = ambient temperature
U_∞ = undisturbed oncoming free-stream velocity
u = Darcy's velocity, x direction
v = Darcy's velocity, y direction
$\bar{x}$ = coordinate measured in the streamwise direction along the surface of a horizontal cylinder or a sphere from the lower point
x = dimensionless distance in the x direction = $\bar{x}/R$
y = coordinate perpendicular to the

---

[1] Department of Engineering Science, National Cheng Kung University, Tainan, Taiwan, Republic of China

[2] Department of Mechanical Engineering, National Cheng Kung University, Tainan, Taiwan, Republic of China

Contributed by the Heat Transfer Division for publication in the JOURNAL OF HEAT TRANSFER. Manuscript received by the Heat Transfer Division September 10, 1984.

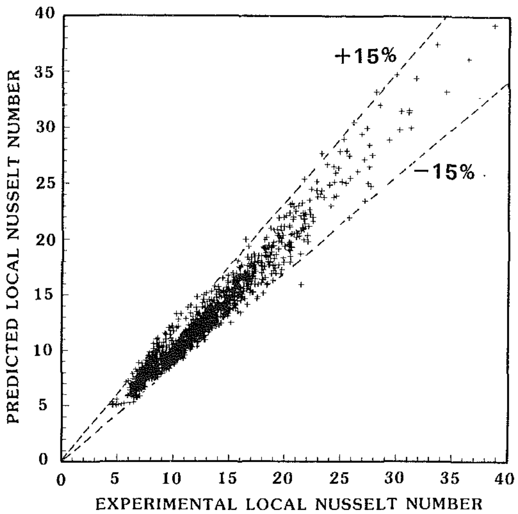

Fig. 3 Comparison between experimental values of Nu_x and those predicted using equations (7)–(9)

($T<950$°C). Figure 2 shows that the function $\mathfrak{F}$ is strongly dependent on the tube-to-particle diameter ratio D/d. For high values of D/d, the Nusselt number values Nu_x approach the $\mathrm{Nu}_{2,x}$ curve for plug flow. This result is consistent with our observations and those of Brinn et al. [11], indicating that the velocity distribution for tube flow of particle beds is uniform across the tube diameter except near the wall where it is about 15 to 20 percent lower. In other words, for large D/d, the bed behavior approaches that of a homogeneous fluid with the same effective physical properties and velocity distribution.

The entire data set (1534 data points) has been used to develop a generalized correlation for $\mathfrak{F}$ as a function of x^+, Pe, and D/d using least-squares fitting. Dependence of $\mathfrak{F}$ on the Archimedes number is not possible to discern since only one gas (air) is used. The following correlation is obtained

$$\mathfrak{F}=\log\{a_0(x^+)^{a_1}(D/d)^{a_2}(\mathrm{Pe})^{a_3}\} \tag{8}$$

where

$$a_0=0.041;\ a_1=0.34;\ a_2=0.63;\ a_3=0.48 \tag{9}$$

Equations (7) through (9) are the main results of this work. They are valid within the following range of variables

$$2.7\times 10^{-4}\le x^+\le 0.11,\ 11\le (D/d)\le 115,\ \text{and}\ 550\le \mathrm{Pe}\le 8000 \tag{10}$$

Figure 3 compares the experimental values of Nu_x with those predicted using the above correlation. The vast majority of the 1534 data points falls within ±15 percent of the experimental values. Analysis of the residuals indicates that the standard error in the predicted Nusselt number is 7.6 percent of the observed value. The 95 percent confidence interval for the percent error in the predicted Nusselt number is ±16.9 percent.

Acknowledgments

Financial support by the Lawrence Livermore National Laboratory is acknowledged.

References

1 Conn, R. W., et al., "SOLASE – A Laser Fusion Reactor Study," University of Wisconsin, Report UWFDM-220, Dec. 1977.

2 Sullivan, W. N., and Sabersky, R. H., "Heat Transfer to Flowing Granular Media," *Int. J. Heat Mass Transfer*, Vol. 18, No. 1, 1975, pp. 97–107.

3 Denloye, A. O. O., and Botterill, J. S. M., "Heat Transfer in Flowing Packed Beds," *Chem. Eng. Sci.*, Vol. 32, No. 5, 1977, pp. 461–465.

4 Nietert, R. E., "Heat Transfer Characteristics of Flowing and Stationary Particle Bed Type Fusion Reactor Blankets," Ph.D. thesis, Nuclear Engineering Department, University of Wisconsin–Madison, 1982.

5 Nietert, R. E., and Abdel-Khalik, S. I., "Thermalhydraulics of Flowing Particle-Bed-Type Fusion Reactor Blankets," *Nuclear Eng. Design*, Vol. 68, 1981, pp. 293–300.

6 Specchia, V., Baldi, G., and Sicardi, S., "Heat Transfer in Packed Bed Reactors With One Phase Flow," *Chem. Eng. Commun.*, Vol. 4, Nos. 2–3, 1980, pp. 361–380.

7 Kunii, D., and Smith, J. M., "Heat Transfer Characteristics of Porous Rocks," *AIChE Journal*, Vol. 6, No. 1, 1960, pp. 71–98.

8 Box, G. E., Hunter, W. G., and Hunter, J. S., *Statistics for Experimenters*, Wiley-Interscience, New York, 1978.

9 Siegel, R., Sparrow, E. M., and Hallman, T. M., "Steady Laminar Heat Transfer in a Circular Tube With Prescribed Wall Heat Flux," *Appl. Sci. Res.* (A), Vol. 7, 1958, pp. 386–392.

10 Kays, W. M., *Convective Heat and Mass Transfer*, McGraw-Hill, New York, 1966, p. 127.

11 Brinn, M. S., Friedman, S. J., Gluckert, F. A., and Pigford, R. L., "Heat Transfer to Granular Materials. Settled Beds Moving Downward Through Vertical Tubes," *Ind. Eng. Chem.*, Vol. 40, No. 6, 1948, pp. 1050–1061.

Mixed Convection Flow Over a Horizontal Cylinder or a Sphere Embedded in a Saturated Porous Medium

Ming-Jer Huang,[1] Kuo-Ann Yih,[1] You-Li Chou,[1] and Cha'o-Kuang Chen[2]

Nomenclature

A = constant; $A=2$ for a horizontal cylinder and $A=3/2$ for a sphere
f = dimensionless stream function
F = function defined in equation (5)
g = gravitational acceleration
h = local heat transfer coefficient
K = permeability of the porous medium
k = thermal conductivity of the porous medium
n = constant; $n=0$ for a horizontal cylinder and $n=1$ for a sphere
Nu = local Nusselt number = hR/k
Pe = Peclet number = $U_\infty R/\alpha$
q_w = local surface heat transfer rate per unit area = $-k\left.\dfrac{\partial T}{\partial y}\right|_{y=0}$
R = radius of the horizontal cylinder or the sphere
r = radial distance from symmetric axis to surface = $R\sin(\bar{x}/R)$
Ra = modified local Rayleigh number = $gKq_wR^2\rho_\infty\beta/(Ak\alpha\mu)$
Sn = function defined in equation (9)
T = temperature
T_∞ = ambient temperature
U_∞ = undisturbed oncoming free-stream velocity
u = Darcy's velocity, x direction
v = Darcy's velocity, y direction
$\bar{x}$ = coordinate measured in the streamwise direction along the surface of a horizontal cylinder or a sphere from the lower point
x = dimensionless distance in the x direction = $\bar{x}/R$
y = coordinate perpendicular to the

---

[1] Department of Engineering Science, National Cheng Kung University, Tainan, Taiwan, Republic of China

[2] Department of Mechanical Engineering, National Cheng Kung University, Tainan, Taiwan, Republic of China

Contributed by the Heat Transfer Division for publication in the JOURNAL OF HEAT TRANSFER. Manuscript received by the Heat Transfer Division September 10, 1984.

surface of a horizontal cylinder or a sphere
α = equivalent thermal diffusivity
β = pseudo-similarity variable, defined in equation (1)
θ = dimensionless temperature
μ = dynamic viscosity
ρ = density of the convective fluid
ξ = transformed axial coordinate = $F(x)/\sin^{n+1}x$
ψ = stream function

Introduction

Recently, mixed convection flow over bodies has been analyzed by Moutsoglu and Chen [1-4]. A numerical scheme is employed to solve the transformed nonlinear boundary layer equations. Both the aiding flow and the opposing flow are considered. They encompass the entire range of mixed convection flow.

The heat transfer characteristics in a saturated porous medium were also very interesting in many engineering applications. Merkin [5] studied the free convection heat transfer of axisymmetric and two-dimensional bodies. Cheng [6] obtained the results of heat transfer over a horizontal cylinder and a sphere. The purpose of this note is to extend the problem, which is similar to that described by Cheng [6], with only surface temperature condition changes to surface heat flux,

$$q_w = -k\frac{\partial T}{\partial y}\bigg|_{y=0}$$

Analysis

With the same assumptions as [6], the governing boundary layer equations on a cylinder or a sphere, which is embedded in a porous medium and is subjected to uniform surface heat flux, will be transformed into the following:

$$f'' = [(\mathrm{Ra}/\mathrm{Pe}^{2/3})/A^{1/2}]^b \xi\theta' \tag{1}$$

$$\theta'' + \tfrac{1}{2}f\theta' - Sn(x)f'\theta = Sn(x)\xi\left(f'\frac{\partial\theta}{\partial\xi} - \theta'\frac{\partial f}{\partial\xi}\right) \tag{2}$$

$$\begin{aligned} &\eta=0; \quad f=0, \quad \theta'=-1 \\ &\eta\rightarrow\infty; \quad f'\rightarrow[A^{1/3}(\mathrm{Pe}/\mathrm{Ra}^{2/3})]^c, \quad \theta\rightarrow 0 \end{aligned} \tag{3}$$

Here primes denote partial derivatives with respect to η. The transformations used are based on forced-flow dominated and buoyancy force flow dominated cases.

$$x=\bar{x}/R, \quad \xi=F(x)/\sin x, \quad \eta=y(A\lambda)^a\sin^{n+1}x/[RF(x)] \tag{4}$$

$$f(\xi,\eta)=\psi/[R^n(A\lambda)^a\alpha F(x)] \tag{5}$$

$$\theta(\xi,\eta)=(T-T_\infty)/\{q_wRF(x)/[k(A\lambda)^a\sin^{n+1}x] \tag{6}$$

where $A=2$, $n=0$ for the cylinder and $A=3/2$, $n=1$ for the sphere. The stream function ψ satisfies the continuity equation, with $r^nu = \partial\psi/\partial y$ and $r^nv = -\partial\psi/\partial x$.

$$F(x)=\begin{cases}(1-\cos x)^{1/2} & n=0 \quad (7)\\ (\cos^3x/3-\cos x+2/3)^{1/2} & n=1 \quad (8)\end{cases}$$

and

$$Sn(x)=\begin{cases}1/2-\cos x/(1+\cos x) & n=0 \quad (9)\\ 1/2-[2(2+\cos x)\cos x]/ & \\ [3(1+\cos x)^2] & n=1 \quad (10)\end{cases}$$

$a=1/2$, $b=1$, $c=0$, $\lambda=\mathrm{Pe}$ for forced-flow dominated case and $a=1/3$, $b=0$, $c=1$, $\lambda=\mathrm{Ra}$ for buoyancy force flow dominated case. The local Nusselt number Nu can be readily shown in the dimensionless form

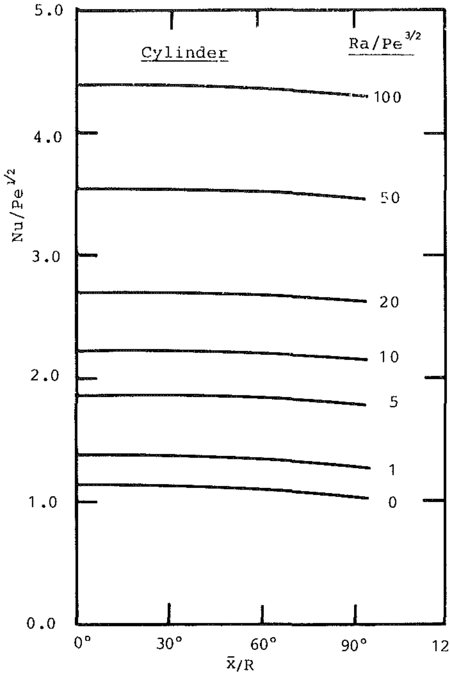

Fig. 1 Angular distributions of the local Nusselt number Nu/Pe$^{1/2}$

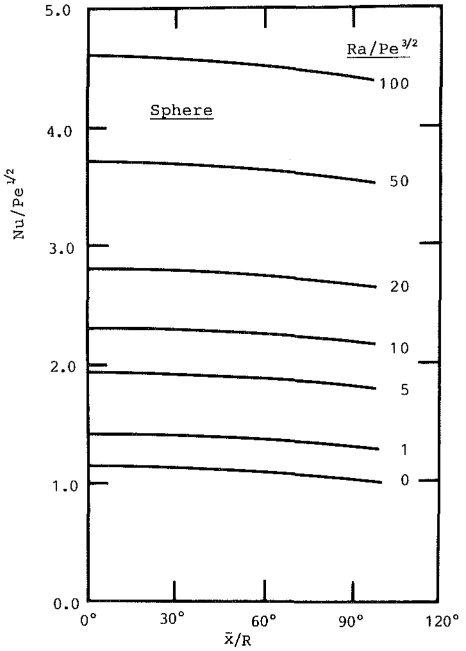

Fig. 2 Angular distributions of the local Nusselt number Nu/Pe$^{1/2}$

$$\mathrm{Nu}=(A\lambda)^a/[\xi\theta(\xi,0)] \tag{11}$$

Numerical Results and Discussion

The system of equations (1)-(3) has been solved by employing an implicit finite difference method [7]. Numerical results are obtained for the effects of the buoyancy force with parameter $\mathrm{Ra}/\mathrm{Pe}^{3/2}$ ranging from 0 to ∞ and the inertia force with parameter $\mathrm{Pe}/\mathrm{Ra}^{2/3}$ covering from 0 to 10.

Based on the forced-flow dominated case, the influence of the buoyancy force on the angular distributions of the local Nusselt number $\mathrm{Nu}/\mathrm{Pe}^{1/2}$ are shown in Fig. 1 for the horizontal cylinder and in Fig. 2 for the sphere cases, respectively. From these two figures it can be found that $\mathrm{Nu}/\mathrm{Pe}^{1/2}$ increases as the buoyancy force increases and

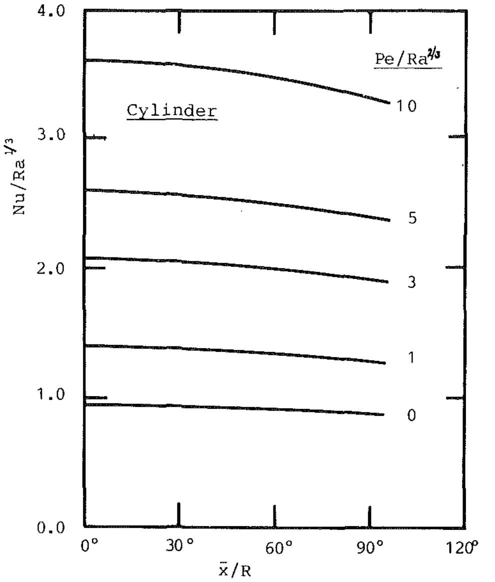

Fig. 3 Angular distributions of the local Nusselt number $Nu/Ra^{1/3}$

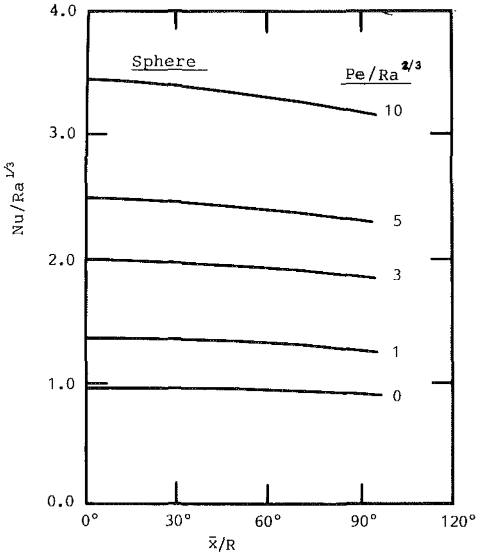

Fig. 4 Angular distributions of the local Nusselt number $Nu/Ra^{1/3}$

decreases with increasing angle from the stagnation point for a given $Ra/Pe^{3/2}$ value.

With consideration of the effect of inertial force on the Nusselt number, $Nu/Ra^{1/3}$ along the surface of the cylinder and the sphere are illustrated in Fig. 3 and Fig. 4, respectively. The figures shown are based on the buoyancy force dominated flow. The Nusselt number $Nu/Ra^{1/3}$ increases with increasing inertial force. Similarly, $Nu/Ra^{1/3}$ also decreases along the surface from the stagnation point.

Conclusion

An analysis for mixed convection over a horizontal cylinder or a sphere in a saturated porous medium has been performed. The investigation of buoyancy force effects on pure forced convection is based on the parameter $Ra/Pe^{3/2}$ with the following magnitudes such that the effects exceed 5 percent departure from pure forced convection:

>0.17 (horizontal cylinder case)
>0.16 (sphere case)

In addition, with 5 percent departure from pure convection, our study includes the effects of inertia force on pure free convection for parameter $Pe/Ra^{2/3}$:

>0.12 (horizontal cylinder case)
>0.11 (sphere case)

The results show that the local Nusselt number increases as buoyancy force or inertial force increases.

References

1 Moutsoglu, A., and Chen, T. S., "Analysis of Combined Forced and Free Convection Across a Horizontal Cylinder," *Canadian J. of Chemical Engineering*, Vol. 55, 1977, pp. 265-271.

2 Moutsoglu, A., and Chen, T. S., "Mixed Convection Across a Horizontal Cylinder With Uniform Surface Heat Flux," *Trans. ASME*, Vol. 99, 1977, pp. 679-682.

3 Chen, T. S., and Moutsoglu, A., "Analysis of Mixed Forced and Free Convection About a Sphere," *Int. J. Heat Mass Transfer*, Vol. 20, 1977, pp. 867-875.

4 Chen, T. S., and Moutsoglu, A., "Mixed Convection About a Sphere With Uniform Heat Flux," *Trans. ASME*, Vol. 100, 1978, pp. 542-544.

5 Merkin, J. H., "Free Convection Boundary Layers on Axi-Symmetric and Two-Dimensional Bodies of Arbitrary Shape in a Saturated Porous Medium," *Int. J. Heat Mass Transfer*, Vol. 22, 1979, pp. 1461-1462.

6 Cheng, P., "Mixed Convection About a Horizontal Cylinder and a Sphere in a Porous Medium," *Int. J. Heat Mass Transfer*, Vol. 25, 1982, pp. 1245-1247.

7 Cebeci, T., and Bradshaw, P., *Momentum Transfer in Boundary Layer*, Hemisphere, Washington, 1977.

Temperature and Heat Flux Distribution in a Natural Convection Enclosure Flow[1]

M. S. Bohn[2] and R. Anderson[2]

Nomenclature

g = acceleration of gravity, m/s^2
H = test cell height, m
k = thermal conductivity, W/m°C
L = test cell length, m
Nu_x = local Nusselt number
$\overline{Nu}$ = average Nusselt number
N_{hw} = number of heated walls
Pr = Prandtl number
q = heat flux, W/m^2
Ra_x = local Rayleigh number, equation (10)
Ra_o = overall Rayleigh number, equation (2)
T_h = temperature of heated wall, °C
T_c = temperature of cooled wall, °C
T = temperature, °C
T_b = bulk temperature, equation (6), °C
T_{fm} = mean temperature with heated boundary layer, equation (11), °C
W = test cell width, m
x = vertical distance from test cell floor, m
y = horizontal distance from heated wall, m
z = horizontal distance from a vertical plane centered on and normal to the heated wall, m
β = coefficient of thermal expansion

---

[1] Prepared for the U.S. Department of Energy, Contract No. DE-AC02-83CH10093

[2] Solar Energy Research Institute, Golden, CO 80401; Assoc. Mem. ASME

Contributed by the Heat Transfer Division for publication in the JOURNAL OF HEAT TRANSFER. Manuscript received by the Heat Transfer Division July 23, 1984.

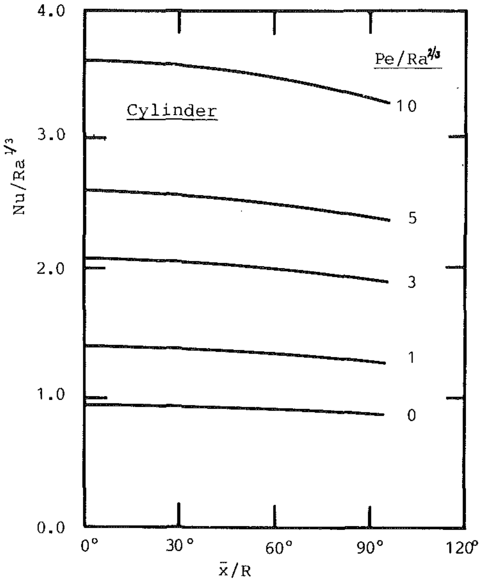

Fig. 3 Angular distributions of the local Nusselt number $Nu/Ra^{1/3}$

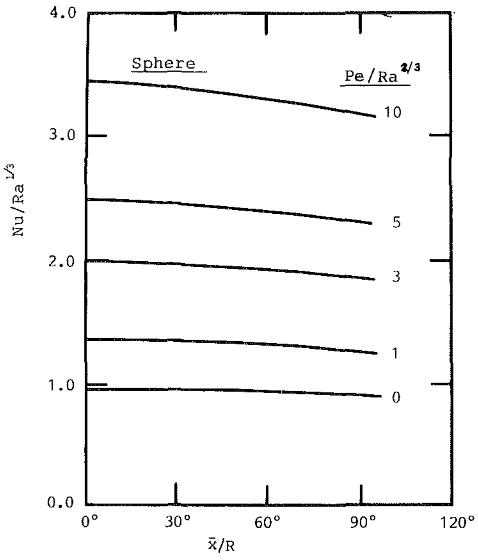

Fig. 4 Angular distributions of the local Nusselt number $Nu/Ra^{1/3}$

decreases with increasing angle from the stagnation point for a given $Ra/Pe^{3/2}$ value.

With consideration of the effect of inertial force on the Nusselt number, $Nu/Ra^{1/3}$ along the surface of the cylinder and the sphere are illustrated in Fig. 3 and Fig. 4, respectively. The figures shown are based on the buoyancy force dominated flow. The Nusselt number $Nu/Ra^{1/3}$ increases with increasing inertial force. Similarly, $Nu/Ra^{1/3}$ also decreases along the surface from the stagnation point.

Conclusion

An analysis for mixed convection over a horizontal cylinder or a sphere in a saturated porous medium has been performed. The investigation of buoyancy force effects on pure forced convection is based on the parameter $Ra/Pe^{3/2}$ with the following magnitudes such that the effects exceed 5 percent departure from pure forced convection:

>0.17 (horizontal cylinder case)
>0.16 (sphere case)

In addition, with 5 percent departure from pure convection, our study includes the effects of inertia force on pure free convection for parameter $Pe/Ra^{2/3}$:

>0.12 (horizontal cylinder case)
>0.11 (sphere case)

The results show that the local Nusselt number increases as buoyancy force or inertial force increases.

References

1 Moutsoglu, A., and Chen, T. S., "Analysis of Combined Forced and Free Convection Across a Horizontal Cylinder," *Canadian J. of Chemical Engineering*, Vol. 55, 1977, pp. 265–271.

2 Moutsoglu, A., and Chen, T. S., "Mixed Convection Across a Horizontal Cylinder With Uniform Surface Heat Flux," *Trans. ASME*, Vol. 99, 1977, pp. 679–682.

3 Chen, T. S., and Moutsoglu, A., "Analysis of Mixed Forced and Free Convection About a Sphere," *Int. J. Heat Mass Transfer*, Vol. 20, 1977, pp. 867–875.

4 Chen, T. S., and Moutsoglu, A., "Mixed Convection About a Sphere With Uniform Heat Flux," *Trans. ASME*, Vol. 100, 1978, pp. 542–544.

5 Merkin, J. H., "Free Convection Boundary Layers on Axi-Symmetric and Two-Dimensional Bodies of Arbitrary Shape in a Saturated Porous Medium," *Int. J. Heat Mass Transfer*, Vol. 22, 1979, pp. 1461–1462.

6 Cheng, P., "Mixed Convection About a Horizontal Cylinder and a Sphere in a Porous Medium," *Int. J. Heat Mass Transfer*, Vol. 25, 1982, pp. 1245–1247.

7 Cebeci, T., and Bradshaw, P., *Momentum Transfer in Boundary Layer*, Hemisphere, Washington, 1977.

Temperature and Heat Flux Distribution in a Natural Convection Enclosure Flow[1]

M. S. Bohn[2] and R. Anderson[2]

Nomenclature

g = acceleration of gravity, m/s^2
H = test cell height, m
k = thermal conductivity, W/m°C
L = test cell length, m
Nu_x = local Nusselt number
$\overline{Nu}$ = average Nusselt number
N_{hw} = number of heated walls
Pr = Prandtl number
q = heat flux, W/m^2
Ra_x = local Rayleigh number, equation (10)
Ra_o = overall Rayleigh number, equation (2)
T_h = temperature of heated wall, °C
T_c = temperature of cooled wall, °C
T = temperature, °C
T_b = bulk temperature, equation (6), °C
T_{fm} = mean temperature with heated boundary layer, equation (11), °C
W = test cell width, m
x = vertical distance from test cell floor, m
y = horizontal distance from heated wall, m
z = horizontal distance from a vertical plane centered on and normal to the heated wall, m
β = coefficient of thermal expansion

---

[1] Prepared for the U.S. Department of Energy, Contract No. DE-AC02-83CH10093

[2] Solar Energy Research Institute, Golden, CO 80401; Assoc. Mem. ASME

Contributed by the Heat Transfer Division for publication in the JOURNAL OF HEAT TRANSFER. Manuscript received by the Heat Transfer Division July 23, 1984.

θ = dimensionless temperature, equation (3)
θ_b = average value of θ in the test cell
ν = kinematic viscosity, m^2/s

Subscripts

x,∞ = value in the core at height x

Introduction

A vast majority of the extensive literature on natural convection in enclosures has been concerned with two-dimensional geometries, that is, an enclosure consisting of two parallel vertical surfaces held at different temperatures and with adiabatic or conducting top and bottom. These studies treat an important class of problems with many practical applications. However, by neglecting the third dimension, complexities present in many real problems are also neglected. Of interest in three-dimensional enclosure is heat transfer between parallel as well as perpendicular vertical walls and how the three-dimensional boundary conditions affect the fluid core. The flows of interest are not three-dimensional flows set up in nominally two-dimensional enclosures as a result of drag at the adiabatic end walls. Here we are interested in three-dimensional flows which result directly from fully three-dimensional boundary conditions.

In a recent experimental effort the problem of heat transfer between parallel and perpendicular vertical walls in a three-dimensional enclosure was treated in detail [1]. Several important features of three-dimensional natural convection enclosure flows were discussed. The testing in [1] was carried out in a water-filled cubical enclosure with an adiabatic top and bottom and isothermal sides at Rayleigh numbers $\sim 10^{10}$. The high Rayleigh numbers are of interest in the study of building heat transfer as well as other practical applications. Several configurations of side wall heating and cooling were tested. It was determined that by judicious choice of a reference temperature, the average Nusselt number correlation equation was only weakly configuration dependent. The correct reference temperature was a bulk temperature defined as the average of the four isothermal wall temperatures. By basing the average Nusselt number on the difference between the wall and bulk temperature, correlation equations for all configurations could be collapsed to a single correlation equation

$$\overline{\mathrm{Nu}} = 0.620\,\mathrm{Ra}_o^{0.250} \tag{1}$$

in the Rayleigh number range $0.3 \times 10^{10} < \mathrm{Ra}_o < 6.0 \times 10^{10}$.

Flow visualization studies indicated that the bulk of the test cell fluid was essentially stagnant; the only substantial motion was that in the boundary layers on the vertical surfaces.

The reader is referred to [1] for a detailed discussion of that work and also of the experimental apparatus and error analysis. The work presented in this paper extends that in [1] to include the effect of three-dimensional boundary conditions on core temperature profiles and on local heat transfer.

Experimental Apparatus

The experimental apparatus was described in detail in [1] and consists of a cubical enclosure with interior dimension 30.5 cm. The enclosure is filled with water to achieve Rayleigh numbers $\sim 10^{10}$ with $T_h \approx 40°\mathrm{C}$ and $T_c \approx 15°\mathrm{C}$. The boundary conditions include an adiabatic top and bottom and four isothermal vertical walls. Spatial variation of temperatures across the heated and cooled walls was less than 10 percent and typically 5 percent of the overall temperature difference $T_h - T_c$, and thus may be considered isothermal. In this work two configurations were tested: one heated wall with three cooled walls and two contiguous heated walls with two contiguous cooled walls. The vertical walls are separated by strips of neoprene insulation which limit the plate-to-plate heat transfer to less than 1 percent of the convection heat transfer. See [1] for a complete discussion of experimental errors.

Three of the vertical walls are cooled or heated by flowing water through heat exchanger channels milled into plates that bolt to the outside of the walls. The remaining vertical wall is electrically heated. Sixteen equal area (58.1 cm^2 each) independent heaters are attached to the outside surface of the electrically heated wall. These heaters are controlled by a microcomputer that can provide an isothermal or constant flux boundary condition on that wall as required. In addition, the microcomputer records the power dissipation for each heater, thereby providing information on local heat transfer from that wall. One thermocouple (copper-constantan) senses the temperature of the center of the zone defined by each heater. The thermocouples were located 1 mm from the inner surface of the wall. In the isothermal mode of operation, the computer senses the temperature of the zone, and if it is below the set point, more power is applied to that zone. A proportional-integral control algorithm is used to determine how long each heater should be left on during each cycle of operation, ~ 10 s. In the second configuration tested (two contiguous heated walls and two contiguous cooled walls) one wall was heated electrically while the second heated wall was heated with hot water.

Given the temperature of the heated plates T_h and the temperature of the cooled plates T_c the overall Rayleigh number is defined by

$$\mathrm{Ra}_o = \frac{g\beta(T_h - T_c)H^3}{\nu^2}\,\mathrm{Pr} \tag{2}$$

The dimensionless local heat transfer coefficient Nu_x is based on the local heat flux q and the difference in temperature between the wall and the bulk fluid; see equation (5). Local heat flux q was determined from local temperature gradient measurements near the heated wall.

Core fluid temperature profiles were measured with a rake consisting of seven 0.08-mm copper-constantan thermocouples. The rake was inserted vertically through one of three slots 6.4 mm wide cut in the top of the enclosure. Each slot was perpendicular to the electrically heated wall, and the three slot locations were on the centerline midway between the two parallel cooled walls, and 7.62 and 12.70 cm from the center line. To minimize flow disturbances at the top boundary, lucite inserts were placed in the unused slots. These fit flush in the slot and gave a smooth surface at the water interface. The thermocouples in the rake were located at 0.010, 0.164, 0.331, 0.497, 0.664, 0.831, and 0.997 cell heights (H) from the bottom of the test cell. A traversing mechanism allowed the rake to be moved in the direction y normal to the heated wall with a resolution of 0.025 mm. The temperature measurement from each thermocouple was made dimensionless with the overall temperature difference between the hot and cold walls

$$\theta = \frac{T - T_c}{T_h - T_c} \tag{3}$$

By linear interpolation, the height x from the bottom where θ took values of 0.1, 0.2, . . . , 0.9 was calculated. Connecting points of equal θ for different rake locations y produces contours of constant θ in the test cell.

Since the traversing mechanism did not allow location of the rake closer than 25.4 mm from any vertical surface, an additional probe was used to measure temperature profiles in the boundary layer on the vertical heated wall of the enclosure. This single junction probe (also 0.08 mm, copper-constantan) inserted into the test cell through an angled sheath, allowed the probe to be placed in contact with the heated surface and traversed out from the surface. In this way, high spatial resolution was achieved as needed in the thermal boundary layer. The ability to relocate the single probe at the exact location where a junction of the rake probe had been located was indicated by an error in θ of less than 0.01.

The local heat flux on the heated wall was calculated by determining the temperature gradient at the wall from the measured boundary layer temperature profile. A least-squares fit of the five temperature measurements near the wall (at distance y = 0, 0.0508, 0.102, 0.152, and 0.203 mm) gives $d\theta/dy$ at the wall. The local heat flux is then

$$q(x) = \frac{d\theta}{dy}(T_h - T_c)k \qquad (4)$$

The correlation coefficient for this least-squares procedure was typically 0.99^+. Equation (4) can be cast in dimensionless form to produce the local Nusselt number

$$\mathrm{Nu}_x = \frac{q(x)}{(T_h - T_{x,\infty})}\,\frac{H}{k} = \frac{d\theta}{dy}H\left[\frac{1}{1-\theta_{x,\infty}}\right] \qquad (5)$$

In [1], the bulk fluid temperature was defined as the area-weighted average of the four isothermal wall temperatures

$$T_b = \frac{1}{4}\,[N_{hw}T_h + (4 - N_{hw})T_c] \qquad (6)$$

where N_{hw} is the number of heated walls in the experiment. This definition was based on a heuristic argument rather than actual core fluid temperature measurements. As mentioned previously, it was shown in [1] that this choice of bulk fluid temperature collapsed data for all heating/cooling configurations onto one curve supporting our argument that the wall-to-bulk temperature difference is the correct temperature difference to use in scaling heat transfer results in enclosures with complex thermal boundary conditions. In this paper we demonstrate that the bulk temperature defined by equation (6) is a good estimate of the actual average core temperature.

Temperature measurement errors are < ±0.25°C, which produces an error in θ of approximately ± 0.01 for $T_h - T_c \approx 28°\mathrm{C}$ for the core temperature profile. This error resulted primarily because two data acquisition systems were used to facilitate data plotting during the measurement of core temperatures and there was some discrepancy in the temperature measured by each system. For the boundary layer measurements only one of the data acquisition systems was used, and the error in θ is ± 0.005 or less. Note that the finite size of the probe junction produces some loss in spatial resolution. A typical thermal boundary layer thickness was 2.5 mm, and the probe junction was approximately 0.48 mm or 19 percent of the boundary layer thickness.

It is interesting to note that making the thermocouple junction by spot welding produces a junction six times the diameter of the individual wires. The effect of this finite probe size is threefold. First, the boundary layer profiles are shifted away from the wall because the junction cannot be placed exactly at the wall surface. Second, the probe will tend to integrate the temperature distribution over the physical extent of the junction. The first effect may be seen in the dimensionless boundary layer temperature profiles which appear to be shifted approximately one junction diameter from the heated wall. These boundary layer profiles were not corrected for this spatial shift. The second effect should have minimal effect since the junction is integrating over a linear portion of the temperature profile and the measured temperature should correspond closely to that at the center of the junction. The third effect of finite probe size is displacement of the streamlines in areas of local velocity shear. Thwaites [2] presents data and calculations for the magnitude of this displacement for pilot-tube type probes and spheres. The controlling parameter is the dimensionless velocity gradient $\alpha = (r/U)\,(du/dy)$ where U is a free-stream velocity, r is the radius of curvature of the pilot tube or sphere, and du/dy is the local velocity gradient.

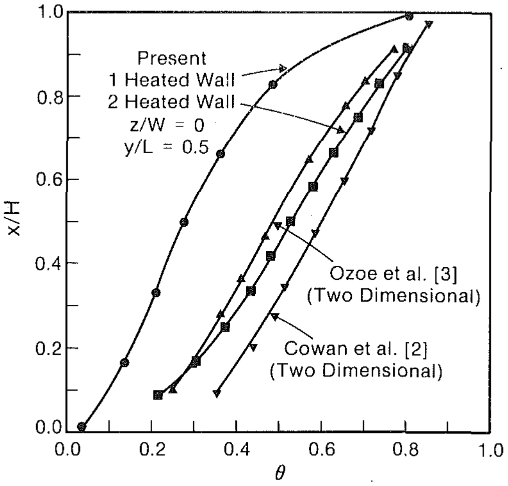

Fig. 1 Temperature distribution for $z/W = 0$, $y/L = 0.5$

Note that since our measurements were made in water where the velocity boundary layer is thicker than the temperature boundary layer, a velocity shear will exist over the entire thermal boundary layer. Using classical solutions for natural convection boundary layers on vertical heated plates and the probe diameter of 0.48 mm, one may show that the dimensionless velocity gradient is approximately 0.01. From Thwaites' results, his Fig. XII.36 for example, it is clear that the probe used in the present study will cause a displacement of streamlines of less than 1 percent of the probe diameter, clearly negligible.

To minimize errors caused by flow interference and to minimize probe conduction errors, the probe lead wires were encased in a 4-mm o.d. glass capillary tube. Assuming the lead wires are at the core fluid temperature where the glass tube joins the steel sheath, the error in indicated temperature caused by conduction along the wires is less than −0.1°C, or an error in θ of -0.004. Results were not corrected for this error.

Results and Discussion

Core temperature distributions were measured in planes defined by z/W = 0.0, 0.25, and 0.417, but are not presented here. The isotherm plots demonstrated that the core is essentially stratified and the temperature profiles in the core are essentially one dimensional in nature. That is, the core temperature may be fully characterized by a vertical temperature gradient alone. For the plane $z = 0$ the center-line temperature profile (along the vertical line at $y = L/2$) and the center-line distribution for the geometry with two heated walls is shown in Fig. 1 along with the center-line temperature distribution in a two-dimensional enclosure [3, 4]. The three-dimensional profile from the present work for a single heated wall appears to be shifted to low values of θ relative to the two-dimensional profiles, while the profile for two heated and two cooled walls compares favorably with the profiles shown in Fig. 1 for the two-dimensional enclosures. In the present experiment, the three cooled walls and one heated wall force the bulk fluid temperature lower than geometries with equal heated and cooled areas. This is consistent with the heuristic argument used in [1] to show that the appropriate bulk fluid temperature should be that given by equation (6).

Since the temperature profile in Fig. 1 is typical of the entire core, the average core temperature θ_b may be calculated from

$$\int_0^1 \theta(x/H)\,d(x/H) \qquad (7)$$

Using the seven measurements of θ in Fig. 1 and using the trapezoidal rule for integration, we find

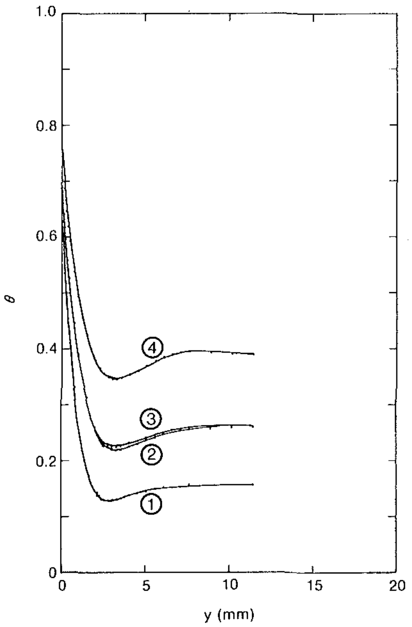

Fig. 2 Boundary layer temperature profiles: (1) $x/H = 0.25$, $z/W = 0$; (2) $x/H = 0.5$, $z/W = 0.25$; (3) $x/H = 0.5$, $z/W = 0$; (4) $x/H = 0.75$, $z/W = 0$

$$\theta_b = 0.303 \tag{8}$$

From equation (6) for $N_{hw} = 1$ we have

$$T_b = (T_h + 3T_c)/4 \tag{9}$$

Inserting equation (9) into equation (3) we find $\theta(T_b) = 0.25$, which is to be compared with 0.303 from equation (8). Repeating this procedure for the geometry with two heated walls we find an average, $\theta(T_b) = 0.44$, whereas using the average of the four wall temperatures gives $\theta_b = 0.50$. In [1], we argued that the difference in temperature between the isothermal wall and the bulk flow temperature is the driving force for the flow in the boundary layer and hence heat transfer. This was confirmed by the heat transfer data. We have shown here that the choice of bulk fluid temperature, equation (6) used in [1], also compares favorably with the actual measured value. These results are restricted to the present geometry, i.e., vertical heated walls only.

Boundary layer temperature profiles are shown in Fig. 2. All the profiles exhibit a large temperature gradient near the wall, reach a minimum near $y = 2.8$ mm, and increase slightly to asymptote to the core temperature for that height x at a distance from the heated wall of about 10 mm. The temperature minimum occurs only for enclosure flows and is apparently related to the interaction between the boundary layer and the stratified core fluid. It has been predicted numerically for air by Chen and Eichhorn [5] and Newell and Schmidt [6] and has been seen experimentally by Eckert and Carlson [7] in air, by Elder [8] in oils, by Ozoe et al. [4] in water, as well as by several other researchers. Note that in the profiles θ $(y = 0) < 1$. This is the θ shift described in the previous section due to the finite probe size. Core stratification is also evident in the vertical shift in asymptote for the four temperature profiles. A lack of three-dimensional effect is demonstrated in the similarity of profiles number 2 and 3 which were for the same height x, but $z/W = 0.25$ and 0.5, respectively.

It is most convenient to present the local heat flux in terms of the local Nusselt number from equation (5). Following Cowan et al. [3], the local Rayleigh number is

$$\mathrm{Ra}_x = \frac{g\beta x^3 (T_h - T_{x,\infty})}{\nu^2} \mathrm{Pr} \tag{10}$$

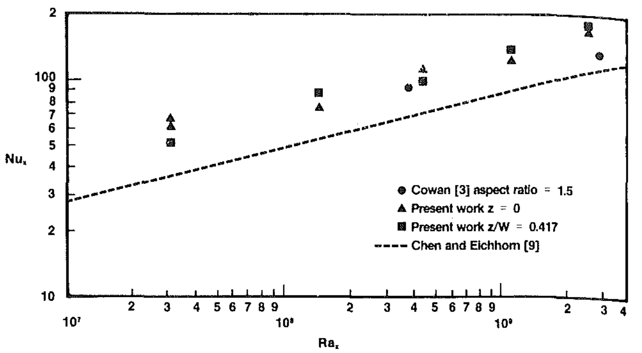

Fig. 3 Local heat flux

where the fluid properties are to be evaluated at the mean film temperature at height x.

The local Nusselt number is plotted as a function of Ra_x in Fig. 3 for the configuration with one heated and three cooled walls. Boundary layer profiles were measured at $x = 7.62$, 11.43, 15.24, 19.05, and 22.86 cm from the test cell floor at $z = 0$ and $z/W = 0.417$ to produce data at the five values of Ra_x shown in the figure. The five locations closest to the wall were used to determine the temperature gradient as discussed previously. In order to be consistent with Cowan et al. [3], fluid properties were evaluated at the mean temperature in the boundary layer at the appropriate height x in the test cell.

There did not appear to be a large difference in Nu_x for the two values of z; however, for $z/W = 0.417$ the two highest Ra_x exhibited relatively large fluctuations in temperature, implying turbulence. Also shown in the figure are the experimental data of Cowan [3] for a two-dimensional water-filled enclosure and the analytical solution of Chen and Eichhorn [5] for a vertical surface in a stratified body of fluid. For the latter, we used the measured core stratification for the configuration with one heated and three cooled walls.

The present data agree favorably with Cowan's data for an enclosure aspect ratio of 1.5 (the lowest he tested). Chen and Eichhorn's results exhibit a slope very nearly 1/4 but are at least 30 percent below the present data and Cowan's data. In the absence of more experimental data it may be difficult to draw firm conclusions at this point. However, since Chen and Eichhorn's analysis was for an isolated vertical surface, i.e., not for an enclosure, the comparison of the present results with Cowan's enclosure data would seem to confirm that the local behavior in the fully three-dimensional enclosure is similar to that in two-dimensional enclosures.

Conclusions

Detailed core temperature measurements in enclosures at high Rayleigh numbers show that, similar to two-dimensional enclosures, a three-dimensional enclosure exhibits core stratification. Temperature in the core varies only in the vertical direction even when the geometry and thermal boundary conditions are strongly three dimensional, as in the present work. The distribution of core temperature is influenced by boundary conditions in a rather simple way. The distribution adjusts itself so that the average core temperature is approximately equal to the average of the four wall temperatures. For the geometry tested with one heated wall and three cooled walls, the isotherms are shifted up relative to the two-dimensional case, or the three-dimensional case with equal heated and cooled areas, giving a lower average core temperature. In the geometry tested with the two heated and two cooled walls, the temperature profile is close to previously published two-dimensional distributions.

These results are to be expected since the boundary layers at the high Rayleigh numbers in this study are thin. This implies that the influence of the boundaries, especially the corners, is only felt in a very small part of the enclosure flow. From the standpoint of building interiors, it appears that local as well as overall heat transfer may be estimated reasonably well from two-dimensional enclosure data. However, room temperature stratification is strongly dependent on boundary conditions and, therefore, cannot be determined from two-dimensional studies.

References

1 Bohn, M. S., Kirkpatrick, A. T., and Olson, D. A., "Experimental Study of Three Dimensional Natural Convection at High Rayleigh Number," ASME JOURNAL OF HEAT TRANSFER, Vol. 106, 1984, pp. 339–345.

2 Thwaites, B., ed., *Incompressible Aerodynamics*, Oxford, 1960.

3 Cowan, G. H., Lovegrove, P. C., and Quarini, G. L., "Turbulent Natural Convection Heat Transfer in Vertical Single Water-Filled Cavities," *Proc. 7th Int. Heat Transf. Conf.*, Munich, Hemisphere, Washington, D.C., 1982, Vol. 2, pp. 195–203.

4 Ozoe, H., Ohmuro, M., Mouri, A., Mishima, S., Sayama, H., and Churchill, S. W., "Laser Doppler Measurements of the Velocity Along a Heated Vertical Wall of a Rectangular Enclosure," ASME JOURNAL OF HEAT TRANSFER, Vol. 105, 1983, pp. 782–788.

5 Chen, C. C., and Eichhorn, R., "Natural Convection From a Vertical Surface to a Thermally Stratified Fluid," ASME JOURNAL OF HEAT TRANSFER, Vol. 98, 1976, pp. 446–451.

6 Newell, M. E., and Schmidt, F. W., "Heat Transfer by Laminar Natural Convection Within Rectangular Enclosures," ASME JOURNAL OF HEAT TRANSFER, Vol. 92, 1970, pp. 159–168.

7 Eckert, E. R. G., and Carlson, W. O., "Natural Convection in an Air Layer Enclosed Between Two Vertical Plates With Different Temperatures," *Int. J. Heat Mass Transfer*, Vol. 2, 1961, pp. 106–120.

8 Elder, J. W., "Laminar Free Convection in a Vertical Slot," *J. Fluid Mechanics*, Vol. 23, 1965, pp. 77–98.

Liquefied Natural Gas (LNG) Plume Interaction With Storage Tanks

K. M. Kothari[1] and R. N. Meroney[2]

Introduction

Natural gas is a highly desirable source of energy for consumption in the United States. Liquefied natural gas (LNG) is stored and transported at about −162°C. If a storage tank or transfer pipe were to rupture and the contents spill out, rapid boiling of the LNG would ensue and liberation of a potentially flammable vapor would result. Studies [1–5] have demonstrated that the cold LNG vapor plume will remain negatively buoyant for most conditions during the dispersion of concern. Thus, it represents a ground-level hazard. This hazard extends downwind from the spill until the atmosphere has diluted the LNG vapor below the lower flammability limit, a local concentration for methane below 5 percent by volume.

This paper describes the experimental measurements of LNG and neutral density plume dispersion in the wake of a single cylindrical obstacle. Additional experiments with added tanks, buildings, and a shelterbelt are described elsewhere [3]. Laboratory tests were conducted at the field scale equivalent continuous LNG spill rate of 30 m^3/min, two wind speeds, 4 and 7 m/sec at 10 m equivalent height, and with neutral atmospheric stability. The experiments were performed with a single cylindrical model tank at scale ratio of 1:250. Configuration 1 is the plane area source case. Configurations 2 to 8 indicate the cylinder position upstream or downstream of the area source along the centerline. The cylinder positions were 0 m, −250 m, −150 m, −50 m, 50 m, 150 m, and 250 m for configurations 2 to 8, respectively.

Experimental Facilities and Simulation Methods

The Environmental Wind Tunnel at Colorado State University was used for all tests performed. This tunnel incorporates special features such as an adjustable ceiling, rotating turntables, transparent boundary walls, and a long test section to permit reproduction of micrometeorological behavior at large scales. A circular area source having an equivalent diameter of 75 m and a cylindrical tank having an equivalent height and diameter of 50 m were constructed. The source gas, 100 percent argon (simulated LNG), or a mixture of 10 percent ethane, 4 percent carbon dioxide, and 86 percent nitrogen (simulated neutral density gas), was stored in a high-pressure cylinder and directed through a flowmeter into the circular area source mounted in the wind-tunnel floor. The area source was consructed so that the discharging gas would exit uniformly through it.

Experiments on micrometeorological phenomenon requires the simulation of atmospheric boundary layer. This layer of the atmosphere is described mathematically by equations of conservation of mass, momentum, and energy [6]. Additionally, it has been determined [7–9] that kinematics and dynamics of flow systems above a certain minimum Reynolds number are independent of its magnitude. The method of similitude [10] describes the scaling parameters needed for simulating LNG plume in the wind tunnel. These considerations lead to specifying equality of Froude number, volume flux ratio, and specific gravity. Since the thermally variable prototype gas was simulated by an isothermal simulation gas, the concentration measurements observed in the model must be scaled. This scaling technique is described elsewhere [2–5].

The velocity and turbulence intensity profiles were measured with a ThermoSystems, Inc. (TSI) 1050 constant temperature anemometer and a 1210 hot-film probe. During calibration of the single film anemometer, the anemometer voltage response values over the velocity range of interest were fitted to an expression of King's law [11] but with a variable exponent. The approach flow velocity profiles were measured at the location of the area source center. The average value of the velocity profile power-law exponent was 0.22. The average values of the prototype frictional velocity were 0.25 m/s and 0.44 m/s corresponding to prototype wind speeds of 4 and 7 m/s. The average value of the prototype surface roughness parameter was 4 cm.

LNG simulation plume measurement were made with a rake of eight hot-wire aspirating probes. The basic principles governing the behavior of aspirating hot-wire probes are discussed elsewhere [12]. The eight instantaneous concentration probes were connected to an eight-channel TSI hot-wire anemometer system. The voltages from the TSI unit were conditioned for input to the analog-to-digital converter by a DC suppression circuit, a passive low-pass filter circuit tuned to 100 Hz, and an operational amplifier of gain five. The measurements of concentration with neutral density source were performed with a gas chromatograph having a flame ionization detector. The details of the concentration measurement techniques are described by Kothari et al. [3, 4].

Results and Discussion

Figure 1 shows plots of ground-level mean concentration versus downwind distance for neutral density and LNG source gas. Concentration isopleths for selected simulations are displayed in Fig. 2. The highest concentrations were observed without any surface obstacle (configuration 1). The storage

---

[1] Project Manager, Gas Research Institute, Chicago, IL 60631; Mem. ASME.

[2] Professor, Fluid Mechanics and Wind Engineering Program, Colorado State University, Fort Collins, CO 80521; Mem. ASME.

Contributed by the Heat Transfer Division for publication in the JOURNAL OF HEAT TRANSFER. Manuscript received by the Heat Transfer Division January 25, 1985.

only felt in a very small part of the enclosure flow. From the standpoint of building interiors, it appears that local as well as overall heat transfer may be estimated reasonably well from two-dimensional enclosure data. However, room temperature stratification is strongly dependent on boundary conditions and, therefore, cannot be determined from two-dimensional studies.

References

1 Bohn, M. S., Kirkpatrick, A. T., and Olson, D. A., "Experimental Study of Three Dimensional Natural Convection at High Rayleigh Number," ASME JOURNAL OF HEAT TRANSFER, Vol. 106, 1984, pp. 339–345.

2 Thwaites, B., ed., *Incompressible Aerodynamics*, Oxford, 1960.

3 Cowan, G. H., Lovegrove, P. C., and Quarini, G. L., "Turbulent Natural Convection Heat Transfer in Vertical Single Water-Filled Cavities," *Proc. 7th Int. Heat Transf. Conf.*, Munich, Hemisphere, Washington, D.C., 1982, Vol. 2, pp. 195–203.

4 Ozoe, H., Ohmuro, M., Mouri, A., Mishima, S., Sayama, H., and Churchill, S. W., "Laser Doppler Measurements of the Velocity Along a Heated Vertical Wall of a Rectangular Enclosure," ASME JOURNAL OF HEAT TRANSFER, Vol. 105, 1983, pp. 782–788.

5 Chen, C. C., and Eichhorn, R., "Natural Convection From a Vertical Surface to a Thermally Stratified Fluid," ASME JOURNAL OF HEAT TRANSFER, Vol. 98, 1976, pp. 446–451.

6 Newell, M. E., and Schmidt, F. W., "Heat Transfer by Laminar Natural Convection Within Rectangular Enclosures," ASME JOURNAL OF HEAT TRANSFER, Vol. 92, 1970, pp. 159–168.

7 Eckert, E. R. G., and Carlson, W. O., "Natural Convection in an Air Layer Enclosed Between Two Vertical Plates With Different Temperatures," *Int. J. Heat Mass Transfer*, Vol. 2, 1961, pp. 106–120.

8 Elder, J. W., "Laminar Free Convection in a Vertical Slot," *J. Fluid Mechanics*, Vol. 23, 1965, pp. 77–98.

Liquefied Natural Gas (LNG) Plume Interaction With Storage Tanks

K. M. Kothari[1] and R. N. Meroney[2]

Introduction

Natural gas is a highly desirable source of energy for consumption in the United States. Liquefied natural gas (LNG) is stored and transported at about −162°C. If a storage tank or transfer pipe were to rupture and the contents spill out, rapid boiling of the LNG would ensue and liberation of a potentially flammable vapor would result. Studies [1–5] have demonstrated that the cold LNG vapor plume will remain negatively buoyant for most conditions during the dispersion of concern. Thus, it represents a ground-level hazard. This hazard extends downwind from the spill until the atmosphere has diluted the LNG vapor below the lower flammability limit, a local concentration for methane below 5 percent by volume.

This paper describes the experimental measurements of LNG and neutral density plume dispersion in the wake of a single cylindrical obstacle. Additional experiments with added tanks, buildings, and a shelterbelt are described elsewhere [3]. Laboratory tests were conducted at the field scale equivalent continuous LNG spill rate of 30 m^3/min, two wind speeds, 4 and 7 m/sec at 10 m equivalent height, and with neutral atmospheric stability. The experiments were performed with a single cylindrical model tank at scale ratio of 1:250. Configuration 1 is the plane area source case. Configurations 2 to 8 indicate the cylinder position upstream or downstream of the area source along the centerline. The cylinder positions were 0 m, −250 m, −150 m, −50 m, 50 m, 150 m, and 250 m for configurations 2 to 8, respectively.

Experimental Facilities and Simulation Methods

The Environmental Wind Tunnel at Colorado State University was used for all tests performed. This tunnel incorporates special features such as an adjustable ceiling, rotating turntables, transparent boundary walls, and a long test section to permit reproduction of micrometeorological behavior at large scales. A circular area source having an equivalent diameter of 75 m and a cylindrical tank having an equivalent height and diameter of 50 m were constructed. The source gas, 100 percent argon (simulated LNG), or a mixture of 10 percent ethane, 4 percent carbon dioxide, and 86 percent nitrogen (simulated neutral density gas), was stored in a high-pressure cylinder and directed through a flowmeter into the circular area source mounted in the wind-tunnel floor. The area source was consructed so that the discharging gas would exit uniformly through it.

Experiments on micrometeorological phenomenon requires the simulation of atmospheric boundary layer. This layer of the atmosphere is described mathematically by equations of conservation of mass, momentum, and energy [6]. Additionally, it has been determined [7–9] that kinematics and dynamics of flow systems above a certain minimum Reynolds number are independent of its magnitude. The method of similitude [10] describes the scaling parameters needed for simulating LNG plume in the wind tunnel. These considerations lead to specifying equality of Froude number, volume flux ratio, and specific gravity. Since the thermally variable prototype gas was simulated by an isothermal simulation gas, the concentration measurements observed in the model must be scaled. This scaling technique is described elsewhere [2–5].

The velocity and turbulence intensity profiles were measured with a ThermoSystems, Inc. (TSI) 1050 constant temperature anemometer and a 1210 hot-film probe. During calibration of the single film anemometer, the anemometer voltage response values over the velocity range of interest were fitted to an expression of King's law [11] but with a variable exponent. The approach flow velocity profiles were measured at the location of the area source center. The average value of the velocity profile power-law exponent was 0.22. The average values of the prototype frictional velocity were 0.25 m/s and 0.44 m/s corresponding to prototype wind speeds of 4 and 7 m/s. The average value of the prototype surface roughness parameter was 4 cm.

LNG simulation plume measurement were made with a rake of eight hot-wire aspirating probes. The basic principles governing the behavior of aspirating hot-wire probes are discussed elsewhere [12]. The eight instantaneous concentration probes were connected to an eight-channel TSI hot-wire anemometer system. The voltages from the TSI unit were conditioned for input to the analog-to-digital converter by a DC suppression circuit, a passive low-pass filter circuit tuned to 100 Hz, and an operational amplifier of gain five. The measurements of concentration with neutral density source were performed with a gas chromatograph having a flame ionization detector. The details of the concentration measurement techniques are described by Kothari et al. [3, 4].

Results and Discussion

Figure 1 shows plots of ground-level mean concentration versus downwind distance for neutral density and LNG source gas. Concentration isopleths for selected simulations are displayed in Fig. 2. The highest concentrations were observed without any surface obstacle (configuration 1). The storage

---

[1] Project Manager, Gas Research Institute, Chicago, IL 60631; Mem. ASME.

[2] Professor, Fluid Mechanics and Wind Engineering Program, Colorado State University, Fort Collins, CO 80521; Mem. ASME.

Contributed by the Heat Transfer Division for publication in the JOURNAL OF HEAT TRANSFER. Manuscript received by the Heat Transfer Division January 25, 1985.

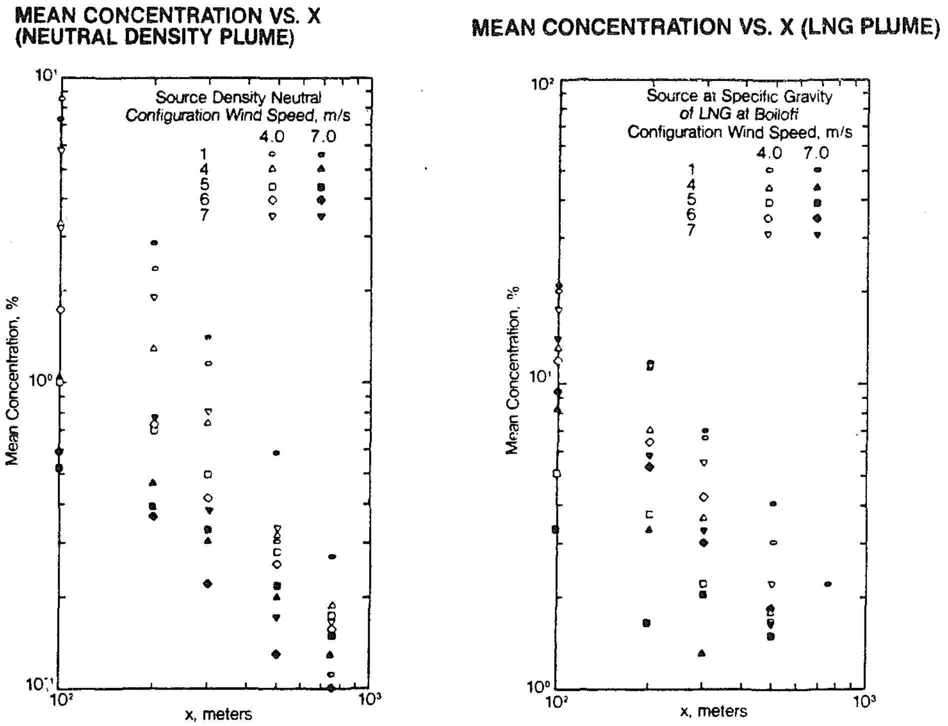

Fig. 1 Mean concentration versus downwind distance for neutral density and LNG plumes

CONCENTRATION ISOPLETHS FOR CONFIGURATION 1 AND WIND SPEED 4 M/SEC

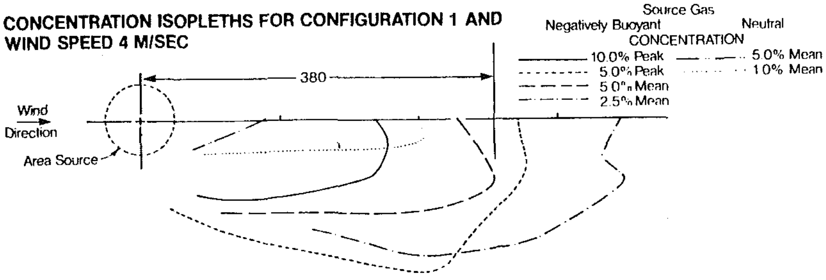

CONCENTRATION ISOPLETHS FOR CONFIGURATION 4 AND WIND SPEED 4 M/SEC

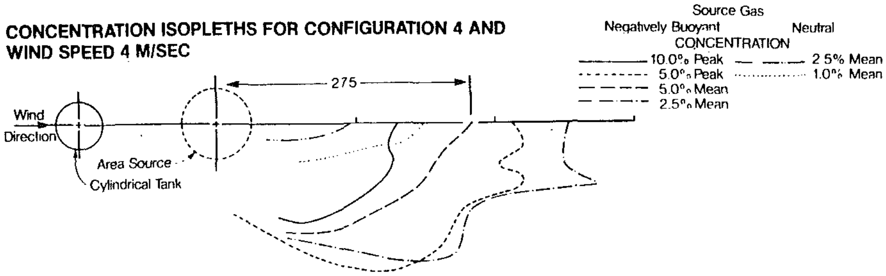

CONCENTRATION ISOPLETHS FOR CONFIGURATION 1 AND WIND SPEED 7 M/SEC

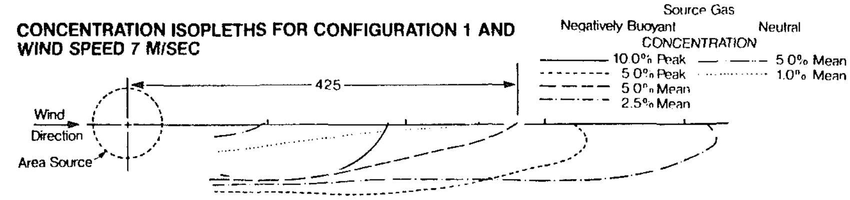

CONCENTRATION ISOPLETHS FOR CONFIGURATION 4 AND WIND SPEED 7 M/SEC

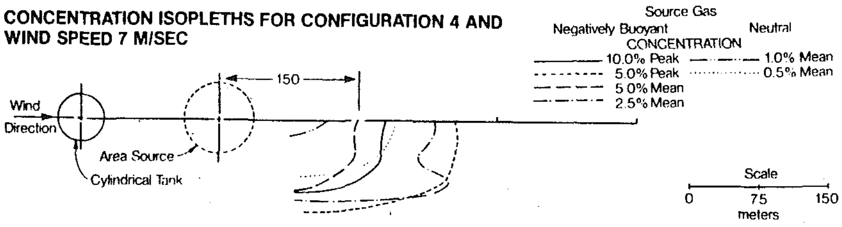

Fig. 2 Concentration isopleths at ground level

Table 1 Comparison of downwind distance to a specific concentration against cylinder position

Wind Speed (m/sec)	LNG Boiloff Rate (m^3/min)	Concentration	R$^{(1)}$ Cylinder at						
			−250m	−150m	−50m	0m	50m	150m	250m
4	30	5% Mean	1.25	1.37	3.57	1.60	1.45	1.27	1.25
4	30	2.5% Mean	1.08	1.25	1.92	1.64	1.25	1.11	1.09
4	30	5% Peak	1.01	1.23	1.75	1.41	1.23	1.12	1.03
7	30	5% Mean	2.27	2.86	7.14	2.86	1.92	1.69	1.02
7	30	2.5% Mean	1.75	2.56	4.35	3.33	1.89	1.67	1.12
7	30	5% Peak	1.27	1.92	2.86	1.89	1.61	1.49	1.06

$$(1)\ R = \left[\frac{\text{Longitudinal Distance without Obstacle}}{\text{Longitudinal Distance with Obstacle}}\right] \text{ @ Specific Concentration Limit}$$

tank generated excess turbulence intensity [13-17], which resulted in additional mixing and corresponding plume dilution. For an LNG spill without tank the lateral plume spread was larger at 4 m/s wind speed than at 7 m/s wind. This resulted in higher concentration at 7 m/s wind speed as compared to 4 m/s wind speed data. However, the 4 m/s wind speed gave higher concentrations as compared to 7 m/s wind speed data for an LNG spill when the storage tank interacted with the plume. The mean concentrations measured with neutral density plumes were about three to five times smaller in magnitude than those observed with LNG plumes. When the cylindrical tank was located upstream of the spill area, the initial dilution for LNG plume (measured at 100 m downwind) was generally two to three smaller than that for the neutral plume data. With the cylindrical tank upstream but close to the spill area the highest plume dilution was observed.

Table 1 summarizes the ratios of distance to a specific concentration with no obstacle to that with an obstacle. The ratios ranged from one to seven under identical wind speed and boiloff conditions. It can be concluded that the effects of the obstacle are major for a distance from three to six times the height of the cylinder. These effects can be attributed to the recirculation zone behind the obstacle enhancing the dispersion of plumes. The entire heavy gas plume is modified by the cylinder wake when the cylinder is upstream of the spill area, whereas the plume divides and is only partly modified by the wake when the cylinder is downwind of the spill area. Greater dilution of the plume occurred with the cylinder upstream of the spill area. However, modifications of the flow structure upstream of the obstacle were also important and resulted in diluting the plume upstream.

The LNG plume tends to have its maximum concentration off the centerline. For configuration 1 the deviation from centerline may be attributed to meandering of the plume from the wind-tunnel centerline due to a slight lateral nonuniformity of the flow. However, for the cylindrical tank interaction cases this deviation may be caused by: (1) higher turbulence intensities in the wake of the tank resulting in higher entrainment, (2) the horseshoe vortices [17] deflecting the ambient air downward from the top of the turbulent boundary layer along the centerline of the obstacle, or (3) the deflection of the plume laterally by the surface obstacle.

Concluding Remarks

This experimental study has shown that the dispersion of heavy or neutrally buoyant plume is remarkably different as a result of its interaction with the surface obstacle. Surface obstacles create a highly turbulent zone downwind of the obstacle and enhance the dispersion. This enhancement of dispersion is expected to reduce the potential hazards associated with the spills of LNG.

References

1 "LNG Safety Program, Interim Report on Phase II Work," Report on American Gas Association Project IS-3-1, Battelle-Columbus Laboratories, 1974.

2 Neff, D. E., Meroney, R. N., Cermak, J. E., "Wind Tunnel Study of Negatively Buoyant Plume Due to LNG Spill," Colorado State University Report No. CER76-77DEN-RNM-JEC22, 1976, p. 241.

3 Kothari, K. M., Meroney, R. N., and Neff, D. E., "LNG Plume Interaction With Surface Obstacles," Gas Research Institute Report No. GRI 80/0095, 1981, p. 140.

4 Kothari, K. M., and Meroney, R. N., "Accelerated Dilution of LNG Plumes With Fences and Vortex Generators," Gas Research Institute Report No. 81/0074, 1982.

5 Meroney, R. N., Neff, D. E., Cermak, J. E., and Megahed, M., "Dispersion of Vapor From LNG Spills—Simulation in a Meteorological Wind Tunnel," Colorado State University Report No. CER76-77RNM-DEN-JEC-MM57, 1977, p. 151.

6 Cermak, J. E., "Applications of Fluid Mechanics to Wind Engineering, a Freeman Scholar Lecture," *Fluid Engineering*, Vol. 97, Ser. 1, No. 1, 1975, pp. 9-38.

7 Schlichting, H., *Boundary Layer Theory*, McGraw-Hill, New York, 1968.

8 Zoric, D., and Sandborn, V. A., "Similarity of Large Reynolds Number Boundary Layers," *Boundary-Layer Meteorology*, Vol. 2, No. 3, 1982, pp. 326-333.

9 Halitsky, J., "Validation of Scaling Procedures for Wind Tunnel Modeling of Diffusion Near Buildings," New York University Report No. TR-69-8, 1969.

10 Kline, S. J., *Similitude and Approximation Theory*, McGraw-Hill, New York, 1965, p. 229.

11 Sandborn, V. A., *Resistance Temperature Transducers*, Metrology Press, 1972, p. 545.

12 Kuretsky, W. H., "On the Use of an Aspirating Hot-Film Anemometer for the Instantaneous Measurement of Temperature,'" Master's Thesis, Department of Mechanical Engineering, University of Minnesota, Minneapolis, MN, 1967.

13 Kothari, K. M., "Stability Stratified Building Wakes," Ph. D. Dissertation, Civil Engineering Department, Colorado State University, Fort Collins, CO, 1979, p. 142.

14 Woo, H. G. C., Peterka, J. A., and Cermak, J. E., "Wind Tunnel Measurements in the Wakes of Structures," Colorado State University Report No. CER75-76HGCW-JAP-JEC40, 1976.

15 Castro, J. P., and Robins, A. G., "The Effects of a Thick Incident Boundary Layer on the Flow Around a Small Surface Mounted Cube," Central Electricity Generating Board Report No. R/M/N795, England, 1975.

16 Counihan, J., "An Experimental Investigation of the Wake Behind a Two-Dimensional Block and Behind a Cube in a Simulated Boundary Layer Flow," Central Electricity Generating Board Report No. RD/L/N115/71, England, 1971.

17 Kothari, K. M., Meroney, R. N., and Peterka, J. A., "The Flow and Diffusion Structure in the Wakes of Cylindrical Obstacles," 4th U.S. National Conference on Wind Engineering Research, Seattle, WA, July 26-29, 1981.

Ignition of Bulk 302 Stainless Steel in Oxygen by Laser Heating

Ke Nguyen[1] and M. C. Branch[1]

Introduction

The effect of an oxidizing environment on the ignition characteristics of 300-series stainless steels has been investigated, largely because of their extensive high-temperature applications. Reynolds [1] resistively heated 302 SS ribbons in a pure oxygen environment at pressures ranging from 0.101 to 0.811 MPa. It was found that 302 SS did not ignite but simply melted at 1650 to 1700 K. Dean and Thompson [2] ignited thin-walled tubular specimens of 300-series stainless steels by resistance heating in an atmosphere of either oxygen, carbon dioxide, or equal mixtures of these gases at pressures of 0.345, 2.068, and 5.516 MPa. All of the 300-series stainless steels, such as 304 SS, 310 SS, 321 SS, and 347 SS, ignited within their melting range (1672–1694 K) in oxygen and mixtures of oxygen and carbon dioxide, at all pressures investigated. No ignition occurred, however, in a carbon dioxide environment. The discrepancies in the results of Reynolds and Dean and Thompson may arise from differences in heating rate and therefore the thickness of the oxide films. Higher heating rates could lead to melting without ignition, whereas lower heating and a thicker oxide layer could allow the specimen to maintain its integrity slightly above the melting temperature and eventually ignite.

Bates et al. [3] studied the ignition behavior of V-notched 302 SS in a high-velocity preheated oxygen flow. The specimen was resistively heated to a predetermined temperature and then fractured in the flowing oxygen at pressures ranging from 2.026 to 6.890 MPa. If ignition occurred, the ignition temperature was assigned as the predetermined temperature. The ignition temperature obtained for 302 SS was a function of oxygen pressures ranging from 590 K at 6.890 MPa to 810 K at 2.026 MPa. These ignition temperatures are much lower than those of Dean and Thompson [2] because of the different method of investigation and different definition of ignition temperature. Differences among all of the studies cited suggest that a careful reconsideration of the development and onset of ignition of stainless steel is warranted.

In the present study, the effect of oxygen pressure on the ignition temperature of cylindrical 302 SS specimens ignited by a focused CW CO_2 laser beam in a cool, static, oxygen environment was investigated. The ignition temperature of 302 SS was determined quantitatively from the specimen temperature history obtained from a fast response, near infrared, two-color pyrometer [4]. The pyrometer was used to record the temperature history of a spot approximately 0.5 mm in diameter, located at the center of the cylindrical 302 SS specimen top surface. In this investigation, ignition signifies the phenomenon preceding the self-sustained combustion event. At ignition the specimen surface temperature increases rapidly from the heating rate trend generated by the external heat source. Earlier results of the ignition phenomena of bulk aluminum alloy using this apparatus have been reported [5, 6].

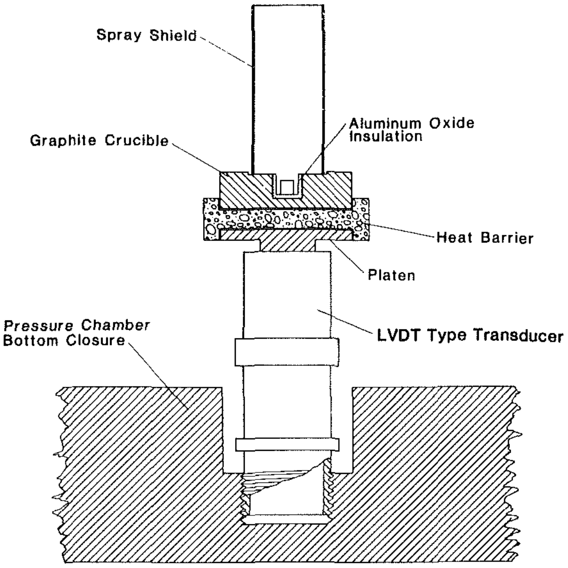

Fig. 1 Cross-sectional view of specimen pedestal

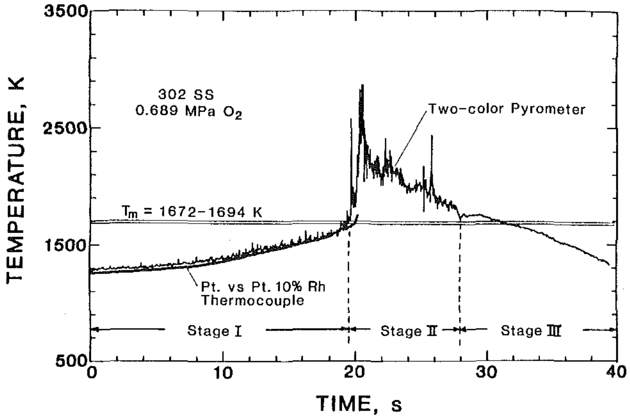

Fig. 2 Comparison between surface temperature measured by two-color pyrometer and interior temperature measured by Pt versus Pt-10 percent Rh thermocouple for CO_2 laser-irradiated cylindrical 302 SS specimen (thermocouple position: 0.3 mm below specimen top surface)

Experimental Apparatus and Procedure

Details of the apparatus and procedure used in the ignition study of 302 SS may be found elsewhere [4–6]; only a brief discussion is given here. The high-pressure combustion chamber consists of the main body and the top and bottom enclosures. The main body was cast from CA 15, a casting version of 410 SS, whereas the enclosures were machined from 410 SS. The combustion chamber has an internal diameter of 12 cm and a height of 23.5 cm, resulting in an internal volume of 2.6 L.

The cylindrical 302 SS specimens (0.15 percent C, 2.0 percent Mn, 1 percent Si, 8–10 percent Ni, 17–19 percent Cr, balance Fe) had a diameter of 5 mm and a height of 5 mm. For runs in which thermocouples were used, a thermocouple well 0.635 mm in diameter was drilled axially at the bottom center of the specimen to within 0.254 mm from the top surface. The cylindrical 302 SS specimen was placed in an aluminum oxide powder-lined well drilled in a graphite block. This block was placed on a foam firebrick which was mounted on the LVDT (Linear Variable Differential Transformer) mass sensor located at the center of the bottom enclosure of the combustion chamber. The complete arrangement is shown in Fig. 1.

Ignition of the cylindrical 302 SS specimens was obtained by laser heating. The CW CO_2 laser beam entered the combustion chamber at the center of the top enclosure of the combustion chamber. Before the laser beam entered the combustion chamber, it was focused by a zinc selenide lens. The focused laser beam had a diameter of approximately 5 mm and an incident average power density of approximately 3.560 MW/m^2.

The temperature measurement system consisted of the narrow-band, two-color pyrometer and thermocouples. The two-color pyrometer was used to record the temperature

---

[1] Mechanical Engineering Department, University of Colorado, Boulder, CO 80309

Contributed by the Heat Transfer Division for publication in the JOURNAL OF HEAT TRANSFER. Manuscript received by the Heat Transfer Division February 19, 1985.

Table 1 Ignition temperature of CO_2 laser-irradiated cylindrical 302 stainless steel SS specimens as a function of oxygen pressure

Pressure, MPa	Average Ignition Temperature and Standard Deviation, K
0.345	1736±19
0.689	1682±32
1.724	1673±15
3.447	1705±49
5.171	1648±22

Note: The melting temperature of 302 Stainless Steel is from 1672 to 1694 K.

history of a 0.5-mm-dia spot located at the center of the cylindrical 302 SS specimen top surface. The pyrometer operated in the near-infrared at two narrow spectral regions with a nominal bandwidth of 10 nm, centered at 0.951 and 1.06 μm. The two-color pyrometer has a maximum time response of 25 μs and a temperature range from 1000 to 4000 K. Internal temperatures of the specimen were measured by W/5 percent Re versus W/26 percent Re and Pt versus Pt/10 percent Rh thermocouples.

Results and Discussion

The ignition and combustion tests were run in a cool, static oxygen environment at pressures ranging from 0.345 to 5.171 MPa. A minimum of four experiments was conducted at each oxygen pressure to minimize the inherent random errors and to check the consistency of the surface temperature at ignition.

Typical temperature curves for a laser-ignited cylindrical 302 SS specimen are shown in Fig. 2. Also shown in Fig. 2 is the temperature of a spot approximately 0.30 mm below the specimen top surface as measured by a Pt versus Pt-10 percent Rh thermocouple. The differences in temperature between the two-color pyrometer and the thermocouple are within those predicted by a theoretical heat transfer model [5]. The complete event can be divided into three distinct stages. Stage I begins with the start of specimen heating and terminates with ignition. This stage is characterized by the formation of an increasingly thick and rough oxide shell. Prior to ignition, numerous hot spots develop on the specimen top surface due to localized cracking of the oxide scale. These hot spots are eventually extinguished perhaps due to the healing ability of the oxide scale by formation of a compact protective scale at the base of the crack. This healing ability of the oxide scale, however, eventually breaks down and one of the hot spots is able to develop into an ignition spot. If the laser heating is turned off prior to this point, the specimen will cool and not ignite. Once established, the ignition spot spreads across the whole specimen top surface and results in ignition of the specimen. The site at which the ignition spot develops varies in a statistically random manner. Stage II corresponds to a much faster oxidation rate between the molten alloy and the oxygen environment and will be referred to as combustion. The beginning of stage II is marked by an increase in both specimen surface temperature and light intensity. The beginning of this stage occurs within the melting range of the alloy (1672–1694 K). Stage III is the cooling period for the oxidation products, during which there is a gradual drop in both temperature and light intensity.

Although other interpretations of the ignition point are possible, in this investigation we have chosen to define ignition as the point at which there exists a change in the slope of the light intensity curve. The ignition temperature was obtained by developing a least-squares fit to the temperature curve for the final few seconds before the point of ignition.

The effect of oxygen pressure on the ignition temperatures of laser-ignited cylindrical 302 SS specimen is shown in Table 1. As seen in this table, 302 SS ignited within its melting range (1672–1694 K) at all oxygen pressures investigated. Results obtained in the present investigation agreed quite well with those obtained by Dean and Thompson [2], even though in their study specimens were resistively heated to ignition.

Acknowledgments

We would like to acknowledge the assistance of James W. Bransford and the National Bureau of Standards, Boulder, for technical assistance and the use of their facilities to conduct this research. The research was supported by the NASA George C. Marshall Space Flight Center and the Air Force Office of Scientific Research.

References

1 Reynolds, W. C., "Investigation of Ignition Temperatures of Solid Metals," NASA *Technology Note TN D-182*, 1959.

2 Dean, L. E., and Thompson, W. R., "Ignition Characteristics of Metals and Alloys," *ARS Journal*, 1961, pp. 917–923.

3 Bates, C. E., et al., "Ignition and Combustion of Ferrous Metals in High Pressure, High Velocity, Gaseous Oxygen," *Jour. Materials for Energy Systems*, Vol. 1, 1979, pp. 61–76.

4 Nguyen, K., and Branch, M. C., "A Near-Infrared Two-Color Pyrometer for Determining Ignition Temperatures of Metals and Metal Alloys," *Rev. Sci. Instrum.*, Vol. 56, No. 9, 1985, pp. 1780–1783.

5 Nguyen, K., "Ignition Characteristics of Bulk 6061 Aluminum Alloy, 302 Stainless Steel and 1018 Carbon Steel in a Pure Oxygen Environment," Ph.D. Thesis, Department of Mechanical Engineering, University of Colorado at Boulder, CO, 1984.

6 Nguyen, K., Bransford, J. W., and Branch, M. C., "Ignition Phenomena of Bulk Aluminum Alloy as a Function of Oxygen Pressure," *Proceedings of 21st JANNAF Combustion Meeting*, CPIA Pub. 412, Vol. 1, 1984, pp. 409–415.

Heat Transfer From a Yawed Finned Tube

F. Samie[1] and E. M. Sparrow[1]

Nomenclature

Nu = average Nusselt number, equation (1)
Re = Reynolds number, equation (2)
T_b = base tube temperature
T_∞ = freestream temperature
β = angular coordinate around circumference
η = fin efficiency
θ = yaw angle (Fig. 1)

Introduction

The effect of yaw on forced convection heat transfer from a finned circular cylinder has, seemingly, not been heretofore investigated. Furthermore, even for the unfinned cylinder, the available experimental information on the effect of yaw does not appear to form a consensus. In the experiments of [1], as the cylinder orientation was varied fom crossflow (yaw angle θ of 0 deg) to a yaw of 60 deg relative to crossflow, the average Nusselt number decreased monotonically. On the other hand, in [2], the Nusselt number increased slightly in the range from $\theta = 0$ to 15 deg and then decreased with further increases in yaw. Still another pattern was encountered in [3]. There, an initial decrease in the Nusselt number between the crossflow and the 30 deg yaw orientations was followed by a slight increase and then by a decrease for yaw angles greater than $\theta = 50$ deg.

Over all, ignoring the aforementioned locally nonmonotonic behavior, the average Nusselt number decreased as the cylinder orientation was varied from crossflow toward parallel flow. (Note that the foregoing discussion was not concerned with fine wires, for which results are surveyed in [4].)

With the foregoing as background, experiments were under-

---

[1] Department of Mechanical Engineering, University of Minnesota, Minneapolis, MN 55455.

Contributed by the Heat Transfer Division for publication in the JOURNAL OF HEAT TRANSFER. Manuscript received by the Heat Transfer Division August 13, 1985.

Table 1 Ignition temperature of CO_2 laser-irradiated cylindrical 302 stainless steel SS specimens as a function of oxygen pressure

Pressure, MPa	Average Ignition Temperature and Standard Deviation, K
0.345	1736 ± 19
0.689	1682 ± 32
1.724	1673 ± 15
3.447	1705 ± 49
5.171	1648 ± 22

Note: The melting temperature of 302 Stainless Steel is from 1672 to 1694 K.

history of a 0.5-mm-dia spot located at the center of the cylindrical 302 SS specimen top surface. The pyrometer operated in the near-infrared at two narrow spectral regions with a nominal bandwidth of 10 nm, centered at 0.951 and 1.06 μm. The two-color pyrometer has a maximum time response of 25 μs and a temperature range from 1000 to 4000 K. Internal temperatures of the specimen were measured by W/5 percent Re versus W/26 percent Re and Pt versus Pt/10 percent Rh thermocouples.

Results and Discussion

The ignition and combustion tests were run in a cool, static oxygen environment at pressures ranging from 0.345 to 5.171 MPa. A minimum of four experiments was conducted at each oxygen pressure to minimize the inherent random errors and to check the consistency of the surface temperature at ignition.

Typical temperature curves for a laser-ignited cylindrical 302 SS specimen are shown in Fig. 2. Also shown in Fig. 2 is the temperature of a spot approximately 0.30 mm below the specimen top surface as measured by a Pt versus Pt-10 percent Rh thermocouple. The differences in temperature between the two-color pyrometer and the thermocouple are within those predicted by a theoretical heat transfer model [5]. The complete event can be divided into three distinct stages. Stage I begins with the start of specimen heating and terminates with ignition. This stage is characterized by the formation of an increasingly thick and rough oxide shell. Prior to ignition, numerous hot spots develop on the specimen top surface due to localized cracking of the oxide scale. These hot spots are eventually extinguished perhaps due to the healing ability of the oxide scale by formation of a compact protective scale at the base of the crack. This healing ability of the oxide scale, however, eventually breaks down and one of the hot spots is able to develop into an ignition spot. If the laser heating is turned off prior to this point, the specimen will cool and not ignite. Once established, the ignition spot spreads across the whole specimen top surface and results in ignition of the specimen. The site at which the ignition spot develops varies in a statistically random manner. Stage II corresponds to a much faster oxidation rate between the molten alloy and the oxygen environment and will be referred to as combustion. The beginning of stage II is marked by an increase in both specimen surface temperature and light intensity. The beginning of this stage occurs within the melting range of the alloy (1672–1694 K). Stage III is the cooling period for the oxidation products, during which there is a gradual drop in both temperature and light intensity.

Although other interpretations of the ignition point are possible, in this investigation we have chosen to define ignition as the point at which there exists a change in the slope of the light intensity curve. The ignition temperature was obtained by developing a least-squares fit to the temperature curve for the final few seconds before the point of ignition.

The effect of oxygen pressure on the ignition temperatures of laser-ignited cylindrical 302 SS specimen is shown in Table 1. As seen in this table, 302 SS ignited within its melting range (1672–1694 K) at all oxygen pressures investigated. Results obtained in the present investigation agreed quite well with those obtained by Dean and Thompson [2], even though in their study specimens were resistively heated to ignition.

Acknowledgments

We would like to acknowledge the assistance of James W. Bransford and the National Bureau of Standards, Boulder, for technical assistance and the use of their facilities to conduct this research. The research was supported by the NASA George C. Marshall Space Flight Center and the Air Force Office of Scientific Research.

References

1 Reynolds, W. C., "Investigation of Ignition Temperatures of Solid Metals," NASA *Technology Note TN D-182*, 1959.

2 Dean, L. E., and Thompson, W. R., "Ignition Characteristics of Metals and Alloys," *ARS Journal*, 1961, pp. 917–923.

3 Bates, C. E., et al., "Ignition and Combustion of Ferrous Metals in High Pressure, High Velocity, Gaseous Oxygen," *Jour. Materials for Energy Systems*, Vol. 1, 1979, pp. 61–76.

4 Nguyen, K., and Branch, M. C., "A Near-Infrared Two-Color Pyrometer for Determining Ignition Temperatures of Metals and Metal Alloys," *Rev. Sci. Instrum.*, Vol. 56, No. 9, 1985, pp. 1780–1783.

5 Nguyen, K., "Ignition Characteristics of Bulk 6061 Aluminum Alloy, 302 Stainless Steel and 1018 Carbon Steel in a Pure Oxygen Environment," Ph.D. Thesis, Department of Mechanical Engineering, University of Colorado at Boulder, CO, 1984.

6 Nguyen, K., Bransford, J. W., and Branch, M. C., "Ignition Phenomena of Bulk Aluminum Alloy as a Function of Oxygen Pressure," *Proceedings of 21st JANNAF Combustion Meeting*, CPIA Pub. 412, Vol. 1, 1984, pp. 409–415.

Heat Transfer From a Yawed Finned Tube

F. Samie[1] and E. M. Sparrow[1]

Nomenclature

Nu = average Nusselt number, equation (1)
Re = Reynolds number, equation (2)
T_b = base tube temperature
T_∞ = freestream temperature
β = angular coordinate around circumference
η = fin efficiency
θ = yaw angle (Fig. 1)

Introduction

The effect of yaw on forced convection heat transfer from a finned circular cylinder has, seemingly, not been heretofore investigated. Furthermore, even for the unfinned cylinder, the available experimental information on the effect of yaw does not appear to form a consensus. In the experiments of [1], as the cylinder orientation was varied fom crossflow (yaw angle θ of 0 deg) to a yaw of 60 deg relative to crossflow, the average Nusselt number decreased monotonically. On the other hand, in [2], the Nusselt number increased slightly in the range from $\theta = 0$ to 15 deg and then decreased with further increases in yaw. Still another pattern was encountered in [3]. There, an initial decrease in the Nusselt number between the crossflow and the 30 deg yaw orientations was followed by a slight increase and then by a decrease for yaw angles greater than $\theta = 50$ deg.

Over all, ignoring the aforementioned locally nonmonotonic behavior, the average Nusselt number decreased as the cylinder orientation was varied from crossflow toward parallel flow. (Note that the foregoing discussion was not concerned with fine wires, for which results are surveyed in [4].)

With the foregoing as background, experiments were under-

---

[1] Department of Mechanical Engineering, University of Minnesota, Minneapolis, MN 55455.

Contributed by the Heat Transfer Division for publication in the JOURNAL OF HEAT TRANSFER. Manuscript received by the Heat Transfer Division August 13, 1985.

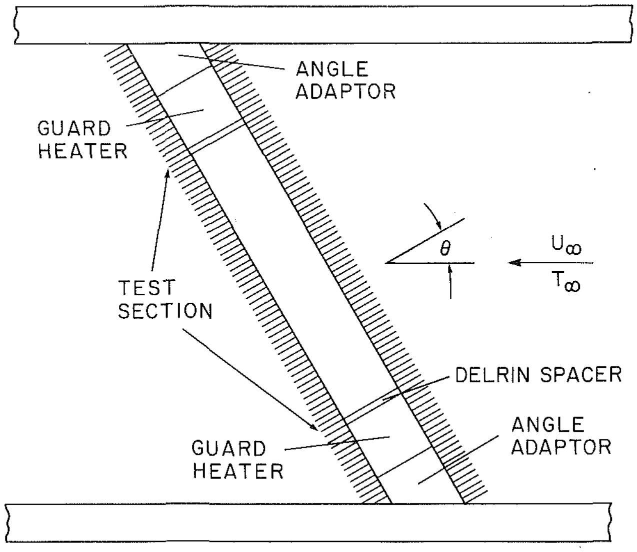

Fig 1 The finned tube in place in the wind tunnel

taken to determine how the heat transfer from a finned circular cylinder responds to yaw. The experiments were performed for crossflow and for yaw angles of 20 and 40 deg. At each orientation, the freestream Reynolds number (based on the diameter of the fin base tube) was varied from 7600 to 34,000. In addition to the average Nusselt number, results will also be presented for the fin efficiency and for the circumferential temperature distribution in the base tube.

Experimental Apparatus

A schematic diagram showing the finned tube in place in a wind tunnel is presented in Fig. 1. As seen there, the finned tube was a composite structure consisting of a heated test section flanked at either end by a guard heater and by a diagonally cut section (the angle adaptor) used to set the angle of yaw. The test and guard sections were common to all of the investigated orientations, with a different angle adaptor used for each.

The finned tube was equipped with annular fins which were made integral with the base tube in order to avoid thermal contact resistance. This was accomplished by fabricating the finned tube from a solid rod and circumferentially grooving the surface of the rod to create the interfin spaces. The test and guard heater sections were made of aluminum, chosen for its high thermal conductivity, low radiative emissivity, and easy machinability. For the angle adaptors, which served both to support the heated portion of the apparatus and to insulate it from the wind tunnel walls, Delrin, a free-machining plastic, was used.

The respective aluminum and Delrin sections had been bored along their axes to provide the finned tube with a hollow center. Individual, separately controlled, uniformly wound heater cores were installed in the test section and in the guard sections. The heater cores were, themselves, hollow to enable the passage of power leads and thermocouple wires, which were drawn out of the apparatus through the angle adaptors.

The external dimensions of all components of the finned tube were made identical, so that the assembled tube was hydrodynamically continuous along its length. The key external dimensions are

fin tip diameter $D_f = 5.715$ cm
base tube diameter $D = 3.175$ cm
interfin gap $S = 0.3175$ cm
fin thickness $t = 0.1058$ cm
fins per inch = 6

The wall thickness of the aluminum base tube, 0.635 cm, was chosen to help minimize temperature variations. The overall axial length of the test and guard sections was 28.89 cm, while the lengths of the angle adaptors corresponding to a given orientation were selected to accommodate the 30.48 cm height of the wind tunnel.

The test section portion of the tube was equipped with eight thermocouples, and three thermocouples were installed in each of the guard sections. The thermocouple junctions were situated about 0.076 cm from the surface of the tube exposed to the airflow in the interfin space. By design, the test section and guard heaters could be rotated as a unit about the axis of the tube, enabling the thermocouples to be positioned at any circumferential location relative to the freestream direction. For the present experiments, temperature measurements were made at 30 deg intervals around the circumference.

During each data run, the temperatures of the adjacent portions of the test section and the guard heaters were matched, thereby eliminating extraneous axial heat losses from the test section. To increase the sensitivity of the temperature-matching procedure, Delrin spacers illustrated in Fig. 1 were positioned between the respective ends of the test section and the guard heaters.

The freestream temperature was measured by a pair of thermocouples situated just forward and to the side of the finned tube, while the freestream velocity was determined with the aid of an impact probe and wall static tap, also positioned forward and to the side of the tube. The finned tube was situated midway between the sidewalls of the 30.48 × 60.96 cross section (height × width) of the wind tunnel. In the crossflow orientation (i.e., zero yaw), the cylinder was vertical. The degree of yaw is defined by the angle θ between the freestream velocity vector and the normal to the cylinder axis, as illustrated in Fig. 1. In the Reynolds number range of the experiments, the turbulence level of the wind tunnel was about 0.4 percent.

Results and Discussion

Data Reduction. The average heat transfer coefficient and Nusselt number for the test section were evaluated from

$$h = Q/(\overline{T_b - T_\infty})(A_b + \eta A_f), \qquad \mathrm{Nu} = hD/k \qquad (1)$$

In the h equation, Q represents the rate of convective heat transfer from the test section to the airflow. Extraneous conduction losses from the test section were suppressed by the guard heaters, and the radiative transfer was estimated and found to be negligible. Consequently, Q was evaluated directly from the electric power input to the test section heater. The quantity $(\overline{T_b - T_\infty})$ is the circumferential-average temperature difference between the base tube and the freestream. As will be demonstrated later, the circumferential variations of $(T_b - T_\infty)$ were not large, ranging from 2-3 percent to 6-7 percent about the mean, depending on the orientation of the finned tube and on the Reynolds number.

The other quantities in the h equation are the exposed area A_b of the base tube, the fin surface area A_f (including both the annular surfaces and the tips), and the fin efficiency η. The latter is unknown and was determined by an iterative process. To begin the iteration, h was evaluated from equation (1) under the assumption that $\eta = 1$. Then, with h and with the dimensions and thermal conductivity of the fins, η was read from Table 2-2 of [5]. This η value was introduced into equation (1), and a new h was evaluated. This h enabled a new η to be read from the table, and the process was continued until convergence.

The fin analysis which is the basis of Table 2-2 of [5] is the conventional one in which the local heat transfer coefficient is assumed uniform along the faces of the fin. In reality, in most fin configurations, the local coefficient will vary with posi-

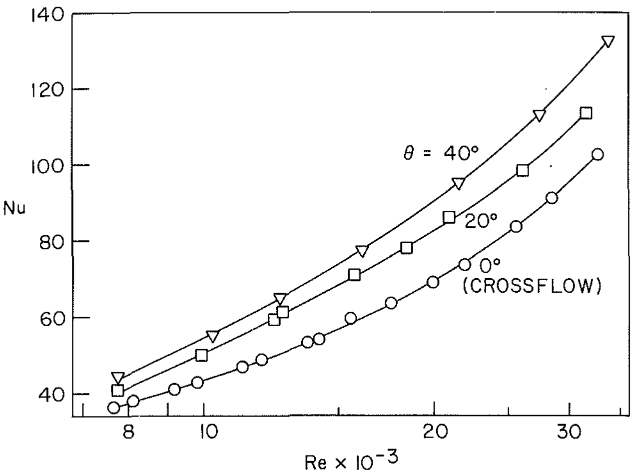

Fig. 2 Nusselt number results

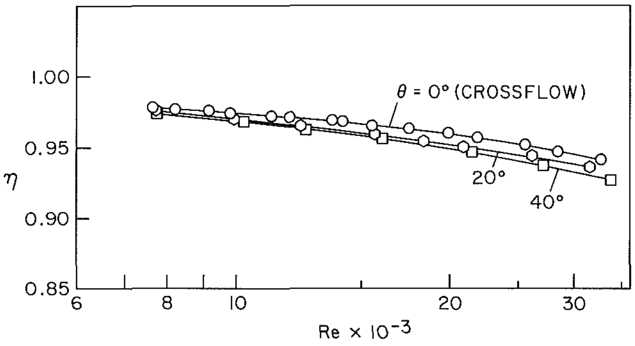

Fig. 3 Fin efficiencies

tion, casting some uncertainty on the accuracy of the η values. For the present experiments, the η values were generally close to unity, ranging from 0.93 to 0.98. In view of this, it is believed that the uncertainties in η did not have a significant effect on the heat transfer coefficients evaluated from the experimental data.

The fluid flow aspects of the problem were expressed in terms of the Reynolds number

$$\mathrm{Re} = U_\infty D/\nu \tag{2}$$

In this equation, U_∞ is the freestream velocity upstream of the finned tube, and D is the diameter of the base tube. Both the kinematic viscosity ν in equation (2) and the thermal conductivity k in equation (1) were evaluated at the reference temperature $\frac{1}{2}(\overline{T_b} + T_\infty)$.

Nusselt Numbers. The finned tube Nusselt numbers are plotted in Fig. 2 as a function of the freestream Reynolds number in the range from 7600 to 34,000. Results are presented for the crossflow orientation (θ = 0 deg) and for yaw angles θ of 20 and 40 deg. For a given freestream Reynolds number, the figure shows that the smallest value of the Nusselt number occurs when the finned tube is in crossflow and that, as the tube is yawed relative to crossflow, the Nusselt number increases. The yaw-related increases in the Nusselt number are in the 20-30 percent range (depending on the Reynolds number) and are, therefore, substantial. It may also be noted that the Nusselt number is more responsive to yaw at smaller yaws (0-20 deg) than at larger yaws (20-40 deg).

It is relevant to compare the just-described response of a finned tube to yaw with the response of an unfinned tube. As indicated in the Introduction, there is an overall trend for the

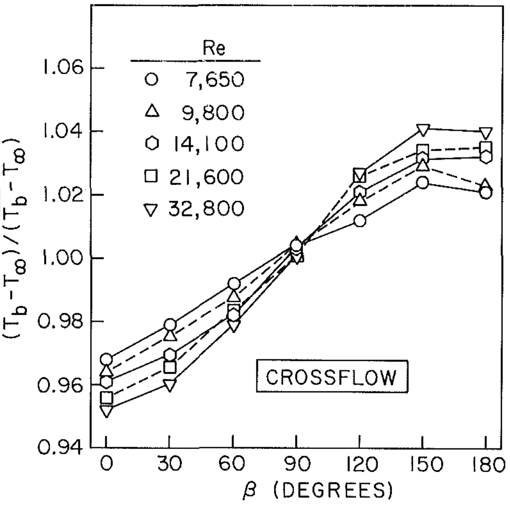

Fig. 4 Circumferential distributions of the base tube temperature, crossflow orientation

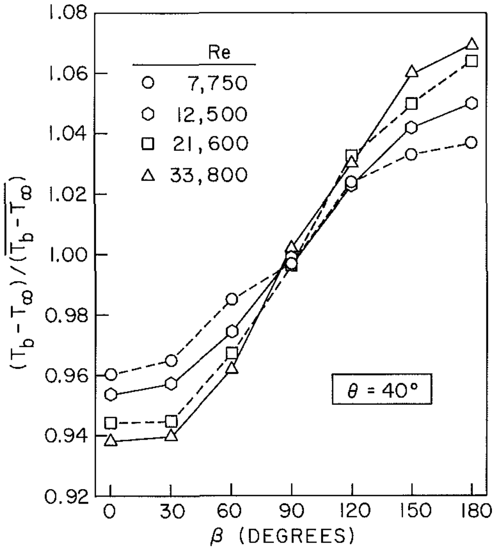

Fig. 5 Circumferential distributions of the base tube temperature, θ = 40 deg yaw

Nusselt number of the unfinned tube to decrease with increasing yaw, although the decrease is not necessarily monotonic. In broad terms, this decrease may be attributed to the decrease of the crossflow velocity component $U_\infty \cos\theta$ with increasing yaw (i.e., increasing θ). The fact that the response of the finned tube to yaw is just opposite to that of the unfinned tube (i.e., an increase in Nusselt number rather than a decrease) is worthy of note. This response requires the activation of enhancement mechanisms to counteract the aforementioned decrease in the crossflow velocity component.

In the absence of fluid flow measurements, the specifics of such enhancement mechanisms are, necessarily, conjectural. One such mechanism is believed to be eddy shedding from the tilted fin tips and the transport of the eddies into the interfin spaces. Also, it is possible that at moderate yaw angles (i.e., the range investigated here), the fluid may encounter less resistance to its entry into the interfin spaces than at zero yaw.

Fin Efficiency. Figure 3 conveys the results for the fin efficiency η. The trends displayed by these results are consistent with the principle that for fixed fin dimensions and thermal conductivity, the efficiency decreases as the convective heat transfer coefficient increases. Since the heat transfer coefficient is lowest for the crossflow orientation and increases with increasing yaw (Fig. 2), so, then, is the efficiency highest for crossflow, decreasing with yaw. By the same token, the efficiency decreases with increasing Reynolds number at a fixed orientation. Furthermore, for the same reason, the efficiency is more sensitive to Reynolds number at larger yaw and is more sensitive to yaw at larger Reynolds numbers.

In general, the η values for the present experiments did not deviate significantly from unity, which is consistent with the use of high thermal conductivity, moderately thick fins. Over all, the efficiency ranged from 0.93 to 0.98, a variation primarily due to the variation of the Reynolds number. At the very most, the yaw-related variation of η was about 1½ percent.

Circumferential Temperature Distributions. Representative results for the circumferential distribution of the base tube temperature are presented in Figs. 4 and 5, respectively, for crossflow and for $\theta = 40$ deg yaw. In each figure, the local tube-to-freestream temperature difference $(T_b - T_\infty)$ is plotted as a function of the coordinate β which specifies the angular position around the circumference of the tube, with $\beta = 0$ deg at the forward stagnation point and $\beta = 180$ deg at the rear stagnation point. On the ordinate, the local temperature difference is normalized by the circumferential-average temperature difference $(\overline{T_b - T_\infty})$.

Each figure contains data for several representative Reynolds numbers in the investigated range. The data were collected at 30 deg intervals around the circumference, but, owing to symmetry, only the range between $\beta = 0$ and 180 deg need be considered in the figures. The data points have been connected by straight-line segments in order to provide continuity.

In general, the tube wall temperature is lowest at the forward stagnation point and increases steadily toward the rear of the tube. The circumferential distribution of $(T_b - T_\infty)$ may also be regarded as an index of the circumferential distribution of the local heat transfer coefficient. Low values of the temperature difference correspond to high values of the transfer coefficient and vice versa. These relationships are, however, strictly qualitative, since the convective heat flux is not circumferentially uniform due to heat conduction in the tube wall.

The figures indicate that the extent of the circumferential variations is qualitatively related to the magnitude of the average Nusselt number, with larger variations at higher Nusselt numbers. Thus, the circumferential variations increase as the Reynolds number increases (at a fixed orientation) and as the yaw angle increases (at a fixed Reynolds number). The actual extent of the circumferential variations is modest—consistent with the use of a moderately thick-walled, highly conducting base tube. For example, in Fig. 4, the deviations from the mean are 3-5 percent in the front of the tube and 2-4 percent at the rear.

References

1 Kazakevitch, F. P., "Effect of the Angle of Incidence of a Gas Stream on the Heat Transfer From a Circular Cylinder," *Zh. Tekh. Fiz.*, Vol. 24, 1954, pp. 1341-1347.

2 Willins, R. E., and Griskey, R. G., "Mass Transfer From Cylinders at Various Orientations to Flowing Gas Streams," *Can. J. Chem. Engng.*, Vol. 53, 1975, pp. 500-504.

3 Kraabel, J. S., McKillop, A. A., and Baughn, J. W., "Heat Transfer to Air From a Yawed Cylinder," *Int. J. Heat Mass Transfer*, Vol. 25, 1982, pp. 409-418.

4 Morgan, V. T., "The Overall Convective Heat Transfer From Smooth Circular Cylinders," in: *Advances in Heat Transfer*, Vol. 11, Academic Press, New York, 1975.

5 Kern, D. Q., and Kraus, A. D., *Extended Surface Heat Transfer*, McGraw-Hill, New York, 1972.

An Empirical Correlation for the Average Heat Transfer Coefficient in Circular Tubes

M. Molki[1] and E. M. Sparrow[2]

Nomenclature

A_x = mass transfer area for a tube of length X
a = coefficient in equation (7)
b = exponent in equation (7)
C = coefficient in equation (1)
D = inside diameter of tube
$\mathfrak{D}$ = mass diffusion coefficient
$\bar{K}_x$ = average mass transfer coefficient over the length X of the tube
LMDD = logarithmic mean density difference, equation (3)
$\dot{M}_x$ = rate of mass transfer for a tube of length X
$\overline{\mathrm{Nu}}$ = average Nusselt number over the length X of the tube
Nu_{fd} = fully developed Nusselt number
Nu_x = local Nusselt number
Pr = Prandtl number
Re = Reynolds number
Sc = Schmidt number
$\overline{\mathrm{Sh}}$ = average Sherwood number over the length X of the tube
Sh_{fd} = fully developed Sherwood number
X = axial coordinate ($X = 0$ corresponds to the tube inlet)
$\rho_{nb,0}$ = naphthalene vapor density in bulk at the tube inlet
$\rho_{nb,x}$ = naphthalene vapor density in bulk at station X
ρ_{nw} = naphthalene vapor density at wall

Introduction

The heat transfer characteristics of turbulent flow in circular tubes with simultaneous velocity and temperature development have been the subject of study by a number of investigators. Although a thorough understanding of the problem requires a knowledge of the local transfer coefficients, it is the average values that are more often needed in practice.

The objective of the present work is to evaluate the average heat transfer coefficient for relatively short circular tubes having a sharp-edged inlet and to develop a new and relatively simple empirical correlation for these results. An existing correlation corresponding to simultaneously developing velocity and temperature profiles, which has appeared in a number of heat transfer textbooks [1, 2], is

$$\overline{\mathrm{Nu}}/\mathrm{Nu}_{fd} = 1 + C/(X/D) \qquad (1)$$

where $\overline{\mathrm{Nu}}$ and Nu_{fd}, respectively, denote the average and fully developed Nusselt numbers, X/D is the normalized axial

---

[1] Department of Mechanical Engineering, Tufts University, Medford, MA 02155

[2] Department of Mechanical Engineering, University of Minnesota, Minneapolis, MN 55455; Fellow ASME

Contributed by the Heat Transfer Division for publication in the JOURNAL OF HEAT TRANSFER. Manuscript received by the Heat Transfer Division December 10, 1984.

conductivity, the efficiency decreases as the convective heat transfer coefficient increases. Since the heat transfer coefficient is lowest for the crossflow orientation and increases with increasing yaw (Fig. 2), so, then, is the efficiency highest for crossflow, decreasing with yaw. By the same token, the efficiency decreases with increasing Reynolds number at a fixed orientation. Furthermore, for the same reason, the efficiency is more sensitive to Reynolds number at larger yaw and is more sensitive to yaw at larger Reynolds numbers.

In general, the η values for the present experiments did not deviate significantly from unity, which is consistent with the use of high thermal conductivity, moderately thick fins. Over all, the efficiency ranged from 0.93 to 0.98, a variation primarily due to the variation of the Reynolds number. At the very most, the yaw-related variation of η was about 1½ percent.

Circumferential Temperature Distributions. Representative results for the circumferential distribution of the base tube temperature are presented in Figs. 4 and 5, respectively, for crossflow and for $\theta = 40$ deg yaw. In each figure, the local tube-to-freestream temperature difference $(T_b - T_\infty)$ is plotted as a function of the coordinate β which specifies the angular position around the circumference of the tube, with $\beta = 0$ deg at the forward stagnation point and $\beta = 180$ deg at the rear stagnation point. On the ordinate, the local temperature difference is normalized by the circumferential-average temperature difference $(\overline{T_b - T_\infty})$.

Each figure contains data for several representative Reynolds numbers in the investigated range. The data were collected at 30 deg intervals around the circumference, but, owing to symmetry, only the range between $\beta = 0$ and 180 deg need be considered in the figures. The data points have been connected by straight-line segments in order to provide continuity.

In general, the tube wall temperature is lowest at the forward stagnation point and increases steadily toward the rear of the tube. The circumferential distribution of $(T_b - T_\infty)$ may also be regarded as an index of the circumferential distribution of the local heat transfer coefficient. Low values of the temperature difference correspond to high values of the transfer coefficient and vice versa. These relationships are, however, strictly qualitative, since the convective heat flux is not circumferentially uniform due to heat conduction in the tube wall.

The figures indicate that the extent of the circumferential variations is qualitatively related to the magnitude of the average Nusselt number, with larger variations at higher Nusselt numbers. Thus, the circumferential variations increase as the Reynolds number increases (at a fixed orientation) and as the yaw angle increases (at a fixed Reynolds number). The actual extent of the circumferential variations is modest—consistent with the use of a moderately thick-walled, highly conducting base tube. For example, in Fig. 4, the deviations from the mean are 3–5 percent in the front of the tube and 2–4 percent at the rear.

References

1 Kazakevitch, F. P., "Effect of the Angle of Incidence of a Gas Stream on the Heat Transfer From a Circular Cylinder," *Zh. Tekh. Fiz.*, Vol. 24, 1954, pp. 1341–1347.

2 Willins, R. E., and Griskey, R. G., "Mass Transfer From Cylinders at Various Orientations to Flowing Gas Streams," *Can. J. Chem. Engng.*, Vol. 53, 1975, pp. 500–504.

3 Kraabel, J. S., McKillop, A. A., and Baughn, J. W., "Heat Transfer to Air From a Yawed Cylinder," *Int. J. Heat Mass Transfer*, Vol. 25, 1982, pp. 409–418.

4 Morgan, V. T., "The Overall Convective Heat Transfer From Smooth Circular Cylinders," in: *Advances in Heat Transfer*, Vol. 11, Academic Press, New York, 1975.

5 Kern, D. Q., and Kraus, A. D., *Extended Surface Heat Transfer*, McGraw-Hill, New York, 1972.

An Empirical Correlation for the Average Heat Transfer Coefficient in Circular Tubes

M. Molki[1] **and E. M. Sparrow**[2]

Nomenclature

A_x = mass transfer area for a tube of length X
a = coefficient in equation (7)
b = exponent in equation (7)
C = coefficient in equation (1)
D = inside diameter of tube
$\mathfrak{D}$ = mass diffusion coefficient
$\bar{K}_x$ = average mass transfer coefficient over the length X of the tube
LMDD = logarithmic mean density difference, equation (3)
$\dot{M}_x$ = rate of mass transfer for a tube of length X
$\overline{\mathrm{Nu}}$ = average Nusselt number over the length X of the tube
Nu_{fd} = fully developed Nusselt number
Nu_x = local Nusselt number
Pr = Prandtl number
Re = Reynolds number
Sc = Schmidt number
$\overline{\mathrm{Sh}}$ = average Sherwood number over the length X of the tube
Sh_{fd} = fully developed Sherwood number
X = axial coordinate ($X = 0$ corresponds to the tube inlet)
$\rho_{nb,0}$ = naphthalene vapor density in bulk at the tube inlet
$\rho_{nb,x}$ = naphthalene vapor density in bulk at station X
ρ_{nw} = naphthalene vapor density at wall

Introduction

The heat transfer characteristics of turbulent flow in circular tubes with simultaneous velocity and temperature development have been the subject of study by a number of investigators. Although a thorough understanding of the problem requires a knowledge of the local transfer coefficients, it is the average values that are more often needed in practice.

The objective of the present work is to evaluate the average heat transfer coefficient for relatively short circular tubes having a sharp-edged inlet and to develop a new and relatively simple empirical correlation for these results. An existing correlation corresponding to simultaneously developing velocity and temperature profiles, which has appeared in a number of heat transfer textbooks [1, 2], is

$$\overline{\mathrm{Nu}}/\mathrm{Nu}_{fd} = 1 + C/(X/D) \qquad (1)$$

where $\overline{\mathrm{Nu}}$ and Nu_{fd}, respectively, denote the average and fully developed Nusselt numbers, X/D is the normalized axial

---

[1] Department of Mechanical Engineering, Tufts University, Medford, MA 02155

[2] Department of Mechanical Engineering, University of Minnesota, Minneapolis, MN 55455; Fellow ASME

Contributed by the Heat Transfer Division for publication in the JOURNAL OF HEAT TRANSFER. Manuscript received by the Heat Transfer Division December 10, 1984.

coordinate, and C is a constant which depends on the inlet geometry (e.g., $C=6$ for sharp-edged inlet [1]). As stated [1, 2], equation (1) is applicable to tubes with length greater than the entry length (about 20 diameters or more) and, as will be discussed later in the paper, fails to predict heat transfer in the developing region.

Also available in the literature is a correlation reported by Al-Arabi [3] for the variation of $\overline{\mathrm{Nu}}/\mathrm{Nu}_{fd}$ with X/D in a circular tube with a sharp-edged entrance, which is purported to be valid for $X/D>3$. It is noteworthy that the functional form of Al-Arabi's correlation is identical to equation (1) provided that C is replaced by $1.683(X/D)^{0.423}$.

The results reported in this paper are based on the experimental data of an earlier work published by the authors [4]. As detailed there, heat transfer coefficients were obtained from mass transfer results by the application of the analogy between the two processes. During the mass transfer experiments, the concentration of the transferred species at the tube wall was maintained uniform, which is analogous to a tube with a uniform wall temperature boundary condition. The particular mass transfer technique employed is the well-known naphthalene sublimation technique. It should be noted that the Schmidt number for sublimation of naphthalene is 2.5, which corresponds to a Prandtl number of 2.5 in the similar heat transfer process. The average Nusselt numbers are reported for Reynolds numbers ranging from 9000 to 88,000.

Data Reduction

The average mass transfer coefficient $\bar{K}_x$ for the length of tube between $X=0$ and $X=X$ was evaluated from the defining equation

$$\bar{K}_x=(\dot{M}_x/A_x)/(\mathrm{LMDD}) \qquad (2)$$

In this equation, $\dot{M}_x$ is the rate of mass transfer for the length X, which is directly obtainable from the experimental data, and LMDD is the logarithmic mean density difference defined as

$$\mathrm{LMDD}=[(\rho_{nw}-\rho_{nb,0})-(\rho_{nw}-\rho_{nb,x})]$$
$$/\ln[(\rho_{nw}-\rho_{nb,0})/(\rho_{nw}-\rho_{nb,x})] \qquad (3)$$

where ρ_{nw} and ρ_{nb} are the vapor densities of the transferred species (naphthalene) at the tube wall and in the bulk of the fluid, respectively. The subscript 0 refers to the tube inlet and X refers to quantities evaluated at a distance X from the inlet. Since the fluid entering the tube was free of naphthalene, $\rho_{nb,0}$ is zero and equation (3) reduces to

$$\mathrm{LMDD}=\rho_{nb,x}/\ln[\rho_{nw}/(\rho_{nw}-\rho_{nb,x})] \qquad (4)$$

By using equations (2) and (4), the average mass transfer coefficients are determined and may be represented in dimensionless form in terms of the Sherwood number

$$\overline{\mathrm{Sh}}=\bar{K}_x D/\mathfrak{D} \qquad (5)$$

in which $\mathfrak{D}$ is the mass diffusion coefficient. With the aid of equations (2)–(5), and for a fixed Reynolds number, $\overline{\mathrm{Sh}}$ was determined at 21 different tube lengths ranging from $X=0.22D$ to $19.08D$. The calculations were performed for five Reynolds numbers spanning the range between 9000 and 88,000.

Results and Discussion

The average Nusselt numbers for Reynolds numbers of 9000 and 88,000 are plotted in the lower diagram of Fig. 1. In this figure, the abscissa X/D is the dimensionless axial distance from the tube inlet over which average coefficients were determined. The Nusselt numbers are normalized by the fully developed values at the same Reynolds number. Thus, the ordinate in Fig. 1 indicates the degree of deviation from the fully developed values.

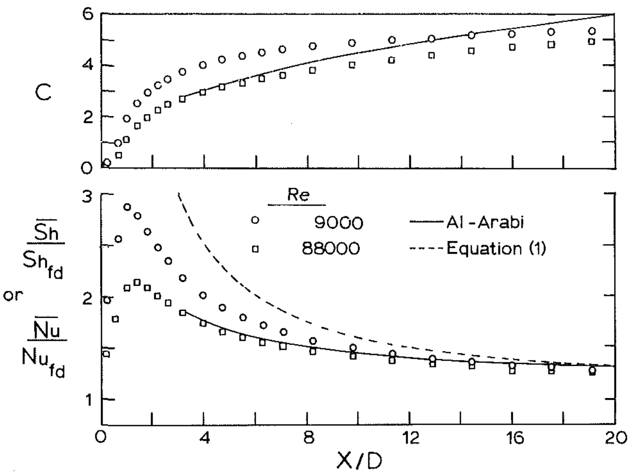

Fig. 1 Variation of the average Nusselt number and the coefficient C with X/D

An overall examination of the figure indicates a common shape of the $\overline{\mathrm{Nu}}/Nu_{fd}$ versus X/D distribution curves for both Reynolds numbers. Starting at the inlet of the tube with a value moderately greater than the fully developed value, the Nusselt number increases rapidly to a maximum, whereupon it begins to decrease and, farther downstream, tends to approach the fully developed value of $\overline{\mathrm{Nu}}=\mathrm{Nu}_{fd}$. This trend is consistent with the flow field in the vicinity of the sharp-edged tube entrance, where flow separation, reattachment, and redevelopment occur. The disturbance caused by the separation ensures that the redeveloping flow is turbulent.

Also shown in Fig. 1 are representations of equation (1) and of the correlation reported by Al-Arabi [3] for Re>7000 and tubes longer than three diameters (i.e., $X/D>3$). As discussed in his paper, Al-Arabi evaluated $\overline{\mathrm{Nu}}$ from

$$\overline{\mathrm{Nu}}=(1/X)\int_0^X \mathrm{Nu}_x dX \qquad (6)$$

and employed graphic integration to determine $\overline{\mathrm{Nu}}$ from the local values of Nu_x reported by other investigators [5, 6, 7] for a sharp-edged inlet. As seen in Fig. 1, for large values of X/D and Re, the results of the present work are in good agreement with those of [3]; however, closer to the tube inlet, where extraneous heat transfers are normally significant for low Reynolds numbers, the average Nusselt numbers of the present work for Re = 9000 are generally higher. The extraneous heat transfers may be due to conductive contact at the upstream end of the tube with structural elements and, perhaps, with electrical power leads. Note that in the present mass transfer experiments, such extraneous transfers do not occur. Another cause of the deviations is that $\overline{\mathrm{Sh}}$ obtained from equations (2)–(5) cannot, in principle, be equal to $\overline{\mathrm{Sh}}$ from the mass transfer counterpart of equation (6). As seen in Fig. 1, the predictions based on equation (1) are not in agreement with the results and, therefore, it may be concluded that equation (1) is not valid in the entry region of the tube.

Attention is now turned to the upper diagram of Fig. 1, where the so-called constant C of equation (1) is plotted as a function of X/D for the two Reynolds numbers. The values of C were determined from equation (1) and from the present values of $\overline{\mathrm{Nu}}/\mathrm{Nu}_{fd}$ at various X/D. As indicated in the figure, C increases rapidly with X/D in the initial part of the entry region, and it also depends on the Reynolds number.

Table 1 Comparison of experimental data with the predictions of equation (7)

Re =	9000			22,000			30,000			44,000			88,000		
X/D	(1)*	(2)**	Error %	(1)	(2)	Error %	(1)	(2)	Error %	(1)	(2)	Error %	(1)	(2)	Error %
2.19	2.59	2.48	4	2.32	2.21	5	2.25	2.15	5	2.17	2.17	0	2.07	2.01	3
2.58	2.39	2.35	2	2.17	2.11	3	2.10	2.05	3	2.04	2.07	2	1.97	1.94	1
3.16	2.19	2.18	0	2.00	1.97	1	1.95	1.93	1	1.90	1.94	2	1.85	1.84	1
4.71	1.86	1.89	1	1.73	1.73	0	1.70	1.71	1	1.67	1.72	3	1.66	1.66	0
6.27	1.69	1.72	2	1.59	1.59	0	1.57	1.57	0	1.55	1.60	3	1.55	1.55	0
8.21	1.55	1.57	1	1.48	1.47	1	1.46	1.46	0	1.45	1.50	3	1.46	1.46	0
11.31	1.43	1.44	1	1.37	1.36	1	1.36	1.36	0	1.36	1.39	2	1.38	1.37	1
14.41	1.35	1.35	0	1.31	1.29	2	1.30	1.29	1	1.30	1.33	2	1.33	1.31	1
17.52	1.30	1.30	0	1.27	1.24	2	1.26	1.25	1	1.26	1.29	2	1.29	1.27	1
19.08	1.28	1.27	1	1.25	1.22	2	1.24	1.23	1	1.24	1.27	2	1.27	1.26	1

* (1) Values of $\overline{\mathrm{Nu}}/\mathrm{Nu}_{fd}$ determined from equation (7)

** (2) Values of $\overline{\mathrm{Nu}}/\mathrm{Nu}_{fd}$ determined from experimental data

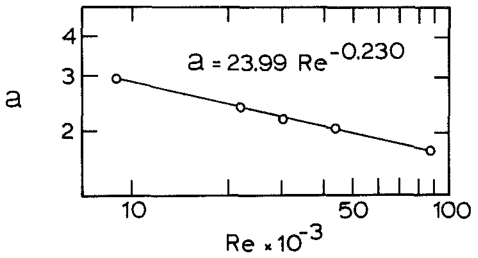

Fig. 2 The coefficient a of the correlation equation (7)

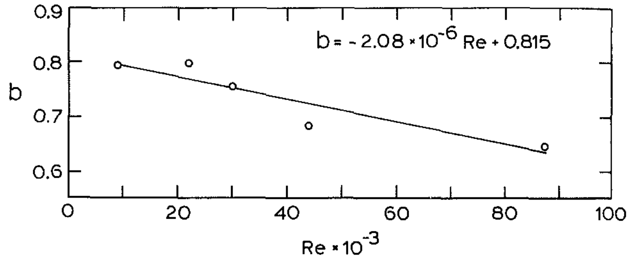

Fig. 3 The exponent b of the correlation equation (7)

Downsteam, however, it appears that the C values approach asymptotically to the constant value of 6.

Also shown in the upper diagram of Fig. 1 are the values of C predicted by Al-Arabi [3] for Reynolds numbers greater than 7000 and $X/D > 3$. As seen there, the agreement between the C distributions is qualitatively good; both support the fact that C is a strong function of X/D. The results of the present investigation, however, point to an additional fact, namely, the dependence of C on Reynolds number. It is, therefore, concluded that equation (1) does not accurately represent the average heat transfer coefficient for $X/D < 20$ in the entry region of the tube, and a new correlation must be found that is valid for a wide range of X/D and also takes the effect of Reynolds number into account.

To achieve this objective, the data shown in Fig. 1 were fit with a least-squares curve having the equation

$$\overline{\mathrm{Nu}}/\mathrm{Nu}_{fd} = 1 + a/(X/D)^b \tag{7}$$

where the variables a and b are functions of Reynolds number, as shown in Figs. 2 and 3. Examination of these figures suggests a linear relationship between the Reynolds number and the variables a and b in their respective system of coordinates. The least-squares fits for a and b are

$$a = 23.99\mathrm{Re}^{-0.230}, \qquad b = -2.08 \times 10^{-6}\mathrm{Re} + 0.815 \tag{8}$$

As shown in Fig. 3, the agreement between the foregoing equation for b and the actual data points is not as good as that for a (Fig. 2). However, the deviations have an acceptably small effect on the prediction of the $\overline{\mathrm{Nu}}/\mathrm{Nu}_{fd}$ distributions. In this regard, Table 1 has been prepared to compare the $\overline{\mathrm{Nu}}/\mathrm{Nu}_{fd}$ values of equation (7) with those of experiment. As seen in this table, aside from a few isolated deviations of 4 and 5 percent, the agreement is very good.

Concluding Remarks

The empirical correlation developed here and expressed by equations (7) and (8) provides a new means for the prediction of average Nusselt numbers in circular tubes with simultaneous development of the velocity and temperature profiles and with sharp-edged inlets. The correlation is applicable to tubes as short as two diameters. Moreover, it was shown that the so-called constant C of the widely used equation (1) is actually a variable which depends on the Reynolds number and the distance from the tube inlet.

References

1 Kays, W. M., and Crawford, M. E., *Convective Heat and Mass Transfer*, 2nd ed., McGraw-Hill, New York, 1980.

2 Karlekar, B. V., and Desmond, R. M., *Heat Transfer*, 2nd ed., West Publishing, St. Paul, MN, 1982.

3 Al-Arabi, M., "Turbulent Heat Transfer in the Entrance Region of a Tube," *Heat Transfer Engineering*, Vol. 3, 1982, pp. 76-83.

4 Sparrow, E. M., and Molki, M., "Turbulent Heat Transfer Coefficients in an Isothermal-Walled Tube for Either a Built-in or Free Inlet," *Int. J. Heat Mass Transfer*, Vol. 27, 1984, pp. 669-675.

5 Mills, A. F., "Experimental Investigation of Turbulent Heat Transfer in the Entrance Region of a Circular Conduit," *J. Mech. Eng. Sci.*, Vol. 4, 1962, pp. 63-77.

6 Cholette, A., "Heat Transfer—Local and Average Coefficients for Air Flowing Inside Tubes," *Chem. Eng. Prog.*, Vol. 44, 1948, pp. 81-88.

7 Boelter, L. M. K., Young, G., and Iverson, H. W., "An Investigation of Aircraft Heaters—Distribution of Heat Transfer Rate in the Entrance Section of a Circular Tube," NACA Tech. Note No. 1451, 1948.

Theory of Fully Developed, Combined Convection Including Flow Reversal

Win Aung[1] **and G. Worku**[2]

Nomenclature

b = spacing between duct walls
D_e = hydraulic diameter
g = acceleration due to gravity
Gr = Grashof number = $g\beta(T_2 - T_0)b^3/\nu^2$
h = heat transfer coefficient
k = thermal conductivity
Nu = Nusselt number = hD_e/k
p = pressure difference = $p' - p''$
p' = static pressure
p'' = hydrostatic pressure
P = dimensionless pressure difference = $p/\rho u_0^2$
r_T = wall temperature difference ratio = $(T_1 - T_0)/(T_2 - T_0)$
Re = Reynolds number = $u_0 b/\nu$
T = temperature
u, v = axial and transverse velocity, respectively
U = dimensionless axial velocity = u/u_0
V = dimensionless transverse velocity = vb/ν
x, y = axial and transverse coordinate, respectively ($x=0$ is duct entrance; $y=0$ is cool wall)
X = dimensionless axial coordinate = $x/b/\text{Re}$
Y = dimensionless transverse coordinate = y/b
β = thermal expansion coefficient
ν = kinematic viscosity
ρ = density
θ = dimensionless temperature = $(T - T_0)/(T_2 - T_0)$

Subscripts

0 = value at duct entrance (i.e., at $x = 0$)
1 = value on cool wall (i.e., at $y = 0$)
2 = value on hot wall (i.e., at $y = b$)
b = bulk value
m = mean value

Introduction[3]

For mixed convection in parallel-plate vertical channels, the study of fully developed flow (FDF) takes on a special significance. In a flow where the flow rate is fixed by the setting on a blower connected to the entrance of the duct (or by some metering device), and where buoyancy effects may not be neglected, the streamwise velocity profile may suffer a pronounced distortion. Typically, buoyancy effects are largest adjacent to heated surfaces; hence, velocities increase in near-wall regions with a concomitant decrease elsewhere due to the fixed flow rate. The combination of a fixed overall upward flow rate at the entrance of the channel and high buoyancy further up (which leads to high fluid flow adjacent to walls) can precipitate a downward flow emanating from the open top of the channel, in order to augment the increased upward flow. Such a flow situation has not been investigated in past studies. Experimental evidence for its occurrence has recently been supplied by Sparrow, Chrysler, and Azevedo [1]. In that case, which deals with a parallel-plate vertical duct having one wall heated at a uniform temperature while the other wall remains at the ambient fluid temperature, it may be inferred from the flow visualization conducted that FDF consists of a parallel-streamline, bidirectional shear flow. Such a flow would be preceded, in the developing region, by a separated flow or flow reversal.

Parallel-streamline, bidirectional shear flow in mixed convection has been discussed in the work of Ostrach [2] and of Lietzke [3]. Cebeci, Khattab, and LaMont [4] recently provided an approximate analysis for the problem. In spite of these studies, the general properties of this class of flows are not adequately understood. For instance, it has not been possible to predict the conditons under which bidirectional flow arises. The objective of the present study is to provide additional insight into the characteristics of the flow. In [5], developing flow in mixed convection between a parallel-plate vertical channel with asymmetric wall temperature has been analyzed. The present paper gives the analysis for FDF. It is assumed that the forced flow entering the duct is in the vertical upward direction. The duct walls are maintained at uniform temperatures (UWT), but provision is made for asymmetric heating in that the two wall temperatures need not be the same.

Analysis

Assuming that when the flow is fully developed the transverse velocity is zero, one gets from equation (1) of [5]

$$\frac{dU}{dX}=0$$

Substituting this into equation (2) of [5], there results the following momentum equation for fully developed flow

$$-\frac{dP}{dX}+\frac{d^2U}{dY^2}+\frac{\text{Gr}}{\text{Re}}\theta=0 \qquad (1)$$

Assuming further that for fully developed flow, the pressure changes linearly (this is shown by the numerical solution of the full equations), and setting a constant slope α to the pressure, there results

$$\frac{d^2U}{dY^2}=-\frac{\text{Gr}}{\text{Re}}\theta-\alpha \qquad (2)$$

The fully developed temperature profile for UWT is characterized by

$$\frac{\partial\theta}{\partial X}=0$$

Substituting the last equation in equation (4) of [5], along with the condition $V = 0$, yields the energy equation (valid at any Prandtl number) for fully developed flow

$$\frac{d^2\theta}{dY^2}=0 \qquad (3)$$

The boundary conditions are

$$\text{At } Y=0:\quad U=0,\quad \theta=r_T$$
$$\text{At } Y=1:\quad U=0,\quad \theta=1$$

Inherent in the above analysis is the idealization that the fluid properties, except for the density in the buoyancy term in the momentum equation, are constant. Note that equations (1) and (3) are different from the system used by Lietzke [3] to study fully developed flow in free convection between vertical parallel plates. Since the channel walls are uniformly heated in [3], the right side of equation (3) is not zero; further, Leitzke

---

[1] Deputy Director, Division of Chemical, Biochemical and Thermal Engineering; and Adjunct Professor, Department of Mechanical Engineering, Howard University, Washington, D.C.; Fellow ASME.

[2] Grove Engineering, Inc., Gaithersburg, MD.

[3] Opinions expressed in this paper are the personal views of the authors.

Contributed by the Heat Transfer Division for publication in the JOURNAL OF HEAT TRANSFER. Manuscript received by the Heat Transfer Division September 19, 1983.

assumed the pressure gradient to be zero. Although this assumption is correct for FDF in pure free convection (in UWT only) as shown in [6], there is no general validity to the assumption of zero pressure gradient in combined convection, whether or not the flow is fully developed.

Using the boundary conditions for θ, equation (3) can be integrated to give the following fully developed temperature profile

$$\theta=(1-r_T)Y+r_T \tag{4}$$

Equation (4) can now be put into equation (2) to yield

$$\frac{d^2U}{dY^2}=-\frac{\mathrm{Gr}}{\mathrm{Re}}\,[(1-r_T)Y+r_T]+\alpha \tag{5}$$

Integration of equation (5) using the velocity boundary conditions results in

$$U=-\frac{\mathrm{Gr}}{\mathrm{Re}}\left[(1-r_T)\frac{Y^3}{6}+r_T\frac{Y^2}{2}\right]+\alpha\frac{Y^2}{2}$$
$$+\left\{\frac{\mathrm{Gr}}{\mathrm{Re}}\left[(1-r_T)\frac{1}{6}+\frac{r_T}{2}\right]-\frac{\alpha}{2}\right\}Y \tag{6}$$

The parameter α still remains to be evaluated. Substitution of equation (6) into equation (7) of [5] then leads to

$$\alpha=-\frac{dP}{dx}=\frac{\mathrm{Gr}}{\mathrm{Re}}\left[(1-r_T)\frac{1}{2}+r_T\right]-12 \tag{7}$$

Substitution of equation (7) into equation (6) leads to the following velocity profile at any value of Gr/Re and r_T

$$U=\frac{\mathrm{Gr}}{\mathrm{Re}}\,(1-r_T)\left(-\frac{Y^3}{6}+\frac{Y^2}{4}-\frac{Y}{12}\right)-6Y^2+6Y \tag{8}$$

For a pure forced flow or a symmetrically heated UWT channel, the FDF streamwise velocity profile has an identical shape and is given by

$$U=6Y(1-Y) \tag{9}$$

By means of equations (4) and (8) given above, and of equations (7) and (8) of [5], an expression for the bulk temperature may be derived, giving

$$\theta_b=\frac{1}{720}\,\frac{\mathrm{Gr}}{\mathrm{Re}}\,(1-r_T)^2+\frac{1}{2}\,(1-r_T)+r_T \tag{10}$$

Limiting Cases of Forced and Free Convection

So far it has been assumed that buoyancy and pressure forces respectively represented by the first and second term on the right side of equation (2) are of equal importance. The limiting case of forced convection is obtained by setting Gr/Re = 0 in equation (2); the same operation applied to equation (8) the gives the velocity distribution in pure forced flow.

The other extreme case of mixed convection, viz., free convection, has been treated in [6]. The latter solution for the axial velocity may be written in terms of the variables utilized herein, giving

$$U=\frac{\mathrm{Gr}}{\mathrm{Re}}\left[(r_T-1)\frac{Y^3}{6}-r_T\frac{Y^2}{2}+(2r_T+1)\frac{Y}{6}\right] \tag{11}$$

It should be noted that in free convection, the flow rate and hence the Reynolds number Re is not an independent quantity, but is an outcome of the solution. Equation (11), however, is given above for the sake of comparison.

Discussion

A graphic representation of the streamwise velocity profile, as derived from equation (8), is shown in Fig. 1(*a*) to 1(*d*) for r_T = 0.0, 0.3, 0.5, and 0.8, respectively. The profile for r_T = 1 is not specifically identified. According to equation (8), the profiles for r_T = 1 at any Gr/Re, and those for Gr/Re $\doteq$ 0 at any r_T, are identical and are in fact given by equation (9). This

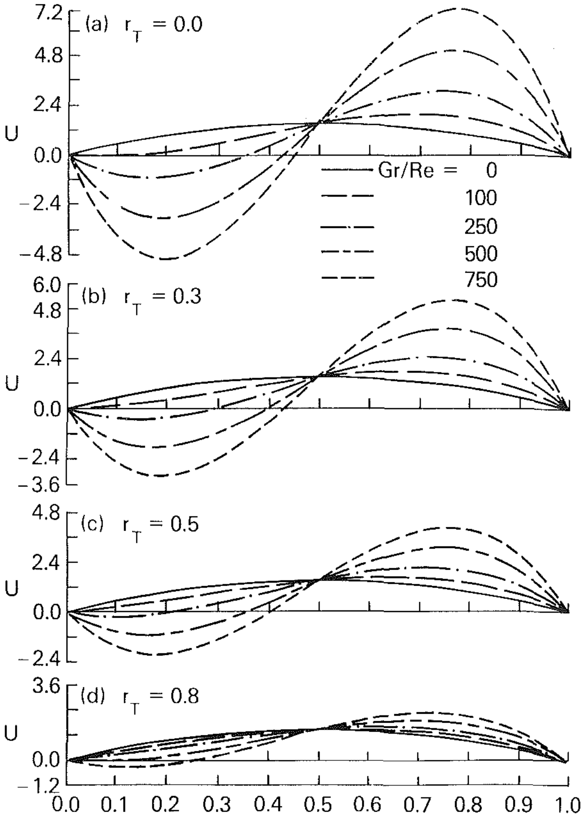

Fig. 1 Velocity distribution as a function of Gr/Re and r_T

profile is therefore indicated by the curves for Gr/Re = 0 in Figs. 1(*a*)-1(*d*). These figures show that at each r_T value, the profiles become increasingly skewed as Gr/Re increases. The skewness is characterized by increased positive velocities near the hot wall (Y = 1) and decreased velocities near the cold wall (Y = 0). At a sufficiently large Gr/Re, the velocities adjacent to the cold wall become negative and both the magnitudes and extents of the reversed flow increase with Gr/Re. All the profiles intersect at Y = 0.5; at this location the velocity is positive in all cases and has a numerical value of 1.5, as an examination of equation (9) quickly shows. This indicates that the extent of the reversed flow region falls short of half the spacing of the channel.

It is possible to deduce an expression or criterion by which to predict whether flow reversal occurs. Figures 1(*a*)-1(*d*) indicate that for $r_T < 1$, the occurrence of flow reversal is given by the condition

$$\left(\frac{dU}{dY}\right)_{Y=0}<0 \tag{12}$$

Appling equation (8), the above translates into

$$(1-r_T)\,\frac{\mathrm{Gr}}{\mathrm{Re}}>72;\qquad r_T<1 \tag{13}$$

That is

$$\left(\frac{\mathrm{Gr}}{\mathrm{Re}}\right)_{\max}=\frac{72}{1-r_T};\qquad r_T<1 \tag{14}$$

Equation (14) gives the maximum value of Gr/Re for which no reversal occurs in FDF. It applies only for $r_T < 1$, since the reversal under discussion is for asymmetric flow. For r_T = 1, the flow reversal, when present, would be located in the vicinity of the center of the channel. In this case, condition (12) is replaced by

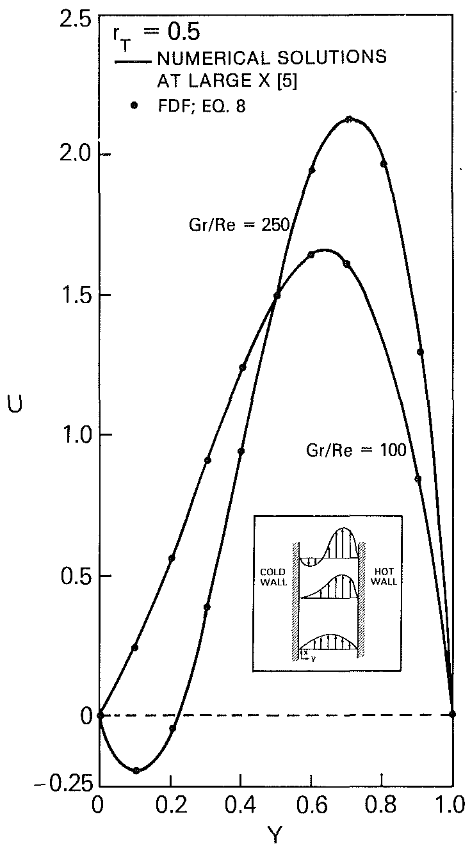

Fig. 2 Comparison of present results with developing flow solutions at large streamwise distances

$$(U)_{Y=0.5}=0; \qquad r_T=1$$

This condition cannot be satisfied by the parabolic profile in equation (9). Thus, in a duct in which the walls are at an identical temperature, there is no flow reversal in FDF.

Next consider the limiting case of free convection. From equation (11), it can be shown that

$$\left(\frac{dU}{dY}\right)_0=\frac{2r_T+1}{6}>0$$

Hence, no flow reversal is possible. In this case the channel top and bottom are open and there is no flow constriction at the channel entrance as is the case in the mixed convection under consideration. On the other hand, the situation may very well be different if the channel is situated in a shallow layer of fluid such that the fluid exiting the channel is recirculated to the entrance. In such a case, the losses incurred by the fluid outside the channel act to decrease the overall flow rate, rendering the situation somewhat akin to mixed convection with external constriction, and may lead to flow reversal of the type discussed earlier. Indeed the experimental study by Sparrow, Chrysler, and Azevedo [1] appears to bear evidence to this mechanism. With one of the channel walls heated to a uniform temperature while the other is left at the same temperature as the fluid entering the channel (this wall was not heated during the 15 min that it took for an experimental run), their experiments correspond to $r_T = 0$. Their measurements do not include the average velocity and hence the Reynolds number is not known; but their data clearly correspond to very large values of Gr/Re. According to equation (14), $(\mathrm{Gr/Re})_{\max} = 72$ for $r_T = 0$; hence there is a strong likelihood of flow reversal in their study. This indeed appears to occur. The resultant flow is stable, with no evidence of transition to turbulence, periodicity, or unsteadiness. However, in general, while buoyancy effects tend to stabilize vertical upward ("assisted") flow, the critical Reynolds number is decreased by buoyancy in downward ("opposed") flow [7]. Thus, the stability of bidirectional shear flow in mixed convection in vertical channels is not a completely resolved issue at this time.

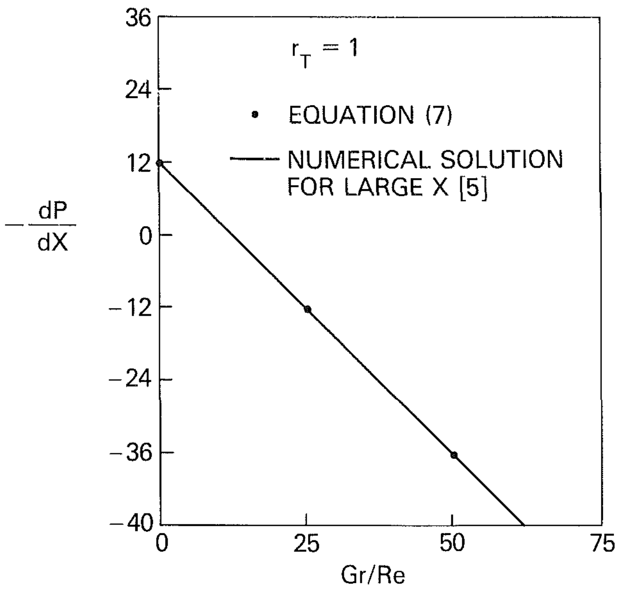

Fig. 3 Pressure gradient as a function of Gr/Re and comparison with developing flow solutions

Figure 2 shows a comparison of equation (8) with the numerical calculations for the developing flow at large values of X where the streamwise velocity profiles do not undergo noticeable further change. For the two asymmetric heating cases indicated, reversed flow occurs for the case of higher buoyancy. In both cases, the agreement of the present FDF solutions with the numerical solutions for large X is excellent.

Figure 3 shows a plot of the gradient of the pressure parameter as a function of Gr/Re. The "dots" designate representative numbers given by equation (7). For all r_T, dP/dX ranges from a value of -12 for pure forced flow (Gr/Re = 0) to progressively larger values as Gr/Re increases, crossing over to positive values. The value of Gr/Re at crossover is given by

$$\frac{\mathrm{Gr}}{\mathrm{Re}}=\frac{24}{1+r_T} \tag{15}$$

The straight line shown in Fig. 3 is taken from the numerical solutions of Aung and Worku [5] in regions of large X where the streamwise velocity profile has ceased to change with X. The present FDF theory is therefore compatible with the developing flow in the asymptotic limit of large X.

A number of interesting observations may be made concerning the bulk temperature. For $r_T = 1$, equation (10) gives the usual result of $\theta_b = 1$. For $r_T < 1$ and sufficiently large values of Gr/Re, equation (10) gives $\theta_b > 1$. This occurs when Gr/Re exceeds a maximum threshold given by

$$\left(\frac{\mathrm{Gr}}{\mathrm{Re}}\right)_{\max}=\frac{360}{1-r_T}; \quad r_T<1 \tag{16}$$

The value of this threshold is greater than that for the initiation of reversed flow as given by equation (14). Thus in this type of mixed convection situations, it is possible for the bulk temperature to exceed the value 1, depending on the values of r_T and Gr/Re. Physically, this apparently perplexing phenomenon may be explained as follows. When a reversed flow occurs, the relatively lower velocity negative flow passes alongside the cool wall and hence carries a lower level of thermal energy. Since the net dimensionless mass flow is fixed, an equal quantity of fluid is added to the fluid flowing in the positive (upward) direction and this fluid flows adjacent to the the hot wall thereby carrying a larger amount of energy. Consequently, the bulk temperature increases as the amount of reversed flow (and hence Gr/Re) increases.

Conclusion

This study provides theoretical results for a class of mixed convection flows between parallel-plate channels in which the net through-flow rates are constant. When the wall temperatures are unequal, it has been shown that a reversed flow situation occurs if the magnitude of the buoyancy parameter Gr/Re exceeds a certain threshold value. When this parameter is much greater than this value, a situation arises in which the bulk temperature of the fluid exceeds the value 1. For symmetric heating of the walls, there can be no flow reversal.

References

1 Sparrow, E. M., Chrysler, G. M., and Azevedo, L. F., "Observed Flow Reversals and Measured-Predicted Nusselt Numbers for Natural Convection in a One-Sided Heated Vertical Channel," ASME JOURNAL OF HEAT TRANSFER, Vol. 106, No. 2, 1984, pp. 325–332.

2 Ostrach, S., "Combined Natural- and Forced-Convection Laminar Flow Heat Transfer of Fluids With and Without Heat Sources in Channels With Linearly Varying Wall Temperatures," NACA TN 3141, 1954.

3 Lietzke, A. F., "Theoretical and Experimental Investigation of Heat Transfer by Laminar Natural Convection Between Parallel Plates," NACA Report 1223, 1954.

4 Cebeci, T., Khattab, A. A., and LaMont, R., "Combined Natural and Forced Convection in Vertical Ducts," *Heat Tranfer 82, Proceedings of 7th International Heat Transfer Conference*, Munich, West Germany, 1982, Vol. 2, pp. 419–424.

5 Aung, W., and Worku, G., "Developing Flow and Flow Reversal in Mixed Convection in a Vertical Channel With Asymmetric Wall Temperatures," ASME JOURNAL OF HEAT TRANSFER, this issue.

6 Aung, W., "Fully Developed Laminar Convection Between Vertical Plates Heated Asymmetrically," *International Journal of Heat and Mass Transfer*, Vol. 15, 1972, pp. 1577–1580.

7 Mucoglu, A., and Chen, T. S., "Wave Instability of Mixed Convection Flow Around a Vertical Flat Plate," *Numerical Heat Transfer*, Vol. 1, 1978, pp. 267–283.

A Model of the Heat Transfer in a Liquid$_3$Liquid Spray Column

D. W. Stamps,[1,2,3] D. Barr,[1,2] and J. A. Valenzuela[1,4]

1 Introduction

Typical temperature profiles within spray columns show discontinuities in the temperature of the continuous phase at the continuous phase inlet. Gier and Hougen [1] suggest that volumes of continuous phase, or wakes, of weak concentration that are attached to the dispersed phase are responsible for the discontinuity of the concentration in the continuous phase in packed extraction columns. Letan and Kehat [2] incorporate the wake as an important heat transfer mechanism in their model of spray column heat exchangers (SCHE) and later present mathematical expressions for temperature distributions in the dispersed [3] and dense [4] packing modes.

In the proposed model, heat is transferred directly from the dispersed phase to the continuous phase as well as indirectly through the wake. The wake growth zone used in the previous model is eliminated since the results of three studies [5–7] show that the length necessary for a wake to be fully established behind a drop may be small when compared with the column length. Letan and Kehat [4] report that the length of the mixing zone is negligible in dense packing. A negligible mixing length is assumed in the proposed model and, even though the mixing length increases as the packing becomes less dense, the results presented later indicate this may not be an unreasonable assumption even for dispersed packing.

2 Model

With the previous assumptions, the entire column is composed of three parallel streams: the upward-flowing dispersed phase (drops), the wakes attached to the drops, and the downward-flowing continuous phase. The flow direction may be reversed without change to the following discussion. Each stream exchanges heat with the other two.

In modeling the heat transfer in a spray column, therefore, the column may be viewed as being composed of three separate heat exchangers: a cocurrent-flow dispersed phase-to-wake heat exchanger, a countercurrent-flow dispersed phase-to-continuous phase heat exchanger, and a countercurrent-flow wake-to-continuous phase heat exchanger. The dispersed phase-to-wake heat exchanger accounts for heat transfer between the drop and the wake. The wake is the attached vortex behind the drop or the upward-flowing continuous-phase fluid trapped between the drops for denser packings. The dispersed phase-to-continuous phase heat exchanger accounts for any heat that is transferred directly between these two phases. This occurs when the fluid in the hydrodynamic boundary layer around the drop is disturbed or destroyed by other drops such that the fluid inside the boundary layer does not flow totally into the wake. Since the volume of the wake is assumed constant through the column length, the supply of fluid into the wake from the hydrodynamic boundary layer must be balanced by the loss of fluid from the wake to the continuous phase. The difference in temperature between the fluid entering and leaving the wake represents a net enthalpy transfer, or energy exchange, from the wake to the continuous phase which constitutes the wake-to-continuous phase heat exchanger.

3 Mathematical Formulation

The following assumptions are employed in the mathematical formulation of the proposed model: (1) insulated column walls, (2) constant fluid properties, (3) steady state, (4) drop size and wake volume are constant along column length, and (5) temperatures are transversely uniform but vary axially.

Control volumes of thickness dz are defined for each stream at a distance z from the dispersed phase inlet. An energy balance combined with the definition of the overall heat transfer coefficient between each phase U_{ij} for each control volume gives

$$\dot{C}_i \frac{dT_i}{dz} = -\sum_{j\neq i} \dot{Q}_{ij} = -\sum_{j\neq i} (UA)_{ij}(T_i - T_j) \qquad i, j = 1,2,3 \quad (1)$$

where the subscripts refer to streams i and j; $\dot{C}$, A, T, and $\dot{Q}$ are the capacity rate, surface area between phases, temperature, and heat transfer rate between phases, respectively. $\dot{C}_3 dT_3/dz$ is negative since stream 3 flows in a direction opposite to the other streams. The energy balance can be rewritten in the vector equation form

$$\frac{d\,\mathbf{T}(z)}{dz} = \mathbf{A}\mathbf{T}(z) \qquad (2)$$

where $\mathbf{T}(z) = [T_1(z), T_2(z), T_3(z)]$ and

---

[1] Department of Mechanical Engineering, Massachusetts Institute of Technology, Cambridge, MA 02139.

[2] Assoc. Mem. ASME.

[3] Current address: Department of Mechanical Engineering, 2250 G. G. Brown Lab, University of Michigan, Ann Arbor, MI 48109.

[4] Current address: Creave, Inc., Hanover, NH 03755.

Contributed by the Heat Transfer Division for publication in the JOURNAL OF HEAT TRANSFER. Manuscript received by the Heat Transfer Division February 25, 1985.

sequently, the bulk temperature increases as the amount of reversed flow (and hence Gr/Re) increases.

Conclusion

This study provides theoretical results for a class of mixed convection flows between parallel-plate channels in which the net through-flow rates are constant. When the wall temperatures are unequal, it has been shown that a reversed flow situation occurs if the magnitude of the buoyancy parameter Gr/Re exceeds a certain threshold value. When this parameter is much greater than this value, a situation arises in which the bulk temperature of the fluid exceeds the value 1. For symmetric heating of the walls, there can be no flow reversal.

References

1 Sparrow, E. M., Chrysler, G. M., and Azevedo, L. F., "Observed Flow Reversals and Measured-Predicted Nusselt Numbers for Natural Convection in a One-Sided Heated Vertical Channel," ASME Journal of Heat Transfer, Vol. 106, No. 2, 1984, pp. 325–332.

2 Ostrach, S., "Combined Natural- and Forced-Convection Laminar Flow Heat Transfer of Fluids With and Without Heat Sources in Channels With Linearly Varying Wall Temperatures," NACA TN 3141, 1954.

3 Lietzke, A. F., "Theoretical and Experimental Investigation of Heat Transfer by Laminar Natural Convection Between Parallel Plates," NACA Report 1223, 1954.

4 Cebeci, T., Khattab, A. A., and LaMont, R., "Combined Natural and Forced Convection in Vertical Ducts," *Heat Tranfer 82, Proceedings of 7th International Heat Transfer Conference*, Munich, West Germany, 1982, Vol. 2, pp. 419–424.

5 Aung, W., and Worku, G., "Developing Flow and Flow Reversal in Mixed Convection in a Vertical Channel With Asymmetric Wall Temperatures," ASME Journal of Heat Transfer, this issue.

6 Aung, W., "Fully Developed Laminar Convection Between Vertical Plates Heated Asymmetrically," *International Journal of Heat and Mass Transfer*, Vol. 15, 1972, pp. 1577–1580.

7 Mucoglu, A., and Chen, T. S., "Wave Instability of Mixed Convection Flow Around a Vertical Flat Plate," *Numerical Heat Transfer*, Vol. 1, 1978, pp. 267–283.

A Model of the Heat Transfer in a Liquid$_3$Liquid Spray Column

D. W. Stamps,[1,2,3] D. Barr,[1,2] and J. A. Valenzuela[1,4]

1 Introduction

Typical temperature profiles within spray columns show discontinuities in the temperature of the continuous phase at the continuous phase inlet. Gier and Hougen [1] suggest that volumes of continuous phase, or wakes, of weak concentration that are attached to the dispersed phase are responsible for the discontinuity of the concentration in the continuous phase in packed extraction columns. Letan and Kehat [2] incorporate the wake as an important heat transfer mechanism in their model of spray column heat exchangers (SCHE) and later present mathematical expressions for temperature distributions in the dispersed [3] and dense [4] packing modes.

In the proposed model, heat is transferred directly from the dispersed phase to the continuous phase as well as indirectly through the wake. The wake growth zone used in the previous model is eliminated since the results of three studies [5–7] show that the length necessary for a wake to be fully established behind a drop may be small when compared with the column length. Letan and Kehat [4] report that the length of the mixing zone is negligible in dense packing. A negligible mixing length is assumed in the proposed model and, even though the mixing length increases as the packing becomes less dense, the results presented later indicate this may not be an unreasonable assumption even for dispersed packing.

2 Model

With the previous assumptions, the entire column is composed of three parallel streams: the upward-flowing dispersed phase (drops), the wakes attached to the drops, and the downward-flowing continuous phase. The flow direction may be reversed without change to the following discussion. Each stream exchanges heat with the other two.

In modeling the heat transfer in a spray column, therefore, the column may be viewed as being composed of three separate heat exchangers: a cocurrent-flow dispersed phase-to-wake heat exchanger, a countercurrent-flow dispersed phase-to-continuous phase heat exchanger, and a countercurrent-flow wake-to-continuous phase heat exchanger. The dispersed phase-to-wake heat exchanger accounts for heat transfer between the drop and the wake. The wake is the attached vortex behind the drop or the upward-flowing continuous-phase fluid trapped between the drops for denser packings. The dispersed phase-to-continuous phase heat exchanger accounts for any heat that is transferred directly between these two phases. This occurs when the fluid in the hydrodynamic boundary layer around the drop is disturbed or destroyed by other drops such that the fluid inside the boundary layer does not flow totally into the wake. Since the volume of the wake is assumed constant through the column length, the supply of fluid into the wake from the hydrodynamic boundary layer must be balanced by the loss of fluid from the wake to the continuous phase. The difference in temperature between the fluid entering and leaving the wake represents a net enthalpy transfer, or energy exchange, from the wake to the continuous phase which constitutes the wake-to-continuous phase heat exchanger.

3 Mathematical Formulation

The following assumptions are employed in the mathematical formulation of the proposed model: (1) insulated column walls, (2) constant fluid properties, (3) steady state, (4) drop size and wake volume are constant along column length, and (5) temperatures are transversely uniform but vary axially.

Control volumes of thickness dz are defined for each stream at a distance z from the dispersed phase inlet. An energy balance combined with the definition of the overall heat transfer coefficient between each phase U_{ij} for each control volume gives

$$\dot{C}_i \frac{dT_i}{dz} = -\sum_{j\neq i} \dot{Q}_{ij} = -\sum_{j\neq i} (UA)_{ij}(T_i - T_j) \qquad i, j = 1,2,3 \qquad (1)$$

where the subscripts refer to streams i and j; $\dot{C}$, A, T, and $\dot{Q}$ are the capacity rate, surface area between phases, temperature, and heat transfer rate between phases, respectively. $\dot{C}_3 dT_3/dz$ is negative since stream 3 flows in a direction opposite to the other streams. The energy balance can be rewritten in the vector equation form

$$\frac{d\,\mathbf{T}(z)}{dz} = \mathbf{A}\mathbf{T}(z) \qquad (2)$$

where $\mathbf{T}(z) = [T_1(z),\ T_2(z),\ T_3(z)]$ and

---

[1] Department of Mechanical Engineering, Massachusetts Institute of Technology, Cambridge, MA 02139.

[2] Assoc. Mem. ASME.

[3] Current address: Department of Mechanical Engineering, 2250 G. G. Brown Lab, University of Michigan, Ann Arbor, MI 48109.

[4] Current address: Creave, Inc., Hanover, NH 03755.

Contributed by the Heat Transfer Division for publication in the Journal of Heat Transfer. Manuscript received by the Heat Transfer Division February 25, 1985.

$$\mathbf{A} = \left\{\begin{array}{ccc} -\left(\frac{(UA)_{12}+(UA)_{13}}{\dot{C}_1}\right) & \frac{(UA)_{12}}{\dot{C}_1} & \frac{(UA)_{13}}{\dot{C}_1} \\ \frac{(UA)_{12}}{\dot{C}_2} & -\left(\frac{(UA)_{12}+(UA)_{23}}{\dot{C}_2}\right) & \frac{(UA)_{23}}{\dot{C}_2} \\ -\frac{(UA)_{13}}{\dot{C}_3} & -\frac{(UA)_{23}}{\dot{C}_3} & \left(\frac{(UA)_{13}+(UA)_{23}}{\dot{C}_3}\right) \end{array}\right\} = \left\{\begin{array}{ccc} a_{11} & a_{12} & a_{13} \\ a_{21} & a_{22} & a_{23} \\ a_{31} & a_{32} & a_{33} \end{array}\right\}$$

The elements a_{ij} are defined for convenient use in the following equations. The solution of equation (2) is

$$\mathbf{T}(z) = \mathbf{P}(z)\mathbf{T}(0) \tag{3}$$

where each element P_{ij} of the matrix **P** is of the form $P_{ij} = \Sigma_{m=1}^{3} K_{ijm} \exp^{C_m z}$ with constants K_{ijm} and C_m of the form

$$K_{ij3} = \frac{1}{(c_1 - c_3)(c_2 - c_3)}(\text{cof}_{ji}(\mathbf{A}) + c_3 a_{ij} + \delta_{ij}((c_3)^2 - c_3 \text{tr}_1(\mathbf{A}))) \tag{4}$$

$$K_{ij2} = \frac{1}{c_1 - c_2}(-a_{ij} - (c_1 - c_3)K_{ij3} + \delta_{ij}(\text{tr}_1(\mathbf{A}) - c_2 - c_3)) \tag{5}$$

$$K_{ij1} = \delta_{ij} - (K_{ij2} + K_{ij3}) \tag{6}$$

$$c_1 = b_6 + b_7 - \frac{b_1}{3} \tag{7}$$

$$c_{2,3} = -\left(\frac{b_6 + b_7}{2} + \frac{b_1}{3}\right) \pm \left(\frac{b_6 - b_7}{2}\right)\sqrt{-3} \tag{8}$$

$$b_k = (-1)^k tr_k(\mathbf{A}) \tag{9}$$

$$b_4 = b_2 - \frac{(b_1)^2}{3} \tag{10}$$

$$b_5 = \frac{1}{27}(2(b_1)^3 - 9b_1 b_2 + 27b_3) \tag{11}$$

$$b_{6,7} = \left(\frac{-b_5}{2} \pm \left(\frac{(b_5)^2}{4} + \frac{(b_4)^3}{27}\right)^{1/2}\right)^{1/3} \tag{12}$$

In equations (4)-(12), $i, j, k = 1, 2, 3$, $\text{cof}_{ji}(\mathbf{A})$ and $\text{tr}_k(\mathbf{A})$ are the cofactor and trace of the kth order of the square matrix **A** respectively, and $\delta_{ij} = 1$ if $i = j$, otherwise $\delta_{ij} = 0$.

These equations can be used to describe columns operating with either dispersed packing, dense packing, or a combination of both packings. The procedure used, however, is different in the latter case.

4 Applications of the Mathematical Formulation

4.1 Dispersed Packing. The temperature of each stream at any location in a column with dispersed packing may be obtained from equation (3) if $T_2(0)$ is known. The inlet temperatures, $T_1(0)$ and T_{in}, are generally specified and $T_3(0) = T_2(0)$. Substituting equation (3) at $z = L$ for $j = 2, 3$ into an equation of the energy balance at $z = L$ ($\dot{C}_2 T_2(L) + \dot{C}_{in} T_{in} = \dot{C}_3 T_3(L)$) yields an expression for $T_2(0)$ in terms of other knowns

$$T_2(0) = T_3(0) = \frac{\left(\frac{\dot{C}_3}{\dot{C}_2} P_{31}(L) - P_{21}(L)\right)T_1(0) - \left(\frac{\dot{C}_3}{\dot{C}_2} - 1\right)T_{in}}{P_{22}(L) + P_{23}(L) - \frac{\dot{C}_3}{\dot{C}_2}(P_{32}(L) + P_{33}(L))} \tag{13}$$

A qualitative temperature profile using equations (3) and (13) is shown in Fig. 1(*a*).

4.2 Dense Packing. If the entire column operates with dense packing, the equations for dispersed packing are applicable with changes only in the numerical value of the constants. If only part of the column is densely packed, then the model can be applied separately to the dispersed packing section and the dense packing section. Equation (3) can be used to calculate the temperature of each stream ($j = 1, 2, 3$) in the dispersed packing section ($0 \leq z \leq z_i$ where z_i is the height of the interface) if $T_2(0)$ is known. Similarly, the temperature of each stream ($j = 1, 2, 3$) in the dense packing section ($z_i \leq z \leq L$) can be calculated using

$$\mathbf{T}'(z) = \mathbf{P}'(z)\mathbf{T}'(z_i) \tag{14}$$

if $T_1'(z_i)$, $T_2'(z_i)$, and $T_3'(z_i)$ are known. Substituting the equations of the energy balance at the interface ($z = z_i$) for both the dispersed phase ($T_1(z_i) = T_1'(z_i)$) and the continuous phase ($\dot{C}_2 T_2(z_i) + \dot{C}_3' T_3'(z_i) = \dot{C}_2' T_2'(z_i) + \dot{C}_3 T_3(z_i)$), the equation of the energy balance at $z = L$ for the wake and continuous phase ($\dot{C}_2' T_2'(L) + \dot{C}_{in} T_{in} = \dot{C}_3' T_3'(L)$), and the constraint that no mixing of the wake with continuous phase occurs at the interface ($T_2(z_i) = T_2'(z_i)$) into equations (3) and (14) (evaluated at $z = z_i$) gives $T_2(0)$ in terms of the specified inlet temperatures ($T_1(0)$ and T_{in})

$$T_2(0) = \frac{-\left(\frac{\dot{C}_{in}}{\dot{C}_2'}\right)T_{in} - \alpha_1 T_1(0)}{\alpha_2 + \alpha_3} \tag{15}$$

$$\alpha_j = \gamma_j^2 - \left(\frac{\dot{C}_3'}{\dot{C}_2'}\right)\gamma_j^3 - \left(\frac{\dot{C}_2}{\dot{C}_3'} - \frac{\dot{C}_2'}{\dot{C}_3'}\right)\beta_{2j}^{23} + \left(\frac{\dot{C}_2}{\dot{C}_2'} - 1\right)\beta_{2j}^{33} \tag{16}$$

$$\gamma_j^k = \beta_{1j}^{k1} + \beta_{2j}^{k2} + \left(\frac{\dot{C}_3}{\dot{C}_3'}\right)\beta_{3j}^{k3} \tag{17}$$

$$\beta_{st}^{mn} = P_{mn}'(L - z_i)P_{st}(z_i) \tag{18}$$

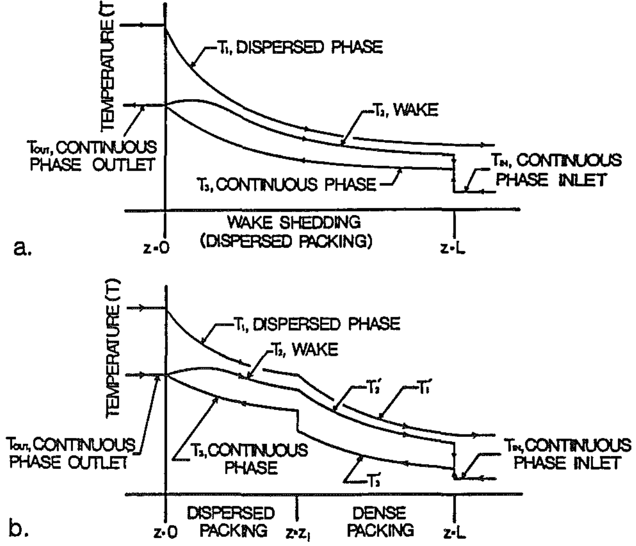

Fig. 1 Typical temperature profiles of the three streams in a SCHE when (*a*) dispersed packing is present in the entire column or (*b*) both dispersed packing and dense packing sections are present in the column; arrows on the temperature profiles indicate fluid flow direction

The temperatures within the dispersed packing section can be determined using equations (3) and (13). The temperatures within the dense packing section can be determined using the energy balances at the interface and equation (14). A qualitative temperature profile is shown in Fig. 1(*b*).

5 Comparison of the Model Predictions With Experimental Data

The matrix **A** in equation (2) may be expressed in terms of five parameters which characterize a spray column with dispersed packing. The first parameter, the recirculation ratio, can be calculated by $\dot{C}_3/\dot{C}_2 = 1/RM + 1$ where R is the ratio of flow rates of the dispersed phase to continuous phase and M is the ratio of the wake volume to drop volume which can be calculated from a correlation by Loutaty and Vignes [8] ($M = (0.275/H + 0.725)^{1.175} - 1$). The second parameter, the capacity ratio, can be calculated by $\dot{C}_4/\dot{C}_1 = 1/rR$ where r is the ratio of the product of the density and specific heat of the dispersed phase to continuous phase. The other three parameters are the number of transfer units (NTU) for each of the three internal heat exchangers:

$$\mathrm{NTU}_{12} = \frac{(AU)_{12}}{\dot{C}_1},\ \mathrm{NTU}_{13} = \frac{(AU)_{13}}{\dot{C}_1},\ \text{and}\ \mathrm{NTU}_{23} = \frac{(AU)_{23}}{\dot{C}_2}.$$

An overall NTU for the SCHE is

$$\mathrm{NTU}_{\mathrm{SCHE}} = \mathrm{NTU}_{13} + \left(\frac{1}{\dfrac{1}{\mathrm{NTU}_{12}} + \dfrac{1}{\mathrm{NTU}_{23}} \dfrac{\dot{C}_4}{\dot{C}_2} \dfrac{\dot{C}_1}{\dot{C}_4}} \right).$$

The first two parameters were calculated for four sets of data [3, 9–11]. The NTU parameter values used ($\mathrm{NTU}_{12} = 7.0$, $\mathrm{NTU}_{23} = 21.0$, and $\mathrm{NTU}_{\mathrm{SCHE}} = 7.0$) were established by adjusting the NTU values until the model predicted the temperatures within ± 16 percent of one set of data [9]. These values were held constant for all other systems with dispersed packing and $\mathrm{NTU}_{\mathrm{SCHE}}$ was increased to 14.0 to provide best results for dense packing data. Ninety percent of the calculated overall effectiveness values, defined as $\epsilon = (T_1(0) - T_1(L))/(T_1(0) - T_{in})$, are within ± 6 percent of the experimental overall effectiveness values.

6 Conclusions

There is good agreement between the model and available data even when large values of NTU_{13} are used in dense packing cases which suggests heat transferred directly between the dispersed phase and the continuous phase should not be a priori set equal to zero as done in previous models. Considering heat transfer between each of the three streams, the SCHE may be modeled as three internal heat exchangers in parallel: dispersed phase-to-wake, wake-to-continuous phase, and dispersed phase-to-continuous phase heat exchanger. Modeling the SCHE in this manner insures the wake temperature will be between the dispersed phase temperature and the continuous phase temperature.

The good agreement between the model's predicted values and the data implies that it may be acceptable to assume instantaneous wake growth and a negligible mixing length for both dispersed and dense packings.

7 Acknowledgments

Partial support from a Shell Companies Foundation grant to the M.I.T. Department of Mechanical Engineering and the assistance of Michael O'Callaghan are gratefully acknowledged.

8 References

1 Gier, T. E., and Hougen, J. O., "Concentration Gradients in Spray and Packed Extraction Columns," *Ind. Eng. Chem.*, Vol. 45, 1953, pp. 1362–1370.

2 Letan, R., and Kehat, E., "Mixing Effects in a Spray-Column Heat Exchanger," *AIChE J.*, Vol. 11, 1965, pp. 804–808.

3 Letan, R., and Kehat, E., "The Mechanism of Heat Transfer in a Spray Column Heat Exchanger," *AIChE J.*, Vol. 14, 1968, pp. 398–405.

4 Letan, R., and Kehat, E., "The Mechanism of Heat Transfer in a Spray Column Heat Exchanger: Dense Packing of Drops," AIChE J., Vol. 16, 1970, pp. 955–963.

5 Lochiel, A. C., and Calderbank, P. H., "Mass Transfer in the Continuous Phase Around Axisymmetric Bodies of Revolution," *Chem. Engng. Sci.*, Vol. 19, 1964, pp. 471–484.

6 Yeheskel, J., and Kehat, E., "The Size and Rate of Shedding of Wakes of Single Drops Rising in a Continuous Medium," *Chem. Engng. Sci.*, Vol. 26, 1971, pp. 1223–1233.

7 Licht, N., and Conway, J. B., "Mechanisms of Solute Transfer in Spray Towers," *Ind. Eng. Chem.*, Vol. 42, 1950, pp. 1151–1157.

8 Loutaty, R., and Vignes, A., "Hydrodynamique d'une Colonne à Pulvérisation Liquide-Liquide à Contre-Courant en Lit Lâche et en Lit Dense," *Chimie et Industrie-Genie Chimique*, Vol. 101, 1969, pp. 231–242.

9 Garwin, L., and Smith, B. D., "Liquid-Liquid Spray-Tower Operation in Heat Transfer," *Chem. Eng. Prog.*, Vol. 49, 1953, pp. 591–602.

10 Woodward, T., "Heat Transfer in a Spray Column," *Chem. Eng. Prog.*, Vol. 57, 1961, pp. 52–57.

11 Markowitz, A., "Heat Transfer in Spray Towers," M.S. Thesis, M.I.T., Department of Mechanical Engineering, 1968.

An Integral Method in Laminar Film Pool Boiling From Curved Surfaces

A. Nakayama[1] **and H. Koyama**[1]

Nomenclature

$A, B, C, D,$
E = shape factors
C_p = specific heat
d = diameter of cylinder (sphere)
f = function for velocity profile
Gr_x = local Grashof number
h = local heat transfer coefficient
h_{fg} = latent heat of vaporization
H = sensible-latent heat ratio
k = thermal conductivity
Nu_x = local Nusselt number
Pr = Prandtl number
R = density–viscosity ratio
T = temperature
u, v = x and y-direction velocity components
x, y = boundary layer coordinates
α = minor to major axis ratio of elliptical cylinder
δ, Δ = vapor film thickness and liquid layer thickness
η, η_l = similarity variables in vapor and liquid layers
θ = function for temperature profile
Λ, Λ_l = shape factors associated

---

[1] Department of Energy and Mechanical Engineering, Shizuoka University, Hamamatsu, 432 Japan.

Contributed by the Heat Transfer Division for publication in the JOURNAL OF HEAT TRANSFER. Manuscript received by the Heat Transfer Division July 30, 1984.

The temperatures within the dispersed packing section can be determined using equations (3) and (13). The temperatures within the dense packing section can be determined using the energy balances at the interface and equation (14). A qualitative temperature profile is shown in Fig. 1(*b*).

5 Comparison of the Model Predictions With Experimental Data

The matrix **A** in equation (2) may be expressed in terms of five parameters which characterize a spray column with dispersed packing. The first parameter, the recirculation ratio, can be calculated by $\dot{C}_3/\dot{C}_2 = 1/RM+1$ where R is the ratio of flow rates of the dispersed phase to continuous phase and M is the ratio of the wake volume to drop volume which can be calculated from a correlation by Loutaty and Vignes [8] ($M = (0.275/H+0.725)^{1.175}-1$). The second parameter, the capacity ratio, can be calculated by $\dot{C}_4/\dot{C}_1 = 1/rR$ where r is the ratio of the product of the density and specific heat of the dispersed phase to continuous phase. The other three parameters are the number of transfer units (NTU) for each of the three internal heat exchangers:

$$\mathrm{NTU}_{12} = \frac{(AU)_{12}}{\dot{C}_1},\ \mathrm{NTU}_{13} = \frac{(AU)_{13}}{\dot{C}_1},\ \text{and}\ \mathrm{NTU}_{23} = \frac{(AU)_{23}}{\dot{C}_2}.$$

An overall NTU for the SCHE is

$$\mathrm{NTU}_{\mathrm{SCHE}} = \mathrm{NTU}_{13} + \left(\frac{1}{\dfrac{1}{\mathrm{NTU}_{12}} + \dfrac{1}{\mathrm{NTU}_{23}} \dfrac{\dot{C}_4}{\dot{C}_2} \dfrac{\dot{C}_1}{\dot{C}_4}} \right).$$

The first two parameters were calculated for four sets of data [3, 9–11]. The NTU parameter values used ($\mathrm{NTU}_{12} = 7.0$, $\mathrm{NTU}_{23} = 21.0$, and $\mathrm{NTU}_{\mathrm{SCHE}} = 7.0$) were established by adjusting the NTU values until the model predicted the temperatures within ± 16 percent of one set of data [9]. These values were held constant for all other systems with dispersed packing and $\mathrm{NTU}_{\mathrm{SCHE}}$ was increased to 14.0 to provide best results for dense packing data. Ninety percent of the calculated overall effectiveness values, defined as $\epsilon = (T_1(0)-T_1(L))/(T_1(0)-T_{in})$, are within ±6 percent of the experimental overall effectiveness values.

6 Conclusions

There is good agreement between the model and available data even when large values of NTU_{13} are used in dense packing cases which suggests heat transferred directly between the dispersed phase and the continuous phase should not be a priori set equal to zero as done in previous models. Considering heat transfer between each of the three streams, the SCHE may be modeled as three internal heat exchangers in parallel: dispersed phase-to-wake, wake-to-continuous phase, and dispersed phase-to-continuous phase heat exchanger. Modeling the SCHE in this manner insures the wake temperature will be between the dispersed phase temperature and the continuous phase temperature.

The good agreement between the model's predicted values and the data implies that it may be acceptable to assume instantaneous wake growth and a negligible mixing length for both dispersed and dense packings.

7 Acknowledgments

Partial support from a Shell Companies Foundation grant to the M.I.T. Department of Mechanical Engineering and the assistance of Michael O'Callaghan are gratefully acknowledged.

8 References

1 Gier, T. E., and Hougen, J. O., "Concentration Gradients in Spray and Packed Extraction Columns," *Ind. Eng. Chem.*, Vol. 45, 1953, pp. 1362–1370.

2 Letan, R., and Kehat, E., "Mixing Effects in a Spray-Column Heat Exchanger," *AIChE J.*, Vol. 11, 1965, pp. 804–808.

3 Letan, R., and Kehat, E., "The Mechanism of Heat Transfer in a Spray Column Heat Exchanger," *AIChE J.*, Vol. 14, 1968, pp. 398–405.

4 Letan, R., and Kehat, E., "The Mechanism of Heat Transfer in a Spray Column Heat Exchanger: Dense Packing of Drops," AIChE J., Vol. 16, 1970, pp. 955–963.

5 Lochiel, A. C., and Calderbank, P. H., "Mass Transfer in the Continuous Phase Around Axisymmetric Bodies of Revolution," *Chem. Engng. Sci.*, Vol. 19, 1964, pp. 471–484.

6 Yeheskel, J., and Kehat, E., "The Size and Rate of Shedding of Wakes of Single Drops Rising in a Continuous Medium," *Chem. Engng. Sci.*, Vol. 26, 1971, pp. 1223–1233.

7 Licht, N., and Conway, J. B., "Mechanisms of Solute Transfer in Spray Towers," *Ind. Eng. Chem.*, Vol. 42, 1950, pp. 1151–1157.

8 Loutaty, R., and Vignes, A., "Hydrodynamique d'une Colonne à Pulvérisation Liquide-Liquide à Contre-Courant en Lit Lâche et en Lit Dense," *Chimie et Industrie-Genie Chimique*, Vol. 101, 1969, pp. 231–242.

9 Garwin, L., and Smith, B. D., "Liquid-Liquid Spray-Tower Operation in Heat Transfer," *Chem. Eng. Prog.*, Vol. 49, 1953, pp. 591–602.

10 Woodward, T., "Heat Transfer in a Spray Column," *Chem. Eng. Prog.*, Vol. 57, 1961, pp. 52–57.

11 Markowitz, A., "Heat Transfer in Spray Towers," M.S. Thesis, M.I.T., Department of Mechanical Engineering, 1968.

An Integral Method in Laminar Film Pool Boiling From Curved Surfaces

A. Nakayama[1] **and H. Koyama**[1]

Nomenclature

$A, B, C, D,$
E = shape factors
C_p = specific heat
d = diameter of cylinder (sphere)
f = function for velocity profile
Gr_x = local Grashof number
h = local heat transfer coefficient
h_{fg} = latent heat of vaporization
H = sensible-latent heat ratio
k = thermal conductivity
Nu_x = local Nusselt number
Pr = Prandtl number
R = density–viscosity ratio
T = temperature
u, v = x and y-direction velocity components
x, y = boundary layer coordinates
α = minor to major axis ratio of elliptical cylinder
δ, Δ = vapor film thickness and liquid layer thickness
η, η_l = similarity variables in vapor and liquid layers
θ = function for temperature profile
Λ, Λ_l = shape factors associated

---

[1] Department of Energy and Mechanical Engineering, Shizuoka University, Hamamatsu, 432 Japan.

Contributed by the Heat Transfer Division for publication in the JOURNAL OF HEAT TRANSFER. Manuscript received by the Heat Transfer Division July 30, 1984.

with velocity and temperature profiles
μ, ν = viscosity and kinematic viscosity
ρ = density

Subscripts

i = vapor-liquid interface
l = liquid layer
w = wall

Introduction

Film pool boiling over a horizontal circular cylinder in a saturated liquid has been analyzed previously by Bromley [1] neglecting inertia and convective terms. Koh [2] treated the film pool boiling on a vertical plate as a two-phase boundary layer problem and solved the full boundary layer equations for both vapor and liquid layers. Nishikawa and Ito [3] subsequently extended this similarity transformation to consider the effects of subcooled liquid on the heat transfer rate. All these analyses, however, are restricted to rather simple geometries such as flat plates and circular cylinders.

The present study employs an integral formulation and suggests a general scheme for the prediction of film boiling heat transfer on bodies of arbitrary geometric configuration. The effects of inertia, convection, and interfacial shear on film boiling are fully considered using the two-phase boundary layer treatment. No semi-analytic methods for film boiling as general as the present one seem to have been reported elsewhere.

Analysis

Figure 1 shows the physical model and coordinate system under consideration. A body heated up to a constant temperature T_w is exposed to a quiescent liquid at its saturation temperature T_i. A usual control volume analysis within the vapor film thickness δ leads to the momentum equation

$$\frac{d}{dx}\int_0^\delta \rho r^* u^2 dy - u_i\frac{d}{dx}\int_0^\delta \rho r^* u\, dy = r^*\left[(\rho_l-\rho)g_x\delta - \mu\frac{\partial u}{\partial y}\bigg|_w + \mu\frac{\partial u}{\partial y}\bigg|_i\right] \quad (1)$$

Likewise, for the saturated liquid boundary layer of thickness Δ, one obtains

$$\frac{d}{dx}\int_\delta^{\delta+\Delta} \rho_l r^* u^2 dy + u_i\frac{d}{dx}\int_0^\delta \rho\, r^* u\, dy = -r^*\mu\frac{\partial u}{\partial y}\bigg|_i \quad (2)$$

where

$$r^* = \begin{cases} 1 & \text{plane flow} \\ r(x) & \text{axisymmetric flow} \end{cases} \quad (3a)$$

and

$$g_x \equiv g\cos\phi = g\left[1-\left(\frac{dr}{dx}\right)^2\right]^{1/2} \quad (3b)$$

The subscript l denotes the liquid properties while terms without supbscripts refer to properties of the vapor. The subscripts w and i refer to the wall and the liquid-vapor interface, respectively. The term g_x refers to the tangential component of the acceleration of gravity related to the wall geometry as described by equation (3*b*)[2]. The following matching condition for the interfacial shear is already implemented in equation (2)

$$\mu\frac{\partial u}{\partial y} = \left(\mu\frac{\partial u}{\partial y}\right)_l \qquad \text{at } y=\delta \quad (4)$$

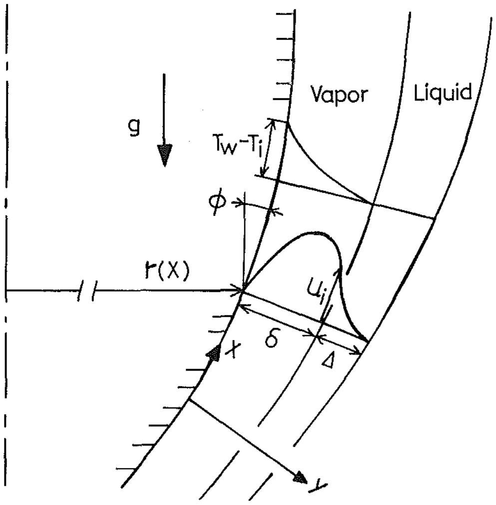

Fig. 1 Physical model and coordinate system

The integral energy equation for the vapor layer is given by

$$\frac{d}{dx}\int_0^\delta \rho\, r^* u\, C_p(T-T_i)dy = r^* k\left(\frac{\partial T}{\partial y}\bigg|_i - \frac{\partial T}{\partial y}\bigg|_w\right) \quad (5)$$

Moreover, an energy balance consideration at the interface leads to

$$h_{fg}\frac{d}{dx}\int_0^\delta \rho\, r^* u\, dy = -r^* k\frac{\partial T}{\partial y}\bigg|_i \quad (6)$$

Since convective terms must vanish at the wall, the second derivatives there must satisfy

$$\Lambda \equiv -\frac{1}{2}\frac{\delta^2}{u_i}\frac{\partial^2 u}{\partial y^2}\bigg|_w = \frac{g_x'\delta^2}{2\nu u_i} \quad (7a)$$

and

$$\frac{\partial^2 T}{\partial y^2}\bigg|_w = 0 \quad (7b)$$

where

$$g_x' \equiv (\rho_l-\rho)g_x/\rho \quad (7c)$$

The shape factor Λ is related to the curvature of the vapor velocity at the wall. In consideration of the conditions above, the velocity and temperature profiles suggested for the vapor film are

$$f(\eta;\ \Lambda,\ C) \equiv u/u_i = C\eta - \Lambda\eta^2 + (1-C+\Lambda)\eta^3 \quad (8a)$$

and

$$\theta(\eta;\ \Lambda_t) \equiv (T-T_i)/(T_w-T_i) = 1-(1+\Lambda_t)\eta + \Lambda_t\eta^3 \quad (8b)$$

where

$$\eta \equiv y/\delta \quad (8c)$$

The shape factor Λ_t accounts for the nonlinearity of the temperature profile, namely, the effect of convection. The velocity profile in the liquid layer, on the other hand, is prescribed as

$$f_l(\eta_l) \equiv u/u_i = 1 - 2\eta_l + \eta_l^2 \quad (8d)$$

where

$$\eta_l \equiv (y-\delta)/\Delta \quad (8e)$$

Equations (8) are substituted into the integral equations (1), (2), (5), and (6), and the integrations are carried out with respect to y. Subsequently, Δ and u_i are eliminated in favor of δ and Λ using equations (4) and (7*a*). After considerable manipulations on equations (1), (2), (5), and (6), one obtains the set of ordinary differential equations

---

[2] dr/dx must be continuous everywhere.

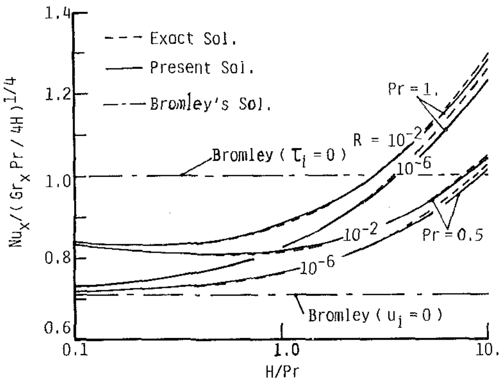

Fig. 2 Heat transfer results on a vertical flat plate

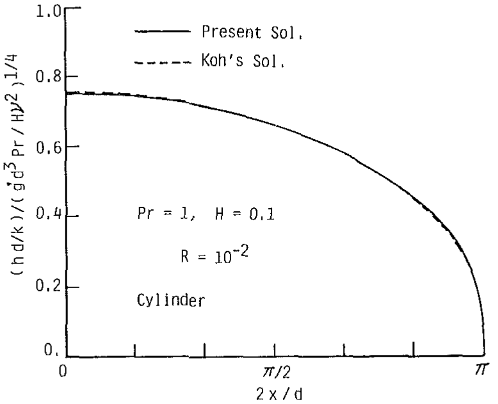

Fig. 3 Heat transfer results on a horizontal circular cylinder

$$
\begin{bmatrix}
1/\zeta, & a_{12}, & a_{13}, & 0 \\
1/\zeta, & a_{22}, & a_{23}, & 0 \\
1/\zeta, & a_{32}, & a_{33}, & 0 \\
1/\zeta, & a_{42}, & a_{43}, & a_{44}
\end{bmatrix}
\begin{bmatrix}
\dfrac{d\zeta}{dx} \\[2ex]
\dfrac{d\Lambda}{dx} \\[2ex]
\dfrac{dC}{dx} \\[2ex]
\dfrac{d\Lambda_t}{dx}
\end{bmatrix}
=
\begin{bmatrix}
b_1 \\ b_2 \\ b_3 \\ b_4
\end{bmatrix}
\tag{9}
$$

where

$$\zeta \equiv (\delta/x)^4 \mathrm{Gr}_x \tag{10a}$$

and

$$\mathrm{Gr}_x \equiv g_x' x^3/\nu^2 \tag{10b}$$

a_{ij} and b_i are given in terms of x, r, ζ, Λ, C, Λ_t, Pr,

$$H \equiv C_p(T_w - T_i)/h_{fg} \tag{11a}$$

and

$$R \equiv \rho\mu/(\rho\mu)_l \tag{11b}$$

These matrix coefficients are listed in the appendix. For given r, Pr, H, and R, the system of equations (9) may be solved by any standard numerical integration scheme (e.g., Runge-Kutta method.) A singularity appearing at $x = 0$ may be removed by expanding around the stagnation point as $\zeta = \zeta|_{x=0} + (x^2/2)d^2\zeta/dx^2|_{x=0} + o(x^4)$ etc., and then solving the resulting set of algebraic equations. A similar procedure for stagnation flows may be found elsewhere [4, 5]. Once the shape factors ζ, Λ, C, and Λ_t are determined, the local Nusselt number $\mathrm{Nu}_x = x/(T_i - T_w)\partial T/\partial y|_{y=0}$ can be evaluated from

$$\mathrm{Nu}_x/\mathrm{Gr}_x^{1/4} = (1 + \Lambda_t)/\zeta^{1/4} \tag{12}$$

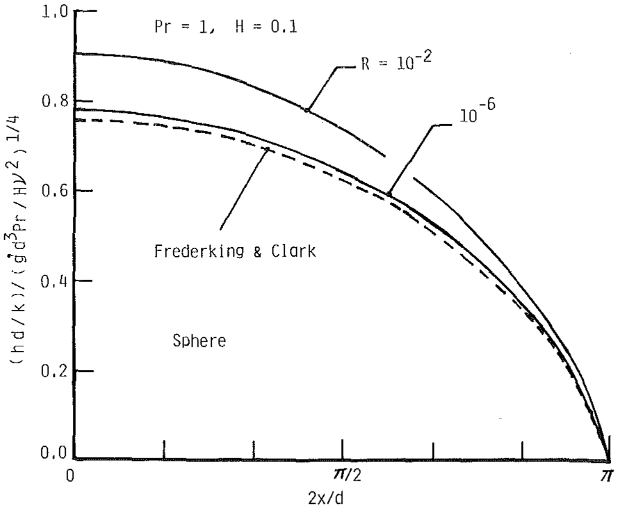

Fig. 4 Heat transfer results on a sphere

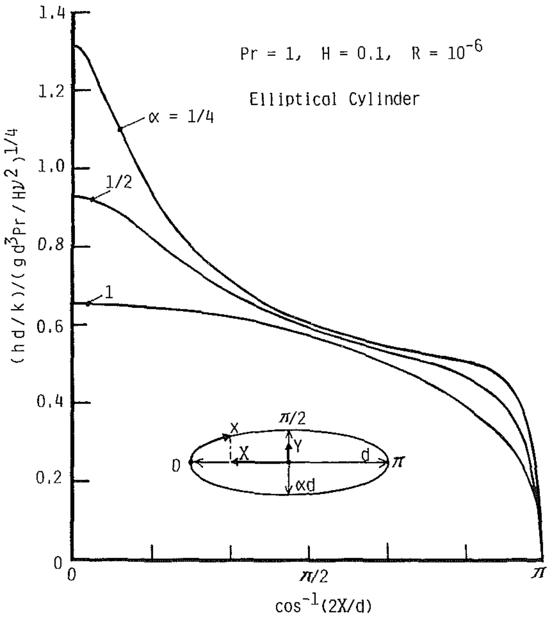

Fig. 5 Heat transfer results on horizontal elliptical cylinders

Results

Figure 2 shows the local heat transfer results along flat plates. Koh's exact solution [2] and Bromley's solutions [1] for zero interfacial shear ($\tau_i = 0$) and zero interfacial velocity ($u_i = 0$) are also indicated in the figure for comparison. The agreement of the present solution with the exact solution appears to be excellent. Bromley's results are in gross error for H/Pr > 10. Discussions on the parametric effects on the heat transfer rate may be found in Koh's original paper [2]. In contrast to film condensation problems [6], the heat transfer level is quite sensitive to R. The ordinate variable in the figure may readily be translated for the overall heat transfer coefficient using the relation $(1/x)\int_0^x h\,dx = (4/3)h$ for the case of a flat plate.

Calculations were carried out for a horizontal circular cylinder with Pr = 1, $H = 0.1$, and $R = 10^{-2}$. The circumferential variation of heat transfer coefficient h is illustrated in Fig. 3 which also shows a solution curve generated using Koh's solution [2] and Hermann's function [7]. The difference between two curves is hardly discernible.

Frederking and Clark [8] extended Bromley's analysis to the film boiling over a sphere. Figure 4 shows a comparison of the present results for a sphere and Frederking and Clark's solution for zero interfacial velocity. It is clearly seen that the postulates made by Frederking and Clark are valid only when R is sufficiently small.

In order to illustrate the generality acquired in the present scheme, calculations were also performed for horizontal elliptical cylinders with different minor to major axis ratios, namely, $\alpha = 1/4$, $1/2$, and 1 (i.e., a circular cylinder). The calculated heat transfer rates are presented in Fig. 5 which indicates rather significant effects of α on the local heat transfer rate.

References

1 Bromley, L. A., "Heat Transfer in Stable Film Boiling," *Chemical Engineering Progress*, Vol. 46, 1950, pp. 221-228.

2 Koh, J. C., Y., "Analysis of Laminar Film Boiling From a Vertical Surface," ASME JOURNAL OF HEAT TRANSFER, Vol. 84, 1962, pp. 55-62.

3 Nishikawa, K., and Ito, T., "Two-Phase Boundary Layer Treatment of Free Convection Film Boiling," *Int. J. Heat Mass Transfer*, Vol. 9, 1966, pp. 103-115.

4 Nakayama, A., Koyama, H., and Ohsawa, S., "An Integral Method in Laminar Film Condensation on Plane and Axisymmetric Bodies," *Letters in Heat Mass Transfer*, Vol. 9, 1982, pp. 443-453.

5 Nakayama, A., Koyama, H., and Ohsawa, S., "Self-Similar Thermal Boundary Layers on Plane and Axisymmetric Bodies," Wärme- und Stoffübertragung, Vol. 18, 1984, pp. 69-73.

6 Koh, J. C. Y., Sparrow, E. M., and Hartnett, J. P., "Two Phase Boundary Layer in Laminar Film Condensation," *Int. J. Heat Mass Transfer*, Vol. 2, 1961, pp. 69-82.

7 Hermann, R., "Heat Transfer by Free Convection From Horizontal Cylinders in Diatomic Gases," NACA TM 1366, 1954.

8 Frederking, T. N. K., and Clark, J. A., "Natural Convection Film Boiling on a Sphere," *Advan. Cryog. Eng.*, Vol. 8, 1963, pp. 501-510.

APPENDIX

Coefficients in Equation (9)

a_{ij} and b_i in equation (9) are listed below:

$$a_{12} = \frac{4}{5B-3A}\left(\frac{\partial}{\partial\Lambda}(B-A) - \frac{2B-A}{\Lambda}\right),$$

$$a_{13} = \frac{4}{5B-3A}\,\frac{\partial}{\partial C}(B-A) \qquad \text{(A1,A2)}$$

$$a_{22} = \frac{1}{2+3RAE}\left(\frac{8}{5}\left(\frac{1}{E} - \frac{2}{\Lambda}\right) - 4RAE\left(\frac{1}{12A} + \frac{1}{\Lambda}\right)\right) \qquad \text{(A3)}$$

$$a_{23} = \frac{\left(RE - \frac{16}{5E}\right)}{2+3RAE}, \quad a_{32} = -\frac{4}{3}\left(\frac{1}{12A} + \frac{1}{\Lambda}\right), \quad a_{33} = \frac{1}{3A} \qquad \text{(A4,A5,A6)}$$

$$a_{42} = \frac{4}{3}\left(\frac{\partial}{\partial\Lambda}\ln D - \frac{1}{\Lambda}\right), \quad a_{43} = \frac{4}{3}\,\frac{\partial}{\partial C}\ln D,$$

$$a_{44} = \frac{4}{3}\,\frac{\partial}{\partial\Lambda_t}\ln D \qquad \text{(A7,A8,A9)}$$

$$b_1 = \left(\frac{24\Lambda(\Lambda - C + 1)}{(5B-3A)\zeta} - 1\right)\frac{1}{x} - \left(\frac{1}{I} - 1\right)\frac{d}{dx}\ln r \qquad \text{(A10)}$$

$$b_2 = \left(\frac{8R\Lambda E^2}{(2+3RAE)\zeta} - 1\right)\frac{1}{x} - \left(\frac{1}{I_l} - 1\right)\frac{d}{dx}\ln r \qquad \text{(A11)}$$

$$b_3 = \left(\frac{8\Lambda(1-2\Lambda_t)H}{3A\Pr\zeta} - 1\right)\frac{1}{x} - \left(\frac{1}{I_t} - 1\right)\frac{d}{dx}\ln r \qquad \text{(A12)}$$

$$b_4 = \left(\frac{8\Lambda\Lambda_t}{D\Pr\zeta} - 1\right)\frac{1}{x} - \left(\frac{1}{I_t} - 1\right)\frac{d}{dx}\ln r \qquad \text{(A13)}$$

where

$$I = \left(1 + \frac{4(B-A)i + (3B-A)j}{5B-3A}\right)^{-1} \qquad \text{(A14)}$$

$$I_l = \left(1 + \frac{4\left(RAE + \frac{2}{5}\right)i + \left(RAE + \frac{6}{5}\right)j}{2+3\,RAE}\right)^{-1} \qquad \text{(A15)}$$

$$I_t = \left(1 + \frac{4i+j}{3}\right)^{-1} \qquad \text{(A16)}$$

where

$$i = \begin{cases} 0 & \text{plane flow} \\ 1 & \text{axisymmetric flow} \end{cases} \qquad \text{(A17)}$$

$$j \equiv \frac{d\ln g_x}{d\ln r} = -r\frac{d^2r}{dx^2}\Big/\left(1 - \left(\frac{dr}{dx}\right)^2\right) \qquad \text{(A18)}$$

$$A \equiv \int_0^1 f\,d\eta = (3 + 3C - \Lambda)/12 \qquad \text{(A19)}$$

$$B \equiv \int_0^1 f^2 d\eta = (30 + 24C + 16C^2 - 10\Lambda - 11C\Lambda + 2\Lambda^2)/210 \qquad \text{(A20)}$$

$$D \equiv \int_0^1 f\theta d\eta = (21 + 49C - 24\Lambda_t - 32C\Lambda_t - 14\Lambda + 11\Lambda\Lambda_t)/420 \qquad \text{(A21)}$$

$$E \equiv -\left.\frac{\partial f}{\partial\eta}\right|_{\eta=1} = 2C - \Lambda - 3 \qquad \text{(A22)}$$

As indicated by equation (A18), j in general is a function of x. However, for the special cases of the stagnation flows around $x = 0$, equation (A18) reduces to

$$j = \begin{cases} 0 & \text{pointed body} \\ 1 & \text{blunt body} \end{cases} \qquad \text{(A23)}$$

Therefore, for example, the integers (i, j) may be given as (0, 0) for a vertical flat plate, (1, 0) for a vertical cone, (0, 1) for the stagnation flow over a horizontal circular cylinder and (1, 1) for the stagnation flow over a sphere. For these cases, similarity solutions exist, and the set of the differential equations (9) reduces to the algebraic equations

$$\zeta = \frac{24\Lambda(1+\Lambda-C)}{5B-3A}I = \frac{8\Lambda RE^2}{3RAE+2}I_l = \frac{8\Lambda\Lambda_t}{\Pr D}I_t = \frac{8\Lambda(1-2\Lambda_t)H}{3A\Pr}I_t \qquad \text{(A24)}$$

The solution curves in Fig. 2 are generated by solving the foregoing equations for ζ, Λ, C, and Λ_t.